

**INVESTIGATION OF ENVIRONMENTALLY FRIENDLY  
POWER GENERATION SYSTEMS FOR LOW-GRADE  
WASTE HEAT RECOVERY**

**By**

**Faisal Ali S Albatati, BEng, MSc**

**Thesis submitted to the University of Nottingham  
For the degree of Doctor of Philosophy**

**JUNE 2015**

# Abstract

From the point of view of energy importance and the environmental impacts associated with conventional energy production methods, and for the purpose of low-grade waste heat recovery, this thesis demonstrates an investigative approach to develop and test a novel, environmentally friendly small-scale Rankine based power generation prototype system. To fulfil the aim, a range of systems of different technologies, and employing different working fluids were investigated to identify the most efficient, cost-effective system for the application. These systems are the absorption power generation system, and the flood expansion power generation system employing CO<sub>2</sub>/Lubricant mixture as the working fluid, the CO<sub>2</sub> SRC power system, and finally the ORC system employing newly developed HFOs and HCFO-R1233zd(E) refrigerants. The CO<sub>2</sub>/lubricant working fluid mixture was experimentally investigated and thermodynamically modelled. The performance of the investigated systems was theoretically evaluated by computer simulations. The results revealed that the ORC outperformed all other investigated systems, achieving thermal efficiency and net thermal power output of 14.36% and 4.81 kW respectively with R1233zd(E). In addition, the evaluation confirmed the capability of the new refrigerants to replace conventional refrigerants. A small-scale R1233zd(E) ORC prototype system utilising a specially developed scroll expander was constructed and tested. In the First Experiment, an automotive motor was utilised as the electric generator. The system's optimum performance was 7.87% thermal efficiency, 1.39 kW expander power output, and 180 W electric power output. The main source of performance limitation was identified as the lower capability of the steam humidifier heat source, in addition to the speed mismatch between the expander and the motor, the poor performance of the circulation pump, and the piping configuration in relation to the positions of heat exchangers. Piping and the position of heat exchangers were altered, the motor was replaced by an alternator and the second experiment commenced in which the best overall experimental performance of 7.6% thermal efficiency, 1 kW expander power output, 246 W electric power output, was achieved. Very poor pump efficiency and a large power loss through the power transmission mechanism to the alternator were observed. Upon completion of the experiments, the theoretically predicted performance was validated, and the experimentally obtained results were compared to those of similar ORCs from literature. The comparison revealed that for the utilised expander type, a mass flow rate of 0.074 kg/s, and a pressure ratio of 4.5, achieves the best expander efficiency of 75%. From an economic point of view, the R1233zd(E) ORC was shown to be a very attractive and safe investment even for scaled-up systems. The thesis concluded that the ORC technology remains the most efficient, flexible technology for low-grade heat recovery, and the evaluation of R1233zd(E) for the first time expressed the attractive potentials of the refrigerant in ORC applications. Finally, justified recommendations were made to replace the heat source and refrigerant pump and to test other types of expander in order to improve the performance of the R1233zd(E) ORC prototype system.

## Acknowledgements

I have been contemplating this moment for a long time, writing the final words in my PhD thesis. However I realised that this work would not have been possible without the unconditional support, trust and love of people around me to whom I will be forever thankful.

I am very grateful to my supervisor Professor Saffa Riffat for his support throughout every step of this work, and the amount of time spent and advice given in numerous discussions to overcome obstacles I faced as this project progressed. I am also grateful to my second supervisor, Dr. Yuehong Su, for his valuable advice and our time spent working together on theoretical and practical issues. Special thanks go to Dr. Xiaoli ma, who worked very closely with me for long sessions and provided help and support all the way through this project.

I also would like to acknowledge Dr. Richard Powell, Mr. Simon Redford, Pera Technology and Mexichem Fluor UK Ltd. for their contribution and the assistance and advice they provided to complete this work.

Lastly, I dedicate this thesis to, and thank my family for their support and unconditional love; to my parents, who raised me with a love of knowledge and always encouraged my pursuits; to my loving sister's presence and frequent visits which have been very supportive; and most of all to my beloved, very patient and encouraging small team of Noora and Abdullah, whose faithful support and understanding will forever be appreciated.

# Table of Contents

<b>ABSTRACT .....</b>	<b>I</b>
<b>ACKNOWLEDGEMENTS.....</b>	<b>II</b>
<b>TABLE OF CONTENTS .....</b>	<b>III</b>
<b>LIST OF TABLES.....</b>	<b>X</b>
<b>LIST OF FIGURES .....</b>	<b>XIII</b>
<b>NOMENCLATURE.....</b>	<b>XX</b>
<b>CHAPTER 1 : INTRODUCTION .....</b>	<b>1</b>
1.1 THE IMPORTANCE AND DEMAND FOR ENERGY .....	1
1.2 ENERGY SOURCES .....	2
1.2.1 <i>Non-Renewable Energy</i> .....	2
1.2.2 <i>Renewable Energy</i> .....	2
1.3 ELECTRIC ENERGY.....	3
1.4 GLOBAL WARMING AND THE GREENHOUSE EFFECT .....	5
1.4.1 <i>The Greenhouse Gases</i> .....	6
1.4.2 <i>International Agreements</i> .....	7
1.5 OZONE LAYER DEPLETION AND REFRIGERANTS .....	8
1.6 INDUSTRIAL WASTE HEAT POTENTIAL IN THE EU.....	10
1.7 THESIS STATEMENT FOR PROBLEMS AND NEEDS.....	12
1.8 THESIS AIMS AND OBJECTIVES.....	13
1.9 NOVELTY OF THE RESEARCH AND THE SMALL-SCALE R1233ZD(E) ORC PROTOTYPE SYSTEM .....	16
1.10 THESIS STRUCTURE .....	16
<b>CHAPTER 2 : A REVIEW OF LOW-GRADE HEAT RECOVERY POWER GENERATION CYCLES .....</b>	<b>19</b>
2.1 INTRODUCTION .....	19
2.2 BACKGROUND .....	19
2.3 THE ORGANIC RANKINE CYCLE (ORC).....	20
2.3.1 <i>Principle of Operation</i> .....	20
2.3.2 <i>Working Fluids Selection Criteria</i> .....	21
2.3.3 <i>Conventional ORC Working Fluids</i> .....	23
2.3.4 <i>Environmentally Friendly ORC Working Fluids</i> .....	25
2.3.4.1 Hydrofluoro Olefin (HFOs) .....	25
2.3.4.2 Hydrochloroflouroolefins (HCFOs) .....	26
2.3.5 <i>Performance of the Environmentally Friendly Working Fluids</i> .	27
2.3.6 <i>Expansion Device</i> .....	29
2.3.6.1 Scroll Expanders .....	30
2.3.7 <i>Applications</i> .....	32
2.3.8 <i>Novel ORC Designs</i> .....	34
2.4 THE SUPER-CRITICAL RANKINE CYCLE (SRC).....	38
2.4.1 <i>Principle of operation</i> .....	38
2.4.2 <i>Working fluids</i> .....	40
2.4.2.1 CO <sub>2</sub> as a Working Fluid .....	41
2.5 CO <sub>2</sub> SRC AND TRC PERFORMANCE AND DESIGN .....	42
2.5.1 <i>Novel CO<sub>2</sub> SRC and TRC Designs</i> .....	45

2.6	ABSORPTION POWER GENERATION CYCLE .....	52
2.6.1	<i>Principle of operation</i> .....	52
2.6.2	<i>Working fluids</i> .....	53
2.6.3	<i>Design and performance of Absorption Power Generation Systems</i> .....	54
2.6.4	<i>Designs for Novel Absorption Power Generation Systems</i> .....	59
2.7	CONCLUSIONS .....	63
2.7.1	<i>ORC</i> .....	63
2.7.2	<i>SRC and TRC</i> .....	65
2.7.3	<i>Absorption Power Generation Cycle</i> .....	66

### **CHAPTER 3 : CO<sub>2</sub>/LUBRICANT OIL MIXTURE AS A WORKING FLUID**

#### **..... 68**

3.1	INTRODUCTION .....	68
3.2	BACKGROUND ON REFRIGERANT/LUBRICANT OIL MIXTURE STUDIES .....	68
3.3	MISCIBILITY AND PHASE EQUILIBRIUM .....	69
3.4	TYPES OF LUBRICANT OIL FOR REFRIGERATION .....	70
3.4.1	<i>Mineral Oils (MO)</i> .....	70
3.4.2	<i>Synthetic Lubricant Oils</i> .....	71
3.4.2.1	<i>Polyol Ester (POE)</i> .....	71
3.4.2.2	<i>Polyalkylene Glycol (PAG)</i> .....	71
3.4.2.3	<i>Polyvinyl Ether (PVE)</i> .....	72
3.4.2.4	<i>Poly-alfa Olefin (PAO)</i> .....	72
3.4.2.5	<i>Alkyl Benzenes (AB)</i> .....	72
3.5	LUBRICANT OIL IDENTIFICATION .....	72
3.6	SELECTION REQUIREMENTS FOR A LUBRICANT OIL IN THE CO <sub>2</sub> /OIL ABSORPTION POWER GENERATION SYSTEM.....	74
3.7	OVERVIEW OF CO <sub>2</sub> /LUBRICANT OIL MIXTURES.....	75
3.8	COMPARISON OF CO <sub>2</sub> SOLUBILITY IN A RANGE OF ABSORBENTS .....	78
3.9	CONCLUSION .....	81

### **CHAPTER 4 : EXPERIMENTAL EVALUATION OF CO<sub>2</sub>/LUBRICANT OIL MIXTURES .....**

#### **..... 83**

4.1	INTRODUCTION .....	83
4.2	MATERIALS .....	83
4.3	THERMOGRAVIMETRIC ANALYSIS (TGA) TEST .....	83
4.3.1	<i>Operating the TGA Apparatus and Conducting the Test Procedure</i> .....	84
4.3.2	<i>Results and Discussion</i> .....	86
4.4	INTELLIGENT GRAVIMETRIC ANALYSIS (IGA) TEST .....	89
4.4.1	<i>IGA principle of operation</i> .....	89
4.4.2	<i>Operating the IGA Apparatus and Conducting the Test Procedure</i> .....	90
4.4.3	<i>Results and Discussion</i> .....	92
4.4.4	<i>IGA Experimental Solubility Data Analysis and Validation</i> .....	94
4.4.4.1	<i>Validation of CO<sub>2</sub>/POE32 Solubility Data</i> .....	95
4.4.4.2	<i>Validation of CO<sub>2</sub>/POE68 Solubility Data</i> .....	96
4.4.4.3	<i>CO<sub>2</sub>/POEs Comparison</i> .....	96
4.4.4.4	<i>Validation of CO<sub>2</sub>/PC Solubility Data</i> .....	98
4.5	ENHANCED ABSORPTION EXPERIMENT .....	99

4.5.1	<i>Operating and Modifying the Absorption Apparatus</i> .....	100
4.5.2	<i>Equipment and Experimental Set-up</i> .....	103
4.5.2.1	Oil Circulation Pump .....	103
4.5.2.2	Charging and Evacuation Equipment .....	104
4.5.2.3	Measurement Devices .....	105
4.5.2.3.1	Measurement Uncertainties .....	105
4.5.2.3.2	Thermocouples .....	105
4.5.2.3.3	Pressure Transducer .....	106
4.5.2.3.4	Data Acquisition .....	107
4.5.3	<i>Results and discussion</i> .....	109
4.5.3.1	CO <sub>2</sub> /POE32 .....	110
4.5.3.2	CO <sub>2</sub> /POE68 .....	116
4.5.3.3	CO <sub>2</sub> /POE32+PC .....	118
4.5.3.3.1	CO <sub>2</sub> /100 ml POE32-10 ml PC .....	118
4.5.3.3.2	CO <sub>2</sub> /100 ml POE32-30 ml PC .....	120
4.6	CONCLUSIONS .....	122

## **CHAPTER 5 : PREDICTION OF THERMODYNAMIC PROPERTIES OF THE CO<sub>2</sub>/LUBRICANT MIXTURES..... 125**

5.1	INTRODUCTION .....	125
5.2	CO <sub>2</sub> /LUBRICANT MIXTURES MODELLING METHODS .....	126
5.2.1	<i>Empirical Correlations</i> .....	126
5.2.2	<i>Cubic EOS Models and the Prediction of Critical Parameters of CO<sub>2</sub>/lubricant Mixtures</i> .....	129
5.2.2.1	Summarised Findings.....	134
5.3	PROPOSED MODELLING APPROACH.....	135
5.3.1	<i>Empirical Correlations</i> .....	135
5.3.2	<i>Cubic EOS Thermodynamic model</i> .....	139
5.3.2.1	CO <sub>2</sub> /POEs model .....	139
5.3.2.2	CO <sub>2</sub> /PC Model .....	143
5.4	IMPLEMENTATION OF THE MIXTURES SPECIFIC ENTHALPY MODELS.....	144
5.4.1	<i>CO<sub>2</sub>/POE Mixtures</i> .....	144
5.4.2	<i>CO<sub>2</sub>/PC Mixture</i> .....	147
5.5	VALIDATION OF THE YOKOZEKI-SRK THERMODYNAMIC MODEL .....	149
5.6	CONCLUSIONS .....	154

## **CHAPTER 6 : THEORETICAL ANALYSIS OF SMALL-SCALE POWER GENERATION SYSTEMS FOR LOW-GRADE WASTE HEAT RECOVERY**

### **..... 156**

6.1	INTRODUCTION .....	156
6.2	GENERAL THERMODYNAMIC MODELS ASSUMPTIONS AND INPUTS.....	156
6.3	THERMODYNAMIC MODELS EVALUATION PARAMETERS .....	157
6.4	CO <sub>2</sub> /LUBRICANT ABSORPTION POWER GENERATION SYSTEM .....	158
6.4.1	<i>Cycle Description</i> .....	158
6.4.2	<i>Thermodynamic Model Assumptions</i> .....	159
6.4.3	<i>Circulation Ratio and Mass Flow Rates</i> .....	159
6.4.4	<i>Heat and Mass Balance of System Components</i> .....	160
6.4.4.1	Heat Exchangers .....	160
6.4.4.1.1	Heat Exchanger Effectiveness.....	160
6.4.4.1.2	The Absorber .....	162
6.4.4.1.3	The Generator.....	162

6.4.4.1.4	The Recuperator Heat Exchanger.....	162
6.4.4.2	Expander.....	163
6.4.4.3	Solution Pump .....	163
6.4.4.4	Throttle Valve .....	164
6.4.5	<i>Simulation Results and Analysis.....</i>	164
6.4.5.1	The Effect of Absorber Pressure: Simulation Case 1 (Base Case) .	165
6.4.5.2	The Effect of Absorber Temperature: Simulation Case 2 .....	168
6.4.5.3	The Effect of Generator Pressure: Simulation Case 3 .....	171
6.4.6	<i>CO<sub>2</sub>/Lubricant Absorption Power Generation Theoretical Analysis Conclusions .....</i>	173
6.5	CO <sub>2</sub> /POE32 FLOOD EXPANSION POWER GENERATION SYSTEM .....	175
6.5.1	<i>Principle of Operation and System Requirements.....</i>	175
6.5.2	<i>Flood Expansion Overview .....</i>	176
6.5.3	<i>Thermodynamic Model of a CO<sub>2</sub>/POE32 Flood Expansion System 178</i>	
6.5.3.1	Cycle Description.....	179
6.5.3.2	Thermodynamic Model Assumptions and Inputs .....	181
6.5.3.3	Heat and Mass Balance of System Components.....	182
6.5.3.3.1	Expander.....	182
6.5.3.3.2	Mixer 2.....	183
6.5.3.3.3	Compression Device.....	184
6.5.3.3.4	Mixer 5.....	184
6.5.3.3.5	The Recuperator Heat Exchanger.....	185
6.5.3.3.6	Mixture Absorber/Cooler.....	187
6.5.3.3.7	Mixture Generator/Heater.....	187
6.5.3.4	Simulation results and analysis .....	188
6.5.3.5	CO <sub>2</sub> /POE32 Flood Expansion Power Generation System Theoretical Analysis Conclusions .....	191
6.6	CO <sub>2</sub> SRC POWER GENERATION SYSTEM .....	193
6.6.1	<i>Cycle Description.....</i>	194
6.6.2	<i>Heat and Mass Balance of System Components.....</i>	195
6.6.2.1	Expander.....	195
6.6.2.2	Compression Device .....	195
6.6.2.3	The Recuperator Heat Exchanger.....	195
6.6.2.4	The CO <sub>2</sub> Cooler Heat Exchanger.....	196
6.6.2.5	The CO <sub>2</sub> Heater Heat Exchanger .....	196
6.6.3	<i>CO<sub>2</sub> SRC Power Generation System Thermodynamic Model Validation .....</i>	196
6.6.4	<i>Simulation Results and Analysis.....</i>	197
6.6.4.1	The Effect of CO <sub>2</sub> Cooler Pressure on the system's performance..	198
6.6.4.2	The Effect of CO <sub>2</sub> Heater Outlet Temperature on System Performance .....	205
6.6.4.3	The Effect of the Turbine's Isentropic Efficiency.....	206
6.6.4.4	The Effect of the Compression Device Isentropic Efficiency .....	207
6.6.4.5	The Effect of the Recuperator Heat Exchanger Effectiveness .....	208
6.6.5	<i>CO<sub>2</sub> SRC Power Generation Theoretical Analysis Conclusions .....</i>	209
6.7	THE ORC SYSTEM EMPLOYING ENVIRONMENTALLY FRIENDLY REFRIGERANTS .....	210
6.7.1	<i>Cycle Description.....</i>	211
6.7.2	<i>Thermodynamic Model Assumptions and Inputs.....</i>	212
6.7.3	<i>ORC System Thermodynamic Model Validation .....</i>	213
6.7.4	<i>Simulation Results and Analysis.....</i>	214

6.7.4.1	Working Fluids Evaluation and Selection.....	214
6.7.4.2	R1233zd(E) ORC Optimised Operating Conditions and Parametric Analysis .....	218
6.7.4.2.1	The Effect of the Expander Isentropic Efficiency .....	221
6.7.4.2.2	The Effect of R1233zd(E) Pump Isentropic Efficiency.....	222
6.7.4.2.3	The Effect of the Recuperator Heat Exchanger Effectiveness ...	223
6.7.5	<i>The ORC System Conclusions</i> .....	224
6.8	CONCLUSIONS .....	225

## **CHAPTER 7 : R1233ZD(E) ORC PROTOTYPE SYSTEM DESIGN AND CONSTRUCTION ..... 227**

7.1	INTRODUCTION .....	227
7.2	ORC PROTOTYPE CONFIGURATION AND DESCRIPTION .....	227
7.2.1	<i>Heat Source</i> .....	230
7.2.2	<i>Heat Sink</i> .....	230
7.2.3	<i>Scroll Expander</i> .....	231
7.2.3.1	Operating Principle .....	231
7.2.3.2	Losses and Internal Leakages .....	232
7.2.3.3	Modification of the Selected Scroll Compressor into the Expander .....	233
7.2.4	<i>Electric Power Generator</i> .....	237
7.2.5	<i>R1233zd(E) Circulation Pump</i> .....	243
7.2.6	<i>Brazed Plate Heat Exchangers (BPHEs)</i> .....	244
7.3	R1233ZD(E) ORC PROTOTYPE BPHE MODEL BY LMTD METHOD .....	247
7.3.1	<i>LMTD</i> .....	247
7.3.2	<i>BPHE Model Assumptions and Inputs</i> .....	248
7.3.3	<i>The BPHE Model Governing Equations</i> .....	249
7.3.3.1	Convective Heat Transfer Coefficient Correlations.....	252
7.3.4	<i>BPHE Model Results and Discussion</i> .....	255
7.4	MEASUREMENT DEVICES.....	256
7.4.1	<i>Data Acquisition System</i> .....	257
7.4.2	<i>Temperature Measurements</i> .....	257
7.4.3	<i>Pressure Measurements</i> .....	258
7.4.4	<i>Flow Rate Measurements</i> .....	259
7.4.5	<i>Tachometer</i> .....	260
7.4.6	<i>Electronic Load</i> .....	261
7.5	SUMMARY.....	265

## **CHAPTER 8 : EXPERIMENTAL INVESTIGATION OF THE R1233ZD(E) ORC PROTOTYPE SYSTEM ..... 266**

8.1	INTRODUCTION .....	266
8.2	COMPRESSED AIR OPEN LOOP EXPANDER-ALTERNATOR EXPERIMENTAL SYSTEM .....	266
8.2.1	<i>Experimental System Configuration and Description</i> .....	266
8.2.2	<i>System Components</i> .....	268
8.2.3	<i>Test Procedure</i> .....	269
8.2.4	<i>Experimental Data Reduction</i> .....	270
8.2.5	<i>Results and Analysis</i> .....	272
8.2.6	<i>Compressed Air Open Loop Expander-Alternator Experiment Conclusion</i> .....	278
8.3	THE R1233ZD(E) ORC PROTOTYPE SYSTEM EXPERIMENTS .....	279

8.3.1	<i>Prototype System Initiation and Starting Procedure</i> .....	279
8.3.2	<i>Prototype System Shutdown Procedure</i> .....	282
8.3.3	<i>Experimental Data Reduction</i> .....	283
8.3.4	<i>Results and Analysis</i> .....	285
8.3.4.1	Experiment 1 .....	285
8.3.4.1.1	First Run .....	286
8.3.4.1.1.1	Temperature and Pressure Profiles .....	286
8.3.4.1.1.2	Performance Profiles .....	291
8.3.4.1.1.3	The Effect of Operating Parameters on System Performance .....	295
8.3.4.1.1.4	First run's Optimum Performance.....	306
8.3.4.1.2	Second run .....	308
8.3.4.1.2.1	Temperature and Pressure Profiles.....	309
8.3.4.1.2.2	Performance Profiles .....	312
8.3.4.1.2.3	The Effect of Operating Parameters on System Performance .....	315
8.3.4.1.2.4	Second run's Optimum Performance .....	321
8.3.4.1.3	Conclusions to Experiment 1 .....	323
8.3.4.2	Experiment 2 .....	324
8.3.4.2.1	Temperature and Pressure Profiles .....	325
8.3.4.2.2	Performance Profiles .....	330
8.3.4.2.3	Second Experiment's Optimum Performance .....	334
8.3.5	<i>R1233zd(E) ORC Prototype System Performance, and Limitations Discussion</i> .....	337
8.3.6	<i>Comparative Analysis of The R1233zd(E) ORC Prototype System's Power Outputs</i> .....	343
8.4	CONCLUSION .....	352

**CHAPTER 9 : ECONOMIC FEASIBILITY ASSESSMENT OF THE R1233ZD(E) ORC SYSTEM AND THE CO2 SRC POWER GENERATION SYSTEM ..... 355**

9.1	INTRODUCTION .....	355
9.2	ECONOMIC ANALYSIS EVALUATION INDICATORS .....	356
9.2.1	<i>System's Specific Cost</i> .....	356
9.2.2	<i>Net Present Value (NPV)</i> .....	356
9.2.3	<i>Internal Rate of Return (IRR)</i> .....	357
9.2.4	<i>Return on Investment (ROI)</i> .....	357
9.3	ECONOMIC ANALYSIS GENERAL ASSUMPTIONS AND INPUTS.....	357
9.4	R1233ZD(E) ORC SYSTEM ECONOMIC ANALYSIS.....	360
9.4.1	<i>R1233zd(E) ORC Systems Components and Costs</i> .....	360
9.4.2	<i>Economic Analysis Results and Discussion</i> .....	365
9.4.2.1	The 5 kW R1233zd(E) ORC System.....	366
9.4.2.1.1	Sensitivity Analysis.....	369
9.4.2.1.1.1	The Effect of the System's Specific Capital Cost.....	369
9.4.2.1.1.2	The Effect of Electricity Costs .....	371
9.4.2.2	The 20 kW R1233zd(E) ORC System.....	372
9.4.2.2.1	Sensitivity Analysis.....	375
9.4.2.2.1.1	The Effect of the System's Specific Capital Costs .....	375
9.4.2.2.1.2	The Effect of Electricity Costs .....	376
9.5	5 KW CO2 SRC POWER GENERATION SYSTEM ECONOMIC ANALYSIS.....	377
9.5.1	<i>System's Components Identification</i> .....	377
9.5.1.1	CO2 Turbine .....	377

9.5.1.2 CO2 pump .....	379
9.5.1.3 Heat Exchangers .....	380
9.5.1.4 Other System Components .....	381
9.5.1.5 Measurement Devices .....	381
9.5.1.6 Components Identification Discussion .....	383
9.5.2 <i>Economic Analysis Results and Discussion</i> .....	385
9.5.2.1 Sensitivity Analysis.....	387
9.5.2.1.1 The Effect of the System's Specific Capital Cost.....	387
9.5.2.1.2 The Effect of Electricity Costs.....	389
9.6 CONCLUSION .....	390
<b>CHAPTER 10 : CONCLUSIONS AND FURTHER WORK .....</b>	<b>393</b>
10.1 CONCLUSIONS .....	393
10.2 RECOMMENDATIONS FOR FURTHER WORK .....	396
<b>BIBLIOGRAPHY .....</b>	<b>399</b>
<b>APPENDIX A .....</b>	<b>419</b>
A.1 IGA EXPERIMENTAL RESULTS .....	419
A.2 GENERAL EMPIRICAL EQUATION TO PREDICT BUBBLE POINT PRESSURE/SOLUBILITY .....	422
<b>APPENDIX B .....</b>	<b>423</b>
B.1 SOLUBILITY, DENSITY AND VISCOSITY CORRELATION COEFFICIENTS OF CO2/ABSORBENTS .....	423
B.2 IDEAL HEAT CAPACITY OF PURE POE COMPOUNDS.....	424
<b>APPENDIX C .....</b>	<b>426</b>
C.1 CO2/LUBRICANT ABSORPTION POWER GENERATION SYSTEM SIMULATION PROGRAM FLOW CHART .....	426
C.2 CO2/POE32 FLOOD EXPANSION POWER GENERATION SYSTEM SIMULATION PROGRAMME FLOW CHART.....	429
C.3 MIXER SUB-ROUTINE FLOW CHART .....	432
C.4 T3 AND T6 RECUPERATOR EXIT TEMPERATURE SUB-ROUTINE FLOW CHART ..	433
C.5 R1233ZD(E) ORC SYSTEM THERMODYNAMIC MODEL CODE.....	434
C.6 THERMAL EFFICIENCY COMPARISON OF THE ORC SYSTEM AND THE CO2 SRC POWER GENERATION SYSTEM .....	437
<b>APPENDIX D .....</b>	<b>439</b>
D.1 R1233ZD(E) SAFETY DATA SHEET .....	439
D.2 BPHE LMTD SUB-ROUTINE FLOW CHART .....	444
<b>APPENDIX E .....</b>	<b>445</b>
E.1 COMPRESSED AIR OPEN LOOP EXPANDER-ALTERNATOR EXPERIMENT'S ELECTRICAL MEASUREMENTS.....	445
E.2 R1233ZD(E) ORC PROTOTYPE'S EXPERIMENTAL RESULTS.....	446
<i>E.2.1 Experiment 1</i> .....	446
<i>E.2.2 Experiment 2</i> .....	450
E.3 R1233ZD(E) ORC PROTOTYPE SYSTEM PERFORMANCE IMPROVEMENT SIMULATED CASES STATE POINTS' PROPERTIES .....	451

## List of Tables

Table 2.1: Thermodynamic and environmental information for the conventional ORC refrigerants.....	24
Table 2.2: Thermodynamic and environmental information for the environmentally friendly HCFO and HFO refrigerants.....	26
Table 2.3: Capacity ranges of expander types. ....	29
Table 2.4: Thermodynamic and environmental information for the conventional SRC refrigerants. ....	41
Table 2.5: Theoretical performance of CO <sub>2</sub> SRC and TRC with ejector. ...	47
Table 3.1: Overview of CO <sub>2</sub> miscibility with different types of lubricant oil .....	75
Table 3.2: List of absorbent candidates and available data. ....	79
Table 4.1: Absorbents and IGA experimental test conditions.....	92
Table 4.2: CO <sub>2</sub> /POE32 IGA solubility data compared to the literature data at -1°C. ....	95
Table 4.3: CO <sub>2</sub> /POE68 IGA solubility data compared to the literature data at 0°C.....	96
Table 4.4: Comparison of CO <sub>2</sub> /POE5 and CO <sub>2</sub> /POE32 IGA solubility data at -1°C. ....	97
Table 4.5: Comparison of CO <sub>2</sub> /POE32 and CO <sub>2</sub> /POE68 IGA solubility data at -1°C. ....	98
Table 4.6: Comparison of CO <sub>2</sub> /PC and CO <sub>2</sub> /POE32 IGA solubility data at -2°C. ....	98
Table 4.7: Comparison of theoretical CO <sub>2</sub> /PC and CO <sub>2</sub> /POE32 solubility data at 30°C.....	99
Table 4.8: Oil circulating pump specifications.....	104
Table 4.9: Names and volumes of the tested absorbents in the enhanced absorption apparatus. ....	109
Table 4.10: Absorbents densities.....	109
Table 4.11: Enhanced CO <sub>2</sub> /POE32 absorption/desorption experimental state points. ....	114
Table 4.12: Enhanced CO <sub>2</sub> /POE32 absorption/desorption experimental results compared to literature solubility data. ....	114
Table 4.13: Enhanced CO <sub>2</sub> /POE68 absorption/desorption experimental state points. ....	116
Table 4.14: Enhanced CO <sub>2</sub> /POE68 absorption/desorption experimental results compared to literature solubility data. ....	117
Table 4.15: Enhanced CO <sub>2</sub> /100 ml POE-10 ml PC absorption experimental state points. ....	119
Table 4.16: Enhanced CO <sub>2</sub> /100 ml POE-10 ml PC absorption experimental results compared to CO <sub>2</sub> /POE32 literature solubility data. ....	120
Table 4.17: Enhanced CO <sub>2</sub> /100 ml POE-30 ml PC absorption experimental state points. ....	121
Table 4.18: Enhanced CO <sub>2</sub> /100 ml POE-30 ml PC absorption experimental results compared to CO <sub>2</sub> /POE32 literature solubility data. ....	122
Table 5.1: Yokozeki-SRK modelling constants for CO <sub>2</sub> and POE lubricant oils. ....	144

Table 5.2: SRK modelling constants for CO <sub>2</sub> and PC. ....	147
Table 5.3: CO <sub>2</sub> /POE3 constants and interaction parameters. ....	149
Table 5.4: CO <sub>2</sub> /POE3 solubility data. ....	149
Table 5.5: Coefficients for CO <sub>2</sub> /POE3 solubility correlation.....	150
Table 6.1: CO <sub>2</sub> /lubricant absorption power generation system-Base case simulation inputs.....	165
Table 6.2: CO <sub>2</sub> /lubricant absorption power generation system-Base case simulation results. ....	166
Table 6.3: CO <sub>2</sub> /lubricant absorption power generation system-Case 2 simulation inputs.....	168
Table 6.4: CO <sub>2</sub> /lubricant absorption power generation system-Case 2 simulation results. ....	169
Table 6.5: CO <sub>2</sub> /lubricant absorption power generation system-Case 3 simulation inputs.....	171
Table 6.6: CO <sub>2</sub> /lubricant absorption power generation system-Case 3 simulation results. ....	171
Table 6.7: CO <sub>2</sub> /POE32 absorption, flood expansion, and CO <sub>2</sub> systems - Base case simulation results. ....	189
Table 6.8: CO <sub>2</sub> SRC power generation system result validation with Cayer et al. ....	197
Table 6.9: CO <sub>2</sub> SRC power generation system simulation cases inputs..	198
Table 6.10: CO <sub>2</sub> SRC power generation system simulation results.....	199
Table 6.11: CO <sub>2</sub> SRC power generation system- Optimum cooler pressures for net thermal power output. ....	203
Table 6.12: ORC thermodynamic model results validation with Shengjun et al. ....	213
Table 6.13: ORC simulations input.....	214
Table 6.14: Optimum operating conditions for environmentally friendly refrigerants in the ORC system. ....	217
Table 6.15: The R1233zd(E) ORC system optimised operating conditions .....	219
Table 7.1: Experimental alternator efficiency. ....	239
Table 7.2: Lynch-LEM-200d-127 motor, general specifications. ....	240
Table 7.3: General specifications of the 3CP1120 triplex plunger CAT pump.....	244
Table 7.4: BPHE characteristics. ....	246
Table 7.5: Heat exchangers LMTD model - plate specifications input. ....	248
Table 7.6: Condenser heat exchanger modelling results. ....	255
Table 7.7: Evaporator heat exchanger modelling results. ....	256
Table 7.8: Recuperator heat exchanger modelling results.....	256
Table 7.9: General specifications for the ORC prototype pressure transducers. ....	258
Table 8.1: Compressed air open loop expander-alternator test results. .	273
Table 8.2: ORC experiment 1, first run – The R1233zd(E) ORC system’s optimum experimental performance .....	306
Table 8.3: ORC experiment 1, first run – The R1233zd(E) ORC system’s optimum experimental performance state points’s properties.....	307
Table 8.4: ORC experiment 1, second run – The R1233zd(E) ORC system’s optimum experimental performance. ....	321

Table 8.5: ORC experiment 1, second run – The R1233zd(E) ORC system’s optimum experimental state points’ properties.....	322
Table 8.6: ORC Experiment 2 - The R1233zd(E) ORC system’s optimum experimental performance.....	334
Table 8.7: ORC experiment 2 - The R1233zd(E) ORC system’s optimum experimental state points’ properties. ....	335
Table 8.8: R1233zd(E) ORC system’s optimum experimental point improvements towards the initially predicted thermodynamic model.....	339
Table 8.9: Comparison between the R1233zd(E) prototype system and Twomey’s experimental results as a function of mass flow rate. ....	351
Table 8.10: Comparison between R1233zd(E) prototype system and Twomey’s experimental results as a function of rotational speed. ....	352
Table 9.1: Annual industrial and domestic electricity prices in the UK....	359
Table 9.2: R1223zd(E) ORC prototype system and scaled-up system’s bill of materials.....	362
Table 9.3: Specific cost of the R1233zd(E) ORC system. ....	365
Table 9.4: Installation costs for the R1233zd(E) ORC system.....	365
Table 9.5: R1233zd(E) ORC system’s economic model inputs. ....	366
Table 9.6: The 5 kW R1233zd(E) ORC system’s economic model results.	367
Table 9.7: The 20 kW R1233zd(E) ORC system’s economic model results .....	373
Table 9.8: The CO2 pump’s general specifications. ....	380
Table 9.9: CO2 power system heat exchanger specifications.....	380
Table 9.10: General specifications for a CO2 solenoid valve.....	381
Table 9.11: 5 kW CO2 power system components and costs in original currencies. ....	382
Table 9.12: CO2 SRC power generation system’s fourth case re-simulation results compared to the original results.....	384
Table 9.13: The 5 kW CO2 power system’s economic model inputs.....	385
Table 9.14: Results for the 5 kW CO2 power system economic model. ..	385

# List of Figures

Figure 1-1: World energy consumption by fuel type.....	3
Figure 1-2: Historical electricity generation by fuel share. ....	4
Figure 1-3: World electric power generation by fuel type.....	4
Figure 1-4: Global temperature increase in the past century .....	5
Figure 1-5: Changes in global greenhouse gas emissions from 1970 to 2010 in different sectors. ....	7
Figure 1-6: The evolution of refrigerants. ....	9
Figure 1-7: Industrial heat demands in the EU, estimated by temperature quality and the manufacturing sector.....	11
Figure 2-1: Temperature variation in the heat addition process- a) Conventional Rankine cycle. b) ORC. ....	21
Figure 2-2: Three types of working fluids .....	22
Figure 2-3: Optimal selection of working fluids for different heat source temperatures.....	23
Figure 2-4: Thermal efficiency of ORC employing low GWP refrigerants, compared to conventional refrigerants; investigated by Varma and Joost.	28
Figure 2-5: Scroll compressor types .....	30
Figure 2-6: Variation of heat source temperatures in different ORC applications. ....	33
Figure 2-7: Market share of each ORC application in terms of the number of units. ....	34
Figure 2-8: Gas turbine waste heat ORC system .....	35
Figure 2-9: Dual loop waste heat ORC system .....	36
Figure 2-10: Solar ORC with reverse osmosis desalination .....	37
Figure 2-11: Temperature variation in the heat addition process for an ORC and an SRC. ....	39
Figure 2-12: The difference between an SRC and a TRC in the CO <sub>2</sub> T-S diagram. ....	39
Figure 2-13: 10 MW CO <sub>2</sub> SRC turbine compared to an equivalent steam turbine.....	45
Figure 2-14: CO <sub>2</sub> TRC with reheating and two-stage expansion .....	46
Figure 2-15: CO <sub>2</sub> SRC or TRC with an ejector .....	46
Figure 2-16: Low/high heat source CO <sub>2</sub> TRC .....	48
Figure 2-17: Low/high heat source CO <sub>2</sub> TRC incorporated with a CO <sub>2</sub> Bryton cycle .....	49
Figure 2-18: Solar CO <sub>2</sub> TRC with LNG cooling and thermal storage .....	50
Figure 2-19: Solar SRC system for combined heat and power .....	51
Figure 2-20: Temperature variation in the heat addition process for ORC, Binary fluid in an absorption cycle, SRC. ....	53
Figure 2-21: Ammonia-water phase diagram. ....	54
Figure 2-22: Schematic diagram of Maloney & Robertson absorption power cycle .....	55
Figure 2-23: Schematic diagram of the Kalina cycle .....	57
Figure 2-24: Schematic diagram of Kalina cycle for cement production waste heat recovery .....	60
Figure 2-25: Schematic diagram of Zheng et al's combined power and refrigeration absorption cycle .....	61

Figure 2-26: Schematic diagram of Zhang and Lior's combined power and refrigeration absorption cycle .....	62
Figure 2-27: Schematic diagram of Wang et al's combined power and refrigeration absorption cycle .....	63
Figure 3-1: Various types of miscibility behaviour.....	70
Figure 3-2: Three POE32 lubricant oils from different sources. ....	73
Figure 3-3: Overview of CO <sub>2</sub> solubility in different common lubricants. ...	76
Figure 3-4: Overview of viscosity of CO <sub>2</sub> /lubricant oil mixtures. ....	77
Figure 3-5: CO <sub>2</sub> solubility comparison in different absorbent candidates at constant temperatures.....	80
Figure 4-1: Schematic view of the SDT Q600 TGA apparatus. ....	84
Figure 4-2: Illustration of the SDT Q600 thermogravimetric analyser.....	85
Figure 4-3: TGA results: a) PC, and b) POE5.....	87
Figure 4-4: TGA results: a) POE32, and b) POE68. ....	88
Figure 4-5: TGA results: a) TG curves for tested absorbents, and b) DTG curves for tested absorbents.....	89
Figure 4-6: Schematic of the IGA apparatus. ....	90
Figure 4-7: IGA-300 .....	90
Figure 4-8: IGA Experiment interface.....	92
Figure 4-9: IGA absorption experiment results.....	94
Figure 4-10: IGA solubility data validation of CO <sub>2</sub> /POE32 at -1°C.....	95
Figure 4-11: IGA solubility data validation of CO <sub>2</sub> /POE68 at 0°C. ....	96
Figure 4-12: Comparison of the results for IGA solubility, from CO <sub>2</sub> /POE5, CO <sub>2</sub> /POE32, and CO <sub>2</sub> /POE68 at -1°C.....	97
Figure 4-13: Absorption test apparatus before modification .....	100
Figure 4-14: A schematic view of the modified absorption test apparatus .....	102
Figure 4-15: Different views of the modified absorption apparatus. ....	102
Figure 4-16: Experimental setup of the absorption apparatus. ....	103
Figure 4-17: Oil circulation pump .....	104
Figure 4-18: CO <sub>2</sub> cylinder, regulator and charging manifold. ....	105
Figure 4-19: K- type thermocouple.....	106
Figure 4-20: Absolute pressure transducer .....	107
Figure 4-21: DataTaker DT80 .....	107
Figure 4-22: The DT80 monitoring interface. ....	108
Figure 4-23: Span calibration coordinates .....	108
Figure 4-24: Enhanced CO <sub>2</sub> /POE32 absorption pressure and temperatures profile.....	110
Figure 4-25: Zoomed-in view of the first enhanced CO <sub>2</sub> /POE32 absorption process. ....	111
Figure 4-26: Zoomed-in view of the first enhanced CO <sub>2</sub> /POE32 desorption process. ....	113
Figure 4-27: CO <sub>2</sub> mass fraction at equilibrium in the CO <sub>2</sub> /POE32 mixture - Theoretical vs. experimental.....	115
Figure 4-28: Enhanced CO <sub>2</sub> /POE68 absorption pressure and temperatures profile.....	116
Figure 4-29: CO <sub>2</sub> mass fraction at equilibrium in the CO <sub>2</sub> /POE68 mixture - Theoretical vs experimental.....	118
Figure 4-30: Enhanced CO <sub>2</sub> /100 ml POE-10 ml PC absorption pressure and temperatures profile. ....	119

Figure 4-31: Enhanced CO <sub>2</sub> /100 ml POE-30 ml PC absorption pressure and temperatures profile. ....	121
Figure 5-1: CO <sub>2</sub> /POE32 vapour pressure at different CO <sub>2</sub> mass fractions .....	128
Figure 5-2: CO <sub>2</sub> /POE32 phase behaviour.....	128
Figure 5-3: Three CO <sub>2</sub> /POE mixtures correlated using the UniOil concept .....	132
Figure 5-4: CO <sub>2</sub> /POE68 vapour pressure at different CO <sub>2</sub> mass fractions .....	137
Figure 5-5: CO <sub>2</sub> /POE68 phase behaviour.....	137
Figure 5-6: CO <sub>2</sub> /PC vapour pressure at different CO <sub>2</sub> mass fractions. ....	138
Figure 5-7: CO <sub>2</sub> /PC phase behaviour. ....	139
Figure 5-8: CO <sub>2</sub> /POE mixture-specific enthalpy sub-routine flow chart. ....	146
Figure 5-9: CO <sub>2</sub> /PC mixture-specific enthalpy sub-routine flow chart. ....	148
Figure 5-10: Comparison of calculated densities for CO <sub>2</sub> /POE3 using different Yokozeki-SRK EOS approaches at 40 bar and variable temperatures.....	151
Figure 5-11: The relative error of densities calculated using different Yokozeki-SRK EOS approaches.....	151
Figure 5-12: Comparison of specific enthalpies using different Yokozeki- SRK EOS approaches calculated at 40 bar and variable temperatures. ..	152
Figure 5-13: The relative error of specific enthalpies calculated using using different Yokozeki-SRK EOS approaches.....	152
Figure 5-14: Comparison of densities calculated using SRK EOS and Seeton and Hrnjak's empirical correlation. ....	153
Figure 5-15: The relative error between calculated densities of CO <sub>2</sub> /POE32 using SRK EOS and Seeton and Hrnjak's empirical correlation at 40 bar and variable temperatures.....	153
Figure 5-16: Comparison of densities calculated using SRK EOS and the empirical correlation developed. ....	154
Figure 5-17: The relative error between densities of CO <sub>2</sub> /POE68 calculated using SRK EOS and the empirical correlation developed at 40 bar and variable temperatures.....	154
Figure 6-1: Schematic of the CO <sub>2</sub> /lubricant absorption power generation system.....	159
Figure 6-2: Simple counter flow heat exchanger.....	161
Figure 6-3: The effect of the absorber's operating pressure on the absorption power generation system's performance at 30°C.....	168
Figure 6-4: The effect of absorber temperature on the absorption power generation system's performance at 10°C. ....	170
Figure 6-5: The effect of the generator's operating pressure on the absorption power generation system's overall performance, at an absorber temperature of 30°C and generator pressure of 100 bar. ....	173
Figure 6-6: Schematics of a) Flood expansion system reproduced from reference, and b) CO <sub>2</sub> /acetone absorption power generation system ....	177
Figure 6-7: Schematic of the CO <sub>2</sub> /lubricant flood expansion system. ....	179
Figure 6-8: Schematic of the CO <sub>2</sub> /lubricant flood expansion system for simulation. ....	181
Figure 6-9: CO <sub>2</sub> /POE32 mixer 2 process flow.....	183

Figure 6-10: Specific heat of CO <sub>2</sub> at expected operating pressures, against the operating temperature range. ....	185
Figure 6-11: Thermal efficiency comparison between the CO <sub>2</sub> /POE32 absorption, flood expansion, and CO <sub>2</sub> systems at base case conditions. ....	190
Figure 6-12: Net thermal power output comparison between CO <sub>2</sub> /POE32 absorption, flood expansion and CO <sub>2</sub> systems at base case conditions. .	191
Figure 6-13: Schematic of the CO <sub>2</sub> SRC power generation system.....	194
Figure 6-14: CO <sub>2</sub> SRC power generation system thermodynamic model validation .....	197
Figure 6-15: CO <sub>2</sub> SRC power generation system-T-S diagram of the base case optimum operating condition. ....	200
Figure 6-16: CO <sub>2</sub> SRC power generation system-P-H diagram of the base case optimum operating condition. ....	200
Figure 6-17: CO <sub>2</sub> SRC power generation system-T-S diagram of the fourth simulation case's optimum operating condition in the super-critical region .....	201
Figure 6-18: CO <sub>2</sub> SRC power generation system-P-H diagram of the fourth simulation case's optimum operating condition in the super-critical region .....	202
Figure 6-19: Simulation results for the CO <sub>2</sub> SRC power generation system performance. ....	204
Figure 6-20: CO <sub>2</sub> SRC power generation system thermal efficiency and net thermal power output as a function of the CO <sub>2</sub> heater outlet temperature .....	206
Figure 6-21: CO <sub>2</sub> SRC power generation system thermal efficiency and net thermal power output as functions of the turbine's isentropic efficiency .....	207
Figure 6-22: CO <sub>2</sub> SRC power generation system thermal efficiency and net thermal power output as functions of the compression device isentropic efficiency. ....	208
Figure 6-23: CO <sub>2</sub> SRC power generation system thermal efficiency and net thermal power output as functions of the recuperator heat exchanger effectiveness. ....	209
Figure 6-24: Schematic of the ORC system.....	212
Figure 6-25: ORC thermodynamic model validation .....	214
Figure 6-26: ORC working fluids performance at 100°C.....	215
Figure 6-27: ORC working fluids performance comparison at 120°C .....	216
Figure 6-28: R1233zd(E) ORC system thermal efficiency and net power as a function of evaporator pressure and dependant super-heating temperature. ....	219
Figure 6-29: R1233zd(E) ORC optimised operating conditions, T-S diagram. ....	220
Figure 6-30: R1233zd(E) ORC optimised operating conditions, P-H diagram. ....	221
Figure 6-31: R1233zd(E) ORC thermal efficiency and net thermal power output as functions of the expander isentropic efficiency. ....	222
Figure 6-32: R1233zd(E) ORC thermal efficiency and net thermal power output as functions of the R1233zd(E) pump isentropic efficiency.....	223
Figure 6-33: R1233zd(E) ORC thermal efficiency and net thermal power output as functions of the recuperator heat exchanger effectiveness.....	223

Figure 7-1: A schematic diagram of the R1233zd(E) ORC prototype system.....	228
Figure 7-2: 3D illustration of the R1233zd(E) ORC prototype system. ...	229
Figure 7-3: 3D illustrations of the R1233zd(E) ORC prototype system with rugged industrial casing. ....	229
Figure 7-4: Heat source - Carel humisteam X-plus EU090 steam humidifier .....	230
Figure 7-5: Heat sink - Corema 56 kW industrial chiller unit. ....	231
Figure 7-6: Scroll expander operation. ....	231
Figure 7-7: Types of internal leakage in scroll expanders. ....	233
Figure 7-8: Sanden TRSA09 .....	233
Figure 7-9: Performance curve of the Sanden TRSA09 compressor. ....	234
Figure 7-10: Views of scroll compressor modification procedures 1.....	235
Figure 7-11: Views of the scroll compressor modification procedures 2 .	236
Figure 7-12: The scroll expander after assembly. ....	236
Figure 7-13: The automotive alternator.....	237
Figure 7-14: A battery supplies the field current to the rotor coil through the brushes and slip rings. ....	238
Figure 7-15: Automotive alternator performance.....	238
Figure 7-16: Lynch-LEM-200d-127 motor, general view. ....	239
Figure 7-17: Lynch-LEM-200d-127 motor performance curve. ....	240
Figure 7-18: Lynch- LEM-200d-127 motor installed on the ORC prototype system.....	240
Figure 7-19: Autoelectro AEC1761 automotive alternator. ....	241
Figure 7-20: Performance curves of a 150 amp-12V DC alternator. ....	242
Figure 7-21: Autoelectro AEC1761 automotive alternator installed on the ORC prototype system. ....	243
Figure 7-22: 3CP1120 triplex plunger CAT pump.....	243
Figure 7-23: The corrugated plates of the BPHEs.....	244
Figure 7-24: Two types of flow pattern in BPHEs. ....	244
Figure 7-25: The chevron angle of the plate heat exchanger.....	245
Figure 7-26: A BPHE as an evaporator and condenser in a refrigeration system.....	246
Figure 7-27: ORC prototype heat exchangers.....	247
Figure 7-28: Simple counter-flow heat exchanger. ....	248
Figure 7-29: Overall thermal resistance in a BPHE. ....	250
Figure 7-30: Agilent 34907A data acquisition system.....	257
Figure 7-31: Pressure transducers installed on the ORC prototype.....	259
Figure 7-32: Variable area flow meter principle. ....	259
Figure 7-33: R1233zd(E) flow meter, Platon FGMT154L. ....	260
Figure 7-34: Condenser cooling water flow meter, Key Instrument FR4500 .....	260
Figure 7-35: Smart T55 digital tachometer.....	261
Figure 7-36: PLZ1004W and PLZ2004WB DC dummy load.....	262
Figure 7-37: Side view of the ORC prototype during construction. ....	262
Figure 7-38: Back view of the ORC prototype during construction.....	263
Figure 7-39: Front view of the final ORC prototype.....	263
Figure 7-40: Back view of the final ORC prototype.....	264
Figure 7-41: General view of the final ORC prototype. ....	264

Figure 8-1: Schematic of the compressed air open loop expander-alternator test bench. ....	267
Figure 8-2: SMC-PF2A703H digital air flow sensor. ....	268
Figure 8-3: Camozzi C401-D000 air filter regulator lubricator unit. ....	268
Figure 8-4: Compressed air open loop expander-alternator test bench set-up. ....	269
Figure 8-5: Voltage and current displayed on the adjustable load screen .....	271
Figure 8-6: Compressed air open loop expander-alternator test's power generation profile. ....	274
Figure 8-7: Generated power variation with air inlet pressure. ....	275
Figure 8-8: Variation in generated power with air flow rate.....	276
Figure 8-9: The expander's isentropic efficiency and the alternator's efficiency. ....	276
Figure 8-10: The relationship between the expander's power output and the alternator's electric power output.....	277
Figure 8-11: The relationship between the expander's power output and the expander's rotational speed. ....	277
Figure 8-12: Variation in air temperature across the expander.....	278
Figure 8-13: Expander-DC electric power generator arrangement.....	285
Figure 8-14: ORC experiment 1, first run - Temperature and pressure profiles. ....	288
Figure 8-15: ORC experiment 1, first run - Overall system performance profile.....	292
Figure 8-16: ORC experiment 1, first run - The effect of expander power output on system performance. ....	297
Figure 8-17: ORC experiment 1, first run - The effect of pressure ratio across the expander on system performance. ....	302
Figure 8-18: ORC experiment 1, first run's parameters relationships.....	305
Figure 8-19: ORC experiment 1, first run - Optimum experimental performance point represented on the R1233zd(E) T-S diagram.....	307
Figure 8-20: ORC experiment 1, first run - Optimum experimental performance point represented on the R1233zd(E) P-H diagram. ....	308
Figure 8-21: ORC experiment 1, second run - Temperature and pressure profiles. ....	311
Figure 8-22: ORC experiment 1, second run - Overall system performance profile.....	314
Figure 8-23: ORC experiment 1, second run - The effect of the expander's power output on system performance. ....	317
Figure 8-24: ORC experiment 1, second run - The effect of the pressure ratio across the expander on system performance.....	319
Figure 8-25: ORC experiment 1, second run's parameters relationships	320
Figure 8-26: ORC experiment 1, second run - Optimum performance point represented on the R1233zd(E) T-S diagram .....	322
Figure 8-27: ORC experiment 1, second run - Optimum performance point represented on the R1233zd(E) P-H diagram .....	323
Figure 8-28: ORC Experiment 2 – temperature and pressure profiles. ...	328
Figure 8-29: ORC Experiment 2 - Overall system performance profiles..	332
Figure 8-30: ORC experiment 2 - Optimum performance point represented on the R1233zd(E) T-S diagram.....	336

Figure 8-31: ORC experiment 2 - Optimum performance point represented on the R1233zd(E) P-H diagram.....	337
Figure 8-32: Improvements of the optimum experimental point towards the initial thermodynamic model T-S diagram. ....	342
Figure 8-33: Improvements of the optimum experimental point towards the initial thermodynamic model P-H diagram. ....	343
Figure 8-34: Comparison between the R1233zd(E) ORC prototype system and preliminary expander-alternator’s experimental results 1. ....	347
Figure 8-35: Comparison between the R1233zd(E) ORC prototype system and preliminary expander-alternator’s experimental results 2. ....	349
Figure 8-36: Comparison between the R1233zd(E) ORC prototype system and Twomey’s experimental results .....	351
Figure 9-1: CPI percentage change from 2010 to 2014. ....	359
Figure 9-2: Exploded view of the R1233zd(E) ORC prototype system. ....	363
Figure 9-3: Cash flow variation for the 5 kW R1233zd(E) ORC system over 20 years. ....	367
Figure 9-4: Net present value of the 5 kW R1233zd(E) ORC system over 20 years. ....	368
Figure 9-5: Net present value of the 5 kW R1233zd(E) ORC system over 5 years. ....	369
Figure 9-6: The effect of specific capital cost on the 5 kW R1233zd(E) ORC system’s economic indicators.....	370
Figure 9-7: The effect of electricity price on the 5 kW R1233zd(E) ORC system’s economic indicators.....	371
Figure 9-8: Cash flow variation for the 20 kW R1233zd(E) ORC system over 20 years. ....	373
Figure 9-9: Net present value of the 20 kW R1233zd(E) ORC system over 20 years. ....	374
Figure 9-10: Net present value of the 20 kW R1233zd(E) ORC system over 5 years. ....	374
Figure 9-11: The effect of specific capital cost on the 20 kW R1233zd(E) ORC system’s economic indicators.....	375
Figure 9-12: The effect of electricity price per unit on the 20 kW R1233zd(E) ORC system’s economic indicators. ....	376
Figure 9-13: Infinity IT10 turbine.....	378
Figure 9-14: Enogia CO2 turbine.....	379
Figure 9-15: Ninjang Yalong Technology CO2 boosting pump.....	380
Figure 9-16: General view of G2H15 high pressure flow sensor. ....	382
Figure 9-17: Cash flow variation throughout the 5 kW CO2 SRC power generation system lifetime. ....	386
Figure 9-18: Net present value of the 5 kW CO2 SRC power generation system.....	387
Figure 9-19: The effect of the specific capital cost of the 5 kW CO2 SRC power generation system’s economic indicators. ....	388
Figure 9-20: The effect of electricity price on the 5 kW CO2 SRC power generation system’s economic indicators.....	389

## Nomenclature

$A$	Heat exchanger heat transfer area [ $m^2$ ]
$a$	EOS attraction parameter [ $J \cdot m^3 / mol^2$ ]
$A_c$	Plate heat exchanger channel crosses sectional area of [ $m^2$ ]
$A_p$	Projected area of a single plate [ $m^2$ ]
$A, B$	Polynomial EOS parameters
$a, b, c$	Correlation coefficients [-]
$b$	EOS volume limiting parameter [ $m^3 / mol$ ]
$b_c$	Channel spacing gap between plates [m]
$Bo$	Boiling number [-]
$C_0$	Capital Cost [\$]
$C_t$	Cash flow
$Co$	Convective number [-]
$cp$	Isobaric specific heat capacity [ $J/kg \cdot K, J/mol \cdot K$ ]
CPI	Consumer price index [%]
$D_h$	Hydraulic diameter [m]
$f$	Fugacity [Pa]
$ff$	Fouling factor [%]
$f, m, K, l$	EOS binary interaction parameters [-]
$Fr$	Froude number [-]
$F_{r1}$	Fluid dependent Constant
$G$	Mass flux [ $kg/m^2 \cdot s$ ]
$g$	Gravitational acceleration [ $9.81 \text{ m/s}^2$ ]
$H$	Molar enthalpy [ $J/mol$ ]
$h$	Specific Enthalpy [ $kJ/kg$ ]
$h_c$	Convective heat transfer coefficient [ $W/m^2 \cdot K$ ]
$h_{fg}$	Refrigerant's latent heat of vaporisation
$I$	Current [Amps]
$i$	Discount rate [%]
IRR	Internal rate of return [%]
$k$	Thermal conductivity [ $W/m^2 \cdot K$ ]
LMTD	Log mean temperature difference [ $^{\circ}C$ ]
$L, w$	Length, and width of a plate [m]

M	Mass [kg]
$\dot{m}$	Mass flow rate [kg/s]
$\dot{m}_r$	Mass flow rate of refrigerant [kg/s]
$\dot{m}_s$	Mass flow rate of solution [kg/s]
N	Number of plates
$n_c$	Number of heat exchanger's cold channels
$n_h$	Number of heat exchanger's hot channels
n	Investment lifetime
NPV	Net present value [\$]
Nu	Nusselt number [-]
O&M	Operation and maintenance costs [\$]
P	Pressure [bar, kPa, Pa]
$p^o$	Atmospheric pressure [ $1.01325 \times 10^5$ Pa]
Pr	Prandtl number [-]
$\dot{Q}$	Heat rate [kW]
R	Resistance [ $\Omega$ ]
R	Universal gas constant [8314.51 J/mol.K]
r	Binary working fluid circulation ratio [-]
Re	Reynolds number [-]
ROI	Return on investment [%]
S	Molar entropy [J/mol.K]
s	Specific entropy [kJ/kg.k]
T	Temperature [ $^{\circ}$ C, K]
t	Wall thickness [m]
U	Overall heat transfer coefficient [ $W/m^2$ K]
u	Velocity [m/s]
$\dot{V}$	Volumetric flow rate [l/min]
V	Voltage [V DC]
V	Volume [ $m^3/kg$ ]
$\bar{V}$	Molar volume [ $m^3/mol$ ]
W	Power [kW]
X	Absorbent mass fraction [kg/kg]
x	Molar fraction [mol/mol]
Z	Compressibility factor [-]

## Greek Letters

$\alpha(T)$	EOS temperature dependent parameter [-]
$\beta_i$	Yokozeki's EOS model coefficients [-]
$\beta$	Chevron angle [rad]
$\varepsilon$	Heat exchanger effectiveness [%]
$\eta$	Efficiency [%]
$\eta_{\text{System}}$	First thermodynamic law thermal efficiency [%]
$\rho$	Density [ $\text{kg/m}^3$ ]
$\tau$	EOS binary interaction parameters [-]
$\nu$	Kinematic viscosity [Cst]
$\omega$	CO <sub>2</sub> mass fraction [kg/kg]
$\omega_f$	EOS acentric factor [-]
$\psi$	Kinematic viscosity correlation constant [1.244068]
$\phi$	Fugacity coefficient [-]
$\phi_f$	Heat exchanger's plate enlargement factor [-]
$\mu$	Dynamic viscosity [ $\text{kg/m s}$ ]

## Superscripts

ID	Ideal
L	Liquid
V	Vapour

## Subscripts

A	Absorber
Abs	Absorber, Absorbed
C	Cooler
c	Critical, cold
(c)	CO <sub>2</sub>
ci	Cold fluid inlet
co	Cold fluid outlet
Cond	Condenser
Des	Desorber, Desorbed
Dk	Two phase
E	Electrical
Electgen	Electrical generator

Evap	Evaporator
Exp	Expander
f	Fluid
G	Generator
Go	Fully developed vapour phase
H	Heater
h	Hot
Hex	Recuperator heat exchanger
hi	Hot fluid inlet
ho	Hot fluid outlet
i,j	Components of a binary mixture
L	Liquid
Lo	Fully developed liquid phase
(m)	Mixture
Net	Net thermal power output
r	Reduced
rl	Refrigerant liquid
T	Total
Trans	Transmitted
W	Water

### **Acronyms**

AB	Alkyl benzene
ASHRAE	American Society for Heating, Refrigerating and Air Conditioning Engineers
ASTM	American Society for Testing and Materials
CFCs	chlorofluorocarbons
CHP	Combined heat and power
DTG	Differential thermogravimetry
EOS	Cubic equation of state model
GDP	Gross domestic product
GHG	Greenhouse gas
GWP	Global warming potential
HCs	Hydrocarbons
HCFCs	Hydrochlorofluorocarbons

HCFOs	Hydrochloroflouroolefins
HFCs	Hydrofluorocarbons
HFES	Hydrofluoroethers
HFOs	Hydrofluoroolefins
IEA	International Energy Agency
IGA	Intelligent gravimetric analysis
ISO	International Standardization Organization
KCS11	Kalina cycle system 11
LLE	Liquid-liquid-equilibrium
MO	Mineral oil
ODP	Ozone depleting potential
OECD	Organisation for Economic Cooperation and Development
ORC	Organic Rankine cycle
PAG	Polyalkylene glycol
PAO	Poly-alfa olefin
PC	Propylene carbonate
PFCs	Perfluorocarbons
POE	Polyolester
PR	Peng-Robinson
PVE	Polyvinyl ether
SRC	Super-critical Rankine cycle
SRK	Soave-Redlich-Kwong
TGA	Thermogravimetric analysis
TRC	Trans-critical Rankine cycle
UNFCCC	United Nations Framework Convention on Climate Change
VLE	Vapour-liquid-equilibrium
VLEE	Vapour-liquid-liquid-equilibrium

## Chapter 1 : Introduction

---

### 1.1 The Importance and Demand for Energy

Energy is a fundamental factor in human development and the economic growth of a country. It is consumed in different forms from various sources in every aspect of daily life, such as heating, lighting, transportation, communication and manufacturing. However, the global energy demand and consumption rate is increasing rapidly, along with the world's population and economies. In the international energy outlook for 2013 [1], the US Information Administration announced that total world energy consumption was 552.85 quadrillion kJ (524 quadrillion Btu) in 2010. A 56% increase in this consumption is expected by 2040. 90% of this energy is predicted to be consumed in countries that are not members of the Organisation for Economic Cooperation and Development (OECD), where the energy demand is driven by long-term economic growth, which is indirectly related to population growth. On the other hand, demand in OECD countries is expected to increase by just 17%.

Besides the growth in world economy, energy demand and consumption is directly related to population growth. In 2013, the world's population reached 7.1 billion, which means it has more than doubled in the past 60 years and is estimated to reach 9.7 billion by 2050 [2]. According to the International Energy Agency (IEA), in their energy outlook for 2012 [3], world population is anticipated to grow from the 6.8 billion reported for 2010, to 8.6 billion in 2035. This growth is expected to occur in non-OECD countries; specifically in Asia and Africa, whereas India's population is expected to exceed China's by 2035. Consequently, it is anticipated that urban populations will increase from 51% in 2010, to 61% in 2035, affecting the amount and type of energy required, as well as energy efficiency.

## 1.2 Energy Sources

Energy can be classified, depending on its source, as non-renewable or renewable energy [4].

### 1.2.1 Non-Renewable Energy

These are the conventional energy sources consumed on the planet. With this type, These binary pairs consist derive from an existing and finite amount of natural stock that cannot be generated or reproduced. These sources are consumed at a more rapid rate than nature can create them. Non-renewable energy sources include nuclear power in the form of uranium and fossil fuels such as oil, natural gas and coal.

### 1.2.2 Renewable Energy

With renewable energy, the energy is derived from natural sources that are available in enormous amounts and which restock themselves over short periods of time. Sources of renewable energy include the sun, wind, water, waste heat, geothermal heat and biomass. However, fossil fuels are the world's primary source of energy, supplying 80% of demand. This is expected to continue through to 2040 at the same percentage rate. With such an accelerated rate of consumption, these sources will be depleted in the coming decades. On the other hand, the shift towards sustainable energy technologies in order to efficiently harness renewable energy sources, along with nuclear energy are growing more rapidly, demonstrating an annual expected increase of 2.8% and 2.5%, respectively. Figure 1-1, below, shows the historical and future projections of energy consumption by fuel type [1].

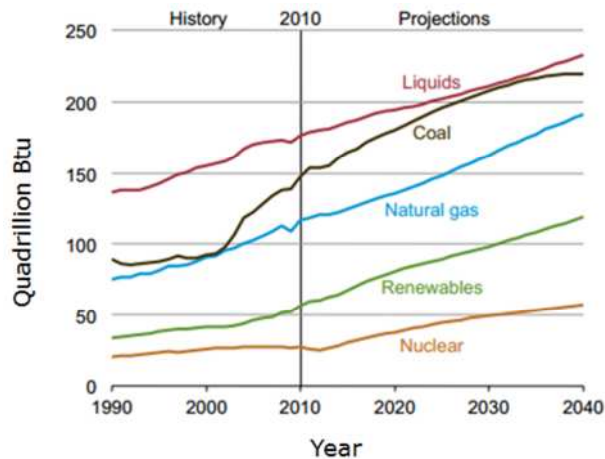


**Figure 1-1: World energy consumption by fuel type. (source:[1])**

### 1.3 Electric Energy

Specifically for electricity, the world's demand is growing twice as fast as total world energy consumption [3]. Future projections suggest that electricity demand will increase by 93% from 20.2 trillion kW in 2010, to 39 trillion kW in 2040 [1]. The main challenge is highlighted by the need for investment to replace the current aging power sector infrastructure, which is mainly coal-fired and thermal-driven. Figure 1-2 shows a historical comparison of the world's electricity consumption between 1973 and 2011. The Figure shows fossil fuel as the dominant source of electricity. However, the share of oil reduced significantly between 1973 and 2011 and was compensated by natural gas and coal. Other sources increased from 0.6% to 4.5%, indicating a rapidly growing sector. These sources comprise renewable energy of different types other than hydropower, including solar, waste heat, geothermal and biomass. This means that the renewable energy share in 2011 amounted to 20.3% of all power produced.

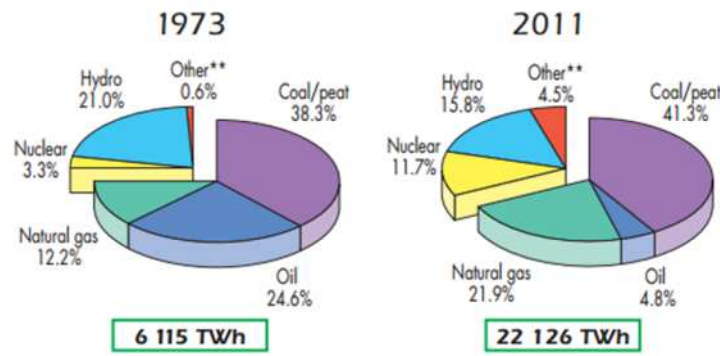


**Figure 1-2: Historical electricity generation by fuel share. (source: [5])**

Although future projections suggest that coal will remain the primary source of power, with an annual increase of 1.8% [1], one third of the existing power infrastructure needs to be replaced. Half of the new capacity will consist of fast-growing renewable sources [3], followed by the second fastest-growing natural gas and nuclear power sources. Figure 1-3 shows historical and future projections for electric power generation by fuel type. The Figure subdivides renewable energy into hydropower and non-hydropower renewable energy.

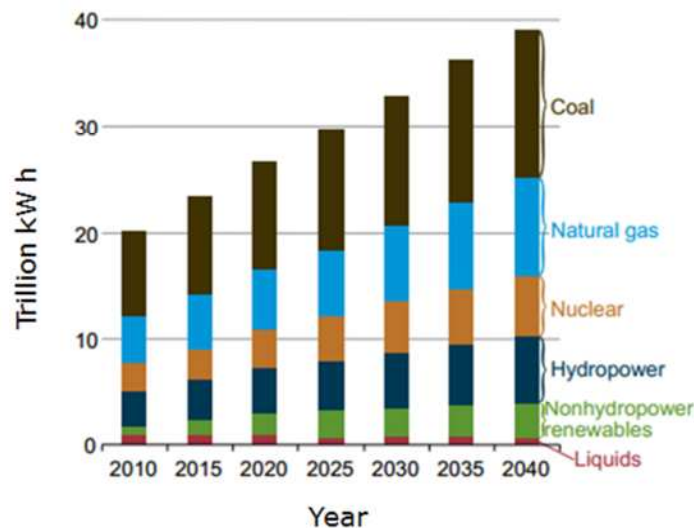


**Figure 1-3: World electric power generation by fuel type. (source:[1])**

It is very important to understand that the projections made by energy organisations do not take into account future international agreements and policies that may be introduced to reduce or limit the growth of fossil fuel consumption. These would be aimed at controlling greenhouse gas (GHG) emissions, the primary source of

global warming. Such agreements could also have an impact on the growth of nuclear power, especially after the Fukushima Daiichi nuclear disaster in 2011, with the possible phasing out of nuclear power generation around the world.

#### 1.4 Global Warming and the Greenhouse Effect

Global warming can be defined as an average increase in temperature which has taken place near the earth's surface, in the air and in the oceans since the middle of the 20<sup>th</sup> century [6]. As shown in Figure 1-4, the average surface temperature of the earth increased by 0.74°C throughout the 20<sup>th</sup> century. However, this temperature has shown a more rapid increase in the past few decades, where the average temperature in 2011 was found to be 0.51°C higher than the temperature recorded for the middle of the 20<sup>th</sup> century [7].

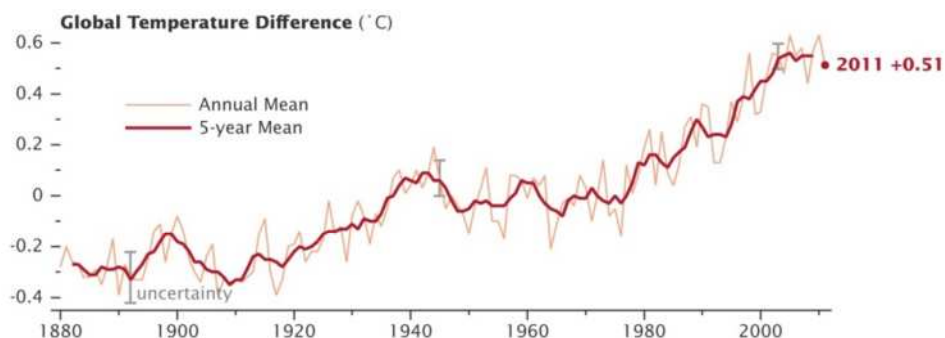


**Figure 1-4: Global temperature increase in the past century (source:[7])**

The greenhouse effect is a natural process whereby the earth maintains its energy balance and warms up by absorbing solar radiation and releasing infrared radiation, according to its surface temperature. However, the greenhouse effect has exhibited continuous acceleration since the Industrial Revolution, due to human activities driven by economic and industrial pressure. Subsequently, greenhouse gas emissions have been released at higher rates into the atmosphere. These highly concentrated gases absorb some of the incoming solar radiation and the outgoing infrared radiation from the earth. Eventually, this trapped heat or radiation is released into the earth's atmosphere, adding to the

incoming solar radiation and causing the earth's surface temperature to increase [8]. Consequently, global warming leads to a serious long-term impact on the environment, affecting the earth's climate and ecosystems, as well as human beings. The most significant impact of global warming is as follows [9, 10]:

- Acceleration of the melting of glaciers and consequent rise in sea level
- The spread of diseases in tropical and temperate regions
- Impact on human health and increased mortality rates, due to a lack of clean water
- Climate change, more frequent and harsh weather events, abnormal season times, stronger and more frequent heatwaves
- Sudden and more frequent flooding
- Ecological damage to agricultural harvests and food supplies.

#### 1.4.1 **The Greenhouse Gases**

The greenhouse emissions emitted by human activities are primarily carbon dioxide (CO<sub>2</sub>), methane (CH<sub>4</sub>), nitrous dioxide (N<sub>2</sub>O), sulphur hexafluoride (SF<sub>6</sub>), and synthetic halocarbons, including chlorofluorocarbons (CFCs), hydrofluorocarbons (HFCs), hydrochlorofluorocarbons (HCFCs), and Perfluorocarbons (PFCs) [10, 11]. Total world greenhouse emissions are measured on the basis of CO<sub>2</sub> equivalents [3], since CO<sub>2</sub>-related emissions are the predominant emissions in the atmosphere, produced by burning fossil fuels. These have increased by 30% in the past 150 years, due to industrialisation, as indicated above [11]. The UN Emissions Gap report of 2012 [12] specified that the total global greenhouse emissions for 2010 contained 50.1 gigatonnes of CO<sub>2</sub> equivalents. This amount is expected to increase by up to 59 gigatonnes in 2020 [13]. Specifically for CO<sub>2</sub>-related emissions, recent records show that 31.2 gigatonnes formed 60% of total world greenhouse emissions in 2010 [3]. This record reached 34.5 gigatonnes in 2012 – an increase of 1.4% [14]. Figure 1-5 shows the historical trend of total global greenhouse gas emissions for the period 1979 to 2010,

by sector. It can be clearly seen that greenhouse gas emissions increased by 25% in 2010, compared to 1990, and almost doubled what was recorded for 1970. As shown, the energy production and conversion sector is the primary contributor to the emissions produced, with rapidly increasing rates.

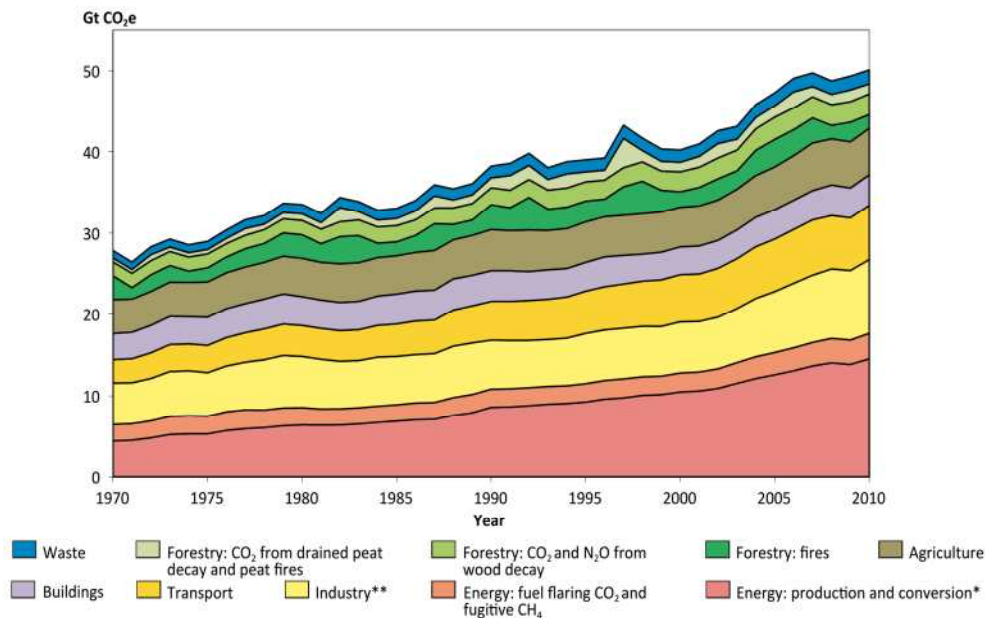


**Figure 1-5. Changes in global greenhouse gas emissions from 1970 to 2010 in different sectors. (source: [12])**

The global awareness of environmental impact and the consequences of greenhouse gas emissions over the past two decades, combined with concerns over the security of energy supplies, have driven governments around the world to draft policies in support of the promotion of renewable energy sources. International agreements have therefore been signed, aiming to limit the effect of greenhouse gas emissions on the world's climate.

#### 1.4.2 International Agreements

The Kyoto protocol was an international agreement within the United Nations Framework Convention on Climate Change (UNFCCC), signed in 1997 by 113 governments. This came into effect in 2005 and expired at the end of 2012. The Agreement's objective was to reduce the overall concentration of greenhouse gas emissions in the atmosphere to 5.2% below the 1990 level, over the period 2008 to 2012. This was intended to prevent dangerous

human interference with the global climate. The Agreement targeted six greenhouse gas emissions: CO<sub>2</sub>, CH<sub>4</sub>, N<sub>2</sub>O, SF<sub>6</sub>, HFCs, and PFCs [15]. The Copenhagen UNFCCC Climate Change Conference held in 2009 was promoted as a last chance and was expected to deliver a legally binding international agreement as a successor to the Kyoto Protocol, subsequent to 2012. Instead, it resulted in a non-binding agreement [16] that supports the reduction of greenhouse gas emissions, the exploration and application of new alternative clean energy sources, and the maintaining of global temperature increases at below 1.5 °C. In other words, an attempt was being made to keep CO<sub>2</sub> concentration in the atmosphere at less than 350 ppm [17].

The European Union, most of the members of which signed the Kyoto Protocol, played a leading role in the Copenhagen Agreement and has collectively recognised the threat of climate change, making decisions to implement its own measures [18]. Europe 2020 is a 10-year strategy proposed by the European Commission in 2010. In the energy-related aspect of the strategy, the Commission has set targets that are even more ambitious than the Kyoto Protocol. These targets are [19]:

- The reduction of greenhouse gas emissions by 20%, compared to the 1990 levels
- Increases in the share of renewable energy in final energy consumption by 20%
- Achieving a 20% increase in energy efficiency.

### 1.5 Ozone Layer Depletion and Refrigerants

Halocarbons are a harmful group of greenhouse gases that either contains chlorine, such as in CFCs and HCFCs, fluorine, as in HFCs, PFCs and SF<sub>6</sub>, or bromine, as in halons. These contribute heavily to the depletion of the ozone layer and increase in global warming [20]. In fact, these substances are involved in everyday activities, mainly as refrigerants. They are also found as cleaning agents, aerosol propellants, and foam-blowing agents. Specifically as

refrigerants, these substances, alongside other non-halocarbons, have been classified into four generations, based on their ultimate target as illustrated in Figure 1-6.

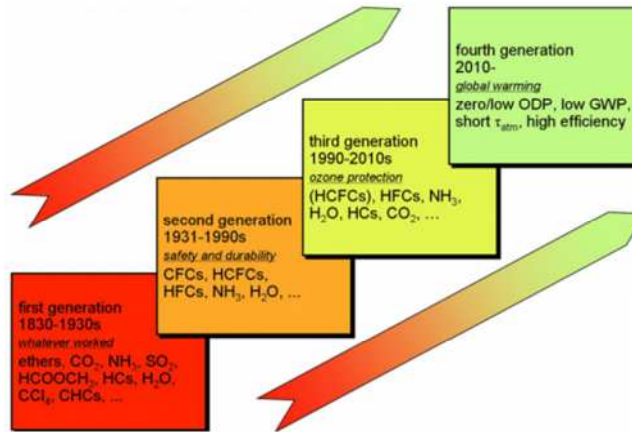


**Figure 1-6: The evolution of refrigerants. (Source: [21])**

The first generation, developed from 1830 to the 1930s, mainly consisted of the use of any substance which could be effective. In the second generation, from 1931 to the 1990s, the main aim in employing refrigerants was safety and durability, which promoted CFCs as the refrigerants of choice. However, CFCs are highly stable. Once they are emitted, they stay in the atmosphere for hundreds or even thousands of years [22]. During their lifetime, they rise to the stratosphere, where they are decomposed by the sun's radiation to release chlorine atoms, which subsequently destroy ozone molecules and deplete the ozone layer [23]. After the ozone hole was discovered over Antarctica, the obligatory Montreal Protocol became effective in 1987, urging the total phasing out of CFCs and other ozone-depleting substances [23].

The phasing out of CFCs promoted the use of HFCs and HCFCs between 1990 and 2010 as non-ozone depleting alternative refrigerants [23, 24]. However, HCFCs are similar to CFCs, but with shorter lifetimes, and far less ozone depletion and global warming effects [22]. Under the Montreal Protocol, they have also been gradually phased out, at a rate of 90% by 2015 and completely by

2020 [20]. HFCs, alongside PFCs and SF<sub>6</sub>, are fluorinated greenhouse gases (F-gases) with no ozone depletion potential, but with high global warming effect, greater than that of CO<sub>2</sub> emissions. Nevertheless, these gases are controlled by the Kyoto Protocol [25]. Notwithstanding the above and despite the fact that the Montreal Protocol addresses the harm caused by HFCs, the Agreement does not bind its signatories to phase them out [26]. However, recently and parallel to the international agreements, the F-gas regulation adopted by the European Union in 2014 became very effective in combating climate change. The regulations aimed to reduce F-gas emissions by two thirds of the 2014 levels, by 2030 and this, with:

- A gradual phasing out of F-gases by limiting their sale in the EU from the beginning of 2015, until one fifth of the sales for 2014 is reached in 2030.
- A ban on the use of F-gases in new equipment. This was recently noted in the automotive industry, where R134a was replaced by the new environmentally friendly R1234yf.
- The prevention of F-gas emissions from existing equipment by conducting frequent and thorough checks, servicing, recovery and disposal of these gases by the end of the equipment's lifetime.

From 2010 onwards, the search for new refrigerants became a priority, where zero or low ozone depleting potential (ODP), low global warming potential (GWP), short atmospheric lifetime, and relatively high efficiency became the governing criteria for fourth generation refrigerants [21].

## 1.6 Industrial Waste Heat Potential in the EU

Among the existing renewable energy sources is the heat generated by industrial processes in the form of flue gas or fluid. This is simply wasted by releasing it into the environment. These industrial processes include chemical and pharmaceutical production, vehicle manufacture, cement and lime production, metal refining and

smelting, glass production, petroleum fluid heaters and many others. It is estimated that around 20 - 50% of industrial energy consumption is waste heat [27]. These enormous amounts of waste heated represent a very attractive potential for heat recovery applications.

The EU's manufacturing sector is very important to its economy, generating around 17.1% of its gross domestic product (GDP). In 2007, it was estimated that the total demand for industrial heating was 13.2 EJ (13.2x10<sup>18</sup>J), with 4.4 EJ (4.4x10<sup>18</sup>J) being for electricity and 8.7 EJ (8.7x10<sup>18</sup>J) for direct heating. The CO<sub>2</sub> emissions associated with this industrial waste heat consist of 537 Mt of CO<sub>2</sub>/year. The most demanding industrial processes as far as energy is concerned across the EU involve metals, chemicals, non-metallic minerals, food, paper and pulp. These account for around 64% of the EU's CO<sub>2</sub> emissions [28]. Furthermore, in terms of temperature profile, the industrial heating requirements across the EU are [29]:

- 43% for high temperatures (>400°C);
- 30% for medium temperatures (100-400°C);
- 27% for low temperatures (<100°C).

Figure 1-7 shows a breakdown of the temperature profile for a range of different industries.

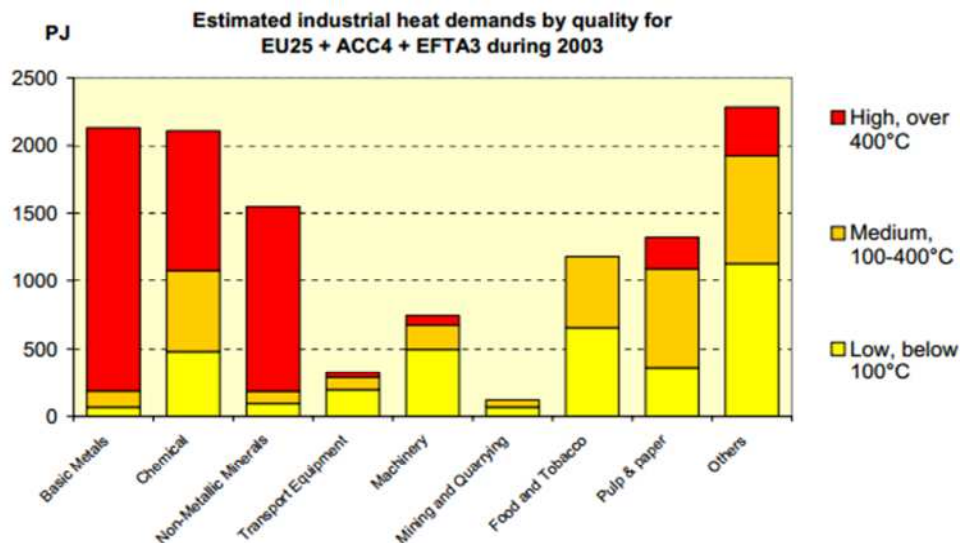


**Figure 1-7: Industrial heat demands in the EU, estimated by temperature quality and the manufacturing sector (source:[29])**

For high quality waste heat at over 400°C, waste heat energy recovery technologies, based on both passive and active technology, have already been successfully developed for a range of industries. Due to the high temperatures required, the systems are inherently thermodynamically efficient and therefore cost-effective to implement. However, a high proportion (27%) of the unavoidable industrial waste heat energy is of low quality, namely below 100°C. Nevertheless, waste heat recovery at lower temperatures is now becoming much more attractive due to increasing energy prices, technological developments and decreasing equipment costs. This portion of heat is suitable for use in active waste heat recovery technologies, where waste heat is converted to a higher temperature or to electricity.

### **1.7 Thesis Statement for Problems and Needs**

A major study on the Competitiveness of European Companies and Resource Efficiency was published in 2011 [30]. It concluded that 'resource efficiency is one of the main challenges the European Union is facing at the moment. Globalisation, the increasing world population and the rise of emerging economies has resulted in increased competition over natural resources across the world. In Europe, various resources are subject to depletion, or are not necessarily extractable'. As a result, EU companies are becoming more dependent on imports and have higher production costs compared to their international competitors, who face less stringent environmental policies. In addition, there are increasing concerns about the effects of emissions on health and the environment. It is therefore important that the EU makes the transition to a low carbon, energy efficient and resource-efficient economy. In the face of these challenges, European companies are adopting several measures to increase the efficiency of the resources they use. For example, the energy intensity of EU industry has fallen by almost 30% since 1990, due to both the introduction of new energy efficient technologies and the recovery of unavoidable waste heat [31].

In the context and for the EU, a disruptive technology step is required to enable the EU's industrial sector to cost-effectively convert low-temperature, unavoidable waste heat energy into useful energy. In so doing, industrial companies which have unavoidable low-grade waste heat streams will have the opportunity to achieve higher energy efficiency and thus help to reduce CO<sub>2</sub> emissions. Consequently, this will enable them to be more competitive with non-EU economies, where environmental legislation is not very strict.

## 1.8 Thesis Aims and Objectives

The current research was conducted in line with a European-funded project under the Seventh Framework Programme. It aims to develop and test a small-scale, novel and thermally driven power generation prototype system for low-grade waste heat recovery from industrial processes in the range of 60°C to 120°C.

The specific objectives of this thesis are as follows:

- To identify the most suitable thermal power generation technology and working fluid that can fulfil the aim of the research based on a comprehensive and up-to-date review conducted on low-grade heat thermal power generation technologies which are mainly based on the Rankine cycle. However, the system developed should introduce a breakthrough by employing an environmentally friendly, non-toxic, non-flammable working fluid, while also achieving relatively high thermal efficiency. The technologies and selected working fluids to be investigated are specifically:
  - (1) The absorption power generation system employing a binary mixture of CO<sub>2</sub>/lubricant as a working fluid. Another new technology using the same working fluid called (Flood expansion) was also investigated, as a substitute to the absorption power generation system.

- (2) The super-critical Rankine cycle power generation system (SRC) employing CO<sub>2</sub> as a working fluid.
  - (3) The organic Rankine cycle power generation system (ORC) employing newly emerged refrigerants, such as HFOs and HCFO-R1233zd(E), evaluated for ORC applications for the first time.
- The developments of thermodynamic models which will enable the accurate evaluation of the theoretical performance of the systems investigated and provide a fundamental understanding of optimum working conditions to yield maximum efficiency and power output.
  - In the case of the CO<sub>2</sub>/lubricant absorption, and flood expansion systems:
    - (1) To identify the most suitable absorbent lubricant for the CO<sub>2</sub> refrigerant from a screened range of refrigeration lubricant oil types and grades based on the maximum CO<sub>2</sub> solubility.
    - (2) To conduct lab-based experiments to examine the thermal stability of the selected lubricants, validate the gathered absorption data, as well as examine the enhancement of the absorption and desorption processes.
    - (3) To produce thermodynamic models that will enable the thermodynamic properties of the selected CO<sub>2</sub>/lubricant mixtures to be predicted, and which will therefore allow a thermodynamic evaluation of the systems.
  - To design and construct a small-scale prototype system based on the selected technology, working fluid, and the

thermodynamic model's simulated optimum operating conditions. However, the technology which was finally selected here was ORC, employing the only recently developed, environmentally friendly R1233zd(E) refrigerant.

- To produce a prototype expansion device suitable for the study's prototype. However, this thesis does not aim to design and construct an expansion device. Instead, a positive displacement scroll compressor that is already commercially available was converted to function as an expander.
- To preliminary evaluate the performance of the prototype expander produced and the electric power generation arrangement by undertaking a lab-based test on a specially constructed bench, where the expander is coupled with an electric generator.
- To practically proof the feasibility, as well as evaluate and monitor the performance of the small-scale R1233zd(E) prototype system by undertaking lab-based tests, where a steam boiler is used to simulate the waste heat flue gas. The system would be instrumented to allow its performance and characteristics to be determined; for example, the system's heat input, mechanical power output and electric power output for a set of given operating conditions.
- To address the sources of destructions, recommend improvements for the system, and validate the thermodynamic model's results with the experimental results.
- To conduct economic evaluation and analysis of the system, in order to assure its economic feasibility and cost-effectiveness by determining the key economic parameters, such as net present value (NPV), payback, internal rate of return (IRR), and rate of interest (ROI), taking into account

the system's performance, manufacturing costs, electricity costs, and operating and maintenance (O&M) costs.

In achieving this, the power generation system developed will offer greatly improved environmental performance due to enhanced efficiency and reduced CO<sub>2</sub> emissions, at a cost which is affordable for the end-user. Consequently, this will lead to significant economic and benefits for manufacturers.

### **1.9 Novelty of the Research and the Small-scale R1233zd(E) ORC Prototype System**

For the first time, the new environmentally friendly HCFO-R1233zd(E) is to be theoretically evaluated for ORC applications. Similarly, for the first time the heat exchangers' sizing for the R133zd(E) are thermodynamically predicted and validated. Consequently, the current research is the first of its kind to experimentally test R1233zd(E) in a specially constructed ORC system, exclusively for this purpose.

Also, one of the major innovations of this work is the deployment of a large scroll expander rated at 7 kW and converted from an automotive compressor. Past studies employing scroll expanders have either used 1 kW scroll expanders with integrated alternators, or larger refrigeration scroll expanders of a hermetic type.

### **1.10 Thesis Structure**

The present work is organised as follows:

**Chapter 2** presents the background of low-grade heat recovery power generation technologies, specifically focusing on Rankine cycle's derivatives. The chapter also provides an overview of the ORC, SRC, and binary fluid absorption power generation cycles, addressing the working fluids, applications, performance, as well as

presents notable and recent state-of-the-art designs for each technology and in different applications.

**Chapter 3** reviews the CO<sub>2</sub>/lubricant oil research background, the lubricant requirements in order to suit CO<sub>2</sub> applications, and identifies the most suitable lubricants for the binary working fluid mixture based on comparison of collected CO<sub>2</sub>/lubricant solubility data.

**Chapter 4** presents the experimental tests carried out on the selected lubricants with CO<sub>2</sub>, where the lubricants' thermal stabilities were evaluated, the absorption data were validated, and the enhancement of absorption and desorption processes was investigated.

**Chapter 5** reviews the most common approaches conducted in literature in order to predict the thermodynamic properties of CO<sub>2</sub>/lubricants. The chapter also presents and describes the proposed thermodynamic model adopted for properties prediction.

**Chapter 6** Presents theoretical and parametric investigations of several small-scale power generation systems covering the reviewed Rankine cycle based technologies, in order to determine the most suitable cycle for the research application, and the prototype systems intended to be constructed and tested. The investigated systems were, namely, the CO<sub>2</sub>/lubricant absorption, the CO<sub>2</sub>/POE32 lubricant flood expansion, the CO<sub>2</sub> SRC, and the environmentally friendly ORC power generation systems.

**Chapter 7** describes the design and construction of the R1233zd(E) ORC prototype system, which was selected for the application, based on the superior performance it has shown in comparison to other theoretically investigated fluids and systems. The prototype system's components are presented, and their principle of operation is described. The chapter also presents and describes the

modification of the automotive scroll compressor into expander and proposes a thermodynamic model for the R1233zd(E) ORC system's heat exchangers' sizing.

**Chapter 8** describes the experimental work carried out preliminarily on the expander-electric power generator, and the main experimental work on the R1233zd(E) prototype system. The chapter also presents and discusses the obtained results, addresses the system's limitations, validates the thermodynamically predicted results, and compares the experimentally obtained outputs to similar systems from literature.

**Chapter 9** Assesses the economic feasibility of the R1233zd(E) ORC power generation system based on the experimentally obtained results. The presented analysis includes two systems of 5 kW and 20 kW intended for mass manufacture. The chapter also presents the outcome of comprehensive market research carried out to identify suitable components for the CO<sub>2</sub> SRC power generation system. Furthermore, the economic feasibility of a 5 kW CO<sub>2</sub> SRC power generation system was analysed based on the theoretically predicted performance.

**Chapter 10** presents a summary of the conclusions of all chapters leading to the final conclusion of the current research, and also presents justified recommendations for further work in order to improve the performance of the R1233zd(E) ORC prototype system.

## Chapter 2 : A Review of Low-Grade Heat Recovery Power Generation Cycles

---

### 2.1 Introduction

This chapter provides a comprehensive overview of the low-grade heat recovery power generation cycles. The chapter presents the background and the most recent state of art of each investigated technology, provides an insight of the performance range of each technology and identifies their applications, employed working fluids and system equipment and highlights the research gaps.

### 2.2 Background

The Rankine cycle is a nineteenth century technology that is based on utilising steam water as a working fluid in a sequence of isentropic/isothermal thermodynamic processes [32] to convert heat into useful work. It is the most used cycle in electric power generation application[33] and has the highest thermal efficiency when compared to other thermodynamic energy conversion cycles [34]. The typical thermal efficiency of the steam Rankine cycle falls in the range of 35% to 40% in the most modern coal fired systems [35]. Water as working fluid offers many advantages, such as very good thermal and chemical stability, high latent and specific heat and the fact that water is abundant, cheap, non-flammable, non-toxic and environmentally friendly[34, 36]. However, the drawbacks encountered with the steam Rankine cycle are mainly excess pressure in the evaporator, the complexity and high cost of the turbine, the compulsory requirement for super-heat in order to prevent condensation during expansion, and the possibility of corrosion of the turbine blades [37]. For these reasons, the conventional steam Rankine cycle is more appropriate for large and centralised systems using high temperature heat sources [36].

With respect to low-grade heat sources and for small and medium system sizes, the conventional steam Rankine cycle becomes

infeasible technically and economically [34, 38] for the mentioned limitations beside the fact that larger system installations are required due to the high specific volume of steam and lower operating temperatures and pressures [39]. In this context, addressing these limitations by replacing the working fluid was the key introduction to various Rankine based thermodynamic cycles such as ORC, SRC, and the binary fluid absorption power cycles that employ a wide range of working fluids and allow the conversion of the enormous amounts of available low-grade heat into useful electricity.

### **2.3 The Organic Rankine Cycle (ORC)**

ORC is a Rankine cycle derivative which has been of growing interest and has been extensively investigated recently in low-grade heat recovery. Large numbers of theoretical and experimental investigations have been carried out in the area of ORCs. The key subjects of these investigations revolve around the selection of working fluids, which is the critical factor in characterising the performance of the system, the investigation and selection of expanders, and the evaluation of ORC performance in different applications.

#### **2.3.1 Principle of Operation**

ORC applies the same concept and has the same configuration as the conventional steam Rankine cycle but on a smaller scale. However, the ORC employs organic working fluids with low boiling points that allow better exploitation of the low-grade heat source. Figure 2-1 illustrates the difference between the temperature variations of the conventional Rankine cycle and the ORC during the heat addition process.

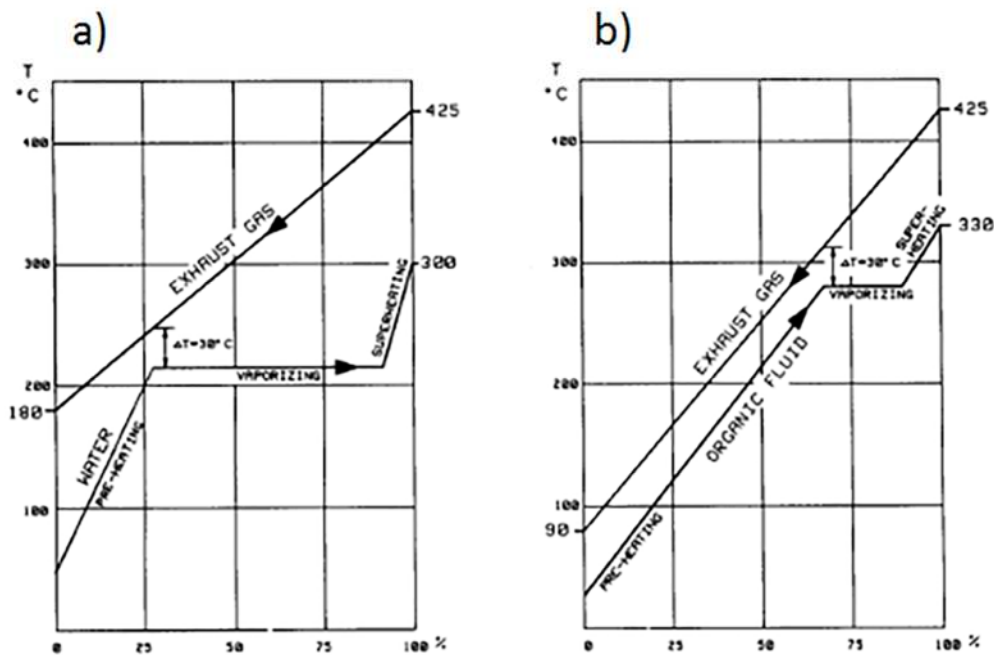


**Figure 2-1: Temperature variation in the heat addition process- a) Conventional Rankine cycle. b) ORC. (Source: [40])**

The ORC technology is well-established and is now becoming attractive because of its flexibility and the availability of all its components, since it is compatible with equipment for refrigeration applications [41]. One of the ORC's advantages is its suitability to fit a large variety of heat sources and sinks characteristics simply by selecting the appropriate working fluid. Another advantage is the ORC's flexibility in employing single stage expanders. These expanders are usually converted from a wide variety of existing refrigeration compressors which are cheap and mass-produced. However, the main disadvantage of ORC technology is the mismatch between the heat source, sink and cycle, due to isothermal heat addition and rejection processes.

### 2.3.2 Working Fluids Selection Criteria

The selection of working fluids is of primary importance and will directly influence the performance and economy of ORC systems [37]. Working fluids can be categorised into three types, according to the slope of their saturation curve of on the fluid's T-S diagram. A positive slope denotes a dry fluid, as in R601; a vertical slope denotes an isentropic fluid, as in R11, and finally, a negative slope

denotes a wet fluid, as in CO<sub>2</sub> and water [42, 43]. Figure 2-2 shows the three types of fluids on a T-S diagram.

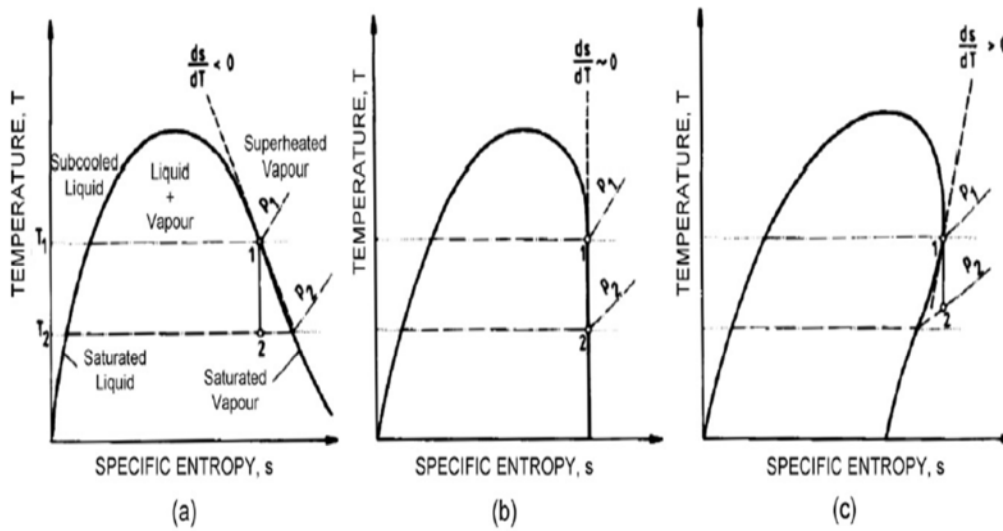


**Figure 2-2: Three types of working fluids- a) wet, b) isentropic and c) dry. (Source: [43])**

Working fluid selection criteria have been extensively investigated in the literature, such as in references [41-45]. A general outline of the selection criteria would suggest that the potential working fluid should have good thermodynamic and physical properties; high thermal and chemical stability; low environmental impact, with low GWP and ODP, and be non-toxic, non-flammable and non-corrosive. The working fluid should also be commercially available and affordable. Specifically for ORCs, Quoilin and Lemort [41] and Chen et al. [42] proposed the use of dry and isentropic fluids, in order to avoid working fluid droplets from damaging the turbine blades. This is something which can occur with wet fluids. Moreover, both studies suggest the use of a recuperator heat exchanger if dry fluids are used. This is explained as being due to the fact that dry fluids will exit the expander in a super-heated state. Consequently, more heat rejection requirements are imposed upon the condenser and the use of a recuperator heat exchanger is important for recovering heat from the super-heated turbine exhaust and increasing ORC efficiency. In this regard, Wang et al. [46] and Li et al. [47] have compared simple and regenerative ORC and reported a 20-30% increase in efficiency when a recuperator is used.

However, with reference to the working fluid requirements, Quoilin and Lemort [41] add that high vapour density is a key requirement in selection, where low density would consequently lead to a larger equipment size, especially in terms of the expander and condenser. The working fluid should also have moderate operating pressure for safety and economic reasons. From an economic point of view, high pressure means a more complex system with high investment costs.

### 2.3.3 Conventional ORC Working Fluids

The most extensively investigated working fluids in terms of theory and experimentation in ORC literature are R600, R600a, and R601 of the dry type, and R245fa, R134a, R123, and R245ca of the isentropic type. These studies include the theoretical evaluation carried out by Wang et al. [48], where it is suggested that the selection of working fluid is mainly determined by the temperature of the heat source, as shown in Figure 2-3.

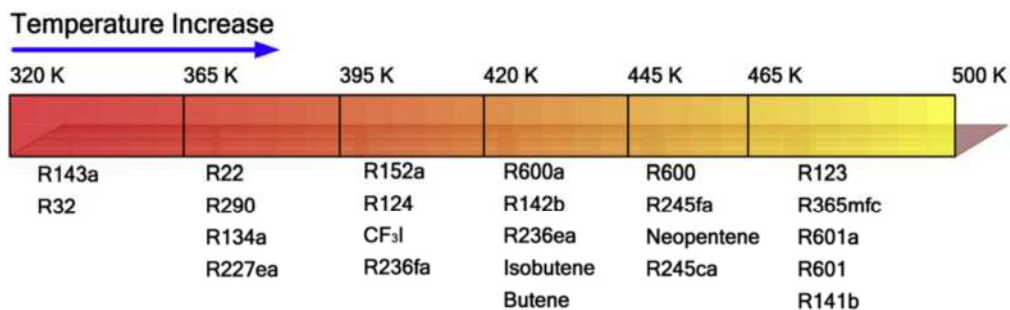


**Figure 2-3: Optimal selection of working fluids for different heat source temperatures. (Source: [48])**

In numerous attempts to fulfil the selection criteria, many studies have been undertaken to screen and evaluate potential working fluids. The most common approach seen in the literature is the evaluation of system performance using a range of working fluids to screen the most suitable fluid for a particular ORC system. The main evaluation parameter in such an analysis is the system's thermal efficiency, which is the ratio of the net thermal power output of the system to the heat input in the system's evaporator.

Another key evaluation parameter is the net thermal power output, which is the difference between the power produced by the expander, and the power consumed by the refrigerant pump.

Saleh et al. [49] evaluated the performance of ORC using 31 working fluids and recommended R245fa, R600, R601a, RE245, RE134, R236ea, and R245ca. Hung [50] specifically investigated dry fluids for waste heat recovery. The study included benzene, toluene, p-Xylene, R113 and R123. The results show that p-Xylene has the greatest thermal efficiency and is suitable for recovering high temperature waste heat sources, while R113 and R123 are more appropriate for low temperature waste heat sources. For dry fluids, Mago et al. [51] theoretically examined the performance of R245ca, R123, R113, and R600. The greatest thermal efficiency was achieved by R113, while the lowest was reached using R600. References [49-51] indicated that the highest efficiency is obtained from the fluid with the highest boiling point. Table 2.1 lists the conventional ORC refrigerants commonly found in literature alongside their critical and environmental properties [37, 52-56].

**Table 2.1: Thermodynamic and environmental information for the conventional ORC refrigerants.**

Refrigerant Type	Refrigerant name	Chemical name	Molecular weight [kg/kmol]	Critical temperature [K]	Critical pressure [bar]	ODP	GWP	ASHRAE Safety group
CFC	R113	1,1,2-Trichlorotrifluoroethane	187.4	487.21	33.92	1	6130	A1
HC	Benzene	1,3,5-Cyclohexatriene	78.11	562.02	48.94	-	-	-
HC	p-Xylene	1,1-Dimethylbenzene	106.17	616.168	35.32	-	-	-
HC	R600	Butane	58.1	425.16	37.96	0	4	A3
HC	R600a	Isobutane	58.1	407.85	36.40	0	3	A3
HC	R601	Isopentane	72.1	469.71	33.58	0	4±2	A3
HC	R601a	Isopentane	72.1	460.93	33.78	0	4±2	A3
HC	Toluene	Methylbenzene	92.14	591.75	41.26	-	-	-
HCFC	R123	2,2-Dichloro-	152.9	456.82	36.62	0.02	77	B1

		1,1,1-trifluoroethane						
HFC	R236ea	1,1,1,2,3,3-Hexafluoropropane	152	412.44	35.02	0	1370	-
HFC	R245fa	1,1,1,3,3-Pentafluoropropane	134	427.2	36.40	0	1030	B1
HFC	R245ca	1,1,2,2,3-Pentafluoropropane	134	447.57	39.25	0	6936	B1
HFC	R134a	1,1,1,2,2-Tetrafluoroethane	102	374.21	40.59	0	1430	A1
HFE	RE134	Difluoroethoxy-difluoromethane	118.03	420.15	34.2	-	6320	-
HFE	RE245	1,1,1-trifluoro-2-Difluoroethoxyethane	150.05	443.15	34.2	-	659	-
Keys: A1: Non-flammable with very low toxicity. A3: High flammability and low toxicity. B1: Non-flammable, with higher toxicity.								

### 2.3.4 Environmentally Friendly ORC Working Fluids

Very recently, new groups of fourth generation refrigerants, namely HFOs and HCFOs have emerged as environmentally friendly refrigerants, with almost no environmental impact. The potential of these refrigerants in ORC applications has become a very popular investigation topic in order to identify new working fluids for ORC applications.

#### 2.3.4.1 Hydrofluoro Olefin (HFOs)

The investigation of halogenated olefins with fluorinated propane isomers is currently endured as a potential low GWP replacement for R134a in automotive applications. This effort is mainly related to the European F-gas regulations. Amongst HFOs, R1234yf is identified as a promising alternative to R134a in automotive applications [57]. R1234ze(Z) and R1234ze(E) are other HFO refrigerants that have been developed to substitute R134a in refrigeration applications, where sink temperature may be as high as 70°C [57, 58]. However, R1234ze has been commercially available as a foam blowing agent [59]. The performance of HFOs is

reported to be similar to that of R134a, with a similar system size and operating pressure. Moreover, they are compatible with available R134a components. Unlike 134a, the R1234yf and both R1234ze types have mild flammability, where they are classified as Class 2 refrigerants. However, to ignite a Class 2 refrigerant, a significantly large amount of energy is required [60].

#### 2.3.4.2 Hydrochloroflourolefins (HCFOs)

In particular, R1233zd(E) was developed by Honeywell as a foam blowing agent and cleaning solvent to replace CFCs, HFCs and HCFCs [61]. However, the refrigerant has been promoted by developers as a promising alternative to R123 and R245fa in ORC applications, high capacity chillers and high temperature applications [62]. Although R1233zd(E) contains chlorine, the refrigerant is non-flammable, non-toxic, has negligible ODP, very low GWP and a very short atmospheric lifetime of 26 days [63].

Table 2.2 presents the critical and environmental properties of the environmentally friendly HCFO and HFO refrigerants [57, 63-66].

**Table 2.2: Thermodynamic and environmental information for the environmentally friendly HCFO and HFO refrigerants.**

Refrigerant type	Refrigerant name	Chemical name	Molecular weight [kg/kmol]	Critical Temperature [K]	Critical pressure [bar]	ODP	GWP	ASHRAE Safety group
HCFO	R1233zd(E)	1-chloro-3,3,3-trifluoropropene	130.496	438.75	35.709	0	>5	A1
HFO	R1234yf	2,3,3,3-tetrafluoropropene	114.042	367.85	33.822	0	4	A2L
HFO	R1234ze(Z)	1,3,3,3-tetrafluoropropene	114.042	423.27	35.33	0	6	A2L
HFO	R1234ze(E)	trans-1,3,3,3-tetrafluoropropene	114.042	382.52	36.3625	0	6	A2L
Keys: A1: Non-flammable with very low toxicity. A2L: Moderate flammability and low toxicity.								

### 2.3.5 Performance of the Environmentally Friendly Working Fluids

Liu et al. [67] has theoretically investigated the potential of HFOs for geothermal application. The study included 8 new HFOs, the performance of which was compared with that of conventional refrigerants, namely R134a, R245fa and R601a. The results show that R245fa has the greatest thermal efficiency of 9.37%, followed by R1234ze(Z) with 8.9%, which indicates the merit and capability of R1234ze(Z) to replace R245fa, if the environmental impact criterion is favoured over performance. Furthermore, the study recommends R1234yf for a heat source temperature of around 120°C, and R1225yeE refrigerant for temperatures of around 150°C.

Yamada et al. [68] expressed the potential of R1234yf refrigerant in ORCs for low to medium waste heat sources. The authors compared the thermal efficiency performance of the new refrigerant alongside intensively investigated high performance refrigerants, such as R134a, R245fa, R601a and ethanol. The results show that R1234yf and R134a have nearly identical performance. The thermal efficiency of R1234yf ranged between 8.8 to 11.4%, depending on the operating conditions. The authors concluded that R1234yf can replace R134a as a working fluid. In addition, R1234yf is suitable for low and medium temperature ORC application with heat source temperatures of up to 170°C, despite the fact it did not demonstrate the best thermal efficiency.

Shu et al. [45] evaluated R124, R134a, R245fa, R600, R600a and R1234yf in their proposed novel dual-loop ORC system for waste heat recovery. The maximum thermal efficiency was 20.07% and 20.06%, achieved by R600 and R245fa, respectively. However, R1234yf achieved the highest net thermal power output and maximum exergy efficiency. Finally, the study recommended the use of R1234yf at high operating loads.

Varma and Joost [66] investigated the potential of several new refrigerants and compared their thermal performance to that of conventional ORC refrigerants, such as R123, R245fa, R601, R134a and toluene. The new refrigerants investigated were R1234ze, R1234yf, DR-2, C6FK, D4 and D5. The ORC investigated has a simple configuration and operates between 80°C and 100°C. The theoretical results were calibrated and minimised according to existing ORCs. The results show that the new refrigerants have fairly good thermal efficiencies and the potential to replace conventional working fluids.

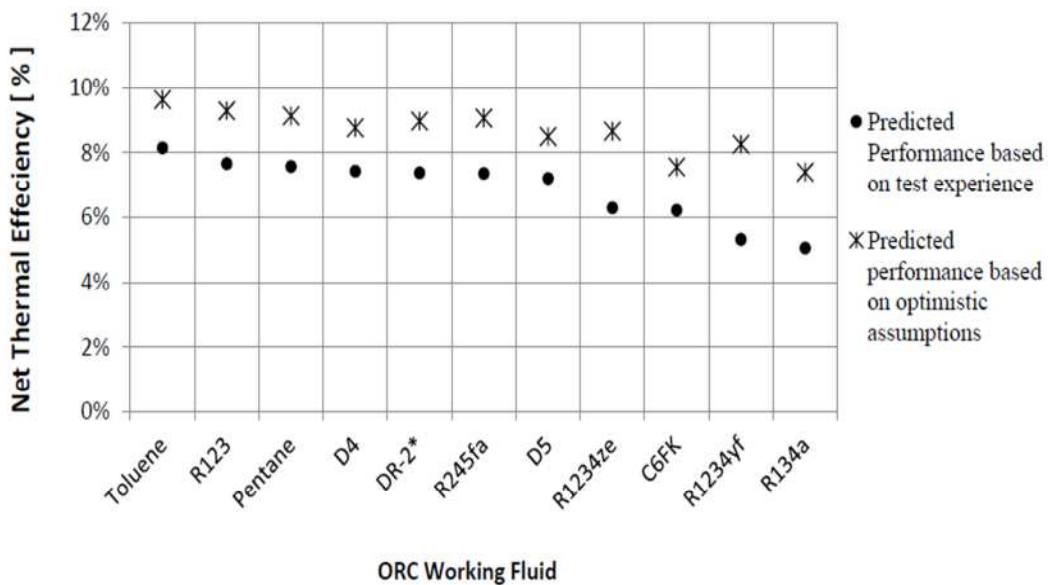


**Figure 2-4: Thermal efficiency of ORC employing low GWP refrigerants, compared to conventional refrigerants; investigated by Varma and Joost.(Source: [66])**

The study concluded that DR-2 is a potential replacement for R123. R1234yf and R1234ze(E), demonstrating a similar performance to R134a, but still with a lower performance than R245fa. However, newly developed, environmentally friendly R1233zd(E) may be a fluid which could replace R245fa. Nevertheless, the properties of R1233zd(E) are still under investigation and the refrigerant is not commercially available.

### 2.3.6 Expansion Device

The expander is the most important piece of equipment in an ORC system and it also has a direct influence on system performance and its economy. Generally, expanders can be categorised into two types: the dynamic (velocity) type and the positive displacement (volume) type. Velocity expanders include axial and radial-flow turbine expanders, and volume types include screw expanders, scroll expanders, reciprocal piston expanders and rotary vane expanders [69]. The capacity ranges of the aforementioned expander types are shown in Table 2.3.

**Table 2.3: Capacity ranges of expander types. (Source: [37])**

Type	Capacity range [kW]
Rotary vane expander	1-10
Scroll expander	1-10
Reciprocating piston expander	20-100
Screw expander	15-200
Radial-inflow turbine	50-500

According to Table 2.3, turbine expanders are suitable for large scale applications. Scroll expanders and rotary vane expanders have limited capacity but are very convenient for small-scale applications. Screw expanders and reciprocating piston expanders may be used for medium-sized ORC applications. It is reported that screw expanders have been widely used for geothermal and waste heat applications [37], while reciprocating piston expanders are widely used in the heat recovery of internal-combustion engine exhausts [70]. Review investigations to be found in the literature have mainly listed experimental work carried out on various types of expansion device, alongside the working fluids employed and the performance characteristics, such as Quoilin et al.'s study [71], which presents a comprehensive review covering different aspects and Song et al.'s study [72], which specifically reviews the performance of scroll expanders in ORC applications.

As the current research is concerned with small-scale ORC systems, the most attractive option is identified as the scroll expanders. For

this reason, scroll expanders are the only reviewed type in order to characterise its performance with different working fluids. However, other types were present in ORC literature such as radial inflow turbines in Yamamoto et al. [73] beside other expanders of volume type such as the screw expander in Smith et al. [74] and Mu et al. [75] , the rotary vane type expander converted from an air compressor in Qiu et al. [76], and the rolling piston expander in Wang et al. [77].

### 2.3.6.1 Scroll Expanders

Scroll expanders have gained interest recently in small-scale ORC systems for the qualities they offer in comparison with other volume expander types. They have few moving parts, with no valves, are mass-produced and cost very little compared to other expansion devices [69]. In general, scroll expanders are modified from commercially available scroll compressors that are used in different applications, as shown in Figure 2-5.

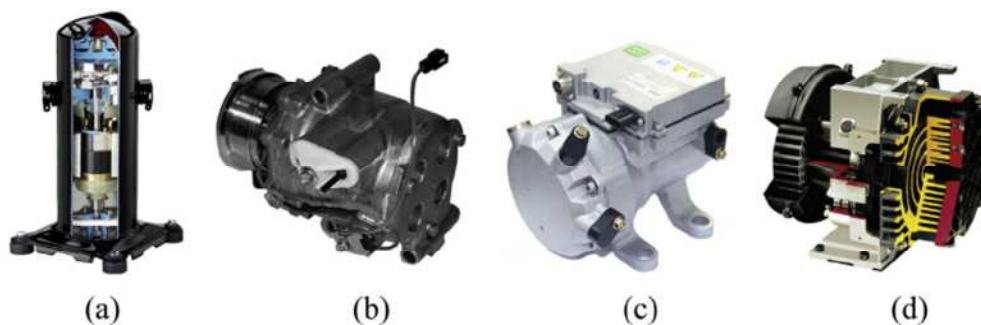


**Figure 2-5: Scroll compressor types - a) hermetic refrigeration b) open drive automotive A/C c) semi-hermetic automotive A/C, and d) air compressor. (Source: [72])**

Figure 2-5 (a) illustrates a hermetic scroll compressor that is used in commercial and residential refrigeration and air conditioning applications. Hermetic compressors come in different sizes, offering a wide range of power and cooling capacities. In this type, the compressor and motor are installed on a common shaft and enclosed in a gas-tight welded container that cannot be opened [72, 78]. The open-drive compressor shown in Figure 2-5 (b) is used widely in automotive air-conditioning systems. It consists of the compressor and an external clutch that engages and disengages the

power transmission [72]. Unlike other compressor types, the motor in this type is external and driven by the automotive engine shaft through either direct coupling or belt and pulley [79]. Figure 2-5 (c) shows the semi-hermetic type, also referred to as the serviceable hermetic type. In this type, the compressor and the motor are installed on a common shaft, similar to the hermetic type [78]. However, unlike the hermetic type, the semi-hermetic compressor is bolted. Therefore, its internal parts are accessible offering the advantage of being serviceable. Furthermore, they are more compact and lighter in weight [80]. Finally, Figure 2-5 (d) illustrates an open drive oil-less air compressor that is used in industrial applications, and externally driven, similar to the open drive automotive air conditioning compressor.

Recent ORC literature is very rich in experimental and theoretical investigations on scroll expanders in relation to ORCs and with different working fluids. Song et al. [72] presented an extensive review of scroll expanders utilising ORCs for low-grade heat recovery. The study gives insights into relevant work covering various aspects, such as performance, technical features, simulation techniques and applications.

Jradi and Riffat [81] and Jradi et al. [82] experimentally investigated a low cost, compact electrical scroll expander of 1 kW electrical capacity. The expander was modified from an automotive A/C compressor in a micro-scale ORC, based on a tri-generation system in [81] and on a micro-CHP in [82]. This ORC system employed environmentally friendly HFE7100 as the working fluid. The reported ORC thermal efficiency was 5.64% and the maximum electric power extracted from the expander was 500W. The reported isentropic efficiency of the expander was in the range of 74.2% to 81%.

Further to the above, Mathias et al. [38] tested a hermetic refrigeration scroll and rotary piston gerotor expanders in a low-

grade heat ORC experimental set-up, employing R123 as the working fluid. The results obtained indicate that both types are suitable for ORC applications. The scroll expander yielded 2.96 kW with an isentropic efficiency of 83%, while the gerotor yielded 2.07 kW with 85% isentropic efficiency.

Moreover, Tarique [83] and Tarique et al. [84] investigated the performance of scroll expanders in an ORC employing R134a as the working fluid. At optimum operation, when the heat source was at 120°C, isentropic efficiency was found to be in the range of 50% to 64%. The maximum power output obtained was 920W, with a thermal efficiency of 8.5% [84].

Li et al. [85] also examined a scroll expander in a laboratory test bench ORC. The system was evaluated employing R245fa and a mixture of R245fa and R601a. R245fa showed thermal efficiency of 4.38% with a scroll expander isentropic efficiency of 71% to 82%, while R245fa/R601a achieved 4.45% thermal efficiency, with an isentropic efficiency ranging from 72.5% to 83.3%. The maximum power output reported was 550W.

### 2.3.7 Applications

ORC applications are based on their heat sources. These applications mainly include biomass, solar, geothermal, and waste heat, including industrial and engine exhausts. The variation of ORC applications along the heat source temperature range is demonstrated in Figure 2-6.



**Figure 2-6: Variation of heat source temperatures in different ORC applications. (Source: [86])**

Several scientific reviews have been conducted to provide up-to-date insights into the current status of ORC technologies, covering various aspects and applications. These investigations have observed similar approaches and are shown to be in agreement. For example, Tchanche et al. [36] reviewed existing applications of ORC and analysed their maturity; Vélez et al. [43] reviewed the current technical, economical and market aspects of ORC in different applications, and Quoilin et al. [41, 71] present a technological and economic survey of the current status of ORCs. These studies discussed ORC applications found in the literature, listing the commercially available ORC systems. However, Tchanche et al. [36] indicated that, geothermal and biomass CHP ORC technologies are already mature, while waste heat recovery ORC systems can expect rapid growth in the near future. Solar ORC systems are being intensely investigated on a smaller scale and large plants are also expected for tropical regions in the future, while Vélez et al. [43] indicated that all applications of ORC are still considered under investigation. However, commercial and experimental systems have grown rapidly. Both Quoilin et al. [41, 71] and Vélez et al. [43] present current commercial ORC distribution per application, as shown in Figure 2-7. The distribution depicted points out the availability of ORCs in the range from kW to several MW and indicates the maturity of ORCs in waste heat recovery, biomass and geothermal application.

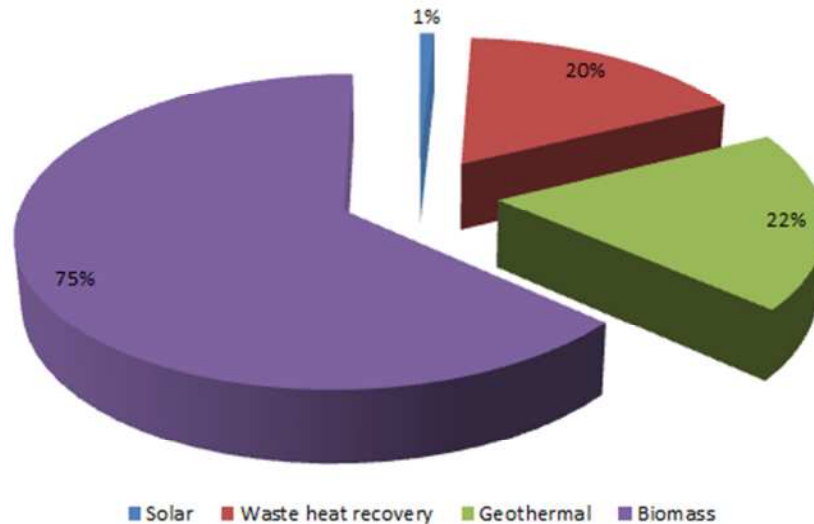


**Figure 2-7: Market share of each ORC application in terms of the number of units. (Source:[41])**

In a different approach, Schuster et al. [87] exclusively reviewed state-of-the-art ORC systems in micro-CHP, biomass, geothermal, solar, and waste heat recovery, while Wong et al. [70] concentrated on waste heat recovery, specifically from internal combustion engine exhausts in automotive applications. The above study reviewed related research developments including various working fluids, configurations and expanders. It also indicates that the main drawback in the application consists of lower efficiency due to lower exhaust temperature and the size of the ORC components to be accommodated, which are rather large.

### 2.3.8 Novel ORC Designs

Besides the commonly studied simple and regenerative configurations, several designs for various applications may be found in the literature. Carcasci and Miliotti [88] theoretically investigated an ORC bottoming cycle in low-medium waste heat recovery from gas turbine power plants, using four dry working fluids, toluene, benzene, cyclopentane and cydhexane. The system incorporated an oil loop to transfer heat to the refrigerant loop, as shown in Figure 2-8. The oil loop was incorporated for safety, in order to avoid explosions resulting from the high flammability of the

selected working fluids. However, the system was simulated at temperatures ranging from 360°C to 400°C.

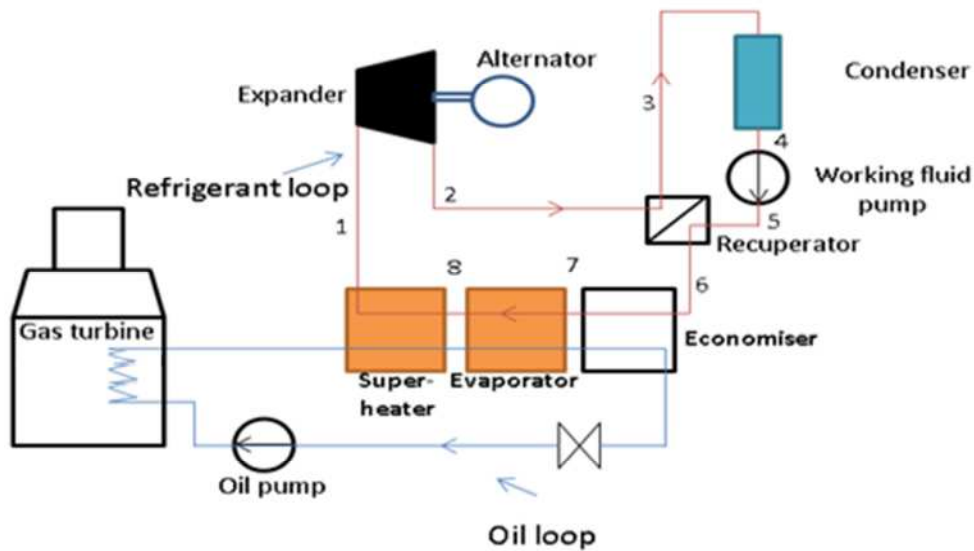


**Figure 2-8: Gas turbine waste heat ORC system reproduced from reference [88].**

As shown in the schematic of the system in Figure 2-8, the hot exhaust from the gas turbine plant heats the oil entering the super-heater, evaporator and economiser, in order for it to heat the working fluid flowing in a counter-direction in the refrigerant loop. The heated working fluid enters the expander and passes through the recuperator, exchanging heat with the condensed working fluid. However, the working fluid finally enters the condenser to be cooled down before it is pressurised by the pump, again. The analysis showed that only cyclohexane requires the super-heater heat exchangers, while other working fluids perform best without the super-heater. However, Carcasci and Miliotti [88] recommends cyclohexane for low temperatures, benzene for medium temperatures and toluene for high temperatures.

Shu et al. [45] propose a novel dual loop organic Rankine cycle consisting of a high temperature loop and a low temperature loop for waste heat recovery from the exhaust, engine coolant and residue from the hot temperature loop. The high temperature loop employs water as the working fluid in a steam Rankine cycle, while the low temperature loop employs a range of different working

fluids in an ORC. Figure 2-9 shows a schematic of the proposed system.

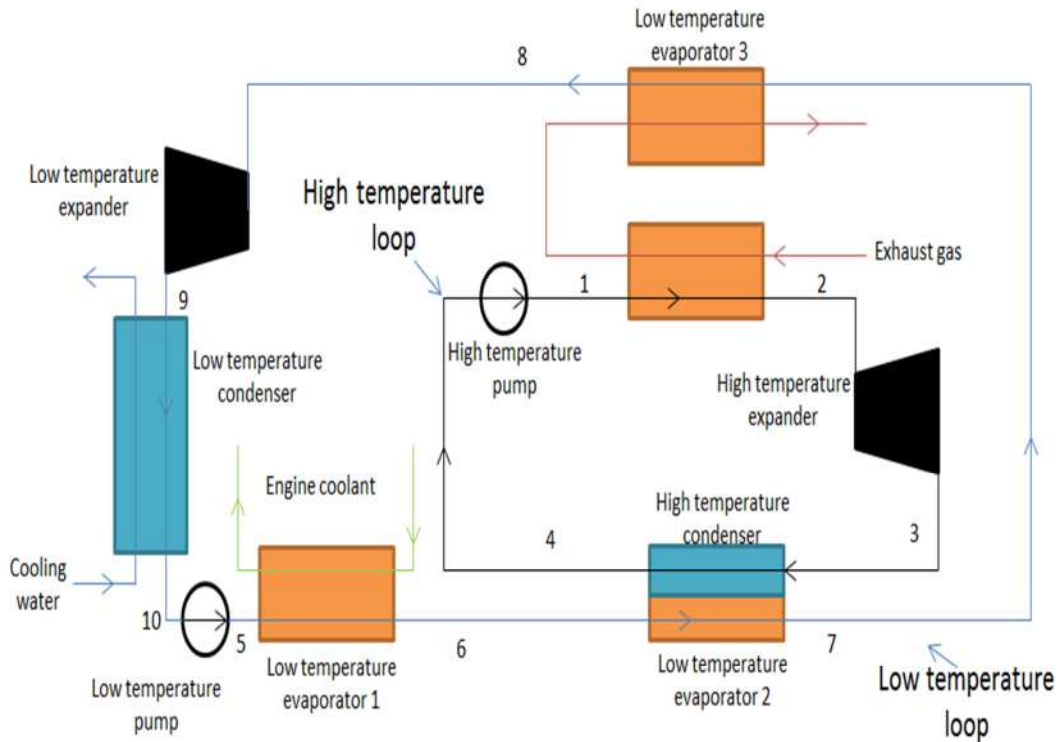


**Figure 2-9: Dual loop waste heat ORC system reproduced from reference [45].**

In this configuration and in order to obtain greater thermal efficiency, the super-heating for the high temperature loop should be maximised but this would be avoided in the low temperature loop, which employs either a dry or isentropic working fluid. The high pressure liquid water at state Point 1 flows into the evaporator to be heated and super-heated by the counter-exhaust stream. The high pressure steam vapour exits at state Point 2 and expands to low pressure through the high temperature expander. The low pressure vapour at state Point 4 passes through the condenser and transfers heat to the working fluid in the low temperature loop. The water vapour then condenses and exits at Point 4, before being pumped to high pressure and the high temperature loop being completed. In the low temperature loop, the high pressure working fluid at state Point 5 is heated by the engine coolant in the first evaporator and exits at state Point 6, before being further heated by the counter-stream of hotter water in the second evaporator and

exiting at state Point 7, and by the residual heat from the exhaust in the third evaporator, before exiting at state Point 8, where it is directed towards the low temperature expander. After expansion, the low pressure vapour at state Point 9 enters the condenser, which is cooled with water so that it exits in a liquid state at state Point 10. It is then pumped again to a higher pressure, where the cycle is completed.

Moreover, Manolakos et al. [89, 90] propose a low temperature solar-driven ORC employing R134a as the working fluid, and incorporating a reverse osmosis sea water desalination system. Figure 2-10 shows a schematic of the proposed system.

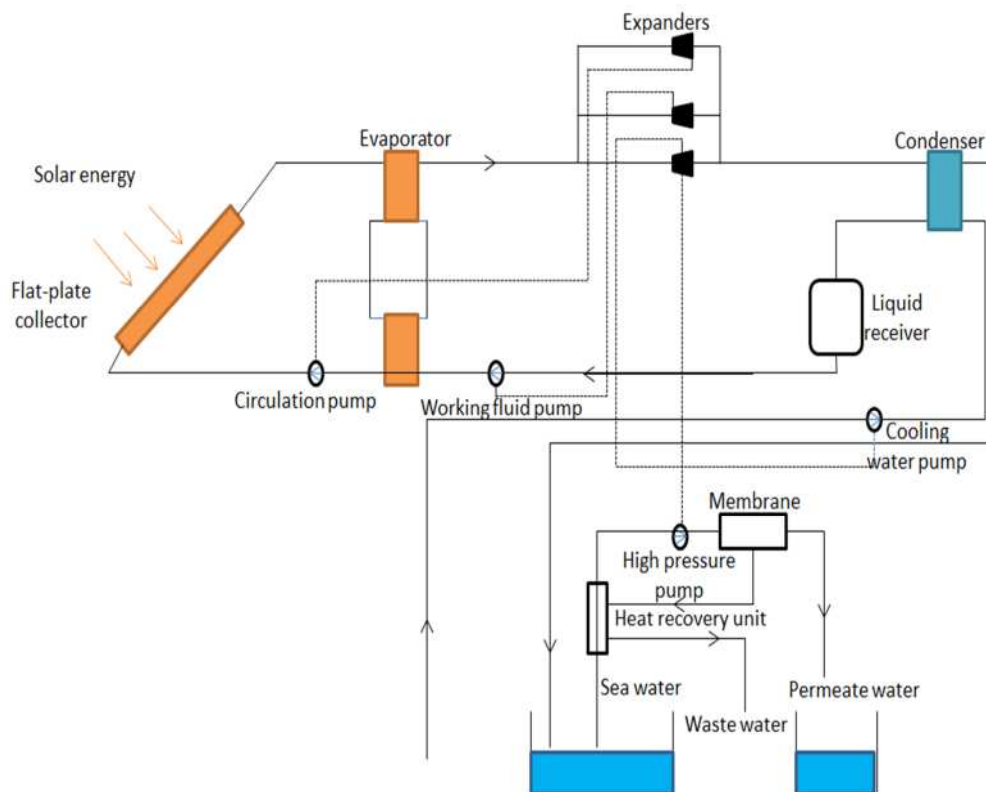


**Figure 2-10: Solar ORC with reverse osmosis desalination reproduced from reference [89].**

The thermal energy produced by the solar collectors is used to evaporate and super-heat the R134a working fluid in the evaporator heat exchanger at 71.7°C and 75°C, respectively. The super-heated R134a vapour drives the expanders and the power output yielded is

used to drive the system pumps, including the desalination unit's high pressure water pump. However, the low pressure vapour at the expander exit is directed towards the condenser, where it is cooled and exits in a liquid state at 35°C, before being pressurised again and directed to the solar collector to complete the cycle. The system was evaluated both theoretically and experimentally. The results show a maximum system efficiency of 4%, expander isentropic efficiency of 65%, and a maximum power output of 2.05 kW.

## 2.4 The Super-critical Rankine cycle (SRC)

Super-critical (SRC) and trans-critical (TRC) Rankine cycles are Rankine cycle derivatives that are used in low-grade heat recovery applications. The vast majority of studies seen in the literature refer to either cycle simply as SRC. In general, nearly all SRC and TRC research, particularly in the investigation of CO<sub>2</sub> as a working fluid, are still in their theoretical phase. However, these studies cover a wide range of applications and have been carried out for the sake of evaluating the performance and feasibility of CO<sub>2</sub> SRC and TRC, proposing novel CO<sub>2</sub> SRC and TRC systems for different applications, in order to improve overall performance, to investigate alternative working fluids performance in comparison to CO<sub>2</sub>, and to compare SRC and TRC performance to that of an organic Rankine cycle (ORC). This section provides a comprehensive review of SRCs and TRCs from the perspective of CO<sub>2</sub> as a working fluid.

### 2.4.1 Principle of operation

The general concept of both cycles is to employ refrigerants with relatively lower critical temperatures and pressures in order to allow operation above the critical point and bypass the two-phase region in the heat addition process [42]. Therefore, the heat addition process takes place non-isothermally, allowing improved thermal match with the heat source temperature glide, the reduction of irreversibility, the avoidance of pinch limitation [91], and optimal thermal efficiency to be gained, with the highest power output

possible [92]. Figure 2-11 shows the heat addition process in both an ORC and an SRC. The isothermal heat addition process causes a mismatch between the working fluid and the gliding temperature of the heat source; it also incites irreversible destruction in the heat addition process.

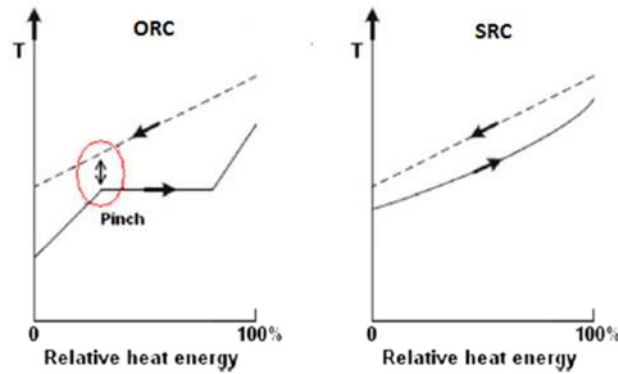


**Figure 2-11: Temperature variation in the heat addition process for an ORC and an SRC. (Source:[93])**

However, the difference between SRC and TRC is simply in the cooling process. In TRC, the heat rejection process takes place isothermally in the sub-critical region, where the working fluid condenses, going through the two-phase region before it is pumped to super-critical state. On the other hand, in SRC, the entire cycle processes take place above the critical point. Therefore, the cooling process in SRC also takes place non-isothermally and a good match with the heat sink is achieved [94]. Figure 2-12 illustrates the difference between SRC and TRC on the CO<sub>2</sub> T-S diagram.

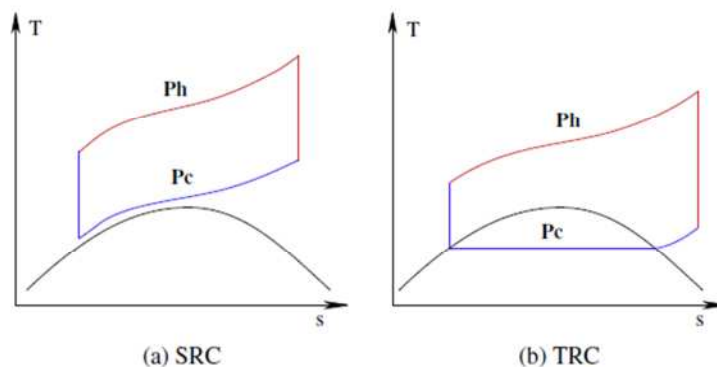


**Figure 2-12: The difference between an SRC and a TRC in the CO<sub>2</sub> T-S diagram. (Source:[94])**

### 2.4.2 Working fluids

Similar to the ORC, the selection of the working fluid is a key element in performance for both the SRC and TRC [95]. Chen et al. [42] recommended wet fluids such as CO<sub>2</sub>; ethane; R143a; R32; R23; R125; R41 and R116 for SRC applications, and indicated dry fluids may be used as well. A similar range of working fluids is seen in Guo et al. [91] and Shengjun et al. [96] comparative studies in geothermal applications. The latter study concluded that R125 constitutes the most suitable working fluid in geothermal applications. Also for geothermal applications, Vidhi et al. [97] indicate that R125 and R143a deliver the best overall performance. Meanwhile, Cayer et al. [98] recommend either CO<sub>2</sub>, ethane, or R125 for industrial waste heat recovery and Baik et al. [99] compared CO<sub>2</sub> and R125, concluding that R125 demonstrates superior performance to that of CO<sub>2</sub>. In addition, Vetter et al. [100] investigated the performance of 10 working fluids, comparing them with CO<sub>2</sub> and propane. R134a was found to have the best performance overall. On the other hand, Zhang et al. [101] concluded that CO<sub>2</sub> outperforms water, propane, ammonia, and R134a in solar applications. In an interesting study by Chen et al. [95], a zeotropic mixture of 70% R134a and 30% R32 was introduced as a working fluid for an SRC cycle and its performance compared to an ORC employing R134a. However, despite the intensive undergoing evaluation of various refrigerants in SRC applications, most of the investigated refrigerants are either subjected to be phased out, or highly flammable such as hydrocarbons. In fact, to date, CO<sub>2</sub> is the most favoured refrigerant for super-critical applications, not only for Rankine based cycles, but also for high efficiency Bryton cycles for medium and high temperature sources, such as in nuclear power and concentrated solar power applications [102-104]. Table 2.4 lists the conventional SRC refrigerants alongside their critical and environmental properties [54, 56].

**Table 2.4: Thermodynamic and environmental information for the conventional SRC refrigerants.**

Refrigerant Type	Refrigerant name	Chemical name	Molecular weight [kg/kmol]	Critical temperature [K]	Critical pressure [bar]	ODP	GWP	ASHRAE Safety group
Natural	R744	CO <sub>2</sub>	44	304.22	73.80	0	1	A1
HC	R170	Ethane	30.07	305.33	48.72	0	5.5	A3
HFC	R143a	1,1,1-Trifluoroethane	84	346.04	37.76	0	4470	A2L
HFC	R32	Difluoroethane	52	351.26	57.82	0	675	A2L
HFC	R23	Trifluoroethane	70	299.1	48.36	0	14800	A1
HFC	R125	Pentafluoroethane	120	339.33	36.29	0	3500	A1
HFC	R41	Fluoromethane	34	317.28	58.97	0	92	-
PFC	R116	Hexafluoroethane	138	293.03	30.42	0	12200	A1
Keys: A1: Non-flammable with very low toxicity. A2L: Moderate flammability and low toxicity. A3: High flammability and low toxicity.								

#### 2.4.2.1 CO<sub>2</sub> as a Working Fluid

CO<sub>2</sub> is a natural refrigerant that possesses many popular environmental and thermodynamic qualities. It was extensively used during the first decade of the 20<sup>th</sup> century, especially in marine applications. However, by the 1950s, CO<sub>2</sub> was replaced by halocarbon refrigerants [105]. In recent years, CO<sub>2</sub> has regained interest and emerged as a promising refrigerant, due to environmental concerns and conventional refrigerants [106] have been phased out. CO<sub>2</sub> is abundant in nature with 0 ODP and 1 GWP over 100 lifetimes. Moreover, it is a non-flammable, non-toxic and inexpensive substance. In addition, it has favourable thermodynamic and transport properties which are well known, even in the super-critical region [107]. On the other hand, the fundamental limitations of using CO<sub>2</sub> are the lower performance compared to other refrigerants, and the complexity of the CO<sub>2</sub> system [106]. In order to achieve condensation in TRC, operation below the critical temperature is required which introduces technical challenges with regard to designing the cooling system. On the

other hand, for both SRC and TRC, the operation above the relatively high critical pressure of CO<sub>2</sub> raises safety concerns and introduces a technical challenge related to design system equipment that could stand such a high operation pressure [42, 91, 94].

## 2.5 CO<sub>2</sub> SRC and TRC Performance and Design

Chen et al. [92] expressed the potential of CO<sub>2</sub> TRC over ORCs as a bottoming cycle in their comparative study between regenerative R123 ORC and CO<sub>2</sub> TRC. The CO<sub>2</sub> TRC showed no pinch limitation and achieved slightly higher output of 8.16 kW, but lower thermal efficiency of 9.2%. Conversely, Guo et al.[108] conducted a thermodynamic and techno-economic comparison between a CO<sub>2</sub> TRC and an R245fa ORC in geothermal applications, in order to determine the maximum net thermal power output with the minimum investment. The results show that the CO<sub>2</sub> TRC achieved the best net thermal power output but at very high pressure in comparison with the ORC. On the other hand, the ORC achieved the best thermal efficiency.

Detailed theoretical studies using several evaluation parameters, such as the first and the second thermodynamic laws efficiencies, net thermal power output, heat exchanger sizes and economic parameters are also present in the literature for the purpose of evaluating and assessing the feasibility of CO<sub>2</sub> SRCs and TRCs, investigating alternative working fluid performance in comparison to CO<sub>2</sub> and comparing the performance of SRCs and TRCs with that of the ORC. Cayer et al. [107] have expressed the potential of CO<sub>2</sub> TRC for heat recovery from low-grade industrial waste heat and carried out a detailed analysis on simple and regenerative configurations of CO<sub>2</sub> TRC using four evaluation parameters. The same authors [98] extended their analysis to a simple TRC configuration and compared the performances of CO<sub>2</sub>, ethane and R125. The study applied six performance evaluation parameters. The comparison showed that R125 achieved the best thermal

efficiency, followed by ethane, and finally CO<sub>2</sub> which is close behind ethane, but at higher pressure. For the net thermal power output, ethane achieved the best net thermal power output, followed by CO<sub>2</sub> and finally, R125. The study concluded that none of the working fluids compared outperformed the others; instead, each system had its own qualities. Furthermore, from an economic point of view, there was an optimum operating point, where the most profitable net thermal power output could be achieved at minimum capital cost. The reported specific net thermal power output and thermal efficiency for CO<sub>2</sub> were 19 kJ/kg and 8.6% respectively.

In a similar approach, Guo et al. [91], favoured R125 over CO<sub>2</sub> in their comparison of a range of working fluids. However, the study indicates that despite the qualities offered by CO<sub>2</sub> as a working fluid, the feasibility of the CO<sub>2</sub> system would mainly rely on the availability and cost of high pressure equipment. The latter opinion corresponds well with the conclusions reached by Vélez et al. [93], who evaluated the performance of simple and regenerative CO<sub>2</sub> TRC for industrial waste heat recovery and reported 6.4% to 9.8% thermal efficiency and 12.6 to 18 kJ/kg specific net thermal power output.

In a different approach, Baik et al. [99] carried out a power based comparison between simple CO<sub>2</sub> and R125 TRCs. The study took into account pressure drop and heat transfer in heat exchangers and concluded that CO<sub>2</sub> showed better pressure drops and heat transfer characteristics but R125 outperformed CO<sub>2</sub> by 14% when the net thermal power output was compared. The reason the CO<sub>2</sub> cycle demonstrated lower power output is mainly due to the large energy input required for the pumping process. However, the reported thermal efficiency and net thermal power output for CO<sub>2</sub> were 8.74% and 17.77 kW respectively.

With regard to system optimisation taking into account different performance evaluation parameters, studies in references [93, 96,

98, 107, 109] indicate that it is impossible to simultaneously optimise all performance evaluation parameters. Instead, there is the option of either trading off or compromising. Moreover, the selection of working fluid will influence the improvement of the selected performance parameter [96]. However, in the context of free heat sources, studies in references [92-94, 98, 99, 107, 110], the aim is to maximise the net thermal power output over thermal efficiency in particular and over other evaluation parameters in general. On the other hand, the reviewed studies in references [96, 109] aim to minimise system cost at the expense of other performance parameters.

Comparing simple and regenerative SRC and TRC configurations, the reviewed studies in references [107, 109, 111] confirm that incorporating a recuperator heat exchanger will marginally improve the system's thermal efficiency and reduce the heater's operating pressure at which maximum thermal efficiency is achieved. However, it does not have any effect on the net thermal power output of the system. Also with the relatively high pressure of CO<sub>2</sub>, studies in references [92, 96, 108] indicated that the CO<sub>2</sub> system would be more compact, with a smaller turbine than is the case with an ORC. This mainly relates to the low specific volume of CO<sub>2</sub> at the expander inlet and the small volumetric expansion ratio in the turbine; a favourable feature, despite lower thermal efficiency, than is the case with other working fluids [96]. Figure 2-13 shows a compact 10 MW CO<sub>2</sub> SRC turbine, compared with a steam turbine.

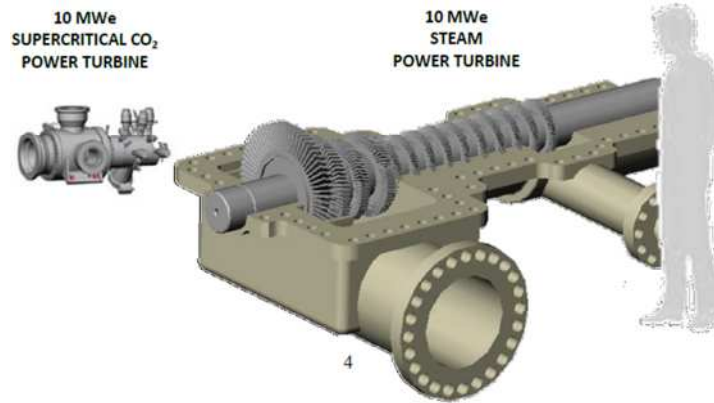


**Figure 2-13: 10 MW CO<sub>2</sub> SRC turbine compared to an equivalent steam turbine.(Source: [112])**

However, for the CO<sub>2</sub> heat transfer surface area, Guo et al. [108] indicate that a greater heat transfer surface area is required for the CO<sub>2</sub> heat exchangers than is seen with ORCs, based on the UA value and the heat transfer coefficient of the CO<sub>2</sub>.

### 2.5.1 Novel CO<sub>2</sub> SRC and TRC Designs

This section presents an up-to-date review of theoretical and experimental studies carried out on CO<sub>2</sub> SRCs and TRCs. For industrial waste heat recovery, Tuo [109] compared a regenerative CO<sub>2</sub> TRC with a proposed regenerative CO<sub>2</sub> TRC with two stage expansion and reheating processes, similar to those seen in water steam Rankine cycles. The aim of the above study was to achieve the best performance possible at minimum cost. Figure 2-14 shows a schematic diagram of the CO<sub>2</sub> TRC re-heating system. The CO<sub>2</sub> is expanded to intermediate pressure at state point 4 and then reheated to the maximum turbine inlet temperature at state point 6, so that it can be expanded through the second stage expander. Thus, overall performance of the CO<sub>2</sub> TRC system can be improved. Nevertheless, the study identifies the optimum operating conditions from a thermodynamic point of view as 84 bar for the CO<sub>2</sub> heater and 57 bar for the CO<sub>2</sub> cooler heat exchangers, concluding that optimum operating conditions are significantly lower from an economic perspective, in order to prove the practicability of the system. This is due to the fact that the pump and turbine are dominant expenses among the cycle components and their cost will

increase significantly as the pressure increases. However, the study reported thermal efficiency and specific net thermal power output of 8.74%, and 17.77 kJ/kg, respectively.

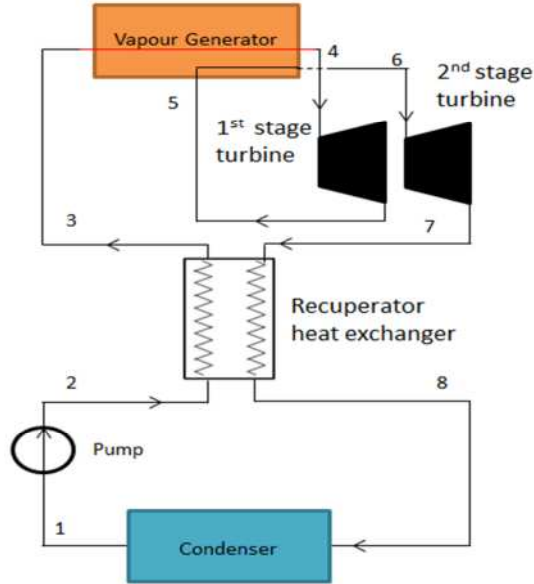


**Figure 2-14: CO<sub>2</sub> TRC with reheating and two-stage expansion reproduced from reference [109].**

For geothermal applications, Li et al. [94] proposed a regenerative CO<sub>2</sub> SRC and TRC, incorporating an ejector as shown in Figure 2-15, in order to maximise the net thermal power output. The study compared the proposed systems with equivalent systems without ejectors.

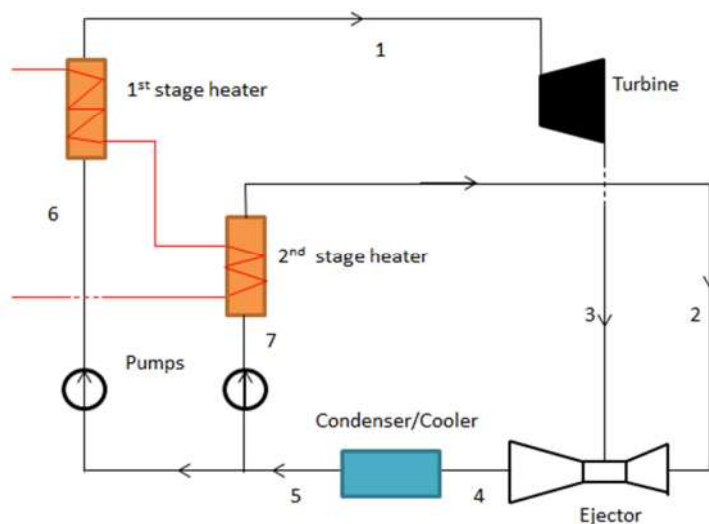


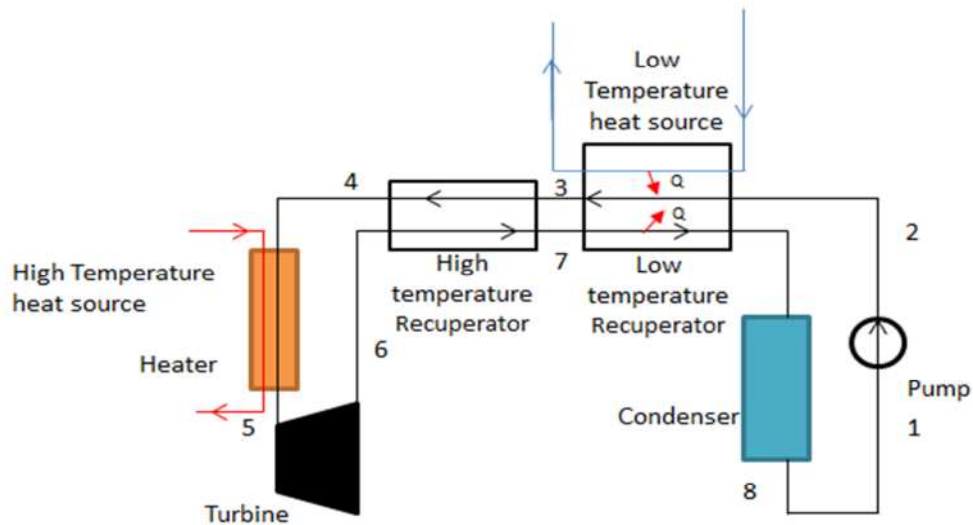
**Figure 2-15: CO<sub>2</sub> SRC or TRC with an ejector reproduced from reference [94].**

As shown in Figure 2-15, the SRC and TRC with an ejector incorporate a second stage heater. The liquid from the second stage heater at state point 2 is used as the primary fluid in the ejector to drag the turbine outlet exhaust at state point 3. Therefore, the turbine inlet pressures decreases and the differential pressure across the turbine increases. As shown in the study's results listed in Table 2.5, the best net thermal power output was achieved in this case by the SRC with an ejector, followed by the TRC with an ejector, then the SRC and finally, the TRC. The results also show that the net thermal power output improved by incorporating the ejector was at the expense of the thermal efficiency, where the TRC showed the best thermal efficiency, followed by the SRC, then the SRC with an ejector, and finally, the TRC with an ejector.

**Table 2.5: Theoretical performance of CO<sub>2</sub> SRC and TRC with ejector. (Source: [94])**

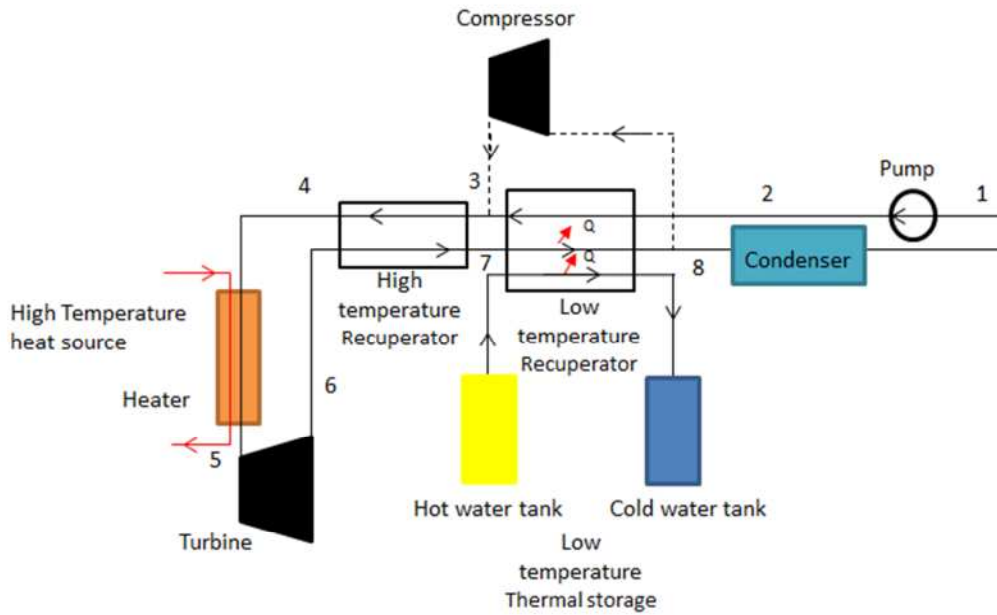
Cycle type	Pressure [bar]	Temperature [°C]	System thermal efficiency [%]	Net thermal power output [kW]
TRC	122.91	60-90	8.19	9.25
SRC	128.58		7.88	9.45
TRC/ejector	124.74		6.23	10.19
SRC/ejector	131.34		6.30	10.32

In a similar approach designed to maximise the net thermal power output, Kim et al. [110] proposed and compared several configurations of a CO<sub>2</sub> TRC and SRC, simultaneously using high and low temperature heat sources for applications like concentrated solar power, combustion, and nuclear power. The configurations studied had adopted both the Rankine and Bryton cycle concepts. Figure 2-16 shows the proposed CO<sub>2</sub> TRC simultaneously using both low and high temperature heat sources and incorporating recuperator heat exchangers for each heat source.



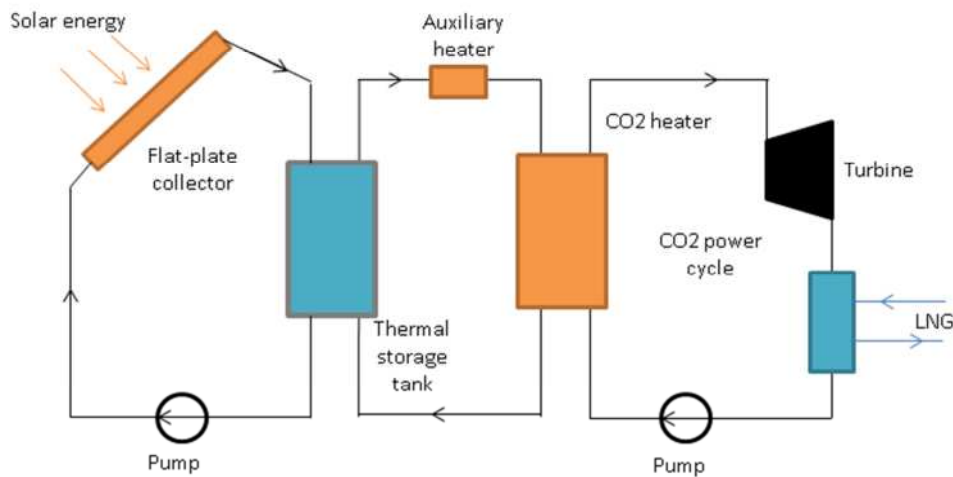
**Figure 2-16: Low/high heat source CO<sub>2</sub> TRC reproduced from reference [110].**

Figure 2-17 shows a proposed system for nuclear plants. The system operates as a TRC during the day and as an SRC Bryton cycle during the night, when the power demand is low. The study concludes that a CO<sub>2</sub> SRC cycle will always have better thermal efficiency than a CO<sub>2</sub> TRC for temperatures lower than 120°C. However, incorporating another low temperature heat source, besides the main high temperature heat source will compensate the difference in CO<sub>2</sub> heat capacity between the low and high temperature sides, which will increase TRC thermal efficiency and makes it more effective than the SRC.



**Figure 2-17: Low/high heat source CO<sub>2</sub> TRC incorporated with a CO<sub>2</sub> Bryton cycle reproduced from reference [110].**

Song et al. [113] proposed a solar driven CO<sub>2</sub> TRC using a liquefied natural gas evaporation system as the heat sink. Figure 2-18 illustrates the proposed system, which consists of two loops: the solar collector loop, comprising the flat plate collector, the thermal storage tank, and the auxiliary heater. The purpose of thermal storage is to compensate the energy required in case of solar energy destruction, while the auxiliary heater provides a backup energy source to maintain the thermal storage temperature supply at a defined reference temperature when needed. The other loop is a simple CO<sub>2</sub> TRC system made of conventional components.



**Figure 2-18: Solar CO<sub>2</sub> TRC with LNG cooling and thermal storage reproduced from reference [113].**

The simulation results show that solar radiation is the main influence on the net thermal power output of the system. In addition, the system shows the capability of producing energy during the night, utilising energy from the thermal storage tank. However, system performance is significantly influenced by the condenser temperature, unlike the turbine inlet temperature. The study reported 8.45 kW for the net thermal power output and 8.48% for the thermal efficiency.

The absence of experimental studies was noted in the literature reviewed, aside from a detailed series of theoretical and experimental studies conducted by Zhang et al. [101, 114-119] and Yamaguchi et al. [120] on their proposed solar-driven, combined power and heat CO<sub>2</sub> SRC cycle, shown in Figure 2-19.

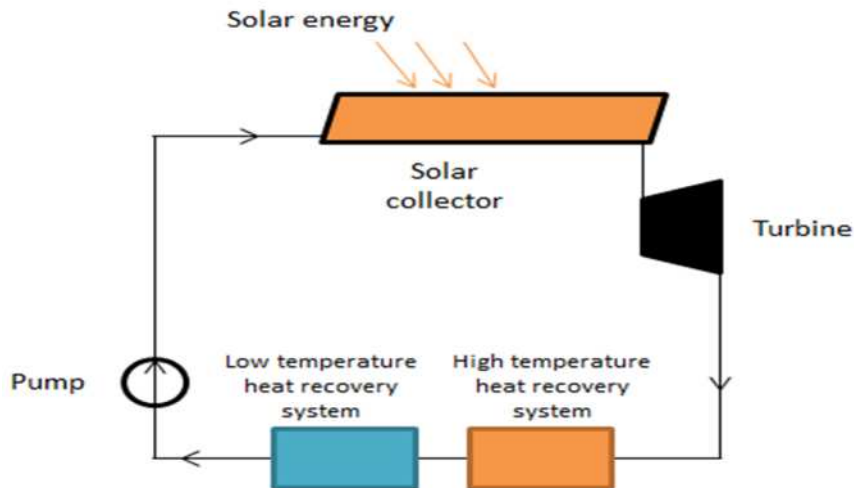


**Figure 2-19: Solar SRC system for combined heat and power reproduced from reference [120].**

As illustrated in Figure 2-19, this system consists of a solar collector of an evacuated type to heat high pressure CO<sub>2</sub> flow in the collector's channels. The super-critical CO<sub>2</sub> then expands through the turbine to produce the system power output. The super-critical CO<sub>2</sub> at the expander exit will still be in a super-heated state and could be utilised as a heat source for an absorption refrigeration system in a high temperature heat recovery system and for a hot water supply in a low temperature heat recovery system, before it is cooled to be pumped again to a higher pressure. However, Zhang et al. [101, 114, 116] carried out detailed theoretical analysis on the proposed system, and experimentally evaluated the system performance throughout the year. The results show a solar collection efficiency of 65% to 70%. The system efficiency obtained was 8.78% to 9.45%, compared to the theoretically calculated values of 10.7 to 11.6 [118]. However it was reported that pump power consumption was not considered in the efficiency calculation, due to the high power consumption of 220W observed while running the system.

It is very important to underline that in all the experiments conducted, the authors used an expansion valve to expand the CO<sub>2</sub>, instead of a turbine, because of the absence of a turbine that

could handle super-critical CO<sub>2</sub> when the studies were conducted. In addition, power generation is assumed to be equal to throttling loss through the expansion valve. This does not represent the real power output, which could be obtained where a real turbine is used. Finally, the studies expressed the potential for system enhancement by replacing the pump with a more efficient one and incorporating a real turbine.

## 2.6 Absorption power Generation cycle

In the literature, most of the studies related to absorption power generation are still in their theoretical phase apart from the well-established Kalina technology. However, these researches mainly focused on proposing either Kalina or Rankine based cycles for low-grade heat recovery in various applications, introducing novel combined power generation and refrigeration cycles, conducting performance evaluations and parametric investigations in order to increase the proposed systems performance.

### 2.6.1 Principle of operation

Absorption power cycles are based on employing binary mixtures as the working fluid. The key objective of the cycle is to allow good exploitation of low-grade heat sources by taking advantage of the mixture heat transfer characteristics where the heat transfer occurs at variable temperatures while at constant pressure [121]. The non-isothermal heat transfer processes allows better temperature glide and match between the cycle and the heat source and sink during the heat addition and heat rejection processes respectively. It therefore avoids the pinch limitation that is usually associated with the Rankine cycle, and reduces exergy destruction in the heat exchangers [107, 122]. Figure 2-20 depicts the difference between the isothermal and non-isothermal heat addition process shown for the ORC, the binary mixture absorption cycle and the SRC respectively.

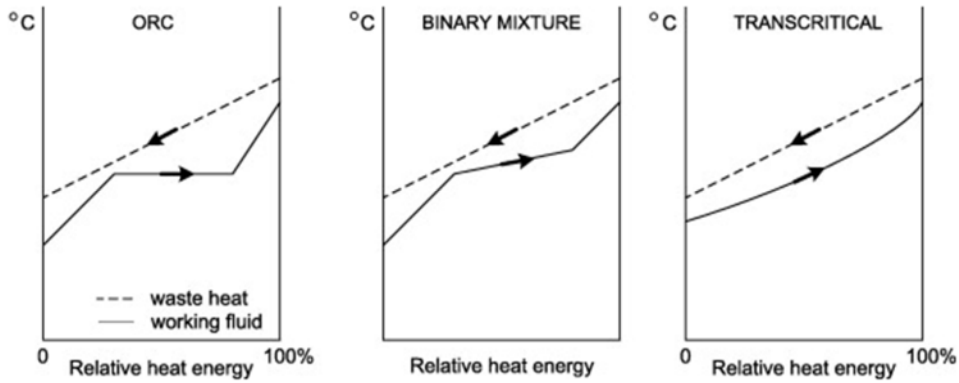


**Figure 2-20: Temperature variation in the heat addition process for ORC, Binary fluid in an absorption cycle, SRC. (Source:[107])**

### 2.6.2 Working fluids

A binary working fluid consists of a refrigerant and an absorbent that behaves like a new fluid altogether [35]. The general requirements for the binary mixture are that in the liquid phase, the mixture must exhibit good miscibility within the cycle operating temperatures and pressures. It also should have favourable transport properties such as viscosity, conductivity and diffusion coefficient that can enhance the heat and mass transfer processes. The difference between the boiling temperature of the pure refrigerant and the mixture at the same pressure should also be as high as possible. In addition, the mixture should be chemically stable, non-corrosive, environmentally friendly, non-toxic, and non-flammable. The refrigerant component of the mixture should have high heat of vaporisation and high solubility in the absorbent component in order to maintain low circulation ratios between the generator and the absorber heat exchangers and therefore achieve lower mass flow rates [123].

Ammonia-water and water-lithium bromide mixtures are the commonly used mixtures where water is the absorbent and ammonia is the refrigerant in the ammonia-water absorption system and water is the refrigerant while lithium bromide is the absorbent in the water-lithium bromide system. However, due to the large specific volume of water and freezing issues, water is not suitable as a refrigerant for low temperature applications [124].

Instead, ammonia-water mixture is the most used working fluid because of its suitability for the combined power and cooling generation application.

Beside the known qualities of water as working fluid, ammonia is widely available, inexpensive, except for its toxicity and flammability. However, the ammonia-water mixture has excellent thermo-physical properties that can be altered throughout the cycle by varying ammonia concentrations [125]. Figure 2-21 shows the ammonia concentration variation with respect to temperature on the ammonia-water phase diagram.

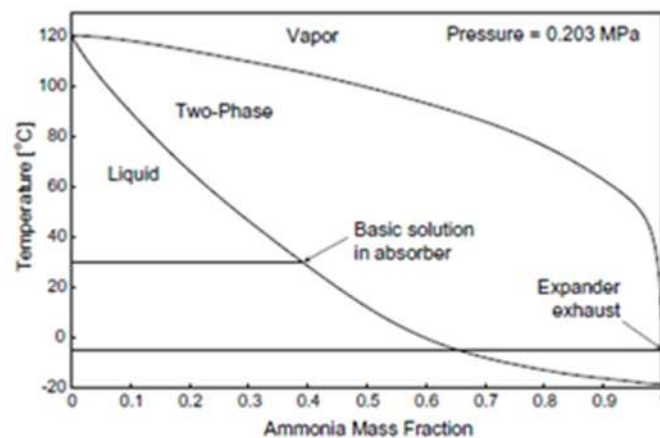


**Figure 2-21: Ammonia-water phase diagram. (Source:[126])**

Other binary pairs were also theoretically evaluated for absorption refrigeration, combined vapour absorption and compression refrigeration applications. These binary pairs consist of HFCs employed as refrigerants and chemicals or alcohols as absorbents [127].

### 2.6.3 Design and performance of Absorption Power Generation Systems

The first known absorption based power cycle was introduced by Maloney and Robertson [128] in the early 1950's. The cycle shown in Figure 2-22 employed ammonia-water as the working fluid and introduced the absorber and the distillation unit which are not used in the Rankine cycle [121]. In this system the boiler delivers a

vapour rich in ammonia through the flash tank to the super-heater. After being super-heated, the vapour expands through the turbine and produces work. The turbine exhaust reunites with the weak solution from the distillation unit and enters the absorber-condenser heat exchanger to absorb the rich vapour in ammonia and generate the basic solution. The basic solution is then pumped to higher pressure and partially heated in the recuperator heat exchanger before entering the flash tank [122]. However, the system concluded that it does not have any significant thermodynamic advantage over the conventional Rankine cycle within the examined operation conditions. Instead, the excessive expansion pressure caused exergy destruction in the condensation-absorption process that occurs at variable temperatures.

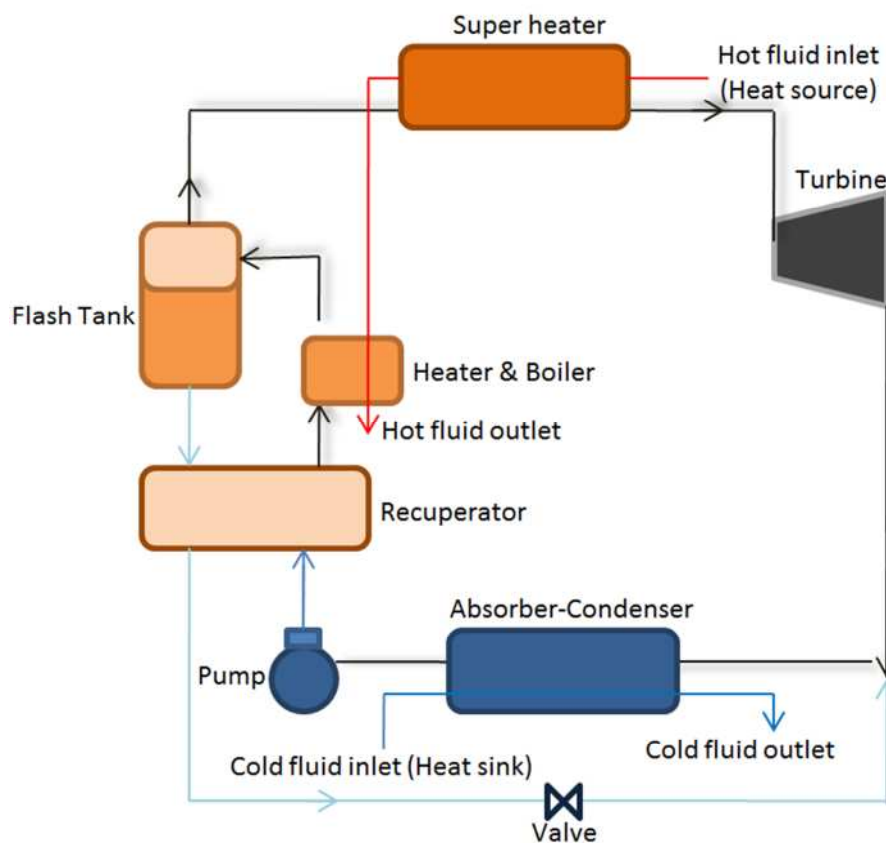


**Figure 2-22: Schematic diagram of Maloney & Robertson absorption power cycle reproduced from reference. [122]**

Kalina [129] proposed an ammonia-water absorption power cycle in the early 1980's, and claimed 1.6% to 1.9% higher thermal efficiency compared to the conventional Rankine cycle. The novelty

of Kalina's work is in adopting variable ammonia-water mixture concentrations in different parts of the cycle and replacing the condensation process with an absorption process that solved the high turbine backpressure and therefore minimised the exergy destruction in the heat rejection process. The operation of the Kalina cycle is illustrated in the cycle schematic diagram presented in Figure 2-23 where the strong vapour mixture from the flash tank is mixed with a bypass basic mixture delivered from the absorber. The mixed working fluid enters the secondary condenser which allows the distillation unit to operate at lower pressure than the vapour generator. Then, the liquid mixture is pumped to the vapour generator pressure to be pre-heated, boiled, and super-heated before it expands through the turbine. The turbine exhaust then partially heats the upcoming counter stream of basic solution on its way to the flash tank. At the exit of the recuperator, the low pressure weak solution reunites with the weak solution from the flash tank and enters the absorber where the absorption takes place at low temperatures and the basic solution is formed. On the absorber outlet, the basic solution is pumped to intermediate pressure and split into two streams. 80% of the stream recovers heat in the recuperator and enters the flash tank, and 20% bypass the flash tank to be mixed with the strong vapour going to the secondary condenser [122].

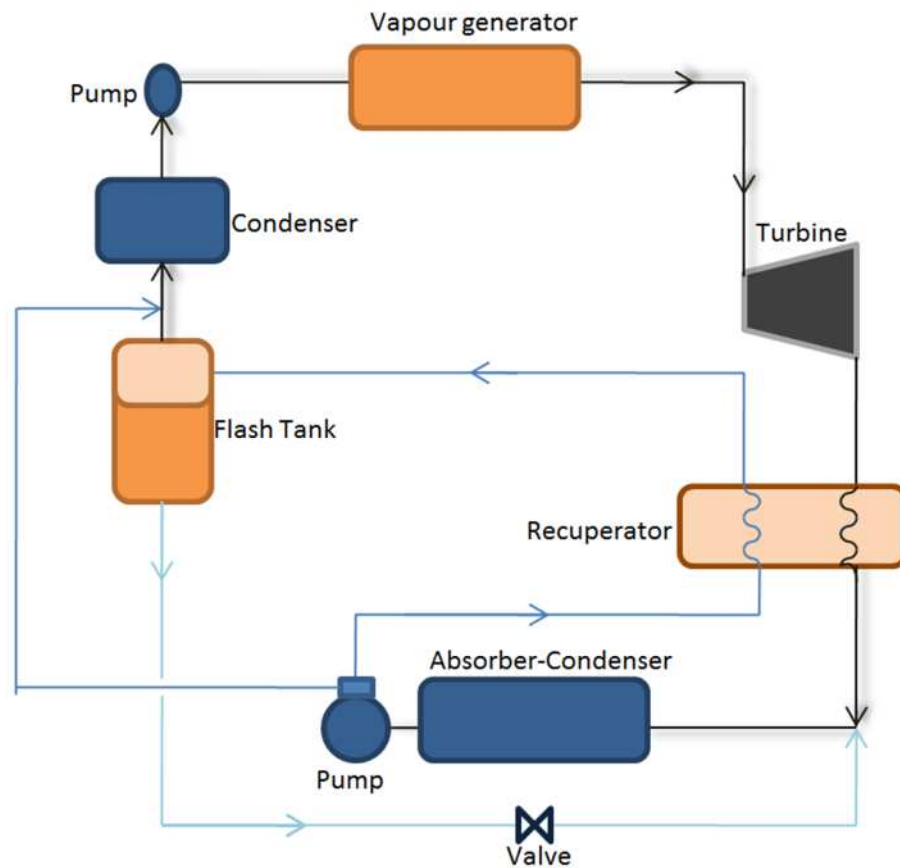


**Figure 2-23: Schematic diagram of the Kalina cycle reproduced from reference. [122]**

Appreciation of Kalina's work has renewed the interest in absorption power generation and has been the introduction of many novel power, and combined power and refrigeration systems that produce power and cooling effect simultaneously.

Based on Kalina's cycle concept, Jawahar, Raja, and Saravanan [130] proposed and parametrically analysed a combined power and cooling cycle. The study reported that the energy consumption in the proposed cycle is lower by 12% compared to separate systems of regenerative ORC and a single effect ammonia-water absorption cooling cycle. However, the reported performance for the proposed cycle was 15.64% for the thermal efficiency, 22.04 kW for the net thermal power output and 0.122 for the power to cooling ratio. For low-grade geothermal heat sources, Li et al. [131] proposed a Kalina cycle system 11 (KCS11) with an ejector that replaces the throttle valve and the absorber in the conventional KCS11. The

modifications reduced the turbine exhaust pressure, increased the power output and the system thermal efficiency. The maximum reported thermal efficiency and net thermal power output for the proposed system were 8.36% and 13.49 kW respectively, compared to 8.16% and 8.16% and 12.77 kW achieved by the conventional KCS11 system.

Based on Rankine's concept, Wang, Dai, and Gao [132] proposed a combined power and cooling absorption cycle. their theoretical evaluation revealed 20.45% thermal efficiency. For the net thermal power output, the study reported 612 kW, while the refrigeration output was 224.608 kW. Xu, Goswami, and Bhagwat [133] proposed a novel solar driven combined power and cooling cycle. The study reported a thermal efficiency of 23.54% and a total net power and cooling output of 99.23 kW. The latter cycle was further extensively analysed by Martin and Goswami [126] who studied the effectiveness of cooling production, and by Sadrameli Goswami [134] who investigated the optimum operating condition for the cycle. Furthermore, Vidal et al.[135] analysed the same cycle taking exergical approach. The reported thermal efficiency and net thermal power output were 15.3% and 52.6 kW respectively. Sun et al. [136] proposed and analysed a combined cycle that uses medium and low waste heat sources, where the medium heat source drives a Rankine based cycle, while the low temperature source in addition to the power sub-system exhaust are used to drive the refrigeration sub-system. The power consumption in the proposed cycle was shown to be lower by 17.1% compared to separate power and refrigeration systems. However, the system achieved up to 18.6% thermal efficiency and 32.6 kW net thermal power output.

#### 2.6.4 **Designs for Novel Absorption Power Generation Systems**

Mirolli [137] proposed a Kalina based system for waste heat recovery from the cement production process. As depicted in the system schematic presented in Figure 2-24, the heat source exhaust boils off and super-heats the working fluid mixture in both heat recovery vapour generators (HRVG1, 2). The super-heated vapour then expands through the backpressure turbine to be cooled and diluted with the weak solution mixture from the downstream of vapour separator/demister, allowing full condensation in the low pressure condenser (LPC). The solution is then pumped to an intermediate pressure and most of the diluted fluid is partially boiled and sent to the vapour separator/demister through heat exchangers and the rest of the solution is mixed with the high concentration vapour stream from the vapour separator/demister. The working fluid is then condensed in the high pressure condenser (HPC) and pumped through the heat recovery vapour generators. In this system, the distillation and condensation sub system (DCSS) is a key component of higher efficiency where the distillation process leans out the ammonia-water mixture in the turbine exhaust just before it enters the low pressure condenser and since a leaner mixture has a lower saturation pressure at a given temperature, the turbine exhaust stream will then condense at a lower pressure. The lower turbine exhaust pressure increases the expansion of the working fluid through the turbine, thus maximizing turbine power.

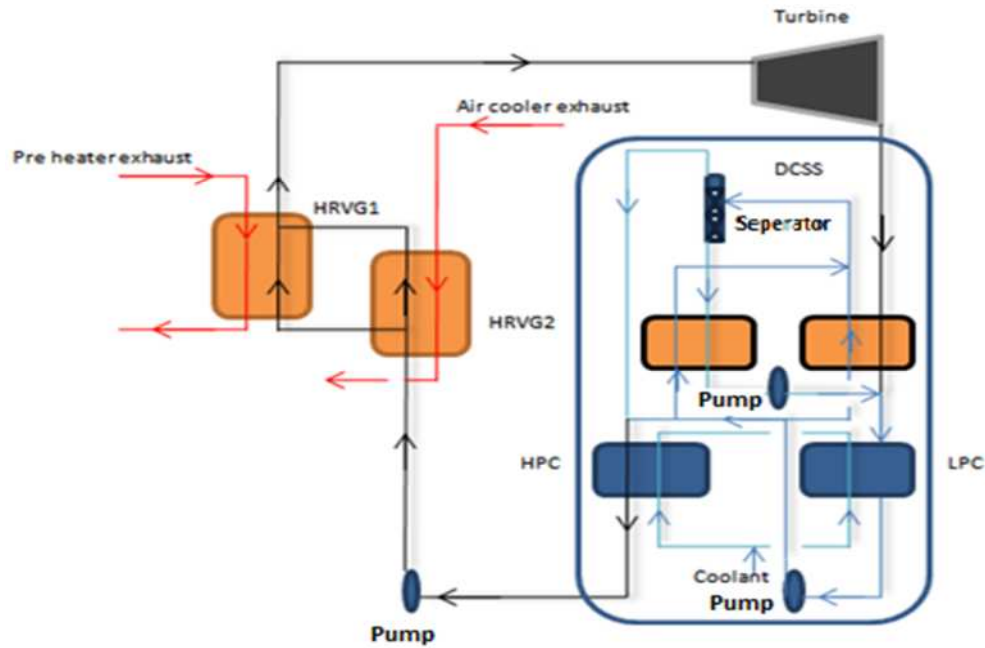


**Figure 2-24: Schematic diagram of Kalina cycle for cement production waste heat recovery reproduced from reference [137].**

Zheng et al. [138] proposed a combined power and cooling absorption cycle based on Kalina's technology and reported system thermal efficiency and net thermal power output of 24.2% and 742.28 kW respectively. To enhance the ammonia-water separation process and acquire higher purity of ammonia for refrigeration, the flash tank of the Kalina cycle was replaced by a rectifier. The proposed system also introduced a condenser and an evaporator between the second absorber and the rectifier as shown in system schematic illustrated in Figure 2-25. With introduced modifications the cycle was able to provide a cooling effect beside power, where the outflow from the top of the rectifier passes through the throttle valve before mixing with the main stream. A splitting/absorption unit is introduced in order to meet different working fluid concentration requirements, integrated with the main cycle and with an ammonia refrigeration cycle.

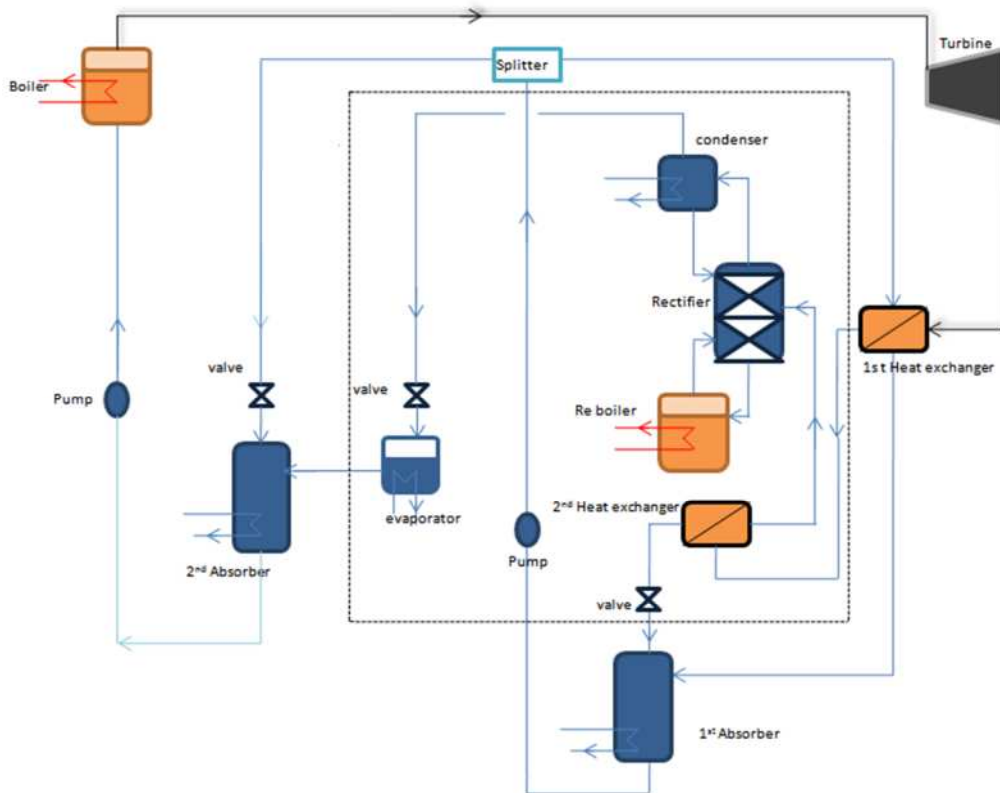


**Figure 2-25: Schematic diagram of Zheng et al's combined power and refrigeration absorption cycle reproduced from reference [138].**

Based on Rankine's principles, Zhang and Lior [125] proposed a combined cooling and power generation cycle that employs ammonia-water mixture as the working fluid. The cycle schematic presented in Figure 2-26 illustrates that the cycle operates in a parallel combined cycle mode as an ammonia-water Rankine cycle and ammonia refrigeration cycle interconnected by absorption, separation and heat transfer processes. A rectifier is introduced to split the feed into two streams, the top outflow stream is rich with ammonia and used for the refrigeration section while the bottom weak outflow is used for power generation. A condenser and a re-boiler are necessary at the top and bottom of the rectifier in order to maintain continuous heat and mass exchange in each rectifier stage. The thermodynamic analysis revealed that the system achieves thermal efficiency and net thermal power output of 27.7% and 724.8 kW respectively. Further investigations were carried out on the cycle where Zhang and Lior [139] proposed general principles for the integration of refrigeration and power systems in order to

increase both thermal and exergy efficiencies. Furthermore, the investigation carried out by Liu and Zhang[140] revealed that there is a certain split fraction for a given basic working fluid concentration at which the maximum system performance is obtained.

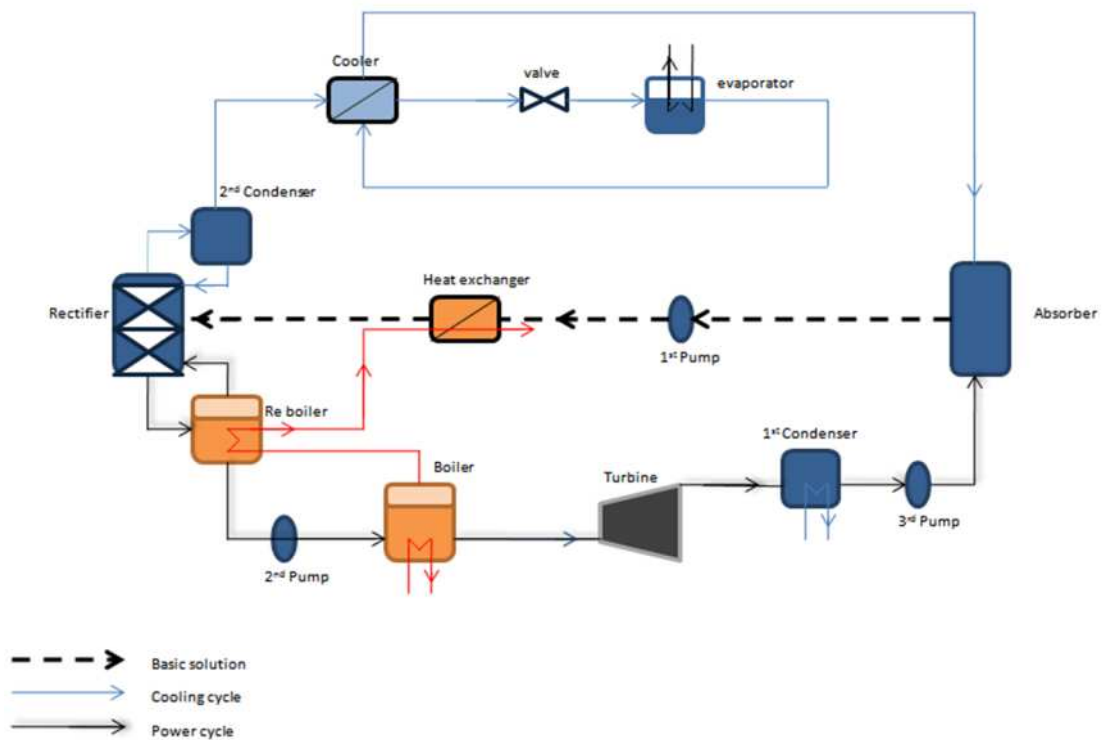


**Figure 2-26: Schematic diagram of Zhang and Lior's combined power and refrigeration absorption cycle reproduced from reference [125].**

Wang et al. [132] criticized the systems proposed in references [125, 139] for their complicity, resulting in higher capital investment, and proposed a Rankine based ammonia-water combined power and refrigeration generation cycle. The cycle eliminated the excessive pumping requirements and the secondary condensers. Further development was carried out on the system in Wang et al. [141], where the refrigeration cycle incorporated an ejector, and the power cycle incorporated an extraction turbine between the heat recovery vapour generator as illustrated in the cycle schematic presented in Figure 2-27. After expansion through the turbine, the exhaust enters the supersonic nozzle of the ejector as the primary vapour. The high velocity vapour at the exit of the nozzle produces a high vacuum at the inlet of the mixing chamber

and drags a secondary vapour from the evaporator into the chamber. After mixing, the two streams become a transient supersonic stream. After passing the constant cross section zone, the subsonic mixed stream discharges from the ejector to the condenser. A fraction of the working fluid stream leaving the condenser enters the evaporator after passing through the throttle valve where it vaporises by absorbing heat from the cooled media and therefore the cooling effect is produced. The rest of the working fluid stream from the condenser is pumped to the boiler pressure to complete the cycle. The reported thermal efficiency and net thermal power output were 14.92% and 114.098 kW respectively.

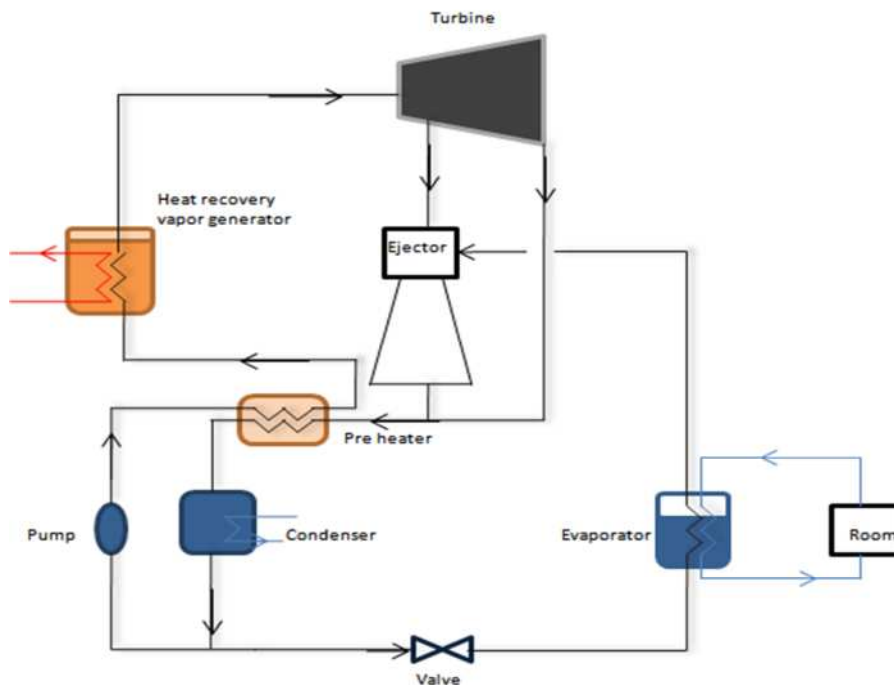


**Figure 2-27: Schematic diagram of Wang et al's combined power and refrigeration absorption cycle reproduced from reference [141].**

## 2.7 Conclusions

### 2.7.1 ORC

The review revealed the attractiveness and flexibility of ORCs for fitting different low-grade heat recovery applications. It also indicated the maturity of several ORC applications and the rapid development of the technology, in comparison with other low-grade heat recovery technologies. However, the main gap is clearly

identified as the unavailability of new working fluids that can fulfil the selection criteria, especially concerning environmental and safety aspects. It is important to underline that although scientific research has screened a wide range of working fluids, there are only a few which are actually used in ORC plants. These fluids include R134a in geothermal applications and low temperature waste heat recovery; R245fa in low-grade waste heat recovery, n-Pentane in low waste heat recovery, and medium temperature geothermal applications and solar ORC in the U.S. [37]. A list of these existing systems, working fluids and manufacturers may be found in several ORC review studies such as in those conducted by Vélez et al. [43].

From an environmental and safety point of view, the importance of identifying new working fluids for ORC applications becomes a matter of urgency as the reviewed recent investigations of several HFOs indicated. Nevertheless, as HFOs alongside HCFO-R1233zd(E) have only very recently appeared in the literature, these refrigerants have not been seen in real ORC applications. Most importantly, the promising HCFO-R1233zd(E) is still not available commercially and its thermodynamic properties are not publicly available. As a result, it has not yet been evaluated either theoretically or experimentally.

In terms of expansion devices, it was noticed that expanders employed in ORC systems suffer from key problems including excessive working fluid internal leakage, thermal losses, lower isentropic efficiency and high costs. The majority of these commercially available expanders are for medium and large-scale applications (>100 kW). However, for small-scale ORC systems, scroll expanders are reported to be the optimal expander option. Several experimental researches were conducted utilising scroll compressors but with major technical problems reported, and relatively expensive prices for those units. To overcome the key problems reported for expanders, scroll expanders modified from

automotive A/C scroll compressors represent the best potential candidates for a small-scale ORC system. Automotive A/C scroll compressors are reported to have high isentropic efficiency, besides their commercial availability and the fact they are mass-produced at low cost. Nevertheless, automotive scrolls are enclosed in a semi-hermetic housing, decreasing the risk of any working refrigerant leakage and therefore allowing more environmentally friendly operation. However, although the utilisation of automotive scroll expanders has been reported in the ORC literature, those researches utilised small scroll expanders rated at 1 kW power output and more rarely, up to ~2 kW.

The identified gaps suggest thermodynamic evaluation of the performance of the new emerging environmentally friendly refrigerants in a small-scale regenerative ORC system, especially the promising R1233zd(E) in order to assess their viability for the proposed power generation prototype system for waste heat recovery.

### 2.7.2 SRC and TRC

The reviewed literature provided sufficient understanding of the concept of SRCs and TRCs in general. It also identified the investigated and recommended working fluids for various applications. The search for new working fluids was found to be a key subject in the studies reviewed beside the assessment of the CO<sub>2</sub> cycle technical and the economic feasibility. However, CO<sub>2</sub> remains the most favoured working fluid for the cycle despite the promotion of HFC-R125, which has better performance, but also has a high GWP of 3500, and therefore it is subjected to be phased out. However, In comparison to its ORC counterparts, CO<sub>2</sub> SRC and TRC proved to have lower thermal efficiency, but higher net thermal power output. Moreover, employing CO<sub>2</sub> as the working fluid enables a compact design for the system and turbine. Nevertheless, the practical feasibility of such a system will heavily depend on the availability of its components, specifically the turbine and the pump.

The experimental studies revealed the absence of a turbine that can handle super-critical CO<sub>2</sub>. For the compression device, if the option is to employ CO<sub>2</sub> TRC, then there are a wide variety of high pressure pumps that can handle pumping the CO<sub>2</sub> liquid. The limitations would be the pump's efficiency and its power consumption, as seen in the reviewed experimental study. Moreover, the inlet pressure of the pump would be limited to certain pressure levels, which may restrict the operation of the system. Pump inlet temperature is another concern, where the CO<sub>2</sub> must be a fully-developed and sub-cooled liquid. In other words, high operating pressure and low temperatures are required for the cooler/condenser heat exchanger. If the option is the adoption of a CO<sub>2</sub> SRC system, a compression device similar to the turbine is required to handle the super-critical CO<sub>2</sub>. In fact, the only available experimental work, namely by Zhang et al. [101, 114-119] and Yamaguchi et al. [120] was carried out from 2005-2007 and is therefore considered outdated. The reason is simply the recent interest shown in CO<sub>2</sub> as a working fluid, from both an environmental and thermodynamic point of view. Additionally, the recent phasing out of CFCs and HFCs has rapidly improved the research and development of equipment which is compatible with CO<sub>2</sub> and most likely to operate in a super-critical state.

For these reasons, both CO<sub>2</sub> SRC and TRC present a potential system for heat recovery from low-grade heat sources, especially nowadays. Therefore, a small-scale regenerative CO<sub>2</sub> SRC power generation system will be theoretically investigated to assess its technical feasibility for the power generation prototype system proposed. Market research will be commenced to identify suitable system components and costs to allow assessment of the system from an economic perspective.

### 2.7.3 Absorption Power Generation Cycle

The absorption power generation cycle review revealed the absence of any working fluid other than the ammonia-water mixture beside

several other working fluid pairs which were rarely reported in literature. In fact, all the reported working fluid pairs, including the ammonia-water do not fulfil the safety and environmental aspects of the working fluid selection criteria. Therefore, the search for new working fluid mixtures consists of completely safe, environmentally friendly components, and the study of their behaviour and impact on the performance of the cycle are much recommended.

For the working fluid mixture employed, the review revealed that the mass fraction of the mixture plays the key rule in characterising the system performance. Several systems configurations showed improved systems performance. This indicates that the configuration also contributes significantly to the overall system performance and therefore it must be considered.

Finally, almost all reviewed absorption power generation cycles are still in the theoretical phase of research and there is no evidence in the literature for a pilot plant, prototype, or experimental, apart from the well-established Kalina power cycle.

For these reasons, the current research proposes a working fluid mixture that consists of the environmentally friendly CO<sub>2</sub> refrigerant and synthetic compressor lubricant oil that is made of environmentally friendly compositions. Several CO<sub>2</sub>/lubricant oil mixtures will be investigated both theoretically and experimentally in order to determine the most suitable lubricant for the mixture. The candidate CO<sub>2</sub>/lubricant oil mixtures will then be thermodynamically modelled in order to obtain the mixtures' thermodynamic properties. Upon thermodynamic modelling of the nominated working fluid mixture pairs, their performance is to be evaluated theoretically in a small-scale absorption power generation system in order to assess its technical feasibility to develop the proposed power generation prototype system for waste heat recovery.

## Chapter 3 : CO<sub>2</sub>/Lubricant Oil Mixture as a Working Fluid

---

### 3.1 Introduction

This chapter presents some background on refrigerant/lubricant oil mixture studies and identifies the conventional lubricant oils currently used in refrigeration applications. A literature review was carried out to investigate the lubricant oil requirements for CO<sub>2</sub> refrigerant and CO<sub>2</sub>/lubricant mixture behaviour. CO<sub>2</sub>/lubricant vapour liquid equilibrium (VLE) solubility data and other properties were collected throughout the literature review, in order to screen a range of potential lubricant oils as CO<sub>2</sub> absorbents. Besides lubricant oils, propylene carbonate (PC) was also investigated as a CO<sub>2</sub> absorbent. The solubility screen comparison resulted in the selection of PC, POE68, POE32 and POE5 for further experimental investigation, in order to validate the collected solubility data.

### 3.2 Background on Refrigerant/Lubricant Oil Mixture Studies

In the open literature, most studies concerned with refrigerant dissolution in refrigeration lubricants were carried out for the purpose of making proper selections of lubricant oil and designing improvements for cycle components in vapour compression refrigeration and air-conditioning applications [142-144].

Due to the dynamic nature of such cycles, compressor oil is liable to migrate from the compressor to other cycle components, even with an oil separator installed. If the oil is miscible with the refrigerant over the cycle's operating temperature and pressure, it will return to the compressor. However, if the oil is immiscible or only partially miscible, and exhibits phase separation at any point in the cycle, several problems will appear. The most obvious is insufficient oil return to the compressor; that could cause damage to the compressor [145]. In addition, oil will accumulate in heat

exchangers, causing flow configuration to decrease the heat transfer coefficients and increase pressure drop, which will affect overall performance [146]. Despite the fact that, in principle, the oil should be fully miscible with the refrigerant [147], high miscibility and solubility tend to reduce the viscosity of the lubricant oil and consequently instigate damage to the compressor [148]. Therefore, the best selection of lubricant oil will depend on both the properties of the oil and the properties of the oil/refrigerant mixture [145].

### 3.3 Miscibility and Phase Equilibrium

Miscibility is defined as the ability of two or more liquids to dissolve into a single homogenous liquid phase [149]. Usually, miscibility is described as the separation temperature where a second liquid phase is formed. It is measured as a function of mixture composition [150].

If the oil is miscible with the refrigerant, a mass of the refrigerant will be absorbed by the oil to form a homogenous liquid phase [151]. In this case, the refrigerant/oil mixture will only exhibit vapour-liquid-equilibrium (VLE) behaviour [152]. At VLE, the refrigerant/oil mixture pressure is always lower than the pressure for the pure refrigerant, where the vapour is formed solely by the refrigerant [151]. If the oil is partially miscible, the refrigerant/oil mixture will exhibit vapour-liquid-liquid-equilibrium (VLLE) phase behaviour; or liquid-liquid-equilibrium phase behaviour (LLE), if the oil is immiscible [152]. In fact, VLE and VLLE are also referred to as solubility, which is defined as the equilibrium mass fraction of an oil or refrigerant in a mixture [153]. The solubility of a refrigerant in oil is strongly dependent on temperature and pressure and has a significant influence on the thermo-physical properties of the resulting mixture [106]. This is due to the fact that the refrigerant changes from being pure, with well-known thermo-physical properties, to a mixture that is poorly understood, with properties that depend on the mixture's composition [154]. Hence, a sound knowledge of the solubility data is essential for being able to

estimate the thermo-physical properties of a refrigerant/oil mixture [155]. The shaded areas illustrated in Figure 3-1 represent various types of miscibility region in refrigerant with lubricant oils.

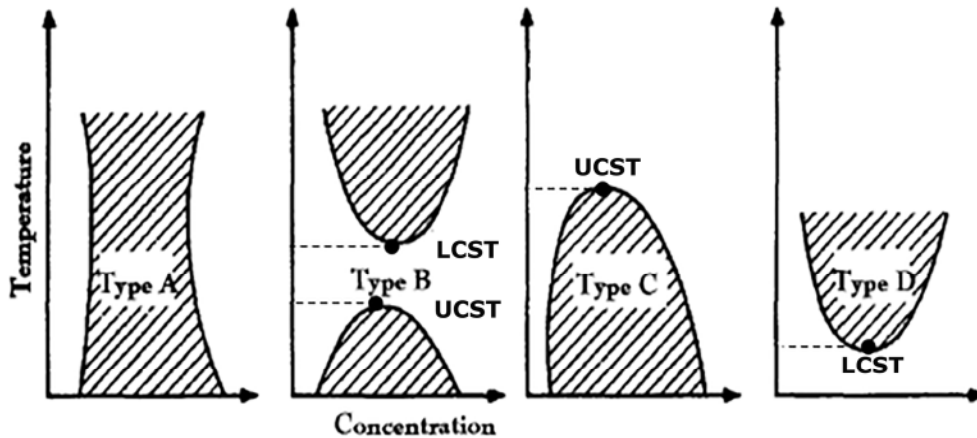


**Figure 3-1: Various types of miscibility behaviour. (Source: [147])**

Upper critical solution temperature (UCST) and lower critical solution temperature (LCST) are the maximum and minimum temperatures where a two-phase behaviour of the mixture may exist. With respect to UCST and LCST, Type A in Figure 3-1 represents the most common phase diagram where the miscibility region exist in the whole temperature range with no critical solution temperature. Type B represents a partially miscible mixture where the miscibility region exists between the UCST and the LCST. Type C represents a mixture with UCST where the miscibility is limited by a high temperature, while type D represents the opposite behaviour where the miscibility is limited by the LCST [156].

### 3.4 Types of Lubricant Oil for Refrigeration

The conventional lubricant oils currently used in refrigeration are either mineral- or synthetic-based. This section identifies the most common types and their applications.

#### 3.4.1 Mineral Oils (MO)

Mineral lubricant oils are used with chlorinated refrigerants [157]. These lubricants are incompatible with the new generations of

refrigerants, including CO<sub>2</sub>, where they show very limited miscibility [145].

### 3.4.2 Synthetic Lubricant Oils

These are synthetic based oils that have replaced mineral oil in refrigeration and air-conditioning applications. Synthetic lubricant oils are categorised in five main groups, and have various solubility behaviours with refrigerants. The main groups of synthetic lubricant oils are:

#### 3.4.2.1 Polyol Ester (POE)

Polyol esters are commercial ester-based lubricants that are widely used in domestic and commercial refrigeration applications. They can be synthesised from a wide variety of materials and biodegradable renewable resources [145]. For this reason, POE lubricants offer flexibility for their design, up to the required physical characteristics [158]. Moreover, POEs are almost completely non-toxic [159] and have excellent thermal stability [160]. On the other hand, POE lubricants are hygroscopic and have a tendency to absorb water. Therefore, good maintenance should be considered to avoid excess moisture within a system [160]. Finally, POEs have been extensively investigated because of their attractive ecological properties and well-established technical performance, which promotes them as a suitable base oil for high performance, environmentally-friendly lubricant oils [159].

#### 3.4.2.2 Polyalkylene Glycol (PAG)

PAG lubricants are used in automotive air-conditioning with R134a refrigerant [160]. They may be customised to exhibit the desired miscibility and solubility with refrigerants [161]. PAG lubricants have a wide range of viscosity indices [162] and excellent lubrication characteristics, but are at the same time extremely hygroscopic and can absorb more water than POE lubricants [160]. Consequently, they may introduce corrosion into a system [163].

Moreover, they are less thermally stable than other synthetic lubricants [150].

#### 3.4.2.3 **Polyvinyl Ether (PVE)**

PVEs are new ether-based lubricants used in refrigeration. The chemical structure of PVE lubricants resembles that of PAG oils, but with some exceptions [158]. For example, they can be compared to POE lubricants, since both are polymer-based oils. As with POE lubricants, the chemical structure of PVEs can be easily modified. However, unlike POE lubricants, PVE lubricants are less hygroscopic, and have lower densities [145]. They are also less thermally stable than POE lubricants and have oxidation characteristics. Nevertheless, the potential for oxidation can be addressed with additives [150].

#### 3.4.2.4 **Poly- $\alpha$ Olefin (PAO)**

Poly- $\alpha$  olefins are synthetic hydrocarbon lubricants [161]. PAO lubricants are used in aerospace, military applications and low temperature ammonia applications [145]. They are also non-hygroscopic [145] and are able to operate at elevated temperatures [161]. Furthermore, they have a wide range of viscosity and good thermal and oxidation stability [164].

#### 3.4.2.5 **Alkyl Benzenes (AB)**

Alkyl benzenes are synthetic hydrocarbon lubricants [145]. AB lubricants are usually used in systems which employ R-22 and R-502 [150]. They are immiscible with most other refrigerants and therefore cannot compete with POE and PAG lubricants [145]. AB lubricants have good thermal and oxidation stability, with relatively lower viscosity indices than mineral lubricants [150].

### 3.5 **Lubricant Oil Identification**

Lubricant oils in refrigeration and air-conditioning applications often refer to commercial products which are varied in their composition and display different performance characteristics. Lubricants of the

same type will also possess diverse properties, which will vary according to their source. Figure 3-2 shows Bobbo et al.'s [165] results for an experimental analysis of three POE32 oils from different manufacturers. The study revealed that even the same ISO grade for the same oil type constitutes different compounds and composition.

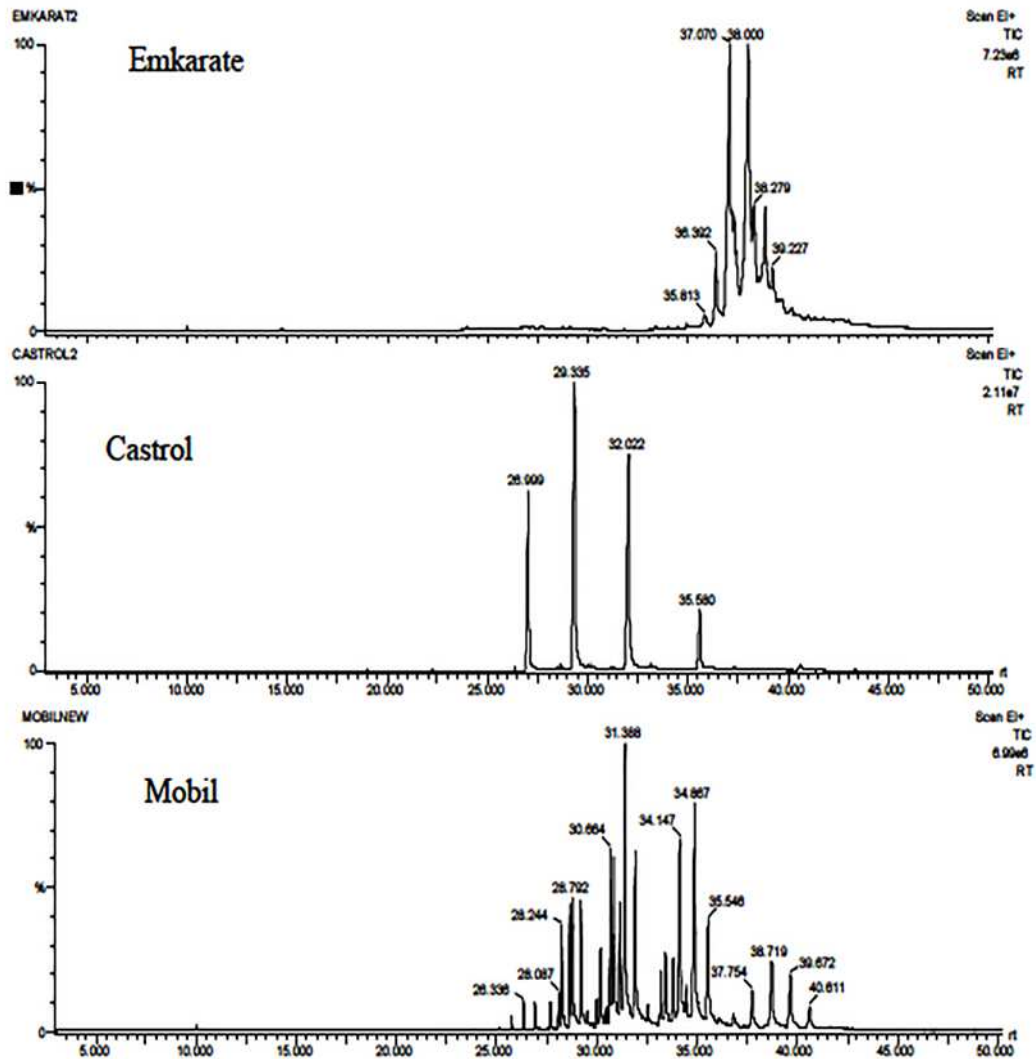


**Figure 3-2: Three POE32 lubricant oils from different sources. (Source: [165]).**

Hence, to identify specific lubricants, the American Society for Heating, Refrigerating and Air Conditioning Engineers (ASHRAE) has established the ANSI-ASHRAE 99-2006 Standard. This standard characterises lubricants by conducting test procedures in accordance with the standards of the American Society for Testing and Materials (ASTM). The principle of this characterisation is to

identify lubricant oils on the basis of their chemical and physical properties, as well as their chemical structure, without reference to their commercial names [166]. The lubricant oil properties are, for example, viscosity and viscosity index; density; colour; pour point, and volatility. Further properties and tests for lubricant/refrigerant mixtures are also described under the ASHRAE standards, such as solubility and mutual solubility with refrigerants, chemical stability, viscosity and density [167].

However, these Lubricants are sold according to the International Standardization Organization's (ISO) viscosity grades [167], where lubricants are identified by their type and ISO viscosity grade. The ISO viscosity grade system (ISO VG) consists of 18 definite kinematic viscosity grades, measured in centistokes (cSt) at 40°C [168]. For example, polyol ester oil with a kinematic viscosity of 32 cSt at 40°C is designated as POE ISO VG 32, POE ISO 32, or simply as POE32. Within every viscosity grade,  $\pm 10\%$  of the median viscosity value is allowed as a limit. Thus, an oil with 140 cSt at 40°C is classified as ISO VG 150 [169].

### **3.6 Selection Requirements for a Lubricant Oil in the CO<sub>2</sub>/Oil Absorption Power Generation System**

To start with, it is very important to understand that CO<sub>2</sub> has a relatively low critical temperature of 31.1°C and a high critical pressure of 73.8 bar. The selection of a suitable lubricant oil to work with CO<sub>2</sub> will therefore depend on the application and the proposed system [170]. For the current research, the proposed absorption power generation system requires operation near or above the critical point of CO<sub>2</sub>. Moreover, the proposed system employs CO<sub>2</sub>/lubricants as working fluid mixtures. Therefore, the selection is influenced by a combination of the thermo-physical properties of the working fluid and high solubility within the operating pressure and temperature range, where the mixture should only exhibit VLE behaviour. The selected lubricant must also display high thermal

and chemical stability, acceptable viscosity, good flow characteristics [171], and low hygroscopicity [158]. Despite the significance of a high solubility factor in selection, such high solubility will lead to a reduction in viscosity, as mentioned previously [172]. Therefore, the CO<sub>2</sub>/lubricant mixture must also be able to provide sufficient lubrication and cooling to hot parts in the pump and expansion device [171]. Moreover, the high pressure associated with CO<sub>2</sub> requires anti-wear properties in the oil, due to the high load on the bearing in the expansion device [158]. Besides the technical requirements for oil candidates, the selected oil should be environmentally friendly, non-toxic, and commercially available.

### 3.7 Overview of CO<sub>2</sub>/Lubricant Oil Mixtures

Investigation of CO<sub>2</sub>/lubricant mixtures has received increasing attention due to the fact that CO<sub>2</sub> has become the promising alternative refrigerant for environmental, safety and economic reasons. Table 3.1 presents an overview of the miscibility of CO<sub>2</sub> with different types of lubricant oils.

**Table 3.1: Overview of CO<sub>2</sub> miscibility with different types of lubricant oil.**

Lubricant Type	Miscibility	Reference
POE	Miscible	[158, 161, 171, 173, 174]
PAG	Partially miscible	[158, 161, 171, 173, 174]
AB	Immiscible	[158, 173]
PAO	Immiscible	[158, 161, 171, 173]
MO	Immiscible	[158, 173]
PC	Miscible	[174]
PVE	Miscible	[158, 174]
AN	Partially miscible	[161]
AN/PAG	Partially miscible	[161]

Hauk and Weidner [171] have compared CO<sub>2</sub>/lubricant mixtures of PAO, PAG and POE types. Their study indicates that the low CO<sub>2</sub> solubility in PAG and PAO types may cause them to become trapped in unwanted places around the system. On the contrary, CO<sub>2</sub> has high solubility in a POE lubricant type and the CO<sub>2</sub>/POE mixture shows good flow characteristics. The above study concludes that either POE or PAG oil types could be used with CO<sub>2</sub>. Meanwhile, Ikeda et al. [174] and Kawaguchi et al. [175] have evaluated the

miscibility, solubility and mixture viscosity, and lubricity of CO<sub>2</sub>/lubricant oil mixtures, with certain additives. The study included POE, PAG and PVE, besides polycarbonate (PC). The above research confirms that CO<sub>2</sub> has high solubility with POE alongside PVE and PC types. However, the authors recommend PAG oil type for CO<sub>2</sub> applications, as the CO<sub>2</sub>/PAG mixture showed better performance with regard to lubricity, viscosity and stability, compared to other mixtures under super-critical conditions. On the other hand, the study indicated that PC showed the worst overall performance.

Randles et al. [173] carried out a critical assessment and screened different types of lubricant oil for CO<sub>2</sub> applications. The study nominated PAG and POE types for further investigation and recommended either to be used with CO<sub>2</sub>. Moreover, Beattie and Karnaz [59] advocated the use of PAG and POE types for CO<sub>2</sub> applications and indicated that the high solubility of CO<sub>2</sub> in POEs eliminates the need for expensive separation techniques and allows the mixture to be used in direct expansion applications. For the PAG type, the main drawbacks consist of its relatively high cost and significant potential to absorb water, besides its limited miscibility. Figure 3-3 shows an overview of CO<sub>2</sub> solubility in various types of lubricant oil.

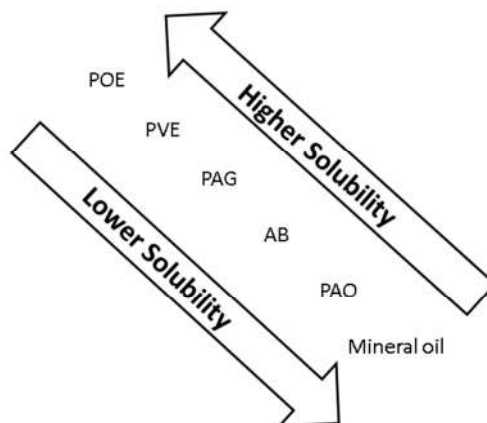


**Figure 3-3: Overview of CO<sub>2</sub> solubility in different common lubricants.**

Furthermore, the studies reviewed confirm that solubility has a significant influence on viscosity and flow behaviour. In Hauk and

Weidner's [171] experimental work, the CO<sub>2</sub>/POE mixture showed the lowest viscosity in all the conditions tested, while CO<sub>2</sub>/PAG had the highest viscosity in all conditions tested, mainly due to the limited solubility and higher viscosity index of the pure PAG oil. In the experimental work conducted in [174, 175], all tested lubricants were of the same ISO viscosity grade but the CO<sub>2</sub>/PAG mixture still showed the highest viscosity. Figure 3-4 shows an overview of several CO<sub>2</sub>/lubricants and the viscosity of their mixtures.

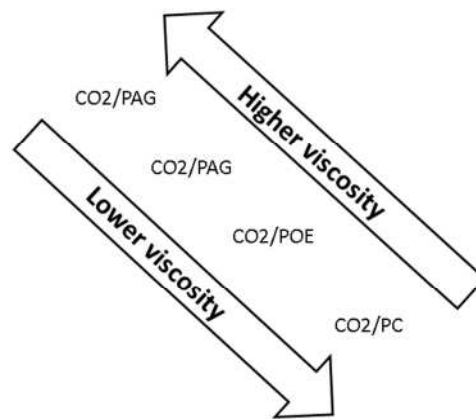


**Figure 3-4: Overview of viscosity of CO<sub>2</sub>/lubricant oil mixtures.**

Besides the reduction in the viscosity of the mixture due to the high CO<sub>2</sub> solubility in POEs, Randles et al. [173] have discussed the potential of foaming. These issues could in fact be resolved by selecting POE lubricants with a higher viscosity index and the use of conventional anti-foaming agents, but with POE and PAG oil types, high moisture levels may also cause problems, as water may react with CO<sub>2</sub> and form carbonic acid. In reality, PAG and POE oils have been used as CO<sub>2</sub> processes gas lubricants without any issues. Further studies reviewed [148, 172, 176-178] clearly identified POE and PAG lubricant oils as the lubricants of choice for CO<sub>2</sub>. However, POE lubricant oils have drawn more attention and had wider market acceptance because of their environmentally friendly and biodegradable characteristics [177].

Other studies on the solubility of CO<sub>2</sub> in liquid solvents may be found in the literature. These studies are mainly concerned with the removal of acidic CO<sub>2</sub> and hydrogen sulphide (H<sub>2</sub>S) from natural

and industrial gas streams [179]. At higher temperatures and pressures, propylene carbonate (PC) is considered as the commonest absorbent for CO<sub>2</sub> [180]. Murrieta-Guevara et al. [181] experimentally measured CO<sub>2</sub> solubility in propylene carbonate (PC). Their study concluded that CO<sub>2</sub> demonstrated good solubility in PC, compared with other absorbents examined. In a similar study, Mantor et al. [180] measured the solubility of CO<sub>2</sub> in PC at elevated pressures and temperatures, where the CO<sub>2</sub> was in a super-critical state. The results confirm the good solubility of CO<sub>2</sub> in PC and correspond with those of previously conducted experimental studies. Although PC has relatively low flash point of 116°C and does not have any lubrication characteristics [182], it could be used to evaluate CO<sub>2</sub>/Lubricant power generation system performance, and be blended with a lubricant of choice for practical investigation.

### **3.8 Comparison of CO<sub>2</sub> Solubility in a Range of Absorbents**

Although the literature reviewed recommends either PAG or POE oil types for CO<sub>2</sub>, further comparison of CO<sub>2</sub>/lubricant oil solubility data should be carried out to determine the highest solubility achieved under the proposed absorption power generation cycle's absorber and generator expected operating conditions, which will give an initial indication of the absorbents to be selected.

Even though many studies have investigated CO<sub>2</sub>/commercial lubricant oil mixtures, the availability of solubility data is still scarce. Few of these published studies include the experimentally obtained solubility data. For the current comparison, the selection of oil candidate types and ISO viscosity grades was essentially based on the availability of VLE solubility data, the range of data, and available information on mixtures properties. Table 3.2 presents a list of the selected lubricant candidates, besides PC, along with data information, range and sources.

**Table 3.2: List of absorbent candidates and available data.**

Absorbent name	Reference	Data type	Temperature range [K]	Maximum pressure [bar]
POE32	[183]	Empirical correlations of solubility, density and kinematic viscosity	243.15 to 398.15	140
POE68	[152, 184]	Solubility data and density [184] Solubility data, density and dynamic viscosity [152]	285.15 to 348 [184] 236.15 to 373.15[152]	121.3 [184] 123.41 [152]
PVE68	[152]	Solubility data, density and dynamic viscosity	253.15 to 373.15	123.26
PAG46	[152]	Solubility data, density and dynamic viscosity	253.15 to 373.15	123.70
AB32	[184]	Solubility data and density	285.15 to 348.15	111.6
PAO68	[185]	Solubility data, density and dynamic viscosity	278.15 to 373.15	153
PC	[180]	Solubility data	299.85 to 377.55	60.9

In the current research, a comparison of solubility at four different temperatures and at variable pressure with correspondingly absorbed CO<sub>2</sub> mass fractions was established. Two low temperatures of 283.15K (10°C) and 303.15K (30°C) were selected as potential absorber temperatures, while the potential temperatures selected for the generator were 353.15K (80°C) and 373.15K (100°C). It is useful to underline that these absorber temperatures and pressures are below the critical point for CO<sub>2</sub>, while the generator temperatures cited are above the critical temperature for CO<sub>2</sub> and the pressures are trans-critical. In addition, the points compared and their trend lines shown in Figure 3-5 are not necessarily the exact same experimental tested points collected from references. The collected solubility data were either correlated or interpolated, as appropriate, to allow comparison under the same pressures and temperatures.

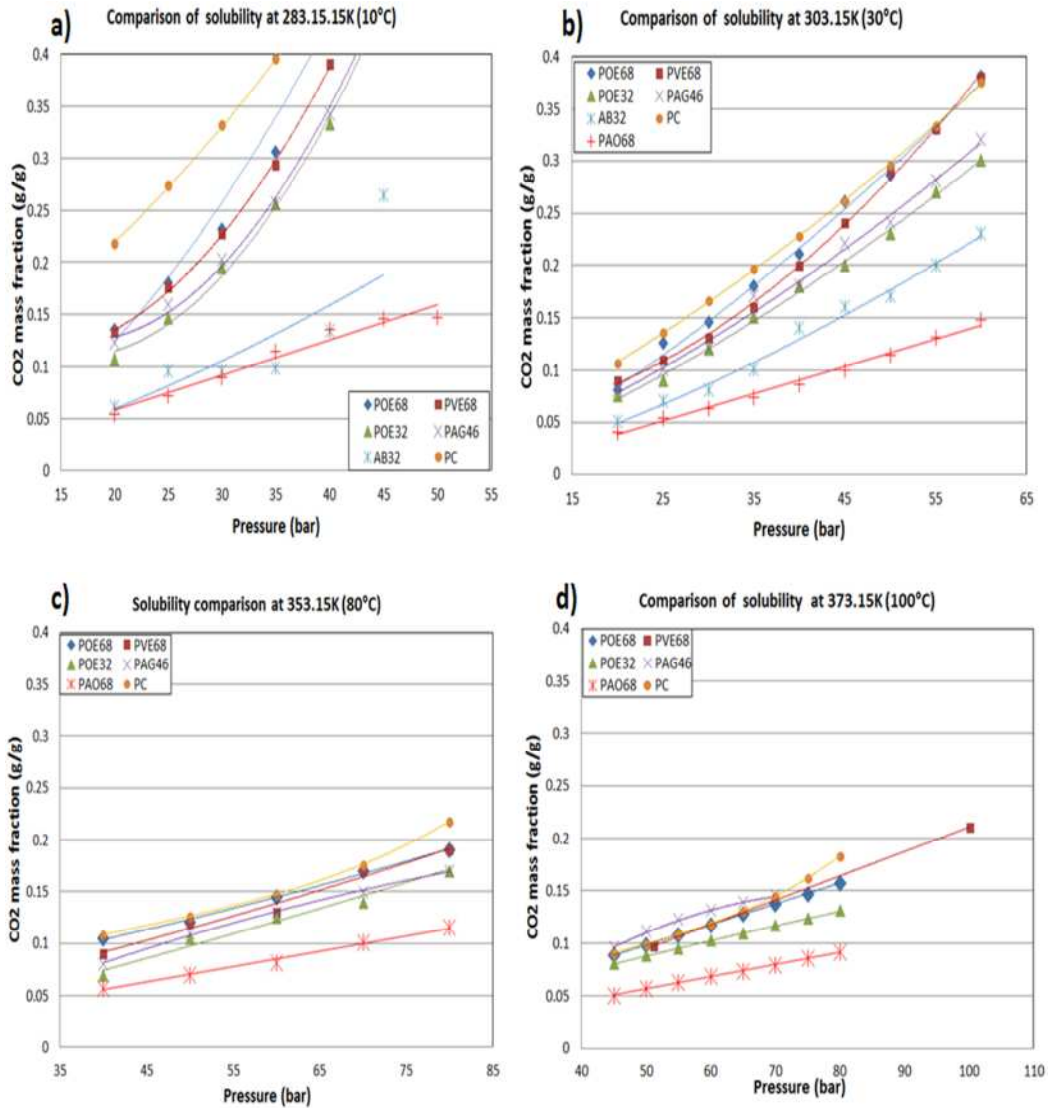


**Figure 3-5: CO<sub>2</sub> solubility comparison in different absorbent candidates at constant temperatures.**

Figure 3-5 shows that CO<sub>2</sub> has the lowest solubility in AB32, followed by PAO68. As shown, both AB32 and PAO68 solubility data deviate from the rest of the absorbents, which seem to cluster together and follow similar trends. This was clearly seen at 283.15K and 303.15K. Moreover, the limited miscibility of AB32 with CO<sub>2</sub> is obvious, where there is no solubility data at 353.15K and 373.15K. Therefore, AB32 and PAG68 will be excluded from further investigation. On the other hand, the remaining absorbents showed satisfactory solubility, but the Figure demonstrates that solubility is higher at lower temperatures and decreases gradually as the temperature increases. Overall, CO<sub>2</sub> showed the highest solubility in PC, followed by POE68, which is nearly similar to CO<sub>2</sub>'s solubility

in PVE68. Similar behaviour may be observed in the case of PAG46 and POE32, where PAG46 is slightly higher than POE32. At 373.15K, CO<sub>2</sub>'s solubility in PAG46 was found to increase unexpectedly, achieving the highest solubility overall.

### 3.9 Conclusion

This chapter presented an overview of the lubricant oil types in refrigeration application and their solubility behaviour with refrigerants in general. The chapter also discussed the lubricant oil requirements in order to work with CO<sub>2</sub> in the proposed CO<sub>2</sub>/lubricant absorption power generation system. Furthermore, various CO<sub>2</sub>/ lubricants solubility data were collected, and the solubility of CO<sub>2</sub> in these lubricants was overviewed from available literature. The available VLE data were then used for solubility comparison in order to identify the most suitable absorbent candidates.

From the solubility comparison, PC and POE lubricant types were selected for further experimental and theoretical investigations, namely to examine the selected absorbants' thermal stability, test and validate the CO<sub>2</sub>/ lubricants solubility data, and examine the agitation effect on the absorption and desorption behaviour on the experimental side. On the theoretical side, the selected CO<sub>2</sub>/absorbents performance will be evaluated in the CO<sub>2</sub>/lubricant absorption power generation system.

Although CO<sub>2</sub> shows the highest solubility in PC, it is quite uncertain whether this is the best absorbent for CO<sub>2</sub>, since it has a low flash point and does not have any lubrication characteristics, thus presenting a drawback for the system operation. On the other hand, it is evident from the reviewed studies and solubility comparisons that the POE oil type makes the best absorbent for CO<sub>2</sub> in the CO<sub>2</sub>/lubricant working fluid mixture since it possesses qualities that are either absent or still unknown in other lubricant types. POE's main qualities may be summarised as:

- Complete miscibility and high solubility with CO<sub>2</sub>.
- Good lubrication and flow characteristics of the CO<sub>2</sub>/POE mixture.
- Does not require a separation system and the CO<sub>2</sub>/POE mixture may be used in direct expansion systems.
- Environmentally-friendly and bio-degradable.
- Currently widely used in commercial and domestic refrigeration systems and is therefore commercially available and at affordable costs.

The CO<sub>2</sub>/POE32 mixture pair will be treated as the primary mixture pair for the above reasons, besides the fact that POE32 is the most commonly used lubricant in related applications. Moreover, the reliability and availability of the extended range of CO<sub>2</sub>/POE32 solubility data and other thermodynamic properties contributed to its selection as the primary mixture pair.

## Chapter 4 : Experimental Evaluation of CO<sub>2</sub>/Lubricant Oil Mixtures

---

### 4.1 Introduction

This chapter presents the experimental work of the nominated absorbent candidates carried out in mixtures with CO<sub>2</sub>. All experiments were conducted in the school of chemistry's laboratory, University of Nottingham. First, the thermal stabilities of the absorbents were examined by means of Thermogravimetric Analysis (TGA) tests. Then the CO<sub>2</sub>/absorbent mixtures were tested to measure their solubility and validate the literature collected data by means of Intelligent Gravimetric Analysis (IGA) tests where the absorption occurs only by diffusion. Finally, enhanced absorption and desorption processes were tested in an especially constructed apparatus in order to examine the agitation effect on the processes. It is important to note that due to the large amount of experimentally obtained data, these results were not included in this thesis unless otherwise indicated. However, they are available in electronic format upon request.

### 4.2 Materials

All materials involved in the following experiments were especially supplied for the current research. The CO<sub>2</sub> gas used was of refrigerant grade (R744), with 99.95% purity, supplied by BOC, UK [186]. The commercial POE compressor oils were Emkarate RL32H, RL68H, and RL5H, supplied directly by the manufacturer, Lubrizol, USA [187], while the PC was supplied by Sigma-Aldrich, UK [182].

### 4.3 Thermogravimetric Analysis (TGA) Test

In the current research application, the absorbent POE lubricants or PC in the mixture are exposed to the high mechanical and thermal stress associated with CO<sub>2</sub>. This may cause thermal degradation and polymerisation results in the formation of heavier fractions [188]. Thus, an examination of the thermal stability of selected absorbents is essential. This section presents the experimental work

on thermal stability, carried out by means of thermogravimetric analysis (TGA).

#### 4.3.1 Operating the TGA Apparatus and Conducting the Test Procedure

TGA analysis is a thermal examination that measures the amount of mass loss in a sample, as a function of time or temperature and in a controlled atmosphere by means of a programmed heating rate [189]. Such a loss in mass might be a result of the evaporation of moisture, chemical decomposition, or the evolution of gases [190]. The common uses of TGA are to determine and quantify compositions [191] and to examine the thermal stability of materials [192]. Figure 4-1 illustrates a schematic view of the SDT Q600 thermogravimetric analyser (TA instruments) used in the experiment [193].

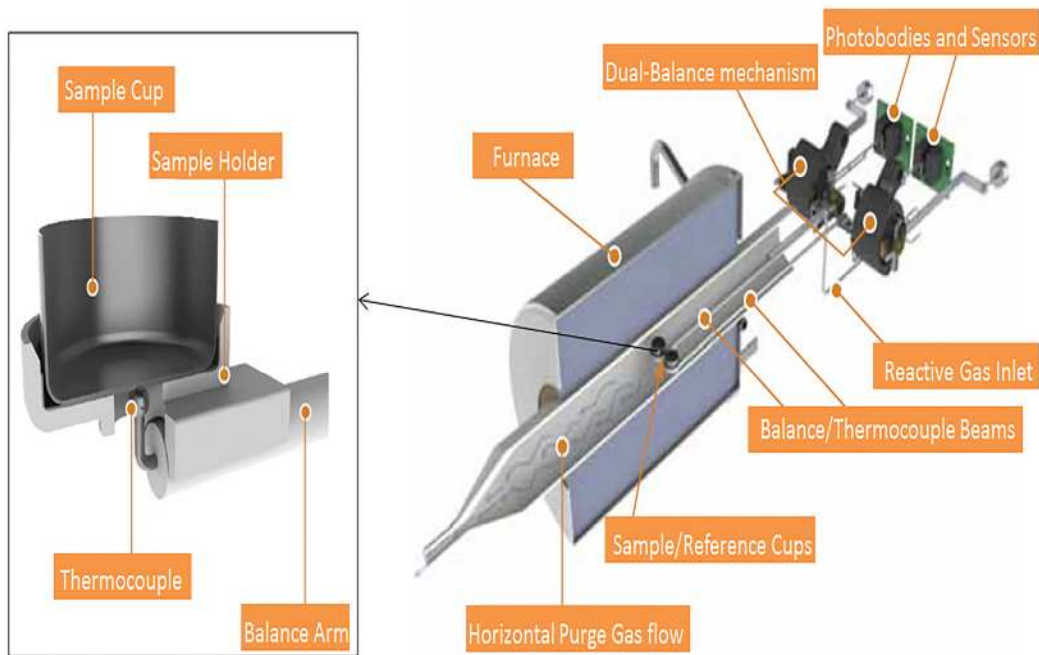


**Figure 4-1: Schematic view of the SDT Q600 TGA apparatus.**

In the TGA analyser shown in Figure 4-1, the sample is loaded into a heat-resistant alumina pan, placed on a high-precision balance and is capable of measuring weights with a balance sensitivity of  $\pm 0.1 \mu\text{g}$  in a gas-tight environment. An electrical furnace heats the sample according to a programmed heating rate, while the sample

temperature is monitored by thermocouples located at the bottom of the sample pan [193]. At frequent intervals, the loss in sample mass is recorded electronically alongside the rate of mass loss represented by the first derivative, with respect to time or temperature [194]. Usually, during such an analysis, the furnace chamber is purged with the desired reaction gas at the known flow rate [191]. However, the gas reaction is not applicable in the case of the experiment currently under study, since the purpose is to examine the thermal stability of the POE oils and PC absorbents. Therefore, all the TGA experiments were carried out in a static-air atmosphere.

The SDT Q600 thermogravimetric analyser used in the current experiment was calibrated by the manufacturer over a temperature range from 150°C to 1250°C. To validate the performance of the SDT Q600, the manufacturer offers certified mass loss reference materials [193]. For the commencement of the experiment, 20 mg of absorbent sample was prepared and loaded in the 90  $\mu$ L alumina sample pan, illustrated in Figure 4-2.

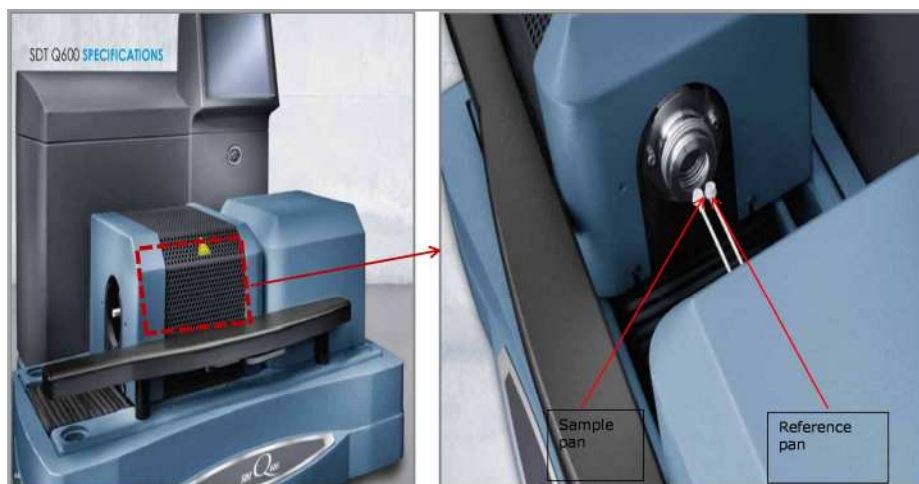


**Figure 4-2: Illustration of the SDT Q600 thermogravimetric analyser.**

Stepwise, the procedure involved heating the sample at a heating ramp rate of 10°C/min, from room temperature up to 944°C, in a static-air atmosphere and for approximately 195 minutes. Experimental data were recorded at one-second intervals.

Subsequently, the collected data were converted to a spreadsheet using the in-built TA Instruments Universal Analysis software.

#### 4.3.2 Results and Discussion

The thermal degradation and decomposition of PC is shown in Figure 4-3(a). The Figure shows the thermogravimetric (TG) curve, alongside its first derivative so-called differential thermogravimetry (DTG) curve. The TG curve represents the process in which mass loss occurs, with the temperature increase. The DTG curve represents the rate of mass loss against temperature, where the mass loss is expressed by the peak. From the DTG curve, it can be seen that the mass loss rate before the peak was relatively slower than after the peak, where the PC sample decomposed completely. The loss of mass started from approximately 65°C and the greatest elimination of the PC sample occurred between 190°C and 200°C, where the TG curve declines. Quite similar degradation behaviour was observed from the POE5 analysis results, but with higher thermal stability. As shown in Figure 4-3(b), the mass loss of the POE5 sample started at approximately 130°C, while the greatest mass loss occurred between 270°C and 290°C, indicated in the DTG curve.

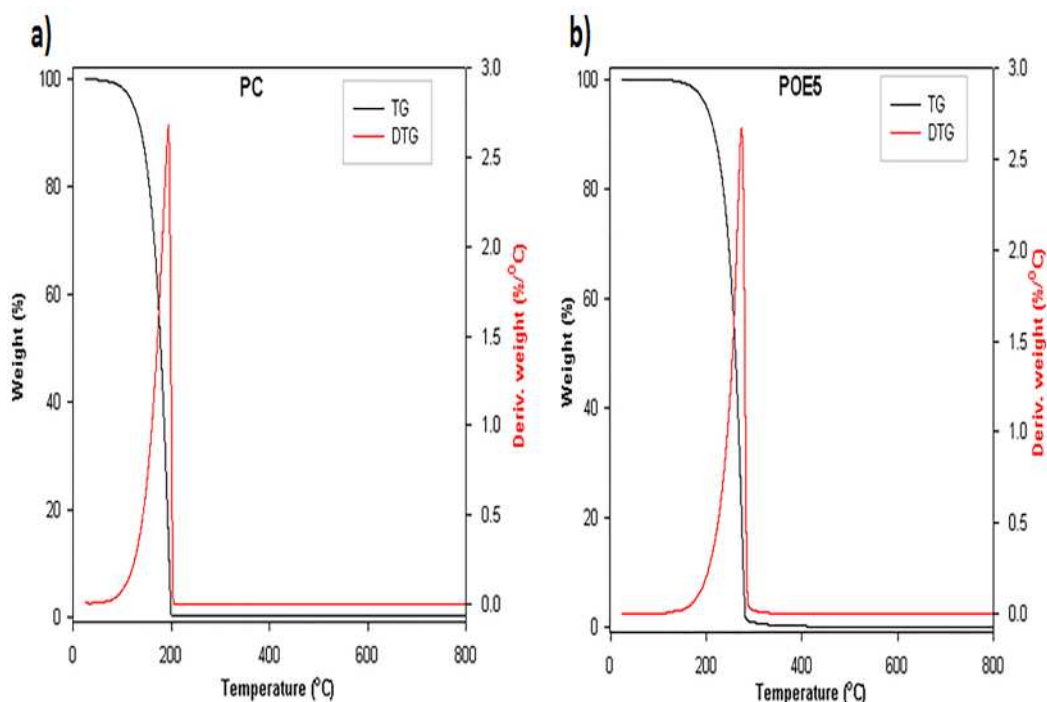


**Figure 4-3: TGA results: a) PC, and b) POE5.**

Higher thermal stability was observed from the POE32 and POE68 analysis. Figure 4-4(a) shows the thermal decomposition of POE32, where sample loss started at 220°C and major sample loss occurred at 335°C. There was further decomposition of residual compounds of the sample at 475°C, represented by the small board peak in the TGA curve. POE68, shown in Figure 4-4(b), exhibited relatively similar behaviour to what was seen in the POE32 sample results. However, the sample loss started at 225°C and major loss occurred at 350°C. The residual compounds decomposed at approximately 500°C.

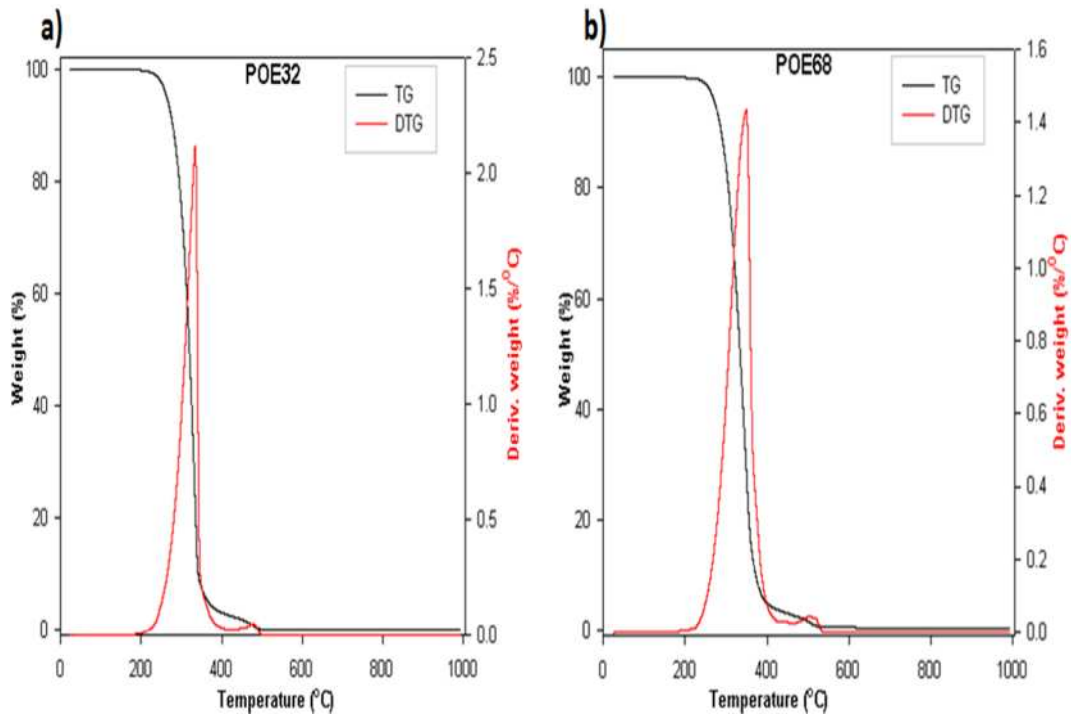


**Figure 4-4: TGA results: a) POE32, and b) POE68.**

A comparison of TG curves is shown in Figure 4-5(a). A clear proportional relationship between the ISO viscosity grade and thermal stability is observed. It can be seen that POE68 displayed the best thermal stability, followed by POE32, with relatively little difference. This was followed by POE5 and finally PC, with the lowest thermal stability. The comparison of DTG curves shown in Figure 4-5(b) also indicates that POE68, followed by POE32, have good thermal stability, with a lower loss rate over a high and wide temperature range, compared to PC and POE5.

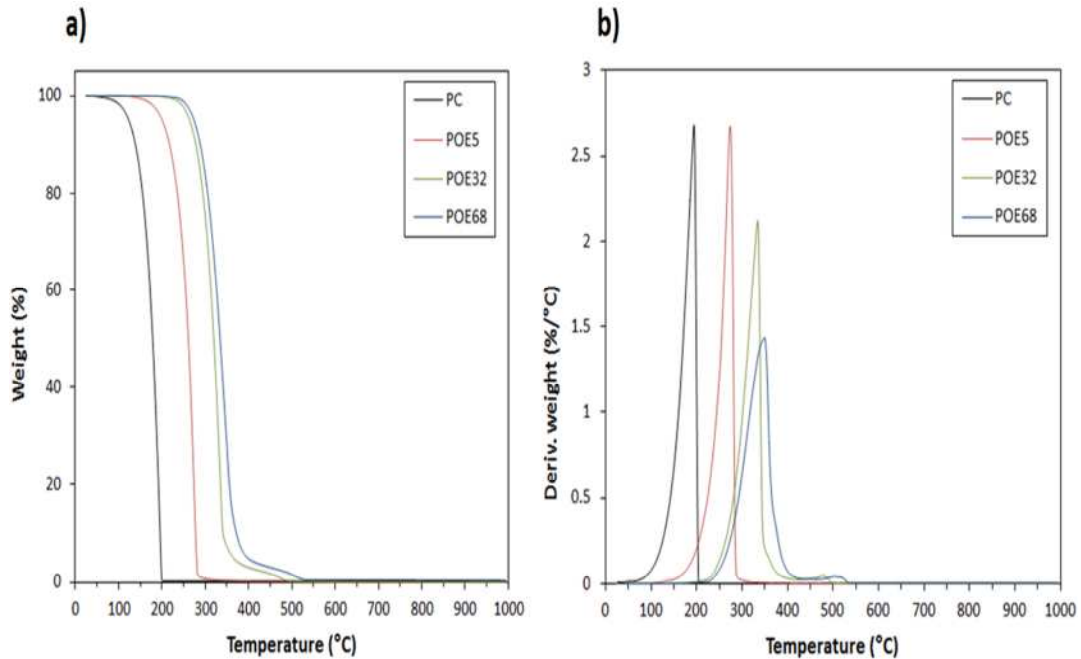


**Figure 4-5: TGA results: a) TG curves for tested absorbents, and b) DTG curves for tested absorbents.**

#### 4.4 Intelligent Gravimetric Analysis (IGA) Test

##### 4.4.1 IGA principle of operation

IGA is a common method of measuring the solubility of gases in liquids. The IGA analyser is a fully automated and computer-controlled microbalance with an automatic gas pressure control that allows the measurement of both absorption and desorption processes by means of isotherms which can record several pressure, temperature and concentration (P-T-x) data points. However, in order to obtain reliable results, sufficient time must be allocated to reach VLE [195]. This means that the absorption in the IGA apparatus takes place only by diffusion and without the interference of absorption enhancement. Figure 4-6 presents a schematic diagram of the Hiden Isochema IGA-003 [196] analyser used to conduct the experiment.

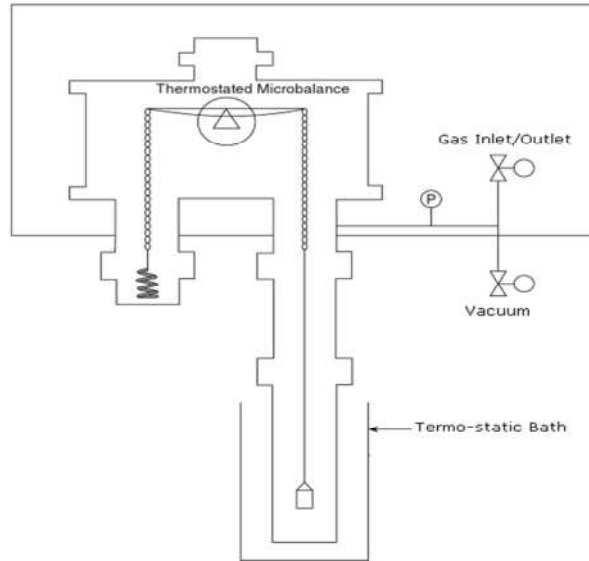


**Figure 4-6: Schematic of the IGA apparatus.**

#### 4.4.2 Operating the IGA Apparatus and Conducting the Test Procedure

CO<sub>2</sub> absorption measurements in selected absorbents were gravimetrically obtained on an IGA-003 Analyser shown in Figure 4-7 and manufactured by Hiden Analytical, UK.

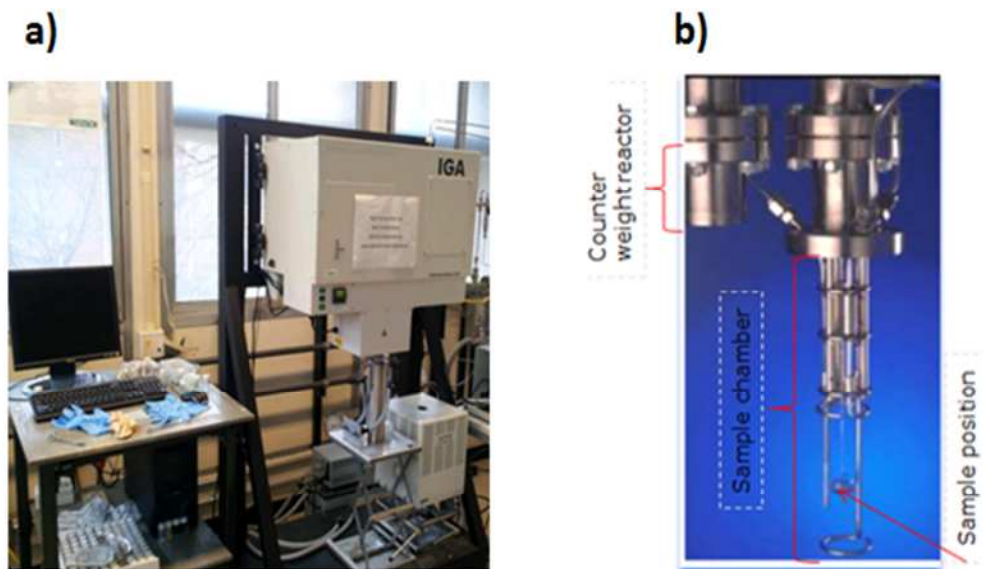


**Figure 4-7: IGA-300 - a) Image of the IGA-300 apparatus, and b) schematic representation of the IGA-003 sample chamber and counter-weight.**

The following experimental procedure was carried out for each absorbent sample. A 60 mg ( $\pm 1$  mg) sample was loaded into the

analyser's microbalance, represented in Figure 4-7(b). This equipment is capable of measuring weights with a resolution of  $\pm 0.02 \mu\text{g}$  over the pressure range of 0 to 20 bar. The sample was degassed at  $150^{\circ}\text{C}$  for 12 hours under a vacuum of  $10^{-6}$  to  $10^{-8}$  bar before commencing the analysis. CO<sub>2</sub> uptake was then gravimetrically determined by measuring the percentage of the sample weight gain due to absorption as a function of time. When the equilibrium was established at the set pressure point, the pressure was then set to the next pressure value and the subsequent uptake measured, until equilibrium was once again established. The pressure values were increased stepwise up to a maximum of 20 bar, followed by desorption on decreasing pressure from 20 to 0 bar. It is very important to point out that the IGA operating temperatures were restricted to sub-zero conditions. For this reason, the experimentally determined isotherms for the purpose of literature collected solubility data validation were in the range of  $-6^{\circ}\text{C}$  to  $0^{\circ}\text{C}$ .

A thermostatic bath consisting of ice and liquefied nitrogen were used to maintain constant temperatures throughout the experiment. The real-time monitoring of pressure, temperature and absorption processes took place using the IGA interface via a computer. Figure 4-8 shows a view of the IGA interface while conducting the experiment, where the process parameters were monitored as shown in Figure 4-8(a) and the absorption graph was created as an isotherm and as a function of pressure and CO<sub>2</sub> mass fraction as shown in Figure 4-8(b). Finally, it is necessary to note that besides real-time monitoring, a portable K-type thermocouple was used to confirm the temperature of the thermostatic bath. The measurement uncertainty was  $\pm 0.15^{\circ}\text{C}$ .

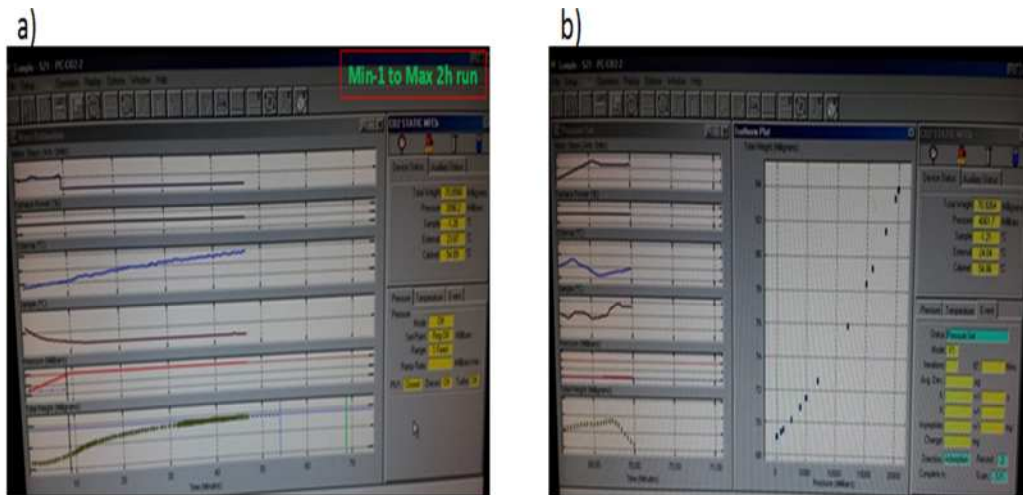


**Figure 4-8: IGA Experiment interface- a) temperature, pressure and absorption over the timeline, and b) derived plot of the absorption isotherm.**

#### 4.4.3 Results and Discussion

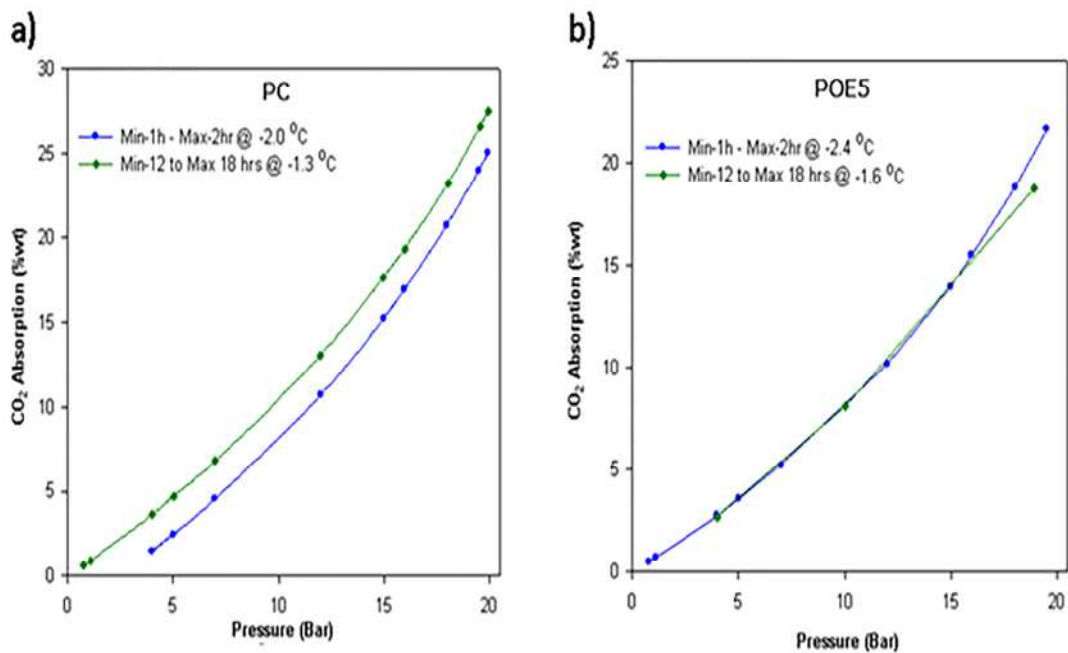
The experimentally obtained data for all the tested absorbent candidates are included in Appendix A.1, alongside the test’s isotherm temperatures. Table 4.1 lists selected absorbents, along with measured isotherms and the minimum and maximum time allowed for each absorption process step to reach VLE. Each isotherm denotes an independent experiment.

**Table 4.1: Absorbents and IGA experimental test conditions**

Name of absorbent	Measured isotherms	Absorption time to achieve VLE at each point
PC	-2.0°C	1 to 2 hours
	-1.3°C	12 to 18 hours
POE5	-2.4°C	1 to 2 hours
	-1.6°C	12 to 18 hours
POE32	-5.9°C	30 minutes to 1 hour
	-1.0°C	1 to 2 hours
	0.0°C	12 to 18 hours
POE68	0.0°C	1 to 2 hours
	-1.1°C	12 to 18 hours

Figure 4-9 shows the absorption results for the absorbents examined at variable isotherms. The results show that time is also an essential factor in the absorption process. This can clearly be seen in the PC results in Figure 4-9(a), where the lower isotherm of -2°C, with a short time step of 1 to 2 hours, showed less CO<sub>2</sub> being

absorbed, when more was supposed to have been absorbed than at the relatively higher isotherm of -1.3°C. The results for the POE5 isotherms in Figure 4-9(b) demonstrated almost identical behaviour up to 15 bar, regardless of time steps or temperature. From 15 to 20 bar, time did not seem to be very influential in the process, where the lowest isotherm of -2.4°C and the shortest time step displayed better absorption than the 12 to 18 hour absorption process at -1.6°C. Similar behaviour can be seen from the results for POE32, presented in Figure 4-9(c). However, the time step for the lowest isotherm of -5.9°C was reduced to 30 minutes to 1 hour. It is important to mention that the 0°C at the 12 to 18 hour test point shown in green was dropped, due to pressure rising above 20 bar. Typical POE-type behaviour is seen in the POE68 results, as presented in Figure 4-9(d), where high CO<sub>2</sub> absorption was achieved by the lower isotherm of -1.1°C during a time step of 12 to 18 hours. However, the lower influence of time is clear from the small deviation in these isotherm results.



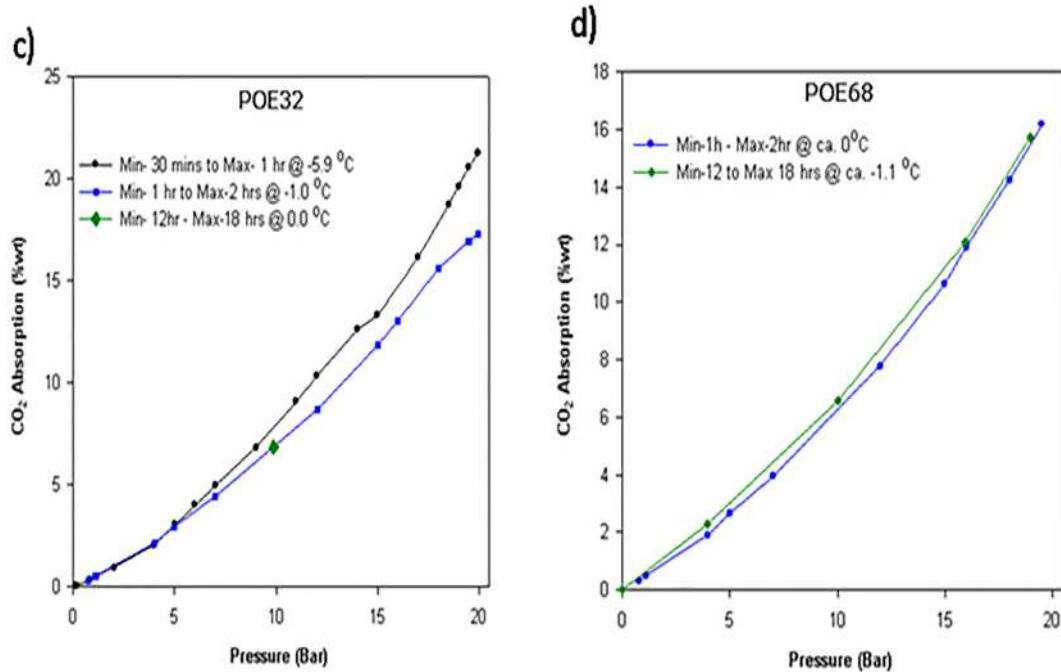


**Figure 4-9: IGA absorption experiment results.**

#### 4.4.4 IGA Experimental Solubility Data Analysis and Validation

Solubility data collected from the literature and presented in Table 3.2, Chapter 3 have been validated by the experimentally obtained IGA results. Depending on the range of IGA results and the range of data available in the literature, the validation range was selected for the pressure region from 10 to 20 bar. However, unfortunately there were no experimental data available in the literature for CO<sub>2</sub>/POE5 at all. For this reason, instead of validating the experimentally obtained data for CO<sub>2</sub>/POE5, they will be compared to the experimental data for POE32, which is the closest ISO viscosity grade available. Moreover, the experimental results for CO<sub>2</sub>/PC are far beyond the bounds of all CO<sub>2</sub>/PC data available in the literature and the extrapolation of these data to establish a comparison is considered invalid. For this reason, CO<sub>2</sub>/PC IGA results will be compared to CO<sub>2</sub>/POE32 IGA results at a selected common temperature within both mixtures tested isotherms range, in order to observe the CO<sub>2</sub>/PC absorption improvement percentage. This percentage is then to be compared to the

absorption improvement percentage for a theoretical case at 30°C and under variable pressure.

#### 4.4.4.1 Validation of CO<sub>2</sub>/POE32 Solubility Data

The isotherm of -1°C was selected to establish a comparison between the experimentally obtained data for IGA and the data collected from the literature from reference [183]. Figure 4-10 shows a comparison between CO<sub>2</sub> mass fractions from both results. Although a slight deviation can be observed, both results appear to be in significant agreement with a maximum relative error of 6.25% found at 12 bar, where the CO<sub>2</sub> mass fraction from reference [183] was 0.075 and the IGA result was 0.08. The results of the comparison alongside relative error are presented in Table 4.2.

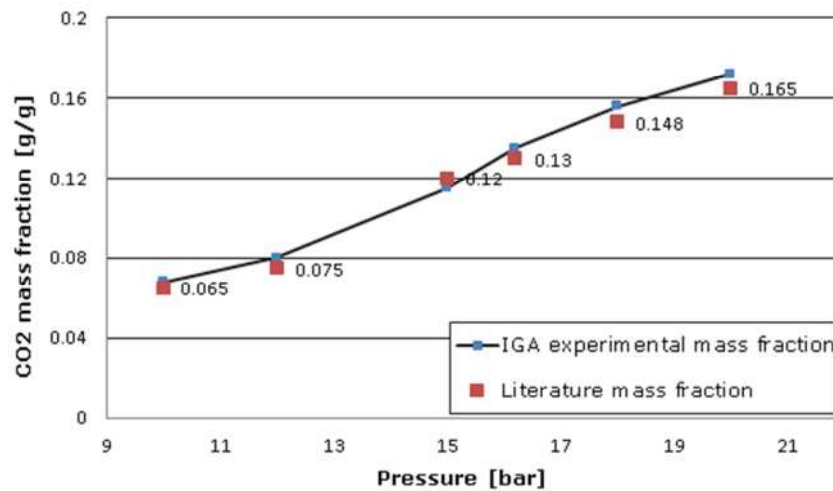


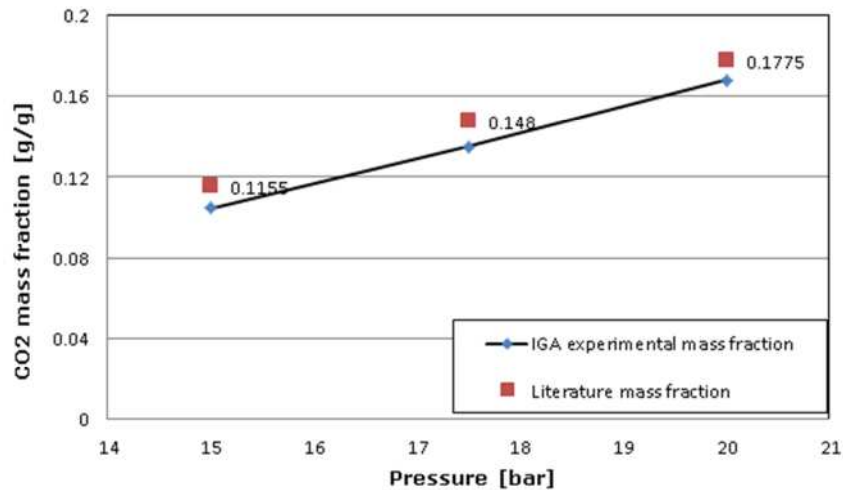
Figure 4-10: IGA solubility data validation of CO<sub>2</sub>/POE32 at -1°C.

Table 4.2: CO<sub>2</sub>/POE32 IGA solubility data compared to the literature data from [183] at -1°C.

Test pressure [bar]	IGA experimental mass fraction [g/g]	Literature mass fraction [g/g] [183]	Relative error [%]
10	0.068	0.065	4.41
12	0.08	0.075	6.25
15	0.115	0.12	4.35
16.2	0.135	0.13	3.70
18	0.156	0.148	5.13
20	0.172	0.165	4.07

#### 4.4.4.2 Validation of CO<sub>2</sub>/POE68 Solubility Data

Figure 4-11 shows a comparison of IGA experimental results for CO<sub>2</sub>/POE68 in comparison to data from reference [152] at 0°C. Despite the greater deviation observed at the first two points, both results are still within a fairly acceptable deviation tolerance, with an average relative error of 8.42%. Moreover, both results follow a similar trend. The maximum relative error was 10%, found at the second point, while the mass fraction found in the literature was 0.148 and the IGA result was 0.135. Table 4.3 lists the results of the comparison and the relative error observed:



**Figure 4-11: IGA solubility data validation of CO<sub>2</sub>/POE68 at 0°C.**

**Table 4.3: CO<sub>2</sub>/POE68 IGA solubility data compared to the literature data from reference [152] at 0°C.**

Test pressure [bar]	IGA experimental mass fraction [g/g]	Literature mass fraction [g/g] [152]	Relative error [%]
15	0.105	0.115	9.524
17.5	0.135	0.148	10.074
20	0.168	0.178	5.655

#### 4.4.4.3 CO<sub>2</sub>/POEs Comparison

Besides using the CO<sub>2</sub>/POE32 IGA results to be compared to the CO<sub>2</sub>/POE5 IGA results, the perfect agreement the CO<sub>2</sub>/POE32 IGA data showed in relation to the literature data endorses the use of CO<sub>2</sub>/POE32 results as a benchmark for comparing other CO<sub>2</sub>/POE results.

Figure 4-12 shows a comparison of CO<sub>2</sub> solubility in POE5, POE32 and POE68 at -1°C, a common temperature within the temperature range tested for the three mixtures. As shown in the Figure, CO<sub>2</sub> has higher solubility in POE5 than it has in POE32, by a maximum of 15.3%, observed at 12 bar. The solubility data compared and the percentage improvement in absorption are shown in Table 4.4. However, since the improvement in solubility is considered to be quite small and due to the absence of solubility data in the open literature, further investigation of CO<sub>2</sub>/POE5 will not be considered.

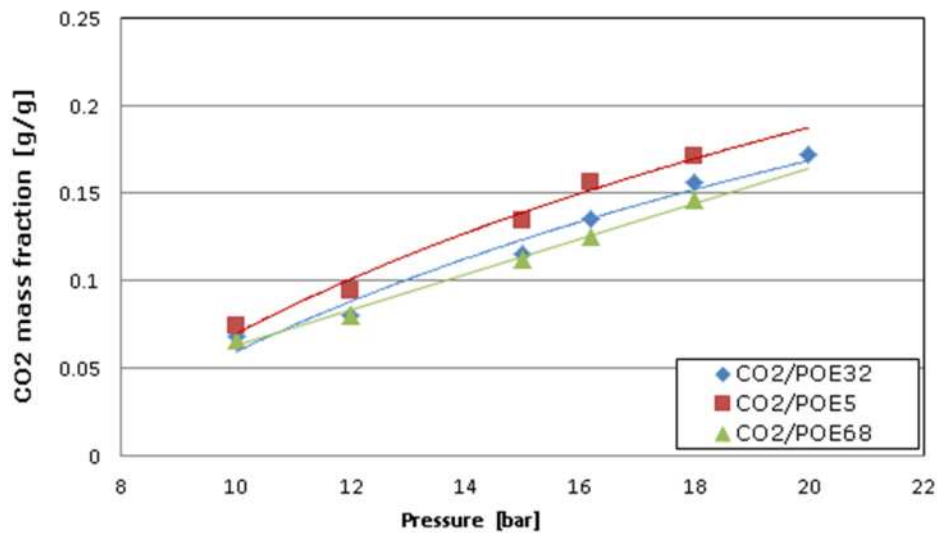


**Figure 4-12: Comparison of the results for IGA solubility, from CO<sub>2</sub>/POE5, CO<sub>2</sub>/POE32, and CO<sub>2</sub>/POE68 at -1°C.**

**Table 4.4: Comparison of CO<sub>2</sub>/POE5 and CO<sub>2</sub>/POE32 IGA solubility data at -1°C.**

Test pressure [bar]	CO <sub>2</sub> /POE5 IGA experimental mass fraction [g/g]	CO <sub>2</sub> /POE32 IGA experimental mass fraction [g/g]	CO <sub>2</sub> /POE5 absorption improvement [%]
10	0.0745	0.068	8.72
12	0.0945	0.08	15.34
15	0.134	0.115	14.17
16.2	0.156	0.135	13.46
18	0.171	0.156	8.77

Besides the deviation observed in the solubility results for CO<sub>2</sub>/POE68 IGA, when compared to the solubility data in the literature, CO<sub>2</sub>/POE68 was found to have a lower mass fraction of CO<sub>2</sub> than CO<sub>2</sub>/POE32 at different test pressures, as can clearly be seen in Figure 4-12. The results of the comparison, presented in

Table 4.5, show a maximum CO<sub>2</sub>/POE32 absorption improvement of 8%, observed at 16.2 bar. The improvement in CO<sub>2</sub>/POE32 absorption over CO<sub>2</sub>/POE68 and the deviation between the CO<sub>2</sub>/POE68 IGA results and those from reference [152] suggest a slight level of inaccuracy in the solubility data from reference [152]. This slight inaccuracy would indicate that CO<sub>2</sub>/POE68 has better absorption than POE32, which is not true. However, this minor discrepancy will not provoke any further evaluation errors once the average deviation between the data from both mixtures is known.

**Table 4.5: Comparison of CO<sub>2</sub>/POE32 and CO<sub>2</sub>/POE68 IGA solubility data at -1°C.**

Test pressure [bar]	CO <sub>2</sub> /POE32 IGA experimental mass fraction [g/g]	CO <sub>2</sub> /POE68 IGA experimental mass fraction [g/g]	CO <sub>2</sub> /POE32 absorption improvement [%]
10	0.068	0.066	3.03
12	0.08	0.08	0
15	0.115	0.112	2.67
16.2	0.135	0.125	8
18	0.156	0.146	6.84

#### 4.4.4.4 Validation of CO<sub>2</sub>/PC Solubility Data

As stated previously, CO<sub>2</sub>/PC IGA data was compared to CO<sub>2</sub>/POE32 IGA data to observe the increased absorption. The isotherm selected for this comparison was -2°C; an isotherm used to evaluate the CO<sub>2</sub>/PC absorption, within the tested temperature range of CO<sub>2</sub>/POE32. Table 4.6 shows the comparison of the IGA results at different pressures, alongside the improvement in CO<sub>2</sub>/PC absorption. An average improvement of 21.84% was observed.

**Table 4.6: Comparison of CO<sub>2</sub>/PC and CO<sub>2</sub>/POE32 IGA solubility data at -2°C.**

Test pressure [bar]	CO <sub>2</sub> /POE32 IGA experimental mass fraction [g/g]	CO <sub>2</sub> /PC IGA experimental mass fraction [g/g]	CO <sub>2</sub> /PC absorption improvement [%]
11.99	0.091	0.107	15.184
14.98	0.122	0.153	20.088
15.98	0.134	0.169	20.768
17.98	0.161	0.207	22.266
19.49	0.178	0.239	25.637
19.94	0.182	0.250	27.082

However, another theoretical comparison case was examined at 30°C and at variable pressure to determine the average improvement in CO<sub>2</sub>/PC absorption behaviour. Table 4.7 shows the results of the comparison alongside the percentage improvement in CO<sub>2</sub>/PC absorption. As shown, an average of 21.62% was observed.

**Table 4.7: Comparison of theoretical CO<sub>2</sub>/PC and CO<sub>2</sub>/POE32 solubility data at 30°C.**

Test pressure [bar]	CO <sub>2</sub> /POE32 theoretical mass fraction [g/g]	CO <sub>2</sub> /PC theoretical mass fraction [g/g]	CO <sub>2</sub> /PC absorption improvement [%]
35	0.15	0.20	23.77
40	0.18	0.23	21.13
45	0.20	0.26	23.39
50	0.23	0.30	22.29
55	0.27	0.33	19.10
60	0.30	0.38	20.10

The average absorption improvement percentage seen in both comparison cases are found to be in good agreement with each other. This agreement indicates a clear sign of validity.

#### 4.5 Enhanced Absorption Experiment

Unlike the IGA experiment, where absorption took place by means of diffusion over a long period to reach VLE, agitation was used in this experiment by means of oil circulation in the absorption chamber. This was introduced to enhance the absorption process and reach VLE in the shortest time possible. For this purpose, absorption testing apparatus was acquired from an external party and modified, in order to adapt it to the purposes of the test. Figure 4-13 shows the original configuration of the apparatus acquired.

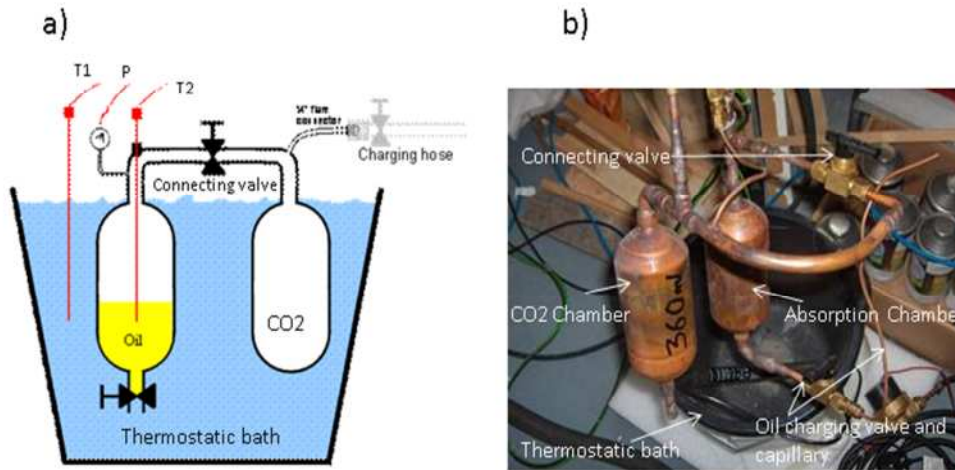


**Figure 4-13: Absorption test apparatus before modification- a) A schematic view of the apparatus, and b) the actual apparatus.**

As shown in Figure 4-13(a), the apparatus has a relatively simple configuration and measures absorption in a similar way to that which was seen in the IGA experiment, where absorption took place solely by diffusion and without any agitation. The apparatus consists of two double-ended copper cylinders of 360 ml each, used as the CO<sub>2</sub> gas chamber and the CO<sub>2</sub>/oil absorption chamber. Both chambers are connected by a valve and submerged in a thermostatic bath. Figure 4-13(b) shows the apparatus lifted out of the thermostatic bath, which is an insulated bucket. The lower valve and capillary on the absorption chamber are for the introduction of a measured quantity of oil when the apparatus is under vacuum.

#### 4.5.1 Operating and Modifying the Absorption Apparatus

The operation procedure of the original apparatus is as follows:  
 Before the commencement of an absorption experiment, both chambers are vacuumed while the connecting valve is open. While vacuuming the apparatus, a specified amount of oil is introduced into the second chamber via the capillary. After the vacuum has been established, the connecting valve is closed and the CO<sub>2</sub> gas is introduced into the first chamber at a known pressure and thermostatic bath temperature. By knowing the CO<sub>2</sub> pressure and temperature, the CO<sub>2</sub> mass in the CO<sub>2</sub> chamber can be easily

determined. However, the second chamber contains the specified oil sample, acts as an absorber when the connecting valve is opened. Once the connecting valve is opened, CO<sub>2</sub> gas travels from the first chamber to the second chamber and equalises the pressure. At that point, the absorption process starts and the CO<sub>2</sub> pressure reduces as it is being absorbed by the oil sample until VLE is reached and no further reduction in CO<sub>2</sub> pressure is observed. The second chamber is equipped with a pressure transducer to enable the pressure reduction resulting from absorption to be monitored. It is also fitted with a K-type thermocouple probe to allow the oil sample temperature to be monitored. Another thermocouple is used to monitor thermostatic bath temperature. It is important to point out that the CO<sub>2</sub> temperature in the first chamber is assumed to be equal to the thermostatic bath temperature because of the very small temperature difference.

Modifications were made to the apparatus by introducing a pump circuit to circulate the oil from the bottom of the absorption chamber, spraying it at the top of the chamber. The key element of either an absorption or desorption process is to ensure a large sorption surface area, and therefore, a very rapid and more efficient sorption process. Otherwise, the rate of absorption or desorption will be limited by the rate of diffusion into the bulk of the oil. This will result in a long sorption process to reach VLE. Figure 4-14 illustrates a schematic view of the modified apparatus, while Figure 4-15 shows different views of the modified apparatus, including the oil circulation pump.

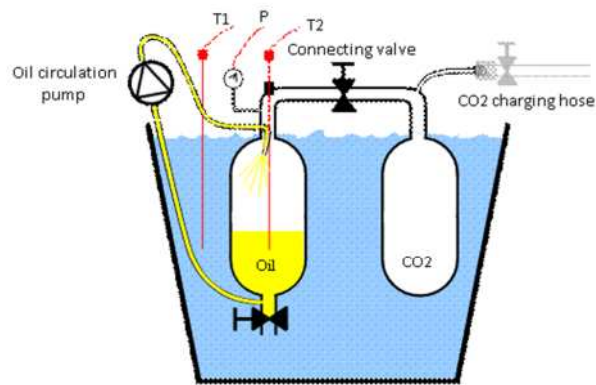


**Figure 4-14: A schematic view of the modified absorption test apparatus.**

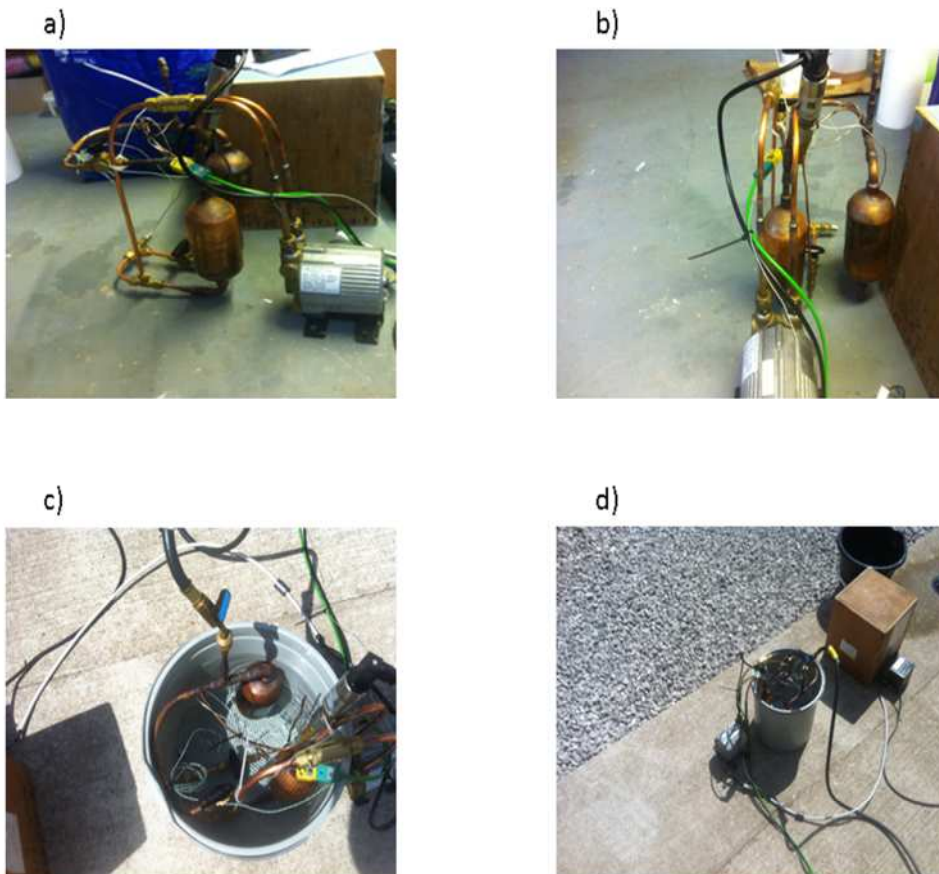


**Figure 4-15: Different views of the modified absorption apparatus.**

After the modification, the total volume of the apparatus was 760 ml, including 40 ml of the extra piping. The operating process of the modified apparatus was similar to what was explained for the original configuration. However, when the CO<sub>2</sub> was introduced into

the absorption chamber, the oil circulation pump was switched on manually to circulate and spray the oil.

#### 4.5.2 Equipment and Experimental Set-up

Besides the chambers, the connecting valve, and the thermostatic bath, the experimental setup comprised other equipment, such as the oil circulation pump, the charging and evacuation arrangement and the measuring devices that will be discussed in this section. Figure 4-16 shows a schematic of the final experimental setup and the experiment's flow process.

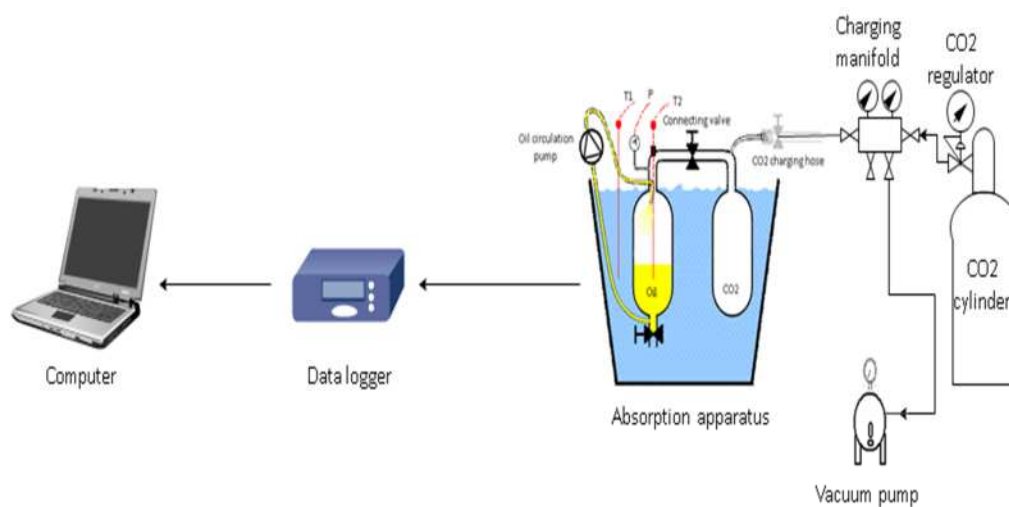


**Figure 4-16: Experimental setup of the absorption apparatus.**

##### 4.5.2.1 Oil Circulation Pump

The oil circulation pump used was a compact, electrically driven rotary vane designed to suit a wide range of applications and manufactured by Fluid-o-Tech, Italy [197]. This pump is an integrated unit which includes a pump and motor, where the motor has no moving parts. The pump has a magnetic drive and 8 selectable speeds controlled via the dual in-line package (DIP) switch on the electronic control box [198]. Figure 4-17(a) shows a general view of the pump and the electronic control box and Figure 4-17(b) shows the pump and the control box installed in the absorption apparatus. Table 4.8 lists the pump's specifications.

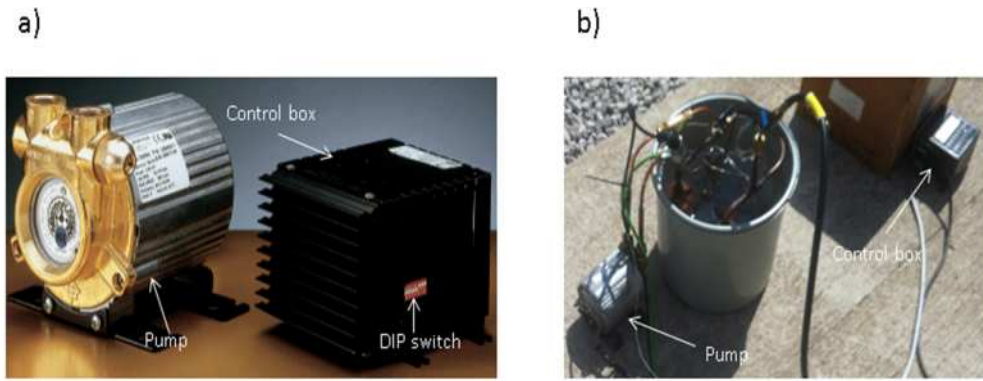


**Figure 4-17: Oil circulation pump - a) General view of the pump and control box (source: [198]), and b) the oil circulation pump and control box installed in the absorption apparatus.**

**Table 4.8: Oil circulating pump specifications.**

Brand	Fluid-o-Tech
Model	TMFR1
Maximum power [W]	250
Voltage [v AC]	230 (3 phase)
Maximum speed [RPM]	3500
Frequency [Hz]	30 to 120
Maximum fluid temperature [°C]	70
Maximum operating pressure [bar]	20

#### 4.5.2.2 Charging and Evacuation Equipment

Other equipment used in the experiment is the common equipment found in refrigeration experiments. A CO<sub>2</sub> regulator was used to provide the CO<sub>2</sub> gas for the charging manifold at the required operating pressure. A four valves refrigeration charging manifold kit, was used to introduce the CO<sub>2</sub> into the CO<sub>2</sub> chamber in the absorption apparatus. A refrigeration vacuum pump was connected to the charging manifold and used to generate a vacuum in the apparatus in order to attain the initial state of the experiment before the introduction of the CO<sub>2</sub> gas and the examined oil sample. The vacuum pump was also used at the end of the experiment to evacuate the apparatus. Figure 4-18 shows the CO<sub>2</sub> cylinder, regulator and charging manifold kit.

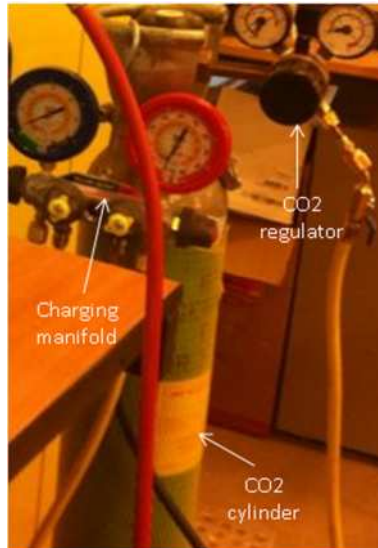


**Figure 4-18: CO<sub>2</sub> cylinder, regulator and charging manifold.**

### 4.5.2.3 Measurement Devices

#### 4.5.2.3.1 Measurement Uncertainties

Measurement uncertainties commonly occur in any experimental work. However, these uncertainties should be minimised to the lowest values possible by calibrating the measurement devices. In addition, the inclusion of the observed uncertainty values in the computation of the transmitted measurements is essential to ensure accurate and reliable measurements. For these reasons, observed uncertainties were indicated for each measurement device and included in the measurement calculations.

#### 4.5.2.3.2 Thermocouples

Common K-type thermocouples with exposed welded tips and miniature plugs were used to measure the thermostatic bath temperature and the oil sample temperature inside the absorption chamber. In this instance, the thermocouples are manufactured by RS [199] and are able to measure temperatures in the range of -75°C to 250°C. Before the acquisition of the absorption apparatus, the thermocouples were calibrated to freezing point and were found to have an uncertainty of  $\pm 0.2^\circ\text{C}$ . Figure 4-19(a) shows a general view of the thermocouple used and Figure 4-19(b) shows its actual installation on the apparatus.

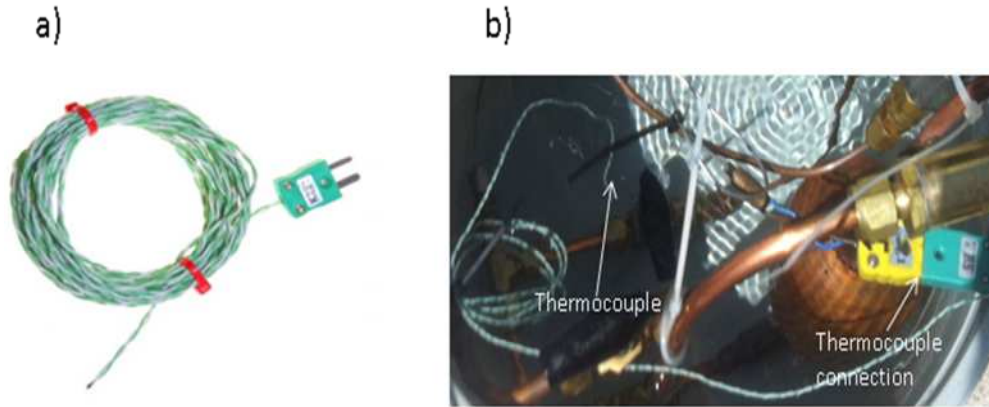


**Figure 4-19: K- type thermocouple - a) General view (source:[199]), and b) thermocouple used to measure the thermostatic bath temperature.**

#### 4.5.2.3.3 Pressure Transducer

An industrial, high performance absolute pressure transducer manufactured by RS [200] was used to measure the pressure changes in the absorption chamber. The transducer has the capability to measure pressure in the range of -1 to 24 bar with a supply voltage in the range of 9 to 32 V DC and an analogue output transmitted in the form of current in the range of 4 to 20 mA. The transducer has an uncertainty of  $\pm 25\%$  of full scale, with the ability to operate across a temperature range of  $-20^{\circ}\text{C}$  to  $135^{\circ}\text{C}$ . Figure 4-20(a) shows a general view of the pressure transducer, while Figure 4-20(b) shows the pressure transducer installed on the absorption chamber. The pressure transducer was calibrated in the test by comparing the charging manifold pressure gauge reading with the real-time transducer readings. Uncertainties of  $\pm 0.13\%$  to  $\pm 0.15\%$  were observed.

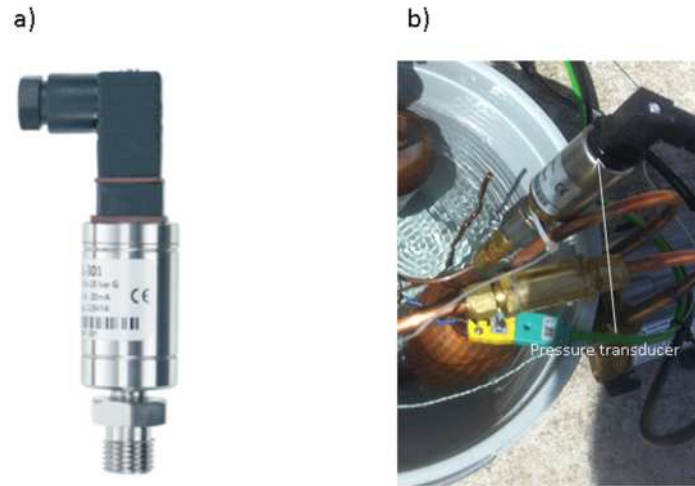


**Figure 4-20: Absolute pressure transducer - a) General view (source: [200]), and b) pressure transducer installed on the absorption chamber.**

#### 4.5.2.3.4 Data Acquisition

Electronic data acquisition of pressure and temperatures as well as operating time was established in order to accurately study the characteristics relating to the apparatus. The data logger used was the DT80, manufactured by dataTaker, Australia [201], which is a very user-friendly data logger with a built-in real-time display and configuration interface that is directly accessible via a Web browser. The DT80 has 15 analogue channels which are able to measure input in voltage, current, resistance and frequency and has an uncertainty of  $\pm 0.1\%$ . The data logger also has 8 digital channels which can be shared with counter-channels and serial channels. Figure 4-21(a) shows a general view of the DT80 data logger and Figure 4-21(b) shows the data logger once the experiment has commenced.

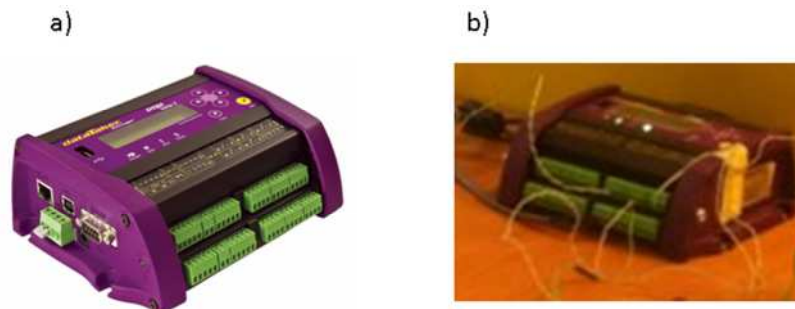


**Figure 4-21: DataTaker DT80- a) General view (source: [201]), and b) the DT80 logger operating while the experiment is in progress.**

However, the data logger configuration interface comprises a wide variety of pre-defined wiring and logging configurations for common instruments and allows for the definition of desired measurements and logging schedules. The range of sensors supported by the interface covers thermocouples of all types, resistance temperature detectors (RTDs), thermistors, monolithic temperature sensors, strain gauges and bridge sensors, as well as a 4 to 20 mA current loop suitable for pressure transducers. Figure 4-22 shows a mimic view created in the DT80 interface for real-time monitoring.

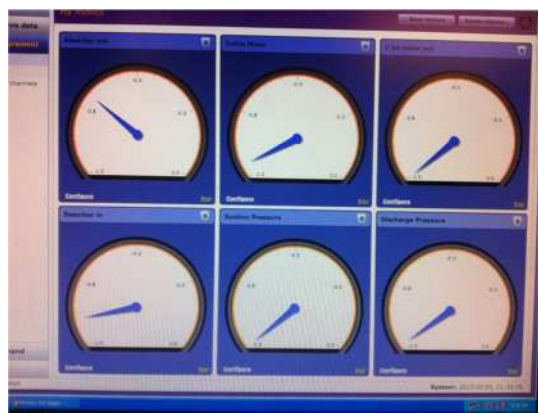


**Figure 4-22: The DT80 monitoring interface.**

Besides support for defining the sensor, the data logger also ensures linearisation, including functions, polynomials and expressions. Figure 4-23 shows an example of a span linearised function [201].

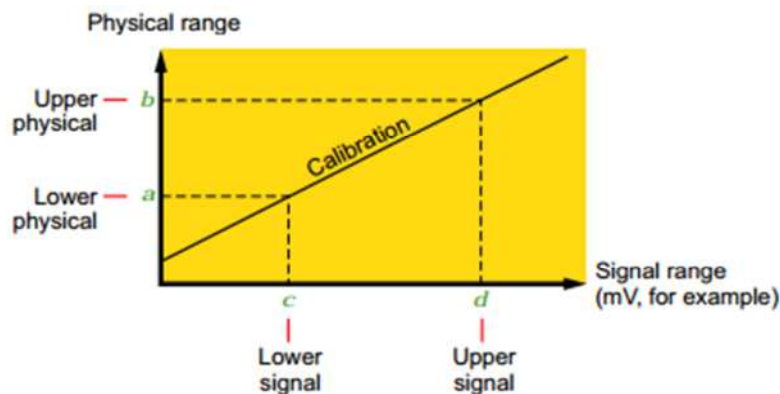


**Figure 4-23: Span calibration coordinates (source: [202])**

As shown in Figure 4-23, the signal value measured in mV DC, for example, is transformed to the physical value by a linear function,

according to the user's definition of the span, as specified in the instrument manufacturer's data sheet [202].

### 4.5.3 Results and discussion

Table 4.9 lists the absorbents included in the enhanced absorption experiment, alongside their measured volumes. PC was tested in a combination of POE32/PC. This is mainly because PC does not have any lubricating characteristics. In addition, two ratios of POE32/PC were tested to investigate the absorption improvement PC may introduce to the POE32 as the main absorbent in the blend. Table 4.10 shows the densities of the absorbents used in the analysis of the experimental results.

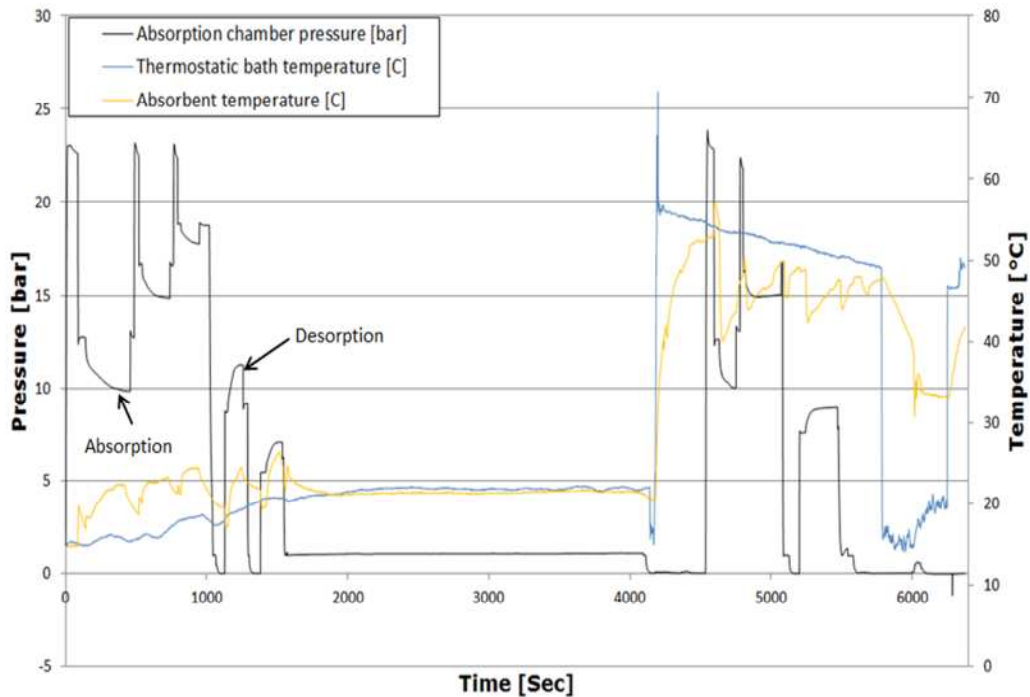
**Table 4.9: Names and volumes of the tested absorbents in the enhanced absorption apparatus.**

Absorbent name	Absorbent volume
POE32	100 ml
POE68	100 ml
POE32/PC	100 ml/10 ml
	100 ml/30 ml

**Table 4.10: Absorbents densities.**

Absorbent name	Density $\left[\frac{kg}{m^3}\right]$
POE32	977
POE68	977
PC	1200

To illustrate the calculation procedure for the solubility results, an absorption process of CO<sub>2</sub> solubility in POE32 was taken as an example to be discussed in detail. The calculation was carried out in Microsoft Excel [203] and was aided by REFPROP 9.0 [204] for the CO<sub>2</sub> properties.

4.5.3.1 CO<sub>2</sub>/POE32

**Figure 4-24: Enhanced CO<sub>2</sub>/POE32 absorption pressure and temperatures profile.**

Figure 4-24 shows the pressure changes in the absorption chamber due to CO<sub>2</sub> absorption or desorption in the POE32 oil sample. As indicated in the Figure, when the absorption takes place, the pressure reduces, while the opposite behaviour is seen for the desorption process. The Figure also shows that the thermostatic bath temperature and oil sample temperature are fairly close to one another; however, the thermostatic bath is more stable. The first three absorption processes and the first two desorption processes took place at lower temperatures, while the fourth and fifth absorption processes alongside the third desorption took place at high temperatures. Figure 4-25 shows a zoomed-in view of the first absorption process indicated in Figure 4-24.

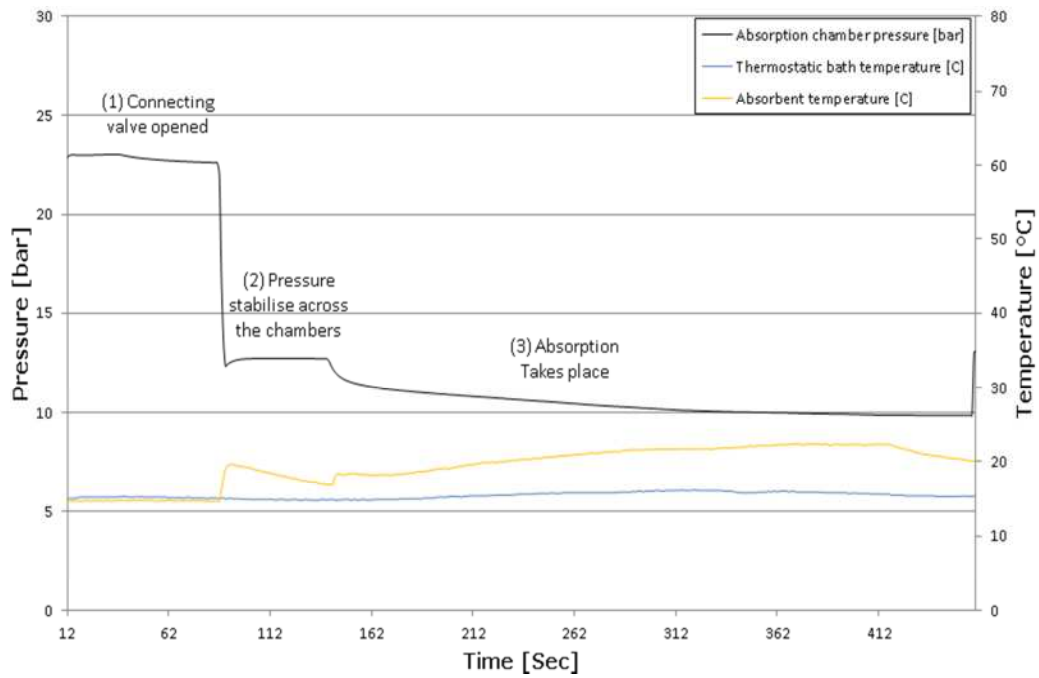


**Figure 4-25: Zoomed-in view of the first enhanced CO<sub>2</sub>/POE32 absorption process.**

As shown in Figure 4-25, the absorption process can be divided into three state points for the purposes of calculation. First, when the connecting valve is closed and the CO<sub>2</sub> exists only in the CO<sub>2</sub> chamber at a known pressure and temperature, a vapour portion, of which the mass is:

$$M_{CO_2_1} = V_1 \rho_{CO_2_1}(P_1, T_{w_1}) \quad (4.1)$$

When the connecting valve is opened, this portion of CO<sub>2</sub> travels across to the absorption chamber and stabilises the pressure at state point 2. The pressure recorded at state point 2 can be predicted by calculation to confirm the procedure for calculating solubility, as:

$$P_{2_{calc}}(\rho_{CO_2_2}, T_2) \quad (4.2)$$

Where

$$\rho_{CO_2_2} = \frac{M_{CO_2_1}}{V_T - V_{oil}} \quad (4.3)$$

It is important to point out that the oil circulation pump is switched on at state point 2. By switching the pump on, the process reaches state point 3, where rapid absorption takes place and is completed within 5.32 minutes instead of hours, as seen in the IGA solubility experiment. If the pump was absent, state point 2 would continue

along the time-line and the pressure would reduce very slowly while diffusion took place. However, the end of the absorption process at state point 3 is identified by the constant pressure along the time-line. At that point the CO<sub>2</sub> mass absorbed in the oil is:

$$M_{CO_2Abs} = (\rho_{CO_2_2} - \rho_{CO_2_3}) (V_T - V_{oil}) \quad (4.4)$$

And

$$\rho_{CO_2_3} (P_3, T_3) \quad (4.5)$$

Where  $T_3$  is taken as the average of the thermostatic bath and oil temperatures. Therefore, the liquid CO<sub>2</sub> mass fraction absorbed in the oil becomes:

$$\omega = \frac{M_{CO_2Abs}}{M_{CO_2Abs} + M_{Oil}} \quad (4.6)$$

Where  $M_{Oil}$  is:

$$M_{Oil} = \rho_{oil} V_{oil} \quad (4.7)$$

The POE32 oil density may be taken as  $977 \frac{kg}{m^3}$ , as given in the oil safety data sheet [205]. Alternatively, a precise calculation of the POE32 density is given by the following correlation, determined through experimental work and especially provided for the current research [206].

$$\rho_{oil} = -0.757 T_{oil_3} + 1198 \text{ Where } T_{oil_3} \text{ is in kelivin} \quad (4.8)$$

For any similar experiment, both absorption and desorption processes are accumulative, where the CO<sub>2</sub> portion absorbed in the first absorption process is added to the CO<sub>2</sub> portion absorbed in the second and so on. Therefore, the CO<sub>2</sub> mass fraction absorbed at the end of the third absorption process shown in Figure 4-24 becomes:

$$\omega_3 = \frac{M_{CO_2Abs1} + M_{CO_2Abs2} + M_{CO_2Abs3}}{M_{CO_2Abs1} + M_{CO_2Abs2} + M_{CO_2Abs3} + M_{Oil}} \quad (4.9)$$

The desorption process follows exactly the same calculation procedure as was explained for the absorption process. However, instead of  $M_{CO_2Abs}$ , the  $M_{CO_2Des}$  is a negative quantity, subtracted from the total absorbed CO<sub>2</sub> mass portion at the end of the third absorption process, where

$$\omega_4 = \frac{M_{CO_2_{Abs1}} + M_{CO_2_{Abs2}} + M_{CO_2_{Abs3}} + M_{CO_2_{Des1}}}{M_{CO_2_{Abs1}} + M_{CO_2_{Abs2}} + M_{CO_2_{Abs3}} + M_{CO_2_{Des1}} + M_{Oil}} \quad (4.10)$$

Figure 4-26 shows a zoomed-in view of the first desorption process. As can be seen, the desorption process is also divided into three state points. While the connecting valve is closed and the CO<sub>2</sub> chamber is at low pressure, with the absorption chamber pressurised from the last absorption process, the connecting valve is opened at state point 1. Next, the pressure will rise across the chambers to stabilise at state point 2. At this point, the oil circulation pump is switched on and rapid desorption takes place until the maximum CO<sub>2</sub> portion is desorbed at the operating pressure and temperature in 1.87 minutes. The CO<sub>2</sub> pressure will rise during the desorption process, showing the opposite behaviour from what is observed in the absorption process.

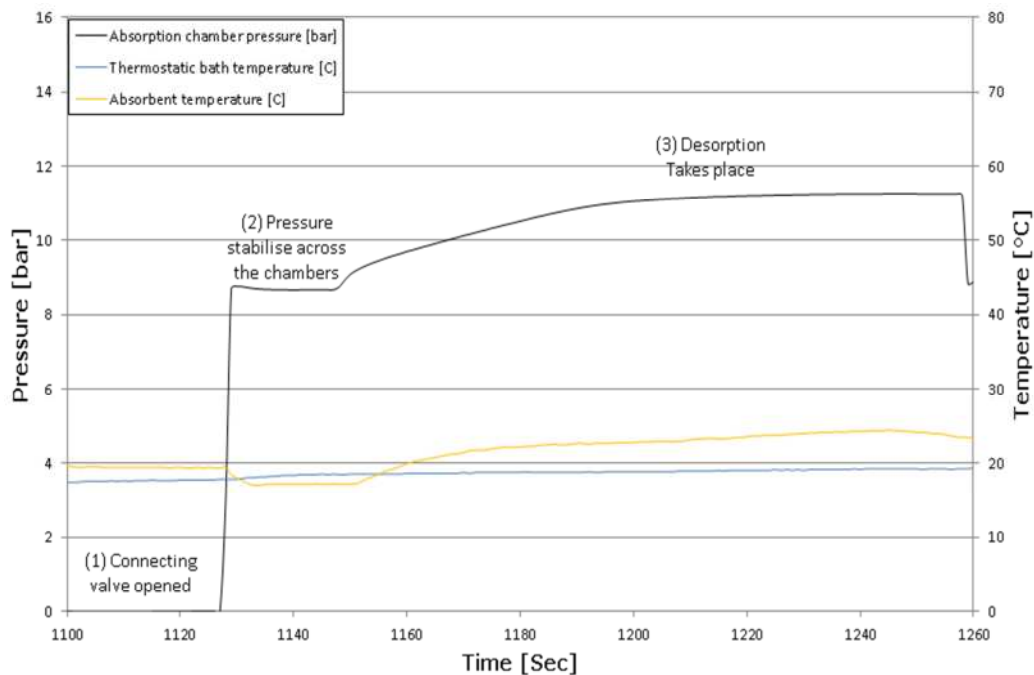


**Figure 4-26: Zoomed-in view of the first enhanced CO<sub>2</sub>/POE32 desorption process.**

The state points analysed for all absorption and desorption processes carried out in the enhanced CO<sub>2</sub>/POE32 experiment and shown in Figure 4-24 are listed in Table 4.11. These state points

were used for the calculation of the CO<sub>2</sub> mass fractions absorbed in the POE32 oil.

**Table 4.11: Enhanced CO<sub>2</sub>/POE32 absorption/desorption experimental state points.**

State point	Pressure [bar]	Thermostatic bath temperature [°C]	Oil sample temperature [°C]
First absorption			
1	22.63	15.1	14.7
2	12.72	14.9	19.1
3	9.86	15.4	21.5
Second absorption			
1	22.58	15.5	18.8
2	16.76	15.7	19.5
3	14.86	16.9	23.1
Third absorption			
1	22.47	17.6	21.4
2	18.82	17.7	21.6
3	17.78	18.3	24.4
First desorption			
1	0.05	17.4	19.7
2	5.41	20.2	21.1
3	11.25	19.2	24.3
Second desorption			
1	0.46	20.2	21.7
2	6.97	20.7	25.4
3	8.71	17.9	18.5
Fourth absorption			
1	23.04	54.2	52.8
2	12.61	53.8	55.6
3	10.03	53.4	43.5
Fifth absorption			
1	21.83	53.3	48
2	16.21	53.2	49.8
3	15.43	53.2	44.4
Third desorption			
1	0	52	48.6
2	7.6	51.7	48.9
3	8.93	50.3	47.4

Table 4.12 shows the analysed experimental results of the enhanced CO<sub>2</sub>/POE32 absorption and desorption, compared to literature data obtained under the same conditions.

**Table 4.12: Enhanced CO<sub>2</sub>/POE32 absorption/desorption experimental results compared to literature solubility data.**

Process	Processing time [Sec]	Total CO <sub>2</sub> mass absorbed [g]	Experimental mass fraction [g/g]	Literature mass fraction [g/g] [183]	Relative error [%]
Absorption 1	326	4.75	0.046	0.044	4.6
Absorption 2	202	7.52	0.071	0.067	6

Absorption 3	131	9.07	0.084	0.079	6.9
Desorption 1	146	5.18	0.050	0.048	4.7
Desorption 2	53	4.16	0.041	0.038	6.9
Absorption 4	114	3.56	0.035	0.034	2.9
Absorption 5	240	5.0	0.049	0.046	5.5
Desorption 3	204	3.12	0.031	0.030	4.7

As shown in Table 4.12, the results indicate that agitation has a very significant influence on both absorption and desorption processes, where the maximum time recorded for a process was 326 seconds in the first absorption process, compared to 1 to 2 hours and 12 to 18 hours, as seen in the IGA experiment. The average absorption time recorded was 202 seconds, while the average desorption time was 134.3 seconds. In addition, the mass fractions determined were shown to be in perfect agreement with the literature's solubility data, with a maximum relative error of 6.9 observed in the third absorption and second desorption. The relative error results of enhanced absorption were found to be within the same range of relative error as was found in the IGA experiment, where the average relative error was 4.9 % and 4.7%, respectively. Figure 4-27 shows the relationship between the literature's theoretical results and the experimentally obtained results for CO<sub>2</sub>/POE32.

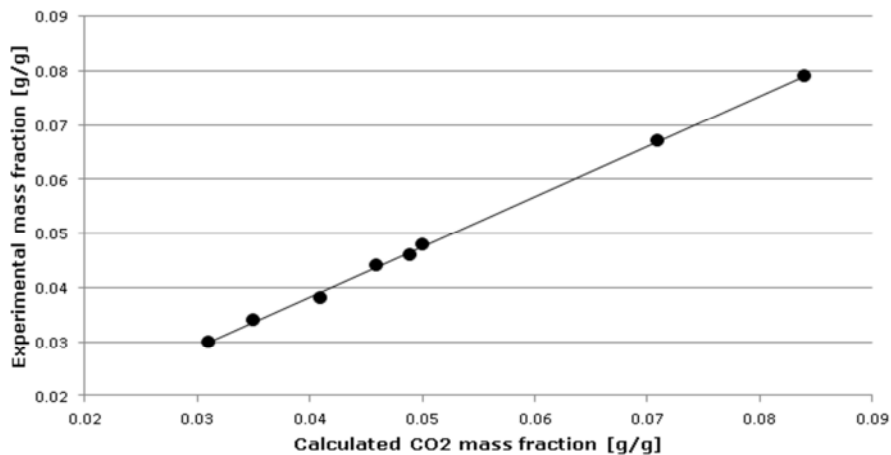


**Figure 4-27: CO<sub>2</sub> mass fraction at equilibrium in the CO<sub>2</sub>/POE32 mixture - Theoretical vs. experimental.**

4.5.3.2 **CO<sub>2</sub>/POE68**

Figure 4-28 shows the experimental results for enhanced CO<sub>2</sub>/POE68 absorption and desorption. As shown in the Figure, two absorption processes took place at the beginning and were followed by a desorption process. Table 4.13 lists the state points used for the calculation of the CO<sub>2</sub> mass fractions in the POE68 oil sample.

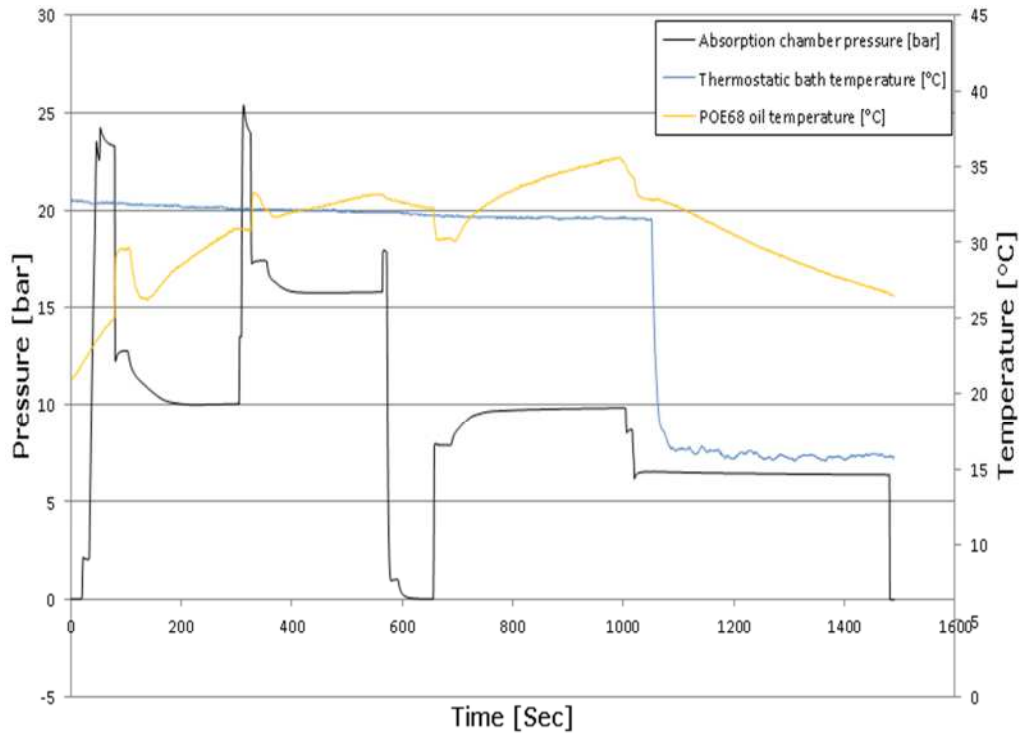


**Figure 4-28: Enhanced CO<sub>2</sub>/POE68 absorption pressure and temperatures profile.**

**Table 4.13: Enhanced CO<sub>2</sub>/POE68 absorption/desorption experimental state points.**

State point	Pressure [bar]	Thermostatic bath temperature [°C]	Oil sample temperature [°C]
First absorption			
1	23.30	32.6	25
2	12.65	32.7	29.5
3	10.06	32.2	30.9
Second absorption			
1	24.36	32.3	30.8
2	17.39	32.3	32.2
3	15.79	32.0	33.2
First desorption			
1	0	31.8	32.3
2	7.91	31.7	30.3
3	9.84	31.7	35.3

The enhanced experimental results analysed for CO<sub>2</sub>/POE68 absorption compared to the results from the literature obtained under the same conditions are shown in Table 4.14.

**Table 4.14: Enhanced CO<sub>2</sub>/POE68 absorption/desorption experimental results compared to literature solubility data.**

Process	Processing time [Sec]	Total CO <sub>2</sub> mass absorbed [g]	Experimental mass fraction [g/g]	Literature mass fraction [g/g] [152]	Relative error [%]
Absorption 1	212	4.27	0.042	0.038	8.26
Absorption 2	212	7.56	0.072	0.056	21.78
Desorption 1	311	4.53	0.044	0.038	15.07

As shown in Table 4.14, both absorption and desorption processes showed improvement with regard to processing time, similar to that seen in CO<sub>2</sub>/POE32. The average absorption time recorded was 212 seconds for the absorption process, while the maximum processing time was observed as 311 seconds in the desorption process. However, the first and third processes were shown to be within the same deviation range as was observed in the IGA experimental results for CO<sub>2</sub>/POE68. On the contrary, the second absorption process demonstrated a significant relative error of 21.78%, in comparison with the literature data. The results were double-checked with a privately provided correlation for CO<sub>2</sub>/POE68 mixture, by Neto and Barbosa [207], which is included in Appendix A.2, and also was checked against CO<sub>2</sub>/POE32 data. The relative error was found to be 26% and 21.6%, respectively. This contradiction suggests that the error could be the result of uncertainty in data logging. However the average relative error from the experimental results was found to be 15%, compared to the 8.42% derived from the results of the IGA experiment. Figure 4-29 shows the relationship between the literature's theoretical results and the experimentally obtained results for CO<sub>2</sub>/POE68.

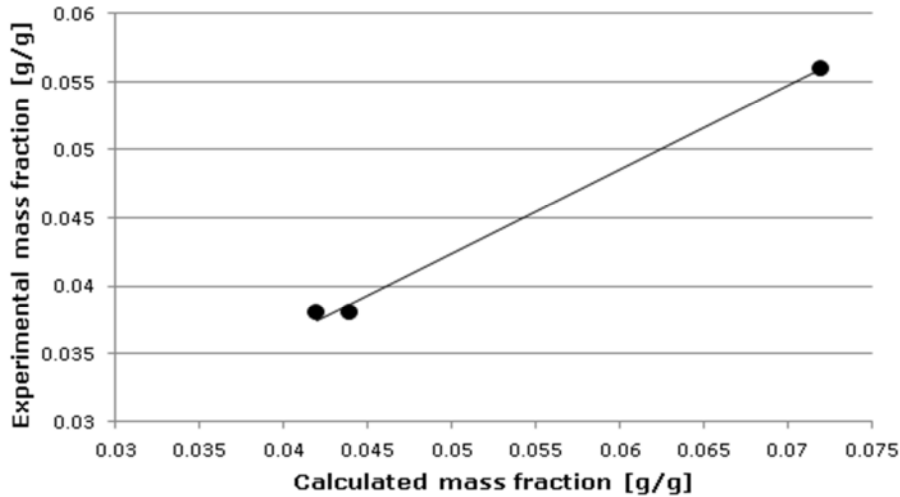


**Figure 4-29: CO<sub>2</sub> mass fraction at equilibrium in the CO<sub>2</sub>/POE68 mixture - Theoretical vs experimental.**

#### 4.5.3.3 CO<sub>2</sub>/POE32+PC

The first blend constituted 100 ml POE32 and 10 ml PC, while the second blend constituted 100 ml POE32 and 30 ml PC. The reason for testing two blend ratios is mainly to investigate the POE32 absorption enhancement attainable through the introduction of a specified amount of PC.

##### 4.5.3.3.1 CO<sub>2</sub>/100 ml POE32-10 ml PC

Figure 4-30 shows the experimental results for the enhanced CO<sub>2</sub>/100 ml POE-10 ml PC absorption. As shown, two absorption processes took place. Table 4.15 shows the state points used for the calculation of the CO<sub>2</sub> mass fractions absorbed in the POE32-PC blend.

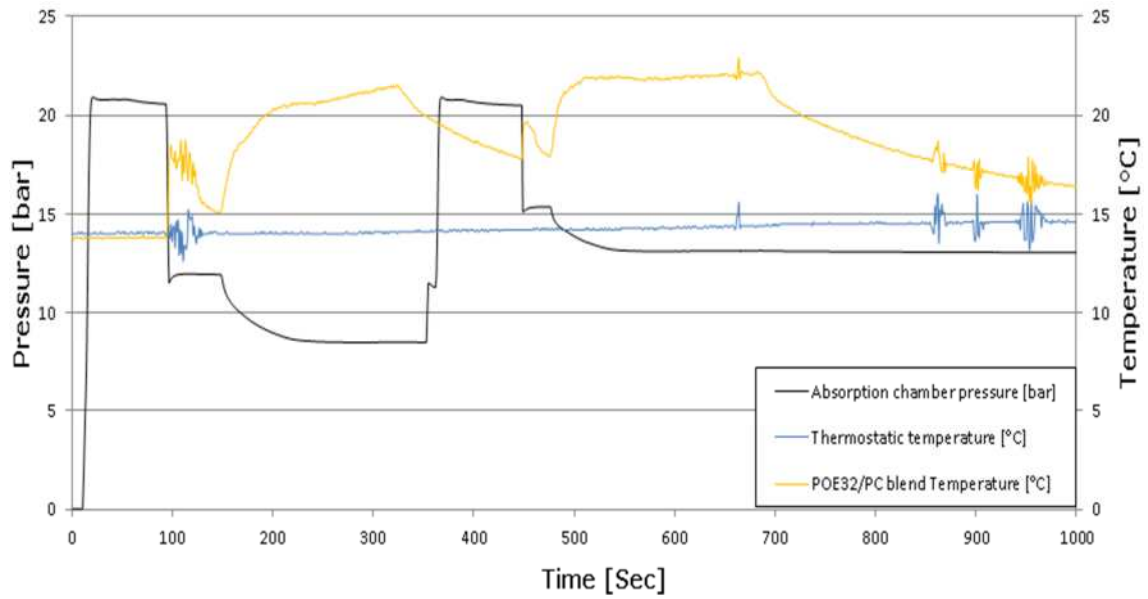


**Figure 4-30: Enhanced CO<sub>2</sub>/100 ml POE-10 ml PC absorption pressure and temperatures profile.**

**Table 4.15: Enhanced CO<sub>2</sub>/100 ml POE-10 ml PC absorption experimental state points.**

State point	Pressure [bar]	Thermostatic bath temperature [°C]	Oil sample temperature [°C]
First absorption			
1	20.57	14	13.8
2	11.91	14	15.2
3	8.504	14.1	20
Second absorption			
1	20.50	14.2	17.90
2	14.2	18	15.37
3	14.1	20	8.50

Table 4.16 shows the analysis of the CO<sub>2</sub>/100 ml POE32 – 10 ml PC experimental results. The mass fraction results of POE32-PC blends were compared to POE32, since the latter forms the higher percentage in the blend. The absorption improvement percentage of blend was taken as a range where the average relative error observed for the CO<sub>2</sub>/POE32 was accounted for.

**Table 4.16: Enhanced CO<sub>2</sub>/100 ml POE-10 ml PC absorption experimental results compared to CO<sub>2</sub>/POE32 literature solubility data.**

Process	Processing time [Sec]	Total CO <sub>2</sub> mass absorbed [g]	Experimental mass fraction [g/g]	CO <sub>2</sub> /POE32 literature mass fraction [g/g] [183]	CO <sub>2</sub> /POE32-PC absorption improvement [%]
Absorption 1	202	4.94	0.043	0.041	5.38-9.80
Absorption 2	90	8.24	0.0588	0.0588	0-4.9

The results shown in Table 4.16 suggest a slight improvement in absorption at the given absorbent blend ratio. This improvement is around 5.38% - where the CO<sub>2</sub>/POE32 relative error was not taken into account - and up to 9.80%, when the average CO<sub>2</sub>/POE32 relative error of 4.9% was considered. Lower absorption improvement was observed in the second absorption process, where it was found to be between 0 and 4.9%. The slight improvement with an average of 6.7% was found to be reasonable, due to the small amount of PC in the blend. However, the second absorption process was completed in a very short time, taking only 90 seconds. It can be seen in Figure 4-30 that the second absorption took place very quickly and the pressure line remained constant. However, the average absorption time was 146 seconds.

#### 4.5.3.3.2 CO<sub>2</sub>/100 ml POE32-30 ml PC

Figure 4-31 shows the experimental results for the enhanced CO<sub>2</sub>/100 ml POE-30 ml PC absorption. Improvements in both absorption and desorption processes are obvious from the pressure data. Two absorption processes took place, followed by desorption process and then two absorption processes at high thermostatic bath and absorbent blend temperatures. Table 4.17 shows the state points used for the calculation of the CO<sub>2</sub> mass fractions absorbed in the POE32-PC blend.

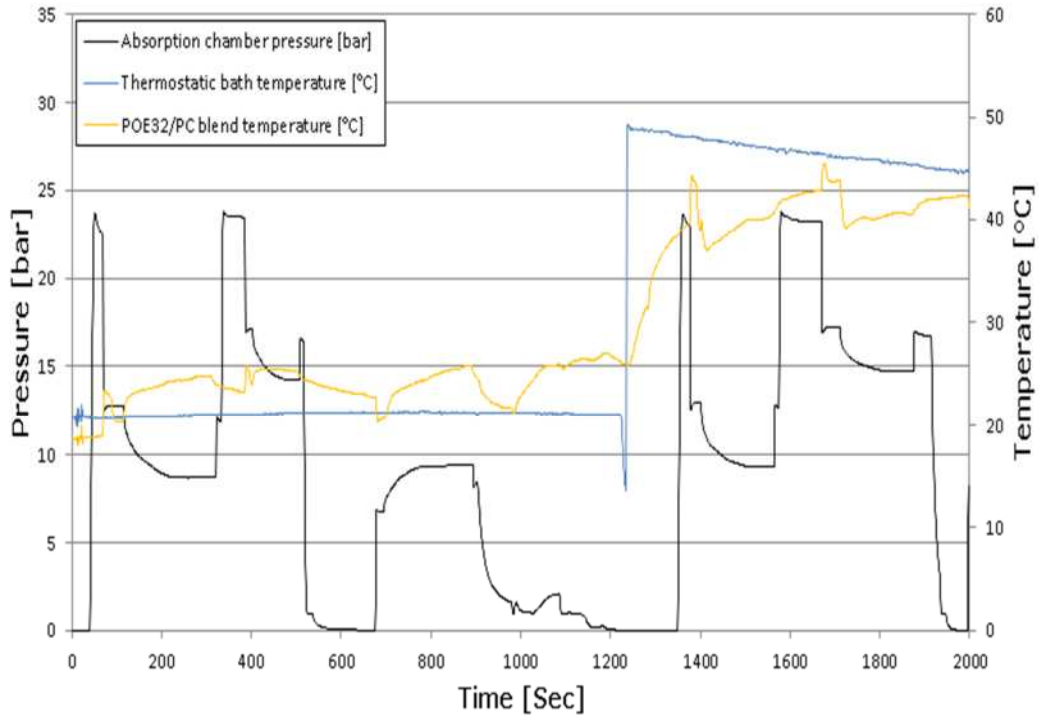


**Figure 4-31: Enhanced CO<sub>2</sub>/100 ml POE-30 ml PC absorption pressure and temperatures profile.**

**Table 4.17: Enhanced CO<sub>2</sub>/100 ml POE-30 ml PC absorption experimental state points.**

State point	Pressure [bar]	Thermostatic bath temperature [°C]	Oil sample temperature [°C]
First absorption			
1	22.54	20.7	19
2	12.78	20.8	20.3
3	8.71	21.1	24
Second absorption			
1	23.42	21.1	23.2
2	17.12	21.1	24.1
3	14.25	21.2	25
First desorption			
1	0.002	21.3	22.8
2	8.35	21.3	23.1
3	9.35	21.3	25.1
Third absorption			
1	22.95	48.1	39.8
2	12.86	47.9	39.5
3	9.29	47	40.3
Fourth absorption			
1	23.17	46.4	43
2	17.16	46.3	45
3	14.71	45.3	40.6

Table 4.18 shows the analysis of CO<sub>2</sub>/100 ml POE32 – 30 ml PC experimental results. Similar to the previous case, the mass fraction results of POE32-PC blends are compared to POE32.

**Table 4.18: Enhanced CO<sub>2</sub>/100 ml POE-30 ml PC absorption experimental results compared to CO<sub>2</sub>/POE32 literature solubility data.**

Process	Processing time [Sec]	Total CO <sub>2</sub> mass absorbed [g]	Experimental mass fraction [g/g]	CO <sub>2</sub> /POE32 literature mass fraction [g/g] [183]	CO <sub>2</sub> /POE32-PC absorption improvement [%]
Absorption 1	215	6.43	0.045	0.0367	20-23.8
Absorption 2	104	10.84	0.075	0.059	20-24
Desorption 1	175	7.15	0.051	0.039	22.8-26.4
Absorption 3	155	4.97	0.036	0.031	15-20.6
Absorption 4	195	8.28	0.0583	0.047	19.43-23.19

As can be seen in the Table, a significant improvement in absorption and desorption was observed, with an average improvement of 21.52%. This improvement was found to be very close to what was observed for CO<sub>2</sub>/PC absorption improvement over CO<sub>2</sub>/POE32 in the IGA experiment, where the average improvement was 21.62%. The maximum processing time recorded for the first absorption process was 215 seconds. The average absorption time observed was 167.25 seconds, which is lower than in the previously examined cases.

#### 4.6 Conclusions

In this chapter, the experimental evaluation of nominated absorbents was presented. POE5, POE32, POE68, and PC were evaluated by means of their thermal stability, solubility behaviour with CO<sub>2</sub>, and enhanced solubility behaviour with CO<sub>2</sub>. The experiments revealed that the most suitable absorbent candidates for CO<sub>2</sub> are POE32 and POE68, where these both showed high thermal stability and good solubility characteristics that suited the application of CO<sub>2</sub>/lubricant absorption power generation, albeit lower than PC and POE5. Finally, enhanced absorption apparatus was acquired and modified to experimentally examine absorption and desorption behaviours and required time to complete the processes when agitation was introduced. However, the results show that absorption and desorption processing times can be enormously reduced from hours to several minutes when agitation by means of oil circulation is applied.

The TGA results show that the PC degradation started at around 65°C, while the POE5 sample started to decompose at 130°C. POE32 and POE68 showed higher thermal stability, where they started to decompose at 220°C and 225°C, respectively. With regard to TGA, it became clear that the POE32 and the POE68 lubricant oils were suitable for the absorption power generation system, where both materials were shown to be able to handle temperatures higher than the proposed generator temperature of 120°C. On the other hand, PC was found to have the lowest decomposition temperature, which was far lower than the anticipated operating temperature. This is a clear indication of its unsuitability for the application. Similarly, however, POE5 was seen to start decomposing at only 10°C higher than the anticipated operating temperature. Therefore, it was considered quite risky for use in the proposed system, apart from the fact that it could limit the operation to even lower temperatures, due to the high pressure associated with CO<sub>2</sub>.

The IGA tests findings show that absorption was significantly influenced by the time VLE was reached. The CO<sub>2</sub>/POE32 IGA results show perfect agreement with the solubility data available in the literature, with a maximum relative error of 6.25%. The CO<sub>2</sub>/POE68 IGA data were found to deviate from the solubility data in the literature by a maximum of 10%, which falls within fairly acceptable bounds. A comparison of solubility data from the literature indicated that POE68 absorb more CO<sub>2</sub> than does POE32. The IGA experiment outcomes show this is not true, where POE32 tended to absorb more CO<sub>2</sub> than POE68 by a maximum of 6.8%. Among the POE lubricants tested, POE5 tended to absorb the most CO<sub>2</sub> mass fractions. In comparison to POE32, POE5 demonstrated an improvement in absorption by a maximum of 15.3%. The CO<sub>2</sub>/PC results illustrate that PC tends to absorb more CO<sub>2</sub> than any of the other lubricants tested. In comparison to POE32, PC showed an average improvement of 21.8%, which was confirmed

by theoretical comparison at 30°C. The average improvement was found to be 21.6%.

The enhanced absorption experimental results show that agitation has a very significant effect on the enhancement of both absorption and desorption process rates, where the processes were completed in just a few minutes, instead of the hours noted in the IGA experiment. The minimum average processing time was 146 seconds, observed in the 100 ml CO<sub>2</sub>/ 10 ml PC, while the maximum average processing time was 212 seconds, observed in the CO<sub>2</sub>/POE68 case. The inconsistency in processing time refers to the solubility behaviour of the mixture and its agitation characteristics. For instance, the more efficiently the mixture was sprayed on the internal surface area of the absorption chamber, the faster the process was completed. Similarly, the speed of the absorbent's circulation is an important factor in time enhancement. Despite enhancement in processing time, the results show that agitation does not have any effect on the amount of CO<sub>2</sub> absorbed. The CO<sub>2</sub> mass fractions yielded by the experiment was seen to be in perfect agreement with the results obtained in the IGA experiment and fell within the same bounds of relative error when compared to the literature data. Significant relative error was found in the second absorption process, pertaining to CO<sub>2</sub>/POE68, which suggests that there was uncertainty in the instruments while data was being recorded. For the CO<sub>2</sub>-PC blend, it was found that a smaller PC ratio in the POE32/PC blend did not have a significant effect in improving absorption. However, when the ratio was increased threefold, the absorption behaviour was significantly enhanced in proportion to the PC increase, where the POE32/PC blend tended to absorb more CO<sub>2</sub> than a pure POE32 absorbent would have done. In fact the absorption behaviour of the blend became similar to that of pure PC, which was examined in the IGA experiment.

## Chapter 5 : Prediction of Thermodynamic Properties of the CO<sub>2</sub>/lubricant mixtures

---

### 5.1 Introduction

The CO<sub>2</sub> solubility in lubricant oils will form a mixture that is poorly understood, with unknown properties. Moreover, commercial lubricants have unknown chemical structures. Therefore, the properties of commercial lubricant oils are also estimated from or referred to their pure compounds. From these facts, it becomes obvious that understanding and correlating the thermodynamic properties of CO<sub>2</sub>/lubricant oil is essential for modelling and evaluating the performance of the CO<sub>2</sub>/lubricant absorption power generation system. However, working with a mixture in an absorption cycle is not straightforward, as it is in pure refrigerant cycles. In mixtures, solubility data are correlated using different approaches [208]. These approaches can be classified into two categories: empirical correlations and thermodynamic models, such as cubic equation of state thermodynamic models (EOS); solution activity models; local composition modelling; group contribution concepts, and perturbed hard chain methods (PHSC) [209]. The majority of these thermodynamic approaches are complex and incorporate the physics and chemistry of mixing, providing little or no advantages in terms of accuracy, when compared to the empirical correlation approach [210]. Generally, however, an excellent fit of solubility data with the correlation and model is a significant sign of validity [211].

Nevertheless, most of the studies available in the literature are not directly related to the determination of the thermodynamic properties of CO<sub>2</sub>/oil mixtures, or cycle performance evaluation. Instead, the vast majority of studies are concerned with correlation and the thermodynamic modelling of refrigerants/lubricants, including CO<sub>2</sub>/POE oil, for the purpose of reproducing experimentally obtained solubility data, such as is seen in [153,

176, 184, 211-213], or looking at developing estimation methods to predict refrigerant/oil properties, based on pure components properties, [147, 214, 215]. This is mainly because measurements of refrigerant/lubricant mixture properties are still considered to be under way and there is still an absence of a universal model to predict properties and describe refrigerant interaction with lubricant oil [152, 216]. This chapter will therefore provide some insight into correlation methods and propose a model approach to determine the CO<sub>2</sub>/lubricant thermodynamic properties essential for the CO<sub>2</sub>/lubricant absorption power generation system.

## 5.2 CO<sub>2</sub>/lubricant Mixtures Modelling Methods

### 5.2.1 Empirical Correlations

In this approach, empirical correlations equations are fitted to a large number of experimental data, such as VLE, density, viscosity and heat capacity data, in order to extract these specific properties for the liquid solution at different temperatures, pressures, and mass fractions, while the vapour phase, which is made purely by the refrigerant is calculated using EOS models [208]. Although empirical correlations are relatively easy to understand and can be rapidly applied, the main drawback of the empirical correlation approach is that their use is limited within the experimental data and a larger quantity of data is required, together with adjustable parameters [210].

Seeton and Hrnjak [183] have developed an equation-based approach for CO<sub>2</sub>/POE32 VLE and VLLE properties. They experimentally obtained solubility data, density and viscosity. Empirical correlations were then developed to fit the experimental data and produce coefficients. All correlations are included in this section, while the coefficients are included in Appendix B.1. Nevertheless, these correlations can only give the CO<sub>2</sub> vapour pressure (5.1), mixture density (5.2) and viscosity (5.3) as functions of liquid CO<sub>2</sub> mass fraction in the mixture and

temperature, for a wide temperature range from -40°C to 120°C, and pressures up to 150 bar:

$$\text{Log}_{10}(P) = a_1 + \frac{a_2}{T} + \frac{a_3}{T^2} + \text{Log}_{10}(\omega) \left( a_4 + \frac{a_5}{T} + \frac{a_6}{T^2} \right) + \text{Log}_{10}^2(\omega) \left( a_7 + \frac{a_8}{T} + \frac{a_9}{T^2} \right) \quad (5.1)$$

$$\rho = b_1 + b_2T + b_3T^2 + \omega(b_4 + b_5T + b_6T^2) + \omega^2(b_7 + b_8T + b_9T^2) \quad (5.2)$$

$$\begin{aligned} \log_e \left( \text{Log}_e(v + 0.7 + f(v)) \right) \\ = c_1 + c_2 \text{Log}_e(T) + c_3 \text{Log}_e^2(T) \\ + \omega(c_4 + c_5 \text{Log}_e(T) + c_6 \text{Log}_e^2(T)) \\ + \omega^2(c_7 + c_8 \text{Log}_e(T) + c_9 \text{Log}_e^2(T)) \end{aligned} \quad (5.3)$$

Where  $f(v) = e^{-v}K_0(v + \psi)$ .  $K_0$  is the zero-modified Bassel function of the second kind and  $\psi$  is a constant, equal to 1.244068.

Although the correlations presented cannot predict other essential properties required for the absorption power generation system modelling, such as specific enthalpy, Seeton and Hrnjak's study [183] still represents a very significant source for the CO<sub>2</sub>/POE32 mixture, since the POE32 lubricant used in the study is of the same POE32 oil brand used in the current research [217]. Therefore, high accuracy results, and perfect agreement were seen for the CO<sub>2</sub>/POE32 in the experimental investigations presented in Chapter 4. Figure 5-1 shows the CO<sub>2</sub> vapour pressure curves at variable CO<sub>2</sub> mass fraction in the CO<sub>2</sub>/POE32 liquid mixture, alongside pure CO<sub>2</sub> pressure, while Figure 5-2 shows the phase behaviour of the CO<sub>2</sub>/POE32 mixture. Both graphs were reproduced using correlations (5.1).

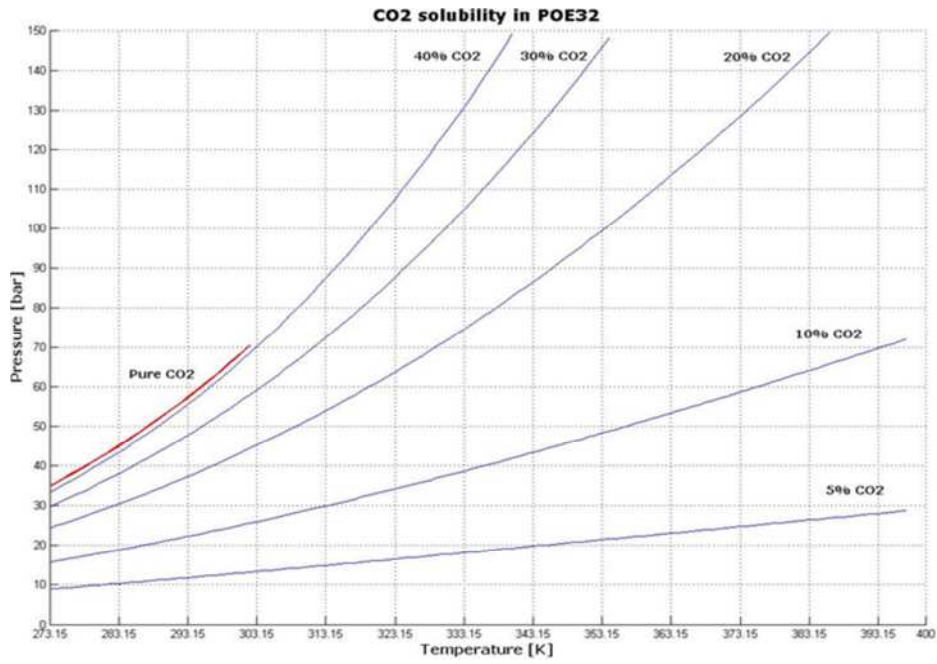


Figure 5-1: CO<sub>2</sub>/POE32 vapour pressure at different CO<sub>2</sub> mass fractions.

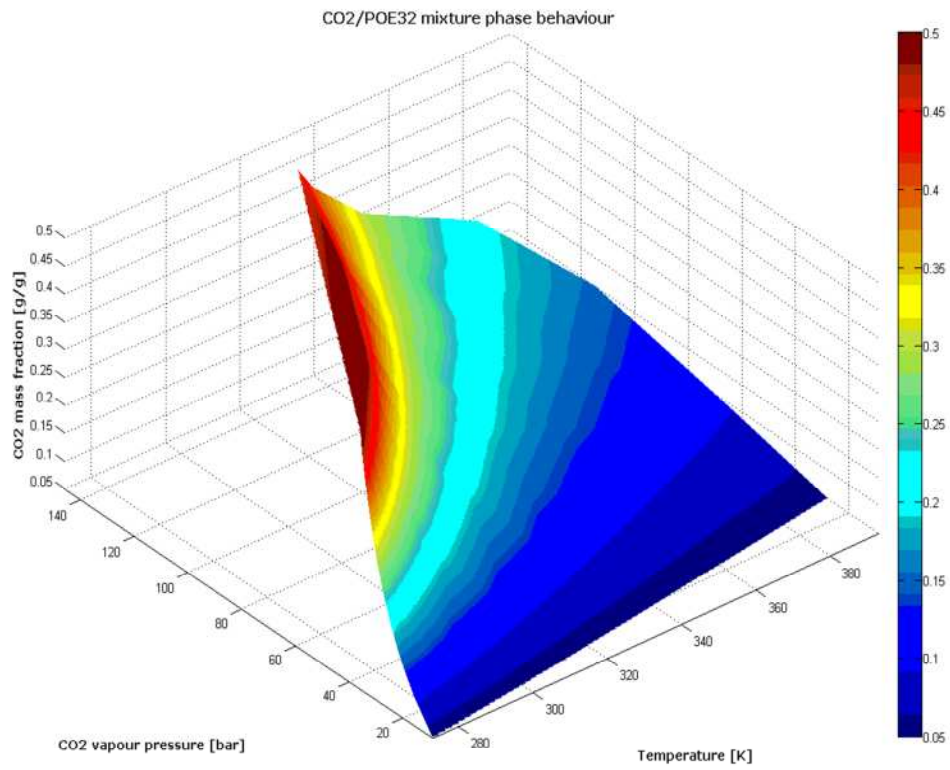


Figure 5-2: CO<sub>2</sub>/POE32 phase behaviour.

With regard to CO<sub>2</sub>/POE68, there were no available correlations in the literature, but through private communication, Neto and

Barbosa [207] provided a polynomial empirical correlation to determine the CO<sub>2</sub> vapour pressure as a function of temperature and mass fraction for both CO<sub>2</sub>/POE68 and CO<sub>2</sub>/AB32 solubility data, published in reference [184]. Unfortunately, the correlation provided was limited to 75 °C - the maximum tested temperature - and therefore, was not very useful for the current research. The document which was originally provided is attached in Appendix A.2.

Several other studies found in the literature present correlations for CO<sub>2</sub>/oil mixtures, such as Pensado et al.'s [154], which provide density and dynamic viscosity correlations for CO<sub>2</sub>/pure POE compound mixtures, derived from their experimentally obtained data. Youbi-Idrissi et al. [151], experimentally obtained CO<sub>2</sub>/commercial PAG oil data and correlated the solubility data in the form of CO<sub>2</sub> vapour pressure, as a function of liquid CO<sub>2</sub> mass fraction in the mixture, as well as temperature. Cavestri [218] suggested generalised equations to correlate the solubility of various refrigerant/oil mixtures and to correlate the viscosity of mixtures as a function of refrigerant mass fraction and mixture temperature. Other refrigerant/oil mixtures and generalised correlations were also found in the literature. However, despite the fact that these correlations would work perfectly for the specific mixtures examined and other mixtures with similar interactions, they would not necessarily work with all types of refrigerant/oil mixtures [210].

### 5.2.2 Cubic EOS Models and the Prediction of Critical Parameters of CO<sub>2</sub>/lubricant Mixtures

Equation of state (EOS) models are well-established thermodynamic models used to predict the P- $\bar{V}$ -T behaviour of pure fluids and mixtures. They are found to be more effective than ideal gas law [219]. Their ability to predict the near and above critical point of fluids makes them very popular, especially when working with

refrigerants with low critical temperatures, such as CO<sub>2</sub> [209]. Amongst the many types of EOS, Soave-Redlich-Kwong (SRK) and Peng-Robinson (PR) are generally the most frequently employed models alongside PC-SAFT for refrigerant/oil mixtures. However, PC-SAFT is a complex approach with different parameters from those usually found in other EOS models. Moreover, the implementation of conventional SRK or PR EOS models requires knowledge of data that are either unavailable or imprecise in the case of lubricant oil, such as critical temperature, critical pressure, molecular weight and acentric factors. This makes both EOS and oil critical properties topics which are usually coupled in researches related to refrigerant/lubricant oil mixtures. Therefore, an extensive investigation of the literature and an estimation of these properties are essential.

The implementation of various conventional and modified versions of EOS models for refrigerant/lubricant oil mixtures, including CO<sub>2</sub>/POE's, are popular and to be seen in many studies in the literature. In a theoretical study conducted by Yokozeki [208] to evaluate the performance of an absorption-refrigeration cycle, the author implemented a generic SRK cubic EOS to model several refrigerant/absorbent mixture VLEs. The study also presented the specific enthalpy equation used and required for SRK EOS. It also included pure POE compounds, treated as commercial POE oils. However, because of the absence of critical parameters, the author estimated the critical properties and ideal polynomial gas coefficients for the pure POE compounds by means of a group contribution method [220] and indicated that a very rough estimation of these properties is sufficient to correlate the VLE data. Although the study did not include commercial POE modelling parameters, it did indeed demonstrate a clear sequence of calculation steps to determine mixture enthalpy using EOS.

In another theoretical study, Yokozeki [211] investigated the solubility of various refrigerants in different lubricant oils. The

author demonstrated complex VLE and VLLE modelling for refrigerants/lubricant oil mixtures using three different cubic EOS. Parameters for Van der Waals (vdW), SRK and PR cubic EOS models were included. The author estimated the critical properties of POE32, POE68 and pure POE compound, PEB8, and examined the sensitivity of the critical properties on the EOS model results, where the critical parameters for PEB8 were replaced by those for POE32. The model results showed a similar degree of accuracy due to the introduced adjustable coefficient  $\beta_1$  for the oil component in the mixture, which compensates for the rough estimation of critical properties in the solubility data fitting process.

It is very important to underline that the  $\beta_1$  coefficient for POEs in Yokozeki's studies [176, 208, 211] has been treated as an adjustable fitting parameter due to its importance in VLE correlations and its strong relationship to the temperature-dependent parameter  $\alpha(T)$  of EOS. Equation (5.4) shows  $\alpha(T)$  in relation to the  $\beta_1$  coefficient in Yokozeki's generic EOS models. The values obtained for the  $\beta_1$  coefficient have been found to be very close to the acentric factors for hydrocarbons with a high molecular weight, in the range of  $1 \pm 0.3$  which renders the  $\beta_1$  coefficient in Yokozeki's models equivalent for the acentric factor in conventional SRK EOS. Equation (5.5) shows  $\alpha(T)$  in relation to the acentric factor,  $\omega_f$ , in the conventional SRK EOS model. In fact, Yokozeki suggests treating the acentric factor in conventional SRK as an adjustable parameter for obtaining more accurate results [211].

$$\alpha(T) = 1 + \beta_1 \left( \frac{T_c}{T} - \frac{T}{T_c} \right) \quad (5.4)$$

$$\sqrt{\alpha(T)} = 1 + (0.48 + 1.574\omega_f - 0.176\omega_f^2) \left( 1 - \sqrt{\frac{T}{T_c}} \right) \quad (5.5)$$

However, Yokozeki [211] also proposes a hypothetical oil concept (UniOil), which has universal constants for critical parameters and coefficients, applicable for any type of oil, for the purpose of modelling. The UniOil approach has 4 to 6 interaction parameters

that are statistically produced from the mixture's solubility data. In another related study, Yokozeki [176] applied the UniOil concept to correlate the solubility data of CO<sub>2</sub>/POE and CO<sub>2</sub>/PAG oil mixtures from reference [151, 171, 185] using his proposed version of SRK EOS. The modelling results show a high level of accuracy when compared with the experimental data and therefore, UniOil has proven its validity and reliability. Figure 5-3 shows Yokozeki's correlation results for three different CO<sub>2</sub>/POE mixtures. The black lines represent the modelling results, while the red dots are the experimental solubility data from reference [185].

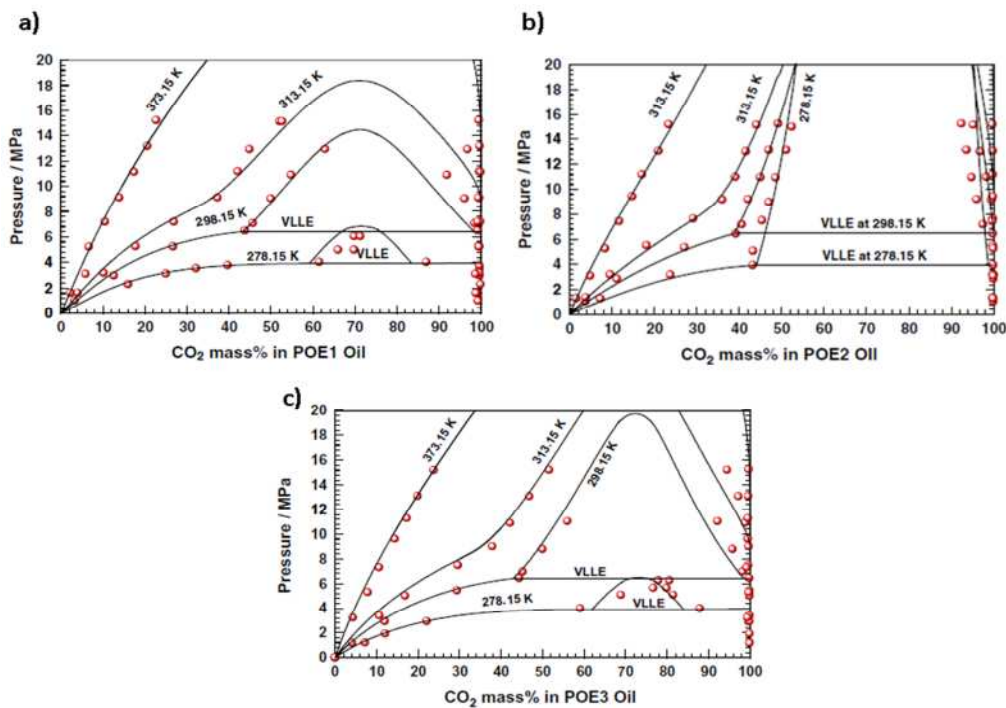


**Figure 5-3: Three CO<sub>2</sub>/POE mixtures correlated using the UniOil concept. (Source: [176])**

A great deal of other research in chemical engineering has been carried out on CO<sub>2</sub>/pure POE lubricant compounds, in order to arrive at a better understanding of the thermodynamic properties of CO<sub>2</sub>/commercial POE, based on their pure compounds. A series of experimental and theoretical studies were conducted by a group consisting of Bobbo et al. [157, 178, 221-223], Fedele et al. [213, 224, 225] and Pernechele et al. [226] to investigate CO<sub>2</sub> solubility in commercial POE oils and their pure compounds. The group experimentally examined the solubility and correlated the data

obtained using modified versions of PR EOS, (Peng-Robinson-Huron-Vidal-UNIQUAC), EOS, or briefly, PR-HV-UNIQUAC, cited in [178, 213, 221-226], and by Peng- Pobinson-Stryjek-Vera, (PRsv), EOS, incorporating Huron-Vidal-UNIQUAC's mixing rules in [157]. These modified versions of conventional PR EOS do not include the acentric factor. In another study related to POE32 oil, conducted by the same group, Bobbo, Fedele and Stryjek [157] experimentally analysed a commercial POE32 (Icematic SW32), produced by Castrol and identified some of the constituents of pure POE compounds. Based on information from these pure compounds, the study presents an estimation of the molecular weight of commercial POE32. The above authors further investigated commercial POE32, POE46 and POE68, in comparison with their pure compounds, and presented an estimation of their molecular weights [178]. In another study relating to a refrigerant/POE32 solution activity model and carried out by the same group, Stryjek et al. [227] experimentally analysed a sample of POE32 of the same commercial brand as is used in the current research and estimated an average molecular weight of 618 kg/kmol. The authors confirmed the value obtained through private communication with Musso [228], who obtained a close value of 610 kg/kmol [227].

In a similar series of studies to investigate POE lubricants with CO<sub>2</sub>, Fandiño et al. [172, 229-231] experimentally obtained solubility data for pure POE compounds and correlated these using a conventional SRK model with two interaction parameters, as in [229], as well as using PC-SAFT EOS, referred to in [230]. These authors also applied both conventional SRK and PR EOS models besides Sako-Wu-Prausnitz (SWP) EOS to correlate the data obtained in [232] and through empirical correlation in [233, 234].

It is apparent from the reviewed literature that the EOS model parameters of pure and commercial oils, including POE, are still vague. Actually, this issue was addressed by Razzouk et al. [235] who predicted SAFT, PC-SAFT, SRK and PR modelling parameters

for pure POE compounds, using a function minimisation method and tuning of the experimentally measured vapour pressure data for pure POE compounds [232-234]. The SRK and PR results were very close and proved the validity of those predicted by Teodorescu, Lugo, and Fernández [236], who had already anticipated the critical parameters for pure POE and PAG compounds in SRK and PR EOS models, using a relatively simple approach. First, the critical pressure of a component was calculated using group contribution methods. Next, the critical temperature and acentric factor were simultaneously adjusted to fit the refrigerant/oil liquid density data. When the model was fitted to the data, Lee-Kesler's [237] method was implemented to calculate the boiling point.

Modelling the CO<sub>2</sub>/PC mixture is relatively easy in comparison with modelling CO<sub>2</sub>/oil mixtures, since both the pure component properties and modelling parameters are known and therefore, any selected thermodynamic model of choice can be directly implemented. Studies related to CO<sub>2</sub>/PC modelling have mainly been conducted using cubic EOS modelling. Murrieta-Guevara et al. [181] derived Henry's law constants and heat solution and correlated the solubility data using SRK EOS. The modelling results compared to those obtained by Isaacs et al. [238], showing that they correspond well. Mantor et al. [180] correlated their experimentally obtained data using Krichevsky-Kasarnovsky's solubility equation.

#### 5.2.2.1 Summarised Findings

- POE32 molecular weight of the same brand used in the current research is confirmed as being in the range of 610 to 618 kg/kmol.
- Both POE32 and POE68's critical parameters of the same brand used in the current research are estimated and made available by Yokozeki [211]. However, the use of these parameters also requires the use of Yakozeki's version of SRK EOS.

- The acentric factor in a conventional SRK model and  $\beta_1$  parameter in Yokozeki's SRK EOS for lubricant oils are in the range of  $1 \pm 0.3$  and are treated as adjustable parameters. Moreover, critical parameters for lubricant oil, which are estimates in the first place, are also treated as adjustable parameters to fit experimental data.
- Using the UniOil EOS approach proposed by Yokozeki will sufficiently correlate experimental data.

### 5.3 Proposed Modelling Approach

As most of the available and reviewed studies are concerned with modelling the phase behaviour of CO<sub>2</sub>/POE or CO<sub>2</sub>/PC and are not directly related to determining thermodynamic properties, a combined empirical-thermodynamic approach is selected to identify the specific enthalpy of the liquid mixture solution at each point around the CO<sub>2</sub>/lubricant absorption power generation system. Nevertheless, the specific entropy of CO<sub>2</sub>/POEs could not be determined, due to the absence of the ideal gas entropy of the lubricant oil, which is essential for entropy modelling. However, the absence of oil entropy does not introduce any error into the absorption power generation system model. Finally, the vapour phase of the mixture is made purely by CO<sub>2</sub> gas which data were calculated using REFPROP 9.0.

#### 5.3.1 Empirical Correlations

The correlation procedure was carried out in a Matlab [239] environment using the Curve Fitting Toolbox. All the correlations developed are presented in this section, while coefficients are included in Appendix B.1. The empirical correlations proposed by Seeton and Hrnjak for solubility, density, and viscosity [183] were used for the CO<sub>2</sub>/POE32 mixture. Extended versions of these equations were also developed to correlate CO<sub>2</sub>/POE68 solubility (5.6) and density (5.7). The results of the equation were validated using a polynomial regression model with least square minimisation method. Equations (5.8) and (5.9) are, respectively, the polynomial

correlations of CO<sub>2</sub>/POE68 solubility and density data. The CO<sub>2</sub>/POE32 viscosity equation (5.3) perfectly correlates CO<sub>2</sub>/POE68 viscosity with the same number of coefficients used by Seeton and Hrnjak.

$$\begin{aligned} \text{Log}_{10}(P) = a_1 + \frac{a_2}{T} + \frac{a_3}{T^2} + \text{Log}_{10}(\omega) \left( a_4 + \frac{a_5}{T} + \frac{a_6}{T^2} \right) + \text{Log}_{10}^2(\omega) \left( a_7 + \right. & \quad \mathbf{(5.6)} \\ \left. \frac{a_8}{T} + \frac{a_9}{T^2} \right) + \text{Log}_{10}^3(\omega) \left( a_{10} + \frac{a_{11}}{T} + \frac{a_{12}}{T^2} \right) \end{aligned}$$

$$\begin{aligned} \rho = b_1 + b_2T + b_3T^2 + \omega(b_4 + b_5T + b_6T^2) + \omega^2(b_7 + b_8T + b_9T^2) & \quad \mathbf{(5.7)} \\ + \omega^3(b_{10} + b_{11}T + b_{12}T^2) \end{aligned}$$

$$\begin{aligned} \text{Log}_{10}(P) = a_1 + a_2T + a_3\omega + a_4T^2 + a_5T\omega + a_6\omega^2 + a_7T^2\omega & \quad \mathbf{(5.8)} \\ + a_8T\omega^2 + a_9\omega^3 \end{aligned}$$

$$\begin{aligned} \rho = b_1 + b_2T + b_3\omega + b_4T^2 + b_5T\omega + b_6\omega^2 + b_7\omega^2T + b_8T\omega^2 + & \quad \mathbf{(5.9)} \\ b_9\omega^3 + b_{10}T^2\omega^2 + b_{11}T\omega^3 + b_{12}\omega^4 \end{aligned}$$

Figure 5-4 and Figure 5-5 show the CO<sub>2</sub> vapour pressure variation in the CO<sub>2</sub>/POE68 mixture at different CO<sub>2</sub> mass fractions compared to the pure CO<sub>2</sub> vapour pressure, and the phase behaviour of the CO<sub>2</sub>/POE68 mixture, respectively, produced using equation (5.6). As seen in the Figures, the CO<sub>2</sub>/POE68 mixture's solubility and phase behaviour are similar to those observed in the CO<sub>2</sub>/POE32 mixture presented in Figure 5-1 and Figure 5-2, but with slightly lower CO<sub>2</sub> vapour pressure and more CO<sub>2</sub> absorbed by POE68.

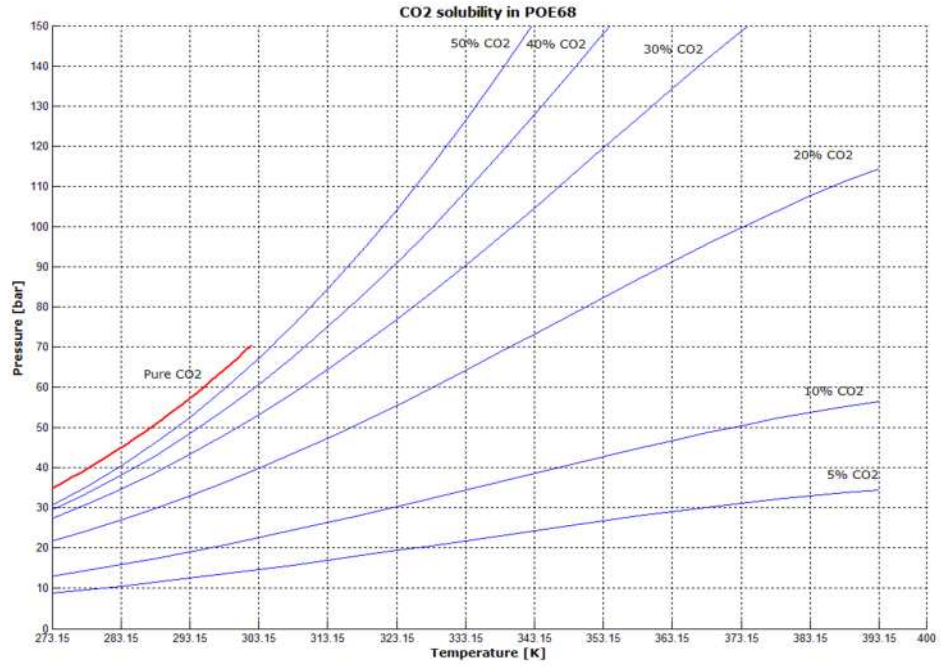


Figure 5-4: CO<sub>2</sub>/POE68 vapour pressure at different CO<sub>2</sub> mass fractions.

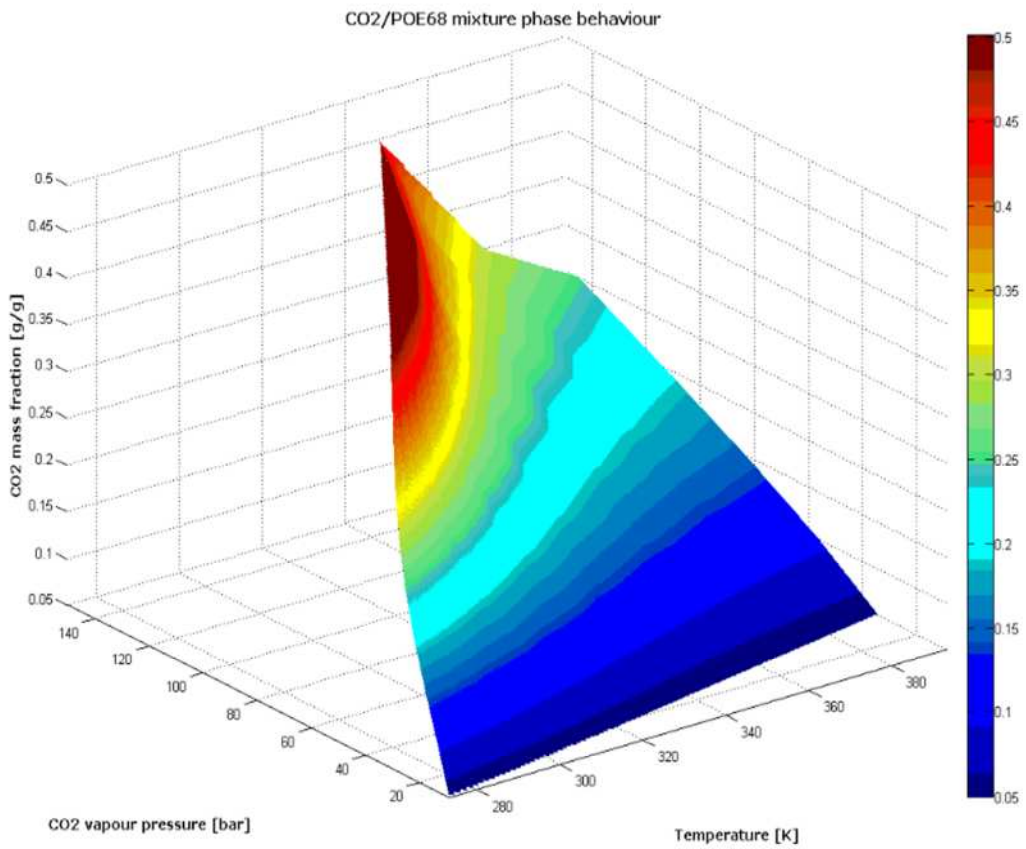


Figure 5-5: CO<sub>2</sub>/POE68 phase behaviour.

The Seeton and Hrnjak equations were found to be unsuitable for the CO<sub>2</sub>/PC mixture. Therefore, the CO<sub>2</sub>/PC solubility data were correlated with a polynomial regression model using the least square method to give a CO<sub>2</sub> mole fraction as a function of temperature and pressure. This was then converted to a mass fraction (5.10). Figure 5-6 and Figure 5-7 show the CO<sub>2</sub> vapour pressure at different mass fractions and the phase behaviour of the CO<sub>2</sub>/PC mixture, respectively. As can be seen from both Figures, CO<sub>2</sub>/PC solubility behaviour differs from what is observed in CO<sub>2</sub>/POE mixtures, where PC tends to accept more CO<sub>2</sub> in the liquid mixture at relatively lower CO<sub>2</sub> vapour pressures than are found in either of the CO<sub>2</sub>/POE mixtures.

$$\omega = a_1 + a_2T + a_3P + a_4T^2 + a_5TP + a_6P^2 + a_7T^2P + a_8TP^2 + a_9P^3 \quad (5.10)$$

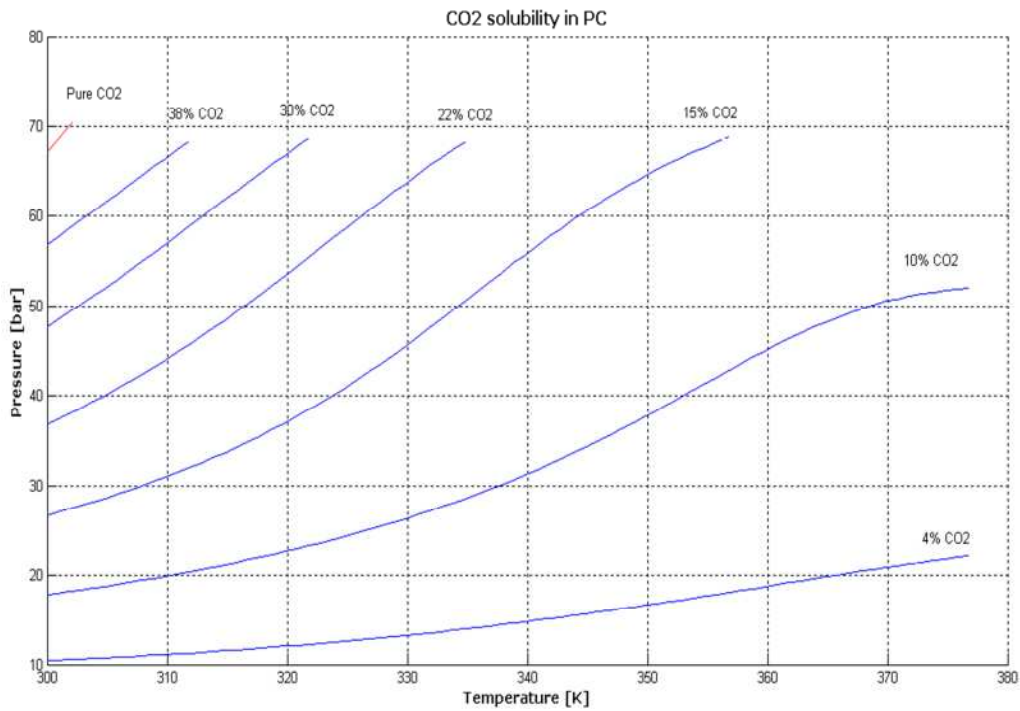
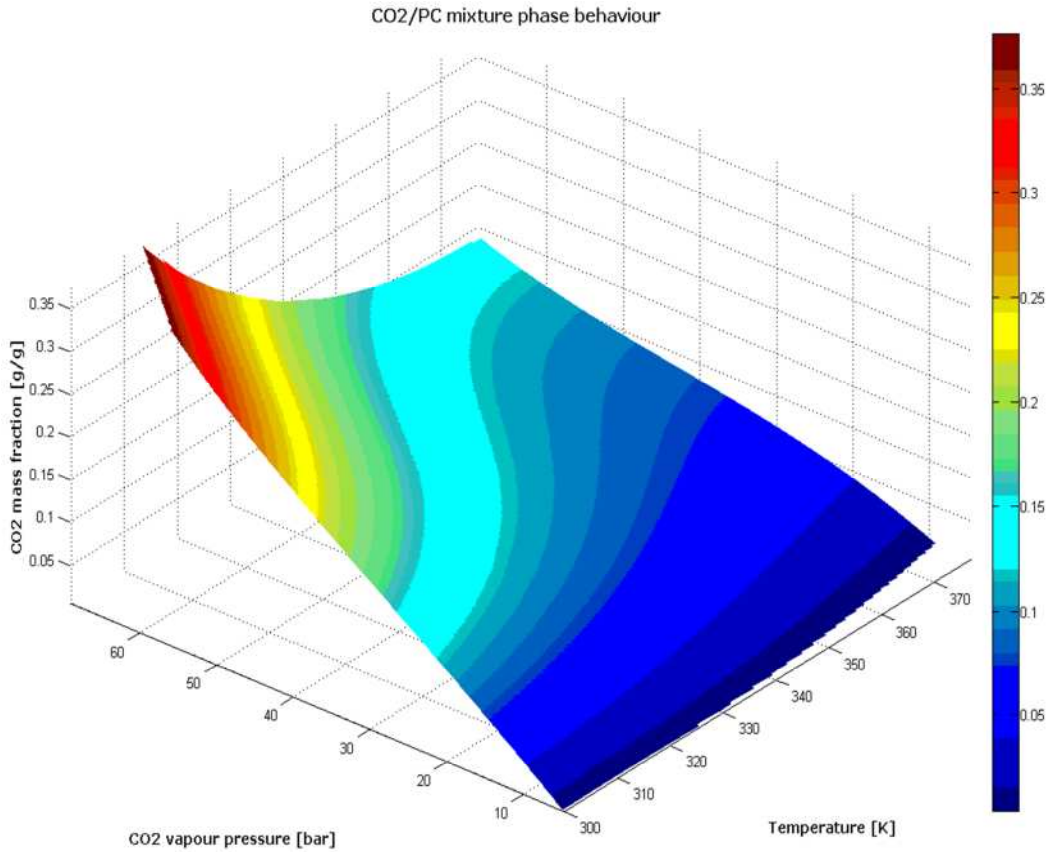


Figure 5-6: CO<sub>2</sub>/PC vapour pressure at different CO<sub>2</sub> mass fractions.



**Figure 5-7: CO<sub>2</sub>/PC phase behaviour.**

### 5.3.2 Cubic EOS Thermodynamic model

#### 5.3.2.1 CO<sub>2</sub>/POEs model

Yokozeki's version of the cubic SRK EOS model [176, 208, 211] was implemented to determine the specific enthalpy of CO<sub>2</sub>/POE32 and CO<sub>2</sub>/POE68, due to the availability of modelling constants. However, Yokozeki's SRK model incorporates several interaction parameters that are not available for either the CO<sub>2</sub>/POE32 or CO<sub>2</sub>/POE68 cases. Therefore, Yokozeki's model was treated as a model with one interaction parameter which resembled a conventional SRK EOS. In general, The SRK EOS model is associated with a standard set of equations which are available in textbooks, articles and software manuals. All equations used for modelling both CO<sub>2</sub>/POE mixtures were taken from reference [176], unless indicated otherwise. Equation (5.11) shows the general form of SRK EOS.

$$P = \frac{RT}{\bar{V} - b} - \frac{a}{\bar{V}(\bar{V} + b)} \quad (5.11)$$

(a) and (b) are the cubic EOS parameters, where (a) is the temperature-dependant attraction parameter [240] and (b) is the volume-limiting parameter [241]. Equation (5.12) shows the polynomial form of SRK EOS in terms of the compressibility factor (Z):

$$Z^3 - Z^2 + (A - B - B^2)Z - AB = 0 \quad (5.12)$$

Where

$$Z = \frac{P\bar{V}}{RT} \quad (5.13)$$

The terms A and B are defined as:

$$A = \frac{aP}{R^2T^2} \quad (5.14)$$

$$B = \frac{bP}{RT} \quad (5.15)$$

And

$$a = \sum_{i=1}^N \sum_{j=1}^N (a_i a_j)^{0.5} f_{ij} (1 - k_{ij}) x_i x_j \quad (5.16)$$

$$b = \frac{1}{2} \sum_{i=1}^N \sum_{j=1}^N (b_i + b_j) (1 - k_{ij}) (1 - m_{ij}) x_i x_j \quad (5.17)$$

Equations (5.16) and (5.17) are Yokozeki's modification for conventional quadratic van der Waals-Berthelot mixing rules for binary mixtures [242]. The temperature-dependent binary interaction parameter  $f_{ij}$  and the conventional binary interaction parameter  $k_{ij}$  are calculated from:

$$f_{ij} = \frac{\tau_{0ij} + \tau_{1ij}}{T + \tau_{2ij}T} \text{ where } f_{ij} = f_{ji}, \text{ and } f_{ii} = 1 \quad (5.18)$$

$$K_{ij} = \frac{l_{ij}l_{ji}(x_i + x_j)}{l_{ji}x_i + l_{ij}x_j} \text{ where } K_{ij} = K_{ji}, \text{ and } K_{ii} = 0 \quad (5.19)$$

Where  $\tau_0, \tau_1,$  and  $\tau_2$  in equation (5.18) and  $l_{ij}$  and  $l_{ji}$  in equation (5.19) are binary interaction parameters that are obtained statistically from solubility data. The  $m_{ij}$  binary interaction

parameter in equation (5.17) is always equal to zero for CO<sub>2</sub>/lubricant mixtures. Moreover, it was found that the  $f_{ij}$  interaction parameter values for CO<sub>2</sub>/lubricant mixtures are always very close to unity. Therefore, for the current model, the  $f_{ij}$  parameter value was taken as unity. This restores the mixing rules in equations (5.16) and (5.17) to the conventional quadratic van der Waals form, with only one binary interaction parameter  $k_{ij}$  in equations (5.20) and (5.21), where  $k_{ij}$  is adjusted to best fit the experimental solubility data [243].

$$a = \sum_{i=1}^N \sum_{j=1}^N (a_i a_j)^{0.5} (1 - k_{ij}) x_i x_j \quad (5.20)$$

$$b = \frac{1}{2} \sum_{i=1}^N \sum_{j=1}^N (b_i + b_j) (1 - k_{ij}) x_i x_j \quad (5.21)$$

For component (i) of the binary mixture in equation (5.20):

$$a_i = 0.42748 \frac{(RT_{ci})^2}{P_{ci}} \alpha_i \quad (5.22)$$

( $\alpha$ ) is the temperature-dependent part of parameter (a), equal to unity when  $T = T_{ci}$  [240]. ( $\alpha$ ) is calculated from the following empirical forms:

$$\alpha_i = \sum_{k=0}^{\leq 3} \beta_k \left( \frac{1}{T_{ri} - T_{ri}} \right)^k, \quad \text{for } T_{ri} = \frac{T}{T_{ci}} \leq 1 \quad (5.23)$$

Or

$$\alpha_i = \beta_0 + \beta_1 [\exp\{2(1 - T_{ri})\} - 1], \text{ for } T_{ri} \geq 1 \quad (5.24)$$

Where  $\beta_k$  are modelling constants for CO<sub>2</sub>, POE32 and POE68, provided in [176, 211].

Furthermore, for component (i) of the binary mixture in equation (5.21):

$$b_i = 0.08664 \frac{RT_{ci}}{P_{ci}} \quad (5.25)$$

Equations (5.22) to (5.25) are also applied to component (j) in the mixture.

The VLE in a mixture is characterised by the equality of the mixture component's fugacity in both the liquid and vapour phases. Fugacity is a thermodynamic function used to substitute pressure in reactions that involve real gases and mixtures [244]. For component (i) in the mixture, the fugacity [220] is:

$$\hat{f}_i^L = \hat{f}_i^V \quad (5.26)$$

Where

$$\hat{f}_i^L = x_i \phi_i^L P \text{ And } \hat{f}_i^V = y_i \phi_i^V P \quad (5.27)$$

For the SRK EOS, the fugacity coefficient [245] becomes:

$$\ln \phi_i = -\ln\left(Z - \frac{Pb}{RT}\right) + (Z - 1) \frac{b_i}{b} - \frac{a}{bRT} \left[ \frac{1}{a} \left( 2a_i^{0.5} \sum_{j=1}^N x_j a_j^{0.5} (1 - k_{ij}) \right) - \frac{b_i}{b} \right] \ln\left(1 + \frac{b}{V}\right) \quad (5.28)$$

As mentioned earlier, due to the very low vapour pressure of lubricant oil, it is assumed as negligible and the vapour phase is then only made by pure CO<sub>2</sub> vapour. Therefore, the mole fraction of CO<sub>2</sub> vapour is taken as unity. The fugacity coefficient equation is applied to the liquid and vapour phases of both binary mixture components (i) and (j). The only difference between the vapour and liquid phase calculation, is replacing the mole fractions and compressibility factors for the phase to be calculated [243].

The molar-specific enthalpy and entropy are calculated using the enthalpy and entropy departure equations (5.29) and (5.30) [246]:

$$\frac{H - H^{ID}}{RT} = Z - 1 - \frac{A}{B} \left[ 1 - \frac{T}{a} \frac{\partial a}{\partial T} \right] \ln\left(1 + \frac{B}{Z}\right) \quad (5.29)$$

$$\frac{S - S^{ID}}{RT} = \ln(Z - b) - \ln \frac{P}{P^\circ} + \frac{A}{B} \left[ \frac{T}{a} \frac{\partial a}{\partial T} \right] \ln\left(1 + \frac{B}{Z}\right) \quad (5.30)$$

Where  $H^{ID}$  and  $S^{ID}$  are the mixture's molar ideal gas enthalpy. ( $H^{ID}$ ) in equation (5.30) is calculated as:

$$H^{ID} = \int_{298.15}^T cp_i x_i dT + \int_{298.15}^T cp_j x_j dT \quad (5.31)$$

298.15K (25°C) was taken as the reference temperature for the enthalpy calculation. The ideal gas enthalpy of POE oils were calculated using the heat capacity correlation and coefficients for pure POE compounds, estimated by Yokozeki [208] and included in Appendix B.2.

### 5.3.2.2 CO<sub>2</sub>/PC Model

Modelling CO<sub>2</sub>/PC is more straightforward, since all the constants of the mixture's components are known. A conventional SRK cubic EOS [240], with one binary interaction parameter was implemented to model the specific enthalpy of the CO<sub>2</sub>/PC mixture. The binary interaction parameter  $k_{ij}$  was found to have very little effect on the results, since all modelling parameters and properties of pure components are known. The model was validated by calculating the pure PC liquid density at 25°C, and atmospheric pressure, which is known to be around 1189  $\frac{kg}{m^3}$  [182]. The conventional SRK EOS has a similar sequence of equations to those presented for CO<sub>2</sub>/POE in section 5.3.2.1., Apart from that, the quadratic mixing rule for the volume limiting parameter (b) in equation (5.21) becomes:

$$b = \sum_{i=1}^N x_i b_i \quad (5.32)$$

In addition, for component (i) in the binary mixture, ( $\alpha$ ), the temperature- dependent part of the attraction parameter (a) in equation (5.22) becomes:

$$\alpha_i^{0.5} = 1 + m_i(1 - T_{ri}^{0.5}) \quad (5.33)$$

Where

$$m_i = 0.48 + 1.574\omega_{f,i} - 0.176\omega_{f,i}^2 \quad (5.34)$$

$\omega_{f,i}$  is the Pitzer acentric factor for component (i), which, along with the critical properties, is commonly used for estimating properties [220].

## 5.4 Implementation of the Mixtures Specific Enthalpy

### Models

Specific enthalpies of the mixtures were programmed in Matlab environment as sub-routines which work alongside several other functions with similar structures to calculate other properties such as temperatures, pressures and densities, in a programme to enable evaluation of the performance of the CO<sub>2</sub>/lubricant absorption power generation system.

#### 5.4.1 CO<sub>2</sub>/POE Mixtures

Two separate sub-routines were developed for the specific enthalpies of CO<sub>2</sub>/POE32 and CO<sub>2</sub>/POE68. Both sub-routines are based on the Yokozeki-SRK model and have a similar calculation procedure. Table 5.1 presents the modelling constants for the pure components used in Yokozeki-SRK to model both mixtures.

**Table 5.1: Yokozeki-SRK modelling constants for CO<sub>2</sub> and POE lubricant oils.**

Constants used for CO <sub>2</sub> /POE mixtures in the Yokozeki-SRK EOS model							
Compound	Molar mass [kg/kmol]	T <sub>c</sub> [K]	P <sub>c</sub> [kPa]	$\beta_0$	$\beta_1$	$\beta_2$	$\beta_3$
CO <sub>2</sub> [176]	44.01	304.13	7377	1.0005	0.43866	-0.10498	0.0625
POE32 [211]	610	864	874	1	0.913	0	0
POE68 [211]	700	746	682	1	1.249	0	0

Figure 5-8 illustrates the specific enthalpy sub-routine for CO<sub>2</sub>/POE mixtures. In the  $k_{ij}$  iteration and interpolation step, the programme first looks for the best  $k_{ij}$  value in a pre-prepared matrix, which covers a wide range of temperatures, pressures and  $k_{ij}$  values for the mixtures. In the event of a  $k_{ij}$  value error, or a breach of the matrix boundaries, the programme will start iterating  $k_{ij}$  from -1 to

1 with very small steps, until equation (5.12) becomes equal to zero and achieves the best fit with the empirically calculated density. In the mixture-specific density calculation step, solving the polynomial form of SRK will yield three root solutions; the smallest positive root being the compressibility factor for the liquid mixture and the largest positive value, if it exists, is the gas compressibility of the mixture.

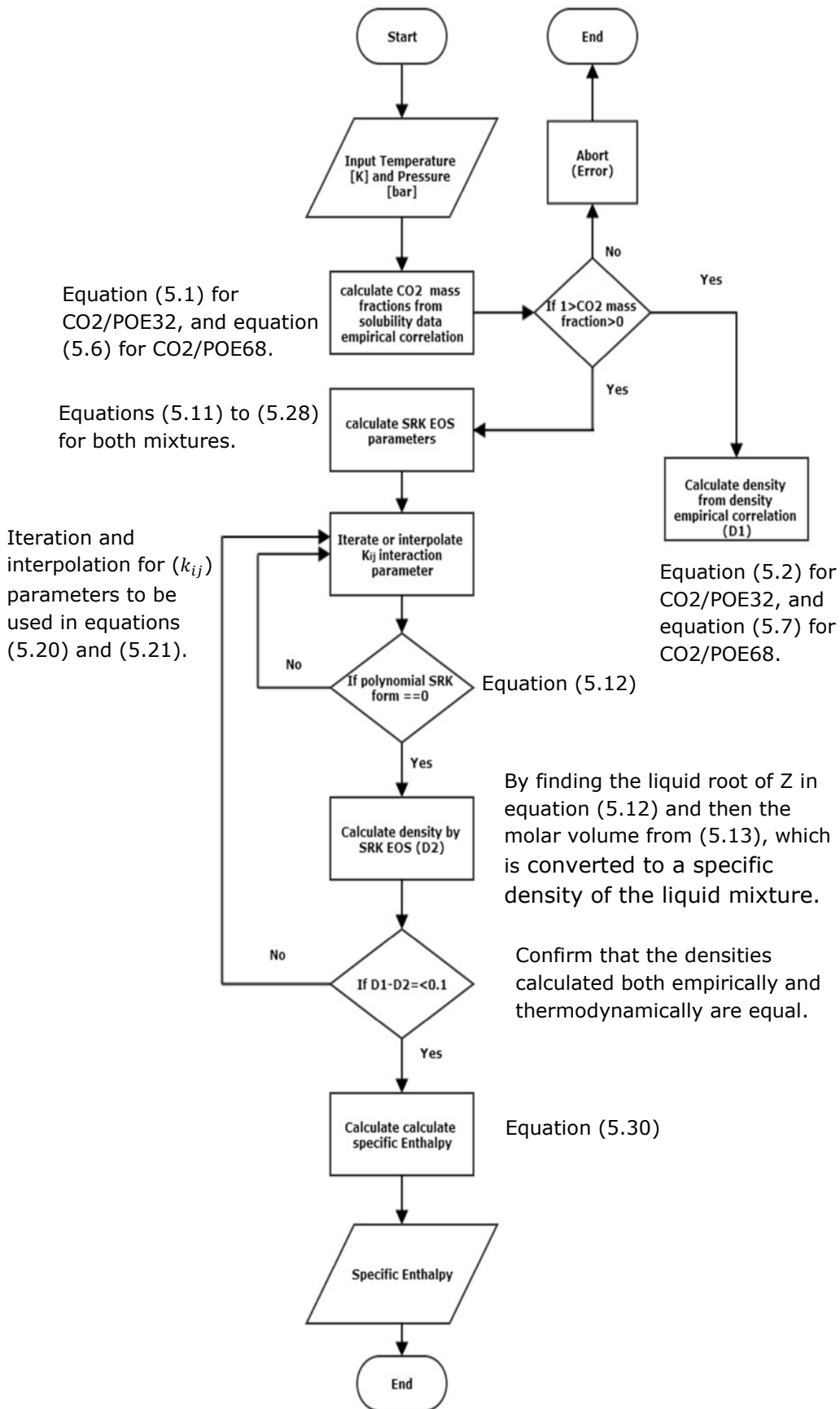


Figure 5-8: CO<sub>2</sub>/POE mixture-specific enthalpy sub-routine flow chart.

### 5.4.2 CO<sub>2</sub>/PC Mixture

Conventional SRK modelling constants for CO<sub>2</sub>/PC are available in some of the literature. For the current model, the constants presented in Table 5.2 were taken from reference [247].

**Table 5.2: SRK modelling constants for CO<sub>2</sub> and PC.**

Constants used for the CO <sub>2</sub> /PC mixture's SRK EOS model				
Compounds	Molar mass [kg/kmol]	T <sub>c</sub> [K]	P <sub>c</sub> [kPa]	$\omega$
CO <sub>2</sub>	44.01	304.13	7377	0.239
PC	102.09	625.15	5705	0.707

The specific enthalpy sub-routine for CO<sub>2</sub>/PC is illustrated in Figure 5-9. In the calculation step for the SRK parameters, the temperature-dependent part ( $\alpha$ ) of parameter ( $a$ ) was calculated by incorporating the acentric factor ( $\omega_f$ ) using equations (5.33) and (5.34). Furthermore, equation (5.32) was used for the mixing rule for parameter ( $b$ ), following the conventional SRK model. The  $k_{ij}$  interaction parameter was interpolated from the temperature- $k_{ij}$  values provided in reference [181] for a temperature range between 25°C and 100°C. However, the interaction parameter seems to have very little influence. This could be regarded as negligible for the CO<sub>2</sub>/PC results and therefore, could be set at 0. The rest of the calculation steps are similar to those carried out for CO<sub>2</sub>/POE mixtures.

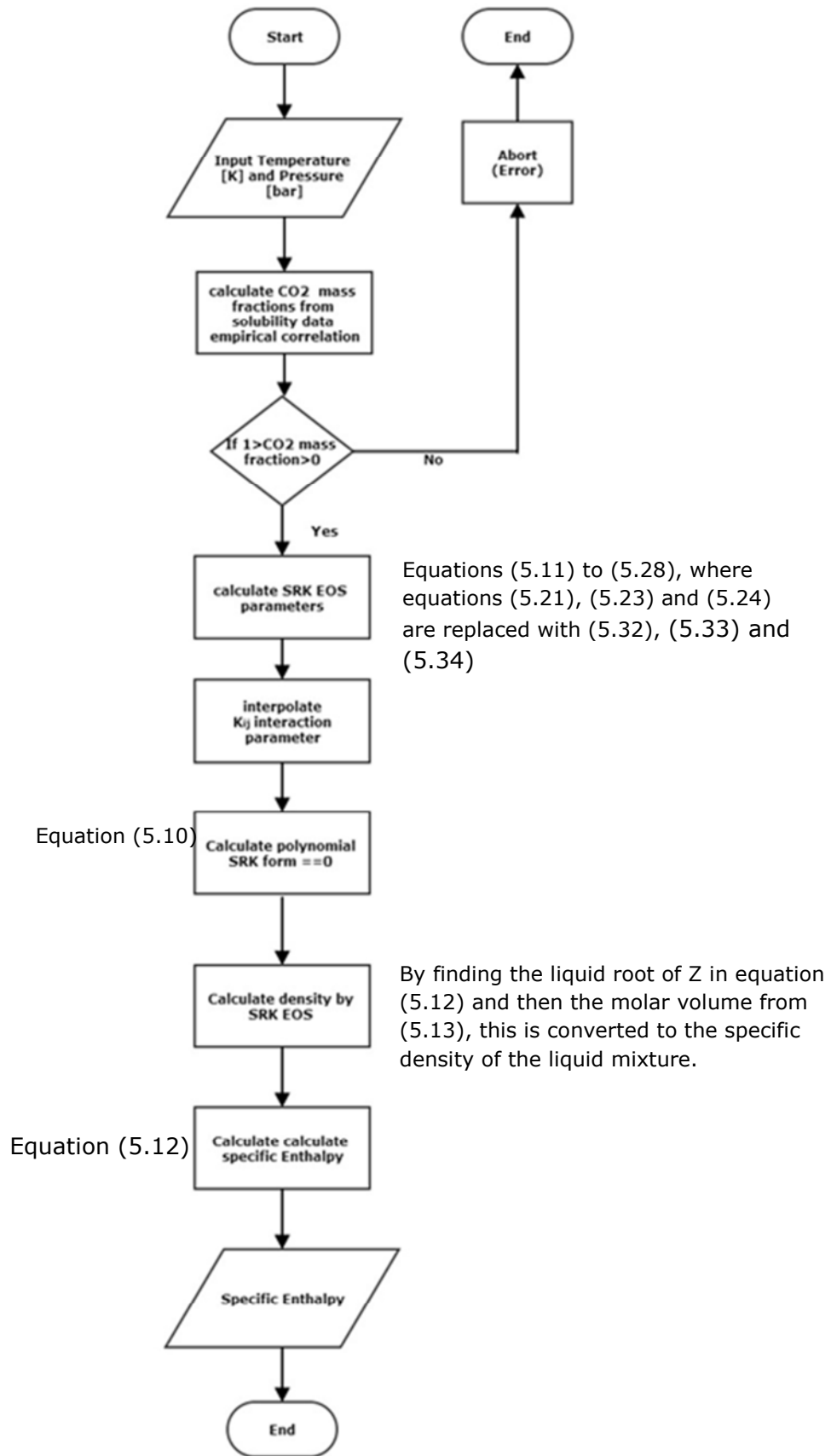


Figure 5-9: CO<sub>2</sub>/PC mixture-specific enthalpy sub-routine flow chart.

## 5.5 Validation of the Yokozeki-SRK Thermodynamic Model

In order to validate the adopted EOS thermodynamic model approach, Yokozeki's-SRK model for the CO<sub>2</sub>/POE3 mixture [176] was used. Constants and interaction parameters proposed by Yokozeki for modelling the CO<sub>2</sub>/POE3 (ISO53) solubility data are shown in Table 5.3, while the experimental solubility data determined and reported by Hauk [185] are presented in Table 5.4. The solubility data were correlated by means of polynomial regression to calculate the CO<sub>2</sub> vapour pressure as a function of temperature and liquid CO<sub>2</sub> mass fraction in the mixture. Equation (5.35) shows the polynomial correlation, while the coefficients are presented in Table 5.5.

**Table 5.3: CO<sub>2</sub>/POE3 constants and interaction parameters. (Source:[176])**

Constants used for the EOS model							
Compound	Molar mass [kg/kmol]	T <sub>c</sub> [K]	P <sub>c</sub> [kPa]	$\beta_0$	$\beta_1$	$\beta_2$	$\beta_3$
CO <sub>2</sub>	44.01	304.13	7377	1.0005	0.43866	-0.10498	0.0625
POE	550	800	950	1	1.15142	0	0
Binary interaction parameters for the CO <sub>2</sub> /POE3 mixture							
$l_{12}$	$l_{21}$	$\tau_{012}$	$\tau_{112}^1$ [K]	$\tau_{212}^2$ [K <sup>-1</sup> ]			
0.039114	0.013294	0.41073	101.56	7.79E-04			

**Table 5.4: CO<sub>2</sub>/POE3 solubility data. (Source: [185])**

Temperature [C]	Pressure [bar]	CO <sub>2</sub> mass fraction[kg/kg]	Temperature [C]	Pressure [bar]	CO <sub>2</sub> mass fraction [kg/kg]
278.15	12	0.072	298.15	11.6	0.041
278.15	19.2	0.121	298.15	29.2	0.12
278.15	29.2	0.221	298.15	54.4	0.294
278.15	39.8	0.591	298.15	64.4	0.444
278.15	50.8	0.689	298.15	69.6	0.452
278.15	56.4	0.767	298.15	87.8	0.5
278.15	62.6	0.779	298.15	110.4	0.56
			298.15	131.8	0.682
Temperature [C]	Pressure [bar]	CO <sub>2</sub> mass fraction [kg/kg]	Temperature [C]	Pressure [bar]	CO <sub>2</sub> mass fraction [kg/kg]
313.15	33.8	0.107	373.15	32.2	0.043

313.15	50.2	0.169	373.15	53	0.079
313.15	74.8	0.296	373.15	73	0.106
313.15	90	0.379	373.15	96	0.144
313.15	109	0.422	373.15	112.8	0.173
313.15	130.8	0.468	373.15	131	0.199
313.15	152.2	0.516	373.15	152	0.238

$$\text{Log}_{10}(P) = a_1 + a_2T + a_3\omega + a_4T^2 + a_5T\omega + a_6\omega^2 + a_7T^2\omega + a_8T\omega^2 + a_9\omega^3 \quad (5.35)$$

**Table 5.5: Coefficients for CO<sub>2</sub>/POE3 solubility correlation.**

Coefficient	CO <sub>2</sub> /POE3 solubility correlation [185]
a1	-4.011
a2	0.02501
a3	10.52
a4	-2.833E-5
a5	-0.02734
a6	-24.2
a7	3.231E-5
a8	0.04573
a9	8.049
Suitability of fit	
SSE	0.0409
$R^2$	0.9844
RMSE	0.04522

Keys:

Summed square of residuals (SSE)

Coefficient of determination ( $R^2$ )

Root mean square error (RMSE)

In the Yokozeki- SRK model, the  $k_{ij}$  and  $f_{ij}$  interaction parameters are given by:

$$k_{ij} = \frac{l_{ij}l_{ji}(x_i + x_j)}{l_{ji}x_i + l_{ij}x_j} \quad \text{where } k_{ii} = 0 \quad (5.36)$$

$$f_{ij}(T) = \frac{\tau_{0ij} + \tau_{1ij}}{T + \tau_{2ij}T} \quad \text{where } f_{ij} = f_{ji} \text{ and } f_{ii} = 1 \quad (5.37)$$

However, the absence of  $\tau$  interaction parameters in the cases of CO<sub>2</sub>/POE32 and CO<sub>2</sub>/POE68 mixtures was compensated by tuning only the  $k_{ij}$  parameter to find the best density fit, where the  $f_{ij}$  parameter value was taken as unity. This was because it was found that the  $f_{ij}$  value for CO<sub>2</sub>/lubricant mixtures is always very close to unity; in other words, it involved treating Yokozeki-SRK EOS as a conventional SRK model, with one interaction parameter  $k_{ij}$ . This approach was validated using the case of a CO<sub>2</sub>/POE3 mixture. As

an example for demonstration, Figure 5-10 shows a comparison of calculated densities at 40 bar and variable temperatures. The black line represents the densities calculated using all interaction parameters for CO<sub>2</sub>/POE3, while the red line represents the densities calculated by tuning only the  $k_{ij}$  parameter. Both results show that they are in close agreement. Figure 5-11 shows the very small relative percentage of error between each model approach.

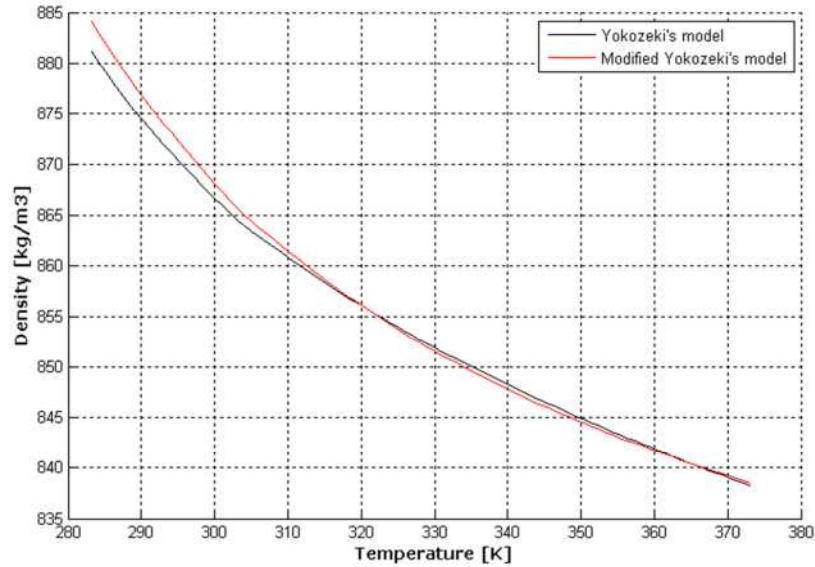


**Figure 5-10: Comparison of calculated densities for CO<sub>2</sub>/POE3 using different Yokozeki-SRK EOS approaches at 40 bar and variable temperatures.**

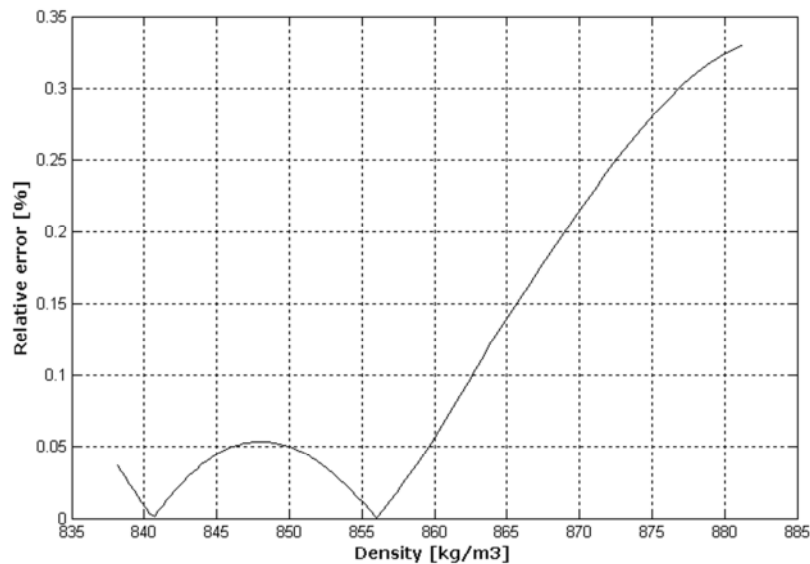


**Figure 5-11: The relative error of densities calculated using different Yokozeki-SRK EOS approaches.**

Figure 5-12 shows specific enthalpies calculated using both approaches with very small relative error being plotted in Figure 5-13.

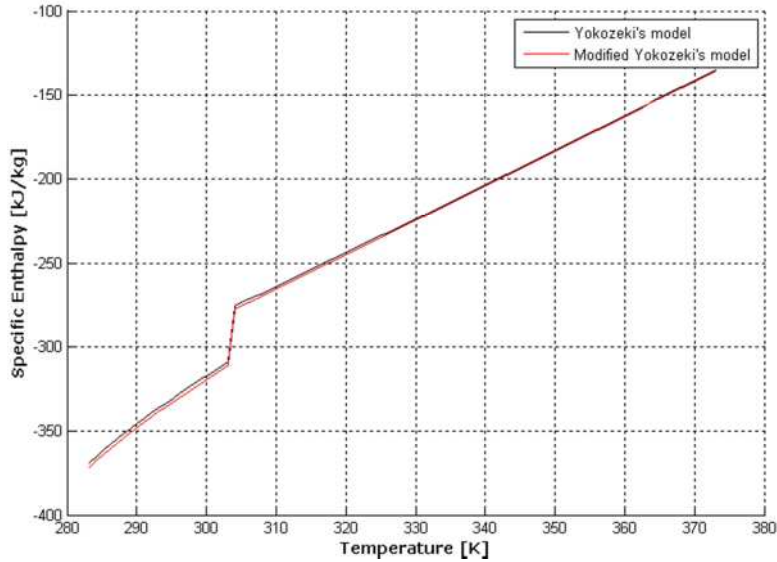


**Figure 5-12: Comparison of specific enthalpies using different Yokozeki-SRK EOS approaches calculated at 40 bar and variable temperatures.**

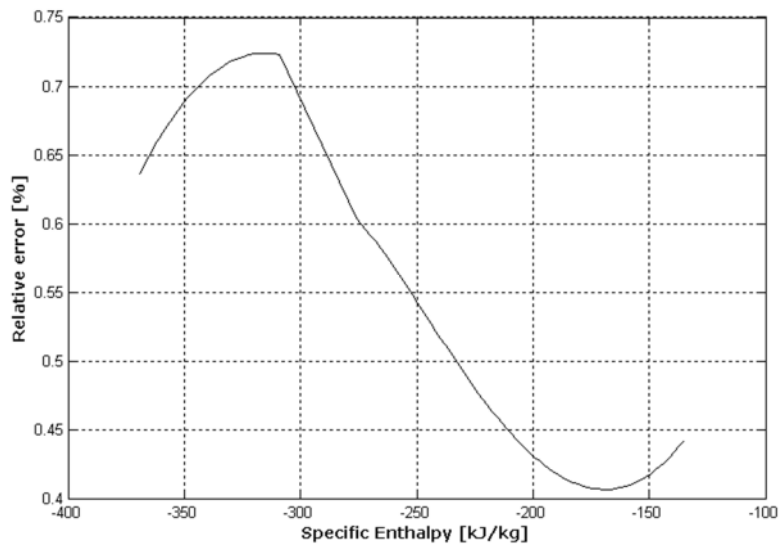


**Figure 5-13: The relative error of specific enthalpies calculated using different Yokozeki-SRK EOS approaches.**

This approach revealed very high accuracy for both CO<sub>2</sub>/POE32 and CO<sub>2</sub>/POE68 mixtures. Figure 5-14 shows the 40 bar and variable temperature demonstration example, where a comparison between the CO<sub>2</sub>/POE32 densities was calculated using an empirical correlation provided by Seeton and Hrnjak [183], indicated in black, and the densities calculated using Yokozeki-SRK with one

interaction parameter, indicated in red. Figure 5-15 illustrates the very small relative error percentage between both methods of density calculation.

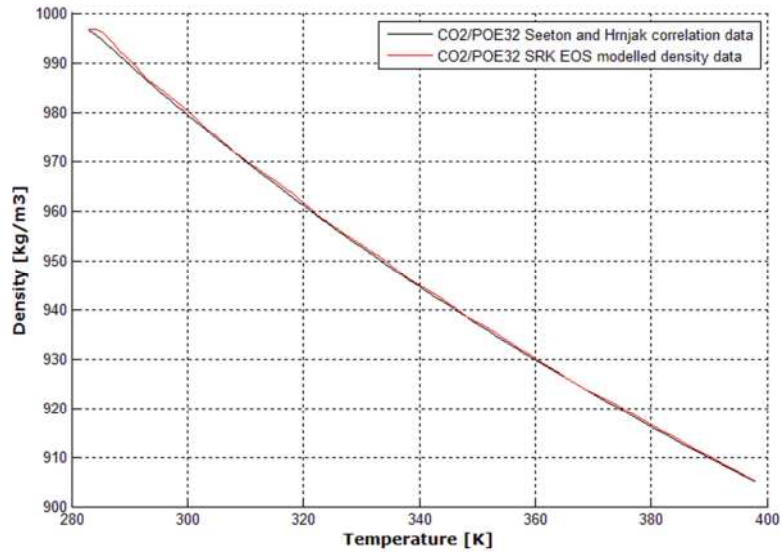


**Figure 5-14: Comparison of densities calculated using SRK EOS and Seeton and Hrnjak's empirical correlation.**

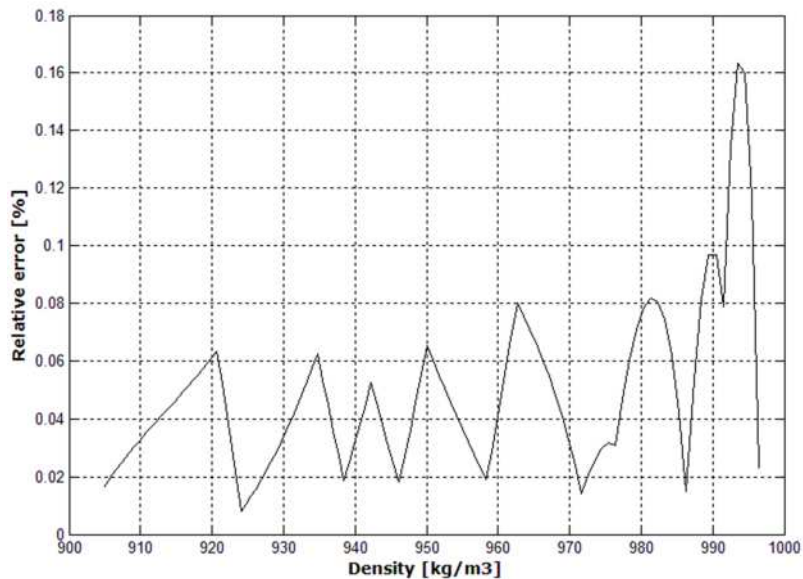


**Figure 5-15: The relative error between calculated densities of CO<sub>2</sub>/POE32 using SRK EOS and Seeton and Hrnjak's empirical correlation at 40 bar and variable temperatures.**

For CO<sub>2</sub>/POE68, Figure 5-16 shows the densities calculated using the empirical correlation developed, indicated in black, and the densities calculated using the Yokozeki-SRK model, indicated in red. Figure 5-17 shows the negligible relative error observed between densities calculated using both methods.

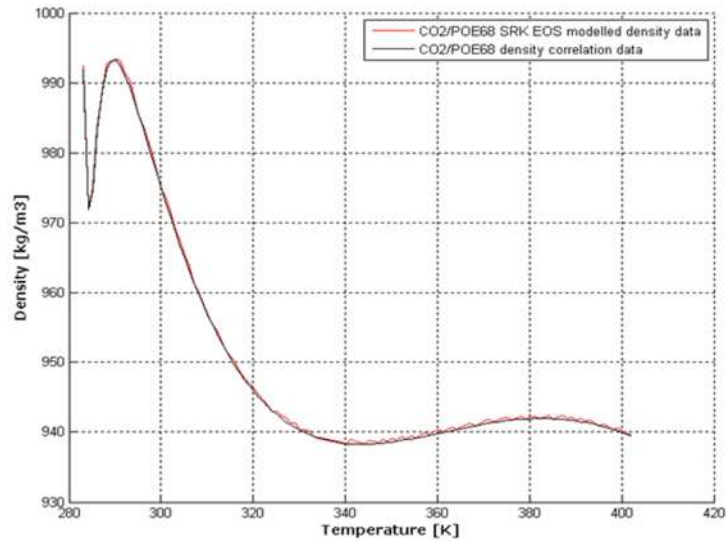


**Figure 5-16: Comparison of densities calculated using SRK EOS and the empirical correlation developed.**

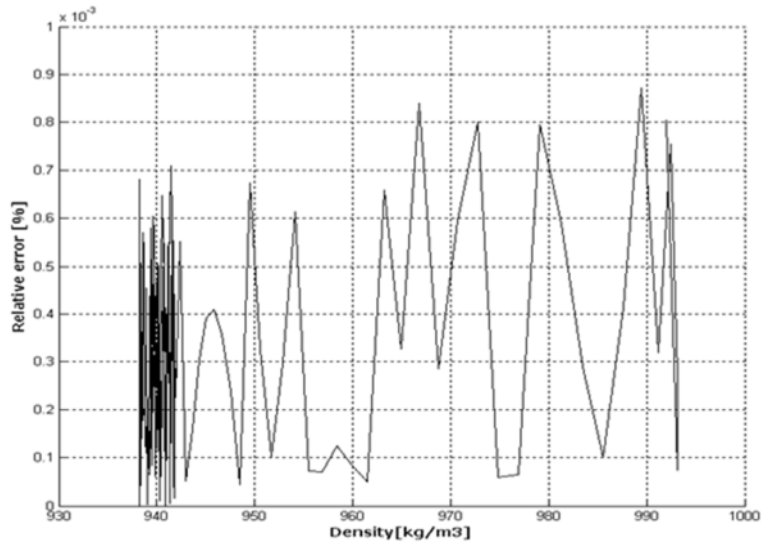


**Figure 5-17: The relative error between densities of CO<sub>2</sub>/POE68 calculated using SRK EOS and the empirical correlation developed at 40 bar and variable temperatures.**

## 5.6 Conclusions

This chapter provided an overview of the current state, and techniques of CO<sub>2</sub>/lubricant thermodynamic modelling. The chapter also identified the EOS thermodynamic model parameters for both POE32, and POE68 lubricants. Consequently, this allowed the selection of the most suitable modelling approach to be carried out in order to determine the CO<sub>2</sub>/lubricant thermodynamic properties. The model approach selected is based on both empirical correlations and EOS thermodynamic model using Yokozeki's

version of SRK EOS. The model equations alongside the model parameters were presented, and the model implementation was explained. A similar approach was also carried out for the CO<sub>2</sub>/PC mixture; however using the conventional SRK model since the available knowledge of both mixture components properties.

Upon determination of the essential thermodynamic properties of the proposed mixtures such as density, viscosity, and specific enthalpy as function of CO<sub>2</sub> mass fraction in the mixture at given temperature and pressure, the CO<sub>2</sub>/lubricant absorption power generation system performance can be evaluated successfully.

## Chapter 6 : Theoretical Analysis of Small-Scale Power Generation Systems for Low-Grade Waste Heat Recovery

---

### 6.1 Introduction

This chapter presents theoretical investigations of performance and parametric characterisation of four regenerative 5 kW power generation systems for low-grade waste heat recovery from industrial processes. The investigated systems technologies are specifically those reviewed Chapter 2, namely the CO<sub>2</sub>/lubricant absorption power generation system, the CO<sub>2</sub> SRC power generation system, and the ORC power generation system employing the new environment friendly refrigerants. In addition, the flood expansion concept using a two-phase working fluid mixture consists of CO<sub>2</sub> gas, and CO<sub>2</sub>/POE32 liquid, was investigated as a substitute for the absorption power generation system upon the poor performance predicted utilising the latter technology.

Iteration-based computer simulations of the investigated power generation systems were introduced in order to describe the performance of each component of each system under different working conditions. These computer programmes were written in a Matlab environment and aided with REFPROP 9.0 software for the refrigerants properties.

### 6.2 General Thermodynamic Models Assumptions and Inputs

In general, all introduced thermodynamic models in this chapter have similar general thermodynamic model assumptions, performance evaluation parameters, inputs, and outputs, unless where indicated otherwise. The general assumptions made for implementing investigated systems models and simulations are as follows:

- The system operates under steady state conditions.
- Compression in the solution pump and expansion in the turbine are assumed to be adiabatic processes, with 90% and 80% isentropic efficiency, respectively.
- Pressure drop and heat loss along the piping system are neglected.
- Changes in the kinetic and potential energy of all streams are neglected.
- All heat exchangers are simulated as counter flow heat exchangers, with a constant effectiveness of 80%.

The thermodynamic models introduced for all systems require specifications of the expansion device power output in kW, and temperatures in kelvin. For the pressures, the models require the input in bar for outlet of either the heat rejection heat exchanger (i.e. the absorber, the CO<sub>2</sub> cooler, and the evaporator), or the heat addition heat exchanger (i.e. the generator, the CO<sub>2</sub> heater, and the evaporator). The programs then iterate the pressure of the unspecified heat exchanger, in order to determine the optimum operating pressure, where the system's thermal efficiency is highest. Likewise, any of the working parameters could be held constant and a selected parameter may be iterated, in order to determine optimum operating conditions and to investigate the influence of different parameters on cycle performance. However, the subsequent solving of the governing equations of each system will enable the system's theoretical performance to be predicted at a single steady state operating point.

### 6.3 Thermodynamic Models Evaluation Parameters

The presented systems were evaluated using the first thermodynamic law thermal efficiency which is the ratio of the net thermal power output from the cycle to the amount of heat input into the generator calculated as

$$\eta_{System} = \frac{(W_{Exp} - W_{Pump})}{\dot{Q}_G} \quad (6.1)$$

The net thermal power output is also a crucial parameter to be considered when evaluating system performance and therefore it was also considered as a system evaluation parameter.

## 6.4 CO<sub>2</sub>/lubricant absorption power generation system

The CO<sub>2</sub>/lubricant absorption power generation system simulation programme was created comprising specially programmed sub-routines for the thermodynamic properties of the CO<sub>2</sub>/lubricants mixtures. The program flow chart is included in Appendix C.1.

### 6.4.1 Cycle Description

Figure 6-1 shows a schematic of the system. The concentrated solution mixture reaches a saturated state in the absorber before it exits at point 3. Then, it flows to the pump, where it is pumped to higher pressure at point 4. Next, the liquid mixture is preheated in the recuperator heat exchanger and exits at point 5, before the concentrated solution flows to the generator, where it is further heated by a flow of flue gas resulting from an industrial process. While in the generator, the CO<sub>2</sub> desorbs from the solution mixture and a high pressure CO<sub>2</sub> vapour is generated. At the CO<sub>2</sub> generator outlet, the stream splits into two in the separator, allowing only CO<sub>2</sub> vapour through the turbine at point 1. The diluted solution under high pressure from which the CO<sub>2</sub> vapour has desorbed enters the recuperator heat exchanger at point 6, to lose its heat to the counter flow stream and exit at point 7, where it is substantially cooled. It will then be throttled to the absorber pressure, at point 8, before entering the absorber. Back to the split stream at the separator, the high pressure pure CO<sub>2</sub> vapour stream flows to the expander inlet at point 1, where it expands to lower pressure at point 2, yielding work output from the system. The low pressure

CO<sub>2</sub> vapour at point 2 enters the absorber, where it joins the downstream from point 8. In the absorber, heat from the system is removed by the heat sink, which is usually water. As the heat is being removed from the system, the solution cools down within the absorber and CO<sub>2</sub> absorption into the absorbent takes place. This is mainly because absorption is an exothermic process and therefore, cooling enhances the absorption process [248]. After the absorption process is completed, the saturated mixture solution exits the absorber at point 3 and the cycle is complete.

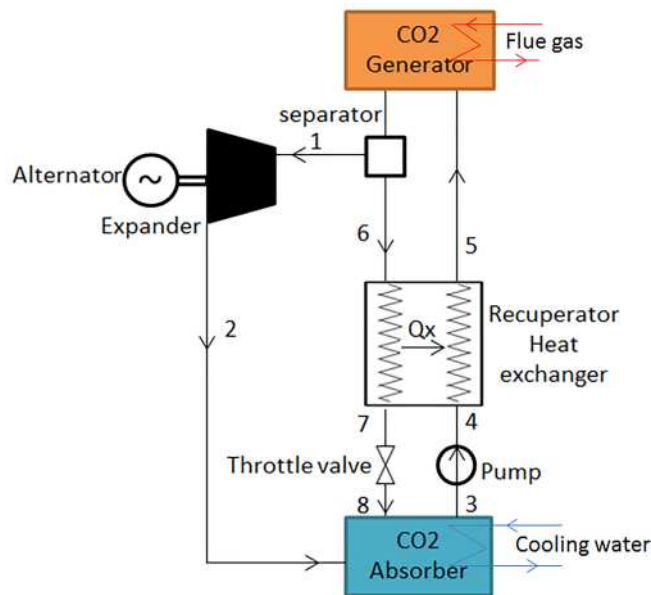


**Figure 6-1: Schematic of the CO<sub>2</sub>/lubricant absorption power generation system.**

### 6.4.2 Thermodynamic Model Assumptions

Beside the general assumptions:

- The throttling valve is assumed to be isentropic.
- Refrigerant vapour from the separator is pure CO<sub>2</sub>, while the weak solution is a saturated liquid. The temperature of each stream is equal to the generator's outlet temperature.
- The solutions at the generator and absorber outlets are always under equilibrium conditions.

### 6.4.3 Circulation Ratio and Mass Flow Rates

Circulation ratio is a key factor that characterises the system performance where it determines the pumping requirements and

size of the system components [249]. The circulation ratio is defined as the ratio of the weak solution mass flow rate to the mass flow rate of the refrigerant [130]. Equation (6.2) shows the circulation ratio, which can also be described in mass fractions of absorbent at the absorber and generator outlets.

$$r = \frac{\dot{m}_s}{\dot{m}_r} = \frac{X_G}{X_G - X_A} \quad (6.2)$$

With respect to the circulation ratio, the mass flow rates at each state point on the schematic diagram of the system shown in Figure 6-1 become:

$$\dot{m}_1 = \dot{m}_2 = \dot{m}_r \quad (6.3)$$

$$\dot{m}_3 = \dot{m}_4 = \dot{m}_5 = \dot{m}_s \quad (6.4)$$

$$\dot{m}_6 = \dot{m}_7 = \dot{m}_8 = \dot{m}_s - \dot{m}_r \quad (6.5)$$

#### 6.4.4 Heat and Mass Balance of System Components

The CO<sub>2</sub>/lubricant absorption power generation system consists of relatively simple components, which can be treated as control volumes with inlet and outlet fluid, heat transfer and work exchange. The basic model for each component consists of a mass balance equation and an energy balance equation, respectively, as discussed in this section.

##### 6.4.4.1 Heat Exchangers

###### 6.4.4.1.1 Heat Exchanger Effectiveness

Heat exchangers play very important roles in thermal cycles, where they are designed to transfer heat between two streams of differential temperature gradients, for the purpose of either heat addition or heat rejection. At this stage, it is necessary to define heat exchanger effectiveness ( $\epsilon$ ), which is the ratio of the actual

heat transfer rate ( $\dot{Q}$ ) to the maximum thermodynamically possible heat transfer rate ( $\dot{Q}_{max}$ ), as shown in equation (6.6) [250].

$$\varepsilon = \frac{\dot{Q}}{\dot{Q}_{max}} \quad (6.6)$$

In a simple counter flow heat exchanger, as shown in Figure 6-2, the actual heat transfer can be determined from either cold or hot streams as:

$$\dot{Q} = \dot{m}_h c p_h (T_{hi} - T_{ho}) = \dot{m}_c c p_c (T_{co} - T_{ci}) \quad (6.7)$$

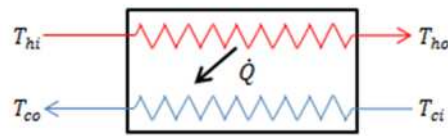


**Figure 6-2: Simple counter flow heat exchanger.**

The fluid with the minimum mass flow rate-specific heat product will exhibit the maximum possible temperature difference between the hot and the cold stream, and the maximum attainable heat transfer rate becomes [251]:

$$\dot{Q}_{max} = (\dot{m}cp)_{min} (T_{hi} - T_{ci}) \quad (6.8)$$

Therefore, the effectiveness is rewritten for the hot and cold streams, respectively as:

$$\varepsilon = \frac{\dot{m}_h c p_h (T_{hi} - T_{ho})}{(\dot{m}cp)_{min} (T_{hi} - T_{ci})} = \frac{\dot{m}_c c p_c (T_{co} - T_{ci})}{(\dot{m}cp)_{min} (T_{hi} - T_{ci})} \quad (6.9)$$

Or simply as:

$$\varepsilon = \frac{T_{hi} - T_{ho}}{T_{hi} - T_{ci}} \text{ if } \dot{m}_h c p_h = (\dot{m}cp)_{min} \quad (6.10)$$

$$\varepsilon = \frac{T_{co} - T_{ci}}{T_{hi} - T_{ci}} \text{ if } \dot{m}_c c p_c = (\dot{m}cp)_{min} \quad (6.11)$$

#### 6.4.4.1.2 The Absorber

Corresponding to the state points on the schematic diagram of the system in Figure 6-1, the mass balance in the absorber is:

$$\dot{m}_3 = \dot{m}_2 + \dot{m}_8 \quad (6.12)$$

With the energy balance as:

$$\dot{Q}_A = \dot{m}_2 h_2 + \dot{m}_8 h_8 - \dot{m}_3 h_3 \quad (6.13)$$

*Also rewritten by incorporating (r) as:*

$$\dot{Q}_A = \dot{m}_r (h_2 + (r - 1)h_8 - r h_3) \quad (6.14)$$

#### 6.4.4.1.3 The Generator

The mass balance in the generator is:

$$\dot{m}_5 = \dot{m}_1 + \dot{m}_6 \quad (6.15)$$

And the energy balance becomes:

$$\dot{Q}_G = \dot{m}_1 h_1 + \dot{m}_6 h_6 - \dot{m}_5 h_5 \quad (6.16)$$

*Also rewritten by incorporating (r) as:*

$$\dot{Q}_G = \dot{m}_r (h_1 - r h_5 + (r - 1)h_6) \quad (6.17)$$

#### 6.4.4.1.4 The Recuperator Heat Exchanger

Generally, the purpose of the recuperator heat exchanger is to recover heat within the system, in order to minimise heat input from the heat source. However, in an absorption system, the recuperator assists the absorption and desorption processes taking place in the absorber and generator, respectively, by cooling the downstream mixture to a temperature where absorption can take place and simultaneously heating the upstream to a temperature where desorption can occur. The mass balance in the recuperator is:

$$\dot{m}_6 = \dot{m}_7 = \dot{m}_5 - \dot{m}_1 \quad \text{and} \quad \dot{m}_5 = \dot{m}_4 = \dot{m}_3 \quad (6.18)$$

And the energy balance becomes:

$$\dot{Q}_{Hex} = \dot{m}_5 h_5 - \dot{m}_4 h_4 = \dot{m}_6 h_6 - \dot{m}_7 h_7 \quad (6.19)$$

*Also rewritten by incorporating (r) as:*

$$\dot{Q}_{Hex} = r \dot{m}_r (h_5 - r h_4) = \dot{m}_r (r - 1)(h_6 - h_7) \quad (6.20)$$

With the recuperator effectiveness being:

$$\varepsilon_{Hex} = \frac{h_6 - h_7}{h_6 - h_4} = \frac{h_5 - h_4}{h_6 - h_4} \quad (6.21)$$

#### 6.4.4.2 Expander

The expander is designed to produce work at the expense of reducing the pressure and enthalpy of the CO<sub>2</sub> vapour. The isentropic efficiency of the expander is the ratio of work performed in the actual process, to the work to be done if the expansion process is reversible and adiabatic [252]. The isentropic efficiency of the expander is:

$$\eta_{Exp} = \frac{h_1 - h_2}{h_1 - h_{2s}} \quad (6.22)$$

Where  $h_{2s}$  is the CO<sub>2</sub> enthalpy at the expander's exit after an isentropic expansion. The power produced by the expander is then:

$$W_{Exp} = \dot{m}_1 (h_1 - h_2) = \dot{m}_1 \eta_{Exp} (h_1 - h_{2s}) \quad (6.23)$$

And

$$\dot{m}_1 = \dot{m}_2 \quad (6.24)$$

#### 6.4.4.3 Solution Pump

The pump is designed to move incompressible fluids by increasing the pressure and enthalpy through the provision of work input. Similar to the expander, the performance of the pump is governed by isentropic efficiency, where it is the ratio of the reversible adiabatic work performed, to the actual work carried out in the process [252]. The isentropic efficiency of the pump is:

$$\eta_{Pump} = \frac{h_{4s} - h_3}{h_4 - h_3} \quad (6.25)$$

Where  $h_{4s}$  is the solution mixture enthalpy at the pump exit, following isentropic compression. The power consumed by the pump is then:

$$W_{Pump} = \dot{m}_3(h_4 - h_3) = \frac{\dot{m}_3(h_{4s} - h_3)}{\eta_{Pump}} \quad (6.26)$$

However, assuming that the liquid solution is incompressible, the energy balance shall be rewritten as:

$$W_{Pump} = \frac{\dot{m}_3 V_3 (P_4 - P_3)}{\eta_{Pump}} \quad (6.27)$$

Where  $V_3$  is the specific volume of the solution mixture at the pump inlet at state point 3, and pressures are in kilopascals. The mass balance across the pump is:

$$\dot{m}_3 = \dot{m}_4 \quad (6.28)$$

#### 6.4.4.4 Throttle Valve

The purpose of a throttle valve is to reduce the fluid flow pressure from the high pressure in the generator, to the lower pressure in the absorber, without any work or heat interaction. Therefore, the mass balance is given as:

$$\dot{m}_7 = \dot{m}_8 \quad (6.29)$$

And the energy balance, as:

$$h_7 = h_8 \quad (6.30)$$

#### 6.4.5 Simulation Results and Analysis

In order to investigate the effect of different parameters on the performance of the CO<sub>2</sub>/lubricant absorption power generation system, a parametric study of the cycle is necessary. The main input parameters involved in such a thermodynamic analysis are the absorber and generator temperatures and pressures. However, in such a system, the absorber is the most complex, yet critical component influencing the system performance. In the absorber, the absorbent absorbs the refrigerant and allows it to be reproduced again in the generator, thus maintaining a continuous flow throughout the cycle. Therefore, the absorber requires continuous cooling to achieve equilibrium at the required temperature and pressure. If the absorber is not cooled, the solution will reach equilibrium very quickly at a high absorbent

mass fraction. Consequently, low refrigerant flow rates circulate around the system, resulting in lower system efficiency [251]. This indicates the very strong dependency of system performance on the absorber's operating temperature and pressure and consequently, the amount CO<sub>2</sub> absorbed.

For these reasons, three simulation cases were carried out, with assumed working condition inputs corresponding to the expected practical working conditions, in order to investigate the effect of different system parameters as a function of the absorber pressure and to determine the optimum operating pressure for the absorber that gives the maximum overall thermal efficiency. It is very important to underline that the CO<sub>2</sub>/PC system simulation is limited to the first two cases because of the relatively low flash point of PC at 116°C [182], the limited solubility data for a maximum pressure of 70 bar, and maximum temperature of 100°C. As for CO<sub>2</sub>/POE mixtures, data on solubility and properties are limited to 120°C; therefore, the effect of generator temperature will not be investigated for temperatures higher than 120°C. Moreover, the CO<sub>2</sub> at the turbine inlet in the first two simulation cases is in a sub-critical state, whereas it is in a super-critical state in the last simulation case.

#### 6.4.5.1 The Effect of Absorber Pressure: Simulation Case 1 (Base Case)

Table 6.1 shows the base case simulation inputs. In this simulation, the CO<sub>2</sub> at the turbine inlet is a super-heated gas in the sub-critical region.

**Table 6.1: CO<sub>2</sub>/lubricant absorption power generation system-Base case simulation inputs.**

Simulation	T <sub>G</sub> [K]		P <sub>G</sub> [bar]		T <sub>A</sub> [K]
	CO <sub>2</sub> /POE's	CO <sub>2</sub> /PC	CO <sub>2</sub> /POE's	CO <sub>2</sub> /PC	
Case 1 (Base Case)	393.15	373.15	70	70	30

Table 6.2 presents the first case simulation results and the optimum absorber operating pressure for each mixture pair. However, the results show that the maximum attainable thermal efficiency of the system using the three pairs is very low, with CO<sub>2</sub>/PC operating at 100°C generator temperature and achieving a maximum thermal efficiency of 1.13% at an absorber pressure of 55 bar, closely followed by CO<sub>2</sub>/POE68 achieving 1.12% at a slightly higher absorber operating pressure of 58 bar. Finally, CO<sub>2</sub>/POE32 achieved the lowest thermal efficiency of 0.68% at an absorber pressure of 58 bar - the same optimum operating pressure observed for CO<sub>2</sub>/POE68. Meanwhile, although CO<sub>2</sub>/PC achieved maximum thermal efficiency, the net thermal power output of 2 kW was found to be lower than the 2.23 kW produced using CO<sub>2</sub>/POE68. Ultimately, CO<sub>2</sub>/POE32 achieved the lowest net thermal power output of 1.57 kW.

**Table 6.2: CO<sub>2</sub>/lubricant absorption power generation system-Base case simulation results.**

Parameter name	CO <sub>2</sub> /PC	CO <sub>2</sub> /POE32	CO <sub>2</sub> /POE68
Optimum absorber pressure [bar]	55	58	58
Generator power [kW]	177.82	232.88	198.28
Absorber power [kW]	175.82	231.30	196.05
Middle heat exchanger power [kW]	187.91	264.32	177.86
Solution pump power [kW]	2.99	3.43	2.77
Working fluid circulation ratio [-]	4.41	4.74	3.79
System thermal efficiency [%]	1.13	0.68	1.12
Net thermal power output [kW]	2.00	1.57	2.23
Absorbent mass fraction at the absorber outlet (weak solution) [kg/kg]	0.66	0.71	0.64
Absorbent mass fraction at the generator outlet (strong solution) [kg/kg]	0.86	0.90	0.87
Pure CO <sub>2</sub> refrigerant mass flow rate [kg/s]	0.46	0.53	0.53
Weak solution mass flow rate (at point 3) [kg/s]	2.01	2.51	2.00
Strong solution (at point 8) mass flow rate [kg/s]	1.55	1.98	1.47

Figure 6-3 (a) shows the effect of absorber pressure on the overall thermal efficiency of the system when operating at 30°C. As shown, for all mixture pairs, the thermal efficiency will first increase to

maximum and then decrease as the absorber pressure increases. Figure 6-3 (b) shows that the system's net thermal power output increases as the absorber pressure increases and the circulation ratio decreases. Figure 6-3 (c) demonstrates that the mass flow rate circulation ratio moves in the opposite direction, where it starts at maximum and then decreases as the absorber pressure increases. This behaviour is explained by equation (6.2), where the circulation ratio is related to absorbent mass fractions at the absorber and generator outlets. As the absorber pressure increases, the absorbent mass fraction at the absorber's outlet decreases. Therefore, the difference between  $X_g$  and  $X_a$  increases, causing the circulation value to drop. However, the high value of the circulation ratio indicates high pumping power requirements and therefore, smaller net thermal power output from the system and lower overall thermal efficiency [208]. In addition, the difference in overall performance between both CO<sub>2</sub>/POE32 and CO<sub>2</sub>/POE68, operating under the same conditions, is related to POE68 oil solubility which suggests that POE68 tends to absorb more CO<sub>2</sub> than POE32 under the similar conditions, as shown in Figure 6-3 (d). However, this behaviour has been shown to be untrue as the experimental tests from Chapter 4 confirmed. The PC, however, tends to absorb more CO<sub>2</sub> than either POEs at lower pressures, resulting in better performance at lower pressure. This behaviour changes after 58 bar, where POE68 absorbs more CO<sub>2</sub> than PC, and achieves the best performance up to 65 bar.

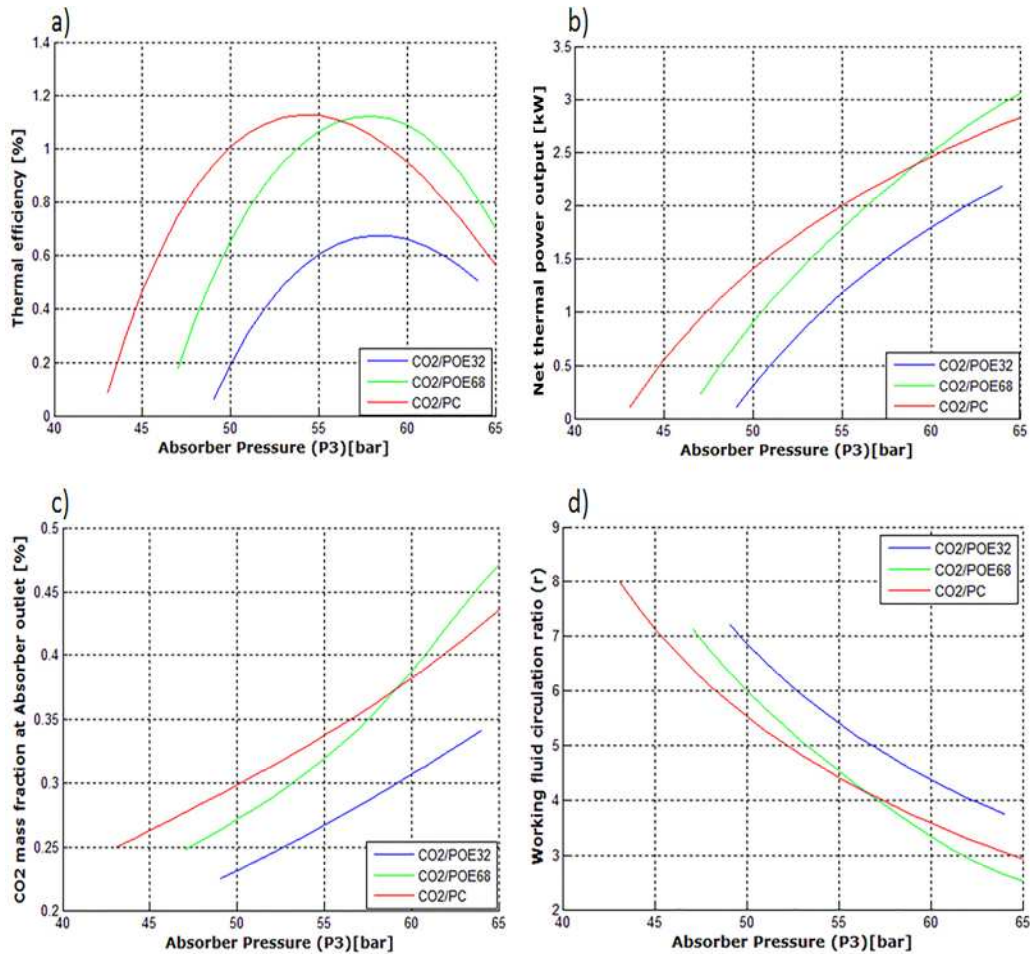


**Figure 6-3: The effect of the absorber's operating pressure on the absorption power generation system's performance at 30°C.**

### 6.4.5.2 The Effect of Absorber Temperature: Simulation

#### Case 2

In this simulation case, the absorber temperature was reduced by 20°C in order to investigate the effect of absorber temperature on system performance and optimum absorber pressure. Table 6.3 shows the simulation inputs.

**Table 6.3: CO2/lubricant absorption power generation system-Case 2 simulation inputs.**

Simulation	T <sub>G</sub> [K]		P <sub>G</sub> [bar]		T <sub>A</sub> [K]
	CO2/POE's	CO2/PC	CO2/POE's	CO2/PC	
Case 2	393.15	373.15	70	70	10

The results listed in Table 6.4 show the significant effect of the absorber's operating temperature on the absorption power system's

performance, when compared to base case simulation results. The results show that a reduction in the absorber's operating temperature will reduce the absorber's optimum operating pressure, and increase the overall thermal efficiency and net thermal power output from the system, as can be seen in the three pairs. Maximum overall thermal efficiency was achieved by CO<sub>2</sub>/POE68. However, unlike the base case simulation results, in this simulation case, CO/POE32 achieved the second highest efficiency and finally, CO<sub>2</sub>/PC. A similar order of net thermal power output was also observed, where CO<sub>2</sub>/POE68 produced the maximum power output, closely followed by the CO<sub>2</sub>/POE32 mixture and finally, CO<sub>2</sub>/PC. Furthermore, in comparison to the base case results, it can be seen that all the energy requirements for all the heat exchangers were significantly reduced by lowering the absorber's working temperature by 20°C.

**Table 6.4: CO<sub>2</sub>/lubricant absorption power generation system-Case 2 simulation results.**

Parameter name	CO <sub>2</sub> /PC	CO <sub>2</sub> /POE32	CO <sub>2</sub> /POE68
Optimum absorber pressure [bar]	43	43	41
Generator power [kW]	110.65	84.24	69.38
Absorber power [kW]	107.88	81.17	65.74
Middle heat exchanger power [kW]	79.60	74.76	35.35
Solution pump power [kW]	2.22	1.93	1.36
Working fluid circulation ratio [-]	3.64	3.09	2.25
System thermal efficiency [%]	2.51	3.64	5.24
Net thermal power output [kW]	2.78	3.07	3.64
Absorbent mass fraction at the absorber outlet (weak solution) [kg/kg]	0.62	0.61	0.49
Absorbent mass fraction at the generator outlet (strong solution) [kg/kg]	0.86	0.90	0.87
Pure CO <sub>2</sub> refrigerant mass flow rate [kg/s]	0.23	0.21	0.19
Weak solution mass flow rate (at point 3) [kg/s]	0.84	0.65	0.43
Strong solution (at point 8) mass flow rate [kg/s]	0.61	0.44	0.24

Figure 6-4 shows the effect of reduction of absorber temperature when operating at 10°C. As shown in Figure 6-4 (a), the system's overall thermal efficiency for all mixture pairs increases gradually

alongside a rise in absorber pressure, up to the point where the maximum CO<sub>2</sub> mass is absorbed in the absorbents shown in Figure 6-4 (d). Figure 6-4 (a) also shows an improvement in thermal efficiency when the absorber temperature is reduced. Figure 6-4 (b) demonstrates further enhanced net thermal power output, brought about by the system through the reduction of absorber temperature. It also shows that a CO<sub>2</sub>/PC mixture pair can produce a higher net thermal power output than is the case with CO<sub>2</sub>/POE32 up to 38 bar. This behaviour changes after that point, where CO<sub>2</sub>/POE32 starts to produce higher net thermal power output, related to the generally lower working fluid circulation ratio of CO<sub>2</sub>/POE32 as shown in Figure 6-4 (c) and therefore, lower pumping power requirements.

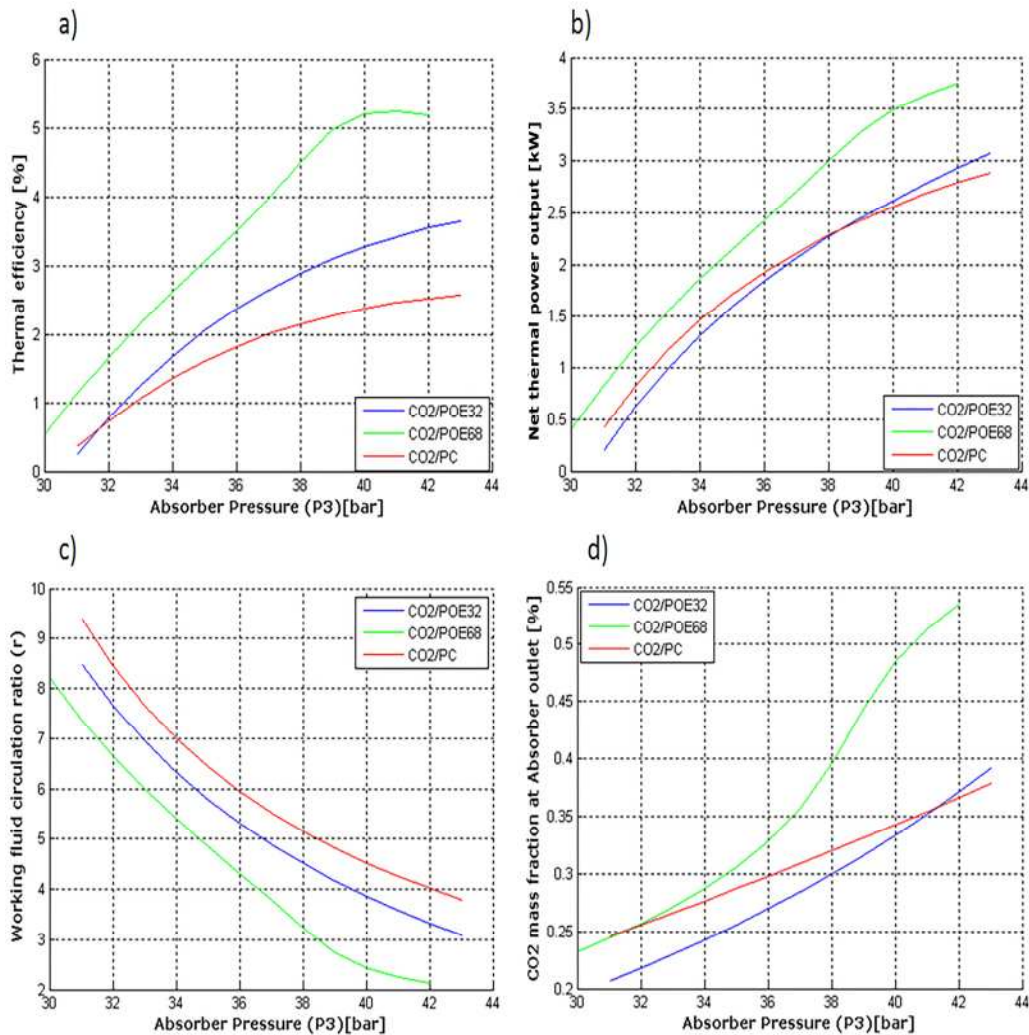


**Figure 6-4: The effect of absorber temperature on the absorption power generation system's performance at 10°C.**

### 6.4.5.3 The Effect of Generator Pressure: Simulation

#### Case 3

In this investigation, the absorber temperature was kept at 30°C, due to its practical feasibility, while the absorber pressure was varied. The generator temperature was kept at 120°C and generator pressure was increased to 100 bar. It is important to mention that the CO<sub>2</sub> at the turbine inlet is in a super-critical state. Table 6.5 shows the simulation's input parameters.

**Table 6.5: CO<sub>2</sub>/lubricant absorption power generation system-Case 3 simulation inputs.**

Simulation	T <sub>G</sub> [K]	P <sub>G</sub> [bar]	T <sub>A</sub> [K]
	CO <sub>2</sub> /POE's	CO <sub>2</sub> /POE's	
Case 3	393.15	100	30

Table 5.10 lists the simulation results alongside the optimum absorber pressure. The results show that the system's thermal efficiency and net thermal power output have a direct dependency on the generator's operating pressure. It can be seen that this is not as influential as the reduction of the absorber's working temperature. However, an increase in generator pressure will also cause the absorbers optimum operating pressure to increase. However, both CO<sub>2</sub>/POE mixture pairs displayed generally low overall thermal efficiency and net thermal power output, with CO<sub>2</sub>/POE68 achieving the greater efficiency and higher net thermal power output. The results also show that the energy requirements for the heat exchangers decreased as the generator pressure increased compared to the base case results.

**Table 6.6: CO<sub>2</sub>/lubricant absorption power generation system-Case 3 simulation results.**

Parameter name	CO <sub>2</sub> /POE32	CO <sub>2</sub> /POE68
Optimum absorber pressure [bar]	70	70
Generator power [kW]	109.02	94.31
Absorber power [kW]	107.47	91.59
Middle heat exchanger power [kW]	90.75	48.05
Solution pump power [kW]	3.45	2.28

Chapter 6: Theoretical Analysis of Small-Scale Power Generation Systems  
for Low-Grade Waste Heat Recovery

Working fluid circulation ratio [-]	3.28	2.33
System thermal efficiency [%]	1.42	2.88
Net thermal power output [kW]	1.55	2.72
Absorbent mass fraction at the absorber outlet (weak solution) [kg/kg]	0.60	0.47
Absorbent mass fraction at the generator outlet (strong solution) [kg/kg]	0.87	0.82
Pure CO <sub>2</sub> refrigerant mass flow rate [kg/s]	0.31	0.31
Weak solution mass flow rate (at point 3) [kg/s]	1.00	0.71
Strong solution (at point 8) mass flow rate [kg/s]	0.70	0.41

Figure 6-5 shows the overall performance of the system at variable absorber pressure. As can be seen, CO<sub>2</sub>/POE68 still demonstrated the best overall performance, where it achieved higher overall thermal efficiency and net thermal power output, and had the lowest working fluid circulation ratio. However this improvement of CO<sub>2</sub>/POE68 over CO<sub>2</sub>/POE32 is directly related to the CO<sub>2</sub>/POE68 solubility data uncertainty, therefore the POE68 performance in reality is very close if not poorer than POE32's.

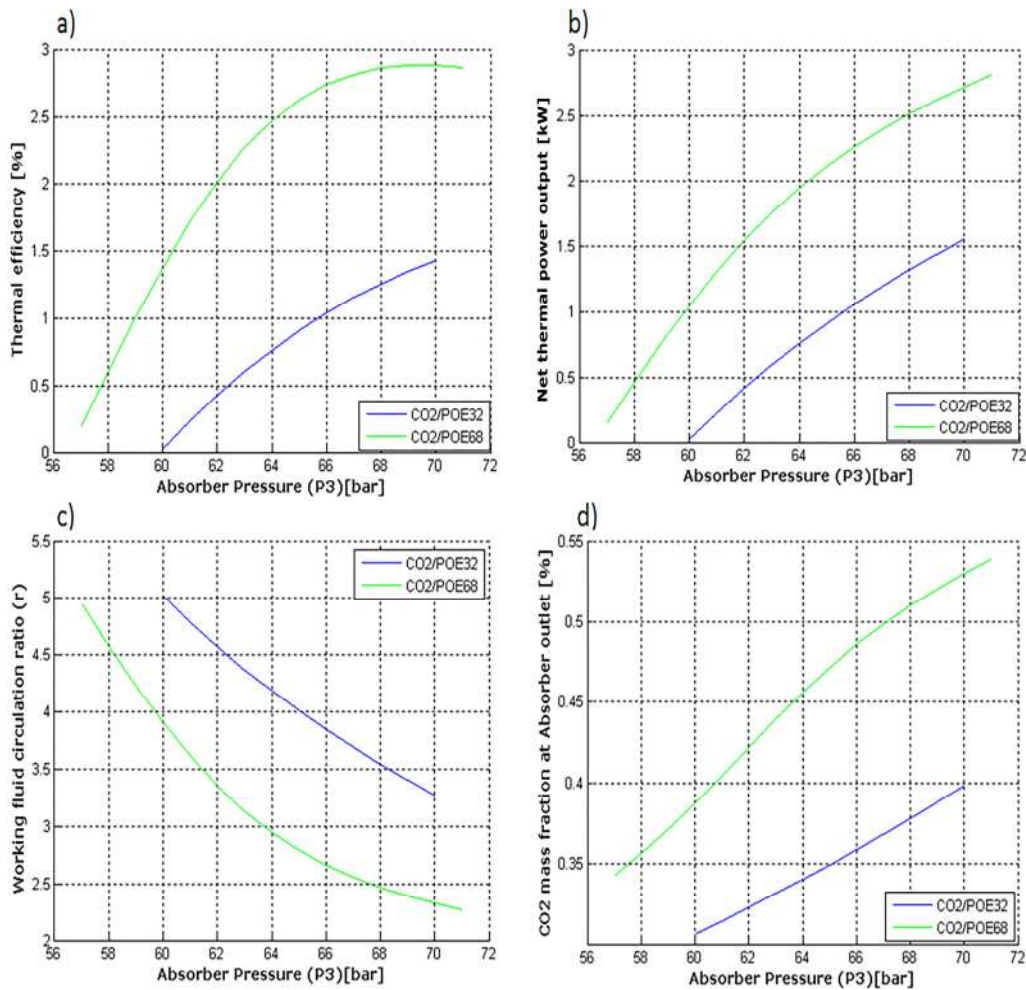


**Figure 6-5: The effect of the generator’s operating pressure on the absorption power generation system’s overall performance, at an absorber temperature of 30°C and generator pressure of 100 bar.**

#### 6.4.6 CO2/Lubricant Absorption Power Generation

##### Theoretical Analysis Conclusions

Three different simulation cases were implemented to compare and investigate the effect of different working parameters on the overall performance of the absorption power cycle, employing three different CO2/absorbent mixture pairs.

The simulation results reveal that all three CO2/absorbent mixture pairs included in the study have very low thermal efficiencies and net thermal power outputs, and require a very large heat exchanger size, compared to other equivalent thermal power technologies,

such as ORC and SRC. The results also show that such a system requires high operating pressures for both the absorber and the generator, with lower temperatures for the absorber. Amongst the three CO<sub>2</sub>/absorbent pairs investigated, CO<sub>2</sub>/POE68 is shown to have the best overall performance, followed by CO<sub>2</sub>/POE32 and then finally, CO<sub>2</sub>/PC.

Moreover, the analysis shows that the thermal efficiency of the system using all three mixture pairs increases significantly as the absorber temperature decreases. Furthermore, the decrease in the absorber working temperature will also cause its optimum working pressure to be reduced. However, considering the absorber cooling conditions, it is difficult in practical terms to achieve absorber temperatures lower than 30°C. The analysis also shows that the system performance increased as the generator pressure increased, but this increase was not as adequate as when the absorber temperature was reduced. In addition, increased generator pressure caused the optimum absorber pressure to increase. Finally, even though the higher generator pressure improved system performance, it is undesirable due to safety issues and difficulties in system construction and component customisation. However, for a practical CO<sub>2</sub>/lubricant absorption power generation system, even lower thermal efficiencies and net thermal power outputs are expected than those seen in the theoretical evaluation, mainly due to the lower isentropic efficiency of commercially available expansion devices as will be discussed in Chapter 9. To conclude, all the drawbacks discussed make further investigation into the CO<sub>2</sub>/lubricant absorption power generation system unfeasible and revive the research on new mixture pairs.

However, a new power generation technology for low-grade heat sources has been under investigation recently. The technology is referred to as (flood expansion), which aims to achieve quasi-static expansion by employing a refrigerant/lubricant working fluid that expands through an expander of positive displacement type.

Consequently, near isothermal expansion is achieved and therefore improved system performance. For the sake of investigating the system's potential as a substitute to the CO<sub>2</sub>/lubricant absorption power generation system, a theoretical model of a flood expansion power generation system that employs a CO<sub>2</sub>/POE32 mixture as a working fluid, was introduced for comparison with the base case results of the CO<sub>2</sub>/POE32 absorption power system, as well as a CO<sub>2</sub> SRC power generation system working under the same operating conditions.

## **6.5 CO<sub>2</sub>/POE32 Flood Expansion Power Generation System**

### **6.5.1 Principle of Operation and System Requirements**

In principle, the purpose of flood expansion is to maximise a system's thermal efficiency and power output by achieving quasi-static or near isothermal expansion [253]. This can be brought about by exploiting the higher heat capacity of a secondary fluid that is expanded at the same time as the refrigerant via the expansion device, thus avoiding the temperature drop which normally occurs in the case of pure refrigerant [254]. The reviewed literature indicates the suitability of POE lubricant oils for use in direct expansion applications [59], but POEs do not seem to be the oils which are most favoured for working with CO<sub>2</sub> in such a system. In contrast to the absorption power generation system, where the high solubility of CO<sub>2</sub> is the key factor in the selection of absorbent fluid, the flood expansion system essentially requires a secondary fluid which is completely immiscible, or just partially miscible with the refrigerant, while also being incompressible and non-chemically reactive with it [255] and where it can achieve good lubrication in the expansion device [256]. These requirements would point to the immiscible lubricants oil types. In fact, these immiscible oils are frequently encountered in both flood expansion and flood compression-related research. For example, the AB oil

type was used in experimental work by Bell et al. [257] and the theoretical research cited in references [254, 255, 258], while PAG lubricant was also seen in reference [256].

In practice, besides the working fluid requirements, the flood expansion system requires a complete separation between the refrigerant and lubricant oil after the expansion process in order to insure that no oil is carried over in the refrigerant loop. Therefore, a separate loop is essential for the lubricant oil, only meeting the refrigerant loop in the expander section so as to achieve quasi-isothermal expansion [257]. Moreover, the nature of the two-phase expansion, limits the options to selecting expanders to only those of positive displacement type, specifically scroll or screw expanders [255].

### 6.5.2 Flood Expansion Overview

Woodland et al. [254] investigated and proposed flood expansion as a simple, low-cost enhancement to ORC systems. Several refrigerants, beside CO<sub>2</sub> were investigated in mixtures with AB lubricant oil and with water. The authors compared the exergy efficiencies of regenerative ORC employing pure refrigerants to the mixture pairs. The results showed an improvement in exergy efficiency of 2% to 4.5% over a heat source temperature, which varied from 110°C to 310°C in the case of the CO<sub>2</sub>/AB lubricant, while the improvement was around 6% in the case of CO<sub>2</sub>/water. In a further theoretical investigation, Woodland et al. [255] compared the performance of CO<sub>2</sub>/water in a flood expansion system to that of CO<sub>2</sub>/acetone absorption power system. The study concluded that flood expansion will always improve system performance, unlike the CO<sub>2</sub>/acetone absorption system which showed very little improvement. However, the authors indicate that water is not the absorbent which should be used in a flood expansion system because it will expand into low quality vapour. Figure 6-6 shows a reiteration of the systems investigated in references [254, 255].

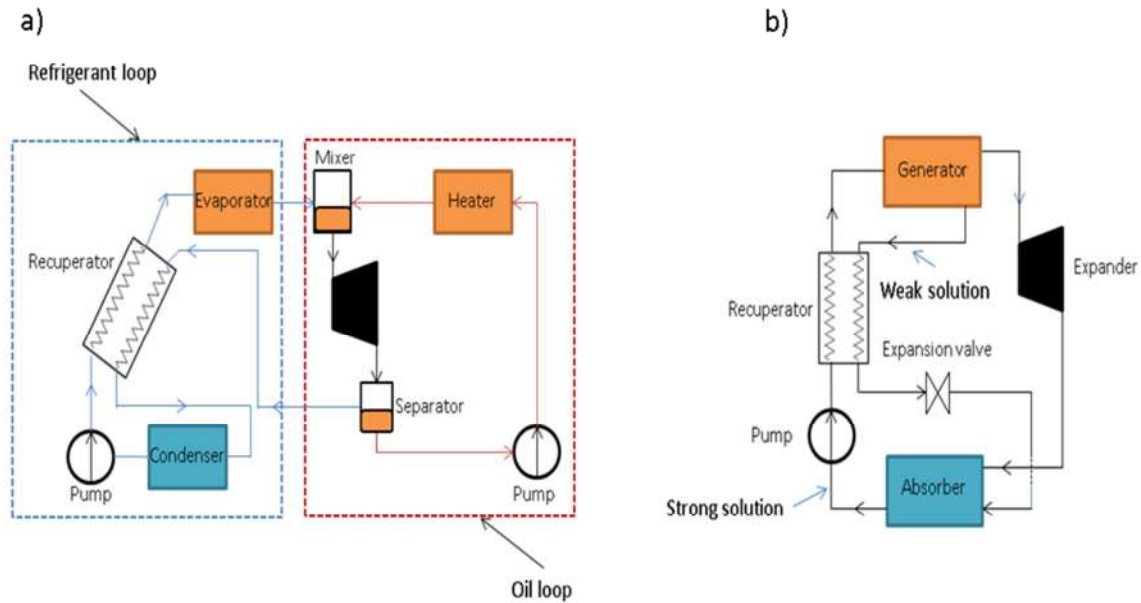


**Figure 6-6: Schematics of a) Flood expansion system reproduced from reference [254], and b) CO<sub>2</sub>/acetone absorption power generation system reproduced from reference [255].**

Bell et al. [257, 259] developed a scroll expander model for refrigerant/oil mixtures, to be used in flood expansion applications. The model was validated by experimental work on a Sanden [260] automotive scroll compressor converted into an expander. The highest isentropic efficiency reported was 65% and the lowest, 35%. The study concluded that flood expansion through this scroll expander would relatively decrease the performance of the expander. Moreover, operating at a lower expander speed would significantly affect its performance, mainly due to leakage, the expander eventually behaving like a throttle valve. In their experimental study on a flood expansion ORC using a hermetic refrigeration scroll expander and employing R245fa/oil, Lemort, Declay and Quoilin [261] confirmed the effect of increased oil mass fraction in reducing the expander isentropic efficiency. Finally, the authors reported a maximum of 71% electrical isentropic effectiveness at an optimum oil mass fraction of 3.2%.

In a theoretical study on CO<sub>2</sub> flood compression refrigeration, Bell et al. [262] investigated the impact of oil solubility on system performance. The results indicate a negative effect of solubility on

system performance, where the COP decreases as the solubility increases. In addition, there is an optimal amount of lubricant oil which depends on the solubility mass fraction under the operating conditions.

In a series of theoretical and experimental studies on two-phase expansion in general, extensive effort was made by the Smith et al. group [263-266] to develop, model and construct twin screw expanders to accommodate the two-phase expansion. The authors indicated the negative effect of the high percentage of lubricant oil on the screw expander's performance [266]. This observation was found to be in agreement with those reported for both the experimentally examined scroll expanders in [257, 261].

Even though flood expansion in principle requires immiscible oil in a separate loop, the potential for a simple regenerative system will be investigated, employing a two-phase mixture of CO<sub>2</sub> gas and CO<sub>2</sub>/POE32 liquid mixture in a single loop, with a defined maximum CO<sub>2</sub>/POE32 liquid mixture mass flow ratio, based on the flood expansion concept. In an ideal world, such a system would deliver lower performance in comparison with a CO<sub>2</sub> system, if CO<sub>2</sub> turbine technology was well established. On the other hand, in a flood expansion system, presuming that both scroll or screw expander technologies are able to handle CO<sub>2</sub>, and the optimum CO<sub>2</sub>/POE32 mass flow ratio has been defined, the low isentropic efficiency of the CO<sub>2</sub> turbine may be compensated by a positive displacement expander. In comparison with the CO<sub>2</sub>/POE32 absorption power generation cycle, this system would be expected to demonstrate better performance, as Woodland et al.'s [255] study indicates.

### **6.5.3 Thermodynamic Model of a CO<sub>2</sub>/POE32 Flood Expansion System**

Similar to the absorption power generation system, the simulation program for the flood expansion power generation system uses the

sub-routines developed for the properties of liquid mixtures. Besides these, new sub-routines were introduced to simulate hypothetical system components, as will be discussed. The program relevant flow chart is included in Appendix C.2.

### 6.5.3.1 Cycle Description

A schematic of the system is shown in Figure 6-7. The two-phase working fluid consists of CO<sub>2</sub>, which could be a super-heated gas, or a super-critical fluid, depending on the operating temperature and pressure, in addition to a CO<sub>2</sub>/POE32 liquid mixture, which is in equilibrium and acts as the high heat capacity medium for achieving near-isothermal expansion. It is essential to emphasize here that the CO<sub>2</sub> phase of the working fluid mixture does not evaporate or condensate in either an evaporator or condenser, respectively, but is only cooled in the working fluid absorber/cooler to remove energy from the system and heated in the generator/heater to gain energy.

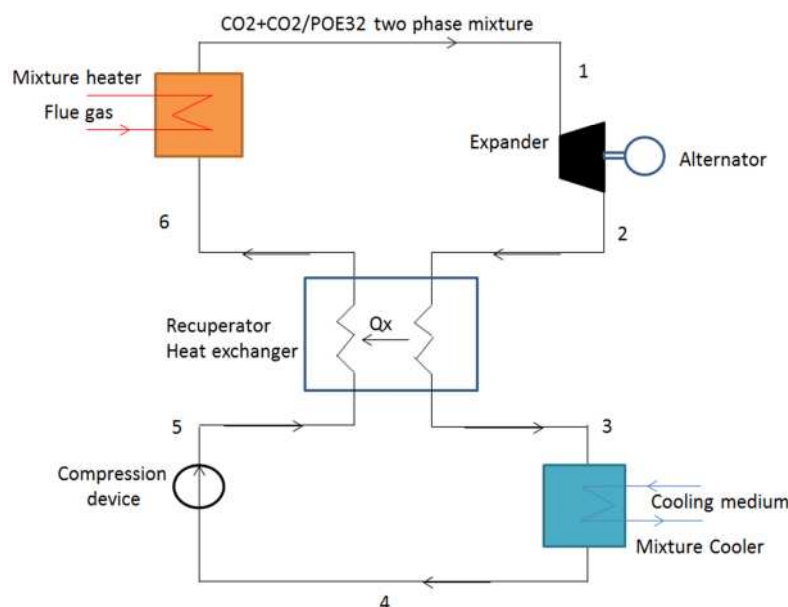


**Figure 6-7: Schematic of the CO<sub>2</sub>/lubricant flood expansion system.**

However, as the system is operating, the working fluid mixture at the known CO<sub>2</sub>/POE32 mass flow rate from the generator/heater outlet at point 1 is directed to the expander, where it expands to a lower pressure at point 2 by flooding the expander and producing the system's work output. At the exit of the expander and due to

the sudden drop in pressure, a small fraction of CO<sub>2</sub> of the CO<sub>2</sub>/POE32 mixture will desorb, thus enhancing expansion performance. Following expansion, the working fluid mixture enters the recuperator heat exchanger, where it loses some of its energy to the upcoming counter stream and therefore a small fraction of the CO<sub>2</sub> gas is absorbed into the coexisting liquid CO<sub>2</sub>/POE32 mixture phase before it exits at point 3 and enters the mixture absorber/cooler. In the absorber/cooler, the CO<sub>2</sub> phase of the mixture, which is normally in its gas phase, but which could also be in its liquid phase, depending on the operating conditions, as well as the liquid CO<sub>2</sub>/POE32 mixture, is further cooled. Consequently, absorption takes place, as per what has been explained for the absorber in the CO<sub>2</sub>/lubricant absorption power generation system. The working fluid mixture then exits the absorber/cooler at point 4, where it is in equilibrium and could take the form of either a fully absorbed solution as in the CO<sub>2</sub>/lubricant absorption power generation system, or a partially absorbed two-phase mixture, depending on the mass flow rate ratios of the CO<sub>2</sub> and CO<sub>2</sub>/POE32 liquid mixture phases.

It is important to understand that the mass flow rate ratio is directly influenced by the CO<sub>2</sub>/POE32 liquid phase mixture mass fractions at the absorber/cooler and generator/heater exits and consequently depends on their operating temperatures and pressures. However, the mixture is directed to the compression device, where it is pumped to the higher pressure side of the system and enters the recuperator heat exchanger at point 5. Here, it is pre-heated by the counter downstream and releases a small fraction of CO<sub>2</sub> from the liquid phase mixture before entering the generator/heater at point 6. In the generator/heater, the working fluid mixture is further heated and the maximum portion of CO<sub>2</sub> desorbs from the CO<sub>2</sub>/POE32 liquid phase, subsequently being added to the co-existing CO<sub>2</sub> phase. Finally, the working fluid mixture exits the generator/heater in equilibrium at point 1, to be expanded, thus completing the cycle.

### 6.5.3.2 Thermodynamic Model Assumptions and Inputs

Due to the complex nature of the working fluid, the expander and the compression device were split into two corresponding hypothetical expanders and compression devices, in order to handle each phase separately. The CO<sub>2</sub>/POE32 mixture liquid phase is assumed to be incompressible in these hypothetical components. Moreover, two hypothetical mixers were introduced after expansion and compression processes, so as to ease the simulation process and take into account the absorption/desorption which occurs while the working fluid mixture is travelling around the cycle. These hypothetical mixers were treated as simple control volumes, with inlets and outlets accounting for heat, mass and mass fraction balance between the two phases of the working fluid. Figure 6-8 illustrates the hypothetical system components used in the model.

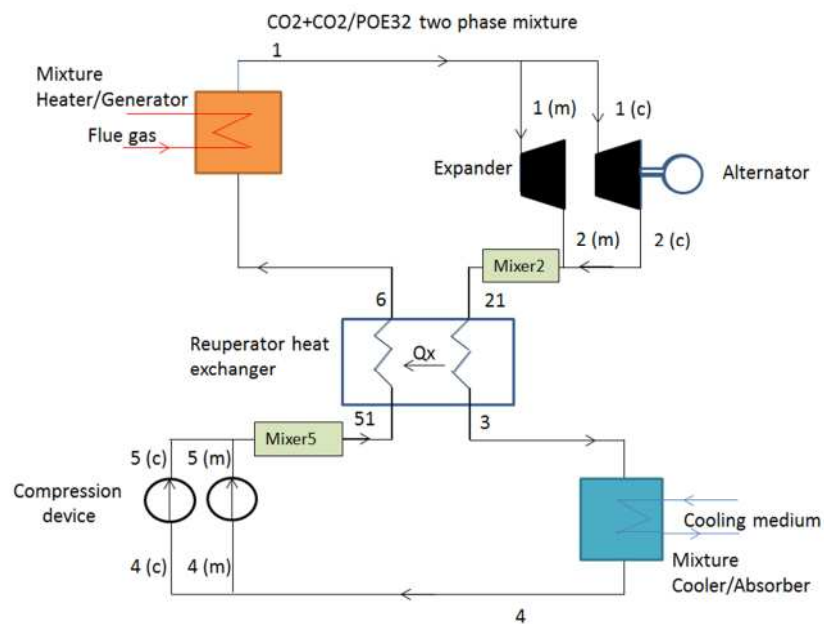


**Figure 6-8: Schematic of the CO<sub>2</sub>/lubricant flood expansion system for simulation.**

1(m), shown in Figure 6-8, denotes the mass flow rate of the CO<sub>2</sub>/POE32 liquid phase entering the expander, while 1(c) denotes the mass flow rate of the CO<sub>2</sub> phase entering the expander. For the current model, the CO<sub>2</sub>/POE32 liquid phase mass flow ratio at point 1 was taken as a simulation input and is limited by the CO<sub>2</sub>/POE32

liquid phase circulation ratio shown in equation (5.11), and described as the mass fraction of the POE32 at the absorber/cooler outlet, to the mass fraction of POE32 at the generator/heater outlet:

$$\dot{m}_{1(m)max} = \frac{X_C}{X_H} \quad (6.31)$$

The above ratio defines the maximum CO<sub>2</sub>/POE32 liquid phase mass flow fraction permitted for expansion through the expander at point 1 in the schematic of the system shown in Figure 6-8. Accordingly, the mass flow rate of the CO<sub>2</sub>/POE32 liquid mixture at the absorber/cooler outlet becomes:

$$\dot{m}_{4(m)} = \frac{X_H \dot{m}_{1(m)}}{X_C} \quad (6.32)$$

In the case where the maximum CO<sub>2</sub>/POE32 mass flow ratio is permitted in the expander, the absorber/cooler will act as an absorber and only a fully absorbed CO<sub>2</sub>/POE32 liquid mixture will exit at point 4. If the CO<sub>2</sub>/POE32 mass flow ratio at point 1 is set to zero, the system will become a CO<sub>2</sub> power generation system.

### 6.5.3.3 Heat and Mass Balance of System Components

Besides the energy and mass balance equations, the balance of the mass fractions of the working fluid mixture components was introduced, due to its direct influence on the cycle. However, this section presents the equations governing the system referred to the system schematic for simulation in Figure 6-8. The subsequent solving of these equations will enable the system's theoretical performance to be predicted.

#### 6.5.3.3.1 Expander

The liquid CO<sub>2</sub>/POE32 mixture phase, mass, energy balance and power output of expander are:

$$\dot{m}_{1(m)} = \dot{m}_{2(m)} \quad (6.33)$$

$$\dot{m}_{1(m)} h_{1(m)} = \dot{m}_{2(m)} h_{2(m)} + W_{Exp(m)} \quad (6.34)$$

$W_{Exp(m)}$  for incompressible fluid could be rewritten as:

$$W_{Exp(m)} = \dot{m}_{1(m)}(P_1 - P_2)V_{1(m)}\eta_{Exp} \quad (6.35)$$

Where pressure is in kilopascals

For the CO<sub>2</sub> phase, the mass and energy balance equations are:

$$\dot{m}_{1(c)} = \dot{m}_{2(c)} \quad (6.36)$$

$$W_{Exp(c)} = \dot{m}_{1(c)}(h_{1(c)} - h_{2(c)}) = \dot{m}_{1(c)}\eta_{Exp}(h_{1(c)} - h_{2s(c)}) \quad (6.37)$$

Where  $h_{2s}$  is the CO<sub>2</sub> exit enthalpy after an isentropic expansion

And the total power output of the expander becomes:

$$W_{Exp(Tot)} = W_{Exp(m)} + W_{Exp(c)} \quad (6.38)$$

### 6.5.3.3.2 Mixer 2

Mixer 2 is where the two hypothetical, separately expanded streams re-join to be balanced under the expander outlet conditions. A block diagram of Mixer 2 is shown in Figure 6-9 to present a simplification of the mixer process.

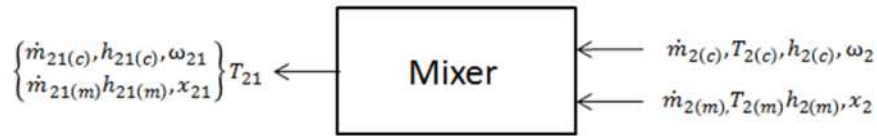


Figure 6-9: CO<sub>2</sub>/POE32 mixer 2 process flow.

After expansion, further quantities of the CO<sub>2</sub> will desorb from the CO<sub>2</sub>/POE32 liquid phase. To compensate for the absence of mixture-specific entropy and to determine the new mass fractions after expansion, the new CO<sub>2</sub> phase mass fraction was determined from the CO<sub>2</sub>/POE32 solubility correlation at known  $T_{2(c)}$  and  $P_2$  and accordingly, the new CO<sub>2</sub>/POE32 liquid phase mass fraction was found. Once the two streams enter the mixer, the mixer sub-routine will iterate values for  $T_{21}$  and determine the mass fractions, mass flow rates and specific enthalpies for both phases, until the mixer energy, mass and mass fraction balance equations (6.39) to (6.41), respectively, are satisfied. The mixer sub-routine is included in Appendix C.3.

$$\dot{m}_{2(m)}h_{2(m)} + \dot{m}_{2(c)}h_{2(c)} = \dot{m}_{21(m)}h_{21(m)} + \dot{m}_{21(c)}h_{21(c)} \quad (6.39)$$

$$\dot{m}_{2(m)} + \dot{m}_{2(c)} = \dot{m}_{21(m)} + \dot{m}_{21(c)} \quad (6.40)$$

$$\dot{m}_{2(m)}X_2 = \dot{m}_{21(m)}X_{21} \text{ and } \dot{m}_{2(c)}\omega_2 = \dot{m}_{21(c)}\omega_{21} \quad (6.41)$$

Where the mass flow rates at the mixer exit are calculated by combining equations (6.39) and (6.40) as:

$$\dot{m}_{21(c)} = \frac{\dot{m}_{2(m)}(h_{2(m)} - h_{21(m)}) + \dot{m}_{2(c)}(h_{2(c)} - h_{21(m)})}{h_{21(c)} - h_{21(m)}} \quad (6.42)$$

$$\dot{m}_{21(m)} = \dot{m}_{2(m)} + \dot{m}_{2(c)} - \dot{m}_{21(c)} \quad (6.43)$$

### 6.5.3.3.3 Compression Device

For the liquid CO<sub>2</sub>/POE32 mixture phase:

$$\dot{m}_{4(m)} = \dot{m}_{5(m)} \quad (6.44)$$

$$W_{Pump(m)} + \dot{m}_{4(m)}h_{4(m)} = \dot{m}_{5(m)}h_{5(m)} \quad (6.45)$$

$W_{Pump(m)}$  for incompressible fluid could be rewritten as:

$$W_{Pump(m)} = \frac{\dot{m}_{4(m)}(P_5 - P_4)V_{4(m)}}{\eta_{Pump}} \quad (6.46)$$

Where pressures are in kilopascals

For the CO<sub>2</sub> phase:

$$\dot{m}_{4(c)} = \dot{m}_{5(c)} \quad (6.47)$$

$$W_{Pump(c)} = \dot{m}_{4(c)}(h_{5(c)} - h_{4(c)}) = \frac{\dot{m}_{4(c)}(h_{5(c)} - h_{4s(c)})}{\eta_{Pump}} \quad (6.48)$$

Where  $h_{4s}$  is the CO<sub>2</sub> exit enthalpy after an isentropic compression

And the total power input of the compression device becomes:

$$W_{Pump(Tot)} = W_{Pump(m)} + W_{Pump(c)} \quad (6.49)$$

### 6.5.3.3.4 Mixer 5

Mixer 5 operates in a similar way to Mixer 2:

$$\dot{m}_{5(m)}h_{5(m)} + \dot{m}_{5(c)}h_{5(c)} = \dot{m}_{51(m)}h_{51(m)} + \dot{m}_{51(c)}h_{51(c)} \quad (6.50)$$

$$\dot{m}_{5(m)} + \dot{m}_{5(c)} = \dot{m}_{51(m)} + \dot{m}_{51(c)} \quad (6.51)$$

$$\dot{m}_{5(m)}X_5 = \dot{m}_{51(m)}X_{51} \text{ and } \dot{m}_{5(c)}\omega_5 = \dot{m}_{51(c)}\omega_{51} \quad (6.52)$$

The mass flow rates at the mixer exit are calculated by combining equations (6.50) and (6.51) as:

$$\dot{m}_{51(c)} = \frac{\dot{m}_{5(m)}(h_{5(m)} - h_{51(m)}) + \dot{m}_{5(c)}(h_{5(c)} - h_{51(m)})}{h_{51(c)} - h_{51(m)}} \quad (6.53)$$

$$\dot{m}_{51(m)} = \dot{m}_{5(m)} + \dot{m}_{5(c)} - \dot{m}_{51(c)} \quad (6.54)$$

Once the parameters are determined for points 21 and 51, points 6 and 3 may be calculated by applying heat and mass balance to the recuperator heat exchanger

### 6.5.3.3.5 The Recuperator Heat Exchanger

The conventional approach to determining the effectiveness of the recuperator heat exchanger is based on the assumption that constant specific heat is invalid for this cycle, as CO<sub>2</sub> phase properties will vary considerably according to whether the CO<sub>2</sub> phase is in a sub-critical state, or approaching the super-critical region. Figure 6-10 shows the significant change in the specific heat of the CO<sub>2</sub> at different expected working pressures along the temperature profile. Therefore, it is essential to take into account the changes in CO<sub>2</sub> properties while balancing the recuperator heat exchanger.

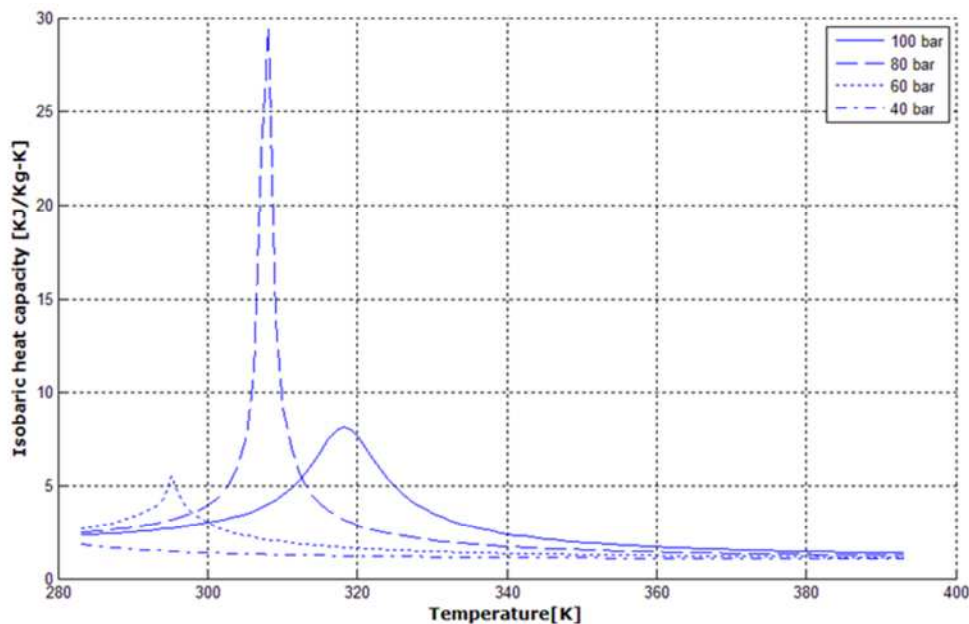


**Figure 6-10: Specific heat of CO<sub>2</sub> at expected operating pressures, against the operating temperature range.**

As suggested by Cayer et al. [107] and implemented in Wang and Zhang's [91] theoretical comparative study, in an ideal recuperator

heat exchanger, two possible situations could arise, depending on which stream has the smaller heat capacity. Either  $T_6$  will have the tendency to increase towards  $T_{21}$ , or the tendency of  $T_3$  may be to decrease towards  $T_{51}$  on the model schematic shown in Figure 6-8. Therefore, the maximum thermodynamic heat transfer possible i.e.  $\dot{Q}_{max}$  is determined as the smaller value of the quantities determined in equations (6.55) and (6.56).

$$\dot{Q}_{max1} = \dot{m}_{21(c)}h_{21(c)} + \dot{m}_{21(m)}h_{21(m)} - \dot{m}_{3(c)}h_{3(c)} - \dot{m}_{3(m)}h_{3(m)} \quad (6.55)$$

*assuming  $T_3 = T_{51}$  and mass flow rates at point 3 are calculated accordingly.*

$$\dot{Q}_{max2} = \dot{m}_{6(c)}h_{6(c)} + \dot{m}_{6(m)}h_{6(m)} - \dot{m}_{51(c)}h_{51(c)} - \dot{m}_{51(m)}h_{51(m)} \quad (6.56)$$

*assuming  $T_6 = T_{21}$  and mass flow rates at point 6 are calculated accordingly.*

Once the  $\dot{Q}_{max}$  is known, the effectiveness becomes:

$$\begin{aligned} \varepsilon_{Hex} &= \frac{\dot{m}_{21(c)}h_{21(c)} + \dot{m}_{21(m)}h_{21(m)} - \dot{m}_{3(c)}h_{3(c)} - \dot{m}_{3(m)}h_{3(m)}}{\dot{Q}_{max}} \\ &= \frac{\dot{m}_{6(c)}h_{6(c)} + \dot{m}_{6(m)}h_{6(m)} - \dot{m}_{51(c)}h_{51(c)} - \dot{m}_{51(m)}h_{51(m)}}{\dot{Q}_{max}} \end{aligned} \quad (6.57)$$

However, to satisfy equation (6.57) and calculate  $T_3$  and  $T_6$ , an iterative sub-routine was created to iterate values for both  $T_3$  and  $T_6$  and calculate enthalpies and mass flow rates, until all sides of equation (6.57) are equal. The sub-routine flow chart is included in Appendix C.4. However, the energy, mass, and mass fraction balance over the recuperator heat exchanger for point 3 are, respectively:

$$\dot{m}_{3(m)}h_{3(m)} + \dot{m}_{3(c)}h_{3(c)} = \dot{m}_{21(m)}h_{21(m)} + \dot{m}_{21(c)}h_{21(c)} \quad (6.58)$$

$$\dot{m}_{3(m)} + \dot{m}_{3(c)} = \dot{m}_{21(m)} + \dot{m}_{21(c)} \quad (6.59)$$

$$\dot{m}_{3(m)}X_3 = \dot{m}_{21(m)}X_{21} \quad \text{and} \quad \dot{m}_{3(c)}\omega_3 = \dot{m}_{21(c)}\omega_{21} \quad (6.60)$$

The mass flow rates at point 3 are calculated by combining equations (6.58) and (6.59) as:

$$\dot{m}_{3(c)} = \frac{\dot{m}_{21(m)}(h_{21(m)} - h_{3(m)}) + \dot{m}_{21(c)}(h_{21(c)} - h_{3(m)})}{h_{3(c)} - h_{3(m)}} \quad (6.61)$$

$$\dot{m}_{3(m)} = \dot{m}_{21(m)} + \dot{m}_{21(c)} - \dot{m}_{3(c)} \quad (6.62)$$

And for point 6

$$\dot{m}_{6(m)}h_{6(m)} + \dot{m}_{6(c)}h_{6(c)} = \dot{m}_{51(m)}h_{51(m)} + \dot{m}_{51(c)}h_{51(c)} \quad (6.63)$$

$$\dot{m}_{6(m)} + \dot{m}_{6(c)} = \dot{m}_{51(m)} + \dot{m}_{51(c)} \quad (6.64)$$

$$\dot{m}_{6(m)}X_6 = \dot{m}_{51(m)}X_{51} \text{ and } \dot{m}_{6(c)}\omega_6 = \dot{m}_{51(c)}\omega_{51} \quad (6.65)$$

The mass flow rates at point 6 are calculated by combining equations (6.66) and (6.67) as:

$$\dot{m}_{6(c)} = \frac{\dot{m}_{51(m)}(h_{51(m)} - h_{6(m)}) + \dot{m}_{51(c)}(h_{51(c)} - h_{6(m)})}{h_{6(c)} - h_{6(m)}} \quad (6.66)$$

$$\dot{m}_{6(m)} = \dot{m}_{51(m)} + \dot{m}_{51(c)} - \dot{m}_{6(c)} \quad (6.67)$$

#### 6.5.3.3.6 Mixture Absorber/Cooler

Now all state points properties are calculated, the mass, energy and mass fraction balance over the absorber/cooler, respectively, becomes:

$$\dot{Q}_A = \dot{m}_{3(m)}h_{3(m)} + \dot{m}_{3(c)}h_{3(c)} - \dot{m}_{4(m)}h_{4(m)} - \dot{m}_{4(c)}h_{4(c)} \quad (6.68)$$

$$\dot{m}_{3(m)} + \dot{m}_{3(c)} = \dot{m}_{4(m)} + \dot{m}_{4(c)} \quad (6.69)$$

$$\dot{m}_{3(m)}X_3 = \dot{m}_{4(m)}X_4 \text{ and } \dot{m}_{3(c)}\omega_3 = \dot{m}_{4(c)}\omega_4 \quad (6.70)$$

#### 6.5.3.3.7 Mixture Generator/Heater

Similar to the absorber/cooler, the mass, energy and mass fraction balance over the mixture generator/heater, respectively, are:

$$\dot{Q}_G = \dot{m}_{1(m)}h_{1(m)} + \dot{m}_{1(c)}h_{1(c)} - \dot{m}_{6(m)}h_{6(m)} - \dot{m}_{6(c)}h_{6(c)} \quad (6.71)$$

$$\dot{m}_{1(m)} + \dot{m}_{1(c)} = \dot{m}_{6(m)} + \dot{m}_{6(c)} \quad (6.72)$$

$$\dot{m}_{1(m)}X_1 = \dot{m}_{6(m)}X_6 \text{ and } \dot{m}_{1(c)}\omega_1 = \dot{m}_{6(c)}\omega_6 \quad (6.73)$$

#### 6.5.3.4 Simulation results and analysis

The CO<sub>2</sub>/lubricant absorption power generation system base case simulation conditions presented in Table 6.1 were used for performance comparison between the flood expansion CO<sub>2</sub>/POE32, the CO<sub>2</sub>/POE32 absorption, and a CO<sub>2</sub> power generation systems operating under the same conditions. In this simulation, the CO<sub>2</sub> phase in both the absorber/cooler and generator/heater was in the form of super-heated gas in the sub-critical region. It is important to note that the generator/heater operates at the edge point where the sub-critical and super-critical regions are divided. However, in order to investigate the effect of CO<sub>2</sub>/POE32 mass flow ratio on the flood expansion system, four ratios were included in the simulation. These flow ratios were 1%, 10%, 20%, and the maximum flow ratio, which was defined by equation (5.11).

Table 6.7 presents the base case simulation results and the optimum absorber/ cooler operating pressures for the three simulated systems: the CO<sub>2</sub>/POE32 absorption system, the CO<sub>2</sub>/POE32 flood expansion system with varied CO<sub>2</sub>/POE32 mass flow ratios allowed through the expander, and finally, the CO<sub>2</sub> power system. The results show that the maximum thermal efficiency attained for all systems was relatively low, with the CO<sub>2</sub> system achieving the maximum thermal efficiency of 3.82% at an absorber/cooler pressure of 59 bar, while the lowest was achieved by the CO<sub>2</sub>/POE32 absorption power system at 58 bar. It is quite interesting to observe that the optimum pressures for all cases were almost similar, apart from the maximum CO<sub>2</sub>/POE32 ratio case of 85%, which yielded its best performance at 51 bar. From the results, it is clear that as the CO<sub>2</sub>/POE32 mass flow ratio increases, the efficiency gradually decreases for the CO<sub>2</sub>/POE32 flood expansion system, in comparison to the CO<sub>2</sub> power system. On the other hand, the heat exchanger energy requirements increase as the mass flow ratio increases, with the energy requirements for the CO<sub>2</sub>/POE32 absorption power system being

the highest. With regard to the net thermal power output, the results suggest that the maximum CO<sub>2</sub>/POE32 mass flow ratio case in the flood expansion cycle would yield 1.66 kW: the maximum output overall, followed by the absorption power system. In comparison, with the maximum CO<sub>2</sub>/POE32 ratio case, the net thermal power output tended to decrease gradually as the flow rate ratio decreased where the CO<sub>2</sub> system yielded 0.99 kW: the lowest net thermal power output. It is important to emphasize here that the maximum CO<sub>2</sub>/POE32 of 85% allowed through the expander is practically impossible, since the expanders usually used are converted compressors, restricted by built-in volumes and therefore, this volume of liquid mixture cannot be accepted. This situation recalls the experimental work of Bell et al. [257, 259], where the scroll expander used was completely flooded, efficiency dropped and the expander started to behave like a throttle valve.

**Table 6.7: CO<sub>2</sub>/POE32 absorption, flood expansion, and CO<sub>2</sub> systems - Base case simulation results.**

Parameter name	CO <sub>2</sub> /POE32 Absorption system	CO <sub>2</sub> /POE32 flood expansion system				CO <sub>2</sub>
		85[Max]	20	10	1	
POE32 ratio percentage through the expander [%]	N/A	85[Max]	20	10	1	N/A
Optimum absorber/cooler pressure [bar]	58	51	58	59	59	59
Generator/heater power [kW]	232.88	63.02	31.76	29.81	26.24	25.85
Absorber/cooler power [kW]	231.308	61.37	30.70	28.75	25.25	24.87
Recuperator heat exchanger power [kW]	264.32	128.48	52.75	48.62	39.98	39.12
Solution pump/compression device power [kW]	3.43	2.16	3.94	3.94	4.01	4.01
Working fluid circulation ratio [-]	4.74	-	-	-	-	-
System thermal efficiency [%]	0.68	2.63	3.34	3.55	3.79	3.82
Net thermal power output [kW]	1.57	1.66	1.06	1.06	0.99	0.99
Pure CO <sub>2</sub> refrigerant mass flow rate through the turbine/expander[kg/s]	0.53	0.15	0.52	0.52	0.58	0.58
POE32 mass flow rate through the expander [kg/s]	-	0.85	0.13	0.06	0.01	0

Figure 6-11 shows the effect of the absorber/cooler pressure on overall thermal efficiency results. The dashed green lines illustrate

the reduction in efficiency as the CO<sub>2</sub>/POE32 ratio increases in comparison to the CO<sub>2</sub> power system shown in red. From 45 bar up to 51 bar, the flood expansion system tended to perform better at different ratios than the CO<sub>2</sub> system. The lowest performance overall was observed for the CO<sub>2</sub>/POE32 absorption system, shown in blue.

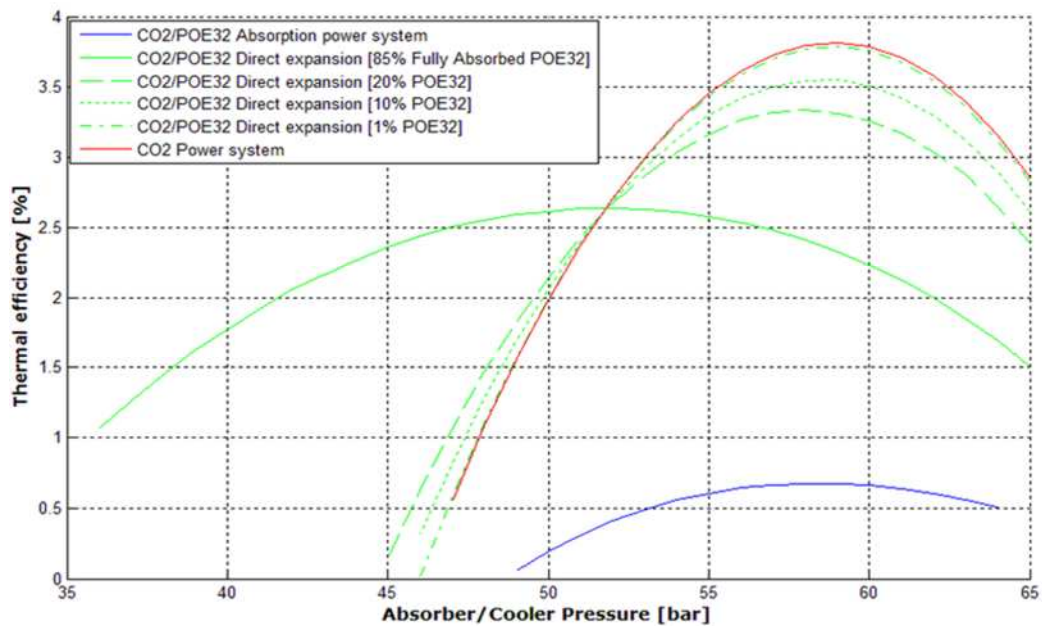


**Figure 6-11: Thermal efficiency comparison between the CO<sub>2</sub>/POE32 absorption, flood expansion, and CO<sub>2</sub> systems at base case conditions.**

Figure 6-12 shows the net thermal power output at variable absorber/cooler operating pressure, as shown, for all cases where the behaviour is proportional, with a fairly linear dependency in the CO<sub>2</sub> power system and the flood expansion system for 1% to 20% CO<sub>2</sub>/POE32 mass flow ratios. It can be seen that the maximum CO<sub>2</sub>/POE32 mass flow ratio case achieved maximum power output, with a significant difference from other flood expansion cases. In addition, regardless of the much lower thermal efficiency seen in the CO<sub>2</sub>/POE32 absorption power system, the system tended to yield the second highest net thermal power output. The CO<sub>2</sub> power system showed the lowest net thermal power output overall. However, the result indicates that as the CO<sub>2</sub>/POE32 liquid mixture flow ratio increased, the net thermal power output also increased, indicated by the green dashed lines. This behaviour confirms the need for a separate loop to contain the lubricant oil, as suggested in

references [254, 255, 257], in order to take advantage of the higher thermal efficiency of the CO<sub>2</sub> system and the flood expansion system's enhanced power output.

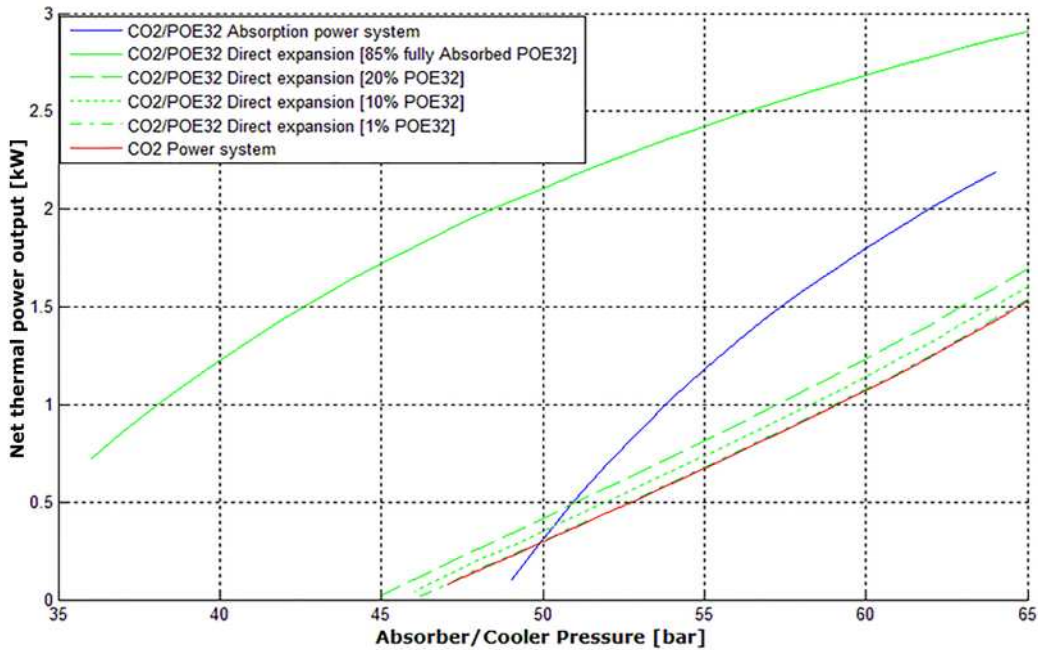


**Figure 6-12: Net thermal power output comparison between CO<sub>2</sub>/POE32 absorption, flood expansion and CO<sub>2</sub> systems at base case conditions.**

### 6.5.3.5 CO<sub>2</sub>/POE32 Flood Expansion Power Generation

#### System Theoretical Analysis Conclusions

Flood expansion by means of CO<sub>2</sub>/POE32 was investigated to examine the advantages of the high heat capacity of POE32 oil to achieve near isothermal expansion, thus improving system performance. In addition, comparative analysis was carried out to compare the CO<sub>2</sub>/POE32 absorption power generation system, the CO<sub>2</sub>/POE32 flood expansion power generation system and a CO<sub>2</sub> power system under base case simulation conditions. The thermodynamic model used has been explained and the results show that CO<sub>2</sub> has the best thermal efficiency. This efficiency will decrease as the CO<sub>2</sub>/POE32 liquid ratio increases. The opposite behaviour was observed with regard to the net thermal power output which increased alongside the rising flow ratio percentage of the CO<sub>2</sub>/POE32.

The reviewed literature points out the advantages and the net thermal power output improvement which can be obtained by adapting the flood expansion concept. Theoretically speaking, such a system showed improvement, in comparison to CO<sub>2</sub>/acetone absorption power generation systems and to regenerative CO<sub>2</sub> and ORCs systems. However, the possibility of implementing such a system in practice still seems remote for several reasons. Besides the fact that research is still underway in this field, the requirements of the flood expansion system present drawbacks in reality. Alongside the total immiscibility of the refrigerant, determination of the optimum oil flow rate ratio is essential. This ratio is subjective from one refrigerant/oil pair to another and the only way to define this ratio is by trial and error. However, the requirement for a separate loop to contain the oil, also presents more challenges related to construction and customisation. In reality, there will be an amount of oil carried out with the refrigerant which may cause durability issues or lead to the need for frequent servicing [253]. Moreover, the additional pumping energy input requirement introduced into the system with the oil loop may be at the expense of the improvement and system efficiency achieved. The expansion device may also present practical difficulties, where the experimental studies reviewed indicate poor performance observed at lower operation speeds, excessive oil flow rate ratios, and internal leakage issues. Safety concerns related to high operating pressures in CO<sub>2</sub> applications arise in conjunction with the customisation and modification challenges already discussed. This also leads to questions being posed about the capabilities of the small-scale scroll and screw expanders which are available nowadays, to handle the high CO<sub>2</sub> pressure. In fact, the studies reviewed which relate to two-phase and CO<sub>2</sub> expansion with screw expanders [263-266], reported a maximum screw expander capability of 85 bar. With some internal modification, the highest achievable pressure would be around 100 bar in such a case. However, there is no such product available commercially despite the fact that an investigation of two-phase expansion with twin

screw expanders has been on-going since the beginning of the 1980s.

From the literature review and the theoretical analysis results, it becomes obvious that regardless of the lower isentropic efficiency of CO<sub>2</sub> turbines, a CO<sub>2</sub> power generation system will have good thermal efficiency and reasonable net thermal power output if the optimum operating conditions are established. In comparison to both the CO<sub>2</sub>/lubricant absorption power generation and the CO<sub>2</sub>/POE32 flood expansion systems, the CO<sub>2</sub> power generation system has a relatively simple configuration, suitable for industrial low-grade waste heat recovery and attractive for commercialization if the system components are available in the market and can stand the high CO<sub>2</sub> operating pressures. Therefore, the potential of CO<sub>2</sub> SRC power generation for waste heat recovery is appealing for further investigation.

## 6.6 CO<sub>2</sub> SRC Power generation system

From a thermodynamic point of view, the greater the temperature differences between the heat sink and the source, the greater the system efficiency. Therefore, CO<sub>2</sub> TRC achieves better efficiency than CO<sub>2</sub> SRC, where low temperature heat sinks are available. SRC performance, on the other hand, is influenced by both CO<sub>2</sub> cooler and heater operating conditions, due to its location above the critical point in the T-S diagram [267].

In this section, a novel concept is adopted to take advantage of both SRC and TRC operating concepts, by utilising two-phase pumping operations to avoid the restriction of condensation in the TRC concept and to allow operation in full SRC mode when desired. The proposed model programme for the system has a similar but simpler flowchart to the CO<sub>2</sub>/POE32 flood expansion system included in Appendix C.2. In other words, it has the same structure, but assuming that the CO<sub>2</sub>/POE32 ratio is zero; therefore it will not be repeated.

### 6.6.1 Cycle Description

In this system, the CO<sub>2</sub> refrigerant does not condensate. Instead, it is only cooled to reject heat to the sink. Moreover, the cycle may operate with sub-critical CO<sub>2</sub> gas or super-critical CO<sub>2</sub> fluid, depending on the heater's operating conditions. Furthermore, the CO<sub>2</sub> introduced into the cooler may either be in a gas or liquid phase, depending on the cooler operating conditions. Figure 6-13 shows a schematic of the CO<sub>2</sub> SRC power generation system, where hot, high pressure CO<sub>2</sub> gas or super-critical fluid from the generator outlet at point 1 expands through the turbine to produce the system power output. After expansion at point 2, lower pressure CO<sub>2</sub> enters the recuperator heat exchanger to lose its heat to the high pressure CO<sub>2</sub> counter stream, before exiting at point 3. The cooled lower pressure CO<sub>2</sub> will then enter the cooler, where it will be cooled further before it exists as liquid or cooled CO<sub>2</sub> gas at point 4. Liquid or gas CO<sub>2</sub> is then pumped or compressed to a higher pressure by the two-phase compression device at point 5 and then preheated in the recuperator heat exchanger before exiting at point 6. The CO<sub>2</sub> is finally directed to the CO<sub>2</sub> heater to be further heated, before it expands through the expander and completes the cycle.

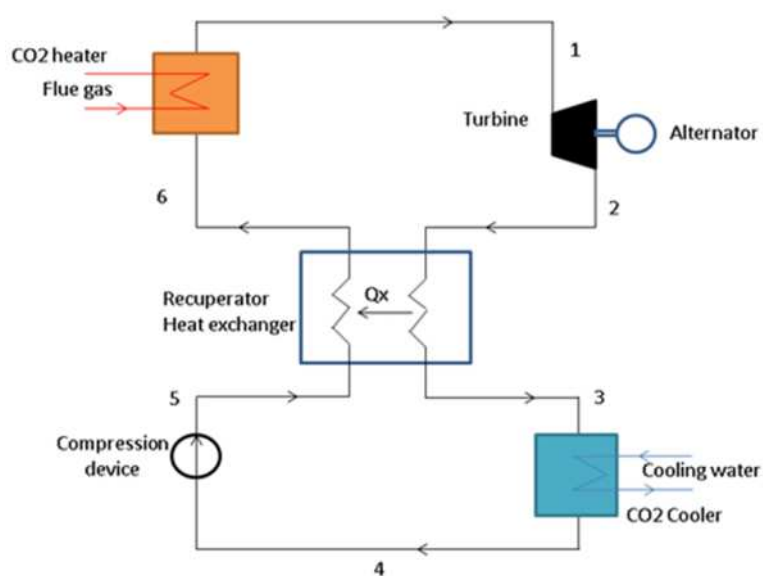


**Figure 6-13: Schematic of the CO<sub>2</sub> SRC power generation system.**

## 6.6.2 Heat and Mass Balance of System Components

Unlike previously simulated systems, the CO<sub>2</sub> SRC power generation system employs a pure refrigerant in a single flow. Therefore, the system governing equations are fairly simple.

### 6.6.2.1 Expander

The turbine's isentropic efficiency is similar to equations (6.22) used for the CO<sub>2</sub>/lubricant absorption power generation system. The CO<sub>2</sub> mass and energy balance equations are similar to equations (6.36) and (6.37), used for the CO<sub>2</sub> phase in the CO<sub>2</sub>/POE32 flood expansion power generation system.

### 6.6.2.2 Compression Device

As stated previously, the CO<sub>2</sub> at the compression device inlet in the current system will either be a super-heated CO<sub>2</sub> gas when the cooler operates in the sub-critical region, or a fully-developed liquid at high cooler pressure above CO<sub>2</sub> critical pressure. Like the turbine, the isentropic efficiency of the compression device is similar to equation (6.25) for the CO<sub>2</sub>/lubricant power generation system, while the mass and energy balance equations are similar to equations (6.47) and (6.48) for the CO<sub>2</sub> phase in the flood expansion system.

### 6.6.2.3 The Recuperator Heat Exchanger

Besides recovering heat within the system and minimising heat input into the system, the recuperator presents another advantage for the CO<sub>2</sub> SRC power generation system from the point of view of safety. It will lower the optimum turbine inlet pressure at which maximum thermal efficiency is obtained. With respect to the significant changes in CO<sub>2</sub> specific heat as illustrated in Figure 6-10, section 6.5.3.3.5, for the recuperator in the CO<sub>2</sub>/POE32 flood expansion system, a similar approach is used for balancing the recuperator in the current system. Therefore, the maximum heat

exchange  $Q_{max}$  will be the lower value of the quantities determined from equations (6.55) and (6.56).

$$\dot{Q}_{max1} = \dot{m}_r(h_2 - h_3) \text{ Assuming } T_3 = T_5 \quad (6.74)$$

$$\dot{Q}_{max2} = \dot{m}_r(h_6 - h_5) \text{ Assuming } T_6 = T_2 \quad (6.75)$$

And the recuperator heat exchanger's effectiveness is expressed as:

$$\varepsilon_{Hex} = \frac{\dot{m}_r(h_2 - h_3)}{\dot{Q}_{max}} = \frac{\dot{m}_r(h_6 - h_5)}{\dot{Q}_{max}} \quad (6.76)$$

#### 6.6.2.4 The CO<sub>2</sub> Cooler Heat Exchanger

For the CO<sub>2</sub> cooler heat exchanger, where the heat is rejected from the system to the sink and the CO<sub>2</sub> gas or liquid is cooled, the power rejected from the system becomes:

$$\dot{Q}_C = \dot{m}_r(h_3 - h_4) \quad (6.77)$$

#### 6.6.2.5 The CO<sub>2</sub> Heater Heat Exchanger

Likewise for the CO<sub>2</sub> heater heat exchanger, where the heat is added to the system by the hot flue gas source and the supercritical CO<sub>2</sub> liquid is heated, the power added to the system becomes:

$$\dot{Q}_H = \dot{m}_r(h_1 - h_6) \quad (6.78)$$

### 6.6.3 CO<sub>2</sub> SRC Power Generation System

#### Thermodynamic Model Validation

The proposed thermodynamic model was validated and compared to the thermodynamic model put forward by Cayer et al. [107] as a regenerative CO<sub>2</sub> TRC power generation system. For the purpose of validation, similar input conditions were applied. The results were found to be in perfect agreement. Table 6.8 shows a comparison for the optimum operating conditions, while Figure 6-14 shows the simulated results in comparison to those obtained by Cayer et.al.[107].

**Table 6.8: CO<sub>2</sub> SRC power generation system result validation with Cayer et al. [107].**

Operation conditions	Current Research	Cayer et al. [107]
CO <sub>2</sub> heater outlet temperature [K]	368.15	
CO <sub>2</sub> condenser outlet Temperature [K]	288.15	
CO <sub>2</sub> heater pressure range [bar]	90-150	
Maximum thermal efficiency CO <sub>2</sub> heater operating pressure [bar]	113	113
Maximum thermal efficiency [%]	8.61	8.6
Maximum specific net thermal power output CO <sub>2</sub> heater pressure [bar]	115	115
Maximum specific net thermal power output [kJ/kg]	18.8	18.8

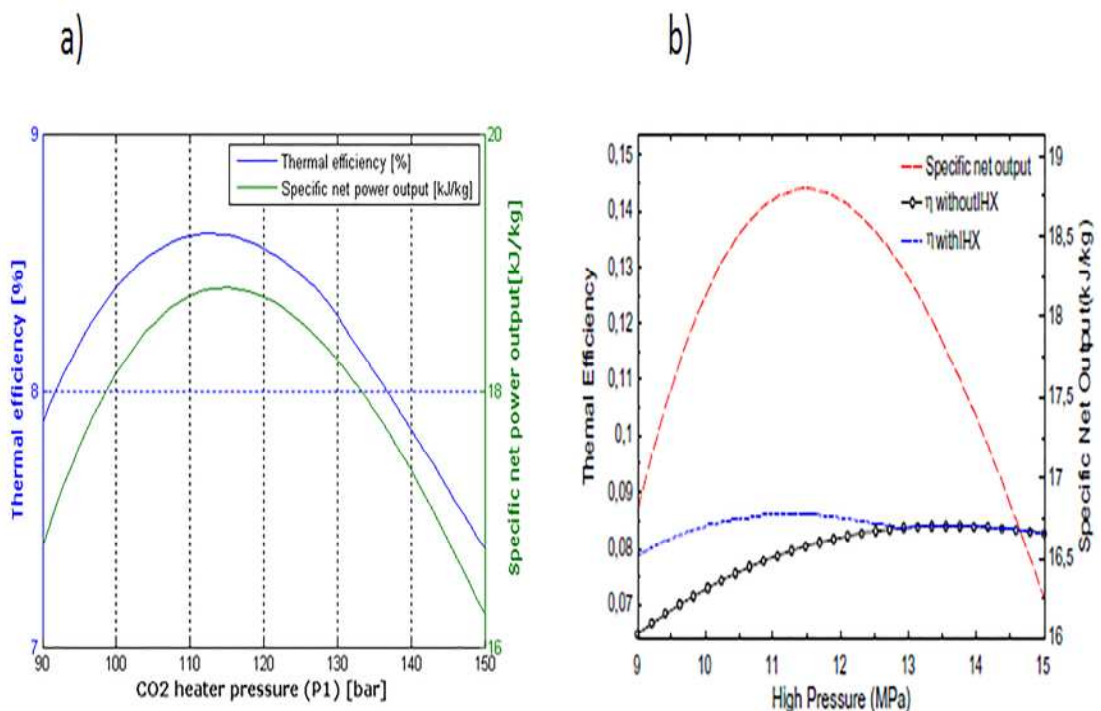


**Figure 6-14: CO<sub>2</sub> SRC power generation system thermodynamic model validation- a) current research results and b) Cayer et al. [107].**

#### 6.6.4 Simulation Results and Analysis

A parametric analysis was carried out in order to determine the optimum working conditions for the CO<sub>2</sub> SRC power generation system, and also to investigate the effect of different operating parameters on the system's thermal efficiency and net thermal power output. To determine the optimum operating pressure for the CO<sub>2</sub> cooler, simulation of the base case as a function of the CO<sub>2</sub>

cooler pressure was carried out, as in previously studied systems. In addition, the effect of CO<sub>2</sub> heater pressure on system performance was investigated in simulation cases 2, 3, and 4. The turbine, compression device and recuperator heat exchanger efficiencies were also very sensitive and have a vital influence on system performance; therefore their effect was also to be investigated.

#### 6.6.4.1 The Effect of CO<sub>2</sub> Cooler Pressure on the system's performance

Table 6.9 lists the inputs used for four simulated cases.

**Table 6.9: CO<sub>2</sub> SRC power generation system simulation cases inputs.**

Simulation	T <sub>H</sub> [K]	P <sub>H</sub> [bar]	T <sub>C</sub> [K]
Case 1 (base case)	393.15	70	303.15
Case 2	393.15	80	303.15
Case 3	393.15	90	303.15
Case 4	393.15	100	303.15

The first simulated case represents the base case simulation conditions, where the system operates exclusively in the sub-critical region, with a turbine inlet pressure directly below the critical pressure of CO<sub>2</sub>. In addition, the CO<sub>2</sub> working fluid is in super-heated gas form at every state point around the cycle shown in the schematic of the system at Figure 6-13. In the second simulation case, the CO<sub>2</sub> on the low pressure side of the system will always be in the sub-critical region in a super-heated gas form and in a super-critical fluid state in the high pressure side of the system, i.e. the compression device exit and turbine inlet. In the third and the fourth simulation cases, the CO<sub>2</sub> will be in a super-critical state in the high pressure side of the system, similar to the third simulation case. In the low pressure side of system in these two cases, the CO<sub>2</sub> working fluid enters the cooler in a super-critical state and converts by cooling to super-heated gas. This happens if the cooler is operating below the critical pressure. If the operating pressure is above the critical pressure and the operating temperature is below

the critical temperature of CO<sub>2</sub>, the working fluid will convert by cooling from its super-critical state to a fully developed liquid when it is cooled. For these reasons, two optimum points are identified for the latter two cases: the cooler operating below critical pressure and above critical pressure of CO<sub>2</sub>. Table 6.10 shows the simulation results for each case alongside the optimum CO<sub>2</sub> cooler operating pressure under which maximum thermal efficiency is achieved.

**Table 6.10: CO<sub>2</sub> SRC power generation system simulation results.**

	Case 1	Case 2	Case 3		Case 4	
Operating region	Sub-critical	Sub-critical	Sub-critical	Super-critical	Sub-critical	Super-critical
Optimum CO <sub>2</sub> cooler pressure [bar]	59	65	71	79	72	82
CO <sub>2</sub> heater power [kW]	25.85	27.72	35.20	55.41	33.01	40.21
CO <sub>2</sub> cooler power [kW]	24.87	26.39	33.18	51.80	30.79	36.70
Recuperator exchanger power [kW]	39.12	32.38	30.42	145.41	18.29	93.71
Compression device power [kW]	4.01	3.67	2.98	1.39	2.79	1.49
System thermal efficiency [%]	3.82	4.78	5.74	6.52	6.69	8.71
Net thermal power output [kW]	0.99	1.33	2.02	3.61	2.21	3.50
CO <sub>2</sub> mass flow rate [kg/s]	0.64	0.49	0.44	0.795	0.33	0.54

Figure 6-15 shows the optimum operating point of the base case on the CO<sub>2</sub> temperature-entropy (T-S) diagram. As shown, CO<sub>2</sub> cooler outlet temperature at state point 4 is just below the critical temperature of CO<sub>2</sub>. Figure 6-16 shows the CO<sub>2</sub> cycle operation on the CO<sub>2</sub> pressure-enthalpy (P-H) diagram. As can be seen, the cycle operates right below the critical pressure of CO<sub>2</sub> in the super-heated gas region.

Chapter 6: Theoretical Analysis of Small-Scale Power Generation Systems for Low-Grade Waste Heat Recovery

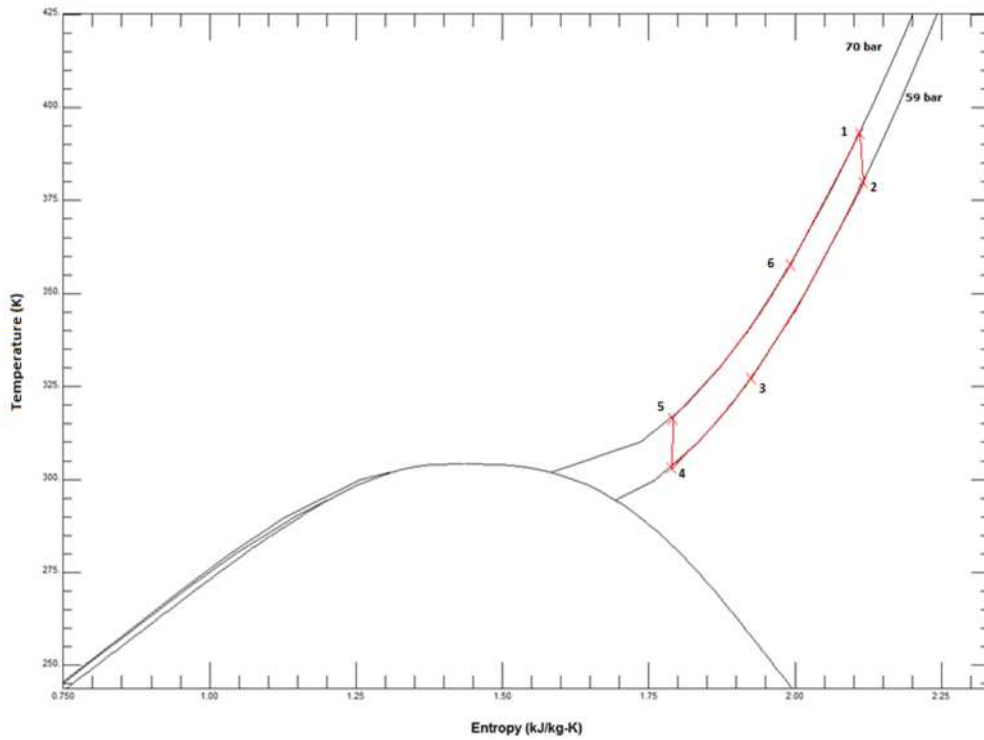


Figure 6-15: CO2 SRC power generation system-T-S diagram of the base case optimum operating condition.

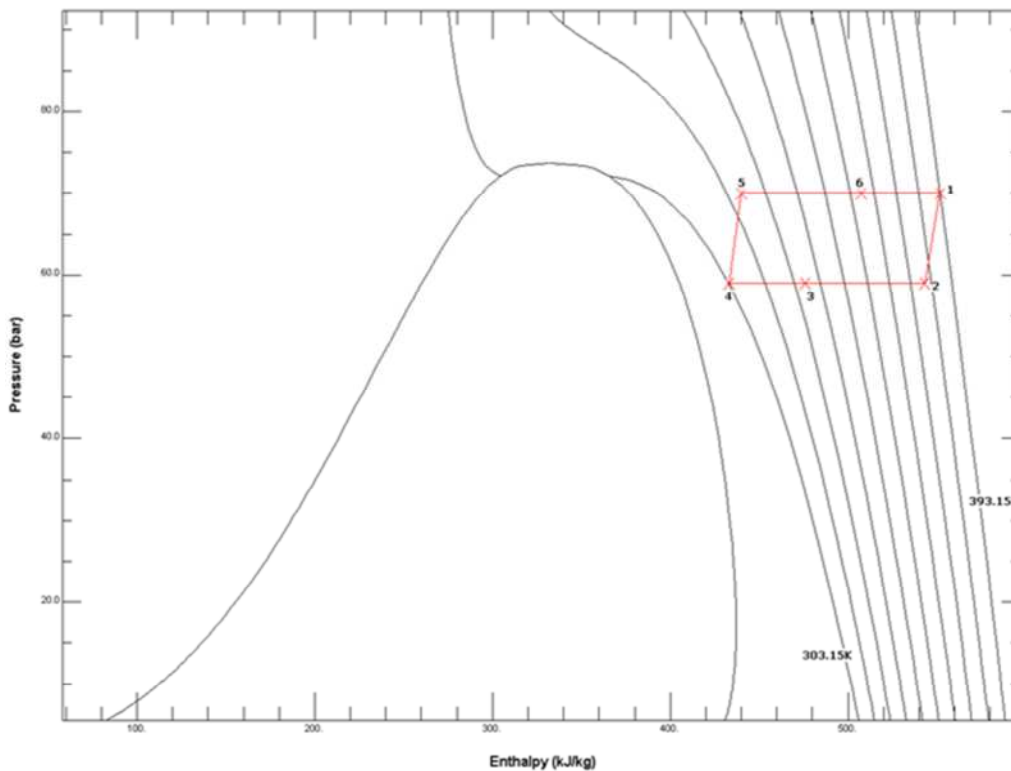
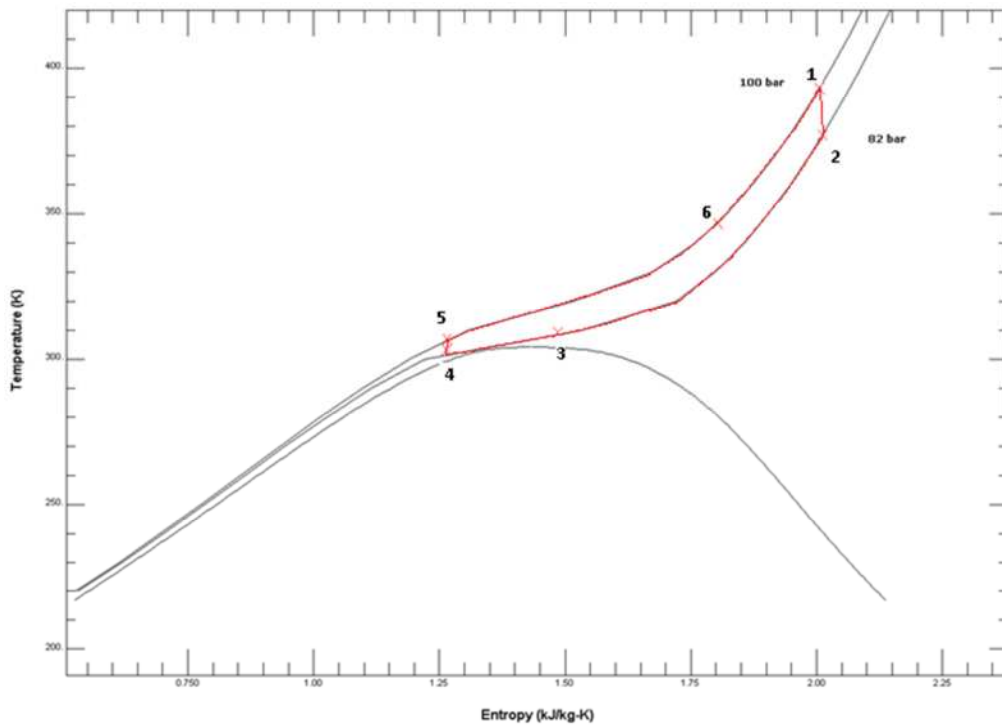
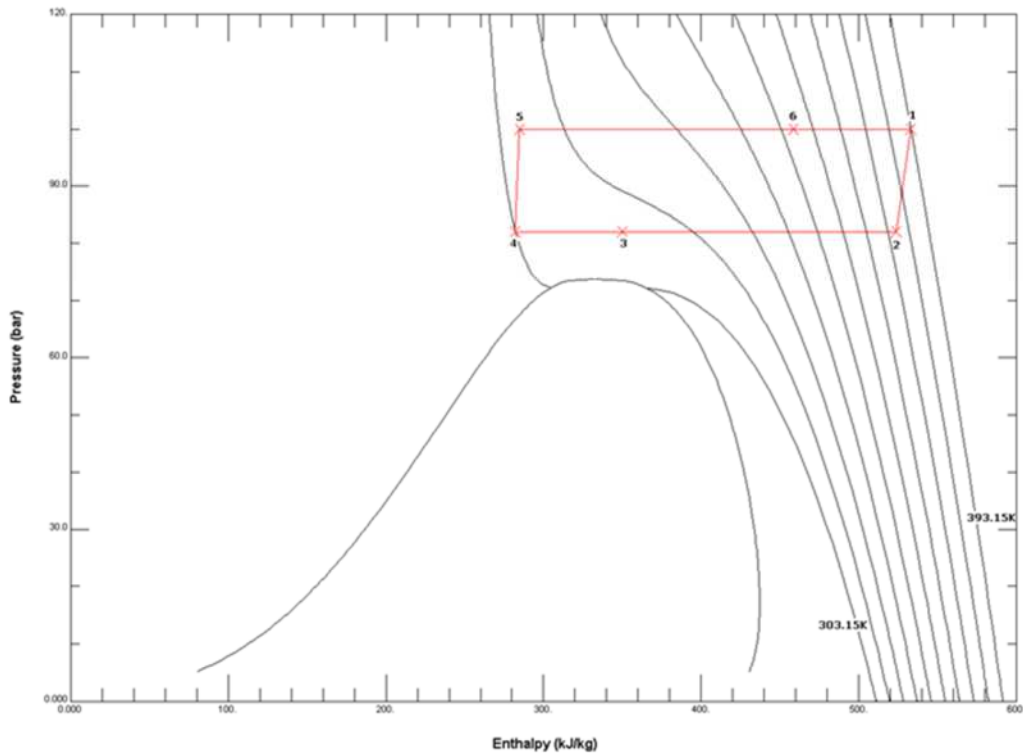


Figure 6-16: CO2 SRC power generation system-P-H diagram of the base case optimum operating condition.

Another example is taken to illustrate the difference when the cycle is operating in the super-critical region. Figure 6-17 shows the cycle operation at the best point of fourth simulation case in the super-critical region, on the CO<sub>2</sub> T-S diagram. As can be seen, the cycle operates exclusively in the super-critical region, apart from the CO<sub>2</sub> cooler exit at state point 4, which is just below the critical temperature of CO<sub>2</sub> in the liquid region. Figure 6-18 shows the cycle operation on the CO<sub>2</sub> P-H diagram. As shown, the cycle operates exclusively above the critical pressure of CO<sub>2</sub>.



**Figure 6-17: CO<sub>2</sub> SRC power generation system-T-S diagram of the fourth simulation case's optimum operating condition in the super-critical region.**



**Figure 6-18: CO<sub>2</sub> SRC power generation system-P-H diagram of the fourth simulation case's optimum operating condition in the super-critical region.**

In general, the results listed in Table 6.10 shows that the optimum CO<sub>2</sub> cooler pressure yielding the best thermal efficiency will increase alongside increasing CO<sub>2</sub> heater pressure. Similar behaviour can be seen for both thermal efficiency and net thermal power output. Compression device power consumption is seen to be very high in the first simulation case and then tends to reduce gradually, as both cooler and heater pressure increase. This confirms what is indicated in the reviewed literature as regards the greater tendency of CO<sub>2</sub> to consume more pumping power than other refrigerants [114].

The energy requirements for the CO<sub>2</sub> heater and cooler tend to increase gradually as the heater pressure increases. This behaviour changes at both sub-critical and super-critical optimum pressure in the fourth case. The energy requirements for the recuperator heat exchanger are in completely the opposite direction and decrease gradually as the heater pressure increases for both sub-critical and super-critical pressures.

It is important to note that in all simulated cases, the optimum operating pressure for achieving the best net thermal power output was not the same pressure that achieved the best thermal efficiency. However, these pressures are very close to those identified for best thermal efficiency. Table 6.11 shows the highest net thermal power output attainable for each simulated case alongside their optimum operating pressures.

**Table 6.11: CO<sub>2</sub> SRC power generation system- Optimum cooler pressures for net thermal power output.**

CO <sub>2</sub> heater Pressure [bar]	Case 1	Case 2	Case 3	Case 4
Operating region	Sub-critical	Sub-critical	Super-critical	Sub-critical
Optimum CO <sub>2</sub> cooler pressure [bar]	60	70	80	87
Net thermal power output [kW]	1.70	1.98	3.16	3.51

Figure 6-19 shows a comparison of the simulation results for all cases. In Figure 6-19 (a), the effect of the CO<sub>2</sub> cooler pressure on the system's thermal efficiency is illustrated for variable CO<sub>2</sub> heater pressures. As shown, the figure demonstrates similar trends for all cases in the sub-critical region where efficiency tends to increase gradually as cooler pressure increases until it reaches its maximum level and then reduces again. The red broken line divides the graph into sub-critical and super-critical CO<sub>2</sub> cooler pressure. As shown, only the latter two simulated cases operate in the super-critical region of the graph. When CO<sub>2</sub> approaches super-critical pressure after maximum sub-critical efficiency is achieved, the enthalpies at the exit of the compression device and the exit of the recuperator heat exchanger on the high pressure side suddenly drop, as phase transformation takes place. These enthalpies increase again steadily as the cycle enters the super-critical pressure region, where thermal efficiency reaches its maximum point. In Figure 6-19 (b), the net thermal power output of the first two simulated cases shows

linear and proportional dependency on CO<sub>2</sub> cooler pressure. This behaviour changes in the latter two cases for the near-critical and super-critical cooler pressures. As shown, the gradual increase changes to fractional increase, which could be regarded as constant net thermal power output. Moreover, the results show that operating at 90 bar CO<sub>2</sub> heater pressure achieves the highest net thermal power output.

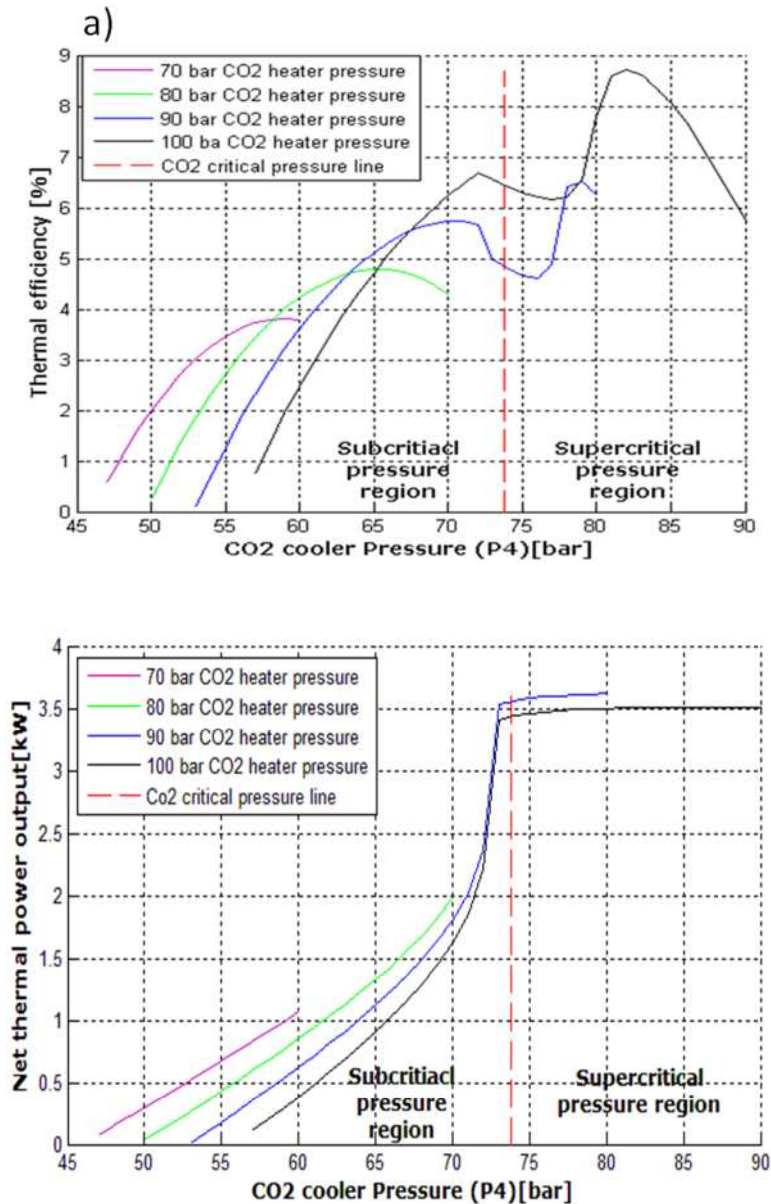


**Figure 6-19: Simulation results for the CO<sub>2</sub> SRC power generation system performance- a) Overall thermal efficiency, and b) Net thermal power output.**

Beside the investigated cases, further parametric investigation was conducted on the system. The effect of cooler temperatures is

thermodynamically obvious: the lower the temperature, the better the overall performance. This effect was illustrated in CO<sub>2</sub>/lubricant absorption power generation system simulation and analysis in section 6.4.5.2 and applicable for all thermal power generation systems. However it will not be investigated for the current system, due to the difficulty of achieving a cooling temperature lower than 30°C in practice. Instead, the effect of the CO<sub>2</sub> heater outlet temperature will be investigated, since this is more likely to be practically achievable.

#### **6.6.4.2 The Effect of CO<sub>2</sub> Heater Outlet Temperature on System Performance**

In this section, the effect of CO<sub>2</sub> heater temperature was investigated by keeping system parameters constant at the base case simulation input and optimum CO<sub>2</sub> cooler pressure while varying the heater outlet temperature from 90°C to 200°C. Figure 6-20 shows a very strong influence of the CO<sub>2</sub> heater outlet temperature on both the thermal efficiency and the net thermal power output. This strong and proportional dependency yields 1.74% and 0.36 kW for the thermal efficiency and the net thermal power output respectively, when heater outlet temperature is 90°C. When heater outlet temperature reaches its maximum at 200°C, the net thermal power output increases up to 1.94 kW while the thermal efficiency reaches 6.73%.

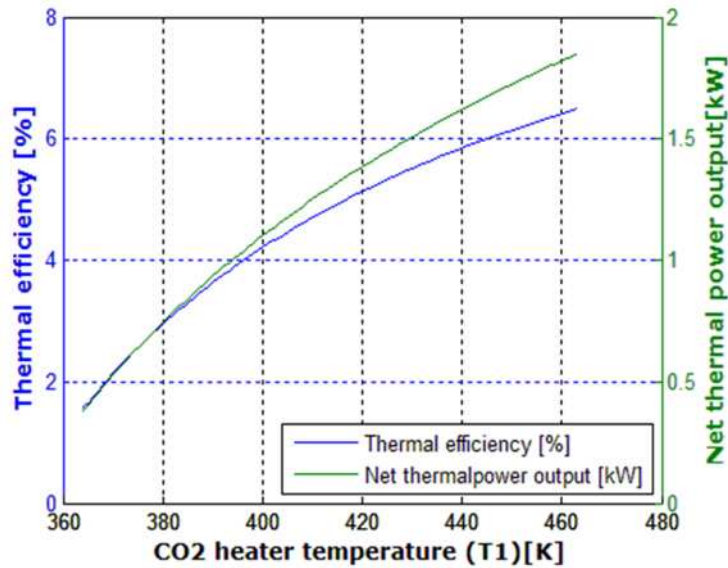


**Figure 6-20: CO2 SRC power generation system thermal efficiency and net thermal power output as a function of the CO2 heater outlet temperature.**

#### 6.6.4.3 The Effect of the Turbine's Isentropic Efficiency

The effect of turbine's isentropic efficiency was investigated by keeping the operation parameters constant at base case conditions and varying the isentropic efficiency of the turbine. Figure 6-21 shows that the system is highly sensitive to turbine isentropic efficiency. The minimum turbine isentropic efficiency acceptable for the selected operating conditions is 70%, which seems to be high for a practical system. As shown, both thermal efficiency and net thermal power output have linear and proportional dependency on the turbine's isentropic efficiency. The minimum thermal efficiency and net thermal power output are 1.43% and 0.41 kW respectively, when turbine efficiency is 70%. The maximum is obviously achieved at isentropic expansion when turbine efficiency is 100%. The thermal efficiency and net thermal power output are 8.33% and 1.79 kW respectively.

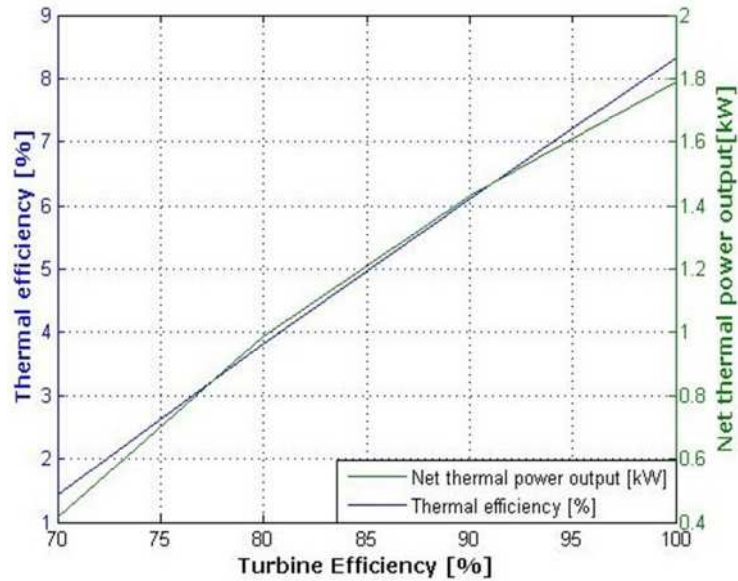


**Figure 6-21: CO2 SRC power generation system thermal efficiency and net thermal power output as functions of the turbine's isentropic efficiency.**

#### 6.6.4.4 The Effect of the Compression Device

##### Isentropic Efficiency

Similar to the turbine efficiency, the effect of the compression device efficiency was investigated by keeping the operating conditions constant and varying the compression device efficiency. The results shown in Figure 6-22 indicate that the minimum acceptable compression device efficiency for the selected operating conditions is 80%, which seems to be very high. However, system performance has linear and proportional dependency, similar to that which is observed for turbine efficiency, but with less effect. The minimum observed thermal efficiency and net thermal power output were 1.89% and 0.49 kW respectively when compression device efficiency was 80%. The maximum results when the compression device efficiency was 100% were 1.39% and 5.34% for thermal efficiency and net thermal power output respectively.

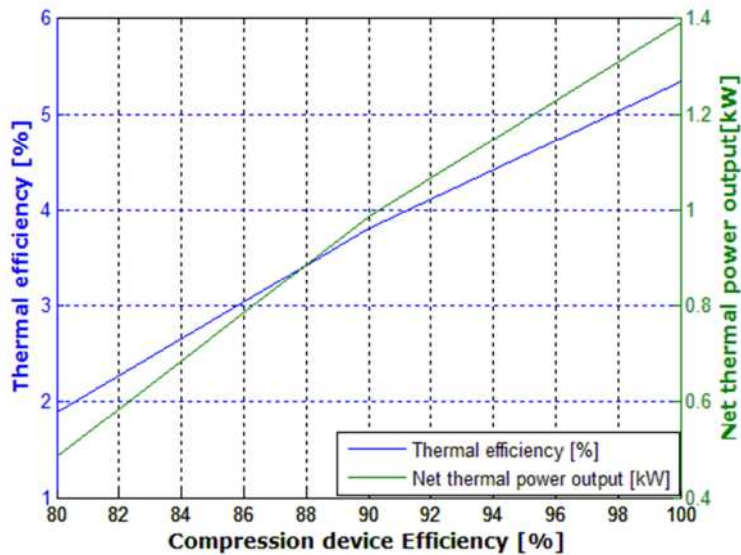


**Figure 6-22: CO<sub>2</sub> SRC power generation system thermal efficiency and net thermal power output as functions of the compression device isentropic efficiency.**

#### 6.6.4.5 The Effect of the Recuperator Heat Exchanger Effectiveness

The recuperator effectiveness was varied from 50% to 100%, while the operating conditions were held constant. Almost all the literature reviewed indicated that the recuperator heat exchanger would marginally increase the CO<sub>2</sub> system's thermal efficiency, without having any effect on the net thermal power output. This behaviour is clearly seen in Figure 6-23. The results show no effect on the net thermal power output at all, while the thermal efficiency indicated a proportional dependency on the recuperator effectiveness. The minimum thermal efficiency was 2.44% when effectiveness was 50% and the maximum thermal efficiency was 6.14% when effectiveness was 100%.

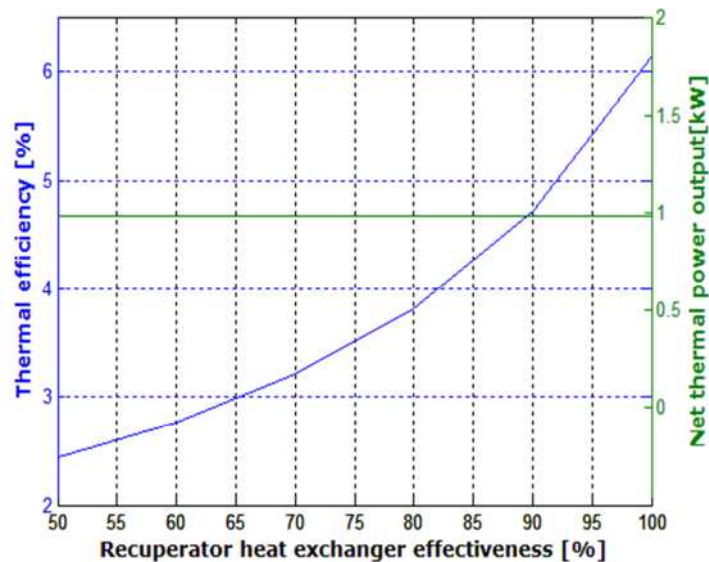


**Figure 6-23: CO<sub>2</sub> SRC power generation system thermal efficiency and net thermal power output as functions of the recuperator heat exchanger effectiveness.**

### 6.6.5 CO<sub>2</sub> SRC Power Generation Theoretical Analysis

#### Conclusions

Four simulation cases at different CO<sub>2</sub> heater pressures were carried out in order to investigate the effect of CO<sub>2</sub> cooler pressure on the overall performance of the CO<sub>2</sub> SRC power generation system. The first simulation case took place exclusively in the CO<sub>2</sub> sub-critical region. In the second case, the high pressure side of the system, i.e. at the compression device exit and at the turbine inlet, were in the super-critical region, while the low pressure side of the system was in the sub-critical region. In the third and the fourth cases, the high pressure side of the system consistently operated in the super-critical region. On the low pressure side, CO<sub>2</sub> entered the cooler as a super-critical fluid to be converted either to gas or liquid CO<sub>2</sub>.

Generally it was observed that thermal efficiency increases as both the CO<sub>2</sub> heater and cooler pressures increase. For the latter simulated cases, there are two optimum operating pressure levels, one in the sub-critical region and the other, which is the highest, is located in the super-critical region.

Parametric investigation was carried out to study the effect of different working parameters on system performance. In general, the system showed a high degree of sensitivity to all investigated parameters. However, system performance showed itself to be heavily dependent on the CO<sub>2</sub> heater exit temperature and the turbine's isentropic efficiency. A similar observation was also made of the compression device and the recuperator heat exchanger, but to a lesser extent.

The minimum acceptable isentropic efficiency for the turbine and the compression device were respectively, 70% and 80%. These isentropic efficiencies seem to be very difficult to achieve in practice. For this situation, different working conditions could be investigated in order to examine their potential for acceptance of lower turbine and compression device efficiencies. However, this is a compromise situation that could be at the expense of the system's thermal efficiency and net thermal power output. If this were the case, the CO<sub>2</sub> SRC power generation performance cannot compete with the well-established ORC technology which has a wide variety of options for highly efficient components and relatively low operating pressures compared to the CO<sub>2</sub> SRC power generation system. To conclude, the feasibility of the CO<sub>2</sub> SRC power generation system is essentially depends on the commercial availability, cost, and efficiencies of the system's components as will be discussed in Chapter 9 for the system's components identification and economic analysis.

## **6.7 The ORC System Employing Environmentally Friendly Refrigerants**

In order to select the best working fluid for the ORC system, this section analyses the potential of new environmentally friendly refrigerants, namely, R1234yf, R1234ze(E), R1234ze(Z), and R1233zd(E), in a regenerative 5 kW ORC system, comparing their thermodynamic performance to that of the conventional ORC

working fluids, specifically, R134a, R245fa, and R123. The section also presents a parametric investigation of the ORC system employing the selected working fluid to study the influence of different parameters on the system performance.

### 6.7.1 Cycle Description

A schematic diagram of the ORC system is shown in Figure 6-24. The high pressure super-heated vapour from the evaporator at state point 1 expands through the turbine and produces the system power output. After expansion, the low pressure, substantially super-heated vapour enters the recuperator exchanger at state point 2 and transfers heat to the high pressure liquid counter-stream, before exiting the recuperator heat exchanger at state point 3. The cooled low pressure refrigerant enters the condenser, where it is cooled further and exits as a sub-cooled liquid at state point 4. The sub-cooled liquid refrigerant is then pumped to a higher pressure at state point 5 and enters the recuperator heat exchanger to be pre-heated, before exiting at state point 6. The pre-heated refrigerant is then directed to the evaporator heat exchanger, where it is heated to evaporation point and further heated to be super-heated before exiting state point 1, to be directed towards the expander. The cycle is then complete.

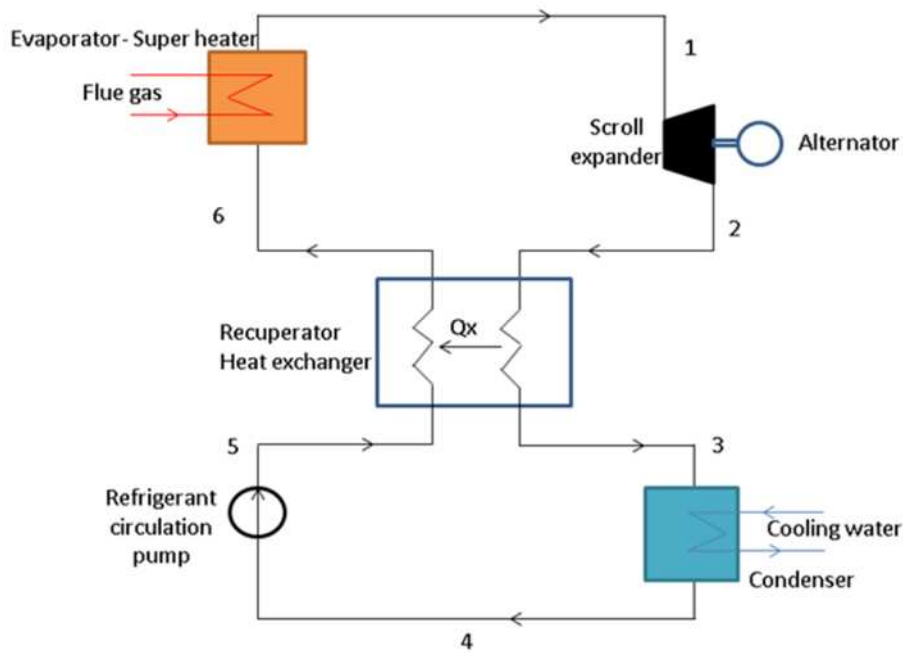


**Figure 6-24: Schematic of the ORC system.**

### 6.7.2 Thermodynamic Model Assumptions and Inputs

The only difference between the current system and the previously investigated systems is that the heat addition and rejection processes in the ORC system take place isothermally where the refrigerant evaporates and is super-heated in the evaporator before being condensed and sub-cooled in the condenser. Therefore the condenser pressure is taken as the corresponding saturation pressure of the selected input condenser's operating temperature. Consequently, an investigation of ORC system performance as a function of evaporator pressure in order to determine the optimum working conditions would seem to be more appropriate than using the condenser pressure as it was implemented in previously investigated systems. In addition, investigating the system as a function of evaporator pressure would require the iteration of the evaporator pressure and, therefore, the evaporation temperature in the simulation programme is taken as the saturation temperature at the iterated pressure, while the super-heated vapour temperature is kept constant at the selected expander inlet temperature. The code of the implemented model is included in Appendix C.5.

### 6.7.3 ORC System Thermodynamic Model Validation

The proposed ORC thermodynamic model was validated and compared to the results presented by Shengjun et al. [96] for a simple ORC employing R134a, R245fa and R123 in geothermal applications. For validation, similar input conditions were used, and the system's thermal efficiency was evaluated as a function of evaporation temperature within the range of 72°C to 84°C. Table 6.12 presents a comparison of the thermal efficiency results obtained from the proposed thermodynamic model, and those reported by Shengjun et al. [96]. As can be seen, the results are in good agreement which is a clear sign of thermodynamic model validity. Figure 6-25 shows a comparison between the current research results and those from Shengjun et al. [96].

**Table 6.12: ORC thermodynamic model results validation with Shengjun et al. [96].**

Evaporator temperature [°C]	Thermal efficiency					
	R123		R134a		R245fa	
	Current research	Shengjun et al. [96]	Current research	Shengjun et al. [96]	Current research	Shengjun et al. [96]
72	9.36	9.30	8.58	8.60	9.20	9.20
76	9.98	9.98	9.05	9.0	9.70	9.58
80	10.63	10.58	9.42	9.45	10.25	10.17
84	11.15	11.08	9.86	9.80	11.75	11.75

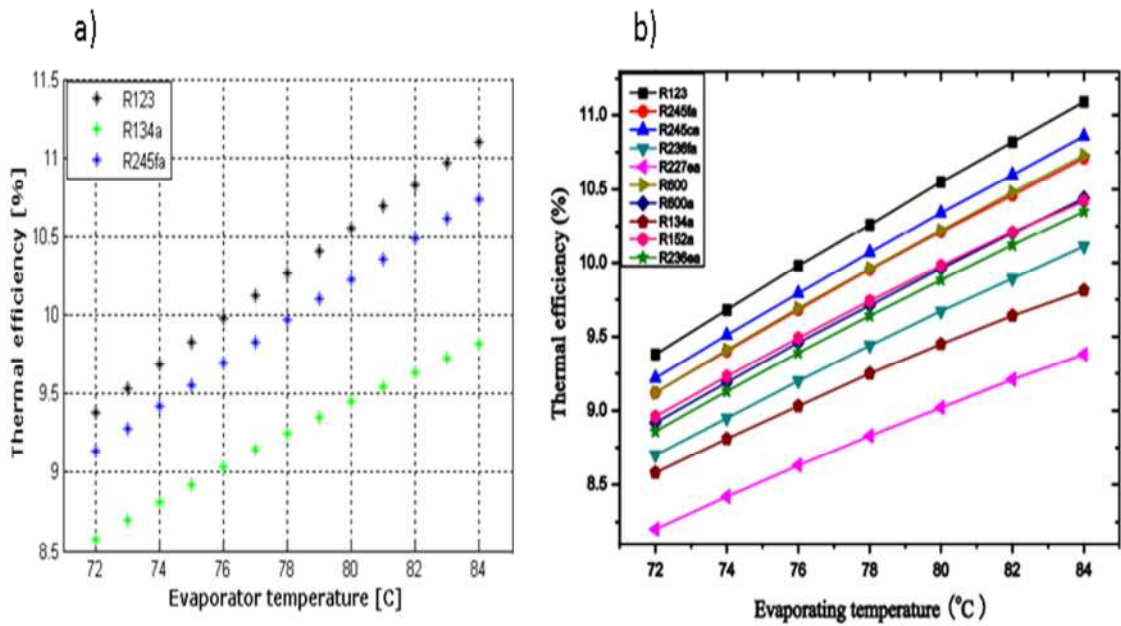


Figure 6-25: ORC thermodynamic model validation, a) Current research results and b) results from Shengjun et al. [96].

## 6.7.4 Simulation Results and Analysis

### 6.7.4.1 Working Fluids Evaluation and Selection

Two cases were simulated at different expander inlet temperatures, in order to compare the new environmentally friendly refrigerants with conventional ORC refrigerants. An average scroll expander isentropic efficiency, reported in the literature at 80%, was used for the ORC system simulations. Table 6.13 shows the input for both simulated cases. Figure 6-26 and Figure 6-27 show the simulation results for thermal efficiency and net thermal power output at 100°C and 120°C respectively.

Table 6.13: ORC simulations input.

Simulation	$T_{\text{expander}}$ [K]	$T_{\text{condenser}}$ [K]
Case 1	373.15	303.15
Case 2	393.15	303.15

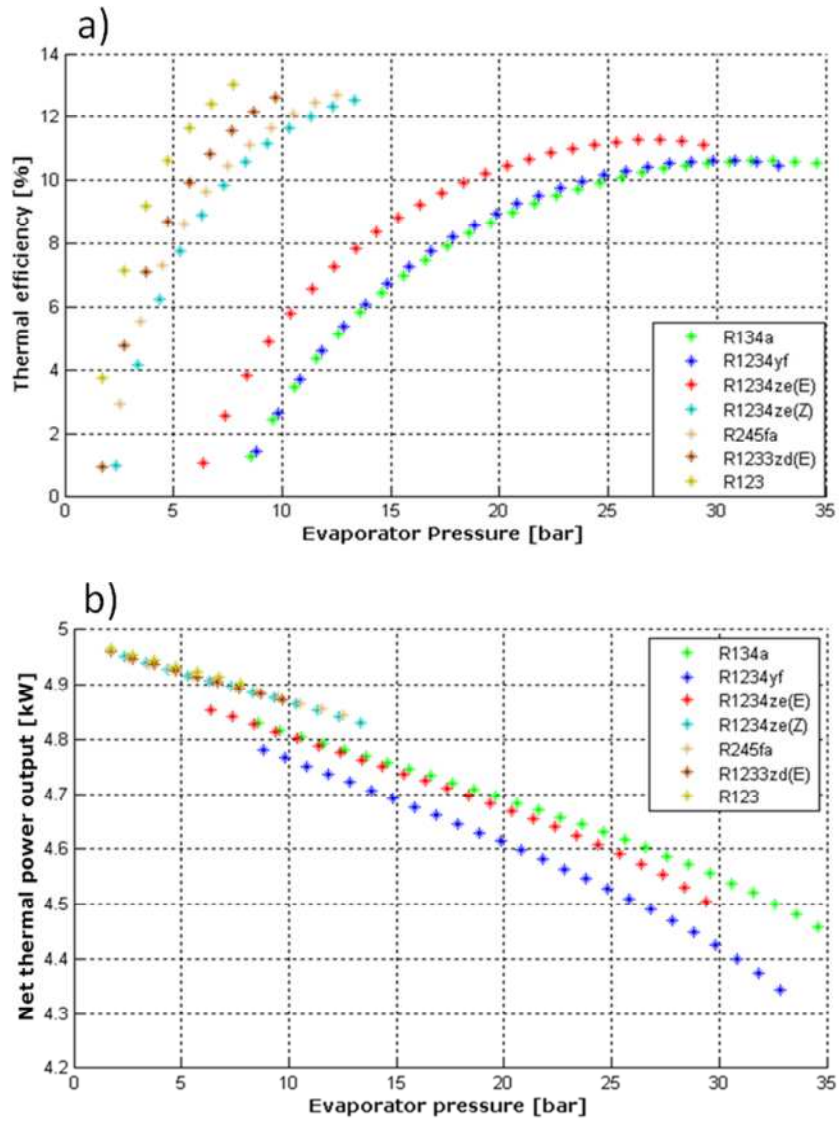
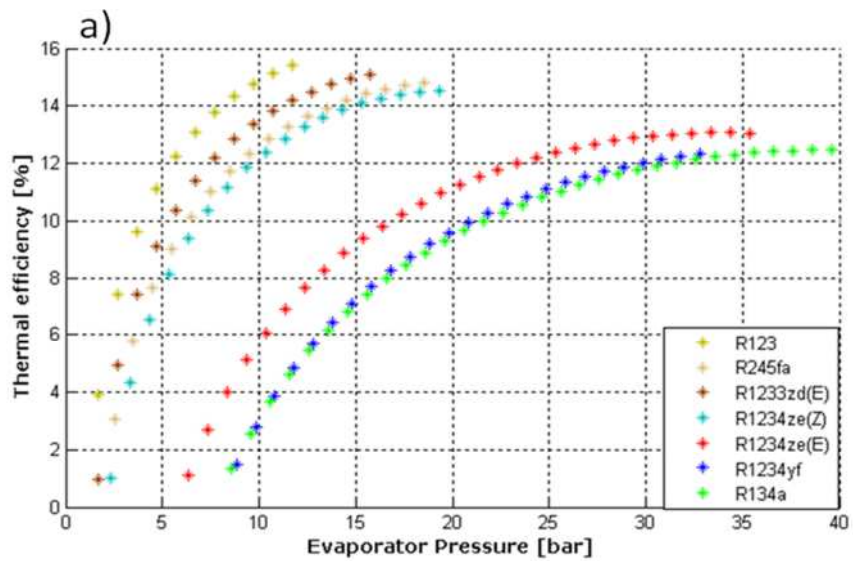
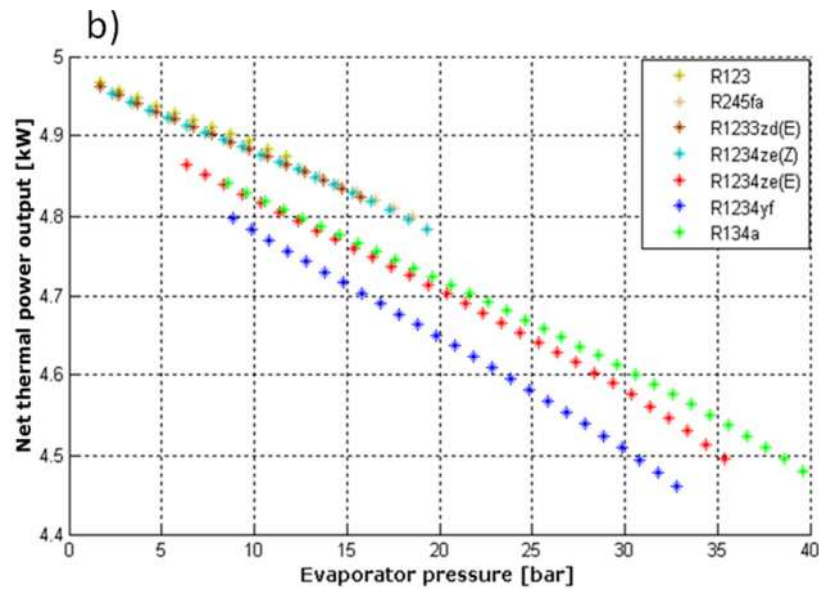


Figure 6-26: ORC working fluids performance at 100°C- a) thermal efficiency, and b) net thermal power output.





**Figure 6-27: ORC working fluids performance comparison at 120°C- a) thermal efficiency, and b) net thermal power output.**

It is clear from the figures that the ORC system using various working fluids outperforms all investigated systems in the current research (See Appendix C.6 for thermal efficiency comparison between the ORC and the CO<sub>2</sub> SRC systems). However, For both cases, the thermal efficiency results in Figure 6-26 (a) and Figure 6-27 (a) indicate that the highest thermal efficiency is achieved using the conventional R123 refrigerant, followed closely by the environmentally friendly R1233zd(E). The environmentally friendly R1234ze(Z) achieved the third highest thermal efficiency with almost identical performance to the conventional R245fa refrigerant. All the refrigerants mentioned subsequently were shown to cluster together and follow a similar trend. On the other hand, the environmentally friendly R1234ze(E) and R1234yf tended to follow a similar trend to the conventional, yet very popular R134a, with R1234yf performance being almost identical. Among the three latter refrigerants, R1234ze(E) showed the highest thermal efficiency. In both simulated cases, the net thermal power output is shown to behave in the opposite direction to thermal efficiency. As shown in Figure 6-27 (b) and Figure 6-26 (b), the net thermal power output starts at maximum and reduces gradually as the evaporator pressure increases. However, this decrease is small. Moreover, super-heating is shown to have an insignificant effect on

the net thermal power output produced when both simulations are compared. However, R1233zd(E) and R1234ze(Z) achieved almost identical net thermal power output to those achieved by R123 and R245fa. R134a generally achieves higher net thermal power output than both R1234yf and R1234ze(E). However, at lower evaporator pressure, R134a and R1234ze(E) achieved similar net thermal power output. Comparing both simulated cases, the results show the positive effect of super-heating on thermal efficiency, where it tends to increase as the expander inlet temperature rises. Super-heating is also shown to allow system operation at a wider range of evaporator pressure, as illustrated in Figure 6-27 (a), compared to Figure 6-26 (a).

Table 6.14 shows the optimum operating conditions that achieve maximum thermal efficiency for the environmentally friendly refrigerants. It is important to underline that the best performance was achieved when the expander inlet temperature was 120°C.

**Table 6.14: Optimum operating conditions for environmentally friendly refrigerants in the ORC system.**

Working fluid	R1234yf	R1234ze(E)	R1234ze(Z)	R1233zd(E)
System thermal efficiency [%]	12.33	13.06	14.51	14.99
Net thermal power output [kW]	4.46	4.53	4.78	4.83
Condenser pressure [bar]	7.8	5.78	2.10	1.55
Evaporator pressure [bar]	32.8	33.36	19.33	15
Evaporator temperature [K]	366.35	378.12	390.73	390.67

The results in Table 6.14 show that R1233zd(E) demonstrates the best performance among the new refrigerants, achieving the highest thermal efficiency and highest net thermal power output at the lowest operating pressure, as well as a super-heat of 2.5°C between the evaporation temperature and the expander inlet. Due to the outstanding performance R1233zd(E) had shown, it was nominated to be employed in the proposed small-scale power generation prototype system for waste heat recovery, and therefore it was further investigated.

#### 6.7.4.2 **R1233zd(E) ORC Optimised Operating Conditions and Parametric Analysis**

Although the optimum working conditions for the R1233zd(E) refrigerant were identified in the previous section, it is important to conduct a parametric investigation appropriate to the practicality of such a system. Therefore, another simulation case was carried out to optimise the anticipated working conditions of the R1233zd(E) ORC system by taking into account the proposed scroll expander's maximum operating pressure of 16 bar based on the manufacturer's data [260], and the effect of super-heating in the evaporator when it is related to the evaporation temperature. Similar to the CO<sub>2</sub> SRC power generation system, the effect of the expander, pump and recuperator heat exchanger efficiencies were also investigated.

However, in this simulation case, the evaporator pressure varied from 4 to 16 bar, while the super-heat temperature was assumed to be 5°C higher than the corresponding evaporation temperature. It is important to underline that the maximum super-heated vapour temperature allowed at the expander inlet is 120°C. The sub-cooled R1233zd(E) liquid temperature at the condenser exit was held constant at 30°C, while the condensation temperature was assumed to be 5°C higher than the sub-cooled temperature.

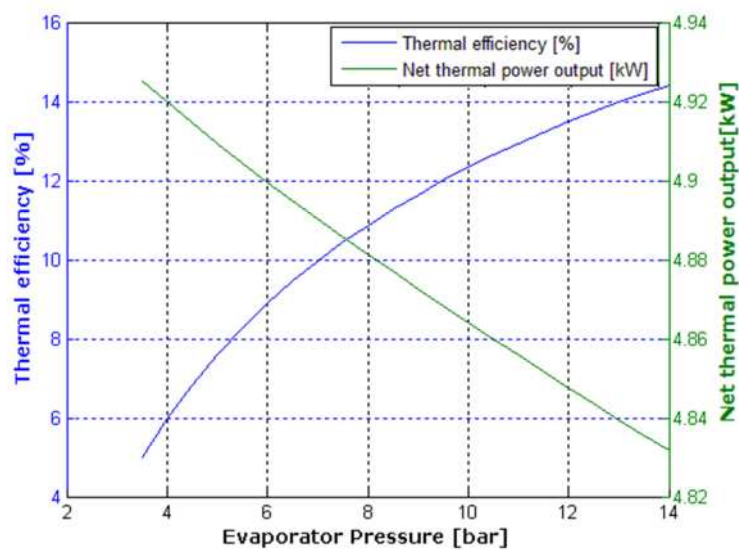
Table 6.15 lists the simulation results for optimum evaporator pressure and operating conditions which are very close to that seen in the second simulated case for working fluid selection in section 6.7.4.1. However, the results show relatively high thermal efficiency and net thermal power output achievable at low optimum evaporator pressure and low condenser pressure, when compared to other ORC refrigerants, as well as other investigated technologies. According to the input conditions for the simulation, the temperature of the super-heated vapour entering the expander is 119.1°C. Generally, heat exchangers' energy requirements are

fairly low, with the recuperator heat exchanger's energy requirements being the lowest. Furthermore, The R1233zd(E) liquid pump consumption was found to be very low.

**Table 6.15: The R1233zd(E) ORC system optimised operating conditions.**

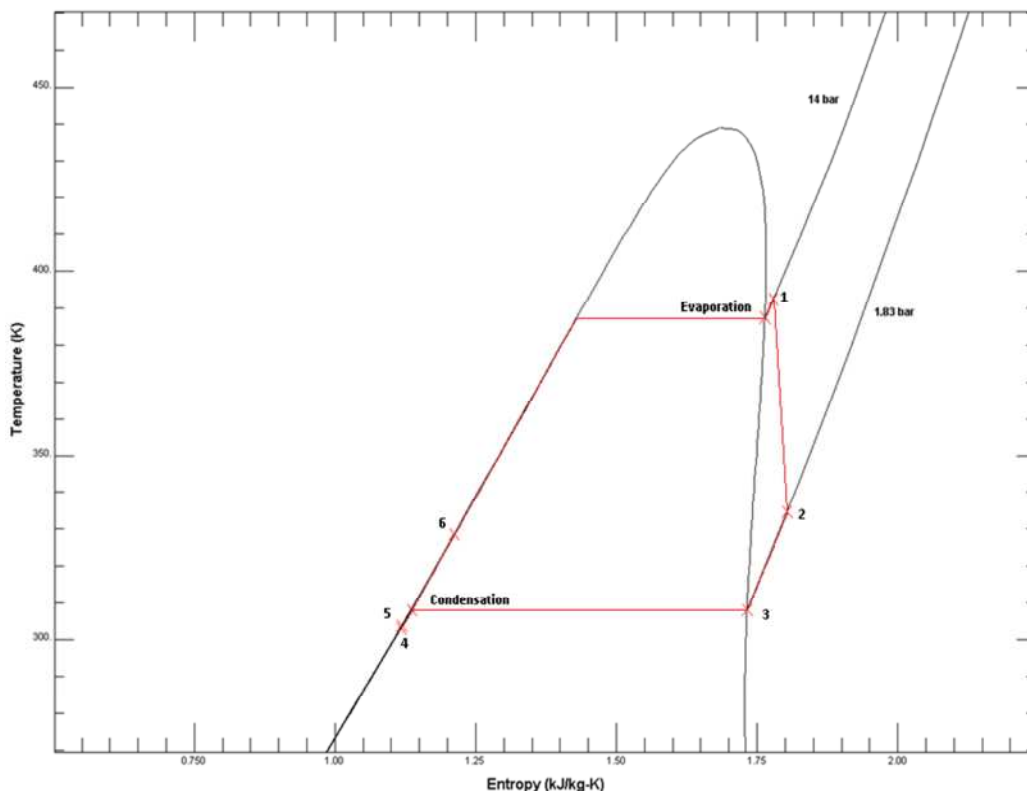
System thermal efficiency [%]	14.34
Net thermal power output [kW]	4.81
R1233zd(E) pump power [kW]	0.1893
Evaporation temperature [K]	387.23
Evaporation pressure [bar]	14
Expander inlet temperature [K]	392.23
Condensation temperature [K]	308.15
Condensation pressure [bar]	1.83
Condenser exit temperature [K]	303.15
Evaporator power [kW]	33.54
Condenser power [kW]	28.73
Recuperator heat exchanger [kW]	4.78
R1233zd(E) mass flow rate [kg/s]	0.15

Figure 6-28 shows that thermal efficiency and net thermal power output move in opposite directions. The system's thermal efficiency starts at its lowest and increases gradually to its maximum as the evaporator pressure increases and the super-heat temperature increases accordingly. On the other hand, the net thermal power output starts at its maximum and reduces in a linear manner, as the evaporator pressure increases. However, this decrease is marginal.



**Figure 6-28: R1233zd(E) ORC system thermal efficiency and net power as a function of evaporator pressure and dependant super-heating temperature.**

Figure 6-29 and Figure 6-30 show the optimised operating conditions on the R1233zd(E) T-S and P-H diagrams, respectively. It is clearly shown on T-S diagrams that R1233zd(E) is a dry working fluid which is able to operate with a minimum superheating temperature. Consequently, the energy requirement for the heat addition could be limited only for evaporation process. This adds another advantage to the qualities the refrigerant offers. Both diagrams reveal that R1233zd(E) enters the condenser as a saturated vapour, indicated at state point 3 and exhibits phase transition and sub-cooling in the condenser. On the other hand, the pre-heat in the counter-flow shown at state point 6 is less effective, where a large portion of latent heat is added by the heat source to reach evaporation and super-heating at state point 1, as shown on the P-H diagram. These observations indicate a low energy requirement for the recuperator heat exchanger and relatively higher evaporator and condenser energy requirements.



**Figure 6-29: R1233zd(E) ORC optimised operating conditions, T-S diagram.**

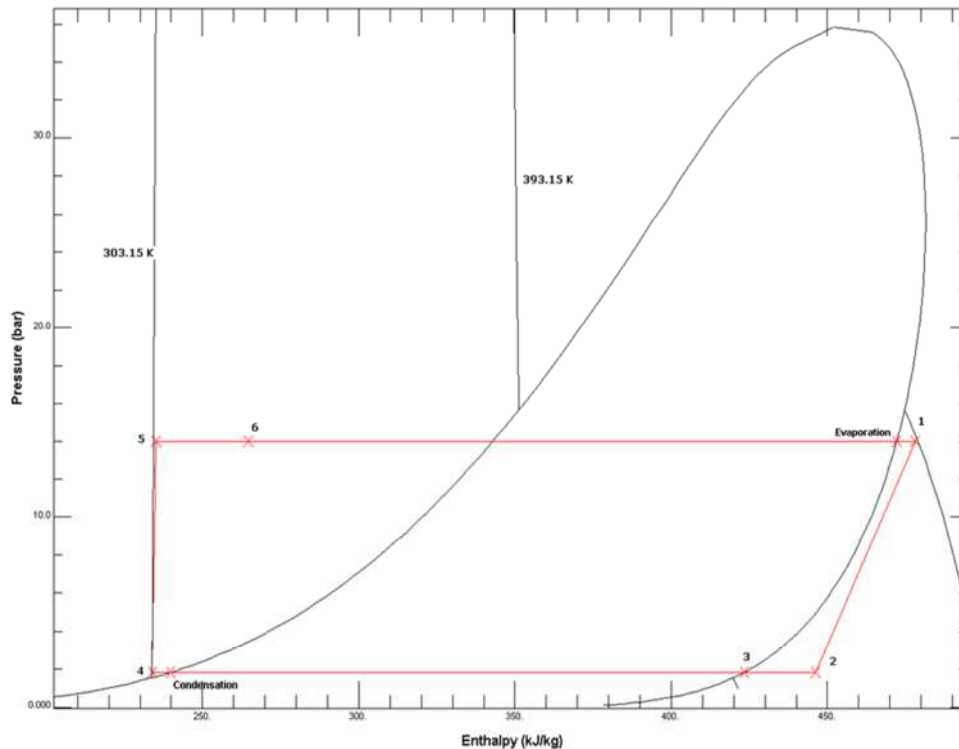


**Figure 6-30: R1233zd(E) ORC optimised operating conditions, P-H diagram.**

#### 6.7.4.2.1 The Effect of the Expander Isentropic Efficiency

The effect of the expander isentropic efficiency was investigated by keeping all parameters held constant under the optimised operating conditions, while varying the expander isentropic efficiency. The results shown in Figure 6-31 indicate a significant influence of the expander isentropic efficiency on the system's thermal efficiency and less effect on the net thermal power output. The system may operate at an expander isentropic efficiency as low as 10%, which is the lowest isentropic efficiency attainable. However, at 10% expander efficiency, the system's thermal efficiency and net thermal power output were 1.54% and 3.48 kW respectively. At isentropic expansion, when the isentropic efficiency of the expander was 100%, the maximum thermal efficiency was 17%, while the net thermal power output was 4.48 kW. As shown in the Figure, the thermal efficiency of the system starts at its lowest and increases gradually in a linear manner as the expander efficiency increases. The net thermal power output tends to increase exponentially, where it increases rapidly when the expander's isentropic efficiency

increases from 10% to 50%. After that, the net thermal power output will increase steadily and slowly towards its maximum value.

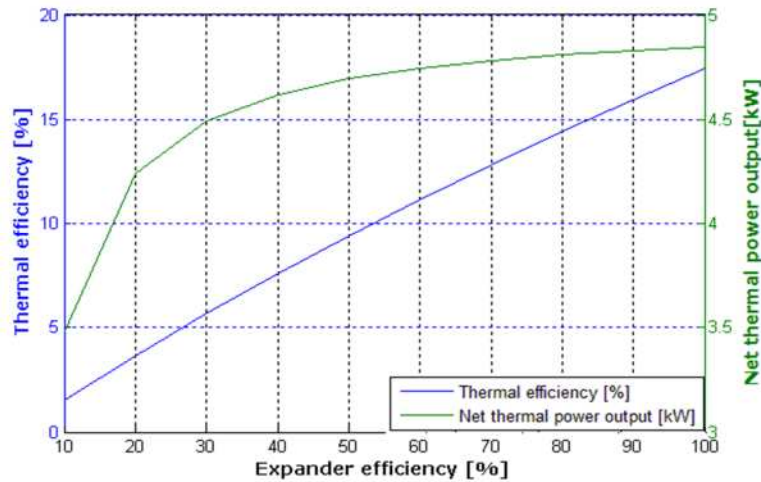


**Figure 6-31: R1233zd(E) ORC thermal efficiency and net thermal power output as functions of the expander isentropic efficiency.**

#### 6.7.4.2.2 The Effect of R1233zd(E) Pump Isentropic Efficiency

Similar to the expander isentropic efficiency, the effect of the R1233zd(E) liquid circulation pump was investigated, keeping the operating conditions held constant at the optimised operating conditions, while varying the pump's efficiency. The results shown in Figure 6-32 indicate that the system would operate with the R1233zd(E) liquid pump at a minimum of 10% for the selected working conditions. The minimum thermal efficiency and net thermal power output attainable were 10.2% and 3.48 kW respectively when the pump's isentropic efficiency was 10%. The maximum results were achieved when the pump's isentropic efficiency was 100%. The maximum thermal efficiency and net thermal power output were 14.54% and 4.85 kW respectively. Both the thermal efficiency and net thermal power output tended to follow similar patterns along the pump's isentropic efficiency axis. Both were observed to increase rapidly between 10% to 50% pump efficiency. After that, they increased steadily towards their maximum values when the isentropic efficiency was 100%.

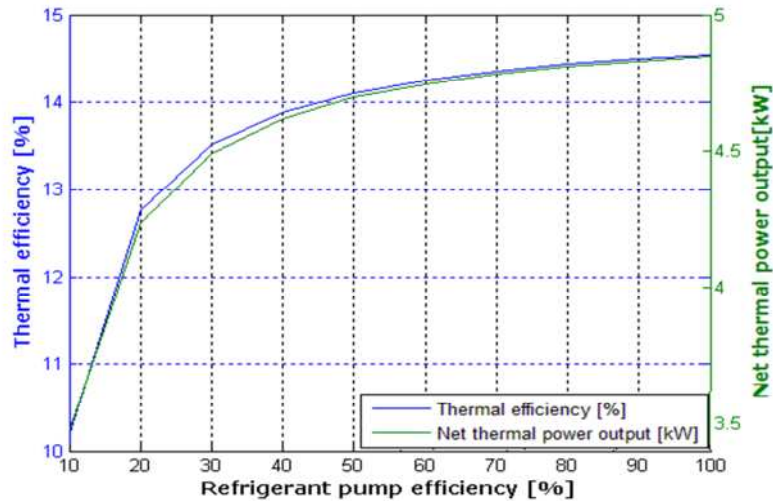


**Figure 6-32: R1233zd(E) ORC thermal efficiency and net thermal power output as functions of the R1233zd(E) pump isentropic efficiency.**

#### 6.7.4.2.3 The Effect of the Recuperator Heat Exchanger

##### Effectiveness

The effect of the recuperator heat exchanger on system performance was also investigated. The results shown in Figure 6-33 show that the effectiveness has no influence on the net thermal power output, as has been confirmed by the CO<sub>2</sub> SRC power generation system simulation and reviewed literature. However, the recuperator heat exchanger was found to marginally increase the system's thermal efficiency in a linear manner from 12.9%, when effectiveness was 10% and up to nearly 15% when effectiveness was 100%.

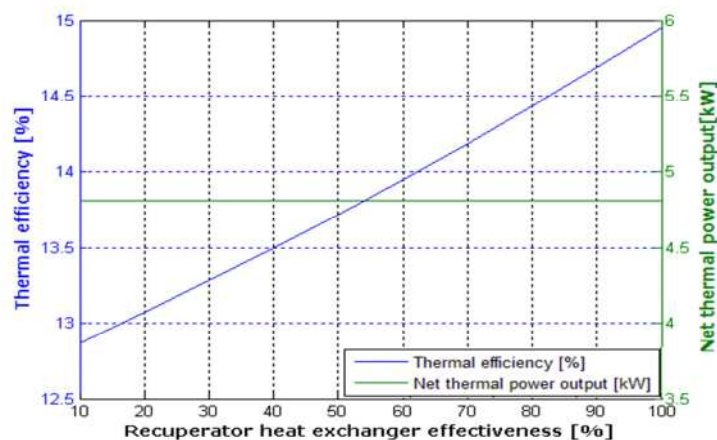


**Figure 6-33: R1233zd(E) ORC thermal efficiency and net thermal power output as functions of the recuperator heat exchanger effectiveness.**

### 6.7.5 The ORC System Conclusions

New, environmentally friendly, low GWP refrigerants were investigated and compared to conventional refrigerants in a 5 kW regenerative ORC system for low-grade heat recovery. The thermodynamic evaluation revealed the capability of the new refrigerants to replace conventional ones. R1233zd(E) showed outstanding performance, similar to R123, while R1234ze(Z) showed similar performance to R245fa. R1234ze(E), and R1234yf showed similar trends to R134a. However, R1234yf showed identical performance to R134a, while R1234ze(E) showed higher performance than both. Therefore, the use of these environmentally friendly refrigerants in ORC applications alongside other refrigeration applications is strongly recommended.

Following the performance evaluation, R1233zd(E) was nominated to be employed in the proposed small-scale power generation prototype system for industrial low-grade waste heat recovery. Further operating condition optimisation, and parametric investigation were conducted on the R1233zd(E) ORC system. The optimised working conditions showed both best thermal efficiency and net thermal power output. Therefore, the optimised working condition characteristics are to be used for developing, constructing, and testing the small-scale R1233zd(E) ORC system, which consequently will be the first of its kind employing the newly developed, environmentally friendly refrigerant.

However, the parametric investigation conducted on the R1233zd(E) ORC showed the significant influence of the expander isentropic efficiency on the thermal efficiency of the system. However this influence is considered marginal on the net thermal power output. The R1233zd(E) pump was shown to have influence on the system thermal efficiency but less than that seen for the expander. Also, similarly to the expander efficiency, the pump efficiency was shown to have a marginal effect on the net thermal

power output. To a minor extent, the recuperator heat exchanger was shown to have an effect on the system thermal efficiency but not the net thermal power output. However, the system showed its ability to operate at the minimum value of any of the latter efficiencies discussed.

## 6.8 Conclusions

In this chapter, four thermal power generation technologies were theoretically investigated in order to assess their technical feasibility and suitability for the proposed small-scale power generation system for low-grade industrial waste heat recovery. All systems, and their thermodynamic model implementation have been described, and their assumptions, inputs, governing equations and outputs have been displayed.

The first investigated system, the CO<sub>2</sub>/lubricant absorption power generation system generally showed very poor thermal efficiencies and net thermal power outputs at extreme pressures for the three investigated mixture pairs. Therefore, the system was considered technically unfeasible and the search for new working fluid mixtures for the absorption power generation technology revives.

The second investigated system was the CO<sub>2</sub>/POE32 flood expansion system. a new technology that aims to improve the system performance by achieving near-isothermal expansion using a mixture of a refrigerant and a high heat capacity liquid which is usually an oil. Although the system showed improved performance when it was compared to the CO<sub>2</sub>/lubricant power generation system, the practicality of such a system remains questionable, mainly because of the system requirements for a separate loop to contain the oil, and the additional pumping requirements associated with the added loop that could finally come at the expense of the main system performance. Furthermore, the system requires the identification of the optimal CO<sub>2</sub>/lubricant mass fraction allowed through the expander. Otherwise, poor system performance is

expected. Instead, to fulfil the aim of such a system, expander surface heating by mean of a jacket can be investigated as a performance improvement alternative in different thermal power generation cycles [253].

The third investigated system was the CO<sub>2</sub> SRC power generation system. The potential of the system was investigated by means of several simulation cases in both sub-critical and supercritical regions. Generally the theoretical analysis showed that the system requires operation at high CO<sub>2</sub> generator pressures in order to yield higher thermal efficiency and net thermal power output. At lower pressures, the compression device i.e. the pump tends to consume higher power. However, from a theoretical point of view the system is considered feasible in the conditions investigated, but requires an expander and a compression device that have very high isentropic efficiencies, which is practically uncertain to be achieved.

The fourth investigated system was the ORC system employing new environmentally friendly refrigerants. The ORC technology in general is attractive, well-established and has the flexibility to adapt differently to any operation condition. The potential of new environmentally friendly refrigerants was investigated theoretically in a regenerative ORC system. The results were compared to conventional popular ORC working fluids. The results showed that the new refrigerants have very close performances to their conventional counterparts. R1233zd(E) showed the highest performance among the new refrigerants, that it is close to the performance of R123. Therefore, it was selected for developing, constructing and testing the proposed small-scale power generation system for low-grade waste heat recovery, based on the optimised working conditions.

## Chapter 7 : R1233zd(E) ORC Prototype System Design and Construction

---

### 7.1 Introduction

This chapter presents the design and construction of the small-scale R1233zd(E) ORC prototype system for low-grade industrial waste heat recovery. The main aims of the prototype system's development and experiments are to:

- Prove the feasibility of the proposed ORC system employing R1233zd(E) for waste heat recovery.
- Experimentally evaluate system performance,
- Identify sources of performance destruction if it exists.
- Validate the system's thermodynamic model by making comparisons with the results of the experiments.

### 7.2 ORC Prototype Configuration and Description

A schematic diagram of the ORC prototype developed is shown in Figure 7-1.

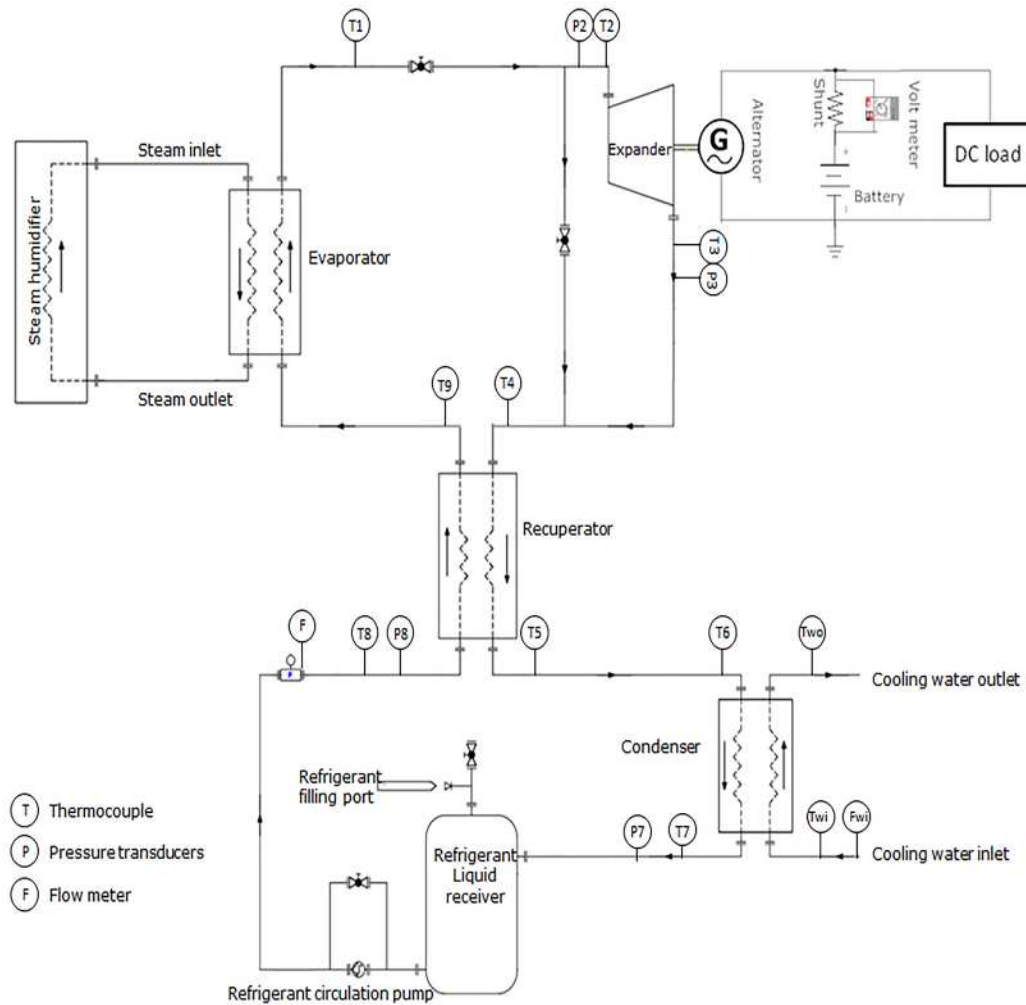


**Figure 7-1: A schematic diagram of the R1233zd(E) ORC prototype system.**

The working fluid is R1233zd(E), and was provided by Mexichem Fluor UK Ltd. [268]. The R1233zd(E) safety data sheet is included in Appendix D.1. However, the prototype heat source is a steam humidifier that supplies saturated steam in the range of 95°C to 101°C to the evaporator heat exchanger, in order to vaporise the working fluid. The scroll expander is an automotive air conditioning compressor, adapted to operate in reverse as an expander. The expander drives an automotive electric power generator through a V-belt. The electric power generator was selected, based on its ability to match the expected rotational speed of the expander. The condenser heat exchanger is cooled by mains water, supplied via an industrial water chiller capable of supplying cooling water at the selected temperature. A 7 litre liquid receiver cylinder is located behind the condenser to receive the condensed refrigerant and to

compensate for the variation in the refrigerant level in the heat exchangers. A triplex plunger pump is used to drive the liquid refrigerant to the evaporator through the recuperator heat exchanger. Before the refrigerant enters the recuperator, it passes through a variable refrigerant area flow meter. All heat exchangers and piping are insulated with rubber thermal insulation. Figure 7-2 and Figure 7-3 show different views of the 3D design of the R1233zd(E) ORC prototype.



**Figure 7-2: 3D illustration of the R1233zd(E) ORC prototype system.**



**Figure 7-3: 3D illustrations of the R1233zd(E) ORC prototype system with rugged industrial casing.**

### 7.2.1 Heat Source

The heat source utilised for the prototype shown in Figure 7-4 is an immersed electrode steam humidifier, manufactured by CAREL [269]. The humidifier is designed for domestic and industrial applications and is capable of supplying heat of up to 67.5 kW, with a maximum steam flow rate of 89.8 kg/h. The steam humidifier is equipped with a digital control panel that allows the energy output capacity, steam flow rate and temperature to be set. Moreover, it is a drum fed by the mains water supply. When the humidifier is operating, the steam generated in the drum is transferred and fed directly to the evaporator heat exchanger via a steam hose.

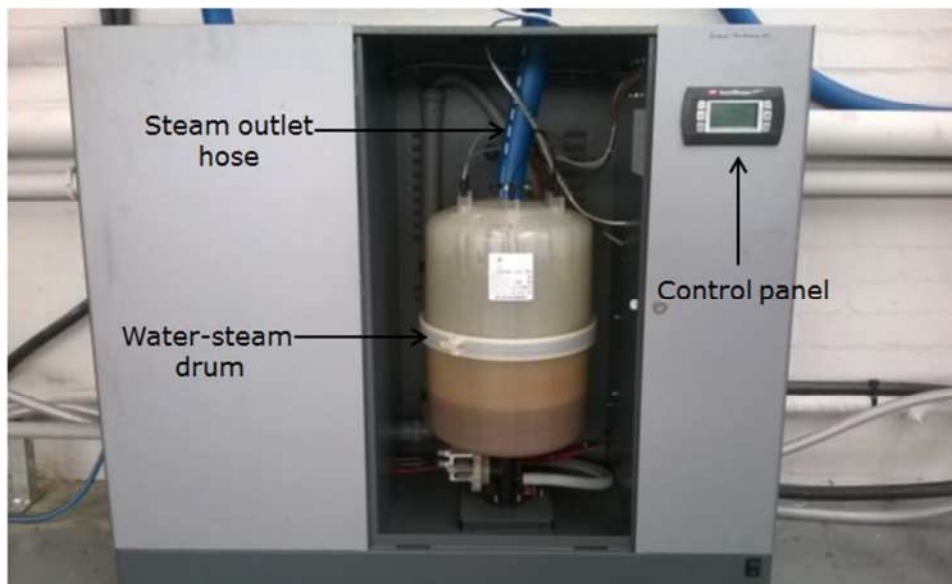


**Figure 7-4: Heat source - Carel humisteam X-plus EU090 steam humidifier.**

### 7.2.2 Heat Sink

The heat sink used for the prototype is a 56 kW industrial chiller unit, as shown in Figure 7-5 and manufactured by Corema [270]. This chiller unit has a tank capacity of 20L, which is fed by mains water at controlled flow rates. The unit is directly connected to the condenser heat exchanger by hoses and is pre-set to deliver a constant supply of desired condenser temperatures.



**Figure 7-5: Heat sink - Corema 56 kW industrial chiller unit.**

### 7.2.3 Scroll Expander

#### 7.2.3.1 Operating Principle

The scroll expander consists of two scrolls: a stationary scroll and an orbiting scroll, which are installed in a position relative to one another. Figure 7-6 illustrates the operating principle of the scroll expander. In reverse operation to the scroll compressor, the working fluid enters the scroll expander from the centre and flows to the periphery. As the high pressure working fluid enters the expander, it creates force that will cause the orbiting scroll to move eccentrically around the stationary scroll. While orbiting, both scroll surfaces make contact at several points and create pockets of trapped working fluid between the scrolls. However, as the orbiting scroll moves, the size of the pockets increases, causing the trapped working fluid to expand at the periphery and be discharged [71, 83].

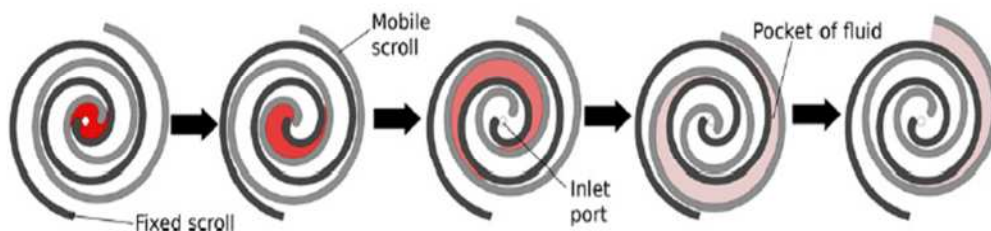


**Figure 7-6: Scroll expander operation. (source: [71])**

### 7.2.3.2 Losses and Internal Leakages

The expander's built-in volume ratio is the ratio of the volume of the expansion chamber at the end of the process to the volume of the intake chamber at the beginning of the process. It is an important parameter, directly related to the scroll geometry and it defines the operation and capacity of the expander [83]. However, the built-in volume ratio may introduce two types of loss which would significantly reduce expansion efficiency. The first type is under-expansion, where the built-in volume ratio is lower than the specific volume ratio of the working fluid. The other type is over-expansion, where the expander's built-in volume ratio is higher than the working fluid's specific volume ratio between the inlet and the outlet [271].

Under-expansion is the most common occurrence in positive displacement expanders, due to the large specific expansion ratios associated with Rankine cycles. Therefore, the expander's built-in ratio is not matched. Consequently, the expansion will be incomplete. Internal leakages are other common losses which occur in scroll expanders. Internal leakage affects volumetric efficiency and reduces the expander's power output, as the high pressure working fluid bypasses the expansion process to the low pressure side. There are two types of internal leakage which can occur in scroll expanders: radial and flank leakage. Radial leakage occurs due to the gap between the top and bottom plate and the scrolls, while flank leakage occurs due to the gap between the flanks of the two scrolls [272].

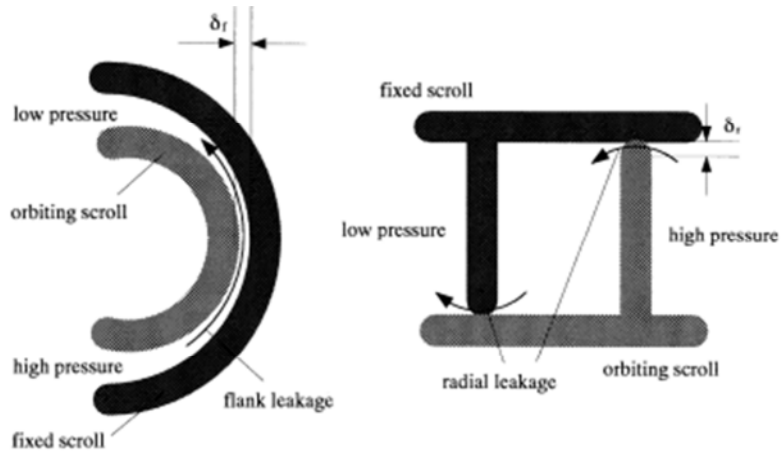


**Figure 7-7: Types of internal leakage in scroll expanders. (source: [272])**

### 7.2.3.3 Modification of the Selected Scroll Compressor into the Expander

The selected expander was converted from a Sanden TRSA09 compressor for automotive air conditioning, as shown in Figure 7-8. The main modification made so that the scroll compressor could work in expander mode, was to remove the check valve located in the compressor's intake compartment at the back of the compressor, as indicated in the cut-away view presented in Figure 7-8 (b). Figure 7-9 shows the performance curve of Sanden TRSA09.

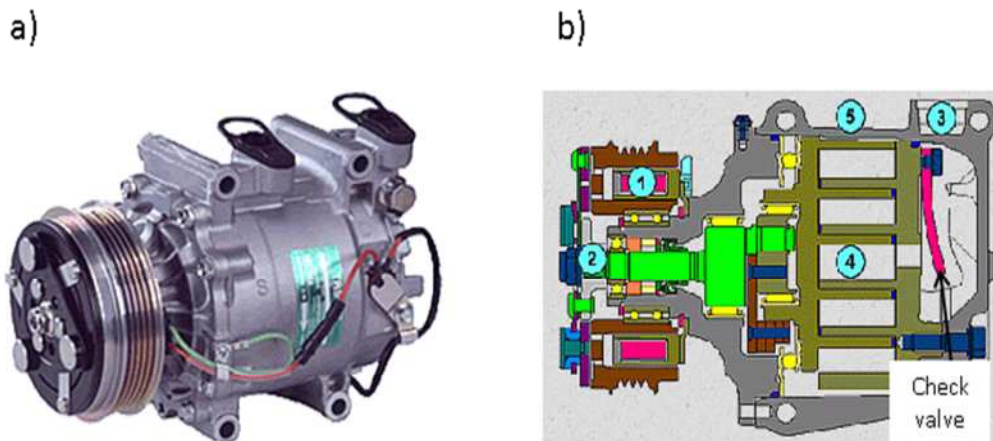


**Figure 7-8: Sanden TRSA09- a) general view, and b) cut-away view. (source: [273])**

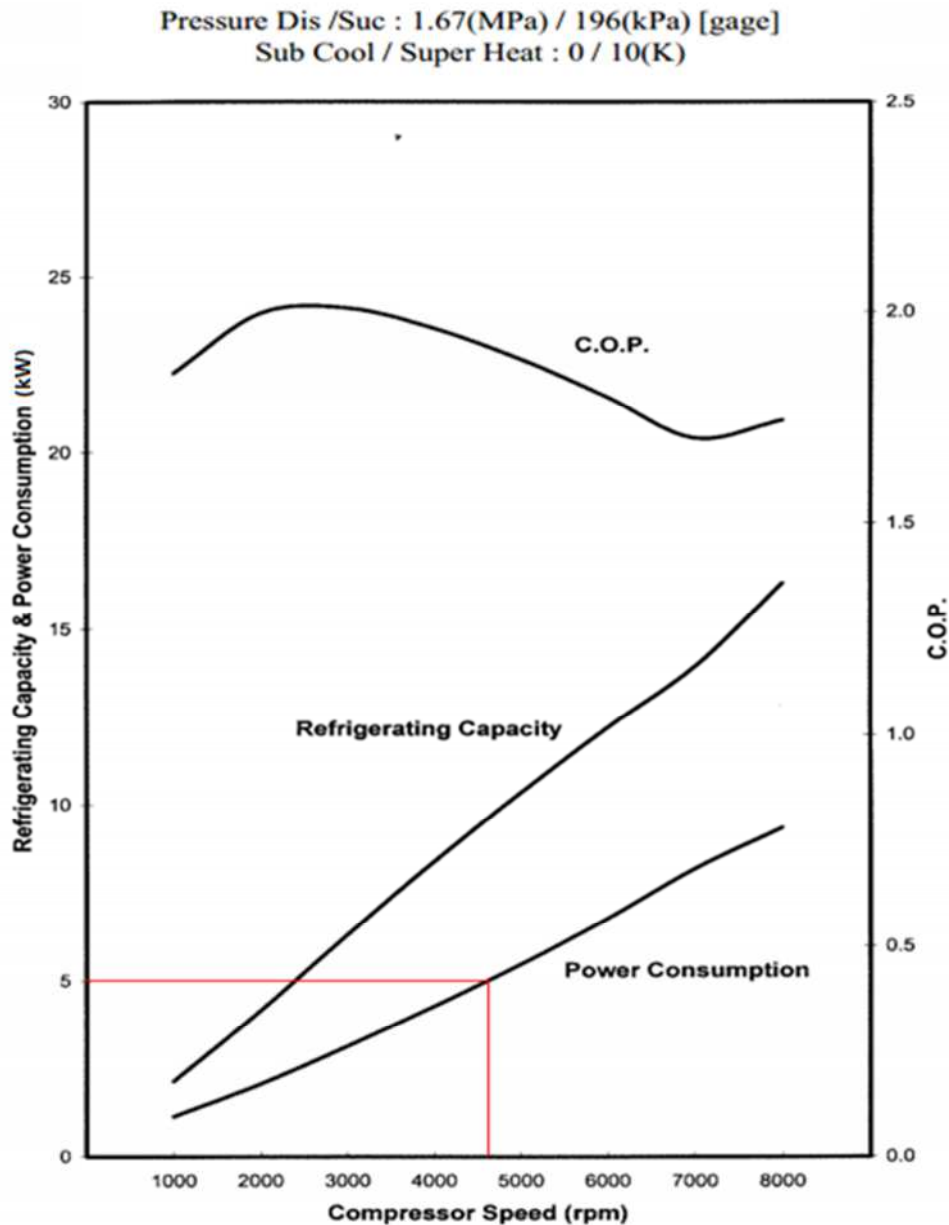


**Figure 7-9: Performance curve of the Sanden TRSA09 compressor.**

The scroll compressor modification procedure is illustrated in Figure 7-10 and Figure 7-11. Figure 7-10 (a) shows a side view of the scroll compressor prior to the commencement of the modification procedure. The compressor was dismantled into two halves and the orbiting scroll was removed, as shown in Figure 7-10 (b). Figure 7-10 (c) presents a zoomed-in view of the orbiting scroll, while Figure 7-10 (d) provides a zoomed-in view of the stationary scroll. As shown at the centre of the stationary scroll, the inlet port for the expander mode is blocked by the check valve.



**Figure 7-10: Views of scroll compressor modification procedures 1- a) side view of the TRSA09 compressor prior modification, b) the dismantled compressor showing stationary and orbiting scrolls, c) a zoomed-in view of the orbiting scroll, and d) a zoomed-in view of the stationary scroll, showing the expander mode inlet port blocked by the check valve.**

In order to reach the check valve, the stationary scroll was also removed from the compressor case. Figure 7-11 (a) shows the inside of the compressor case, which is the compressor's intake chamber after the stationary scroll has been removed. It also shows the check valve placed on the stationary scroll plate wall. Figure 7-11 (b) presents another view of the check valve and the back of the compressor case. The check valve was removed, as depicted in Figure 7-11 (c), and the expander parts re-assembled as the conversion procedure was being completed. However, as part of the modification procedure, customised inlet and outlet port adaptors were installed on the expander following assembly, as illustrated in Figure 7-12.

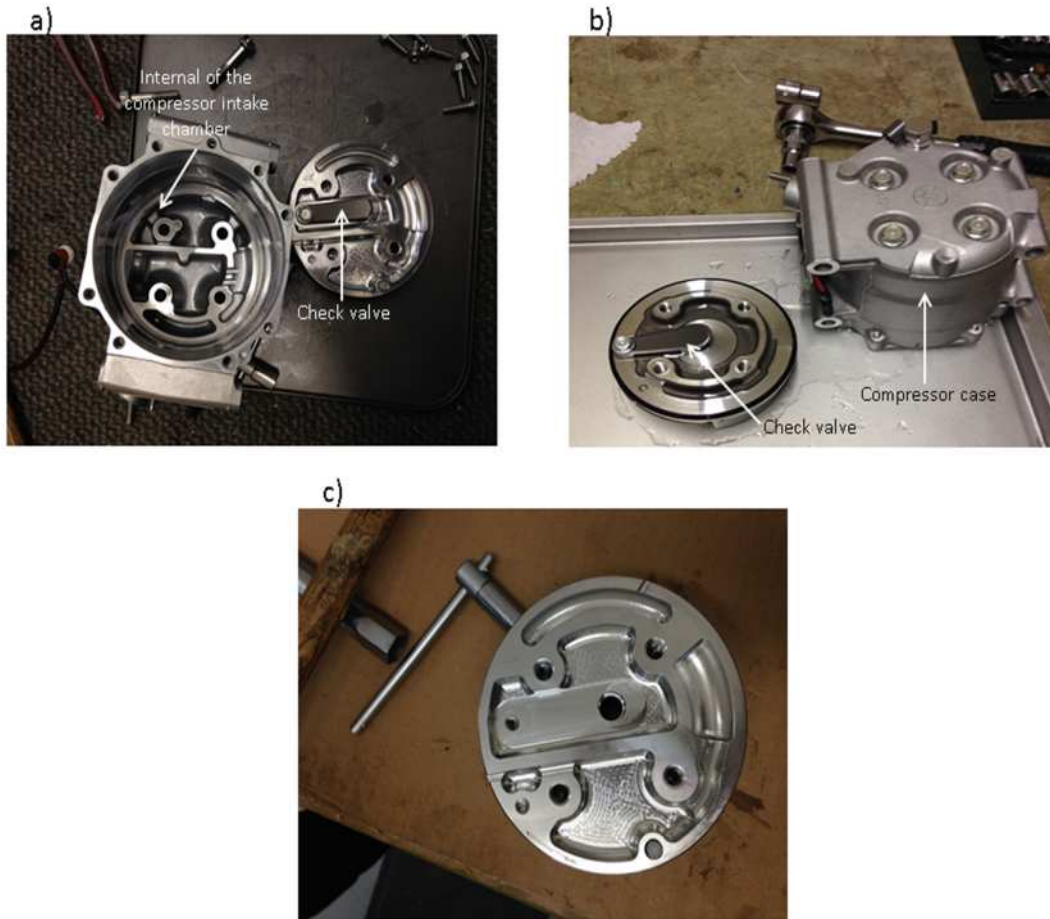


**Figure 7-11: Views of the scroll compressor modification procedures 2- a) the inside of the compressor's intake chamber and the check valve on the stationary scroll plate, b) a view of the compressor case and the check valve, and c) the check valve removed from the stationary scroll plate.**

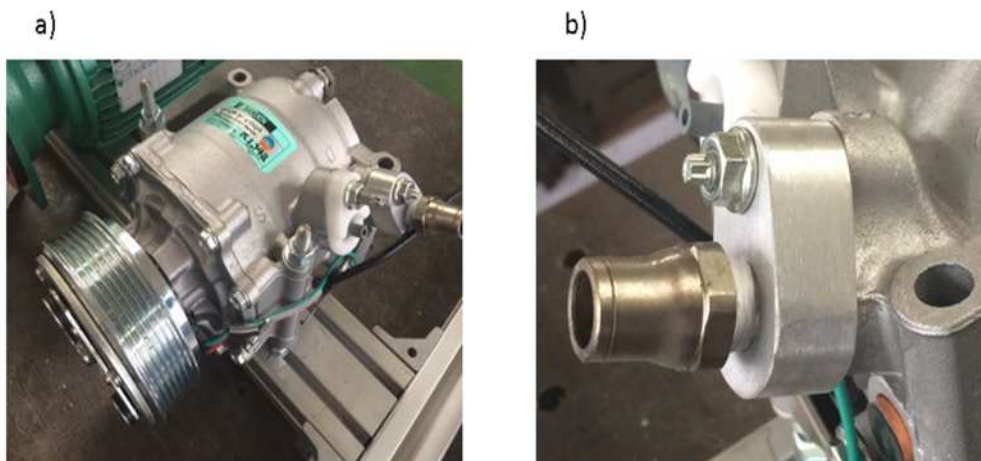


**Figure 7-12: The scroll expander after assembly- a) scroll expander with custom port adaptor, and b) zoomed-in view of one of the port adaptors.**

### 7.2.4 Electric Power Generator

Either DC or AC generators have similar operating principles. The objective of the generator is to convert the mechanical power produced by the expander into electrical power. The generator consists of a rotating driven assembly called the rotor, which fits into a stationary assembly called the stator, leaving a small air gap. The stator's assembly comprises the output wire winding, arranged around its periphery, while the rotor assembly consists of a coil of wires acting as an electromagnet. Figure 7-13 (a) presents a general view of an automotive alternator, showing the rotor and stator. Figure 7-13 (b) depicts the assembly components.

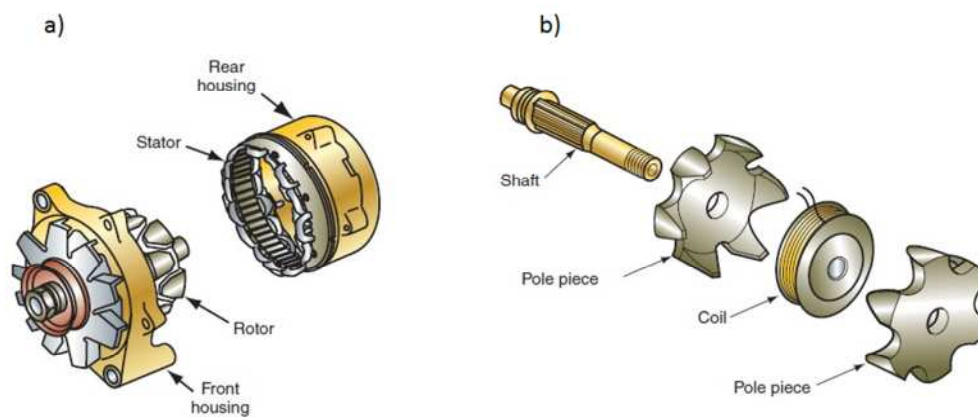


**Figure 7-13: The automotive alternator- a) general view, and b) rotor components. (Source:[274])**

The operation of the alternator is excited by a small amount of current called the field current, supplied by a connected battery, as illustrated in Figure 7-14. This current flows through a brush and slip ring mounted on the rotor shaft to the electromagnetic coil, creating the magnetic field. From there, it flows back through another slip ring and brush in order to leave. The strength of the magnetic field will be determined by the level of the field current passing through, which consequently determines the electrical power output. However, as the rotor rotates inside the stator with a small air gap, the magnetic field energises the stator windings and the maximum current is induced [275].

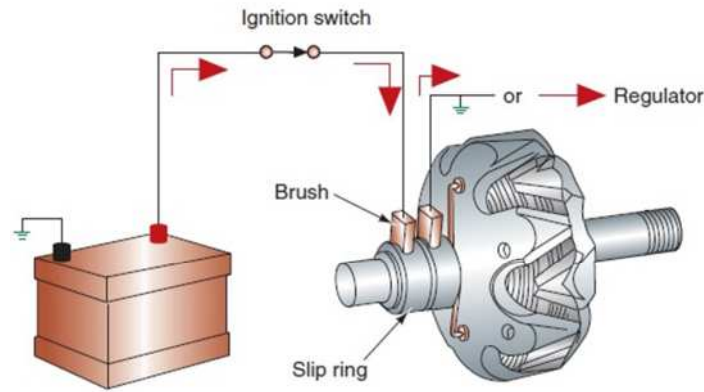


**Figure 7-14: A battery supplies the field current to the rotor coil through the brushes and slip rings. (Source:[274])**

Almost all automotive alternators are three-phase Lundell alternators, also called claw pole alternators. They are equipped with a passive diode rectifier to convert the generated AC current into DC. They are also equipped with an internal voltage regulator. This will maintain a constant voltage output of 14 or 28 V DC by adjusting the field current [276] to match the nominal lead-acid battery charging voltage of 12V DC or 28V DC in small and large vehicles, respectively [277]. In an automotive-related experimental study, Whaley et al. [277] investigated the extraction of the maximum power output from alternators. Figure 7-15 shows the study results.

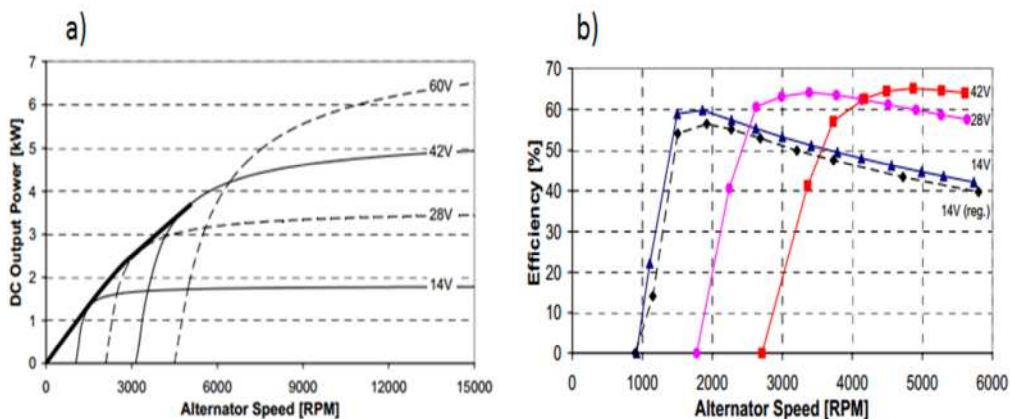


**Figure 7-15: Automotive alternator performance- a) output power against alternator speed at different output voltages, and b) alternator efficiency against alternator speed. (Source: [277])**

The results shown in Figure 7-15 (a) indicate that there is a minimum rotational speed at which the alternator will start to generate power. This minimum speed will increase as the output

voltage rises, which consequently means larger alternators, originally made for larger vehicles. Figure 7-15 (b) shows the variation in alternator efficiency for varying V DC output along rotational speeds. The peak efficiency achieved is shown in Table 7.1.

**Table 7.1: Experimental alternator efficiency. (Source: [277])**

Output DC voltage [V DC]	Peak efficiency [%]
14	65
14	60
28	64
42	65

However for the current ORC system, automotive alternators do not seem to be the best option since the requirement of considerably high rotational speeds in order to maximise the electric power output as illustrated in Figure 7-15. For this reason, two options were considered for the R1233zd(E) ORC prototype system. The first option was to utilise an automotive axial gap DC brushed motor, manufactured by the Lynch Motor Company Ltd, UK [278] and shown in Figure 7-16.



**Figure 7-16: Lynch-LEM-200d-127 motor, general view. (Source: [279])**

The motor is able to operate as a generator and is capable of producing electrical power outputs up to 12.5 kW at a rotational speed of 3900, as shown in the motor performance curve in Figure 7-17. Table 7.2 reveals the general specifications of the motor and Figure 7-18 presents a view of the motor installed on the ORC prototype.

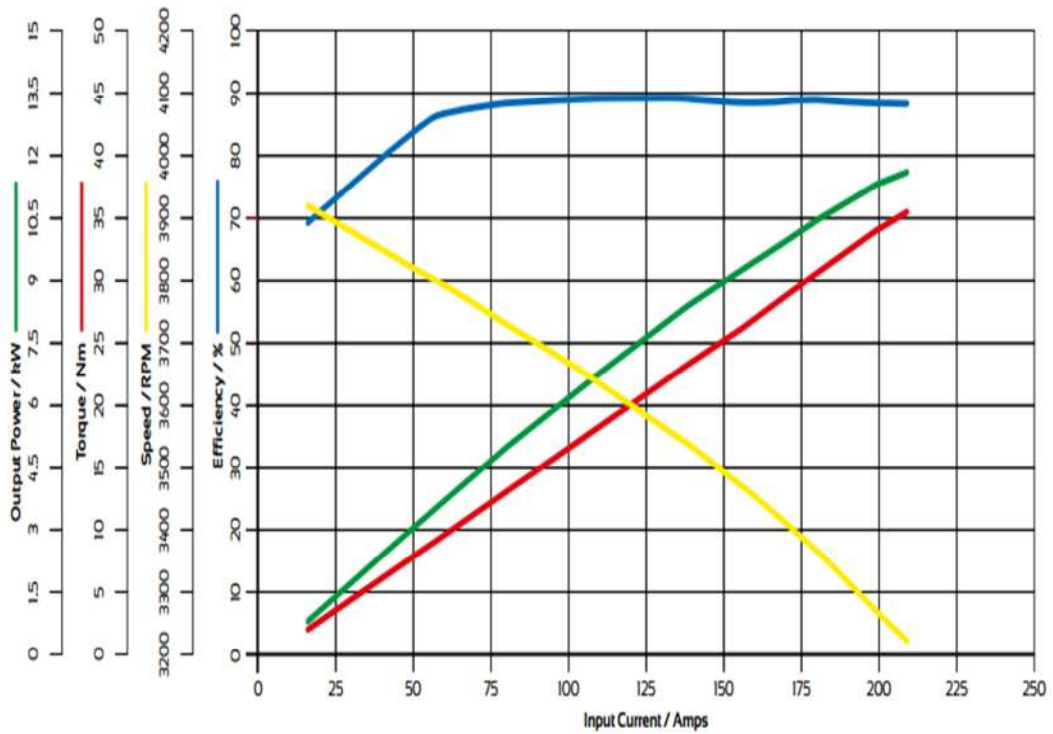


Figure 7-17: Lynch-LEM-200d-127 motor performance curve. (Source: [278])

Table 7.2: Lynch-LEM-200d-127 motor, general specifications.

Rated volts [VDC]	72
Rated current [A]	200
Rated power [kW]	12.5
Speed constant [rpm/V]	50
Efficiency [%]	92

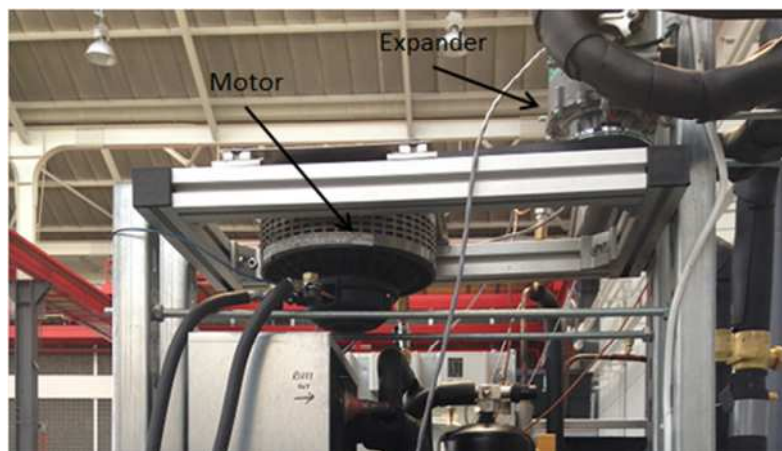


Figure 7-18: Lynch- LEM-200d-127 motor installed on the ORC prototype system.

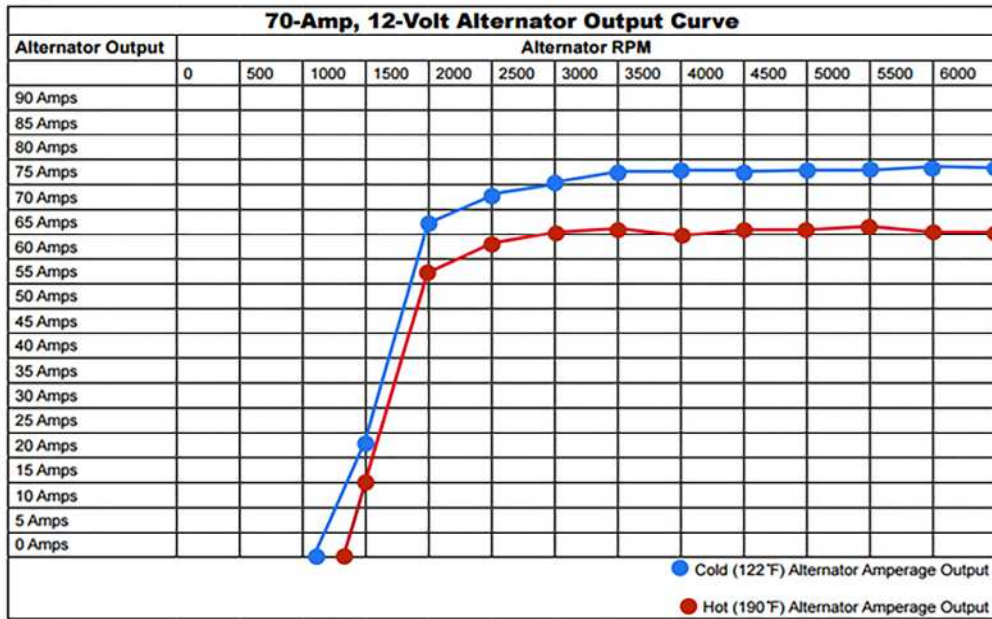
The second option is to utilise a conventional automotive alternator, capable of producing 1.8 to 2.1 kW. This option was considered for preliminary test of the modified expander operation in an expander-generator compressed air open loop system set-up. It was also considered as a back-up solution and trade-off option in the event of unexpected abnormality in ORC system operation and performance, which prevented the motor generator from rotating at its minimum speed of 3200 RPM, as will be discussed in Chapter 8. However, the alternator utilised is shown in Figure 7-19 and is manufactured by Autoelectro, UK [280]. It has a rated output of 150 amps and 12V DC.



**Figure 7-19: Autoelectro AEC1761 automotive alternator. (Source:[280])**

Unfortunately, according to the alternator manufacturer, the alternator's performance curve is not available as public information. Instead, there are many standard equivalent alternator replacements that provide their performance curves. Several equivalent alternator performance curves from different manufacturers were compared. All alternators presented nearly identical performance. Figure 7-20 shows the performance curves of two alternative alternators of similar ratings. The curves in Figure 7-20 (a) indicate that the alternator starts to produce power at just off 1000 RPM and at a temperature of up to 48°C, while it starts producing power at nearly 1250 to 1300 RPM, when the temperature is as high as 87°C. A similar curve for high temperatures is shown in Figure 7-20 (b) for another alternator. Figure 7-21 shows a view of the selected alternator installed on the ORC prototype.

a)



b)

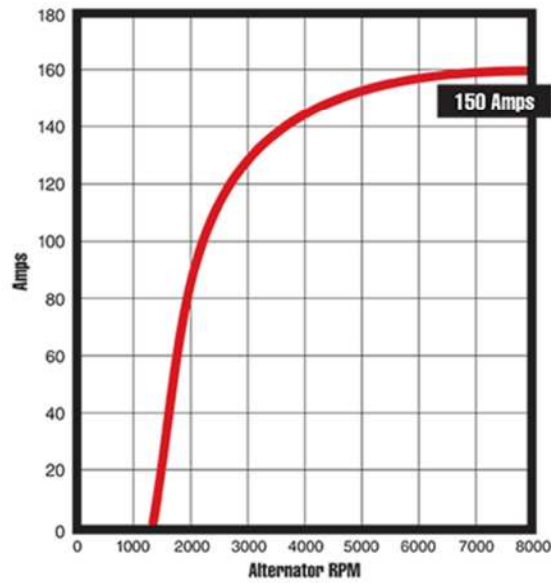


**Figure 7-20: Performance curves of a 150 amp-12V DC alternator. (Source: a) [281], and b):[282])**

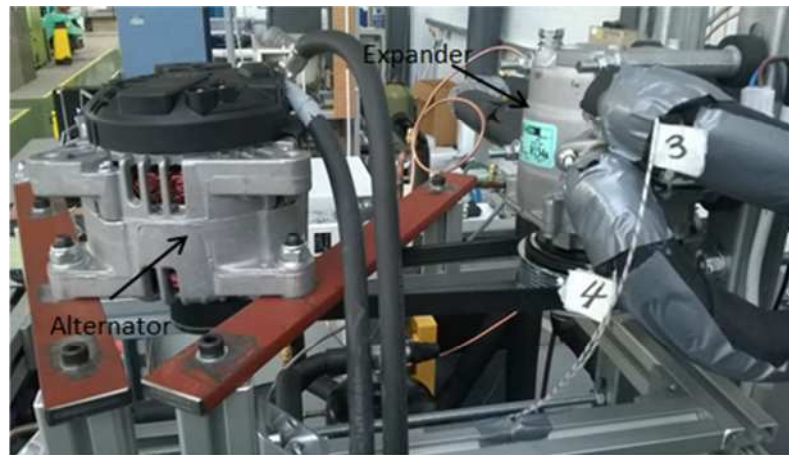


**Figure 7-21: Autoelectro AEC1761 automotive alternator installed on the ORC prototype system.**

### 7.2.5 R1233zd(E) Circulation Pump

The pump utilised in the system was a variable speed motor driven triplex plunger pump, manufactured by CAT Pumps Ltd., UK [283] and shown in Figure 7-22 (a).

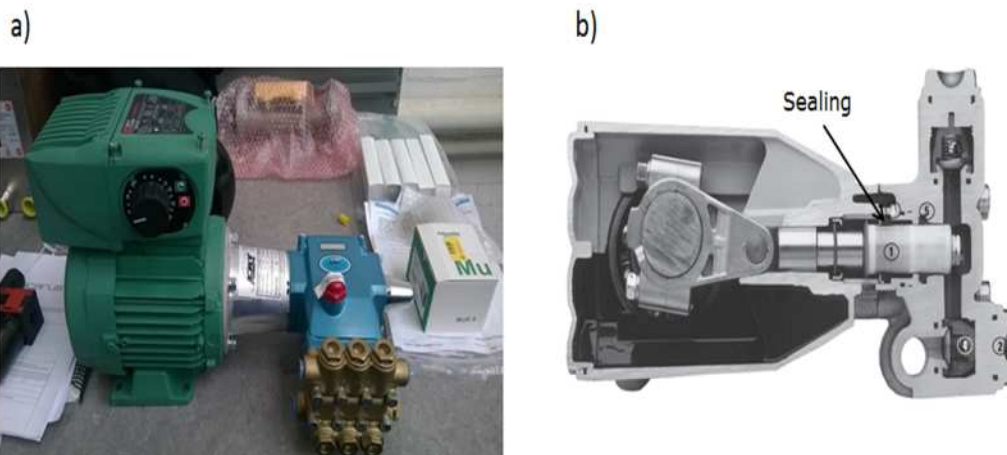


**Figure 7-22: 3CP1120 triplex plunger CAT pump- a) pump and motor during installation, and b) cut-away view of the pump (source: [284])**

To ensure optimum operation with refrigerants, the pump was customised by the manufacturer who replaced the standard sealing material with PTFE material as indicated in the cut-away view in Figure 7-22. In addition, the standard motor was replaced with a motor which consumed less power in order to suit the ORC application. Table 7.3 lists the general specifications for the pump.

**Table 7.3: General specifications of the 3CP1120 triplex plunger CAT pump.**

Plunger stroke [mm]	12.7
Maximum flow rate [L/min]	13.2
Minimum pressure [bar]	From flood
Maximum pressure [bar]	151
Motor power consumption [kW]	0.75
Motor maximum speed [RPM]	950

### 7.2.6 Brazed Plate Heat Exchangers (BPHEs)

BPHEs are made of a packed series of thin corrugated stainless steel plates that are brazed together by either copper or nickel. Figure 7-23 shows the corrugated plates of BPHEs.



**Figure 7-23: The corrugated plates of the BPHEs. (Source: [285])**

The spaces between plates become the flow channels, where each of the two heat exchanger fluids flows in alternate channels in the opposite direction: so-called counter-current flow. There are two flow patterns in BPHEs: single pass, where the fluids flow through the exchanger in a single direction, and a multi-pass flow arrangement, where the flow changes paths. However, single pass is the standard, most commonly used configuration [286]. The two types of flow pattern are illustrated in Figure 7-24.

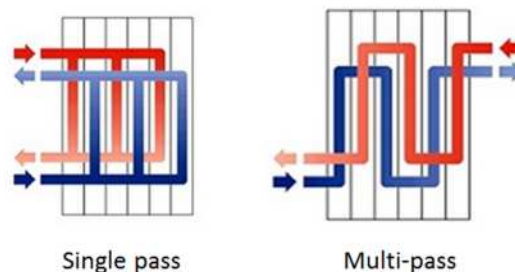


**Figure 7-24: Two types of flow pattern in BPHEs. (Source: [286])**

One of the main parameters characterising the performance of plate heat exchangers in general is the chevron angle, which is the angle

of the plate's corrugations, as shown in Figure 7-25. A high chevron angle will result in high heat transfer, but will also lead to high pressure drops and vice versa for low chevron angles. Therefore, careful selection of the chevron angle should be taken into consideration when designing plate heat exchangers to ensure efficient operation [250].

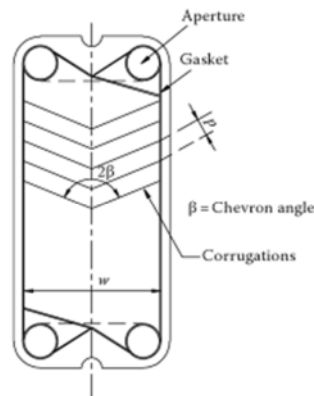


**Figure 7-25: The chevron angle of the plate heat exchanger. (Source: [250])**

The general features of BPHEs include a very compact size, low weight, and the ability to withstand higher pressure. This is mainly due to the brazing, which eliminates the use of frames or gaskets seen in other types of plate heat exchanger. Typical applications of BPHEs are generally found in refrigeration evaporators and condensers, HVAC systems and process applications [287]. Figure 7-26 shows the counter-flow direction in single pass BPHEs, used respectively as an evaporator and condenser in a refrigeration system.



**Figure 7-26: A BPHE as an evaporator and condenser in a refrigeration system. (Source: [285])**

For the ORC prototype system, three stainless steel single pass BPHEs were utilised as a condenser, an evaporator, and a recuperator, as shown in the system configuration schematic in Figure 7-1. The heat exchangers were manufactured by Kaori in Taiwan [288] and were specially designed for refrigeration applications. Since the thermodynamic properties of R1233zd(E) were unavailable, all the thermodynamic properties at inlets and outlet state points were provided for the manufacturer. The proposed heat exchangers characteristics are listed in Table 7.4.

**Table 7.4: BPHE characteristics.**

Heat exchanger/model	Condenser/K205	Recuperator/K205	Evaporator/I070
Number of plates	30	70	86
Dimensions [mm]	528x246x86	528x246x182	304x124x216.4
Volume [l]	6.73	16.01	2.03
Heat transfer area [m <sup>2</sup> ]	3.08	7.47	2.40
Maximum pressure [bar]	30	30	30
Maximum temperature [°C]	200	200	200

Figure 7-27 (a) presents a view of the heat exchanger utilised in the ORC prototype before installation. Figure 7-27 (b) shows an installed and thermally-insulated heat exchanger in the ORC prototype system.

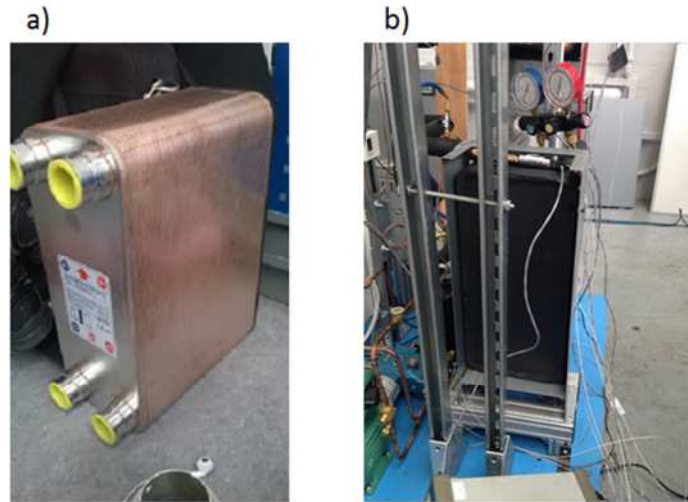


**Figure 7-27: ORC prototype heat exchangers- a) before installation, and b) an installed and thermally insulated heat exchanger.**

However, parallel to the manufacturer's determination of the heat exchangers' characteristics and for validation reasons, the heat exchangers' heat transfer area calculation was carried out as part of the current research using logarithmic mean temperature difference (LMTD) method and was compared to the BPHE characteristics provided by the manufacturer.

### **7.3 R1233zd(E) ORC Prototype BPHE Model by LMTD**

#### **Method**

For the R1233zd(E) ORC prototype, heat exchangers were modelled using an LMTD approach. Three separate iterative sub-routines were developed for the system's three heat exchangers in a Matlab environment and assisted by REFPROP 9.0 for R1233zd(E) properties. These sub-routines were integrated into the previously presented R1233zd(E) ORC thermodynamic system model in Chapter 6 and attached in Appendix C.5.

#### **7.3.1 LMTD**

The LMTD is the logarithmic average of the temperature difference between the two fluids of the heat exchanger [289]. LMTD is illustrated in the simple counter-flow heat exchanger shown in Figure 6-2 and the equation (7.1).

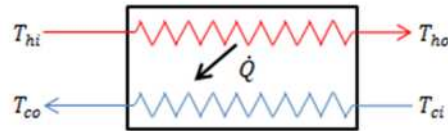


**Figure 7-28: Simple counter-flow heat exchanger.**

$$LMTD = \frac{(T_{hi} - T_{co}) - (T_{ho} - T_{ci})}{\ln \frac{(T_{hi} - T_{co})}{(T_{ho} - T_{ci})}} \quad (7.1)$$

The LMTD is the maximum driving force for heat transfer in a counter-flow heat exchanger [250]. Therefore, the higher the LMTD, the greater the heat transfer and vice-versa. The LMTD method is a common heat exchange, design and sizing method, with a standard set of equations which are widely available in textbooks on heat exchangers and ORC-related articles, such as [290, 291]. The method involves the heat exchanger energy load, flow temperatures and mass flow rates, as shown in equation (7.2). It is compatible for use with other heat exchanger design approaches, such as effectiveness and effectiveness-NTU (Number of Transfer Units Method) [292].

### 7.3.2 BPHE Model Assumptions and Inputs

The heat exchangers' sub-routines apply the outputs relevant to the R1233zd(E) ORC thermodynamic model as inputs alongside the heat exchangers' plate geometry specifications, listed in Table 7.5 and collected from the heat exchanger manufacturer's catalogue [293] according to the proposed heat exchangers models, and reference [294].

**Table 7.5: Heat exchangers LMTD model - plate specifications input.**

	Condenser and recuperator	Evaporator
Kaori model	K205	I070
Plate material	Stainless steel 316	Stainless steel 316
Plate length [mm]	456	250
Plate width [mm]	246	124
Distance between plates [mm]	2	2
Chevron angle [°]	45	45

Surface enlargement factor [ $\phi_f$ ]	1.17	1.17
Fouling factor percentage [%]	2	2

The main assumptions made for conducting the model are as follows:

- Pure counter-current, single pass heat exchangers, with a constant effectiveness of 80%, are assumed.
- 5°C pinch temperature is assumed between the steam and cooling water inlets and the R1233zd(E) ORC system corresponding state points.
- Pressure drops and friction effects were neglected.
- All heat exchangers were modelled as one-zone heat exchangers where the two-phase condensation and evaporation transition is assumed as occurring throughout the heat exchanger. Therefore, the streams' inlet and outlet temperatures are averaged.

### 7.3.3 The BPHE Model Governing Equations

The governing equations of the R1233zd(E) ORC BPHE model are equations (7.1) to (7.31). The subsequent solution of these will allow the heat exchangers' surface areas, LMTD, overall heat transfer coefficients, and the outlet temperatures and mass flow rates of the steam heat source and cooling water sink to be predicted. It is important to note that the heat transfer area is the key output of interest. It allows comparisons to be made with the manufacturer's proposed heat exchangers. However, the sub-routines developed could be altered to deliver any calculated heat exchanger characteristic. The principle of the implemented model is illustrated in a flow chart included in Appendix D.2. However, all general equations used were taken from Gebrehiwot [295], unless otherwise indicated:

$$\dot{Q} = U.A.LMTD = \dot{m}_h(h_{hi} - h_{ho}) = \dot{m}_c(h_{co} - h_{ci}) \quad (7.2)$$

Where (U) is the overall heat transfer coefficient and (A) is the heat transfer surface area, defined as:

$$A = N A_p \quad (7.3)$$

Where (N) equals the number of plates and  $A_p$  is the projected area of a single plate given by multiplying the dimensions of the plate, as shown in equation (7.4):

$$A_p = Lw \quad (7.4)$$

Determining the overall heat transfer coefficient involves the heat exchanger's geometric characteristics and the detailed properties of fluids flowing in both sides of the heat exchanger - where this is defined as a function of the convective heat transfer coefficients of both fluid streams in the heat exchanger, thermal resistance due to conduction through plate thickness, and fouling resistance. These elements are illustrated in Figure 7-29, while the overall thermal heat transfer coefficient is provided by equation (7.5).

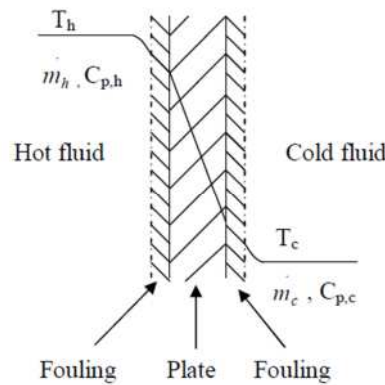


**Figure 7-29: Overall thermal resistance in a BPHE. (Source: [295])**

$$U = \frac{1}{\left(\frac{1}{h_{c,hot}} + \frac{1}{h_{c,cold}} + \frac{t}{k_p}\right) \left(1 + \frac{ff}{100}\right)} \quad (7.5)$$

Where  $h_{h,hot}$  and  $h_{c,cold}$  are the convective heat transfer coefficients of the heat exchanger's fluids in the hot and cold sides, respectively. (t) is the thickness of the heat exchanger's plate, (k) is the heat exchanger plate material conductivity, and (ff) is the fouling factor percentage. The heat transfer coefficient of either the hot or cold fluid is given by:

$$h_c = \frac{Nuk_f}{D_h} \quad (7.6)$$

Where (Nu) is the dimensionless Nusselt number,  $k_f$  is the thermal conductivity of the fluid, and  $D_h$  is the hydraulic diameter. The

hydraulic diameter of the plate heat exchangers has two definitions. The first definition is similar to two wide parallel plates, with a spacing of ( $b_c$ ) between the plates [296], written as:

$$D_h = 2 b_c \quad (7.7)$$

The second definition is more physically accurate and is based on a three-dimensional variable cross-sectional area duct as:

$$D_h = \frac{4V_{void}}{A_{wetted}} = \frac{2 b_c}{\phi_f} \quad (7.8)$$

Where  $V_{void}$  is the void volume between plates,  $A_{wetted}$  is the wetted surface area between them. In the second term of equation (7.8),  $\phi_f$  is the surface enlargement factor, which is the ratio of the actual surface area developed to the projected surface area [297]. The surface enlargement factor value is provided by the manufacturer. However, for corrugated plate heat exchangers, Han et al. [294] and Naik and Matawala [298] suggest a value of 0.17. Referring once again to equation (7.6), determining the dimensionless Nusselt number will depend on the dimensionless Reynolds and Prandtl numbers and is calculated using various correlations, depending on the fluid characteristics, stream type, phases of the flow, and subjected to experimental determination. However, the general calculations for Prandtl and Reynolds numbers are respectively given in equations (7.9) and (7.10).

$$Pr = \frac{cp\mu}{k_f} \quad (7.9)$$

( $cp$ ) is the heat capacity of the fluid, and  $\mu$  is the fluid's dynamic viscosity.

$$Re = \frac{\rho u D_h}{\mu} \quad (7.10)$$

Where ( $\rho$ ) is the fluid density, ( $u$ ) is the actual fluid velocity. Claesson [296] suggests taking advantage of the actual fluid velocity, assuming a two-dimensional flow. Therefore, the actual velocity becomes the velocity of the fluid as it flows in the corrugations, rather than using the mass flow velocity. However, the relationship between the mass flow velocity and the actual velocity becomes:

$$u = \frac{u_m}{\cos\beta} \quad (7.11)$$

Where  $u_m$ , is the mass flow velocity and  $\beta$  is a chevron angle converted from degrees to radians. The mass flow velocity is given by:

$$u_m = \frac{G}{\rho} \quad (7.12)$$

Where (G) is the mass flux of the fluid. The mass flux is calculated as:

$$G = \frac{\dot{m}}{A_c n} \quad (7.13)$$

Where  $\dot{m}$  is the mass flow rate,  $A_c$  is the cross-sectional area of a single channel, and (n) is the number of channels the fluid flows through. The cross-sectional area of a single channel is the spacing between the plates ( $b_c$ ), multiplied by the width of the plate (w).

$$A_c = b_c w \quad (7.14)$$

The numbers of channels in both the hot and cold sides of the heat exchanger are respectively given in equations (7.15) and (7.16), where (N) is the number of plates.

$$n_h = \frac{N - 2}{2} \quad (7.15)$$

$$n_c = \frac{N}{2} \quad (7.16)$$

Once all the general parameters have been determined, the Nusselt number can be calculated for each stream on both sides of the heat exchanger.

### 7.3.3.1 Convective Heat Transfer Coefficient

#### Correlations

For a fully developed turbulent stream in a plate heat exchanger, the forced convection heat transfer is generally correlated as:

$$Nu = C_1 Re^{C_2} Pr^{C_3} \left( \frac{\mu_{fw}}{\mu_f} \right)^n \quad (7.17)$$

where the coefficients  $C_1$   $C_2$   $C_3$  and (n) are dependent on the plate geometry and flow pattern, with the typical values that are usually

reported in the literature [297]. The fluid dynamic viscosity at the wall and  $\mu_{fw}$  and the fluid stream viscosity  $\mu_f$  may be assumed to be similar. Therefore, the last term of the correlation could be neglected. However, the convective heat transfer coefficient for the water side in the condenser is calculated using the correlation proposed by Longo [299], based on Muley and Manglik's [300] experimental study on the heat transfer of the turbulent flow of water in the plate heat exchangers.

$$Nu = 0.2121Re^{0.78}Pr^{1/3} \quad \left[ \begin{array}{l} 5 < Pr < 10 \\ 200 < Re < 1200 \end{array} \right] \quad (7.18)$$

The condensation heat transfer coefficient is calculated using the condensation correlation proposed by Kuo et al. [301] and is shown in equation (7.19) for R410A in the plate heat exchangers. This correlation was used widely by Quoilin et al. [271, 291, 302] in ORC systems and proved to yield highly accurate results:

$$h_c = h_{c,rl} [0.25Co^{-0.45}Fr_l^{0.25} + 75 + Bo^{0.75}] \quad (7.19)$$

Where  $h_{c,rl}$  is the refrigerant liquid's single-phase convective heat transfer coefficient, calculated as:

$$h_{c,rl} = 0.2092 \left( \frac{k_{fl}}{D_h} \right) Re_l^{0.78} Pr_l^{1/3} \quad (7.20)$$

$Co$ ,  $Fr_l$ , and  $Bo$  in equation (7.19) are, respectively, the non-dimensional, convective, Froude, and boiling numbers, defined as:

$$Co = \left( \frac{1-x}{x} \right)^{0.8} \left( \frac{\rho_g}{\rho_l} \right)^{0.5} \quad (7.21)$$

Where  $(x)$  is the mean quality of the working fluid and  $\rho_l$ , and  $\rho_g$  are the densities of the liquid and gas refrigerant, respectively:

$$Fr_l = \frac{G_{Cond}^2}{\rho_l^2 g D_h} \quad (7.22)$$

Where  $G_{Cond}$  is the mass flux of the refrigerant in the condenser, and  $(g)$  is the gravitational acceleration. Finally, the boiling number is:

$$Bo = \frac{Q_{Cond}}{G_{Cond} h_{fg}} \quad (7.23)$$

Where  $h_{fg}$  is the refrigerant's latent heat of vaporisation.

The refrigerant's film heat transfer coefficient in the recuperator heat exchanger, the super-heating in the evaporator, and the steam heat source were calculated using the single-phase correlation developed by Bogaert and Böles [303] and presented by Claesson [296]:

$$Nu = B_1 Re^{B_2} Pr^{\frac{1}{3}} e^{\frac{6.4}{Pr+30}} \left( \frac{\mu_{fw}}{\mu_f} \right)^{\frac{0.3}{(Re+6)^{0.125}}} \quad (7.24)$$

Where the coefficients  $B_1$  and  $B_2$  were taken from the similar correlation developed by Muley [304], also presented in reference [296]. After adding the coefficients and neglecting the variation in dynamic viscosity, equation (7.24) becomes:

$$Nu = 0.44 \left( \frac{\beta}{30} \right)^{0.38} Re^{0.5} Pr^{\frac{1}{3}} e^{\frac{6.4}{Pr+30}} \quad \begin{matrix} [30^\circ \leq \beta \leq 60^\circ] \\ [30 \leq Re \leq 400] \end{matrix} \quad (7.25)$$

$$Nu = A B Re^C Pr^{\frac{1}{3}} e^{\frac{6.4}{Pr+30}} \quad \begin{matrix} [30^\circ \leq \beta \leq 60^\circ] \\ [Re \geq 1000] \end{matrix} \quad (7.26)$$

Where:

$$A = 0.2668 - 0.006967\beta + 7.244 \cdot 10^{-5} \beta^2 \quad (7.27)$$

$$B = 20.7803 - 50.9372\varphi_f + 41.1585 \varphi_f^2 - 10.1507\varphi_f^3 \quad (7.28)$$

$$C = 0.728 + 0.0543 \sin\left(\frac{2\pi\beta}{90} + 3.7\right) \quad (7.29)$$

The convective evaporation heat transfer coefficient in the evaporator was calculated using the flow's boiling heat transfer correlation developed by Donowski and Kandlikar [305] for R134a in plate heat exchangers and modified by Claesson [296] to handle heat transfer coefficients when vapour quality is above 90%. Here, it is important to note that R134a has been used widely as a reference refrigerant for heat exchanger modelling and sizing by different manufacturers. However, the convective evaporation heat transfer coefficient is:

$$h_c = \left\{ [h_{c,DK}(1-x)^{1/3}]^{0.8} + (h_{c,GO}x^3)^{0.8} \right\}^{1/0.8} \quad (7.30)$$

where  $h_{c,GO}$  is the heat transfer coefficient of the flow assumed to be fully in the vapour phase and calculated using single-phase

correlations from (7.24) to (7.29). The term  $h_{c,DK}$  is the heat transfer coefficient of the two-phase refrigerant given by Donowski and Kandlikar [305] as:

$$h_{c,DK} = (2.312Co^{-0.3}0.512 + 667.3Bo^{2.8}F_{fl}0.338)(1 - x)^{0.003}h_{c,LO} \quad (7.31)$$

Where  $h_{c,LO}$  is the heat transfer coefficient of the flow assumed to be a fully-developed liquid and calculated using the single-phase correlations from (7.24) to (7.29).  $F_{fl}$  is a fluid-dependant parameter and is taken as a unity for stainless steel plates. The convective and boiling numbers are calculated for the evaporation process using equations (7.21) and (7.23).

### 7.3.4 BPHE Model Results and Discussion

For the anticipated prototype system operating conditions presented in Chapter 6, Table 6.15, the system's BPHE sizing modelling results are presented in Table 7.6 to Table 7.8 and compared to the heat exchanger characteristics provided by the manufacturer [306]. However, in general, the results obtained proved to be in satisfactory agreement with the manufacturer's proposed characteristics.

**Table 7.6: Condenser heat exchanger modelling results.**

Condenser heat exchanger	Model	Manufacturer
Cooling water inlet temperature [°C]	20	20
Cooling water outlet temperature [°C]	31.85	28
Cooling water mass flow rate [kg/s]	0.86	0.87
LMTD [°C]	5.81	4.97
Heat transfer area [m <sup>2</sup> ]	3.18	3.08

The condenser modelling results show a slight deviation of 0.1 m<sup>2</sup> between the heat transfer area calculated and the manufacturer's proposed heat transfer area. The LMTD deviation was 0.84°C and the cooling water outlet temperatures were found to deviate by 3.85°C. The cooling water mass flow rates proved to be very close and deviated by just 1.2%.

**Table 7.7: Evaporator heat exchanger modelling results.**

Evaporator heat exchanger	Model	Manufacturer
Heating steam inlet temperature [°C]	130	130
Heating steam outlet temperature [°C]	115.1	122
Heating steam mass flow rate [kg/s]	0.53	0.15
LMTD [°C]	28.79	25
Heat transfer area [m <sup>2</sup> ]	2.83	2.40

The heat transfer area obtained from the modelling of the evaporator heat exchanger was found to deviate from the manufacturer's proposed heat transfer area by 0.43 m<sup>2</sup>. The LMTD deviation was 4.8°C, while the steam outlet temperature was found to deviate by 6.9°C and the heating steam's mass flow rates were found to deviate by 3.9%.

**Table 7.8: Recuperator heat exchanger modelling results.**

Recuperator heat exchanger	Model	Manufacturer	Deviation [%]
LMTD [°C]	5.12	5.95	13.94
Heat transfer area [m <sup>2</sup> ]	6.7	7.47	13.43

Finally, the recuperator heat exchanger heat transfer areas were found to deviate by 1.04 m<sup>2</sup>, while the LMTD deviated by 0.83°C. The relatively larger heat transfer area difference observed in the recuperator heat exchanger is presumed to relate to several factors, such as the general deviations observed in the condenser and evaporator and the effect of pressure drop, where it was accounted for in the manufacturer's calculation, but neglected in the LMTD model implemented.

#### 7.4 Measurement Devices

This section presents the measurement devices installed in the ORC prototype. The measurement devices will basically enable the monitoring and acquisition of different operating parameters of the system. Consequently, they will enable the system's performance to be evaluated and compared with that theoretically predicted.

### 7.4.1 Data Acquisition System

Data acquisition and the monitoring of temperatures and pressures, as well as operating time were established using the Agilent 34907A data acquisition system [307] shown in Figure 7-30. This unit is a powerful data acquisition system equipped with three module card slots that allow the measurement of 20 to 120 channels. It also supports 11 different types of measurement, including various temperature sensors, AC and DC voltages, resistance, current, and frequency. The unit has a capacity to perform measurements with an uncertainty of  $\pm 0.004\%$  for V DC and  $\pm 0.06\%$  for V AC. The monitoring and configuration of the system is carried out via the supported interface software, which enables the real time monitoring of physical quantities and the generation of graphs. Alternatively, the data acquisition unit could be monitored and configured through the unit's front panel and display monitor.

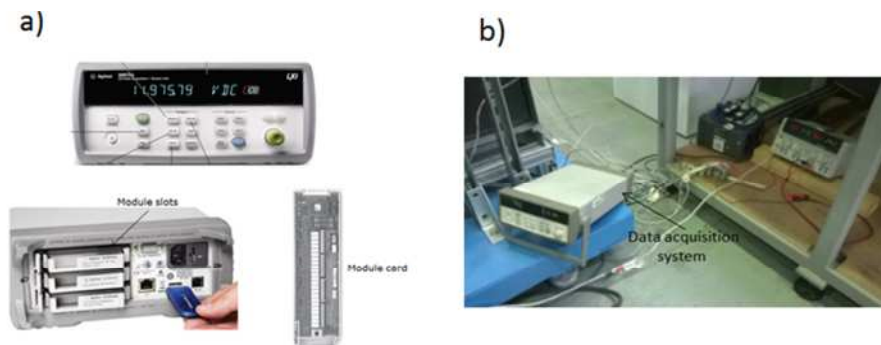


**Figure 7-30: Agilent 34907A data acquisition system- a) Different views of the Agilent 34907A data acquisition system (Source: [307]), b) data acquisition system during ORC system operation.**

### 7.4.2 Temperature Measurements

Temperature measurements were performed at various points around the system, as the configuration's schematic shows in Figure 7-1. The thermo-couples used were of a conventional K-type, similar to those described in Chapter 4, section 4.5.2.3.2, for the enhanced absorption experiment. These thermo-couples were calibrated at boiling point prior to installation. The uncertainty observed was around  $\pm 0.2$  °C.

### 7.4.3 Pressure Measurements

Four gauge-pressure transducers of two measurement ranges manufactured by RS were installed in different places on the ORC prototype, as indicated in the system's configuration schematic in Figure 7-1. Two of the transducers at the expander outlet and inlet of the condenser are able to measure gauge pressure between 0 and 10 bar. The other two transducers installed at the expander inlet and the outlet of the R1233zd(E) circulation pump are able to measure gauge pressure within the range of -1 to 24 bar. Both transducer types have an uncertainty of  $\pm 0.25\%$  of full scale. Uncertainties, as well as the conversion from gauge readings to absolute pressure readings were taken into account during the configuration of the pressure transducers in the data acquisition interface. In addition, initial real time comparison took place during system operation, by comparing the pressure readings transmitted and the connected charging manifold. The uncertainties observed were found to be between  $\pm 0.10$  and  $\pm 0.13\%$ . Table 7.9 lists the general specifications for the pressure transducers used and Figure 7-31 shows two pressure transducers installed on the ORC prototype.

**Table 7.9: General specifications for the ORC prototype pressure transducers.**

	Type 1	Type 2
Quantity	2	2
Pressure transducer range	0 to 10	-1 to 24
Manufacturer	RS [200]	RS [308]
Input [V DC]	9 to 32	12 to 36
Output [mA]	4 to 20	4 to 20
Temperature range [°C]	-20 to 135	-20 to 125



**Figure 7-31: Pressure transducers installed on the ORC prototype.**

#### 7.4.4 Flow Rate Measurements

Two variable area flow meters from different manufacturers and with different capabilities were utilised in the ORC prototype to measure the R1233zd(E) refrigerant flow rate around the system and the cooling water flow rate supplied by the chiller to the condenser. The principle of variable area flow meter operation is to measure a float position in a precision machined tapered tube, as shown in Figure 7-32. When the fluid flows inside the tube, it raises the float up the tube until the up-thrust from the flow reaches equilibrium with the weight of the float.

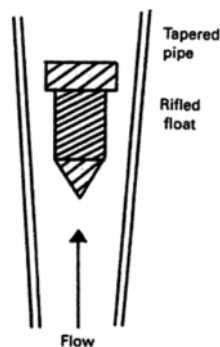


**Figure 7-32: Variable area flow meter principle. (Source:[309])**

However, in the case of the R1233zd(E) flow meter utilised, a magnetic electron beam was welded in the float casing, thus driving the external indicator to display the flow rate. Figure 7-33 shows the R1233zd(E) flow meter as manufactured and customised by Roxspur [310], specifically according to the refrigerant properties. The flow meter is able to operate under extreme working conditions

and is capable of measuring flow rates within the range of 50 to 500 L/h and with an uncertainty of  $\pm 2\%$  of full scale deflection.



**Figure 7-33: R1233zd(E) flow meter, Platon FGMT154L.**

Figure 7-34 shows the condenser cooling water flow meter installed on the chiller outlet's piping arrangement. The flow meter is a transparent, scaled acrylic tube with a stainless steel float, manufactured by Key Instruments [311]. The flow meter is capable of operating at maximum pressure and temperatures of 6.9 bar and 65°C, respectively. It is also able to measure water flow rates from 0.5 L/min to 20 L/min, with an uncertainty of  $\pm 3\%$  of full scale.



**Figure 7-34: Condenser cooling water flow meter, Key Instrument FR4500.**

#### 7.4.5 Tachometer

The rotational speed of the expander was measured using a digital optical non-contacting tachometer, capable of measuring RPM speeds within the range of 0.19 to 100,000 RPM, with an uncertainty of 0.05% as shown in Figure 7-35. To allow the tachometer to track the rotation and ensure high accuracy readings, a black electrical insulation tape was affixed to the expander clutch wheel, as shown in Figure 7-35 (b).

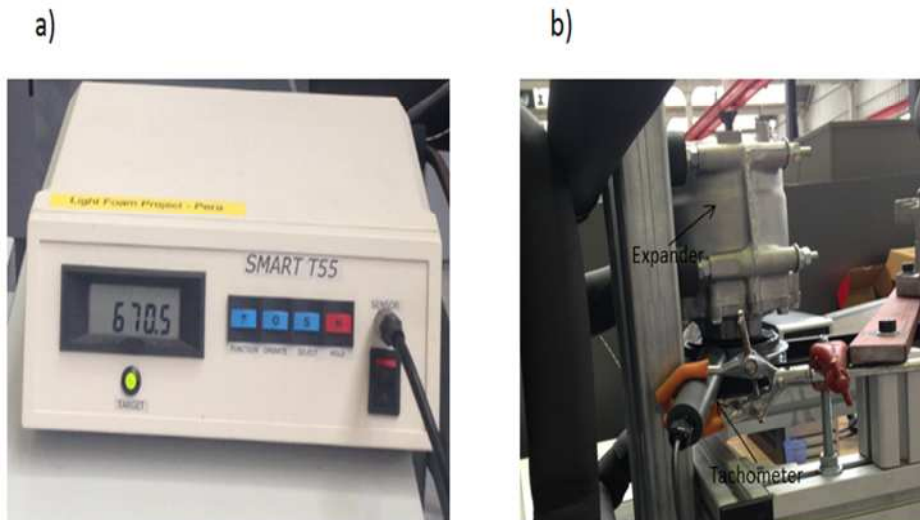


**Figure 7-35: Smart T55 digital tachometer- a) tachometer receiver, and b) tachometer measuring the rotational speed of the expander.**

#### 7.4.6 Electronic Load

The electrical load used to measure the electricity output from the ORC system was a dummy DC load designed to generate electricity demands similar to those found in different applications for testing purposes. The load was hired from Telonic, UK [312], and consists of two units shown in Figure 7-36. The PLZ1004W, which is the main unit, is capable of handling up to 1 kW electrical power and 200 amps was coupled to the PLZ2004WB booster unit, allowing the load to handle up to 9 kW electrical power and 1800 amps. The load is capable of operating in different modes, such as constant power, constant voltage, constant current, constant resistance, and combinations of these parameters.



**Figure 7-36: PLZ1004W and PLZ2004WB DC dummy load.**

All the components described above were installed in a frame to form the R1233zd(E) ORC prototype. Figure 7-37 and Figure 7-38 show views of the prototype during construction, while different views of the final prototype system are shown in Figure 7-39 to Figure 7-41.



**Figure 7-37: Side view of the ORC prototype during construction.**



Figure 7-38: Back view of the ORC prototype during construction.

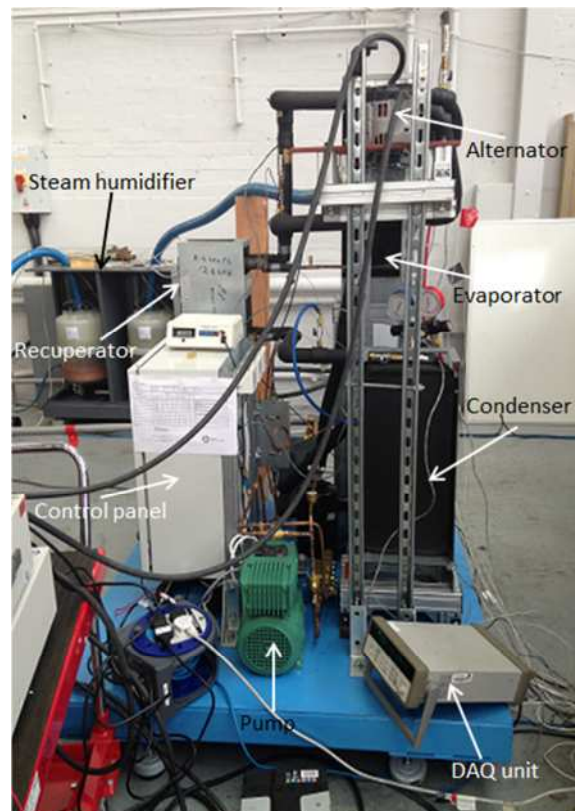


Figure 7-39: Front view of the final ORC prototype.



**Figure 7-40: Back view of the final ORC prototype.**



**Figure 7-41: General view of the final ORC prototype.**

## 7.5 Summary

This chapter has presented a comprehensive overview of the configuration and final illustrations of the R1233zd(E) ORC prototype system. It has also provided a detailed description of the system components' specifications and their operating principles. The scroll expander's modification procedure was explained and illustrated, and the options considered for the electric generator were discussed. Measurement devices installed on the prototype system were presented, along with their measurement capabilities and uncertainties.

In addition to the above, the chapter presents the BPHEs characteristics provided by the heat exchangers manufacturer, based on the refrigerant properties supplied and implemented in the study. Due to the fact that R1233zd(E) has never been modelled for ORC systems or heat exchangers, it was essential to carry out heat exchanger modelling as part of the current research and also to validate the BPHEs characteristics' provided by the manufacturer. The heat exchanger modelling was carried out using the LMTD approach and the inputs and assumptions made, the outputs, and the governing equations were presented and explained. The output results were compared to the characteristics of the heat exchangers provided by the manufacturer. The comparison showed that both results are in fairly good agreement with slight deviation. The similarity between the results is a good indication of the proposed model's validity and also presents an indication of the average R1233zd(E) heat exchanger size, since it has never been modelled before in the literature.

## Chapter 8 : Experimental Investigation of The R1233zd(E) ORC Prototype System

---

### 8.1 Introduction

This chapter describes the experimental testing performed on the expander-alternator preliminary test bench and the main R1233zd(E) ORC prototype system. The chapter presents the test procedures, experimental parameters adopted and the evaluation and analysis of the results obtained via experimentation throughout the phases of its progress. The chapter also identifies the system limitations and demonstrates the experimentally obtained performance improvement towards the thermodynamic model performance characteristics by mean of three simulated cases. Finally, the R1233zd(E) prototype system's outputs were compared to similar parameters obtained from equivalent ORC systems from literatures.

### 8.2 Compressed Air Open Loop Expander-Alternator Experimental System

#### 8.2.1 Experimental System Configuration and Description

A preliminary experimental test was carried out to evaluate the operation and electrical output of the scroll expander connected to the proposed automotive alternator via a V-belt; compressed air was used as the working fluid in an open loop test bench system. The schematic of this is shown in Figure 8-1. An open loop configuration was adopted to allow easy adjustment of the selected operating pressure without restrictions. Compressed air was applied as the working fluid, mainly because of its availability and due to the fact that it is safe for release into the atmosphere. Therefore, the system configuration was simpler. Moreover, air has very well-known thermodynamic properties that could be assumed to behave

like an ideal gas, thus allowing simpler and more accurate experimental data analysis.

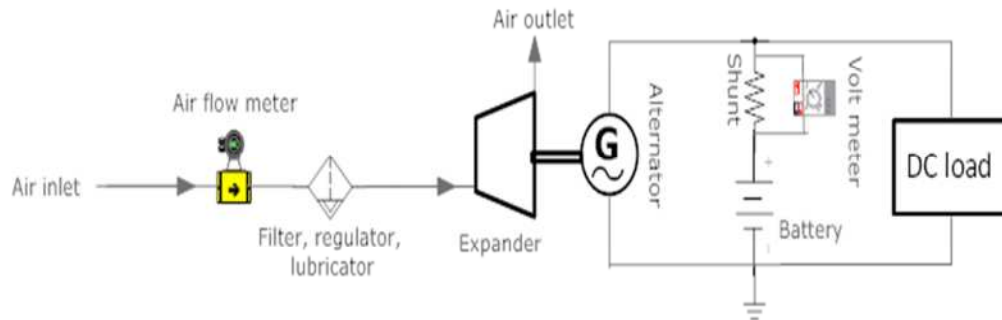


**Figure 8-1: Schematic of the compressed air open loop expander-alternator test bench.**

As shown in Figure 8-1, the system consists of a workshop compressed air supply line, sourced from the workshop's central air compressor. This compressed air line is capable of supplying compressed air at a maximum pressure of 7 bar. This may be regulated at the required operating pressure. The compressed air was delivered to the expander through system components using rubber hoses capable of withstanding the operating pressure. The air flow rate was measured by a digital air flow sensor before being directed to the filter-regulator-lubricator unit. The function of the latter is to strain the compressed air and eliminate any particles and liquids, regulate the air pressure delivered to the expander at a constant output rate, and add controlled amounts of oil to the air stream, thus minimising friction in the expander. After the air has received this treatment, it is directed to the expander where it expands to atmospheric pressure, causing the expander to spin. This consequently rotates the alternator before exiting the test bench system.

The spinning alternator is connected to the external adjustable electrical load, which allows measurements of the system's electrical power output, alongside the voltage and amperage. An automotive battery is also integrated within the circuit to initially energise the rotor electromagnet coil and generate the magnetic field. Moreover, it is important to note that the fully-charged

battery functions as a capacitor, where the alternator utilised is a 3-phase alternator which produces an AC current rectified to DC. As a result, there will be various ripples in the voltage output that require smoothing, in order to provide a steady DC voltage output [313, 314]. A shunt resistor of 60mV/200A and a voltmeter were connected to the battery loop in order to measure the battery current. This measured current may flow in or out of the battery, depending on the voltage produced by the electric power generator where it flows into the battery, when the generator's voltage is higher than the battery voltage and vice-versa.

### 8.2.2 System Components

The major system components are the same as those utilised for the R1233zd(E) ORC prototype system. Besides these components, the system comprises the digital air flow sensor manufactured by SMC, Japan [315]. This air flow sensor is capable of measuring flow rates in the range of 150 l/min to 3000 l/min and is equipped with an LED display, as shown in Figure 8-2.



**Figure 8-2: SMC-PF2A703H digital air flow sensor. (source:[315])**

The system also includes the filter-regulator- lubricator unit, shown in Figure 8-3 and manufactured by Camozzi [316]. This unit has the capability to handle inlet pressures of up to 16 bar and supply outlet pressure of up to 10 bar.



**Figure 8-3: Camozzi C401-D000 air filter regulator lubricator unit. (source: [316]).**

Two portable K-type thermocouples were used to monitor air temperature at the expander's inlet and outlet.

### 8.2.3 Test Procedure

Figure 8-4 shows the compressed air open loop experimental test bench assembly.

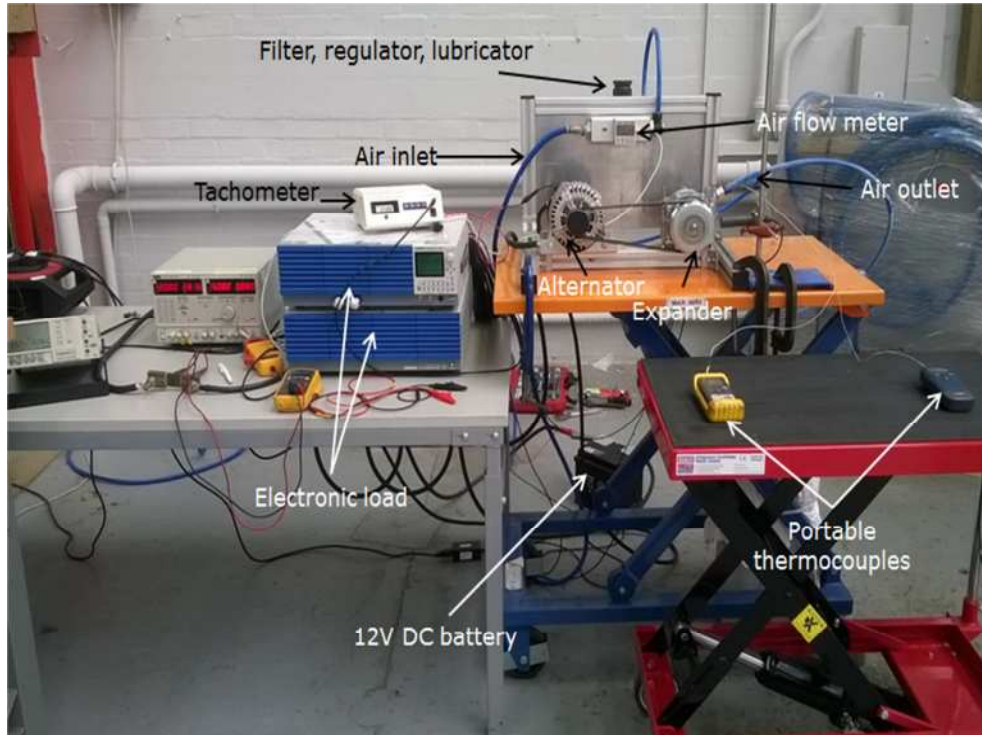


**Figure 8-4: Compressed air open loop expander-alternator test bench set-up.**

The experimental test aims to run the system at different air pressures from 3 to 6 bar and to examine the performance of the scroll expander and the power output obtained. The main challenge encountered during the test was the fluctuation in air supply resulting in obvious pressure drops, mainly caused by the upstream compressor cycling to suit demand during the test. Consequently, the system never operated in a continuous steady state. For this reason, each run lasted for several minutes to ensure sufficient air supply for reasonable power output.

The measurements of the experimental tests were recorded manually; where each recorded point represented an independent test. This was mainly due to the short duration of the tests and the

fact that all utilised measuring devices were equipped with displays that permitted the accurate monitoring of operating parameters. The test procedure conducted was as follows:

- Set the required test load on the adjustable load.
- Set the required test pressure by adjusting the regulator on the workshop's main compressed air line.
- Record the time and the set test pressure in a prepared log book.
- Open the air inlet valve to allow air into the system.
- When the expander and alternator rotate, observe the voltage and current readings until they reach a steady state. Record air flow rate, voltage, current and temperatures.
- Once the measurement record has been established, the air inlet valve is shut down and the test is complete.

#### 8.2.4 Experimental Data Reduction

The performance of the expander and the electric generator was evaluated from the experimental recorded data using Microsoft Excel, aided by REFPROP 9.0 for air properties. The air inlet and outlet enthalpies were determined by the known inlet and outlet temperatures and pressures. The recorded air volumetric flow rate in l/min was converted into mass flow rate kg/s through knowledge of the air inlet density as:

$$\dot{m}_{air} = \left( \frac{\dot{V}_{air}}{60} / 1000 \right) \rho_{air} \quad (8.1)$$

The expander's power output and isentropic efficiency were also calculated for air using equations (6.37) and (6.22), respectively.

It was assumed that the transmission V-belt connecting the expander and the electric generator has an efficiency of 90%, where the initial V-belt efficiency is in the range of 94%-97%, with

the possibility of deteriorating by 5%. Then the power transmitted to the electric generator by the V-belt will be:

$$W_{Trans} = W_{Exp} \eta_{Belt} \quad (8.2)$$

The electrical power output from the system was calculated from the alternator's electrical circuit shown in the schematic of the system in Figure 8-1 as the total power consumed by the adjustable load and the power directed to the battery. The power consumed by the load is simply calculated by the measured voltage and current displayed on the load screen, as shown in Figure 8-5, where:

$$W_{Eload} = I_{Load} V_{Load} \quad (8.3)$$

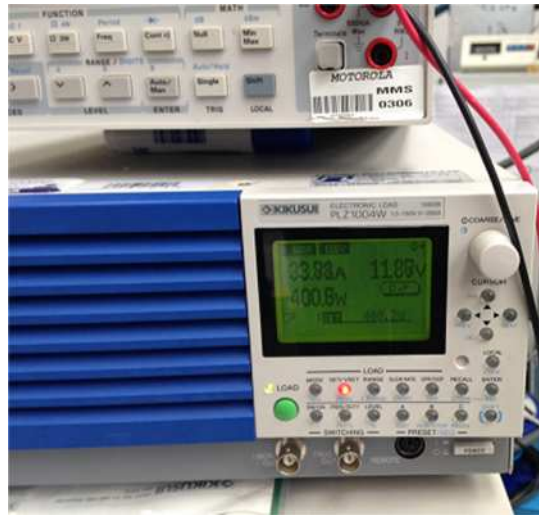


**Figure 8-5: Voltage and current displayed on the adjustable load screen.**

The power directed to the battery is:

$$W_{Ebattery} = I_{Battery} V_{Battery} \quad (8.4)$$

Where  $I_{Battery}$  is calculated by measuring the voltage across the shunt as:

$$I_{Battery} = \frac{V_{Shunt}}{R_{Shunt}} \quad (8.5)$$

And  $R_{Shunt}$  is the shunt-rated resistance at 60mV/200A. However, the total electric power produced and the alternator efficiency, are given respectively as:

$$W_E = W_{Eload} + W_{Ebattery} \quad (8.6)$$

$$\eta_{Electgen} = \frac{W_E}{W_{Trans}} \quad (8.7)$$

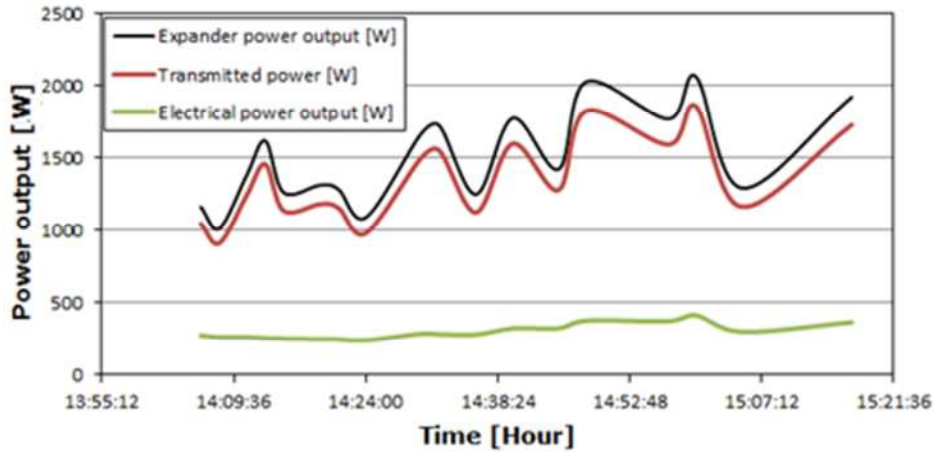
### 8.2.5 Results and Analysis

Table 8.1 presents the complete test conditions and analysed results. The recorded currents, voltage, and power outputs are included in Appendix E.1. The results generally show very high expander isentropic efficiency. However, although low alternator efficiencies were observed, the electric power outputs under all tested conditions were able to fulfil the power demands set on the adjustable electric load. Test number 16 in Table 8.1, represents the optimum result obtained, where the system delivered maximum electric power output. The expander produced 2 kW, with an isentropic efficiency of 96.33%. A small portion of this power was lost through the transmission mechanism delivering 1.86 kW to the alternator. However, a larger portion of this power was also lost due to the alternator's low efficiency. The power converted into useful electricity amounted to just 416.02W, indicating a low alternator efficiency of only 22.39%. It is important to note here that the electric power output was obtained at the maximum tested air inlet pressure of 5.4 bar, which subsequently produced the maximum recorded expander power output. Throughout the experiment, the expander air outlet temperature at atmospheric pressure was shown to be very low.

**Table 8.1: Compressed air open loop expander-alternator test results.**

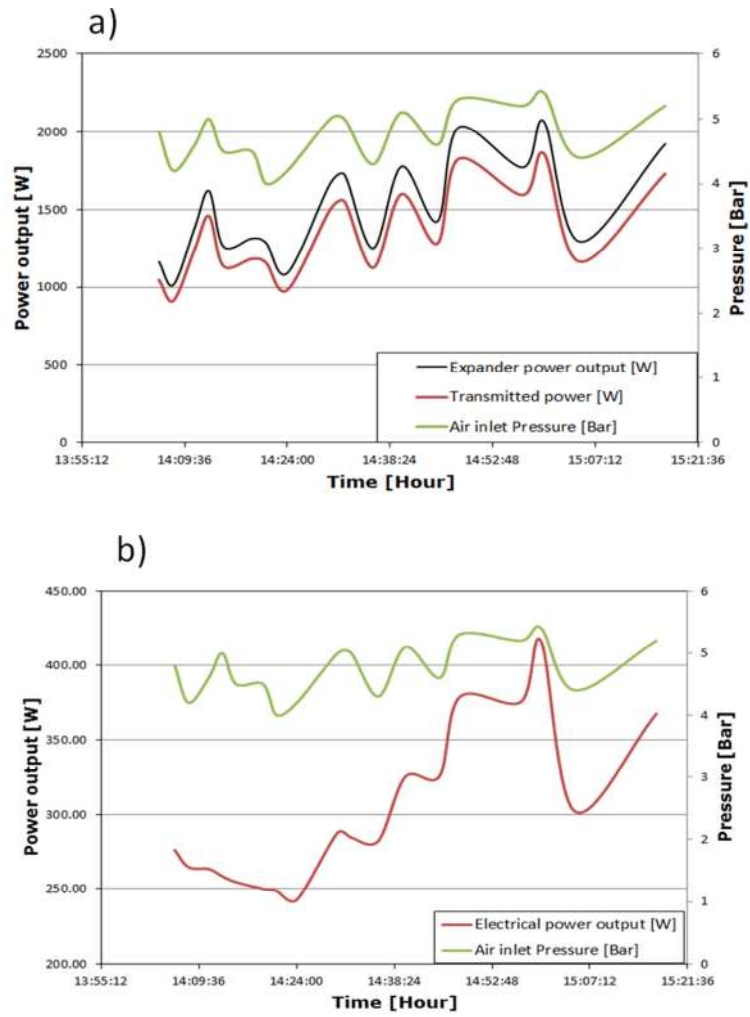
Test	Load power setting [W]	Air inlet Pressure Bar	Pressure ratio [-]	Air volumetric flow Rate [l/min]	Expander rotational speed [RPM]	Air inlet temperature [°C]	Air outlet temperature [°C]	Expander power output [W]	Expander isentropic efficiency [%]	Transmitted power [W]	Electric power output [W]	Alternator efficiency [%]
1	200	4.80	4.66	1000	3580	16.20	3.30	1163.32	93.61	1046.98	276.12	26.37
2	200	4.20	4.08	715	2650	16.60	-0.90	1014.38	96.27	912.94	264.67	28.99
3	200	4.60	4.47	840	2895	16.50	-2.10	1384.15	96.06	1245.74	263.40	21.14
4	200	5.00	4.85	930	3070	16.30	-1.90	1620.36	95.46	1458.32	258.49	17.73
5	200	4.50	4.37	805	2830	16.40	-1.70	1263.17	96.05	1136.85	254.57	22.39
6	200	4.50	4.37	805	2850	16.50	-2.30	1313.98	96.23	1182.59	250.08	21.15
7	200	4.00	3.88	910	2990	16.30	-1.90	1285.65	96.68	1157.08	248.75	21.50
8	200	4.20	4.08	705	2580	16.20	-2.80	1091.23	96.62	982.11	243.04	24.75
9	243	5.00	4.85	890	2920	16.30	-3.20	1667.60	95.82	1500.84	287.78	19.17
10	243	5.00	4.85	920	2994	16.10	-3.40	1724.88	95.81	1552.39	284.49	18.33
11	243	4.30	4.17	720	2580	16.70	-4.10	1250.17	96.87	1125.15	282.27	25.09
12	291	5.10	4.95	870	2730	16.30	-4.50	1777.22	96.02	1599.50	325.45	20.35
13	291	4.60	4.47	680	2340	16.70	-6.70	1422.81	97.03	1280.53	325.66	25.43
14	342	5.30	5.15	840	2540	16.60	-7.00	2029.09	96.42	1826.18	378.91	20.75
15	342	5.20	5.05	800	2380	16.80	-5.30	1770.84	96.22	1593.76	375.53	23.56
16	342	5.40	5.24	840	2430	16.70	-6.90	2064.60	96.33	1858.14	416.02	22.39
17	276	4.40	4.27	660	2320	16.90	-6.00	1293.50	97.14	1164.15	302.02	25.94
18	342	5.20	5.05	880	2740	16.40	-5.40	1922.64	96.15	1730.37	367.63	21.25

Figure 8-6 presents the variation in the power generation profile along the test timeline. As shown, the electric power produced by the alternator was very low, compared to the power generated by the expander and the power transmitted to the alternator via the transmission belt. This is an indication of low alternator efficiency.

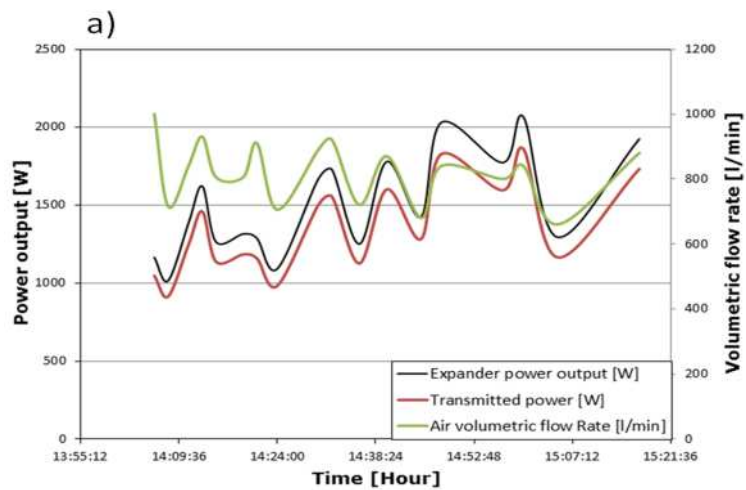


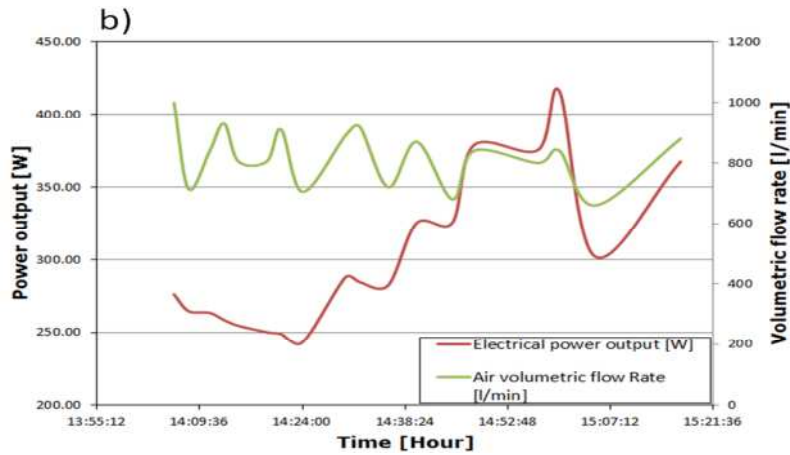
**Figure 8-6: Compressed air open loop expander-alternator test's power generation profile.**

Figure 8-7 (a) shows the variation in expander-generated and transmitted power, along with the variation in expander inlet pressure. The relationship indicates that the expander power output is directly proportional to the expander inlet pressure. Figure 8-7 (b) shows the relationship between the expander inlet pressure and the alternator's electric output. The alternator's electric power output indicates proportional dependency on the expander inlet pressure. However, this relationship is not as strong as what is observed in Figure 8-7 (a), due to the lower electric conversion efficiency. Similar behaviour was noted for power output variation in relation to air flow rate, as shown in Figure 8-8.



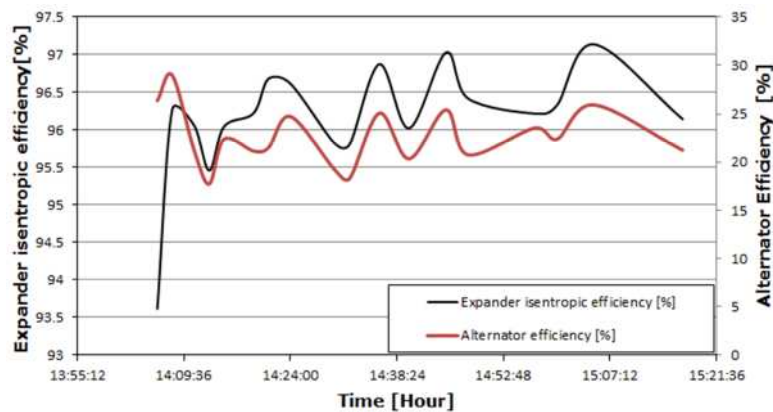
**Figure 8-7: Generated power variation with air inlet pressure- a) power generated and transmitted by the expander, and b) the alternator's electric power output.**





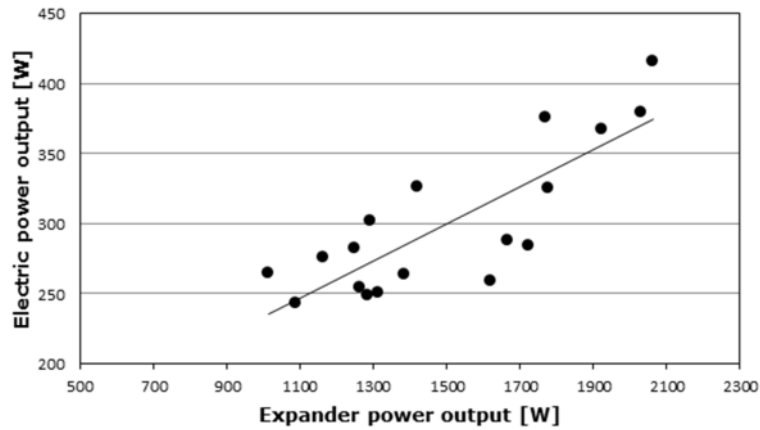
**Figure 8-8: Variation in generated power with air flow rate- a) Power generated and transmitted by the expander, and b) the alternator’s electric power output.**

Figure 8-9 presents the expander’s isentropic efficiency and the alternator’s efficiency throughout the experiment. As shown, both efficiencies followed a similar pattern, but at different levels, where the lowest expander isentropic efficiency was 93.6% and the maximum was 97.1%, with an average efficiency of 96.15%. On the other hand, the alternator’s efficiencies are shown to have been low throughout the experiment, where the lowest alternator efficiency was 17.7% and the maximum observed efficiency was 29%, with an average of 22.57%.



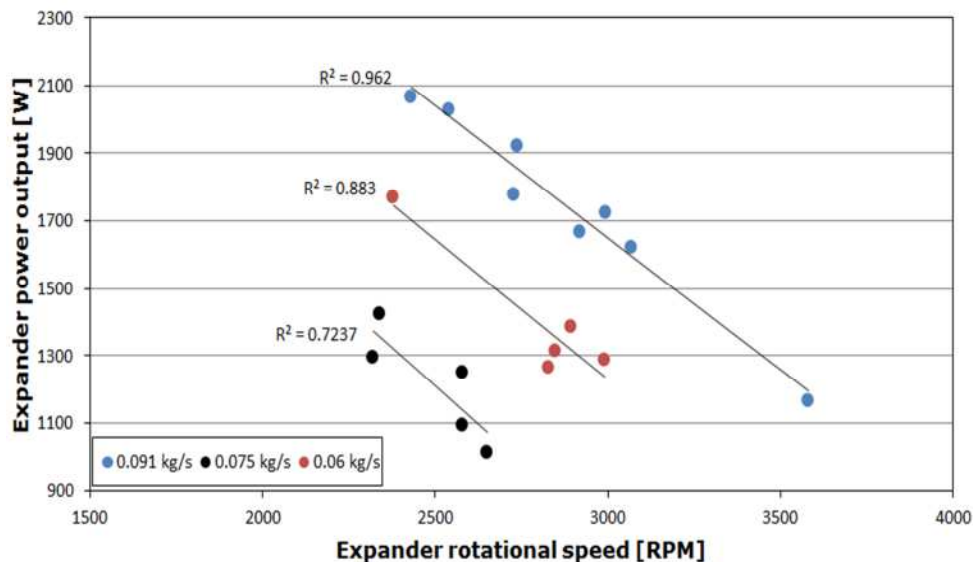
**Figure 8-9: The expander’s isentropic efficiency and the alternator’s efficiency.**

Figure 8-10 shows the relationship between the expander’s power output and the alternator’s electric power output. Despite the low electric power converted, the results show a coefficient of determination of 67%, indicating the value of the relationship.



**Figure 8-10: The relationship between the expander’s power output and the alternator’s electric power output.**

The expander’s power output showed strong dependency on the expander’s rotational speed which is also related to the air mass flow rate, as shown in Figure 8-11. To demonstrate this relationship, the recorded results were categorised into three groups, depending on the air mass flow rate, measured as  $0.06 \text{ kg/s} \pm 0.005$ ,  $0.075 \pm 0.005$ , and  $0.091 \pm 0.005$ . For each mass flow rate, the expander’s power output was at its maximum at the minimum rotational speed and reduced gradually as the rotational speed increased. However, throughout the experiment, the expander’s rotational speed varied between 2320 RPM to 3580 RPM.



**Figure 8-11: The relationship between the expander’s power output and the expander’s rotational speed.**

The temperature profile across the expander is shown in Figure 8-12. As can be seen, the air temperature at the expander inlet was

steady throughout the experiment at an average of 16.5°C. The outlet temperature is shown to have varied, depending on the operating characteristics, where the minimum observed temperature was -7°C and the maximum was 3.30°C.

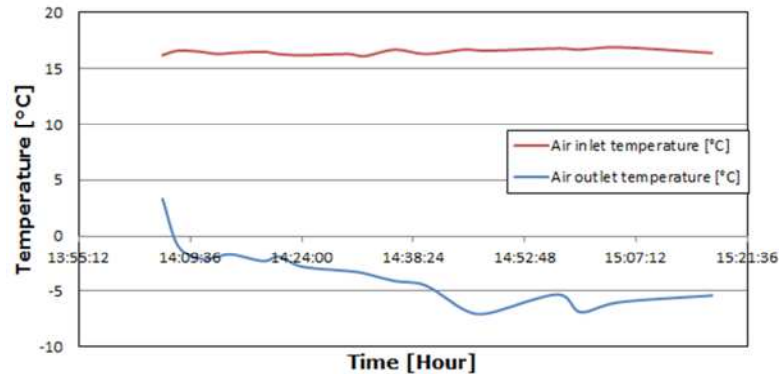


**Figure 8-12: Variation in air temperature across the expander.**

## 8.2.6 Compressed Air Open Loop Expander-Alternator

### Experiment Conclusion

A preliminary test was carried out to examine the performance of the scroll expander and the automotive electric generator's power output in a specially constructed test bench. The results show that the expander operates at high isentropic efficiency and produces reasonable power output, which is dependent on the expander's pressure ratio and the air flow rate. The electric power generator is shown to have had very low efficiency, compared to the expander, which consequently resulted in low electric power output. This suggests either large power losses through the transmission mechanism, or a speed mismatch between the expander and the electric power generator. The maximum electric power produced was 416W, with an alternator efficiency of 22.39%, when the expander produced a power output of 2 kW, with an isentropic efficiency of 96.33%.

This observed performance could be reflected in the case of the R1233zd(E) ORC prototype system when the alternator is used as the electric power generator. Presuming that the expander was able to produce a 5 kW power output, the losses by transmission would

reduce the power delivered to the alternator to 4.5 kW. Subsequently, an alternator with an efficiency of 22.39% would yield 1.007 kW electric power output.

For the above reason, the automotive DC motor is to be used as the primary electric power generator in the first experiment, on the R1233zd(E) ORC prototype system.

### **8.3 The R1233zd(E) ORC Prototype System Experiments**

Several experiments were conducted on the R1233zd(E) ORC prototype system. Two sets of experiments, which represent the best performance obtained from the system, have been analysed and presented in this thesis. In the first experiment, two tests were conducted and the automotive DC electric motor was used as the electric power generator. Due to poor system performance as a result of a rotational speed mismatch between the expander and the DC motor, and the physical position of the refrigerant which prevented it from moving freely around the system, it was decided that the system's piping should be modified to ensure free movement of the refrigerant, consequently altering the heat exchanger heights. After these modifications were made, the second experiment was conducted. However, the DC motor was replaced by the automotive alternator and battery arrangement in order to evaluate any improvement it may make to the electric power output.

#### **8.3.1 Prototype System Initiation and Starting Procedure**

Before and during the commencement of the tests on the R1233zd(E) ORC prototype system, the following procedure, including precautionary measures, was followed to ensure safe and proper operation:

- Checking around the ORC prototype system to ensure there were no loose components and all the main valves were fully open.
- Before charging the R1233zd(E) refrigerant, pressurising the prototype system with nitrogen of up to 10 bar and monitoring via the connected DAQ unit through the interface software for about an hour, for obvious leaks. Once it was confirmed there was no leakage, leak testing by means of a soap and water solution on every pipe and joint in the system. Having established that no leakage had occurred, increasing the pressure on the system to 15 bar, and then monitoring the system for another hour through the computer interface. After the integrity of the experimental rig had been confirmed, releasing the nitrogen from it. At lower pressure, vacuuming the rig to remove any remaining nitrogen.
- After integrity had been confirmed, closing all by-pass valves on the prototype system and establishing that all main-line valves were fully open.
- Confirming that the temperature thermocouples and pressure transducers fitted properly in positions around the system and observing transmitted signals via the DAQ unit interface software, in order to verify the functionality of the instrumentation.
- Ventilating the lab space to allow removal of any refrigerant emission in the event of leakage, even though R1233zd(E) is a non-hazardous substance. This step was necessary as there might be exceptional cases of allergy due to the potential sensitivity of personnel involved in the test.

- Having the system charged with R1233zd(E) by a qualified sub-contractor.
- Supplying the chiller with clean water from the mains supply through the piping arrangement. Switching on the chiller and setting the temperature for water delivery on the front panel. Once the required temperature had been achieved, opening the chiller outlet valve to deliver cooling water to the condenser and set the chiller outlet flow rate using the water flowmeter.
- Filling the steam humidifier with clean water from the mains supply via the connected hose and valve arrangement. Switching on the front control panel of the humidifier and setting the heating capacity percentage, along with the steam supply temperature kept at its maximum of 104°C. However, the maximum steam supply observed during the test was in the range of 93 to 101°C, due to the humidifier's cut-in and cut-out sequence.
- Preparing the test log book and starting the data-logging process using a connected personal computer. Saving this information in a file for data analysis at a later point in time. It is important to underline here that the DAQ unit only allowed the monitoring and recording of pressure and temperature readings. Other test data were recorded manually in the log book at intervals, once a steady operating state was established. These data consisted of cooling water and R1233zd(E) mass flow rates, boiler supply capacity and mass flow rate, expander rotational speed and the external adjustable load's set load, voltage, amperage, and battery voltmeter readings.

- Once the steam humidifier was warmed up and running at the desired capacity and temperature, switching on the ORC prototype system control panel and turning on the R1233zd(E) refrigerant circulation pump using the On/Off-speed control knob. The pump speed was kept to a minimum at the beginning of the test and raised steadily and gradually while monitoring the R1233zd(E) flow meter, until the desired flow rate was established and differential pressure created.
- At this stage, all the system components were involved in performing their duty to operate the ORC prototype system. When the R1233zd(E) refrigerant in the evaporator had vaporised, due to the heat supplied by the boiler, the expander became operational and subsequently rotated the connected electric power generator to generate electric power output.

Once the expander and alternator are rotating, the key objective is to maximise the expander's rotational speed and subsequently, the expander power output, which will result in the maximum attainable electric power output from the generator. However, the expander's rotational speed and power output are proportionally dependent on the expander's inlet pressure and the pressure ratio across the expander.

### 8.3.2 **Prototype System Shutdown Procedure**

The shutdown procedure involves general safety checks carried out after the experimental tests have been completed, in order to ensure a safe experimental system and to avoid any incidents after the system has shut down. First, the steam humidifier is shutdown from its front panel and left to cool down. This step will cause the expander and alternator arrangement to slow down until they stop rotating, due to the absence of a heat supply. The cooling water and the R1233zd(E) are left to run for a while to allow condensation

of the refrigerant and to cool the hot surfaces. When the monitored system temperatures have cooled down, the pump is turned off from the prototype system control panel and the condenser's cooling water inlet valve is closed. The same procedure is applied to the steam humidifier valves supplying the evaporator. The chiller is then switched off from the front panel. After that, all power supplies to the boiler, chiller, and prototype system are to be isolated and the shutdown procedure is complete.

### 8.3.3 Experimental Data Reduction

Recalling the ORC prototype system schematic Figure 7-1 in the previous chapter, the heat input in the system's evaporator is given by:

$$\dot{Q}_{Evap} = \dot{m}_r(h_1 - h_9) \quad (8.8)$$

The useful heat provided by the steam humidifier can be calculated as:

$$\dot{Q}_{Steam} = \dot{m}_{steam}(h_{steam\ in} - h_{steam\ out}) \quad (8.9)$$

However, for the current experiments, this information was available and recorded from the steam humidifier control panel throughout the tests.

The R1233zd(E) mass flow rate was calculated using the refrigerant's density at the pump's exit, alongside the expander's power output, efficiency, and transmitted power. All were calculated similarly, as described in 8.2.4 but applied for R1233zd(E) at state point 8, and 2, 3 on the prototype system schematic, respectively.

The heat transferred in the recuperator heat exchanger is a product of the mass flow rate and the refrigerant's enthalpy change across the sides of the heat exchanger, where:

$$\dot{Q}_{Hex1} = \dot{m}_r(h_4 - h_5) \quad \text{for the low pressure side of the system} \quad (8.10)$$

And

$$\dot{Q}_{Hex2} = \dot{m}_r(h_9 - h_8) \quad \text{for the high pressure side of the system}$$

The heat rejected from the condenser by the cooling water supplied by the chiller is given by:

$$\dot{Q}_{Cond} = \dot{m}_r (h_6 - h_7) \quad (8.11)$$

The R1233zd(E) circulation pump input power is calculated as:

$$W_{Pump} = \dot{m}_r (h_8 - h_7) \quad (8.12)$$

And the pump efficiency is:

$$\eta_{Pump} = \frac{h_{8S} - h_7}{h_8 - h_7} \quad (8.13)$$

The system's net thermal power output is calculated as:

$$W_{Net} = W_{Exp} - W_{Pump} \quad (8.14)$$

And the prototype system's thermal efficiency becomes the ratio of the net thermal power output to the energy input into the evaporator:

$$\eta_{System} = \frac{W_{Net}}{\dot{Q}_{Evap}} \quad (8.15)$$

It is important to note that the system's electric power output is not thermodynamically related to the system's operating conditions and output, other than the expander's power output and the power transmitted by the transmission belt. This is similar to the system's electrical efficiency, which is related purely to the heat input from the heat source. However, the electric power output from the system could be determined in two ways, depending on the electric generator utilised. When the automotive alternator is used, the electric power output is calculated in a way similar to that presented in equations (8.3) to (8.6) for the preliminary test. When the automotive DC motor is used, the configuration of the expander-electric power generator becomes simpler, as illustrated in Figure 8-13 and the electric power output from the system becomes the load displayed on the adjustable load and given in equation (8.3).

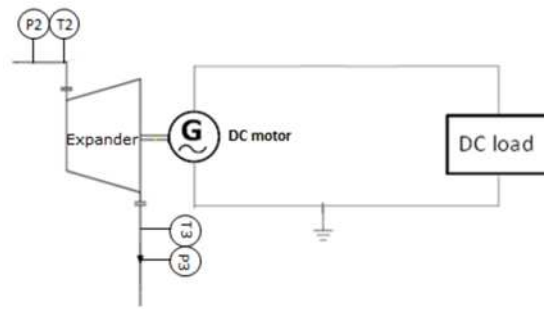


**Figure 8-13: Expander-DC electric power generator arrangement.**

And the prototype system's electrical efficiency becomes the ratio of the electric power output to the energy input from the steam humidifier heat source:

$$\eta_{Elect} = \frac{W_E}{\dot{Q}_{Boiler}} \quad (8.16)$$

### 8.3.4 Results and Analysis

The performance of each system component was obtained from the recorded data, analysed in a Matlab environment, using similar programme to that presented for the ORC system thermodynamic model, presented in Appendix C.5. The only difference is that the ORC prototype system analysis programme uses the experimentally obtained data as inputs to evaluate the performance of the system instead of the user defined inputs, as in the thermodynamic model. Due to the large amount of experimental data, only data points recorded in the log book were included in this thesis (see Appendix E.2). However, raw experimental data are available upon request.

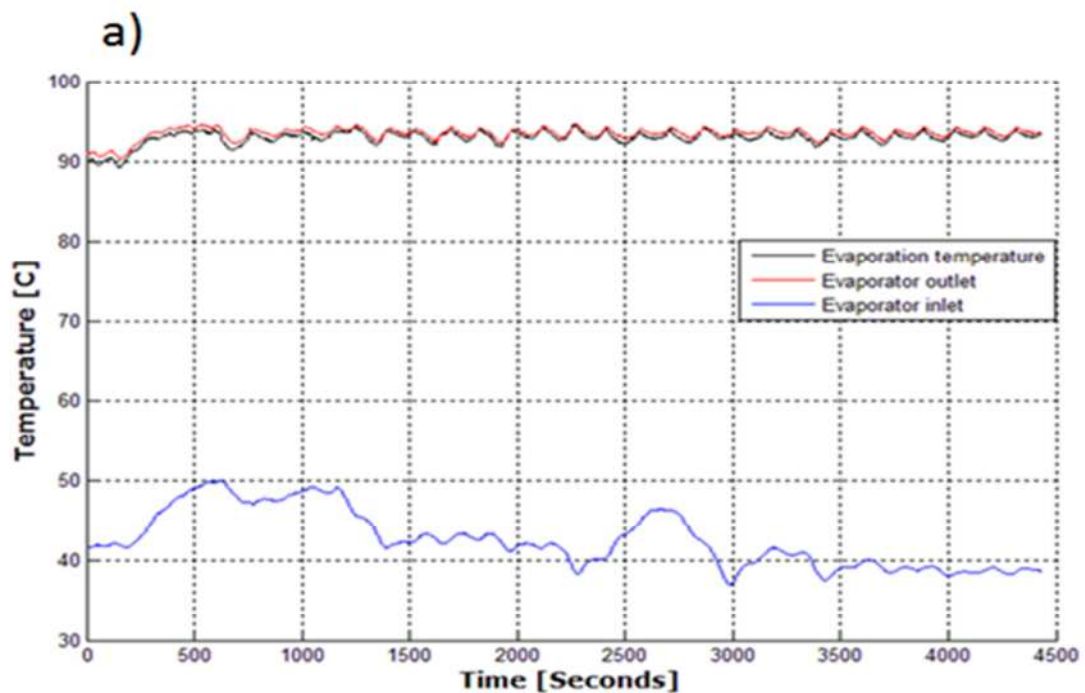
#### 8.3.4.1 Experiment 1

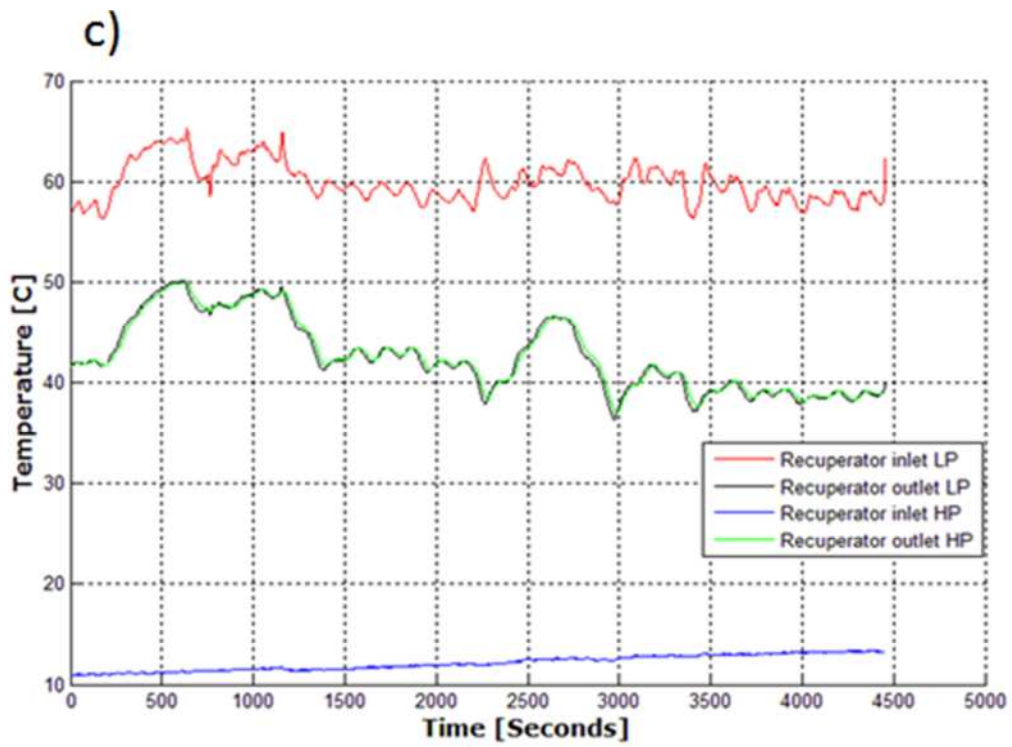
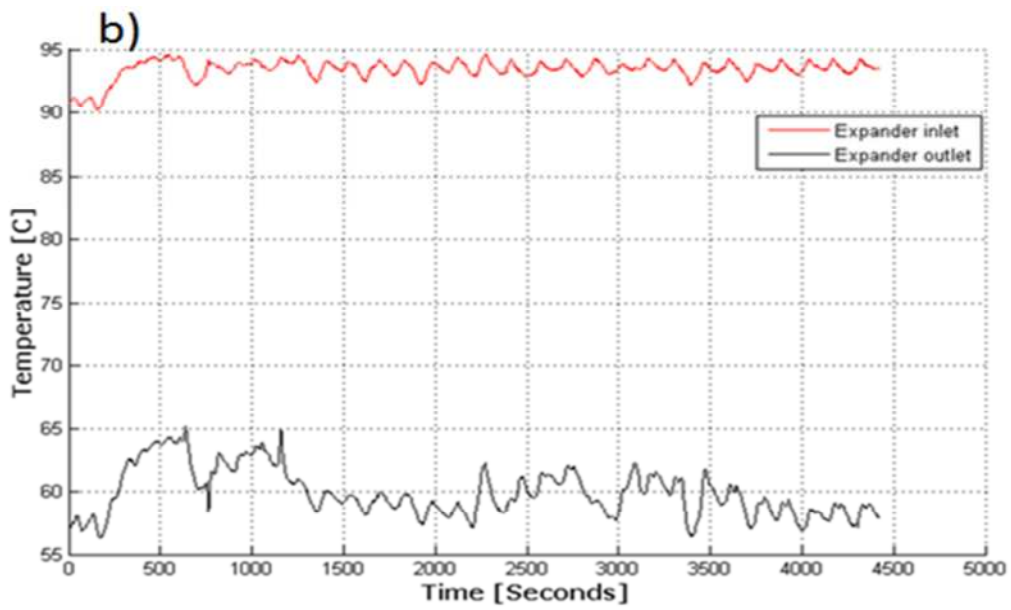
The experiment conducted consisted of two tests. The heat input has varied during the tests, while the steam temperature was set to maximum throughout the experiment and fluctuated from 95°C to 101°C. For the cooling water supply to the condenser, the flow rate was set at set at 20 l/min throughout the tests.

### 8.3.4.1.1 First Run

In this run, the heat input into the evaporator was increased gradually throughout the test. On the condenser side, the cooling water supply was set at 10°C at the chiller throughout the test. Different mass flow rates of R1233zd(E) were set during the test, where it was increased gradually to its maximum, before it was reduced again.

#### 8.3.4.1.1.1 Temperature and Pressure Profiles





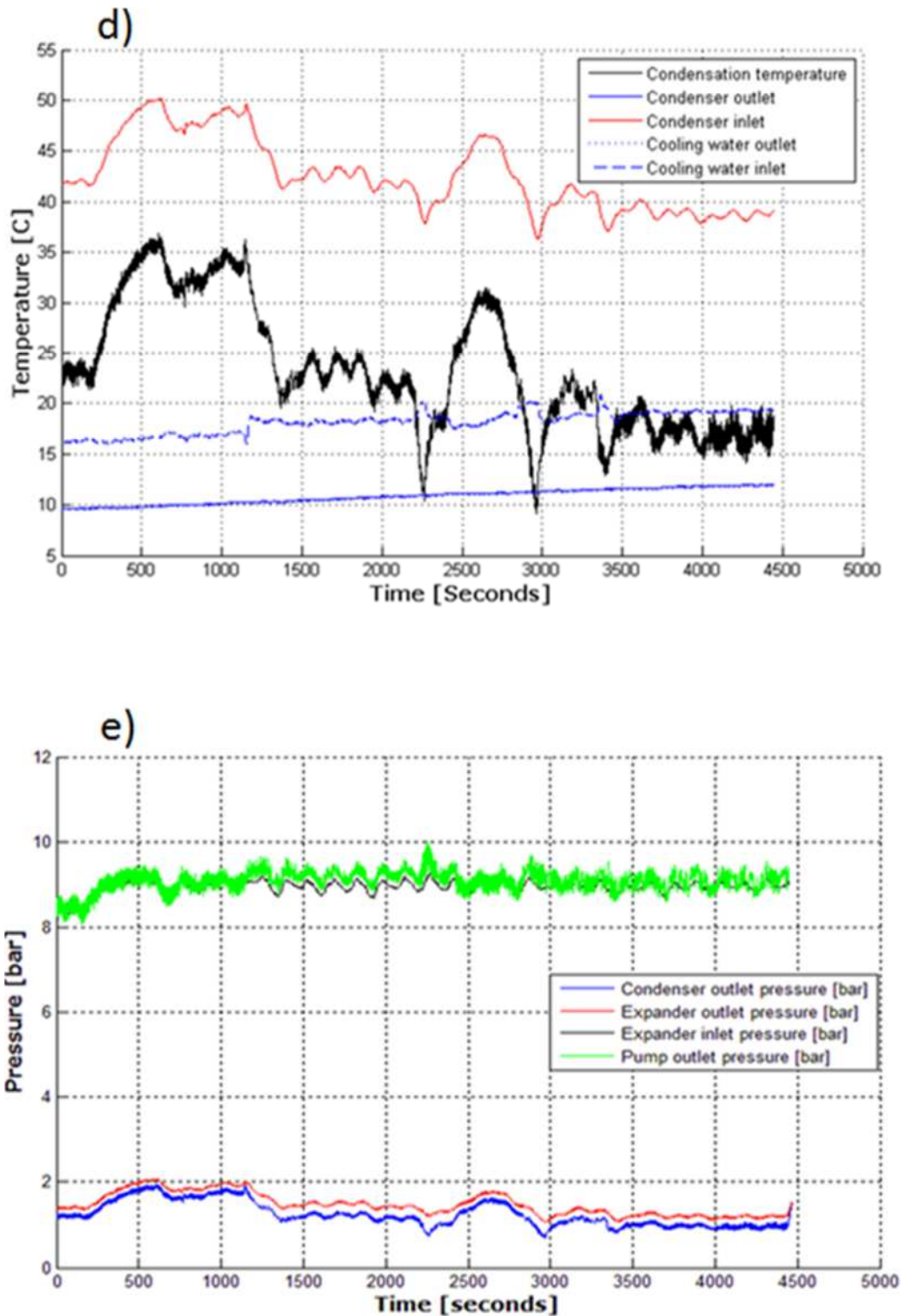


**Figure 8-14: ORC experiment 1, first run - Temperature and pressure profiles.**

Figure 8-14 (a) shows the evaporator's temperature profile along the test timeline. As can be seen, the evaporator's outlet temperature is super-heated to slightly above the evaporation temperature throughout the test. The evaporator's outlet

temperature varied between 90.20°C and 94.61°C, while the evaporation temperature was in the range of 89.26°C to 94.61°C. The evaporator's inlet temperature was lower by almost half, compared to the evaporator's exit temperature, ranging between 36.97°C to 50.06°C.

Figure 8-14 (b) presents the expander's temperature profile. The super-heated R1233zd(E) stream from the evaporator outlet expands through the scroll expander and exits at temperatures in the range of 56.32°C to 65.17°C.

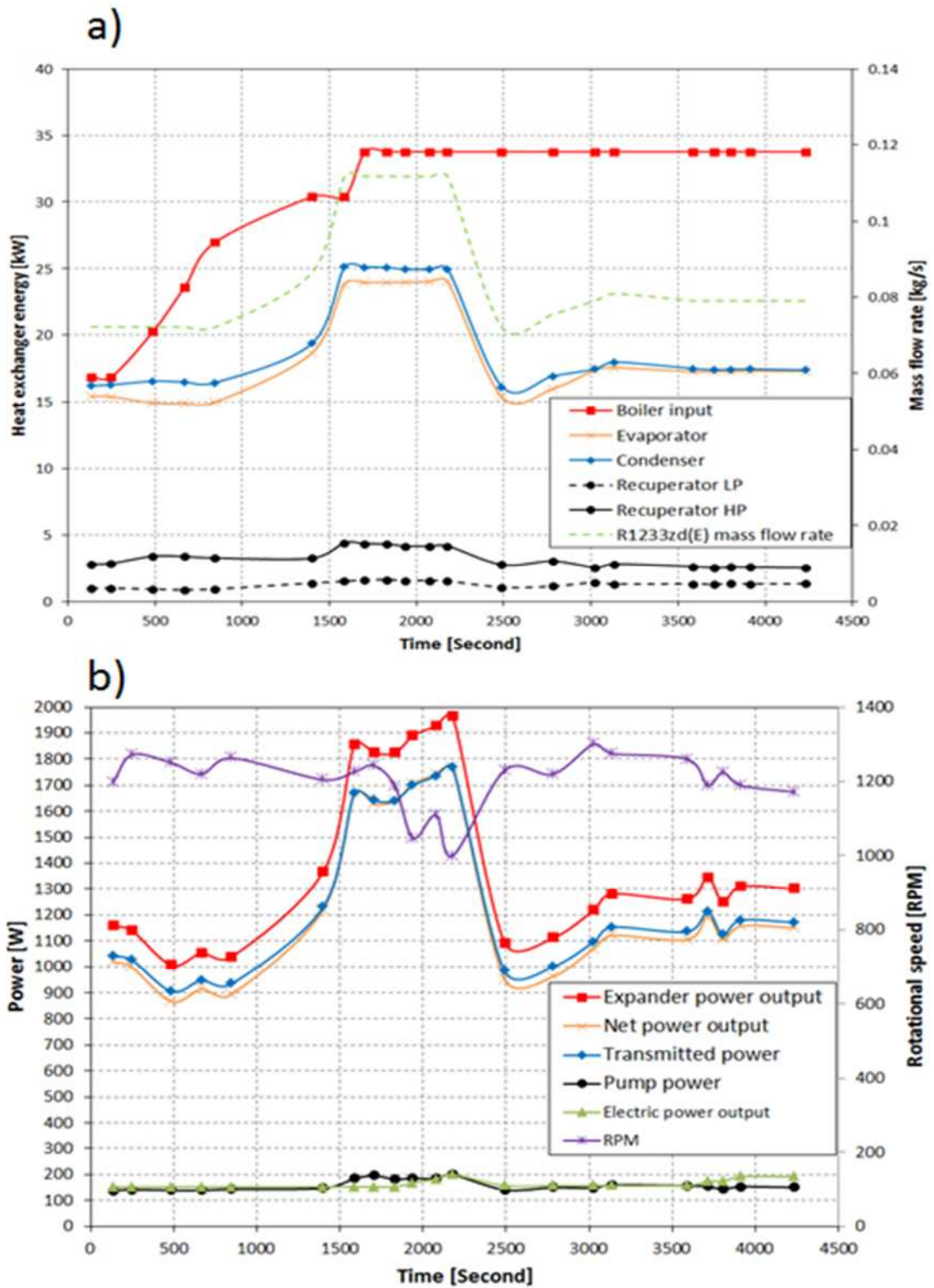
Figure 8-14 (c) shows the recuperator heat exchanger's temperature profile. It is clear that the recuperator inlet from the expander exhaust had the highest temperature, while the high pressure inlet after the pump exhibited the lowest temperatures, varying from 10.87°C to 13.35°C. The outlets on both sides of the recuperator had relatively similar temperatures, with mean values of 42.44°C and 42.76°C for the high pressure and low pressure side, respectively.

Figure 8-14 (d) shows the variation in condenser temperature throughout the test. As shown, the partially cooled refrigerant from the recuperator entered the condenser at temperatures varying between 36.26°C and 50.12°C, to condensate at temperatures between 9.1°C and 36.84°C, before exiting at sub-cooled temperatures between 9.58°C and 11.98°C. The temperature of the cooling water supplied by the chiller was almost identical to that of the condenser exit, while the cooling water outlet after heat rejection was higher and within the range of 15.92°C to 20.85°C.

The pressure profile of the system during the test is presented in Figure 8-14 (e). As shown, slight pressure drops were observed on both the high and low pressure sides of the system. For the high pressure side of the system, the pump's outlet pressure was in the range of 8.1 to 10 bar, while the expander's inlet pressure ranged

between 8.19 and 9.25 bar. However, the fluctuations in the pump's exit pressure readings indicate destruction in the pumping process. On the low pressure side, the expander's outlet pressure was in the range of 1.06 to 2.07 bar; at the condenser outlet, the pressure dropped and varied from 0.70 to 1.95 bar.

8.3.4.1.1.2 Performance Profiles



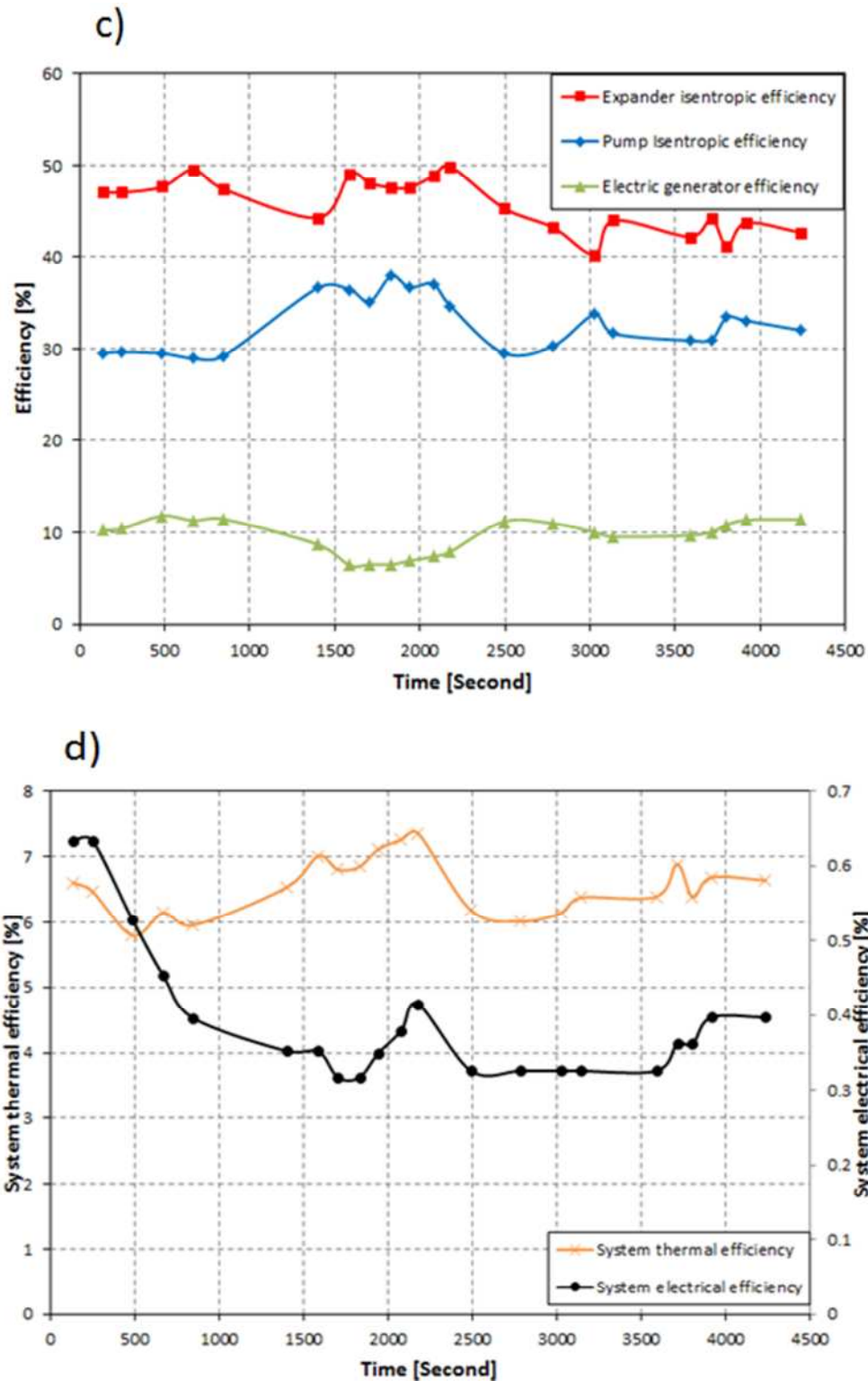


**Figure 8-15: ORC experiment 1, first run - Overall system performance profile.**

Figure 8-15 (a) shows the variation in the steam humidifier’s heat supply to the system and the heat exchangers’ energy at the data points analysed when the system was operating under steady state conditions. As shown, the steam humidifier’s heat supply was

increased gradually from 16.88 kW to 33.75 kW, slightly higher than the thermodynamically anticipated optimum evaporator input of 33.54 kW – determined and presented in Chapter 6, Table 6.15 - where it continued to supply heat at a constant rate. The heat exchangers' energy levels were increased gradually, alongside the heat input. However, they were shown to be strongly dependent on the R1233zd(E) mass flow rate, where the heat exchangers' energy increased alongside the increase in mass flow rate and correspondingly decreased when the mass flow rate was reduced, following similar patterns. The evaporator's energy level ranged from 15 kW to 24 kW, while the condenser's ranged between 16.1 kW and 25 kW. The energy on the high pressure side of the recuperator heat exchanger varied from 2.5 kW to 4.40 kW, while the energy on the low pressure side varied between 0.87 kW and 1.62 kW.

Figure 8-15 (b) shows the power generation and consumption profile of the test, alongside the expander's rotational speed during the test. A similar dependency on the mass flow rate may be observed for the expander's generated power, and transmitted power, as well as the net thermal power output from the system, alongside the power consumed by the pump. This behaviour was also observed for the electrical power generated, but to a lesser extent, because of low electric power generator efficiency. Although the expander did not produce the predicted power output, it achieved a peak power output of 1966W, while the electric power output from the connected electric power generator was way lower than anticipated. This indicates that the system has very low electrical efficiency and very low electric power generator efficiency, due to the unsuitability of the DC motor used, where it barely got going to produce a maximum output of only 140W. The reason for this relates to a mismatch in rotational speed, where the expander could not supply sufficient rotational speed to meet the minimum speed requirements of the electric power generator, as may be

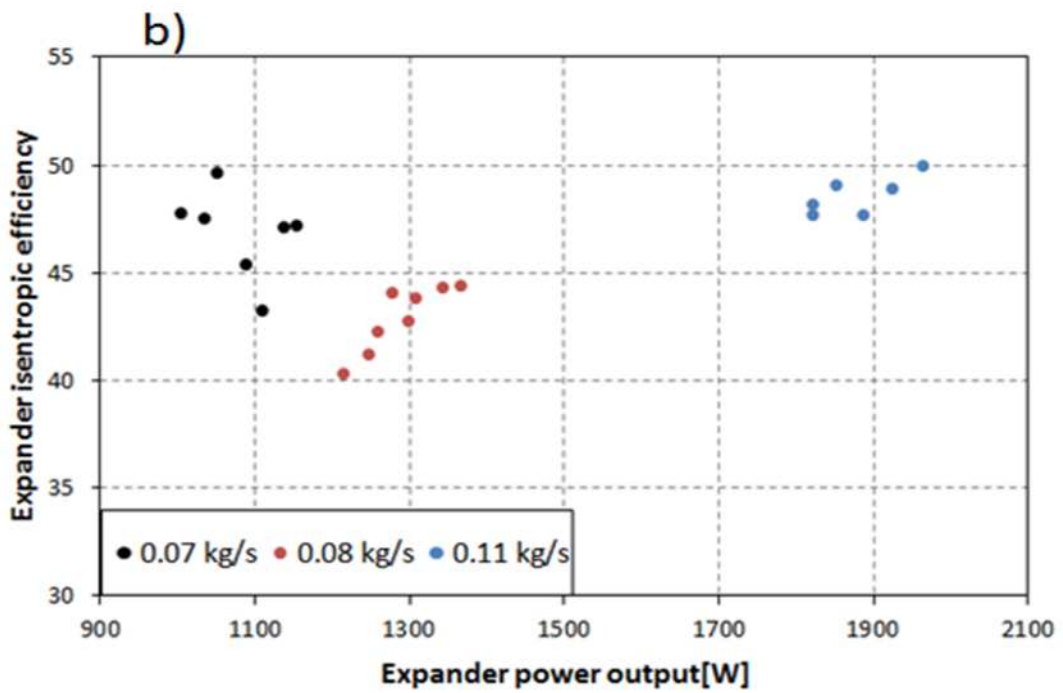
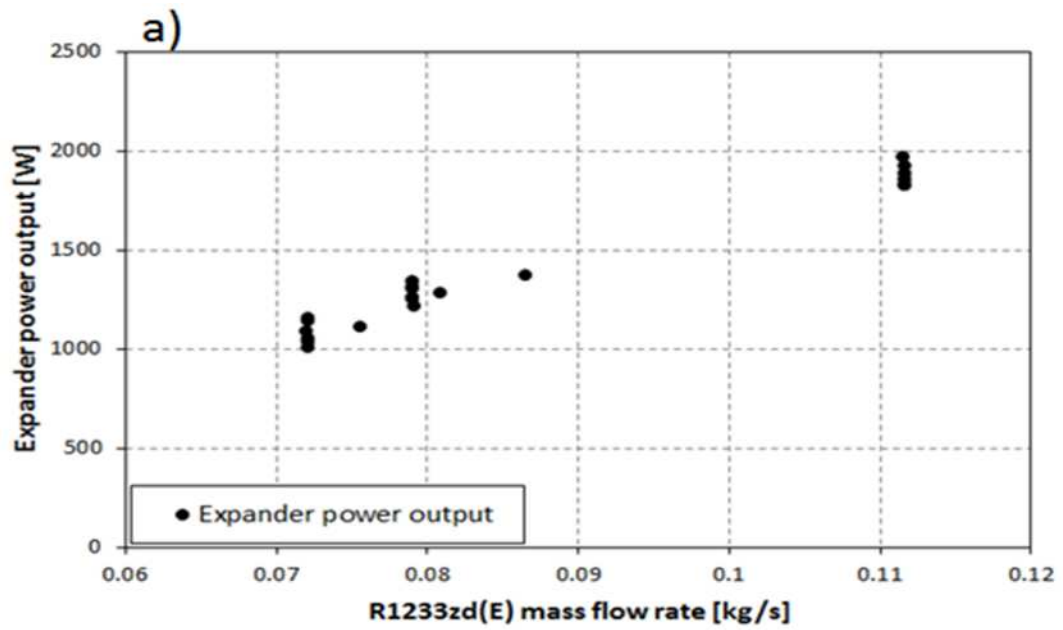
recalled from the motor performance curve presented in Chapter 7, Figure 7-17.

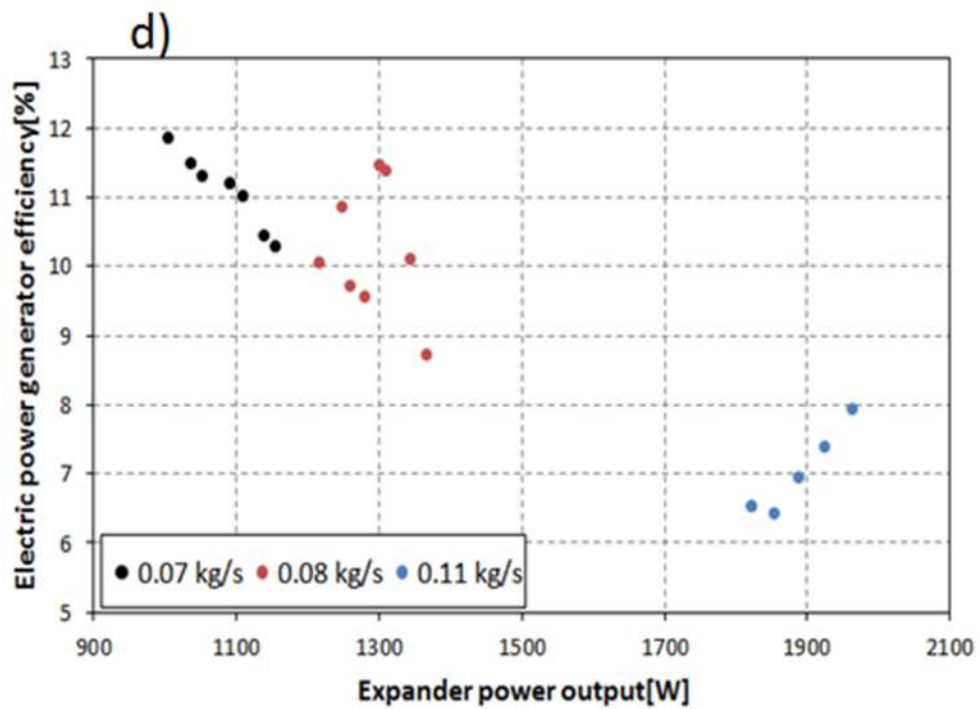
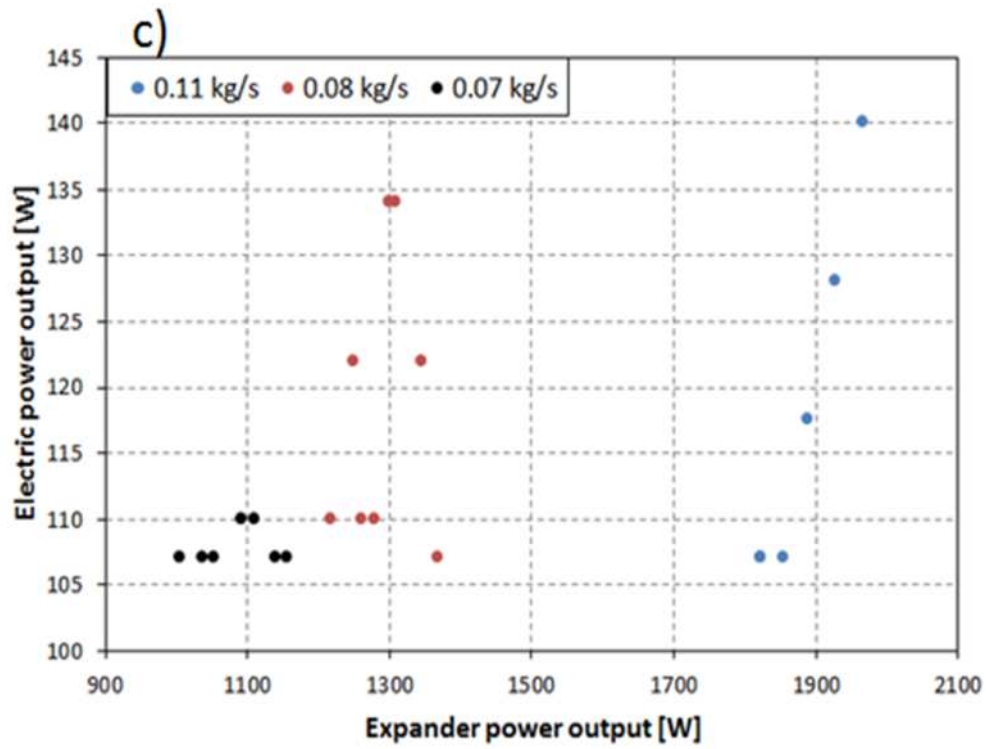
Figure 8-15 (c) shows that the expander, pump and electric generator efficiencies are below expectations. The expander's isentropic efficiency varied from 40.27% to 49.88% throughout the test, while the refrigerant circulation pump proved to have very low efficiency, ranging between 28.9% and 37.9%. Finally, the electric power generator showed the lowest efficiency during the test, ranging from 6.4% to 11.8%.

Figure 8-15 (d) shows the system's thermal efficiency and electrical efficiency throughout the test. As can be seen, the thermal efficiency varied from 5.79% to 7.35%; while the electrical efficiency was very low ranging from 0.31% to 0.63%. The Figure also shows that the system's thermal efficiency improved when the mass flow rate was increased. On the other hand, the electrical efficiency started at its maximum and gradually dropped, only to increase again gradually and slowly once the mass flow rate was raised.

### 8.3.4.1.1.3 The Effect of Operating Parameters on System Performance

#### Performance





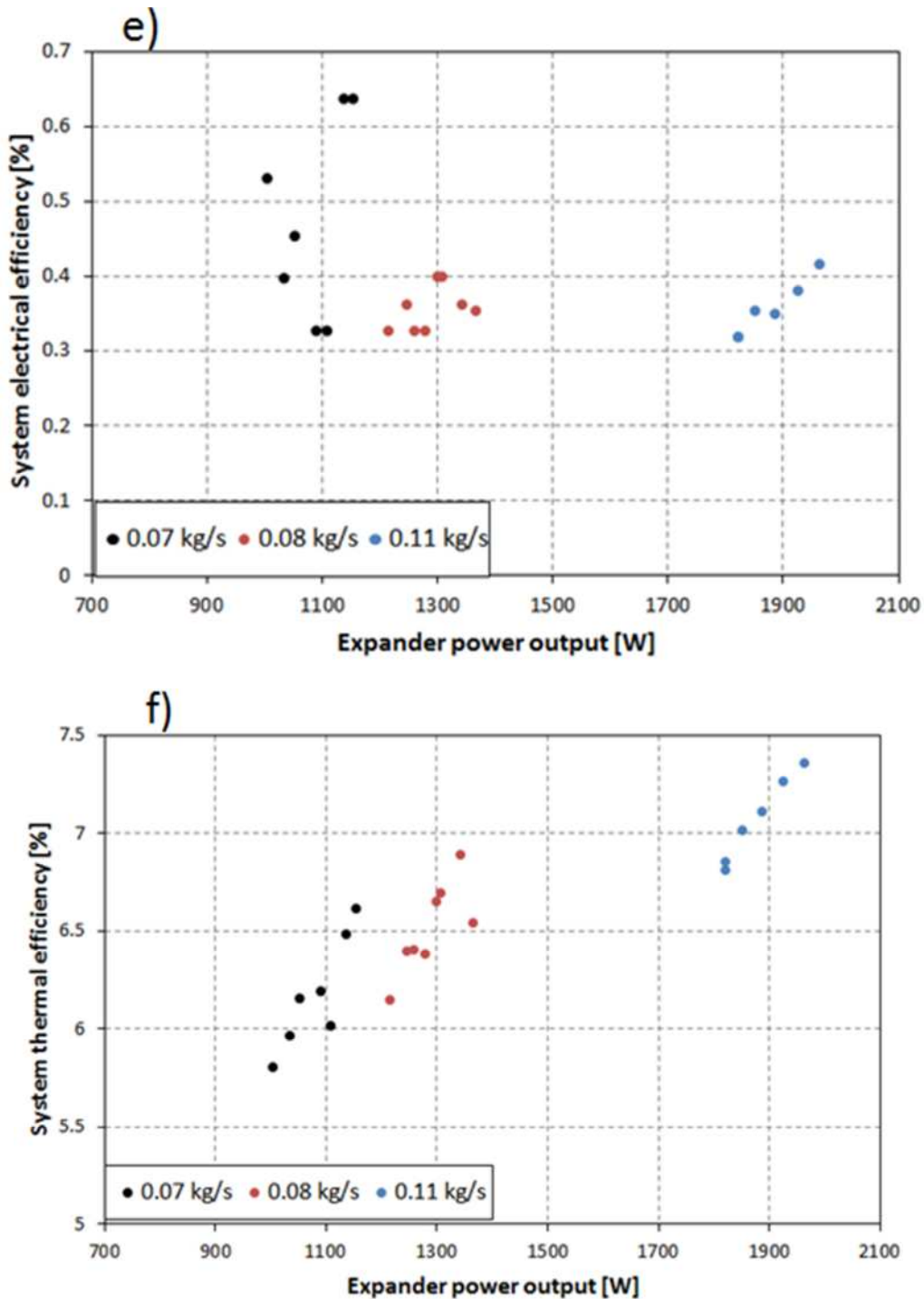


**Figure 8-16: ORC experiment 1, first run - The effect of expander power output on system performance.**

In order to effectively study the effect of changing system parameters on the system's performance, the recorded data were categorised into three groups, depending on the R1233zd(E) mass flow rate, measured as 0.07 kg/s  $\pm$ 0.005, 0.08 kg/s  $\pm$ 0.005, and 0.11 kg/s. Figure 8-16 shows the effect of the mass flow rate on the expander's power output and the system's performance

parameters as a function of the expander's power output. Figure 8-16 (a) shows the dependent linear relationship of the expander's power output on the mass flow rate, where the power output rose to its maximum at the peak R1233zde(E) mass flow rate of 0.11 kg/s.

Figure 8-16 (b) shows the expander's isentropic efficiency for various mass flow rates as a function of the expander's power output, where it can clearly be seen that for every mass flow rate tested, the expander's isentropic efficiency gradually increased and subsequently, the expander's power output increased. The Figure also shows the range of power output achieved at each mass flow rate, where it ranged from 1823W to 1965.88W at the maximum mass flow rate of 0.11 kg/s. When the mass flow rate was 0.08 kg/s, the power output ranged between 1217.27W and 1367.87W. At the lowest mass flow rate of 0.07 kg/s, the power output proved to be less consistent and ranged from 111.36W to 1156W. For both minimum and maximum mass flow rates, the isentropic efficiency was demonstrated as being within similar limits, although slightly lower for 0.08 kg/s.

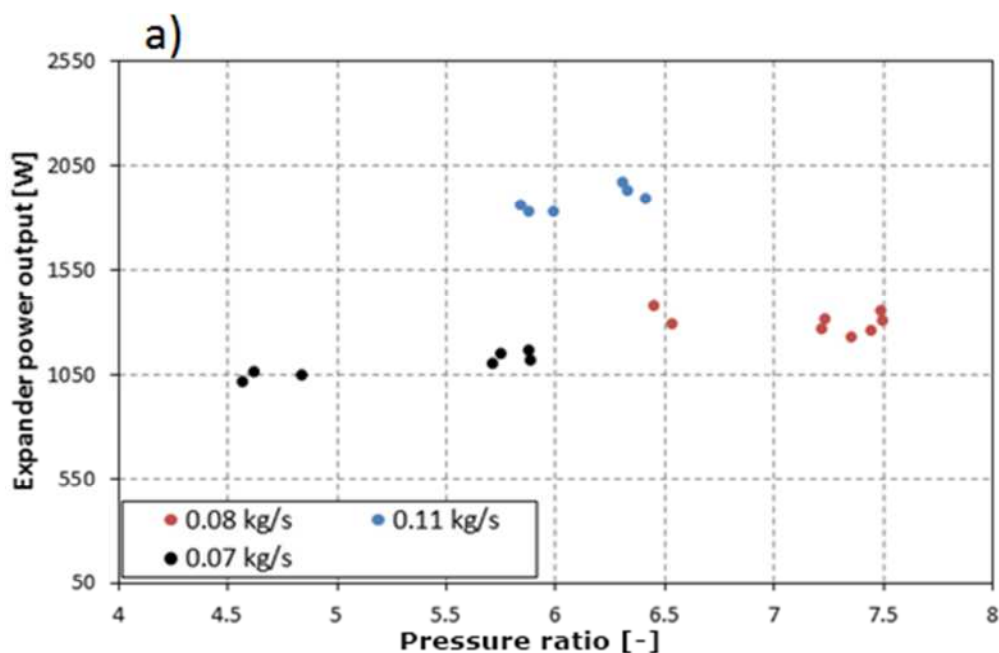
The electric power output results in Figure 8-16 (c) show a perfectly linear relationship between the mass flow rate and the electric power output, when the mass flow rate was 0.11 kg/s. At lower flow rates, these results were inconsistent and exhibited fluctuations, even though the expander's power output was seen to have increased.

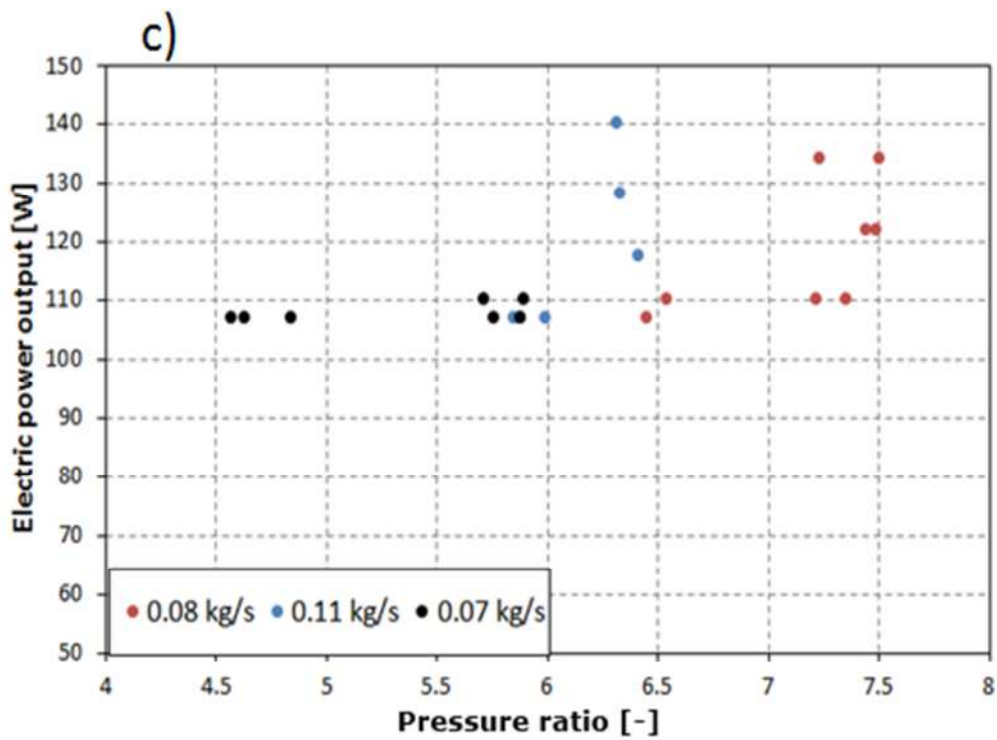
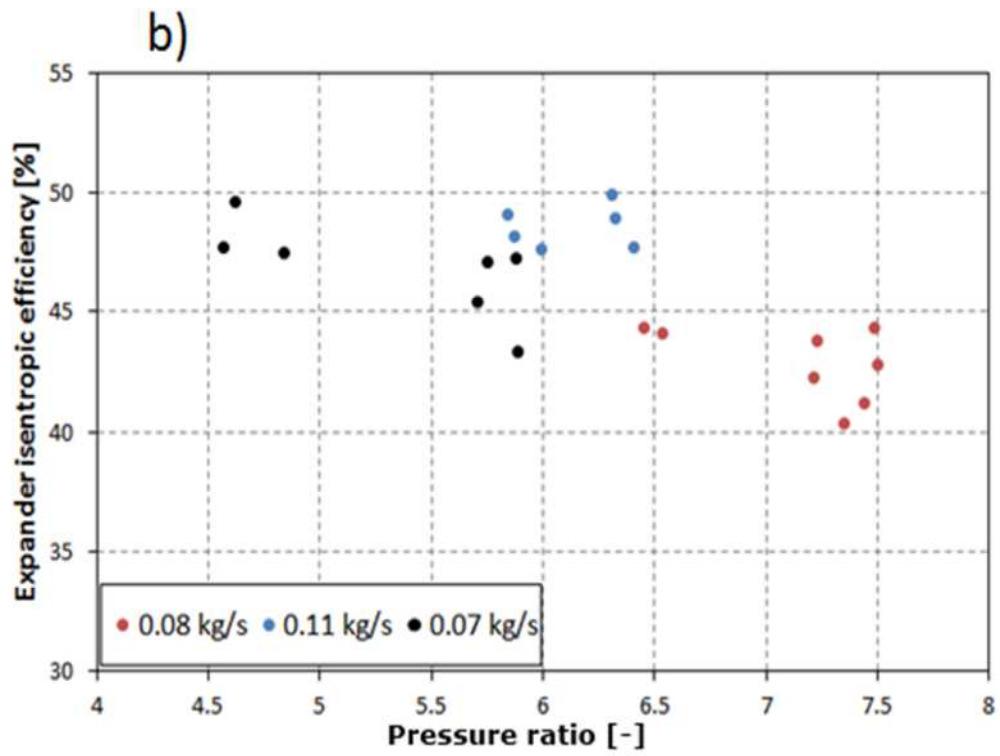
Figure 8-16 (d) shows that the electric power generator's efficiency tended to reduce in a linear manner from 11.8% down to 8.6%, as the expander's power output increased at the 0.07 and 0.08 kg/s flow rates. However, efficiency increased by a few points to reach 12%, when the mass flow rate was 0.07 kg/s. At the maximum mass flow rate, the electric generator's efficiency was shown to be

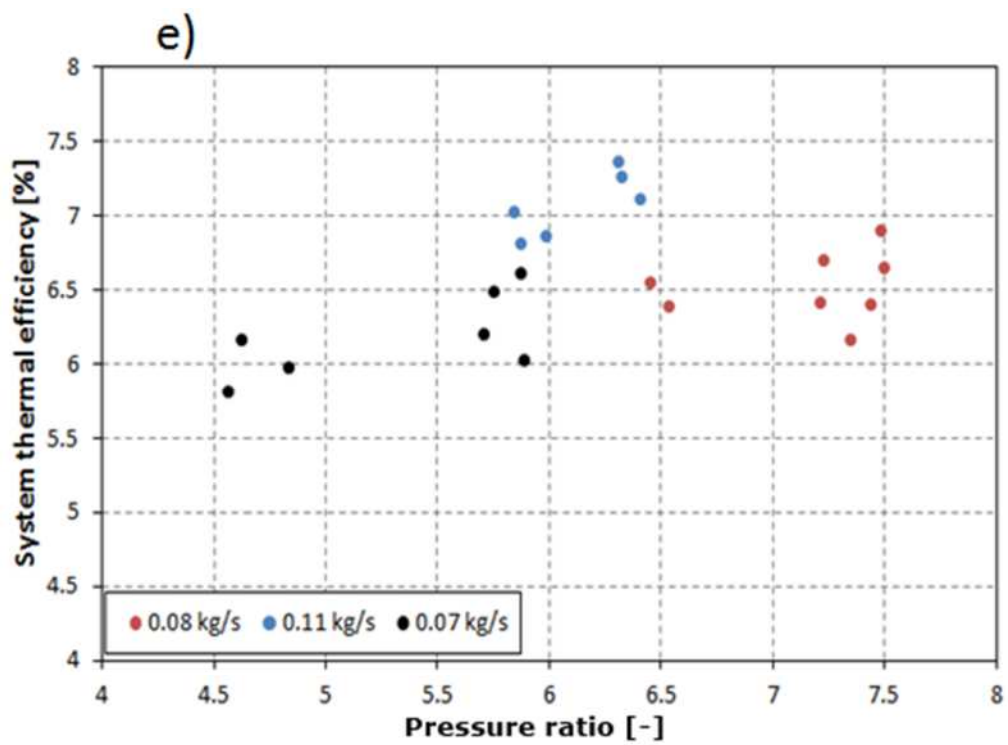
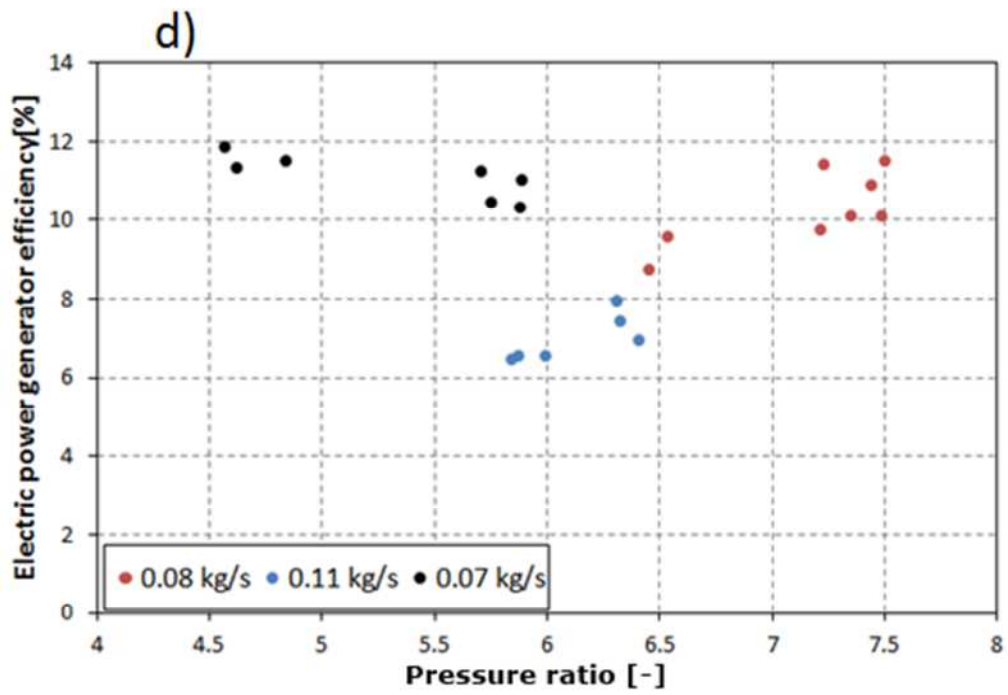
the lowest; however, the linear reduction behaviour changed to a linear increase as the expander's power output increased.

The system's electrical efficiency shown in Figure 8-16 (e) is directly related to the electric power output and the system's heat input. Since there were fluctuations observed in the electric power output at 0.07 and 0.08 kg/s and a gradual increase in heat from the source, the system's electrical efficiency was shown to be less consistent at lower mass flow rates. For the maximum mass flow rate, a linear increase in the system's electrical efficiency could be seen, similar to the electric power output behaviour and electric power generator efficiency behaviour observed for the same mass flow rate.

As expected, Figure 8-16 (f) shows that higher mass flow rates mean higher expander power output and thermal efficiency. As shown for each mass flow rate, thermal efficiency increases gradually as the expander's power output increases. However, the system's thermal efficiency is directly related to the net thermal power output from the system, which is in turn related to the power produced by the expander and consumed by the pump.







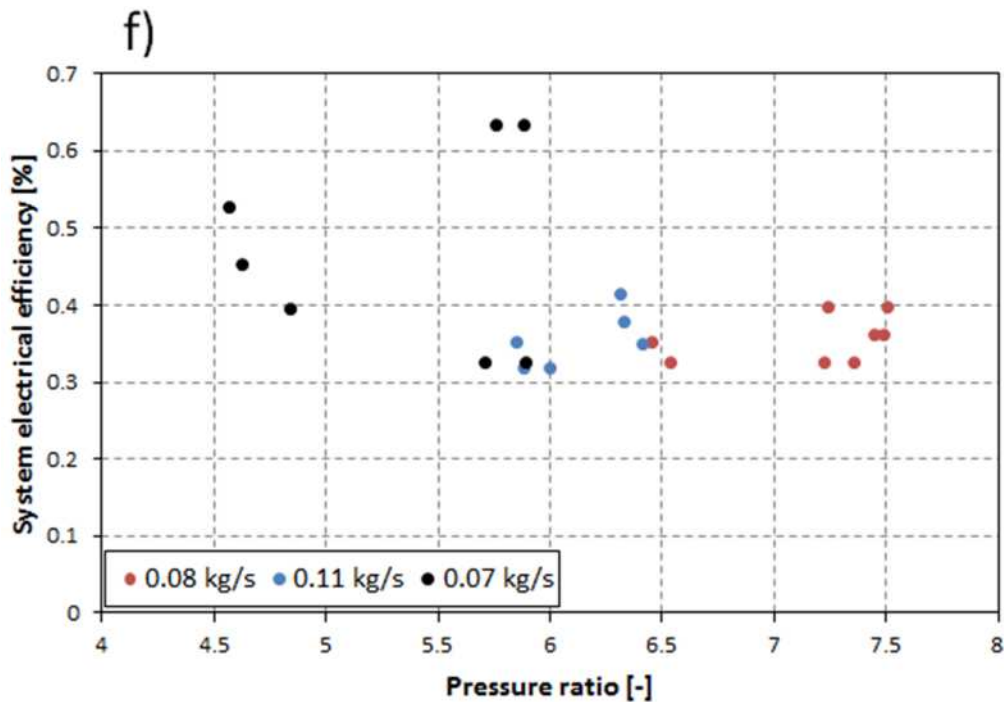


**Figure 8-17: ORC experiment 1, first run - The effect of pressure ratio across the expander on system performance.**

Figure 8-17 presents the effect of the pressure ratio across the expander on the system's performance. As shown in Figure 8-17 (a) from the results for 0.07 kg/s and 0.08 kg/s, the expander's power output gradually rose as the expander pressure ratio increased. At the maximum mass flow rate, the results show that the expander's power output increased significantly at lower expander pressure ratios, from 5.8 to 6.3.

Figure 8-17 (b) shows that the expander's isentropic efficiency behaved in a completely opposite manner to the expander's power output. Shown for the 0.07 and 0.08 kg/s results, the isentropic efficiency tends to be at its maximum at the lowest pressure ratio and decreases gradually as the ratio is increased. At the maximum mass flow rate of 0.11kg/s, the isentropic efficiency was found to decrease in a similar manner to that observed for lower mass flow rates, however at a higher level.

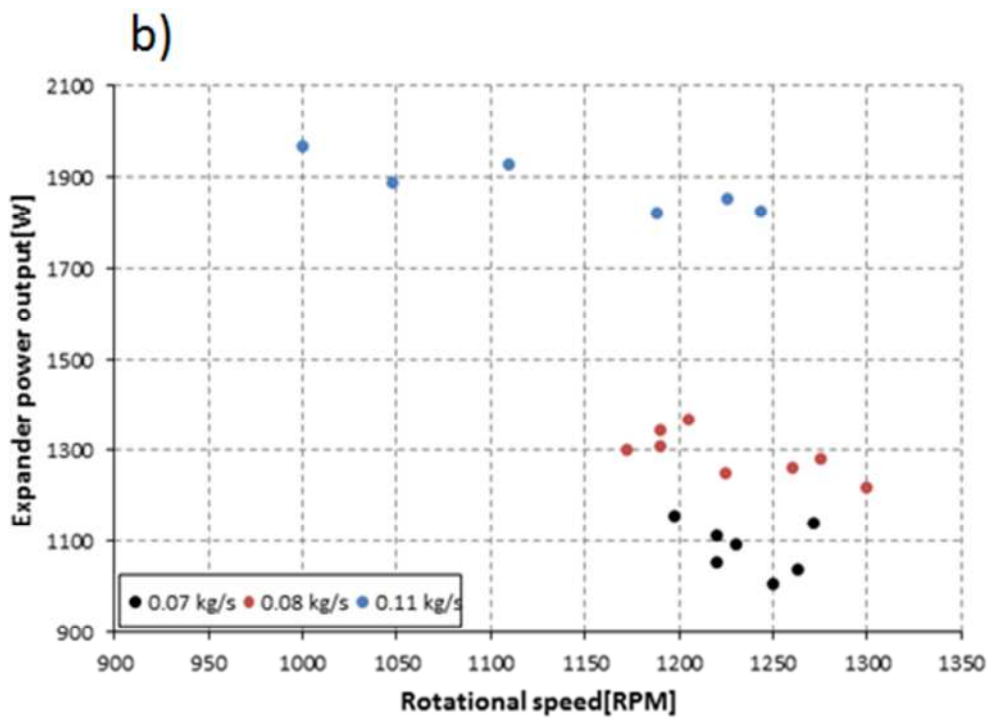
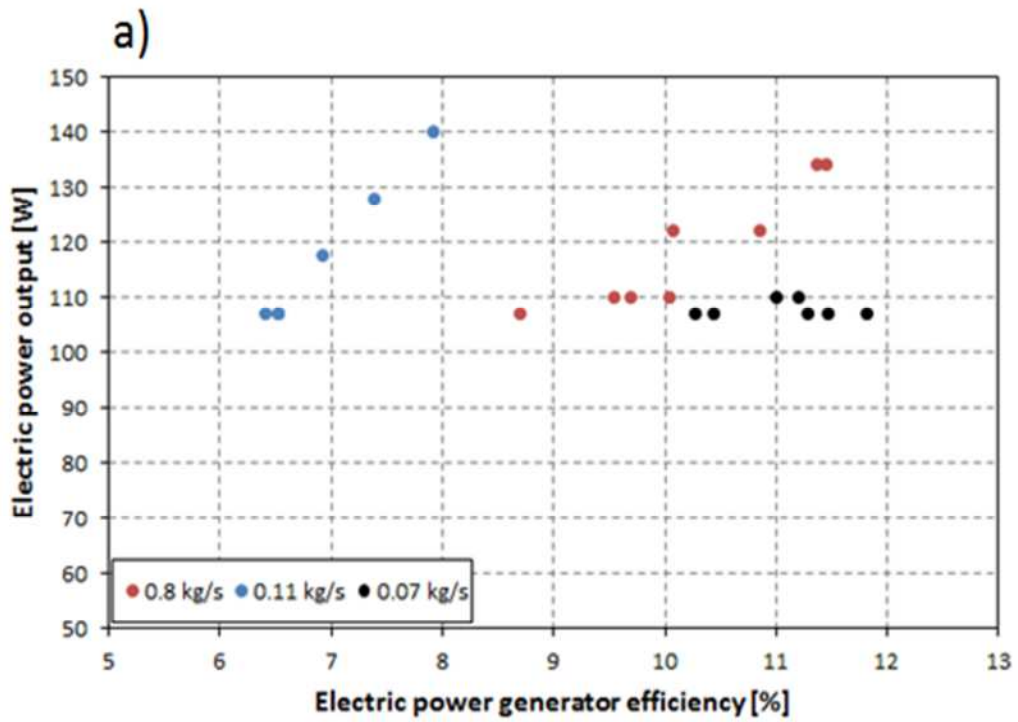
The behaviour of the electric power output can be more clearly seen as a function of the pressure ratio in Figure 8-17 (c), where it tends

to gradually increase alongside the pressure ratio, in a similar way to the expander's power output. However, it showed less steady behaviour at a mass flow rate of 0.08 kg/s, where the electric power output increased significantly.

For the electric power generator's efficiency, Figure 8-17 (d) illustrates that this reduced gradually with an increase in the pressure ratio at 0.07 kg/s, as per the isentropic efficiency results. Nevertheless, this is unlike the behaviour which can be seen for both the 0.08 and 0.11 kg/s results, where efficiency increased alongside the pressure ratio and was at its lowest when the mass flow rate was at its maximum, followed by the 0.08 kg/s results.

Similar to the behaviour observed for the expander's power output, the system's thermal efficiency shown in Figure 8-17 (e) increased gradually with the rise in pressure ratio for the 0.07 and 0.08 kg/s results, while the 0.11 results also show a gradual increase, but at a higher level. However, the data are less clustered due to the effect of the pump's power consumption on the net thermal power output.

Finally, the system's electrical efficiency in Figure 8-17 (f) is demonstrated at its maximum, at the lowest pressure ratio and lowest mass flow rate, after which it remains between 0.3% to slightly above 0.4%, as the pressure ratio is increased for the 0.08 and 0.11 kg/s mass flow rates.



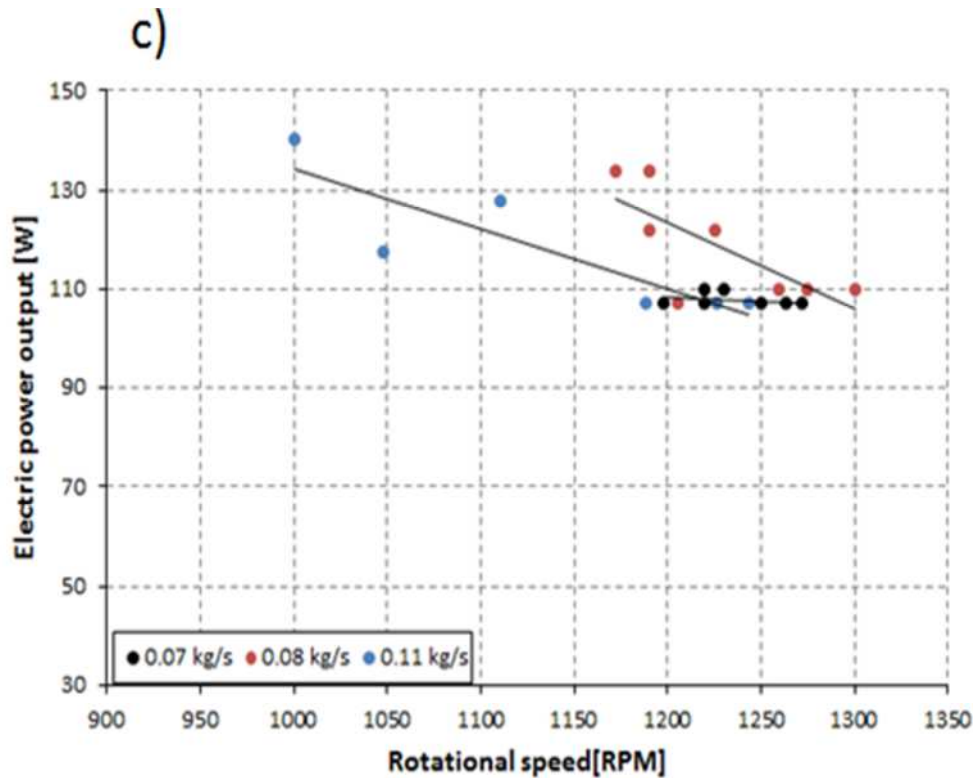


**Figure 8-18: ORC experiment 1, first run’s parameters relationships- a) the relationship between the electric power generator’s efficiency and electric power output; b) the relationship between the expander’s rotational speed and the expander’s power output, and c) the relationship between the expander’s rotational speed and electric power output.**

Figure 8-18(a) presents the relationship between the electric power generator’s efficiency and the electric power output from the system. As shown, the lowest efficiency was at the maximum mass flow rate, where the maximum electric power output was achieved, while maximum efficiency was obtained at the lowest mass flow rate, when the lowest electric power output was generated. However, at 0.08 kg/s and 0.11 kg/s, the electric power output increased in a linear manner, corresponding to increases in efficiency. On the other hand, at 0.07 kg/s, the electric power output increased slightly at two points before decreasing again.

Figure 8-18(b) and Figure 8-18(c) show the effect of the expander’s rotational speed on the expander’s power output and electric power output, respectively. In both Figures and for each mass flow rate, the expander’s power and the electric power outputs were at their

maximum at the lowest rotational speed and decreased gradually as the rotational speed increased.

#### 8.3.4.1.1.4 First run's Optimum Performance

The analysis revealed that maximum system's thermal efficiency, expander's power output, expander's isentropic efficiency and electric power output were achieved at the same experimental point, but this did not apply to the electric power generator's efficiency or the system's electrical efficiency. Table 8.2 lists the optimum performance achieved in the first ORC prototype system run.

**Table 8.2: ORC experiment 1, first run – The R1233zd(E) ORC system's optimum experimental performance**

System thermal efficiency [%]	7.35
System electrical efficiency [%]	0.41
Expander power output [W]	1966
Expander isentropic efficiency [%]	49.86
R1233zd(E) pump power [W]	199
R1233zd(E) pump efficiency [%]	34.69
Net thermal power output [W]	1767
Electric power output [W]	140
Electric power generator efficiency [%]	7.91
R1233zd(E) mass flow rate [kg/s]	0.11
Evaporator pressure [bar]	8.91
Expander inlet temperature [°C]	93.45
Condenser pressure [bar]	1.41
Condenser exit temperature [°C]	10.85
Steam humidifier heat input [kW]	33.75
Evaporator power [kW]	24.02
Condenser power [kW]	24.97
Recuperator heat exchanger LP side [kW]	1.52
Recuperator heat exchanger HP side [kW]	4.16

As shown in Table 8.2, the expander's inlet temperature was just a fraction higher than the evaporation temperature. However, this does not affect system performance because of the dry nature of R1233zd(E), where the expansion process occurs in the superheated region on the T-S diagram. Table 8.3 shows the system's state points alongside their properties for the optimum experimental performance. Figure 8-19 and Figure 8-20 illustrate the optimum experimental performance of the first run represented on the R1233zd(E) T-S and P-H diagrams, respectively. The state

points in both diagrams correspond to the ORC prototype schematic presented in Figure 7-1, while point 3S and the dashed line represent the isentropic expansion.

**Table 8.3: ORC experiment 1, first run – The R1233zd(E) ORC system’s optimum experimental performance state points’s properties.**

State point	Temperature [°C]	Pressure [bar]	Enthalpy [kJ/kg]	Entropy [kJ/kg-°C]
Evaporation	93.276	8.9127	461.05	1.756
2	93.45	8.9127	461.23	1.7565
3	57.781	1.4114	443.76	1.8121
3S	36.822	1.4114	425.96	1.7565
5	41.27	1.4114	429.7	1.7685
Condensation	27.206	1.4114	230.63	1.1066
7	10.846	1.4114	212.02	1.0429
8	12.049	8.9127	213.65	1.0466
9	42.063	8.9127	248.29	1.162

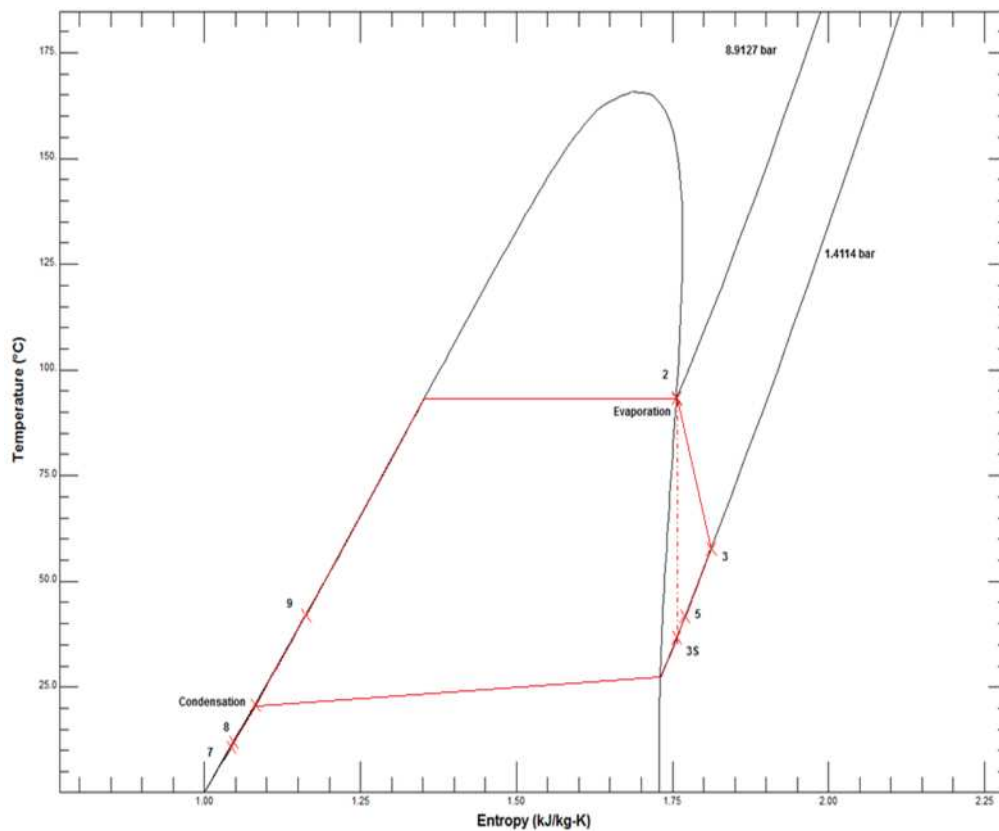


**Figure 8-19: ORC experiment 1, first run - Optimum experimental performance point represented on the R1233zd(E) T-S diagram**

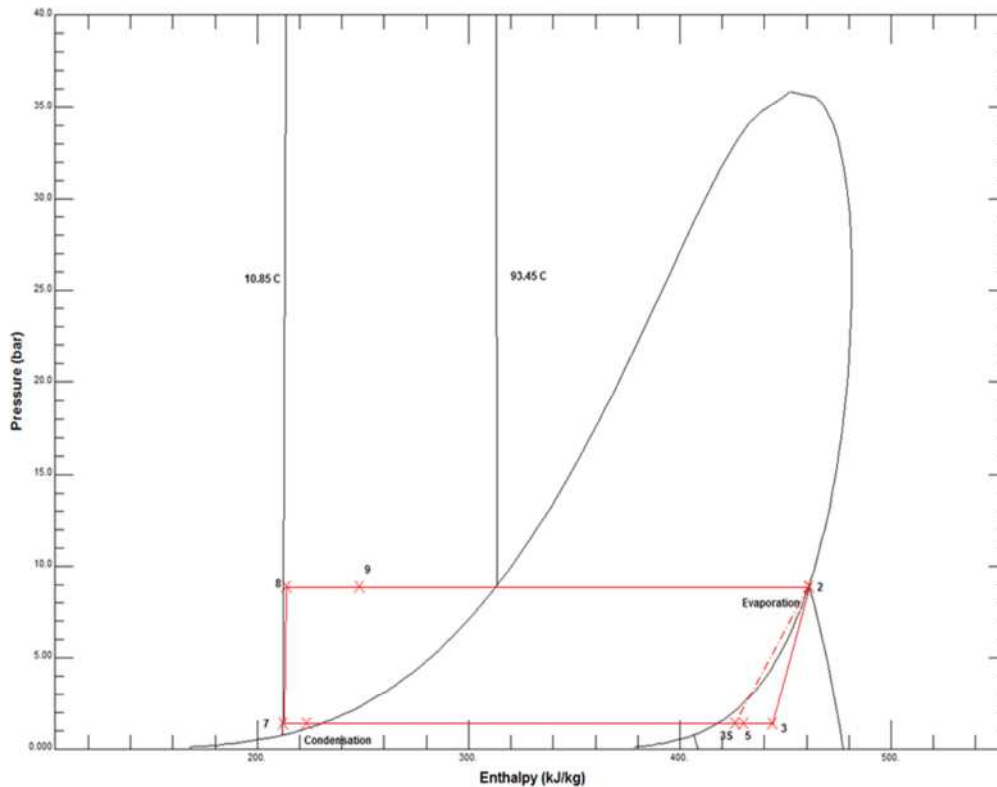


**Figure 8-20: ORC experiment 1, first run - Optimum experimental performance point represented on the R1233zd(E) P-H diagram.**

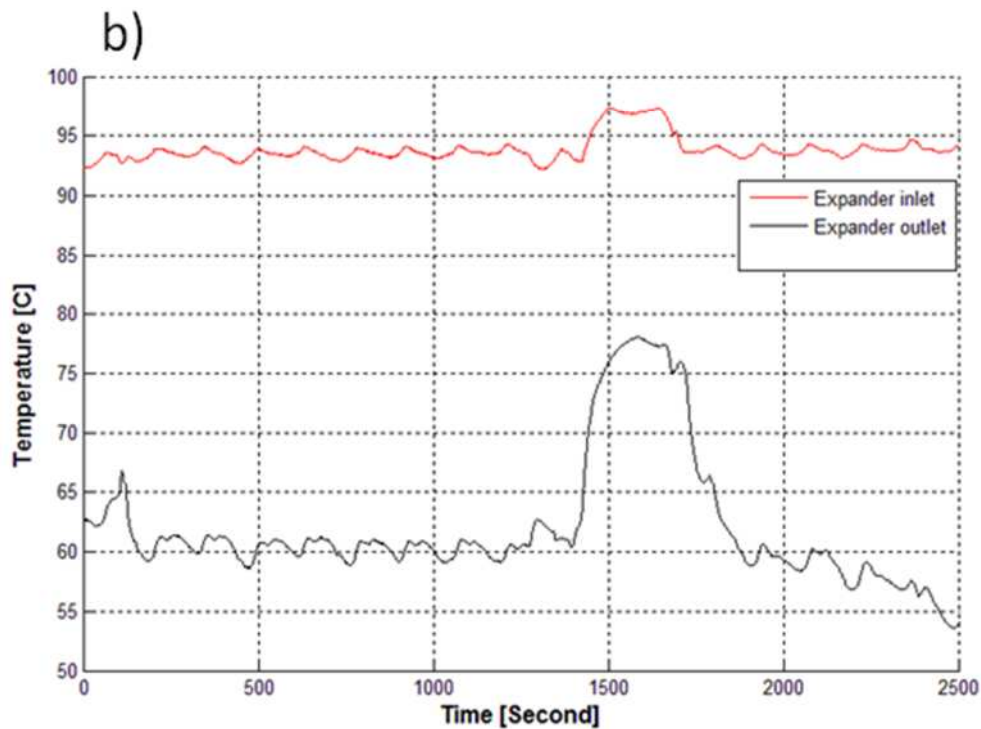
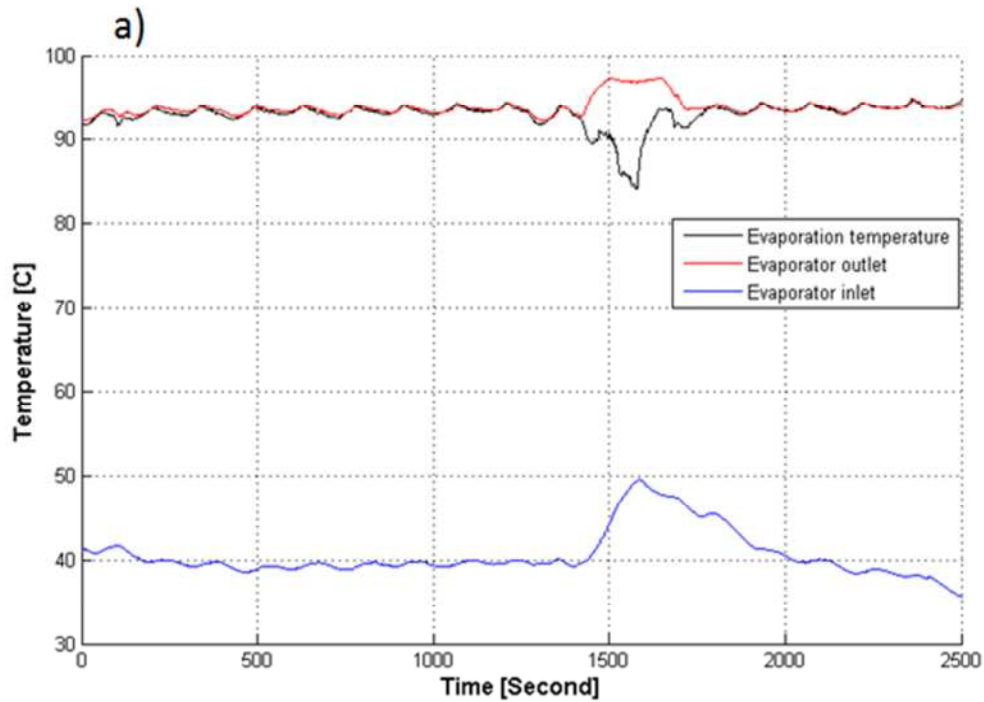
Although the first system run did not achieve the theoretically predicted optimum performance in Table 6.15, Chapter 6, it showed acceptable ORC characteristics that could be significantly improved. However, the main obstacle preventing achievement of the theoretically predicted performance is mainly the lower capability of the utilised heat source, which showed relatively lower temperatures than those anticipated. On the operational side, it was pointed out that the pump irreversibility represented by the excessive fluctuation of pressure at the pump outlet and the poor pump efficiency, alongside the low electric generator performance, contributed significantly to the poor overall system performance.

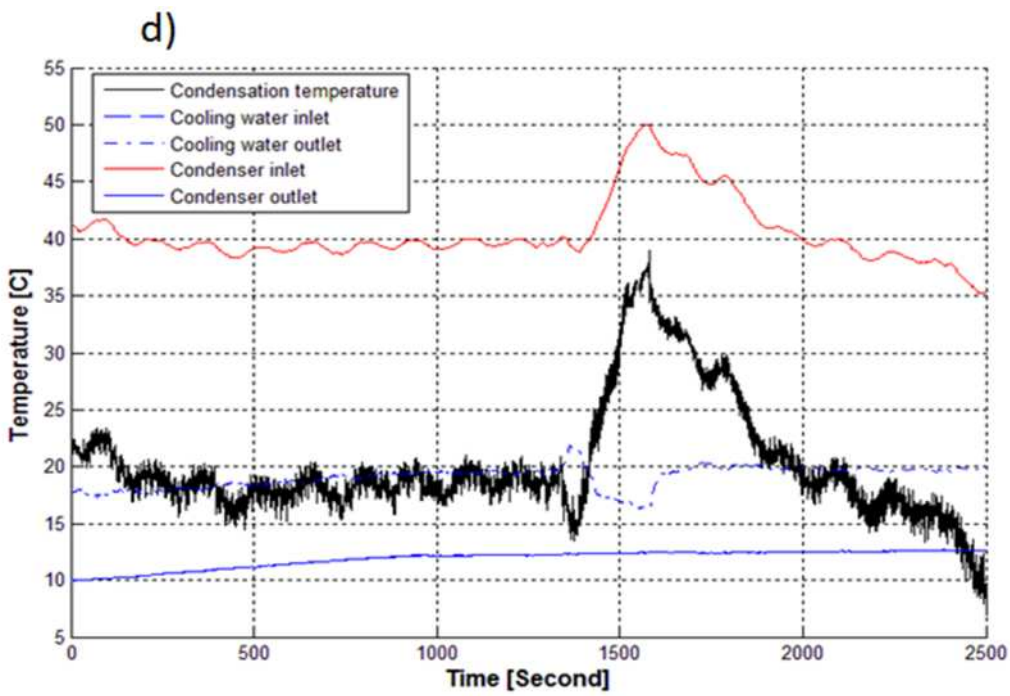
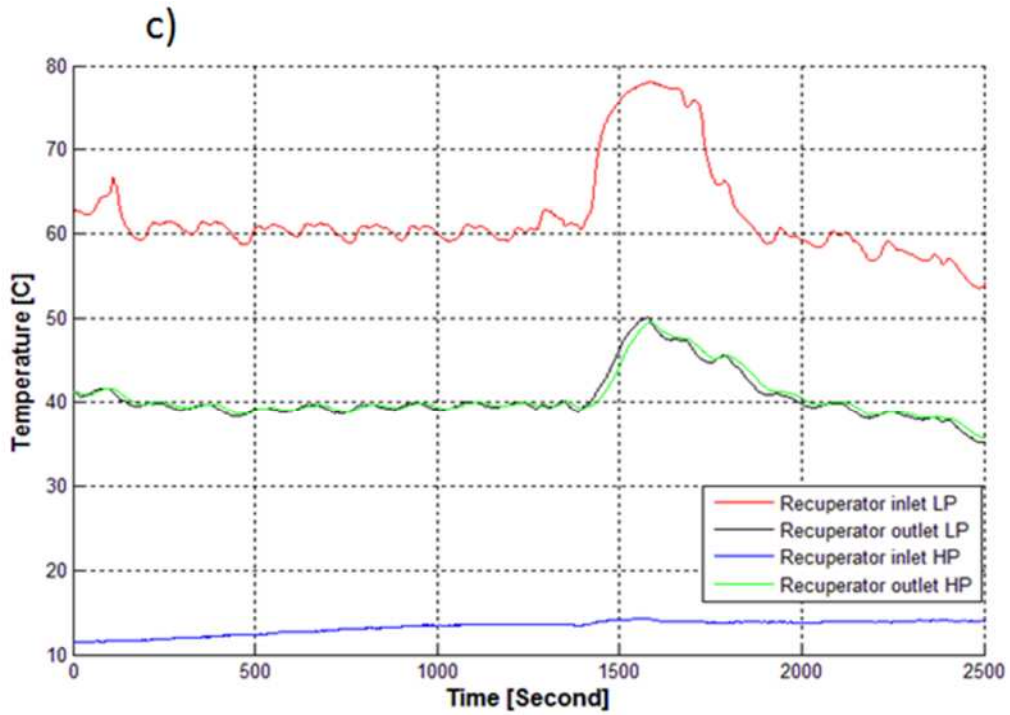
#### 8.3.4.1.2 Second run

It was decided to first investigate the pump before addressing the problem of the electric power generator. The experiment was commenced by keeping the R1233zd(E) mass flow rate held constant at its minimum of 0.07 kg/s in an attempt to avoid interfering with the pump's operation, contemplating a reduction in

its performance destruction. Consequently, the pressure ratio was also kept constant during the test. The heat supply from the steam humidifier was maintained at 33.75 kW. The cooling water temperature was kept between 10°C and 12°C throughout the test.

### 8.3.4.1.2.1 Temperature and Pressure Profiles





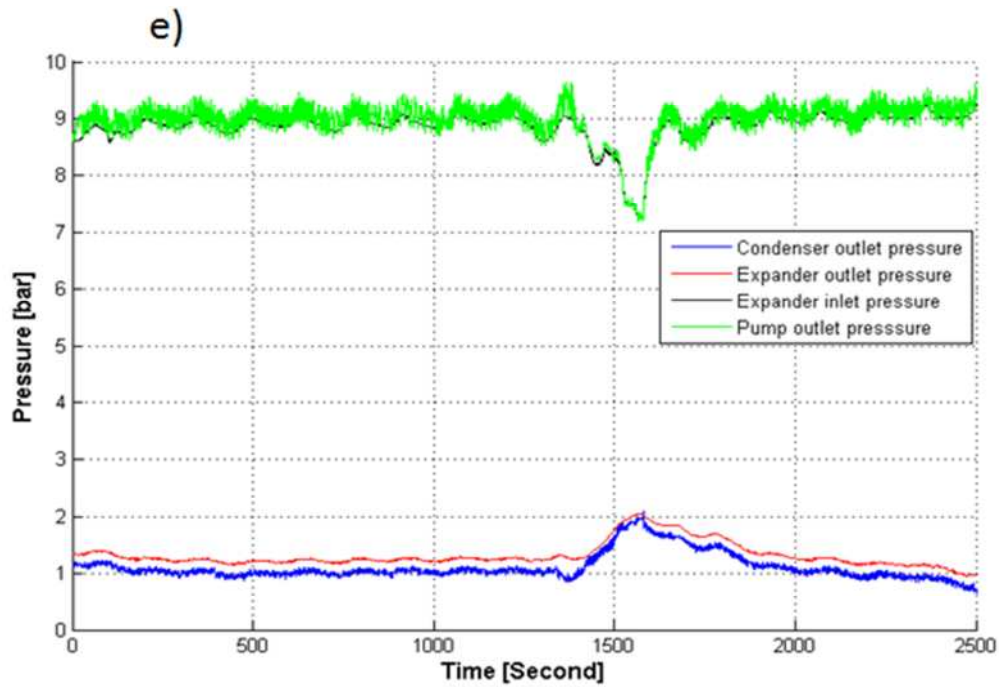


**Figure 8-21: ORC experiment 1, second run - Temperature and pressure profiles.**

Figure 8-21(a) shows the evaporator's temperature profile during the second run of the experiment. Similar behaviour can be seen to that which was observed in the first run. The evaporator's inlet temperature ranged from 35.72°C to 49.65°C while the outlet was in the range of 92.22°C to 97.35°C, just above the evaporating temperature, which varied between 84.23°C and 94.85°C.

Figure 8-21(b) shows the variation in expander's inlet and outlet temperatures during the run, where the expander's outlet temperature varied between 53.59°C and 78.12°C.

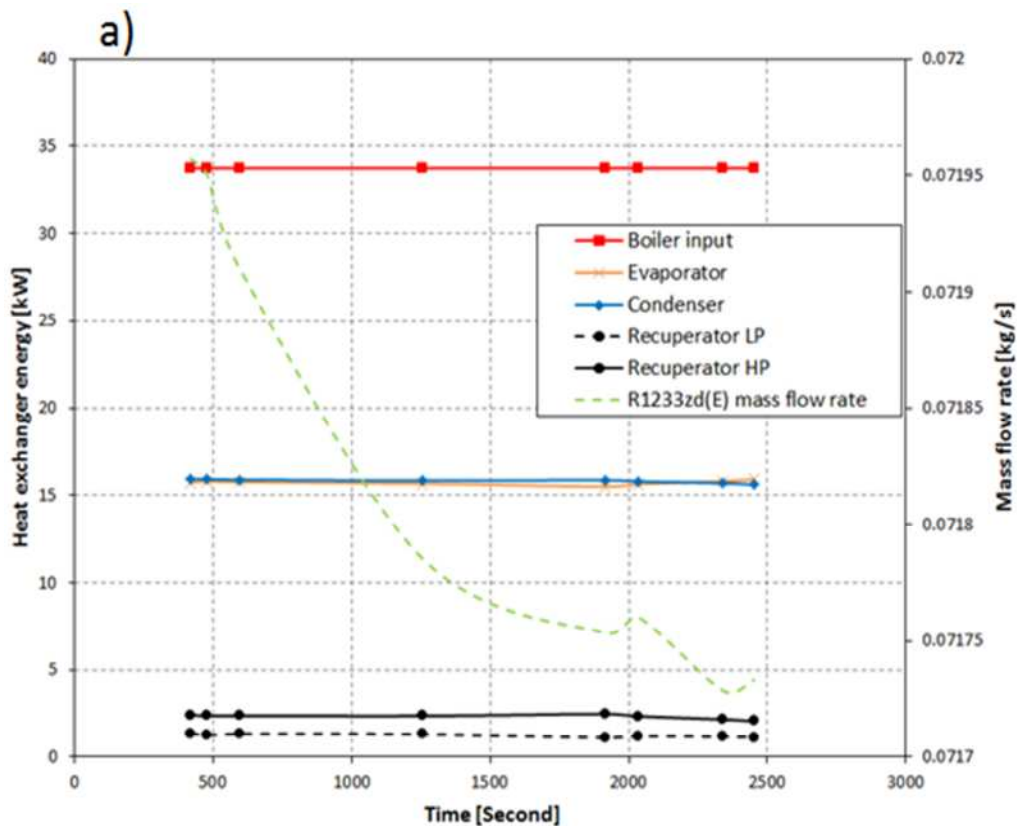
Figure 8-21(c) presents the recuperator's temperature profile, where the expander's exhaust entered the recuperator and exited at temperatures between 35.18°C and 50.02°C. On the high pressure side, the R1233zd(E) stream entered the recuperator at temperatures ranging from 11.41°C to 35.72°C and exited at evaporator's inlet temperatures.

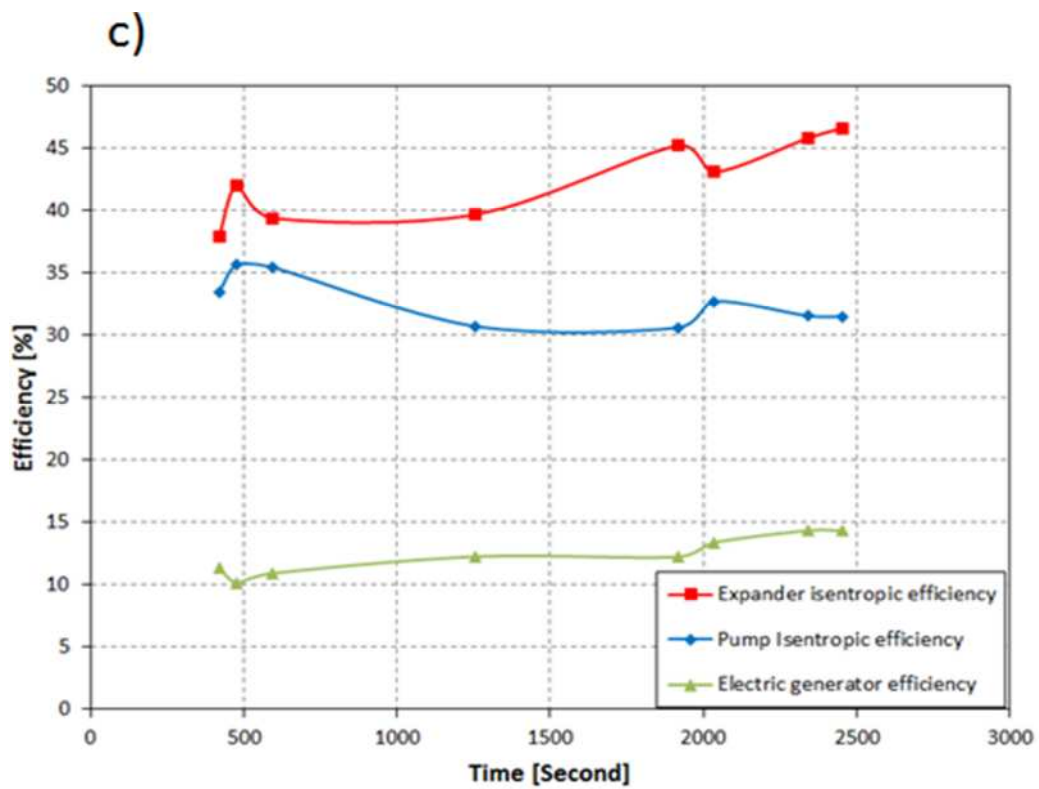
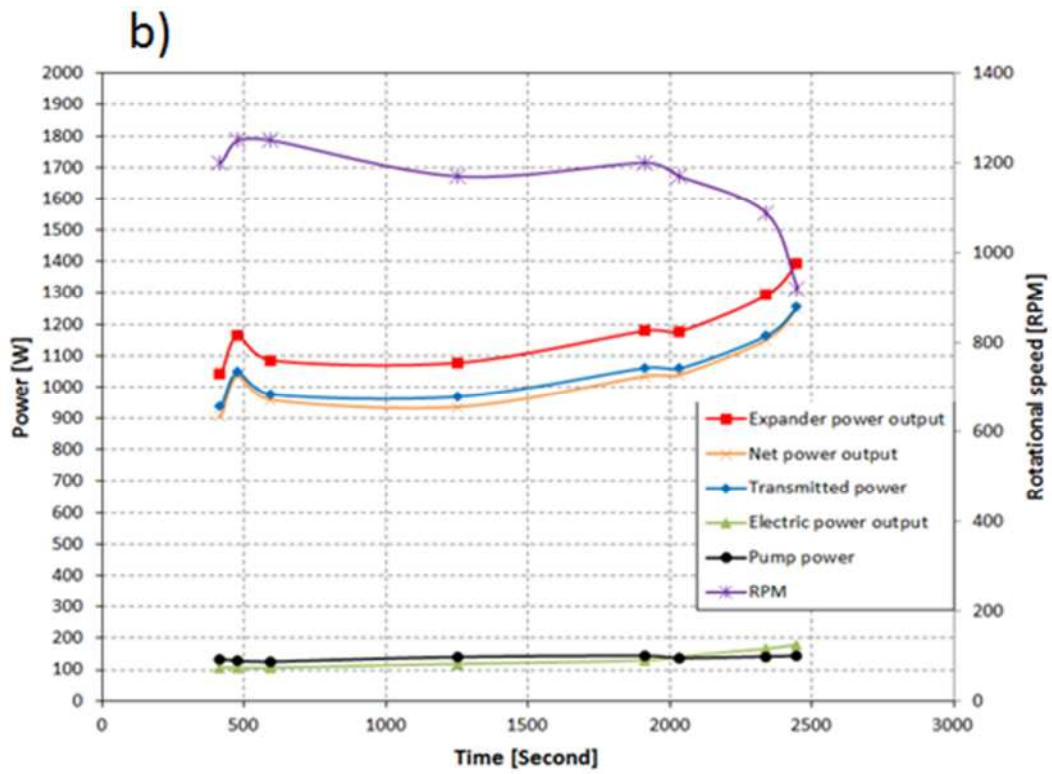
Figure 8-21(d) shows the condenser's temperature profile throughout the run. The partially cooled refrigerant stream exited

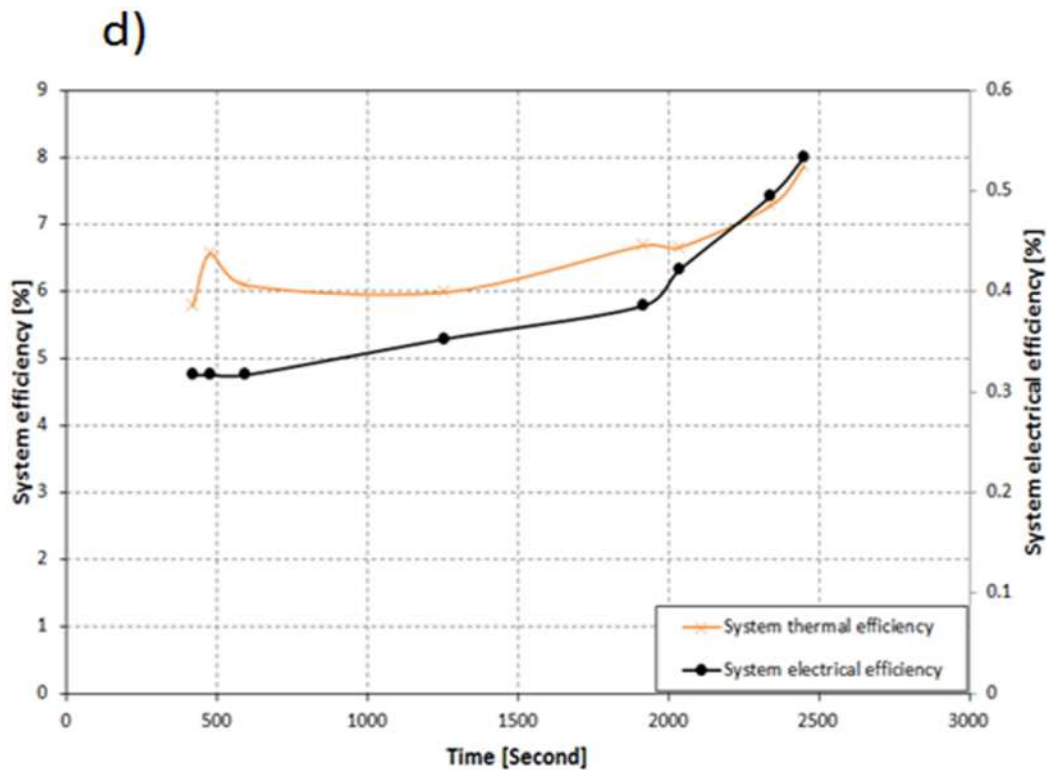
the recuperator and entered the condenser to condensate at temperatures between 7.89°C and 38.98°C, before exiting at temperatures between 9.92°C and 12.69°C. The cooling water exited at temperatures between 16.30°C and 21.85°C after heat rejection.

Figure 8-21(e) shows the pressure profile of the system during the second run. Similar to the first run, slight pressure drops occurred and the excessive fluctuation of pressure at the pump’s outlet was still evident, even though the mass flow rate was kept constant during the run. However, for the high pressure side, the pump’s outlet pressure ranged between 7.19 and 9.65 bar, while expander’s inlet pressure ranged between 7.23 and 9.23 bar. On the low pressure side, the expander’s outlet pressure was in the range of 0.96 to 2.05 bar. At the condenser outlet, the pressure dropped slightly and varied in the range of 0.69 to 2.1 bar.

### 8.3.4.1.2.2 Performance Profiles







**Figure 8-22: ORC experiment 1, second run - Overall system performance profile.**

Figure 8-22 (a) presents the heat exchangers' energy and mass flow rate variation profile for the duration of the test. As shown, the test began when the steam humidifier's heat supply reached 33.75 kW and was kept constant until the end of the run. The mass flow rate was also held constant at  $0.07 \text{ kg/s} \pm 2 \times 10^{-3}$ . The Figure shows that the heat exchangers' energy remained almost constant at all recorded points. The evaporator and condenser were constant between 15 kW and 15.9 kW, while the recuperator's low pressure side was at  $1 \text{ kW} \pm 0.3$ , the high pressure side being at  $2 \text{ kW} \pm 0.4$ .

Figure 8-22 (b) presents the power generation and consumption profile, where the expander's power output, transmitted power, and the net thermal power output from the system increased gradually along the timeline. A similar pattern was observed for the electric power output, but still at very low rates and with very poor performance. However, the maximum power output produced by the expander was 1394.82W and the maximum electric power output was 180W. It can be seen that the rotational speed of the

expander started at its maximum and reduced gradually to its minimum, where the maximum power output and electric power were produced. In fact, the improvement in performance was not related to the rotational speed of the expander. Instead, it was found to be directly related to the gradual increase of the expander's isentropic efficiency and the electric power generator's efficiency. The pump's power consumption remained fairly stable, ranging from 126W to 143W throughout the test.

Figure 8-22 (c) presents the expander, pump and electric generator efficiencies during the test. Both the expander's isentropic efficiency and electric generator's efficiency were seen to increase gradually along the test timeline, where the expander's efficiency was 37.88% at the beginning of the test and reached its maximum of 46.61% by the end of the test. The electric power generator's efficiency was in the range of 10.2% to 14.35%. The pump was found to have low efficiency that gradually decreased during the test, even though the flow rate was kept constant throughout. However, the pump efficiency was within a similar range to that observed in the first run and ranged between 30.62% and 35.66%.

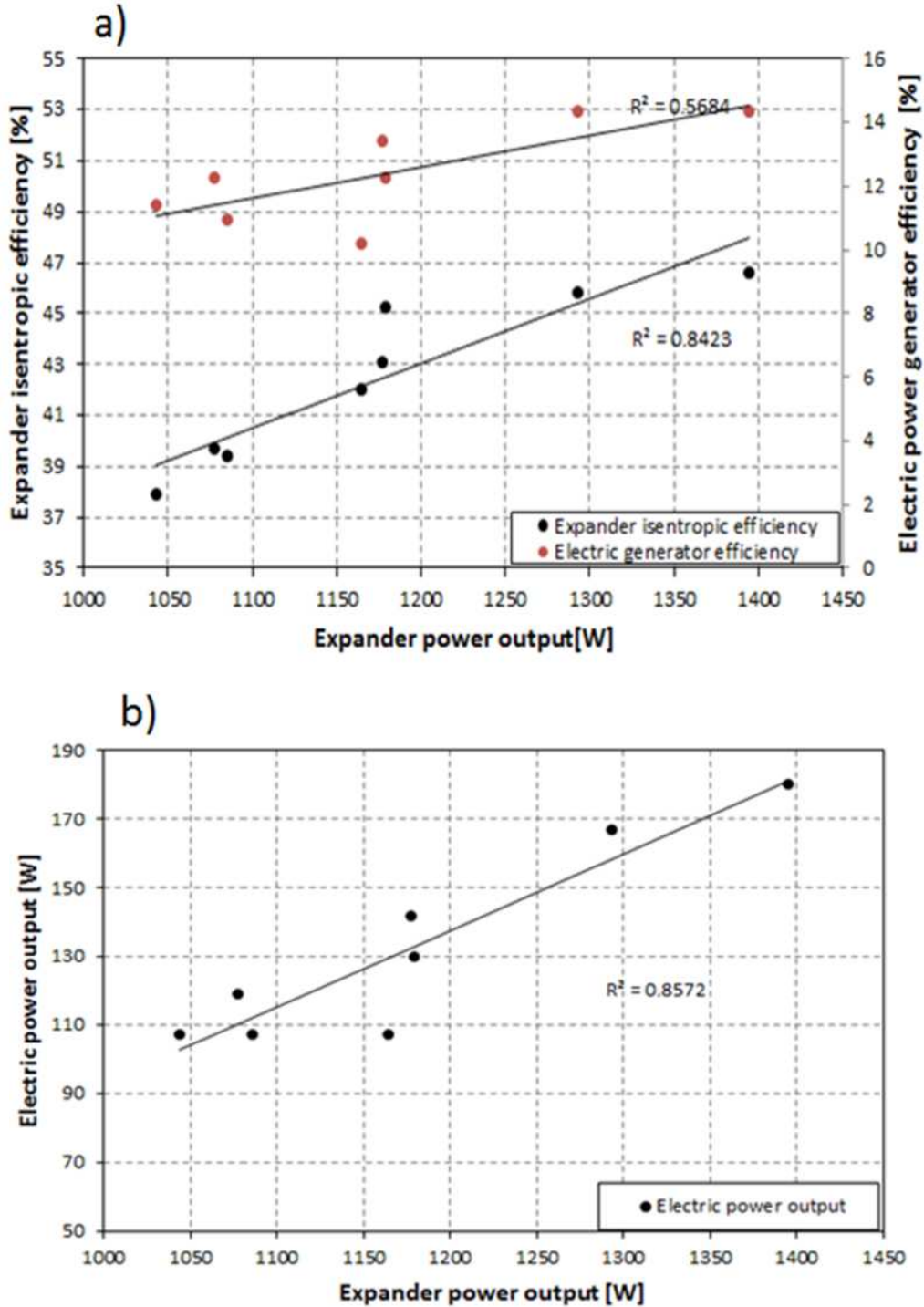
Finally, Figure 8-22 (d) shows the system's thermal and electrical efficiencies. As illustrated, both efficiencies increased gradually until the end of the test. The system's thermal efficiency was in the range of 5.77% to 7.87%, which is slightly higher than those obtained from the first run. The system's electrical efficiency was slightly lower than the results from the first run and was in the range of 0.31% to 0.53%.

#### 8.3.4.1.2.3 **The Effect of Operating Parameters on System**

##### **Performance**

Similar to the first test, the effect of variation in the system's parameters on its performance is investigated here. However, unlike the first test, the second test involved a single mass flow rate

throughout the duration of the run. Therefore, more obvious behaviour can be observed for other changing parameters. Figure 8-23 presents the system performance as a function of the expander's power output.



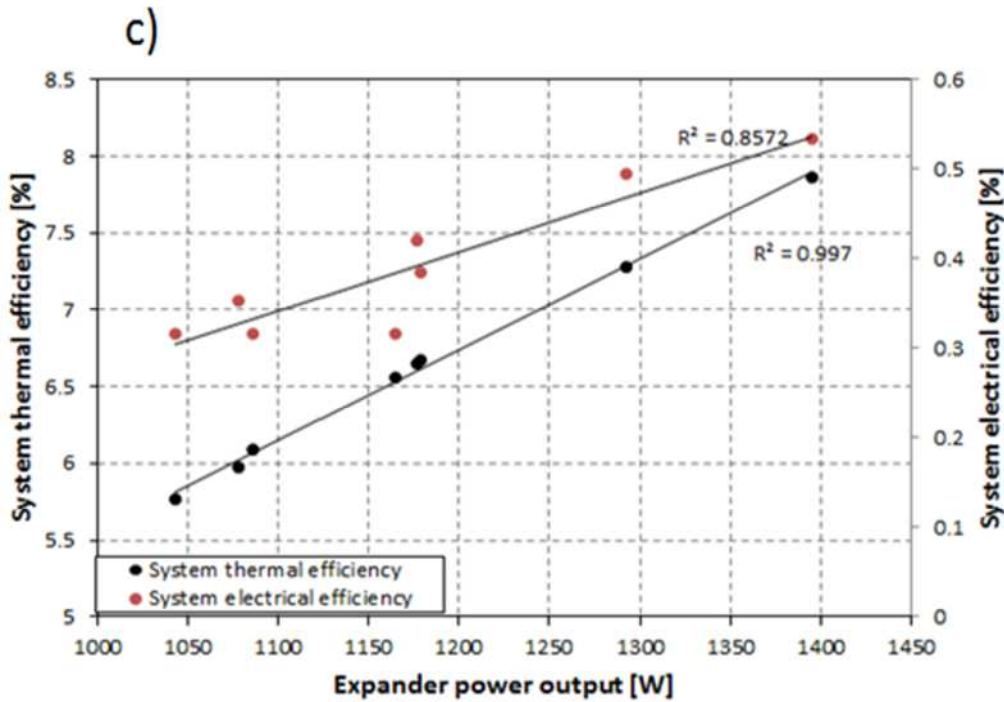
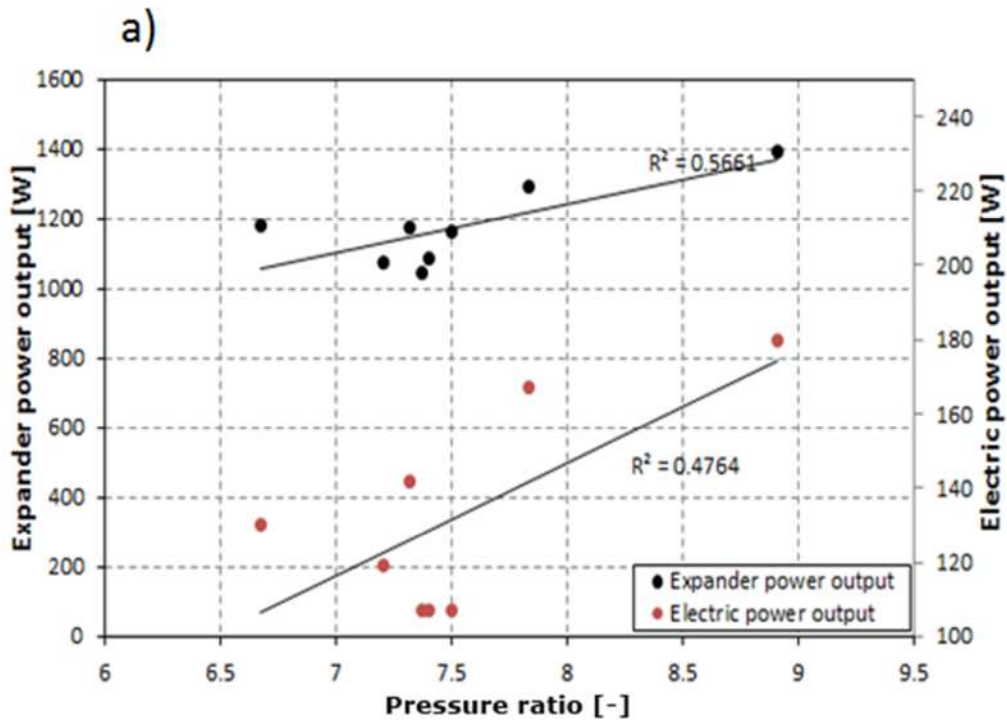


**Figure 8-23: ORC experiment 1, second run - The effect of the expander's power output on system performance.**

In Figure 8-23 (a), the effect of the expander's power output on the expander's isentropic efficiency and electric power generator at single mass flow rate shows that both efficiencies increased gradually and in a linear manner to their maximum levels with increased expander's power output. Other obvious behaviour of a similar nature can also be seen in the electric power output, in relation to the expander's power output in Figure 8-23 (b). Accordingly, linear and steady increases in the system's thermal and electrical efficiencies were observed, as shown in Figure 8-23 (c).

Figure 8-24 presents the effect of the pressure ratio across the expander on the system's performance. Figure 8-24 (a) shows that the expander's power output and the electric power output from the generator are proportional to the pressure ratio across the expander. Unlike the general behaviour of the expander's isentropic efficiency observed in the first test, Figure 8-24 (b) shows that the expander's isentropic efficiency increased proportionally with the pressure ratio across the expander, in the same way as the 0.11

kg/s flow rate case in the first test. However, the Figure also shows that the electric power generator's efficiency increased alongside the pressure ratio, similar to what was seen from the first test results. Figure 8-24 (c) illustrates how the system's thermal efficiency is also proportional to the increase in the pressure ratio. However, more consistent behaviour can be seen for the system's electrical efficiency, compared to the results observed from the first test, where they were shown to increase as the pressure ratio increased.



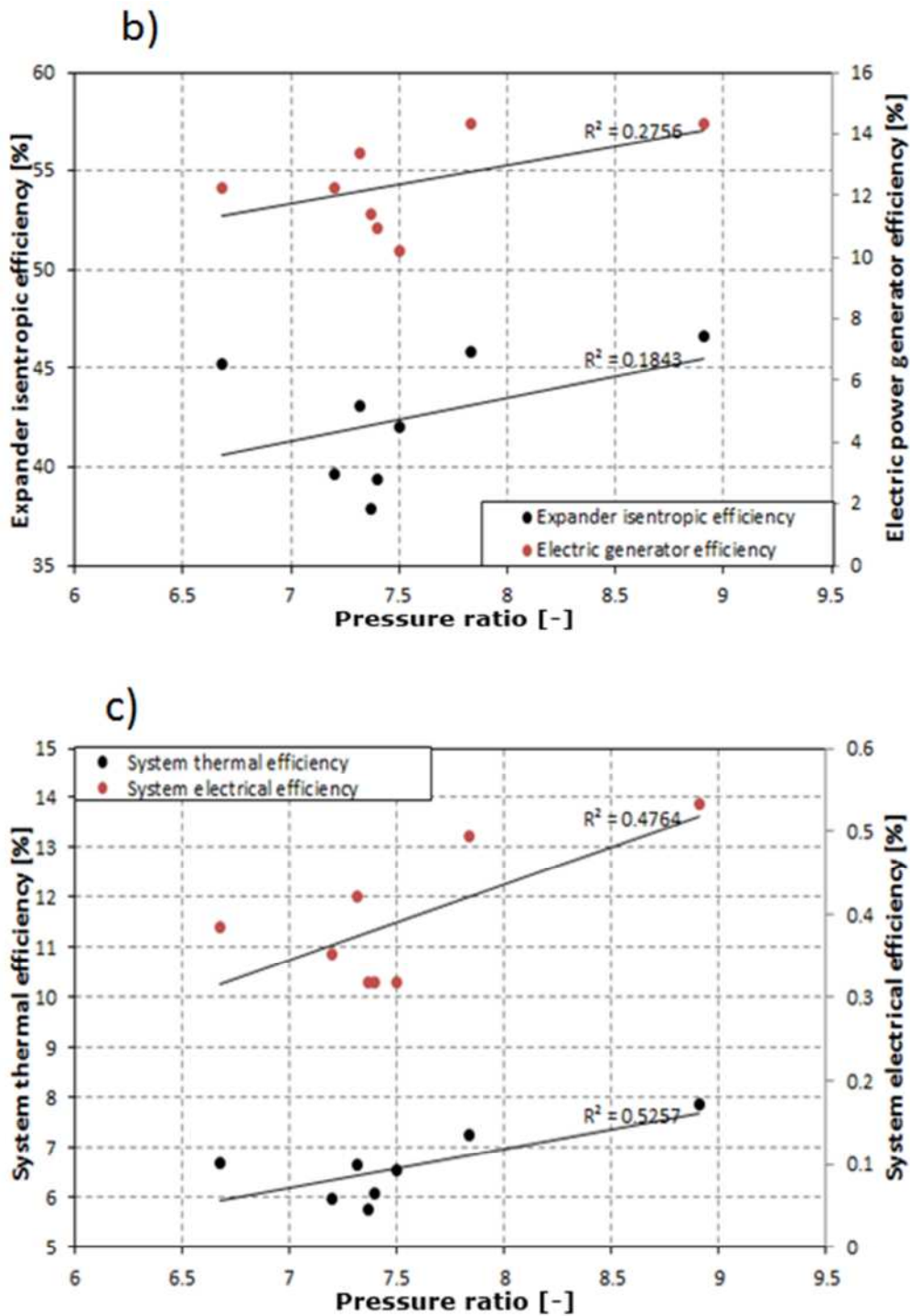


**Figure 8-24: ORC experiment 1, second run - The effect of the pressure ratio across the expander on system performance.**

Figure 8-25 (a) shows the expander’s power output and the electric power output as functions of the expander’s rotational speed. Both outputs showed similar behaviour, where they were at their maximum at the minimum rotational speed and reduced gradually as the rotational speed increased. However, the difference between

the expander's power output and the electric power output indicates low electric generator efficiency. The relationship between the electric power generator's efficiency and the electric power output is shown in Figure 8-25 (b), where the electric power output increased as the electric generator's efficiency increased.

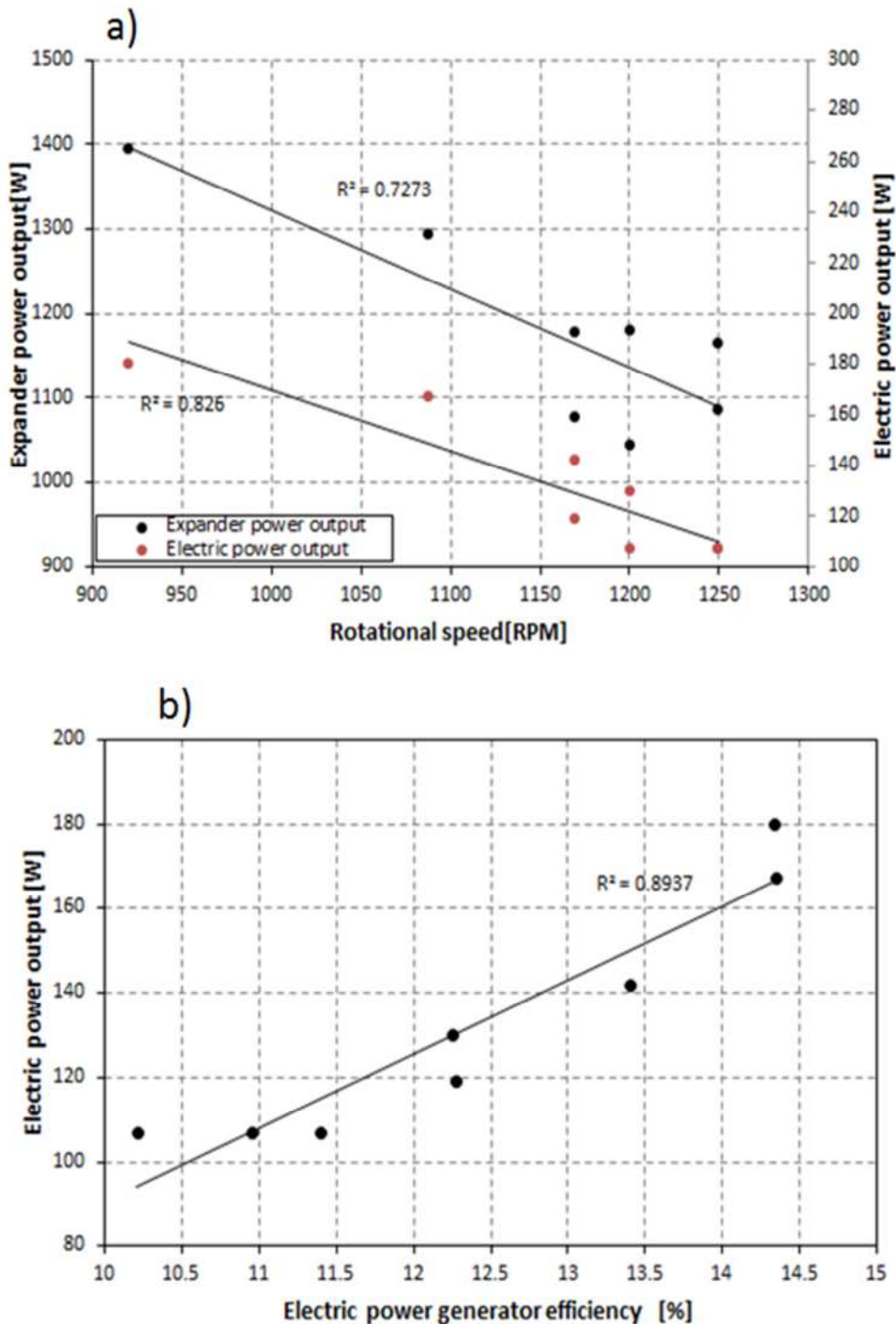


**Figure 8-25: ORC experiment 1, second run's parameters relationships- a) The relationship between the expander's rotational speed, the expander's power output, and the electric power output, and b) the relationship between the electric power generator's efficiency and the electric power output.**

#### 8.3.4.1.2.4 Second run's Optimum Performance

In the second run, the optimum experimental point yielded the greatest thermal and electrical efficiencies, as well as the maximum expander's and electric power generator's outputs. It also yielded the maximum expander's isentropic efficiency and the second highest electric power generator's efficiency. Table 6.15 presents the second run's optimum performance characteristics.

**Table 8.4: ORC experiment 1, second run – The R1233zd(E) ORC system's optimum experimental performance.**

System thermal efficiency [%]	7.87
System electrical efficiency [%]	0.533
Expander power output [W]	1394.83
Expander isentropic efficiency [%]	46.61
R1233zd(E) pump power [W]	143.86
R1233zd(E) pump efficiency [%]	31.50
Net thermal power output [W]	1250.97
Electric power output [W]	180
Electric power generator efficiency [%]	14.34
R1233zd(E) mass flow rate [kg/s]	0.072
Evaporator pressure [bar]	9.06
Expander inlet temperature [°C]	93.65
Condenser pressure [bar]	1.01
Condenser exit temperature [°C]	12.61
Steam humidifier heat input [kW]	33.75
Evaporator power [kW]	15.9
Condenser power [kW]	15.61
Recuperator heat exchanger LP side [kW]	1.12
Recuperator heat exchanger HP side [kW]	2.05

As was demonstrated when lower and constant mass flow rates were implemented, the system's thermal and electrical efficiencies were slightly higher than those achieved in the first run, even though the power output produced by the expander was lower by 572W, compared to the first run. However, the expander's isentropic efficiency was slightly lower than in the first run. The electric power generator's efficiency showed significant improvement, where it was 7.91% in the first run and almost doubled to reach 14.34% in the second run. The electric power output had also improved from 140W in the first run to 180W in the second run. The results also show that the heat exchangers' energy levels were lower than those seen in the first run. Table 8.5 presents the optimum experimental performance state points'

properties, while Figure 8-19 and Figure 8-20 present illustrations of the optimum performance point on the R1233zd(E) T-S and P-H diagrams, respectively.

**Table 8.5: ORC experiment 1, second run – The R1233zd(E) ORC system’s optimum experimental state points’ properties.**

State point	Temperature [°C]	Pressure [bar]	Enthalpy [kJ/kg]	Entropy [kJ/kg-°C]
2	93.65	9.06	461.38	1.7564
3	53.07	1.01	440.53	1.8228
3S	28.044	1.01	419.71	1.7564
5	35.55	1.01	426.37	1.7782
Condensation	17.921	1.01	219.98	1.0707
7	12.606	1.01	213.98	1.0499
8	13.986	9.06	215.83	1.0542
9	36.979	9.06	242.27	1.1427

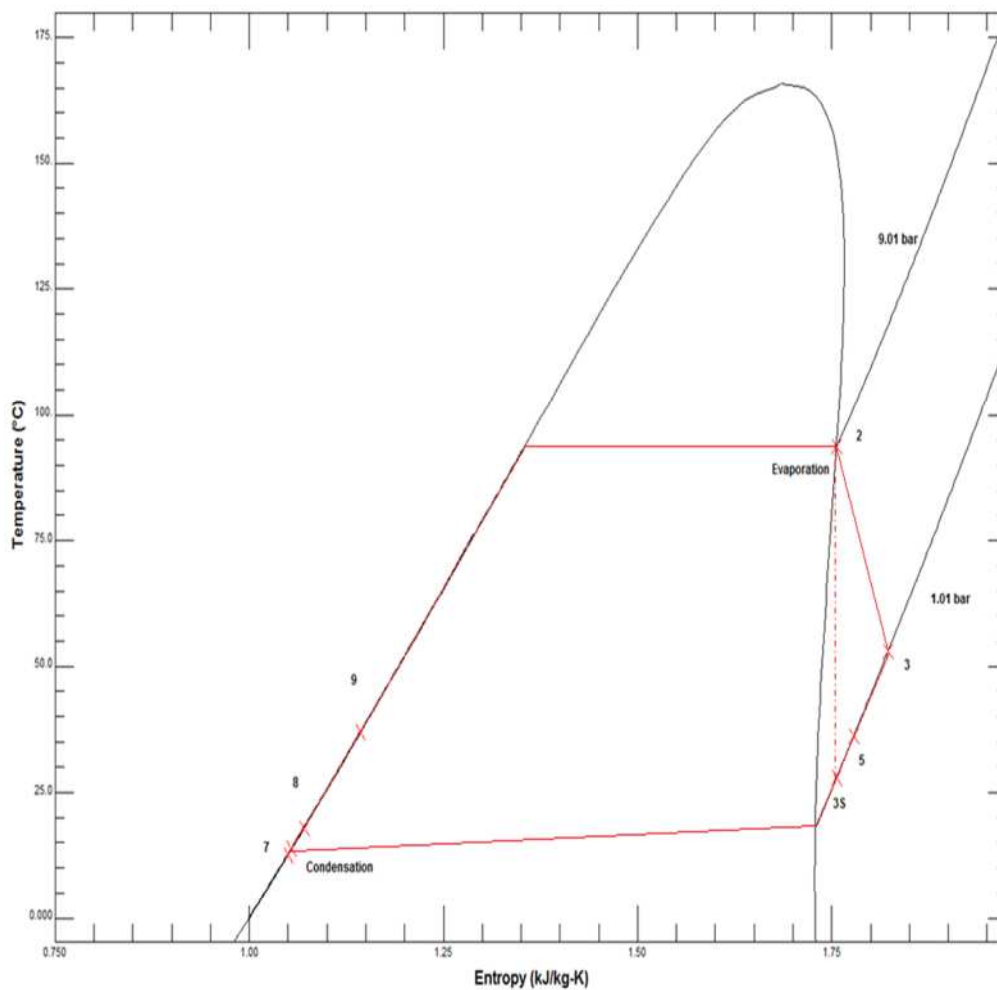


**Figure 8-26: ORC experiment 1, second run - Optimum performance point represented on the R1233zd(E) T-S diagram**

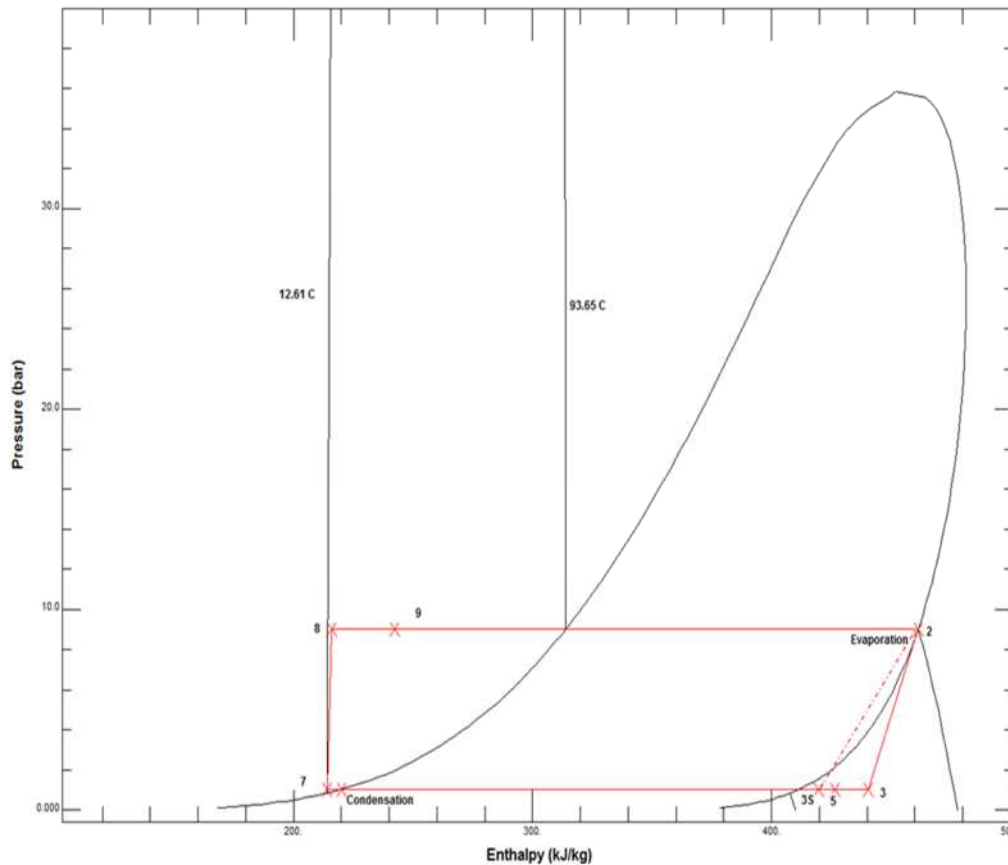


**Figure 8-27: ORC experiment 1, second run - Optimum performance point represented on the R1233zd(E) P-H diagram**

#### 8.3.4.1.3 Conclusions to Experiment 1

The first experiment provided an insight into the effect of operating parameters, such as the expansion ratio and the refrigerant mass flow rate, on system's performance. However, both tests showed that the system's thermal performance was lower by almost half of what had been predicted theoretically. The maximum expander power output achieved was just slightly under 40% of the anticipated power output. However, the main source of the lower performance is the steam humidifier heat source which could not achieve the anticipated temperature of 120°C, and therefore directly affected the expander's power output and its rotational speed. Subsequently, the expander was not able to transmit the power and speed required by the electric power generator in order to produce the anticipated electric power output, and resulted in the poor electric generator's efficiency and electric power output. In addition, the R1233zd(E) circulation pump showed low efficiency,

and chocking at some points during the test, which also contributed to the lower performance of the system.

Because of the problems addressed above, it was decided to suspend the experiment and replace the DC motor with the automotive alternator used in the expander-alternator preliminary test. The pump was investigated by running it while the prototype system was shut down. The refrigerant was observed through the sight glass installed on the pump's exit line. It was noticed that the refrigerant's flow does not increase consistently when the pump speed is increased. Eventually, there was no sign of working fluid passing through the sight glass which was an indication that the refrigerant might have overflowed the condenser, and was not able to move freely to the pump and to the other system's components. This could be due to a piping configuration in relation to the pump location and heat exchangers' positions which may have caused the refrigerant to overflow the condenser. Therefore it was decided to alter the system piping lengths and bends and also alter the heat exchanger heights. To make these modifications, the system was isolated and the R1233zd(E) was recovered in order to carry on safely with these modifications.

#### 8.3.4.2 **Experiment 2**

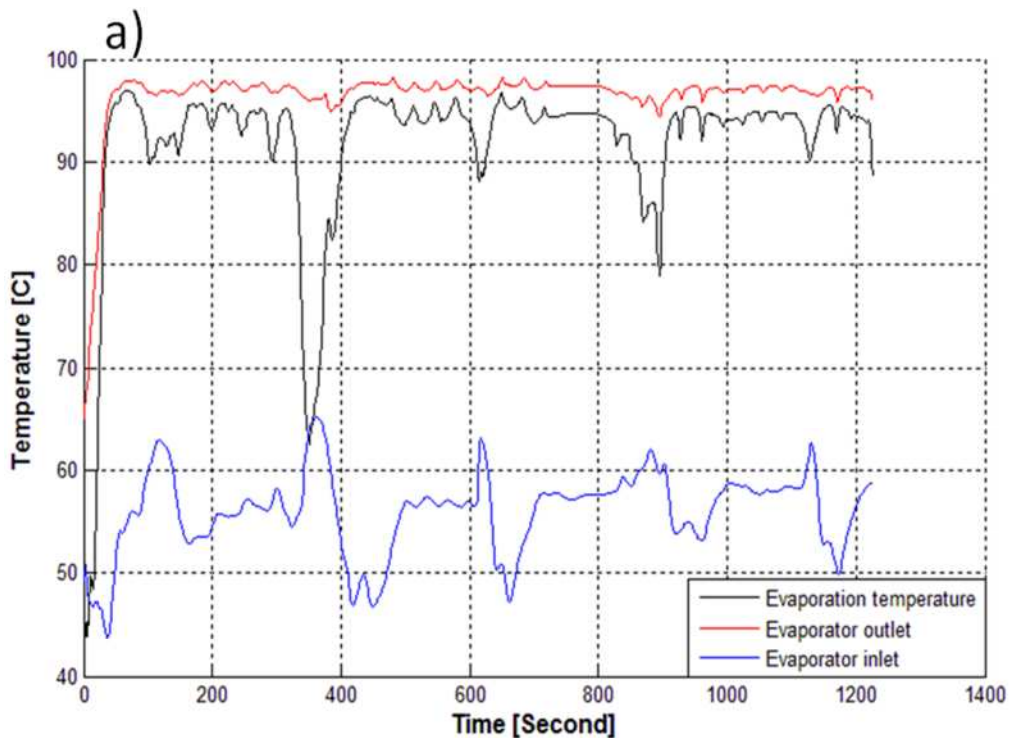
After the ORC prototype system modifications were completed, the system was initiated to commence the second and final experiment on the system using the automotive alternator as an electric power generator. The experiment consisted of one run that yielded the maximum performance characteristics attainable from the system with the current configuration.

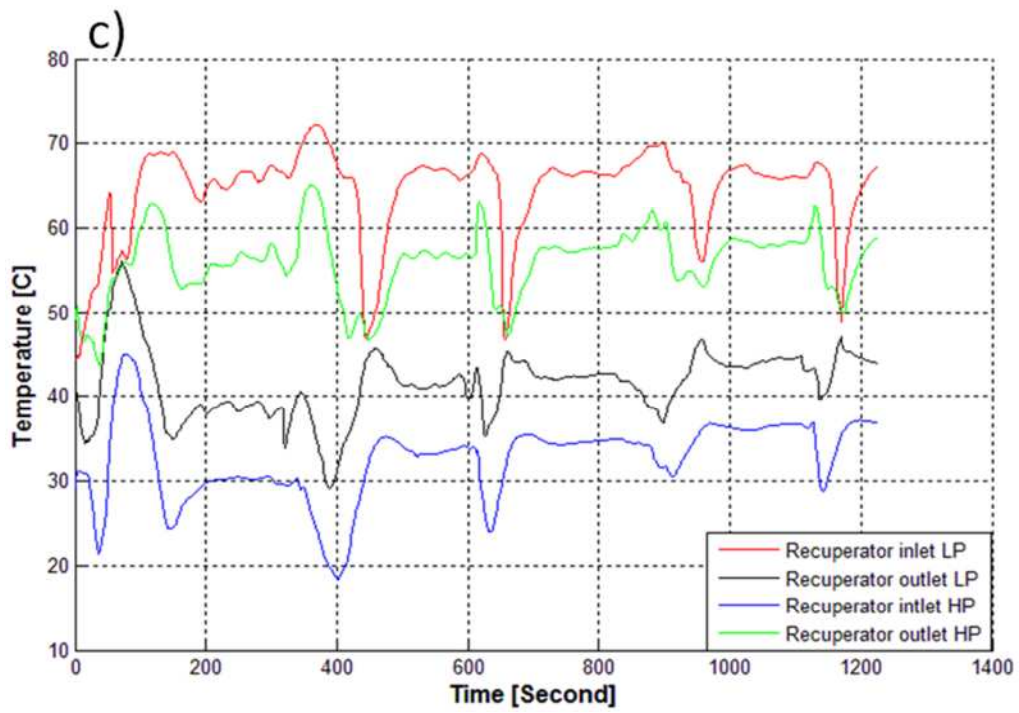
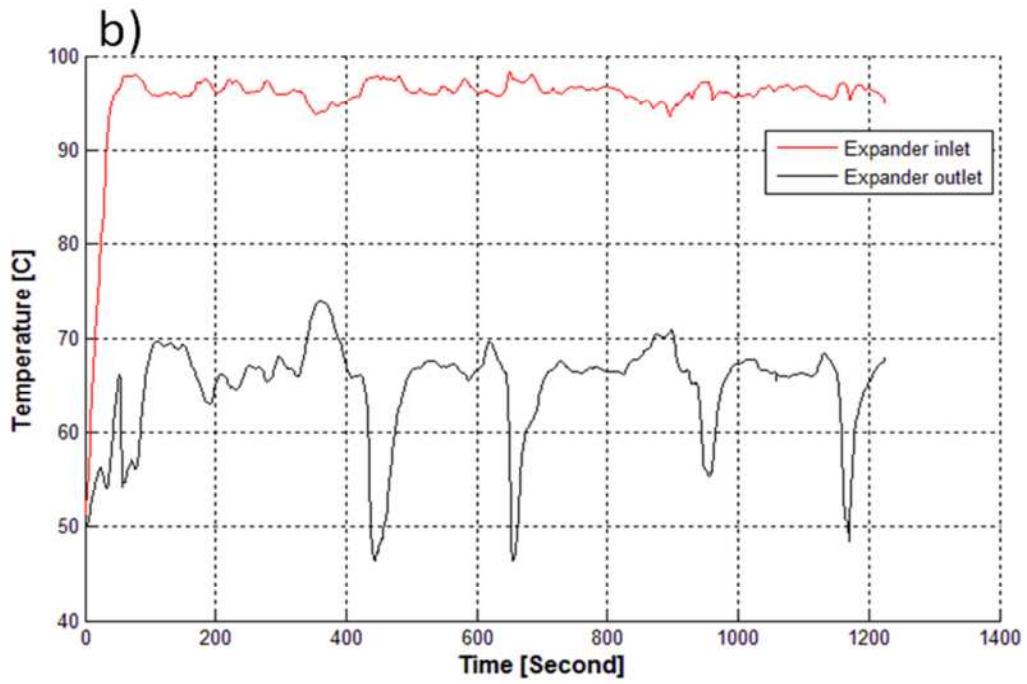
It is important to note that the pressure transducer at the condenser's outlet was not installed after the modifications, due to damage incurred to the transducer connection during the removal of instruments required for the modifications. Instead, the expander's outlet pressure transducer was considered sufficient for

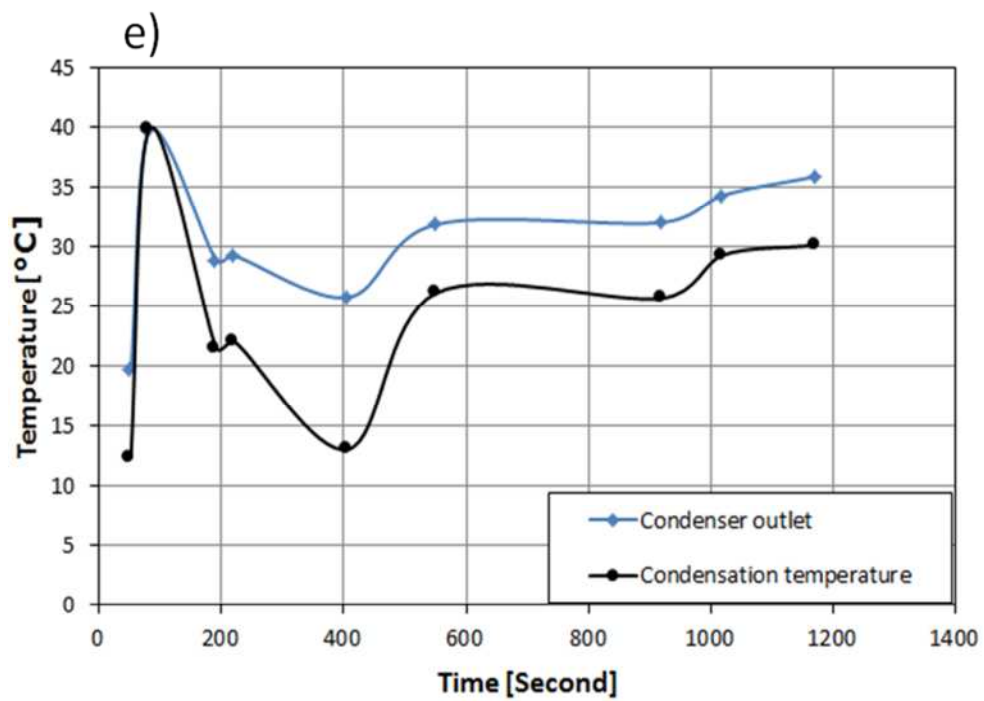
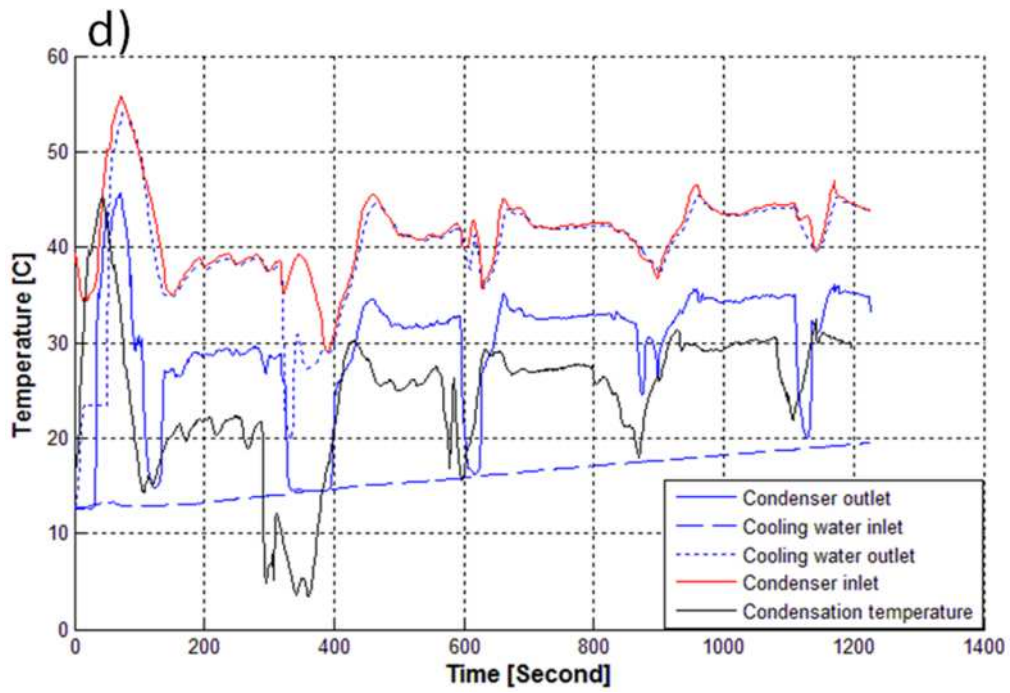
monitoring and analysing the low pressure side of the system, as a result of the very slight pressure drops seen in the results of the first experiment. Furthermore, the results of the second experiment show that both the expander's and the electric power generator's power outputs were below expectations, due to several factors, which will be discussed.

However, similar to the first run of the first experiment, the heat input into the system's evaporator varied during the experiment, while the steam temperature was set at its maximum. On the condenser side, the cooling water supply was set at flow rates from 3 to 4 l/min while the temperature was increased gradually from 11°C to 20°C.

#### 8.3.4.2.1 Temperature and Pressure Profiles







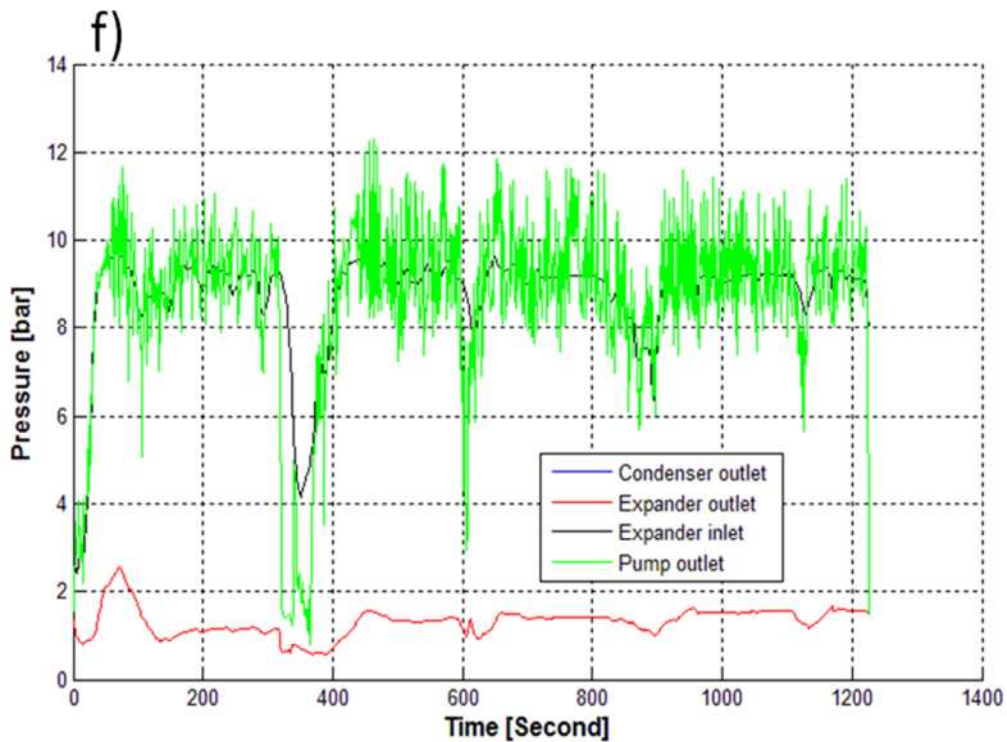


**Figure 8-28: ORC Experiment 2 – temperature and pressure profiles.**

Similar to the first experiment, Figure 8-28 presents the temperature and pressure profile of the second experiment. Figure 8-28 (a) shows the temperature profile of the evaporator where its inlet temperatures ranged from 43.69°C to 65.17°C, while the outlet showed fairly stable temperatures averaging 96.53°C. Evaporation temperatures varied between 41°C and 96.92°C. As can be seen, super-heating was improved by an average of 4.81°C, thus contributing to an improvement in overall system efficiency.

Figure 8-28 (b) shows the temperature difference between the expander’s inlet and outlet during the experiment. The expander’s outlet temperatures varied between 46.44°C and 74°C.

The recuperator’s temperature profile is presented in Figure 8-28 (c). This illustrates how further improvement in heat recovery took place in the recuperator heat exchanger, compared to the results of the first experiment. On the high pressure side, the outlet temperatures increased significantly, in contrast to the inlet temperatures, which ranged from 18.33°C to 45.1°C. On the low

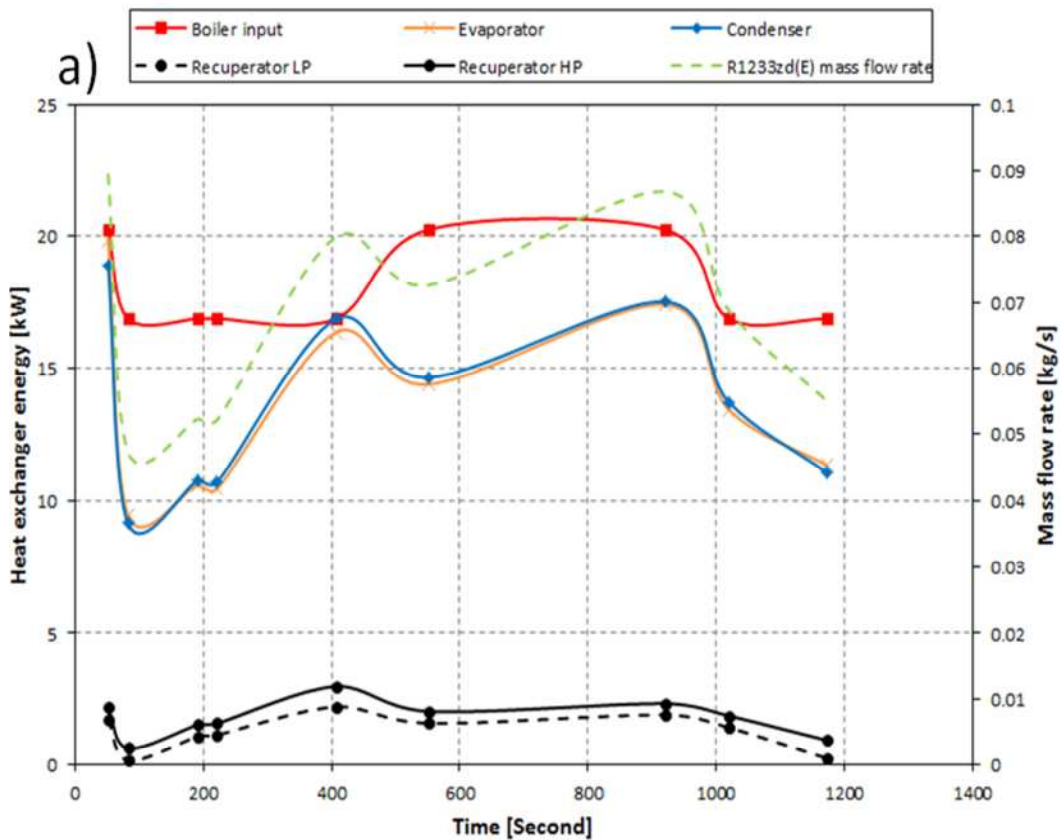
pressure side, the expander's exhaust lost its heat to the counter-flow stream and exited at temperatures between 29.17°C and 56.07°C.

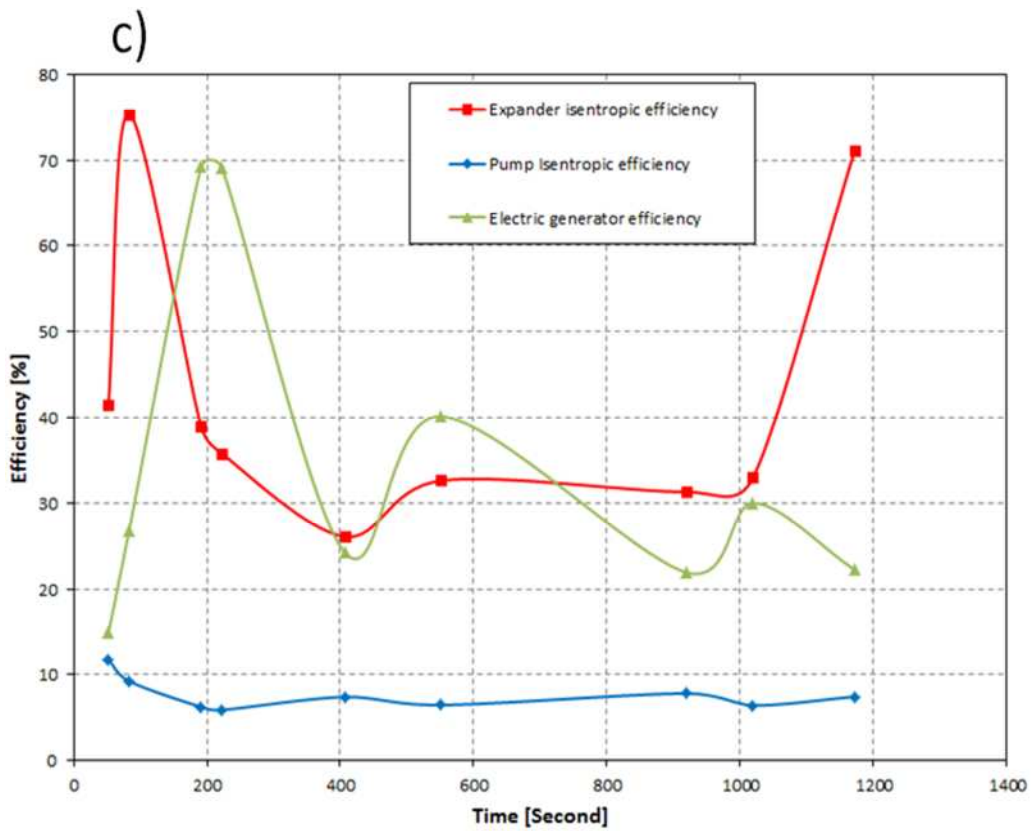
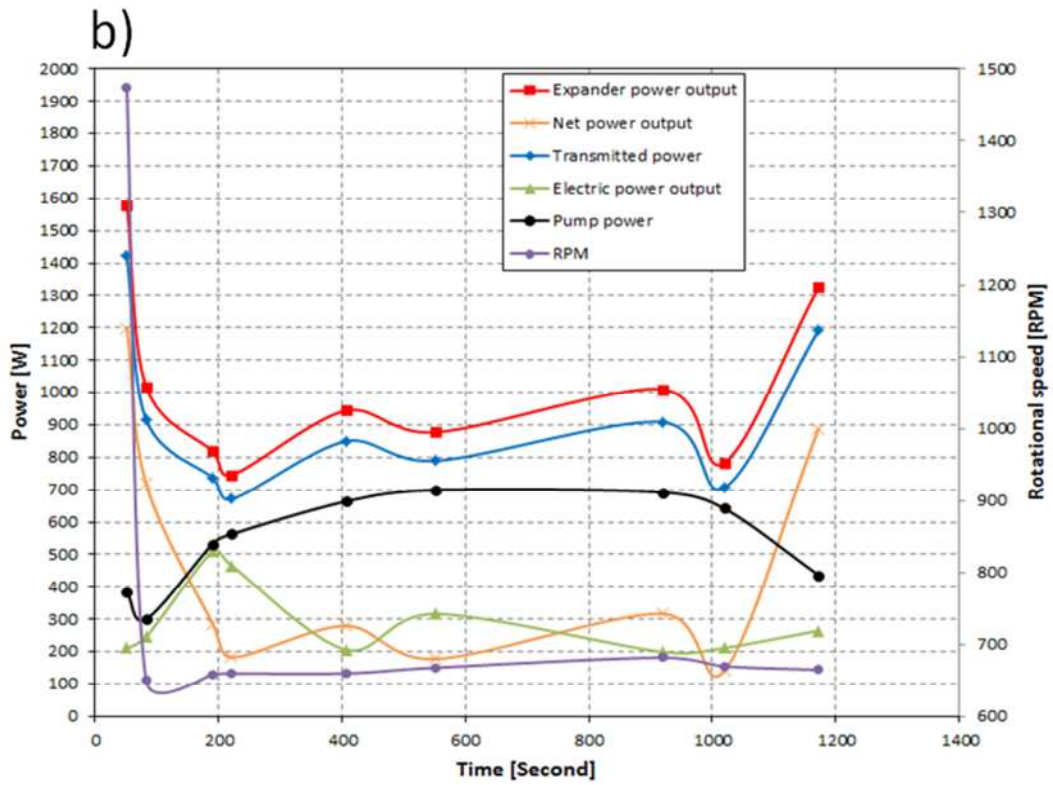
The condenser temperature profile of the experiment is shown in Figure 8-28 (d). The partially cooled R1233zd(E) stream entered the condenser, and exited at 12.60°C at the beginning of the test, and then increased up to 45.78°C. Likewise, the cooling water exited the condenser at temperatures of 12.76°C to 54.39°C. As shown, condensation occurred at a few points along the experiment timeline. At the remaining points, the refrigerant exited the condenser in a partially condensed or gas state, depending on the difference between the exit and condensation temperatures. Consequently, this affected the operation of the circulation pump and contributed further to the system's performance destruction related to the pump poor performance already pointed out. Among the manually recorded data points in the logbook, the analysis revealed that condensation only occurred at the second point, where the R1233zd(E) exited the condenser sub-cooled by only 0.2°C, as shown in Figure 8-28 (e). For this reason and in order to establish a comparison between the experimental data points, it was assumed that condensation occurred at the condenser's operating pressure and the refrigerant exited the condenser sub-cooled by 1°C, where appropriate.

Figure 8-28 (f) shows the system's pressure profile during the experiment. As shown, the pump operation exhibited excessive vibration, where the pressure fluctuation increased significantly, in contrast to what was observed in the first experiment. These may be compared with similar pressure readings obtained for the expander's inlet pressure, indicated in black. This behaviour is a result of several factors, mainly the incomplete condensation process, which may eventually lead to cavitation, besides the very low pump efficiency indicated previously. However, it also suggests that the refrigerant stream flows back into the pump, either

because of an improper connection to the pump, the pump's liquid line being too small or an inappropriate pump location within the system. For this reason, the expander's inlet pressure was taken into account in the analysis of the high pressure side of the system. However, on the high pressure side of the system, the average pressure during the experiment was 8.86 bar with a maximum recorded pressure of 9.67 bar. On the low pressure side, a wider pressure range was observed than in the first experiment, where the pressure varied from 0.89 to 2.55 bar.

### 8.3.4.2.2 Performance Profiles





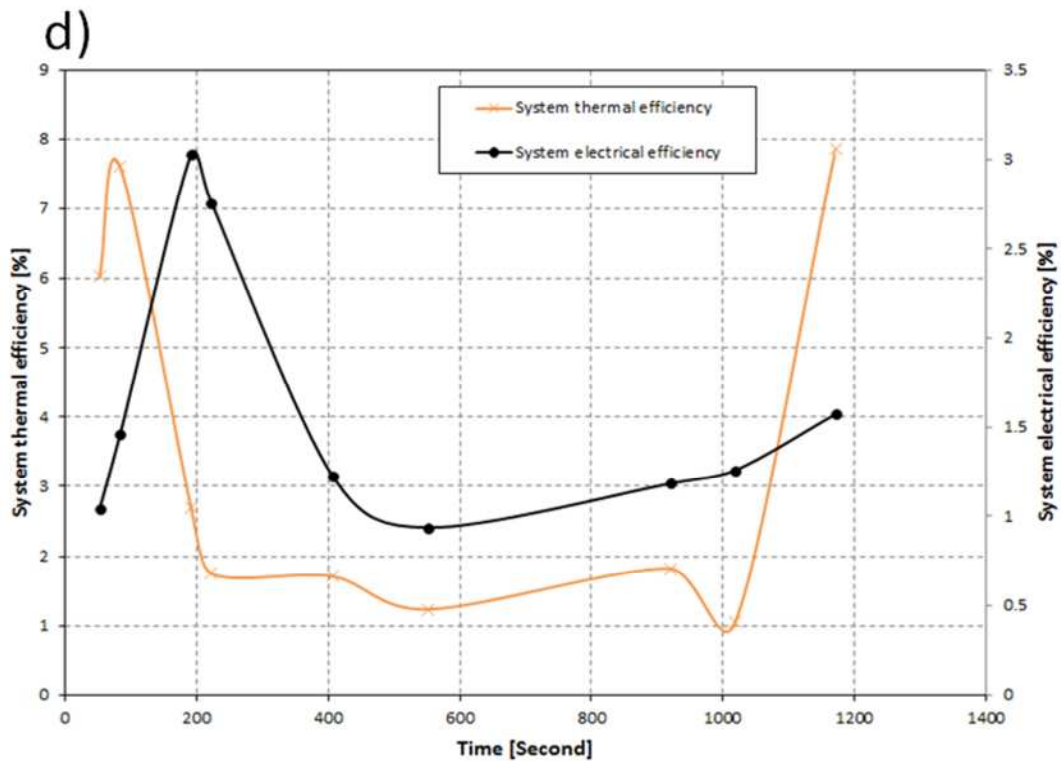


**Figure 8-29: ORC Experiment 2 - Overall system performance profiles.**

Figure 8-29 (a) presents the heat exchangers' energy profile and the R1233zd(E) mass flow rate variation for the experimental points recorded. As shown, at the first point, the steam humidifier's heat supply was 20.25 kW. This was reduced to 16.88 kW for four recorded points, before being increased again to 22.25 kW for two points and then reduced once more to 16.88 at the end of the test. The mass flow rate was also altered during the experiment, where it varied from 0.047 to 0.089kg/s. The Figure also confirms the heat exchangers' energy dependency on the R1233zd(E) mass flow rates. The evaporator's energy input varied from 9.44 kW to 19.82 kW, while the condenser's rejected energy was also within the same range and varied from 9.14 kW to 18.88 kW. The energy on the recuperator's low pressure side was in the range of 0.16 kW to 2.20 kW, while on the high pressure side, it ranged from 0.62 kW to 3 kW.

Also similar dependency is confirmed for the power generation and consumption profile presented in Figure 8-29 (b). As shown, the expander's power output ranged between 746W and 1580W;

slightly lower than the power output range achieved in the first experiment. The net thermal power output exhibited severe reductions throughout the experiment, due to the power consumption increased by the pump, besides its very low efficiency and unstable operation. However, the net thermal power output ranged from 141W to 1196.50W, where the pump's power consumption increased gradually from its minimum of 300W to its maximum of 699.57W, before dropping again. Electric power output showed significant improvement using the automotive alternator as the electric power generator. However, this improvement remained below the expected output from the system, where the electric power output varied from 199.51W to 510.34W. The Figure also shows the rotational speed of the expander recorded during the experiment and ranged between 650 RPM and 1475 RPM.

Figure 8-29 (c) shows that the expander's isentropic efficiency reached high levels when the pressure ratios across the expander were low. When the pressure ratio was 4.37, the expander's isentropic efficiency reached its maximum of 75.42% and when the ratio was 5.75, the expander's efficiency was 71.23%. This behaviour confirms the dependency of the expander's isentropic efficiency on the pressure ratio, where a lower pressure ratio results in higher efficiency and vice-versa. It also shows agreement with the experimental results obtained by a smaller expander from the same manufacturer, published in reference [81]. However, when the pressure ratio increased, the expander's efficiency decreased to reach similar levels to that observed in the first experiment, with an average of 43% and a lowest value of 26.15%. The poor performance of the pump can also be seen clearly in the Figure, where the pump's efficiency was at its maximum of 11% at the first point, before dropping to below 10% for the rest of the duration of the experiment. However, the electric generator's efficiency exhibited a major increase when the automotive alternator was utilised, where it reached 69.2% at the third and fourth points analysed and showed an average of 38% throughout the test.

Figure 8-29 (d) shows the system's thermal and electrical efficiency. At the first two points, the system achieved thermal efficiencies of 6% and 7.6%, respectively. However, an obvious reduction in thermal efficiency occurred due to the pump's increased power consumption during the experiment. When the pump's power consumption was reduced again at the end of the experiment, a maximum efficiency of 7.86% was achieved, almost equal to the best thermal efficiency demonstrated in the second run of the first experiment. Although the system's electrical efficiency was still below expectations, it can be seen that efficiency improved significantly using the automotive alternator, where the maximum electrical efficiency achieved was 3%, while the lowest achieved electrical efficiency for the system was nearly 1%, which is higher than any efficiency obtained in the first experiment.

#### 8.3.4.2.3 Second Experiment's Optimum Performance

Unlike the first experiment, the effect of the expansion ratio and R1233zd(E) mass flow rate on system performance in the second experiment seems difficult to characterise because of the continuous alteration in pressure and mass flow rate during the experiment, besides the incomplete condensation and abnormal operation of the R1233zd(E) circulation pump. Nevertheless, the results of the second experiment show that there was no single experimental point where most of the maximum system characteristics were achieved, as was the case in the first experiment. However, trading off characteristics and knowing that only the second point constituted a fully completed ORC cycle process, it was selected as the optimum performance point. The results are presented in Table 8.6.

**Table 8.6: ORC Experiment 2 - The R1233zd(E) ORC system's optimum experimental performance.**

System thermal efficiency [%]	7.6
System electrical efficiency [%]	1.46
Expander power output [W]	1019.54
Expander isentropic efficiency [%]	75.42
R1233zd(E) pump power [W]	300

R1233zd(E) pump efficiency [%]	9.27
Net thermal power output [W]	718.31
Electric power output [W]	245.99
Electric power generator efficiency [%]	26.82
R1233zd(E) mass flow rate [kg/s]	0.047
Evaporator pressure [bar]	9.38
Expander inlet temperature [°C]	97.66
Condenser pressure [bar]	2.15
Condenser exit temperature [°C]	39.67
Steam humidifier heat input [kW]	16.88
Evaporator power [kW]	9.45
Condenser power [kW]	9.14
Recuperator heat exchanger LP side [kW]	0.16
Recuperator heat exchanger HP side [kW]	0.62

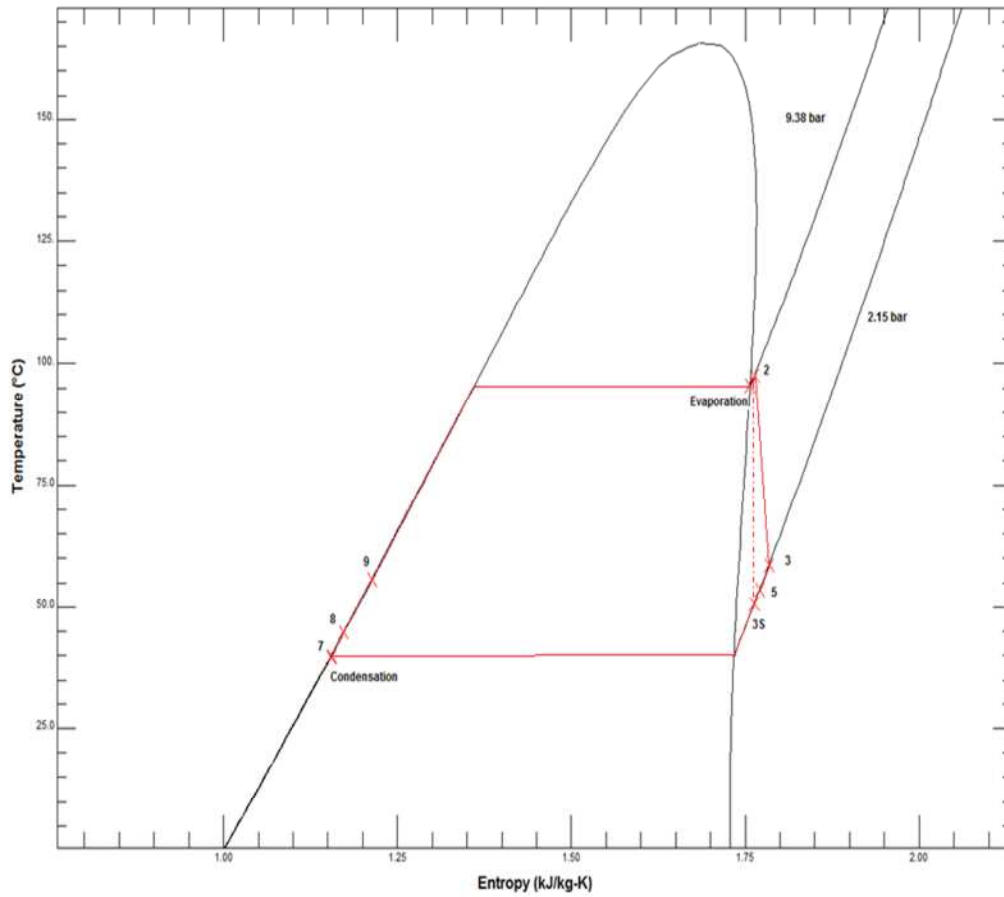
As shown, the system achieved thermal efficiency within a similar range to those achieved in the first experiment. The expander's isentropic efficiency was at its highest level by far and the heat exchangers' energy at its lowest here. Similarly, the R1233zd(E) mass flow rate was at its lowest, compared to the first experiment. The pump's efficiency was shown to be the lowest among the optimum points recorded, with only 9.27% and a relatively higher power consumption, which resulted in lower net thermal power output. As shown, the expander's inlet temperature was at its highest, compared to the first experiment's results, with a superheating temperature of 2.12°C.

Table 8.7 presents the system's state points' properties, while Figure 8-30 and Figure 8-31 show representations of the optimum performance point on the R1233zd(E) T-S and P-H diagrams, respectively. A state point called 8S was added to the P-H diagram to illustrate the enthalpy difference between the isentropic and actual pumping processes.

**Table 8.7: ORC experiment 2 - The R1233zd(E) ORC system's optimum experimental state points' properties.**

State point	Temperature [°C]	Pressure [bar]	Enthalpy [kJ/kg]	Entropy [kJ/kg-°C]
Evaporation	95.553	9.3809	462.33	1.7569
2	97.663	9.381	464.62	1.7631
3	58.721	2.147	443.06	1.7845
3S	50.688	2.147	436.05	1.7631
5	53.623	2.147	438.6	1.771
Condensation	39.88	2.1518	245.5	1.1549

7	39.674	2.147	245.26	1.1541
8	44.84	9.381	251.62	1.1724
8S	39.991	9.381	245.84	1.1541
9	55.733	9.381	264.83	1.2132



**Figure 8-30: ORC experiment 2 - Optimum performance point represented on the R1233zd(E) T-S diagram.**

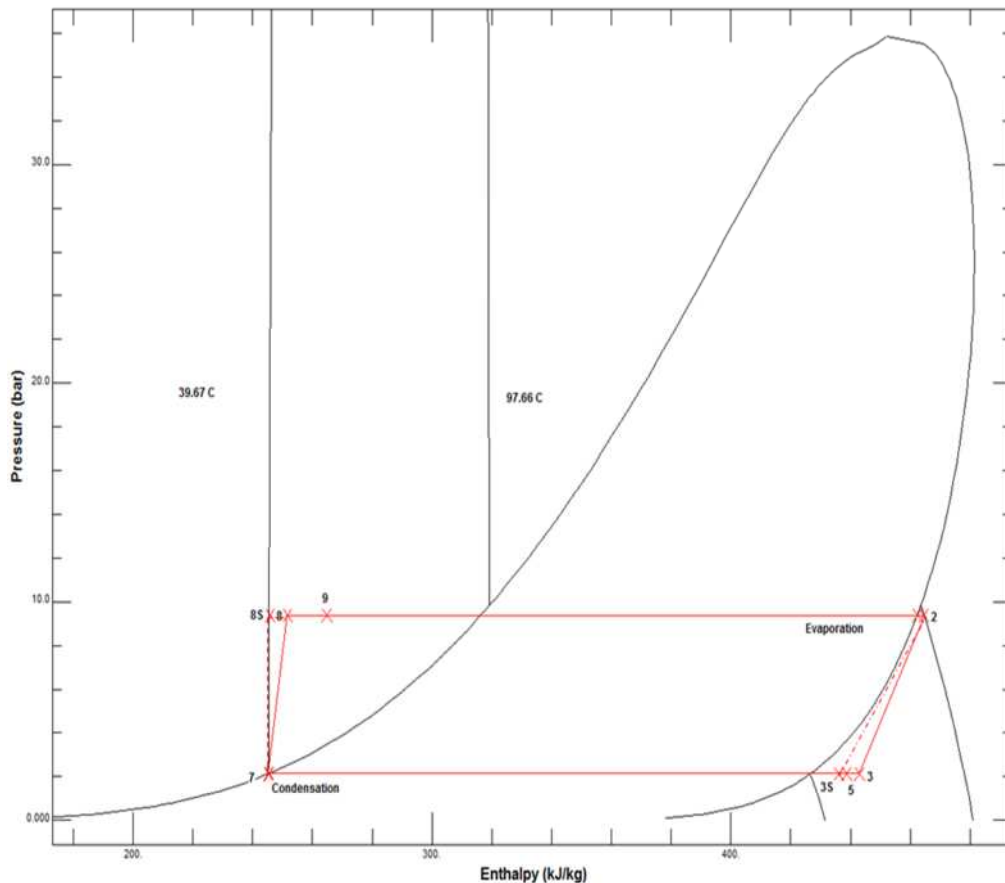


**Figure 8-31: ORC experiment 2 - Optimum performance point represented on the R1233zd(E) P-H diagram.**

### 8.3.5 R1233zd(E) ORC Prototype System Performance, and Limitations Discussion

Comparing both conducted experiments, the second experiment achieved the maximum electric power output of 500W and the best experimental overall performance characteristics represented by the second experiment's optimum performance that could be attained with the current configuration and equipment capabilities. Generally, the major obstacles limiting the achievement of higher system performance consisted of:

- The lower capability of the steam humidifier heat source to generate sufficient super-heat and maintain a constant heat supply; this was due to the cut-in and cut-out behaviour. The latter resulted in drops in heat supply at some points. Also,

most importantly, it was unable to reach the target expander's inlet temperature of 120°.

- The poor performance of the R1233zd(E) circulation pump, which consequently resulted in higher power consumption and disallowed the achievement of the mass flow rate of 0.15 kg/s predicted from the theoretical thermodynamic model as a means of achieving 5 kW expander power output.
- The low efficiency of the electric power generator, which resulted in reduced electrical power output from the system.
- To a lesser extent, the low isentropic efficiency of the expander; however, this isentropic efficiency showed great improvement in the second experiment, with around 4.5% less than the anticipated efficiency of 80%.
- The fact that the theoretical thermodynamic model may assume system component efficiency, but still not able to predict the losses occurring during the system's operation, such as heat exchangers' effectiveness, expander shaft losses, power transmission losses and magnetic losses in the electric power generator.

However if the above limitations are overcome; for instance, if the pump operates at an average isentropic efficiency of 80% as is usually seen in plunger type pumps, the electric generator had an average efficiency of 80%, and to lesser extent if the recuperator heat exchanger operated with an average effectiveness of 80%, then significant improvement in system performance is therefore expected.

Using the optimum experimental point achieved, three thermodynamic models were implemented to demonstrate the R1233zd(E) prototype system's performance improvements towards the theoretically predicted system performance, where the limitations addressed were overcome. These cases include:

- Case 1: The system operates under the optimum experimental point's operating conditions established, but with 80% pump's and electric generator's efficiencies.
- Case 2: The system operates under the optimum experimental point's operating conditions established, but with 80% expander's, pump's, and electric power generator's and recuperator's heat exchanger efficiencies. In addition, 5°C super-heat and sub-cooling were assumed for the evaporator and condenser, respectively.
- Case 3: the system operates under the theoretical thermodynamic model operating conditions, but with the optimum experimental point's R1233zd(E) mass flow rate and heat input from the heat source.

Table 8.8 presents the results of the three simulated cases, in relation to the optimum experimental point results and the initially predicted thermodynamic model results. The three simulated cases state points' properties are presented in Appendix E.3.

**Table 8.8: R1233zd(E) ORC system's optimum experimental point improvements towards the initially predicted thermodynamic model.**

	Experimental	Case 1	Case 2	Case 3	Thermodynamic model
System thermal efficiency [%]	7.58	10.42	11.05	14.43	14.43
System thermal efficiency Improvement [%]	-	2.84	3.47	6.85	6.85
System electrical efficiency [%]	1.46	4.35	4.77	6.42	10.67
Expander power output [W]	1019.55	1019.55	1117.1	1505.40	5000
Expander isentropic efficiency [%]	75.42	75.42	80	80	80
R1233zd(E) pump power [W]	302.95	34.84	35.18	57.1	189.7
R1233zd(E) pump efficiency [%]	11.29	80	80	80	80
Net thermal power output [W]	716.59	984.16	1081.92	1448.30	4810.3
Electric power output [W]	245.99	733.69	804.31	1083.89	

Electric power generator efficiency [%]	26.80	80	80	80	80
R1233zd(E) mass flow rate [kg/s]	0.047	0.047	0.047	0.047	0.15
Evaporator pressure [bar]	9.38	9.38	9.38	14	14
Expander inlet temperature [°C]	97.66	97.66	100.55	119.38	119.38
Condenser pressure [bar]	2.15	2.15	2.15	1.84	1.84
Condenser exit temperature [°C]	39.67	39.67	34.88	30	30
Steam humidifier heat input [kW]	16.88	16.88	16.88	16.88	33.75
Evaporator power [kW]	9.45	9.44	9.79	10.04	33.33
Condenser power [kW]	9.14	9.14	8.71	8.59	28.52
Recuperator heat exchanger LP side [kW]	0.16	0.16	1.17	1.39	4.62
Recuperator heat exchanger HP side [kW]	0.62	0.62	1.17	1.39	4.62

As shown in Table 8.8 for the first case, significant system improvement could be achieved merely by resolving the pump and electric power generator issues. Most of the system's characteristics remained similar to the optimum experimental point, apart from the higher thermal efficiency, which would increase by 2.84% to reach 10.42%, due to the pump's power consumption being reduced by 268W, consuming just 34.84W. Consequently, the net thermal power output would increase from 716.59W to 984.16W. The improvement in electric generator efficiency would also increase the electric power from the system by 66.5%, from 245.99W to 733.69W, enhancing the system's electrical efficiency by 2.89%.

In the second case, further improvement in system performance could be obtained where the expander's power output increases from 1019.55W to 1117.1W, as a result of the expander's isentropic efficiency rising from 75.42% to 80%. Therefore, the net thermal power output from the system would increase to 1081.92W and would subsequently further increase up to 11.05% for the system's thermal efficiency would be achieved. Although the effectiveness of the recuperator heat exchanger was set at 80% in this case, the

results suggest a very marginal influence of the effectiveness of the recuperator heat exchanger on the system's thermal efficiency. However, the electric power output would be expected to further increase up to 804.31W, while the system's electrical efficiency would increase only slightly, compared to the first case, reaching 4.77% at the experimentally observed heat input from the steam humidifier.

In the third case, when the operating conditions were changed to the initial thermodynamic model input, the system's thermal efficiency showed a significant increase, reaching 14.43%. As the mass flow rate was maintained at a level similar to what was experimentally obtained, the power output from the expander was expected to increase to 1505.40W, 47.7% higher than experimentally obtained output. The pump's power consumption also increased to 57.1W, due to the change in operating pressure. However, the net thermal power output from the system reached 1448.30W, which subsequently increased the system's thermal efficiency. In this case and because of higher expander's power output, the electric power output expected from the system would be 1083.89W and the system's electrical efficiency at the experimental steam heat input would increase by up to 6.42%.

Likewise, for the initial thermodynamic model, when the mass flow rate was increased by up to 0.15 kg/s, the expected power output from the expander was 5 kW at 80% expander's isentropic efficiency. The expected electric power output would therefore be 4.8 kW, while the system's electrical efficiency would be expected to reach 10.68% at the maximum experimental heat supply of 33.75 kW observed in the first experiment. The required heat supply could be even higher, due to the limitations of the steam humidifier being addressed, restricting a continuous and constant heat addition process during the experiment. Figure 8-32 and Figure 8-33 show a comparison between cases of system operation

improvement from Table 8.8, illustrated on the R1233zd(E) T-S and P-H diagrams, respectively.

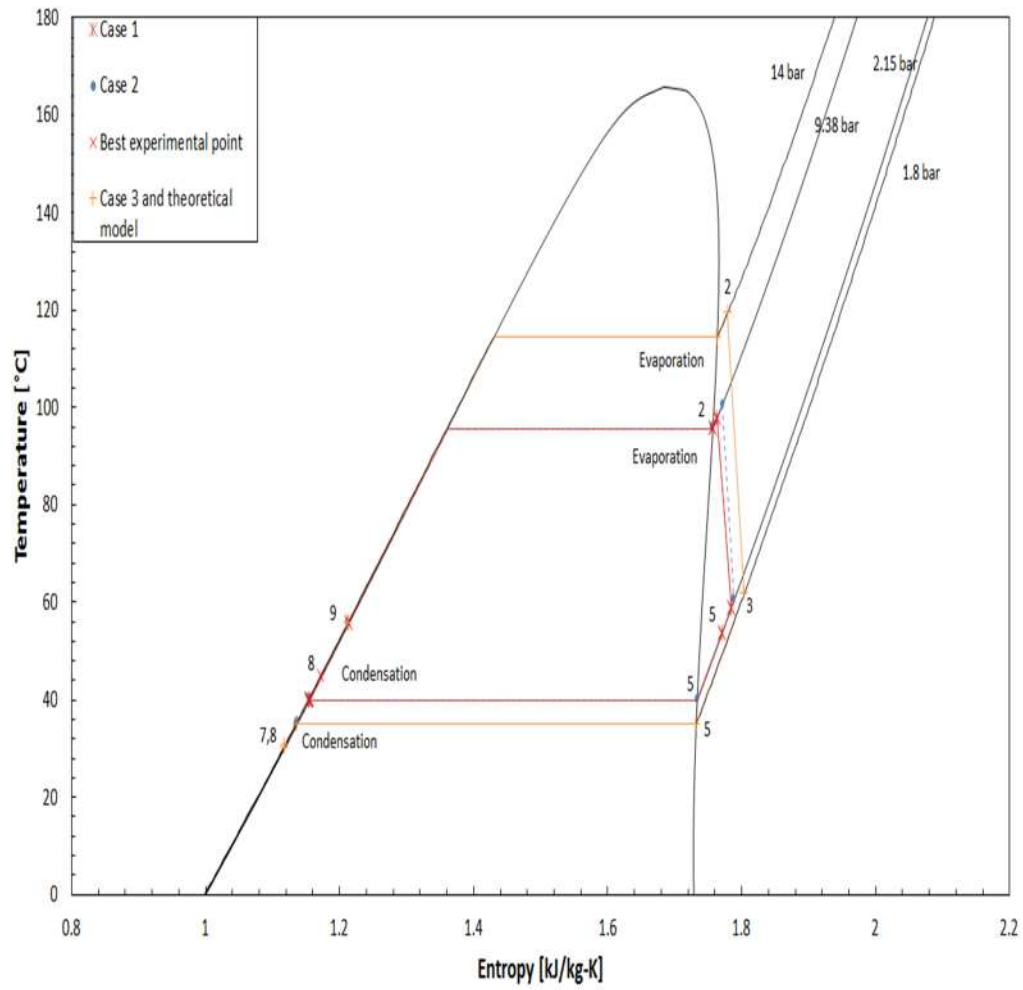


**Figure 8-32: Improvements of the optimum experimental point towards the initial thermodynamic model T-S diagram.**

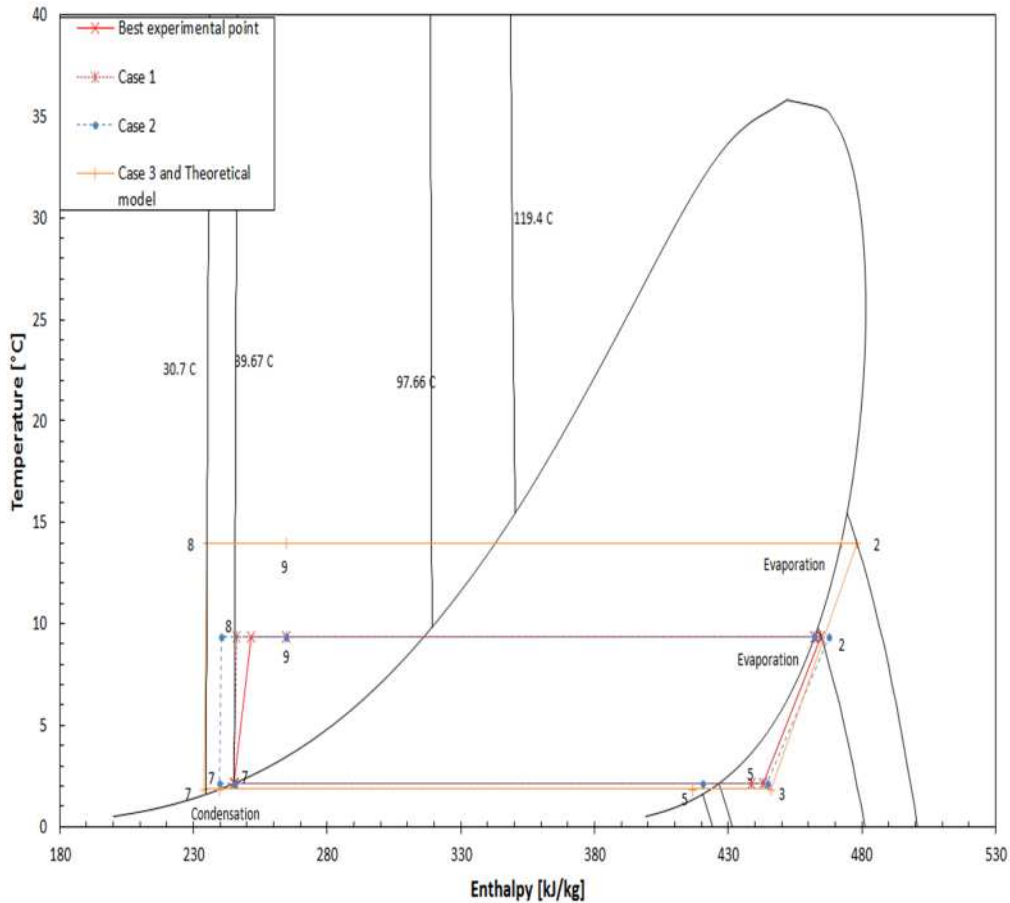


**Figure 8-33: Improvements of the optimum experimental point towards the initial thermodynamic model P-H diagram.**

The enhanced continuity of system components efficiencies demonstrated in Table 8.8 and illustrated in Figure 8-32 and Figure 8-33, indicates the initial thermodynamic model's validity in relation to the experimentally obtained results, since all presented cases were closely correlated.

### 8.3.6 Comparative Analysis of The R1233zd(E) ORC Prototype System's Power Outputs

The system's performance was compared to other experimental ORC systems reported in the literature. Jradi and Riffat [81] conducted experimental work on a micro-CHP system that employed HFE7100 as a working fluid. The system utilised a similar expander to the one used in the current research, but with an internal electric generator and maximum capacity of 1 kW. The optimum performance was achieved at a refrigerant mass flow rate

of 0.047 kg/s, a pressure ratio of 4.64, and an expander isentropic efficiency of 74.23%, these being identical to the optimum experimental point characteristics obtained from the R1233zd(E) ORC prototype system in the current research. However, the maximum electric power output obtained from their experiment was 500W, with an electric generator's efficiency of 81%. At the optimum experimental point, the micro-CHP system achieved 5.64% ORC thermal efficiency and 4.16% electrical efficiency.

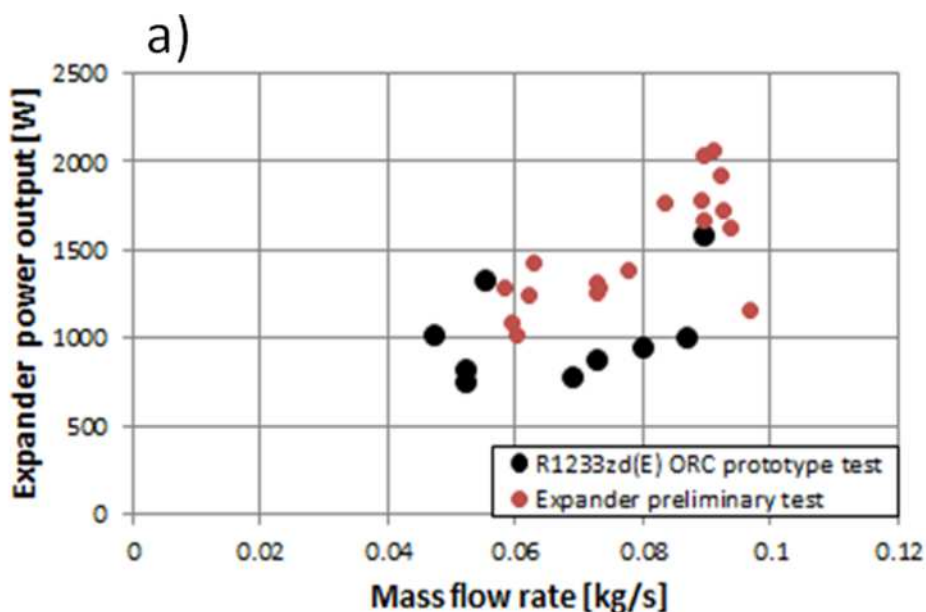
With the same micro-CHP system, Qiu et al. [76] employed HFE7000 as a working fluid and utilised a modified air motor as an expander, connected to an automotive alternator via a transmission belt. The best performance was achieved at a mass flow rate of 0.31 kg/s and an expander isentropic efficiency of 53.92%, where the expander's power output was 1690W and the electric power output achieved was 860.7W, yielding an electric generator efficiency of 50.94%. The thermal efficiency was 3.78%, while the electrical efficiency was 1.41%.

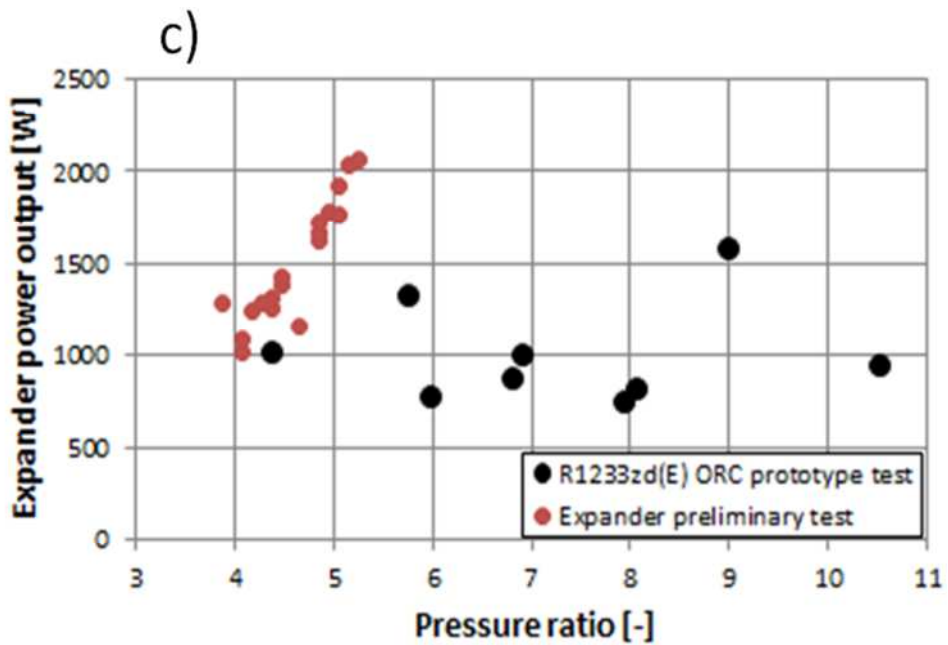
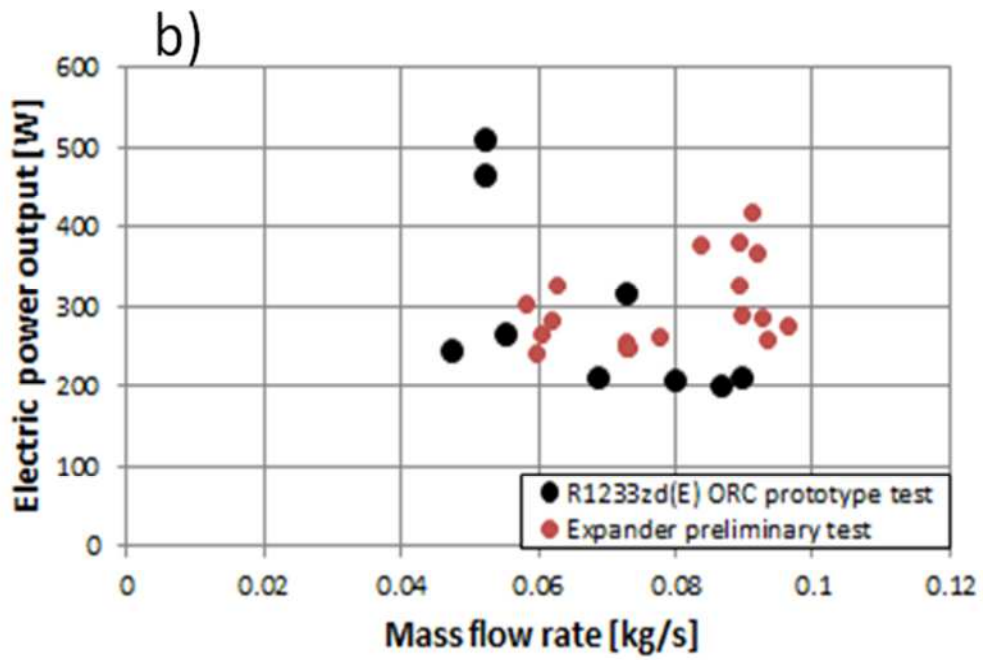
Zhou et al. [317], on the other hand, utilised a 5 kW scroll expander connected to a 2 kW alternator via a transmission belt in an ORC system employing R123 as a working fluid. The results show that the best performance was achieved at a 215°C heat source temperature and 10.8 bar evaporator's pressure. However, although the thermal efficiency reported for the system was as high as 8.5%, the expander's isentropic efficiency was only 57% and the maximum power output was 645W, without any mention of the electric power output or efficiency of the electric generator.

In relation to the R1233zd(E) ORC prototype system, the identical characteristics of the expander's performance and optimum mass flow rate reported in reference [81] suggest that 0.047kg/s could be the optimal expander design mass flow rate at which maximum isentropic efficiency is achieved, since this was not observed in the result from reference [76] with another type of expander, on the

same system and under similar operating conditions. However, this optimal mass flow rate is related to the pressure ratio across the expander and could also be related to the expander's inlet, outlet ports and piping sizes. Nevertheless, it is highly unlikely that it relates to the under expansion phenomena or the design's built-in volume ratio, since greater expander's power output was achieved at higher mass flow rates. Furthermore, the high electric generator's efficiency achieved using the internal electric generator from reference [81] confirms speed mismatch between the expander and both utilised electric power generators for the R1233zd(E) ORC system, and the very high power loss occurring as a result of power transmission through the belt. This behaviour could be observed for the micro CHP system in the results of reference [76], when the expander with integrated alternator was replaced by an expander-alternator arrangement similar to that used in the R1233zd(E) ORC prototype system.

However, this relationship between the expander-alternator arrangement and the system's outputs was confirmed by carrying out performance comparisons between the R1233zd(E) ORC prototype system results from the second experiment and the preliminary expander-generator air open-loop test, as shown in Figure 8-34 and Figure 8-35.





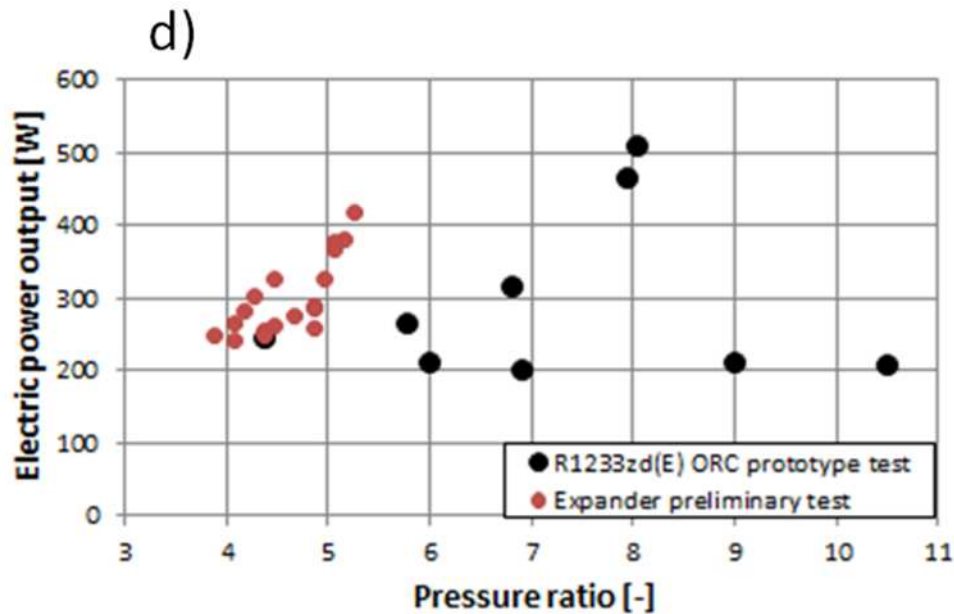


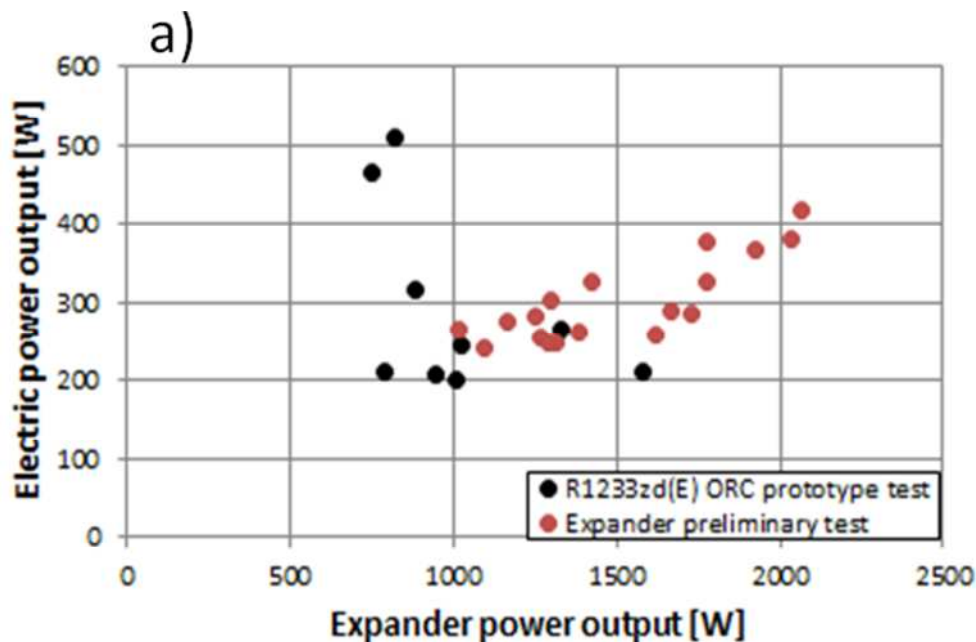
**Figure 8-34: Comparison between the R1233zd(E) ORC prototype system and preliminary expander-alternator’s experimental results 1 - a) Mass flow rate-expander’s power output, b) mass flow rate-electric power output, c) pressure ratio-expander’s power output, and d) pressure ratio-electric power output.**

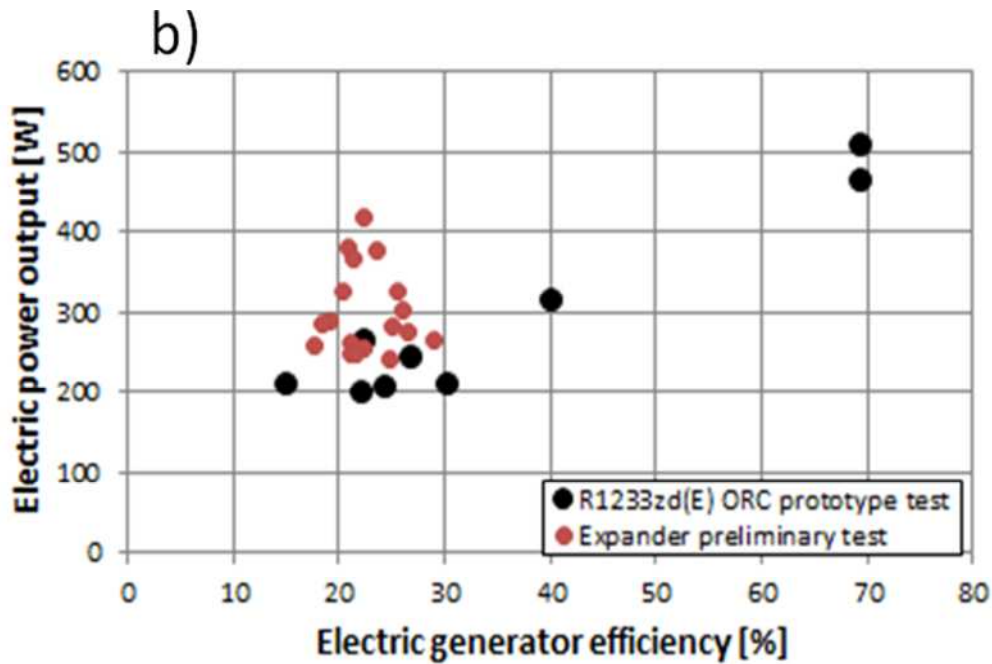
In Figure 8-34(a), the expander’s power output as a function of the mass flow rate shows that there were at least two experimental points with close results, considering the difference between the working fluid properties and experimental conditions. Here, the R1233zd(E) achieved 1580W at 0.09 kg/s and the preliminary test showed 1667W at a similar mass air flow rate. At lower mass flow rates, the R1233zd(E) ORC achieved 1325W at 0.55 kg/s, while the preliminary test achieved 1293.5W at 0.06 kg/s of air.

The comparison of the electric power output presented in Figure 8-34(b) shows a less close relationship between both results, mainly because of changes in the electric generator’s efficiency. However, the results from 0.05 kg/s to 0.08 kg/s showed to be within similar level where the R1233zd(E) ORC system achieved 265.4W at 0.055 kg/s while the preliminary test achieved 264.67W at 0.06 kg/s of air. Similarly, the R1233zd(E) achieved 212.1W and 254.57W at 0.068 and 0.07 kg/s, respectively, compared to the 206.2W and 263.4W achieved at 0.08 kg/s of air in the preliminary test.

Because of the differences in pressure ratio range in both experiments, it was found that only one experimental point fell in the comparison region when the pressure ratio was around 4 in both experiments, as shown in Figure 8-34(c). It is important to emphasise that this point is the optimum experimental point recorded for the R1233zd(E) ORC prototype system, where 1019W expander power output was achieved at a pressure ratio of 4.37, while the closest points observed from the preliminary experiment were 1017.38W and 1091.23W at a 4.1 pressure ratio across the expander.

For the electric power output, the comparison presented in Figure 8-34(d) shows that there are also two preliminary test points which perfectly match the best R1233zd(E) ORC optimum point, at which 250W was achieved with a 4.37 pressure ratio, compared to the 254.6W and 263.4W achieved at a ratio of 4.37 and 4.47, respectively, in the preliminary test.





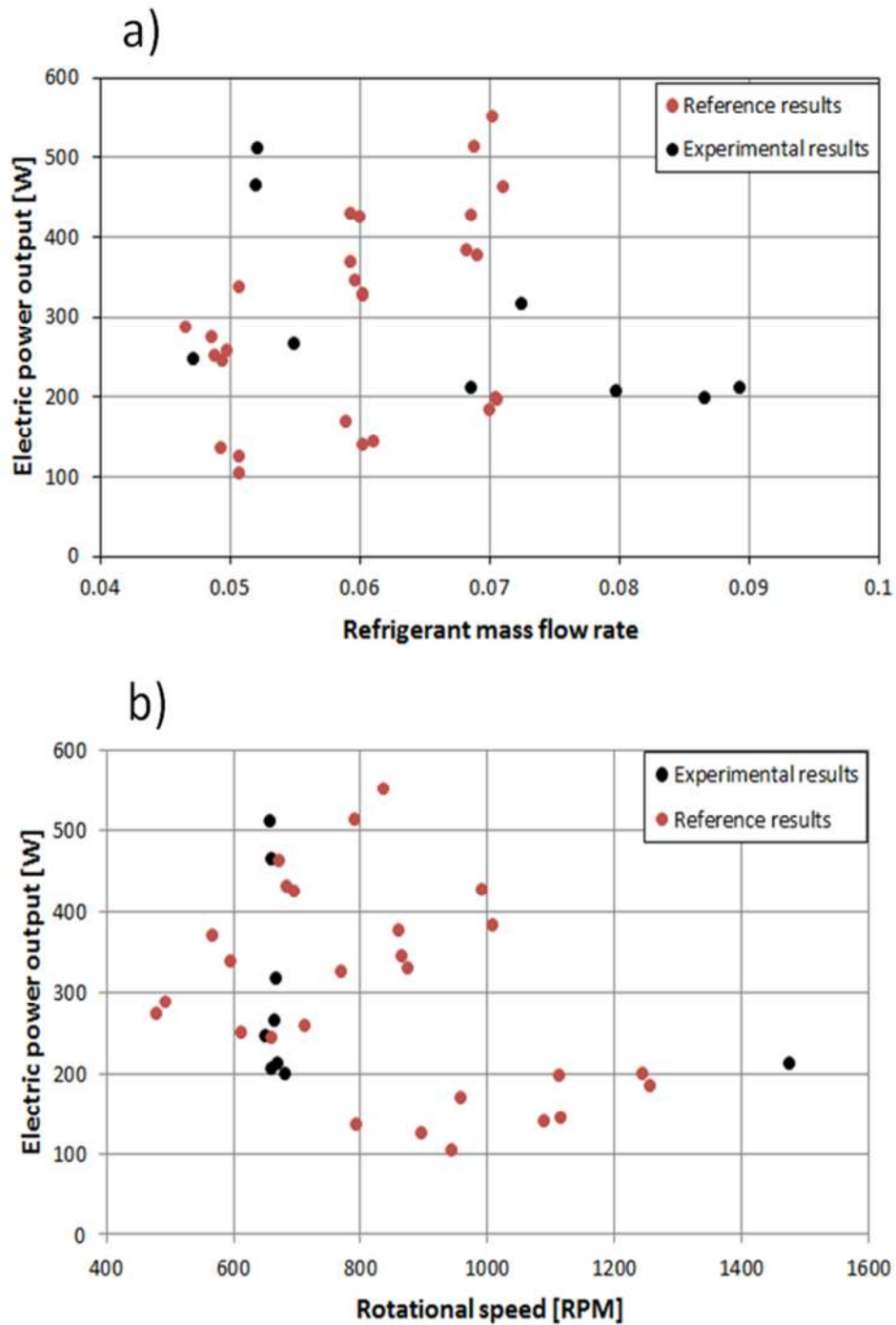
**Figure 8-35: Comparison between the R1233zd(E) ORC prototype system and preliminary expander-alternator's experimental results 2 - a) expander's power output- electric power output, and b) electric power generator's efficiency-electric power output.**

Figure 8-35(a) presents a comparison between the expander's power output and the electric power output of both experiments. As shown, at least two of the R1233zd(E) experiment results fall between several data points amongst the preliminary test results. Besides the optimum R1233zd(E) point and equivalent preliminary test results, the comparison shows that while the R1233zd(E) ORC system achieved 265.4W electric power output at 1325.76W expander power output, while the preliminary test achieved electric power output of between 250.8W to 263.4W at an expander power output, ranging from 1263W to 1384.15W.

Figure 8-35(b) shows a comparison of the generator efficiency in both experiments with regard to electric power output. As can be seen from both tests, the majority of points fall between 15% and 30% efficiency for the electric power generator at different electric power outputs, apart from three R1233zd(E) experimental points that showed outstanding efficiency. However, the results show that there are at least two R1233zd(E) ORC experimental points which are very close to several preliminary test results. When the

R1233zd(E) ORC electric power generator's efficiency was 22.24%, the electric power output achieved was 265.4W, while the preliminary test showed 22.39% electric power generator's efficiency at 254.57W, and 21.14% electric power generator's efficiency at 263.40W. Similarly, the optimum R1233zd(E) experimental point achieved a 26.8% electric power generator's efficiency at 245.99W, while the closest preliminary experimental results were 24.75% efficiency, when the electric power output was 243W.

An equivalent ORC system to the R1233zd(E) ORC prototype was found in the literature, where Twomey [318] built and tested a system that employs R134a as a working fluid and utilised a similar expander, automotive alternator electric power generator, and pump to those utilised in the R1233zd(E) ORC prototype system. A comparison between the results of the second experiment and the equivalent results from reference [318] as a function of mass flow rate, and as the expander's rotational speed is presented in Figure 8-36(a) and Figure 8-36(b), respectively. As can be seen in Figure 8-36(a), the comparison of the electric power output shows that at least four points are within a similar range, but with slight deviation related to the difference in mass flow rates, refrigerant characteristics, and system component efficiency during the tests. A stronger relationship between the electric power output and rotational speed can also be seen in Figure 8-36(b), where the electric power output from both results is shown to be similar between 600 RPM to 800 RPM and 200W to 465W. Table 8.9 and Table 8.10 list the experimental points compared as a function of mass flow rate and rotational speed, respectively.



**Figure 8-36: Comparison between the R1233zd(E) ORC prototype system and Twomey's [318] experimental results - a) as a function of mass flow rate, and b) as a function of rotational speed.**

**Table 8.9: Comparison between the R1233zd(E) prototype system and Twomey's [318] experimental results as a function of mass flow rate.**

R1233zd(E) ORC prototype experimental results		Twomey [318] results	
Mass flow rate [kg/s]	Electric power output [W]	Mass flow rate [kg/s]	Electric power output [W]
0.047	250	0.049	250.4

0.068	212	0.076	199.4
0.055	265.4	0.5	257.4
0.072	316	0.069	377.1

**Table 8.10: Comparison between R1233zd(E) prototype system and Twomey’s [318] experimental results as a function of rotational speed.**

R1233zd(E) prototype experimental results		Twomey [318] results	
Rotational speed [RPM]	Electric power output [W]	Rotational speed [RPM]	Electric power output [W]
660	465	673	462.7
650	250	661	244
665	265.4	712	254.4

Although the results from reference [318] show higher electric power output at a wider range of rotational speeds, but within a narrower mass flow rate range, the results are shown to be in fair agreement with those obtained from the second experiment of the R1233zd(E) ORC prototype system. Furthermore, the comparison of the results confirm the limitation of the electric power generator to producing electric power output of less than 1 kW, even though the expander was able to produce higher power output.

#### 8.4 Conclusion

This chapter has presented the investigation carried out on two experimental set-ups. A preliminary test was carried out to examine the performance of the scroll expander and the automotive alternator’s power output on a specially constructed test bench. The results show that the expander operates at high isentropic efficiencies and produces reasonable power output. However, the alternator as the electric power generator showed very low efficiency compared to the expander, which consequently resulted in low electric power output. This suggests large power losses through the transmission mechanism and speed mismatch between the expander and the electric power generator. The maximum electric power produced was 416W with an alternator efficiency of 22.39%, when the expander yielded a power output of 2 kW, with an isentropic efficiency of 96.33%.

The R1233zd(E) ORC prototype system was investigated by means of two experiments. The experimental data recorded and analysed provides an insight into the system's characteristics and performance. In both experiments, the power output and the thermal efficiency achieved were lower than the thermodynamically predicted performance with regard to the limitations of the heat source, electric power generator and poor pump performances indicated in both experiments. However, the first experiment consisted of two tests, the first demonstrating that the optimum system performance characteristics were achieved at the same point, where maximum thermal efficiency was 7.35% and maximum expander power output was 1966W, whereas the maximum electric power output was only 140W. In the second test and at a single mass flow rate, the results showed a slight improvement, where the thermal efficiency was 7.87% and the expander's power output was 1394.83W, with an electric power output of 180W. However, in both tests, the system's electrical efficiency was lower than 1%. The poor pump efficiency and automotive DC motor electric power generator's efficiency were pointed out, besides the fluctuations in pump pressure exhibited. After investigation, the DC motor was replaced by the automotive alternator utilised in the preliminary test and the required component positioning, as well as the re-working for optimum liquid flow were carried out.

After modification, the second experiment was initiated. The second experiment showed very poor pump's efficiency compared to the first experiment, where the pump's power consumption was higher and resulted in poor net thermal power output and lower thermal efficiency at most of the recorded points. It was pointed out that condensation did not occur in most points throughout the experiment, where the condenser outlet temperature was higher than the condensation temperature. This is mainly related to the relatively high temperatures and low flow rates of the cooling water. The incomplete condensation consequently contributed

heavily to the poor pump's performance and caused further performance destruction. However, the second experiment achieved relatively higher electric power output and electric generator's efficiency, but was still much lower than anticipated. It was noted that unlike the first experiment, the maximum expander's power output, electric power output, the system's thermal efficiency and the system's electric efficiency were obtained at different points. However, the second experiment achieved the optimum overall performance attained from experiments, where the system achieved 7.6% thermal efficiency, 1.46% electric efficiency, 1019.54W expander power output and 250W electric power output. However, although the obtained results were below anticipation, the system demonstrated its technical feasibility, and the ability for further system's performance improvement, upon solving the limitations addressed. However, the improvement of the experimentally obtained performance towards the initial thermodynamic model was demonstrated using the three cases, where the drawbacks highlighted were assumed to have been solved. The cases presented in relation to the experimentally obtained results and the initially conducted thermodynamic model showed good signs of agreement, indicating the validity of the predicted results.

Finally, the optimum experimental point, which was obtained from the second experiment, was compared to that of the preliminary experiment and the results of equivalent ORC systems in the literature. The comparison revealed that for the expander type utilised, a pressure ratio of around 4.5% and a mass flow rate of 0.047 kg/s were the optimal operating parameters. However, although the expander's power output was fairly reasonable, a large portion of this power was lost through the transmission mechanism, and the rotational speed mismatch.

## Chapter 9 : Economic Feasibility Assessment of the R1233zd(E) ORC system and the CO<sub>2</sub> SRC Power Generation System

---

### 9.1 Introduction

In this chapter, an economic feasibility analysis of the R1233zd(E) ORC system was carried out, based on the optimum experimental results. However, two systems of 5 kW and 20 kW were included in the analysis and assumed to be intended for mass manufacture. A description of the system's equipment breakdown costs were also presented for both systems based on the knowledge of the R1233zd(E) prototype system costs. In addition, the economic feasibility of the previously theoretically investigated CO<sub>2</sub> SRC power generation system was also assessed in the chapter, for the purpose of producing a prototype system similar to that developed for the R1233zd(E) ORC system. Therefore, the outcome of comprehensive market research is presented, carried out to identify commercially available equipment which can produce a 5 kW CO<sub>2</sub> power system.

For both investigated technologies, the specific financial data for the analysis was introduced and the profitability of investment in each system was expressed by economic indicators such as net present value (NPV), internal rate of return on investment (IRR), return on investment (ROI), and pay back (PP). For each system, sensitivity analysis was also presented to assess the economic viability of the system against key factors which contribute directly to the cost of the system, such as its specific capital cost and the price of electricity. The analysis was carried out in US dollars, where all system component costs were converted using 0.63 £/\$ and 1.25 €/€/\$ exchange rates reported for the 11<sup>th</sup> of November 2014. This is because the main systems components that contribute heavily to their capital costs are priced in US dollars.

## 9.2 Economic Analysis Evaluation Indicators

### 9.2.1 System's Specific Cost

It is important to define the system's specific capital cost; an economic term associated with renewable energy technologies. The specific capital cost is the total capital cost per kW, as given in equation (9.1). It allows for more accurate investigation of the system's economic feasibility, it gives an estimation of the capital cost for scale-up, and also allows for comparisons between different technologies [319].

$$\text{Specific capital cost} = \frac{\text{System total capital cost [\$]}}{\text{System capacity [Kw]}} \quad (9.1)$$

### 9.2.2 Net Present Value (NPV)

NPV is the difference between the capital cost of the system and the present value of future cash flow discounted at the given rate. The cash flow when the system is operating is the difference between the benefits, i.e. the annual electricity price saved by investing in the system, and the annual costs of operation and maintenance (O&M). The NPV decision will depend on the sum of the present value of future cash flow. For a feasible investment, the NPV should be positive and exceed the capital cost of the system. The larger the NPV value, the greater the value of the investment added. On the other hand, a negative NPV indicates an investment which is not feasible [320]. NPV has a wide variety of formulas; however they all lead to the same answer. Equation (9.2) shows the most appropriate formula for the current study:

$$NPV = -C_0 + \sum_{t=1}^n \frac{C_t}{(1+i)^t} \quad (9.2)$$

Where  $C_0$  is the capital cost of the system;  $C_t$  is the cash flow at year number (t) during (n) which is the lifetime of the system; and (i) is the discount rate. The term  $\frac{C_t}{(1+i)^t}$  is the present value of future cash flow in year (t).

### 9.2.3 Internal Rate of Return (IRR)

IRR is the critical discount rate of investment at which the NPV is equal to zero. Therefore, it can be found by solving equation (9.2) for variable (i) when the NPV is assumed to be equal to zero. For an acceptable investment, the IRR value should be higher than the originally set discount rate [321].

### 9.2.4 Return on Investment (ROI)

ROI is one of the most popular economic evaluation criteria. It simply measures the efficiency of an investment, taking into account non-cash values, such as system depreciation. ROI directly compares the magnitude and timing of net profit from an investment with the time and magnitude of costs. For an acceptable investment, the ROI should be positive. High ROI results indicate attractive investment gains in comparison with costs [322]. Equation (9.3):

$$ROI = \frac{\text{Total system revenue} - \text{System total capital cost}}{\text{System total capital cost}} \quad (9.3)$$

## 9.3 Economic Analysis General Assumptions and Inputs

For the analysed systems, the modelling assumptions made were reliant on the availability of information on similar existing systems. The United States Office of Technology Assessment [323] reported a life expectancy of 20 years for ORC systems based on commercially available units. Similar lifespan was reported by Obernberger and Thek [324] based on experience with ORC systems in geothermal applications. In their refrigeration and air-conditioning equipment life expectancy chart, ASHRAE [325] reported an expected lifetime of 19 years for commercial heat pumps, which usually utilises similar equipment to those found in ORC systems. However, similar lifespan was assumed in many feasibility assessment and economic analysis studies in the ORC

literature, such as in references [44, 326-328]. Therefore, a lifespan of 20 years was considered in the current analysis, including all components, unless where indicated otherwise. In addition, an 8% annual depreciation rate was taken for the system, as suggested by Jung et al. [44].

Operating and maintenance (O&M) costs were found to be very close for a wide range of ORC applications. For an existing ORC plant, which is 95% available throughout the year, David et al. [329] reported €0.01/kWh; a similar rate as that reported for a large scale existing ORC CHP biomass plant [330]. For geothermal applications, the US Department of Energy [331] reported \$0.01 to \$0.03/kWh. Unfortunately, there was no available information for O&M costs in supercritical CO<sub>2</sub> applications. However, the O&M costs for nuclear applications, which are usually associated with supercritical CO<sub>2</sub> applications, were found to be \$0.015/kWh [332], which is in the same range reported for ORC applications. For the current analysis, the O&M costs were assumed to be \$0.012/kWh, the average of the reported O&M costs, while the availability of the system was also assumed to be 95% throughout the year; similar to reported existing ORC systems.

The discount rate used in the analysis was 3.5%, which is the standard rate suggested by HM treasury [333] for periods ranging from 0 to 30 years. The consumer price index (CPI) is an economic factor that has a direct influence on O&M. The UK's Office for National Statistics publishes annual percentage changes to CPI [334]. Figure 9-1 shows the statistical data for CPI from September 2010 to September 2014. The average CPI percentage of these data was taken for the current analysis and was found to be 2.99%.

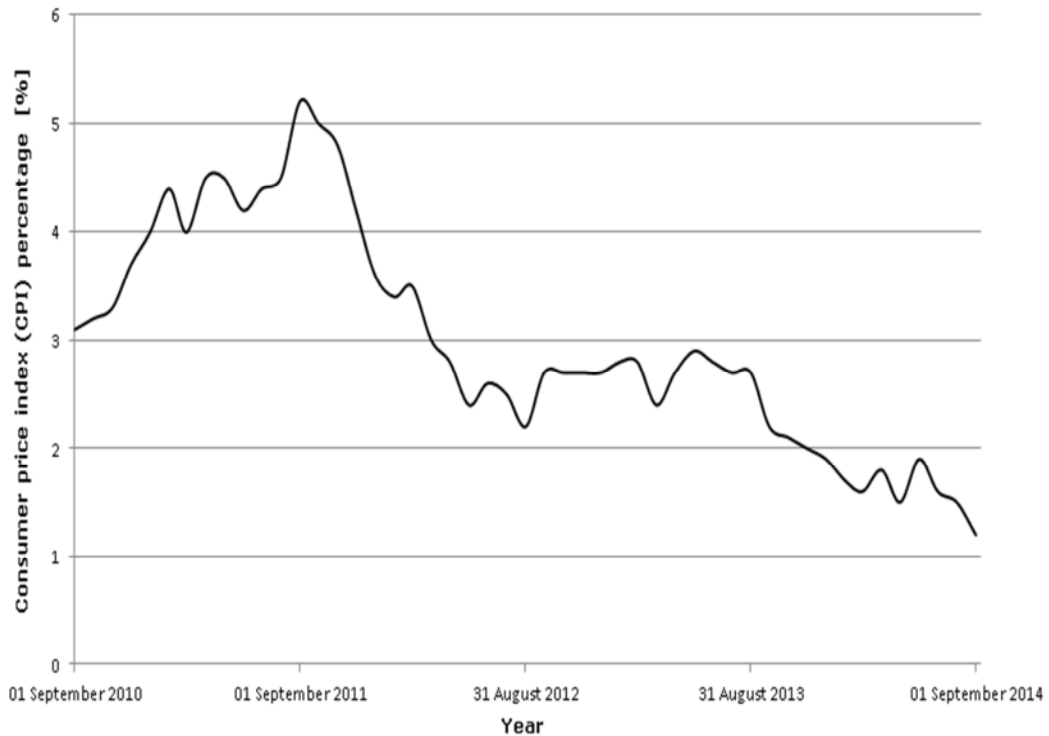


**Figure 9-1: CPI percentage change from 2010 to 2014.**

The department of energy and climate change, UK [335] publishes annual international energy price statistics for comparison. Table 9.1 shows both industrial and domestic electricity prices, including taxes and the annual percentage increase from 2010 to 2013.

**Table 9.1: Annual industrial and domestic electricity prices in the UK. (source: [336, 337])**

Year	Industrial electricity price [pence/kWh]	Annual increase percentage [%]	Domestic electricity price [pence/kWh]	Annual increase [%]
2010	7.84		11.85	
2011	8.08	3.11	12.99	9.56
2012	8.47	4.78	13.64	5.02
2013	8.94	5.58	14.64	7.35

The data in Table 9.1 show a fluctuation in the percentage increase for domestic electricity prices, with an average increase of 7.31%. Industrial electricity price percentage increase, on the other hand, has steadily risen over the years with an average of 4.49%. For these reasons, the electricity price for the first year of system operation was taken as the industrial electricity price for 2013, with an anticipated price escalation of 4.49%.

## 9.4 **R1233zd(E) ORC System Economic Analysis**

This section presents an economic analysis of the R1233zd(E) ORC system, taking into consideration the system's experimental performance, manufacturing costs, potential market and economic feasibility. The analysis will only include the expander's power output and specifically excludes the experimentally obtained electric power output, which proved to be significantly low, due to the low electric power generator's efficiency and power losses. An assumption was also made for the R1233zd(E) pump, where it was anticipated to operate effectively with 80% efficiency, since the experimental results showed very low pump's efficiency and relatively high power consumption at the optimum experimental point, which is generally abnormal for fluid pumps, and is attributed to a number of issues addressed, such as improper connection, back flow, and small pipeline sizes.

### 9.4.1 **R1233zd(E) ORC Systems Components and Costs**

Based on the optimum experimental point's result, where expander power output was nearly 1 kW, two systems of 5 kW and 20 kW were included in the analysis and assumed to be intended for mass manufacture. However, the 5 kW system was selected for the analysis in order to assess the economic potential of a small-scale system, while the 20 kW system was analysed in order to examine the potential of a scaled-up system. Therefore, in relation to the experimentally achieved power output, it is assumed the 5 kW and 20 kW systems would require 5 and 20 expanders, respectively.

A bill of materials for the R1233zd(E) ORC prototype was generated and accordingly, the cost of the potential larger systems were estimated. The bill of materials shown in Table 9.2 depicts the individual cost, description and quantity for each component assembled on the prototype system. In addition, it shows the cost of individual components and quantities for the 5 kW and 20 kW systems, where the prices were predicted for the mass manufacture

of these systems. Therefore, each component was discounted by 25% from the original price, due to price breaks from purchasing bulk quantities. Figure 9-2 illustrates an exploded view of the prototype system's individual components.

PART NUMBER	DESCRIPTION	PROTOTYPE - MATERIAL COST (€)	PROTOTYPE QUANTITY	TOTAL PROTOTYPE COST (€)	SKW QUANTITY	SKW SYSTEM COST (€)	20KW QUANTITY	20KW SYSTEM COST (€)
1	Side Panel Assy	356.57	2.00	713.14				
1.1	Side Panel	N/A	1.00	N/A				
1.2	Joggle Plate	N/A	1.00	N/A				
2	Housing Lid	436.94	1.00	436.94				
3	Corner Assembly RH	263.09	2.00	526.18				
3.1	Corner Support	N/A	1.00	N/A				
3.2	Corner Support Top Plate	N/A	1.00	N/A				
3.3	Corner Support Bottom Plate	N/A	1.00	N/A				
3.4	Lifting Eye Screw Boss	N/A	1.00	N/A				
4	Corner Assy LH	263.09	2.00	526.18				
4.1	Corner Support	N/A	1.00	N/A				
4.2	Corner Support Top Plate	N/A	1.00	N/A				
4.3	Corner Support Bottom Plate	N/A	1.00	N/A				
20	Base Assy	512.00	1.00	512.00				
4.4	Lifting Eye Screw Boss	N/A	1.00	N/A				
5	Panel Support Angle Assy	48.04	4.00	192.15				
5.1	Panel Angle Support	48.04	1.00	48.04				
6	Panel Angle Support	48.04	4.00	192.15				
7	Front Panel Assy	251.43	1.00	251.43				
7.1	Front Panel	N/A	1.00	N/A				
7.2	4 Phase 32A Isolator Switch	45.79	1.00	45.79				
7.3	Green Control Indicator	5.15	3.00	15.44				
7.4	Emergency Stop Button	30.18	1.00	30.18				
7.5	Label Front Panel	12.80	1.00	12.80				
7.6	Reset Button	17.59	1.00	17.59				
7.7	Stop Button	21.20	1.00	21.20				
7.8	Start Button	17.55	1.00	17.55				
8	Rear Panel Assy	270.63	1.00	270.63				
8.1	Rear Panel	N/A	1.00	N/A				
21	Eye Bolt	10.37	4.00	41.47				
9	Heat Exchanger HX204	282.34	1.00	282.34				
10	Scroll Compressor	326.40	1.00	326.40				
11	Heat Exchanger HX201	246.64	1.00	246.64				
12	Heat Exchanger HX203	477.84	1.00	477.84				
13	3cP1120 Pump, Drive & Transmission	2163.20	1.00	2163.20				
14	Anti Vibration Feet	13.15	4.00	52.58				
15	Valve Plate	38.40	1.00	38.40				
16	Rating Plate	6.40	1.00	6.40				
17	Storage Tank	102.40	1.00	102.40				
18	Brake & Swivel Castor	33.84	4.00	135.37				
19	LEM-200-D127 Motor	1280.00	1.00	1280.00				
22	Control Box Support	180.02	2.00	360.04				
23	Control Box	97.36	1.00	97.36				
24	Pipes & Valves	384.00	N/A	384.00				
25	Screws, Nuts & Bolts	25.60	N/A	25.60				
26	Refrigerant Gas	512.00	1.00	512.00				
27	Paint For All Metal Work	318.1696	1	318.1696				
				<b>TOTAL:</b>	<b>10679.60</b>	<b>6633.84</b>	<b>15740.79</b>	

Table 9.2: R1223zd(E) ORC prototype system and scaled-up system's bill of materials.

## Chapter 9: Economic Feasibility Assessment of the R1233zd(E) ORC system and the CO2 SRC Power Generation System

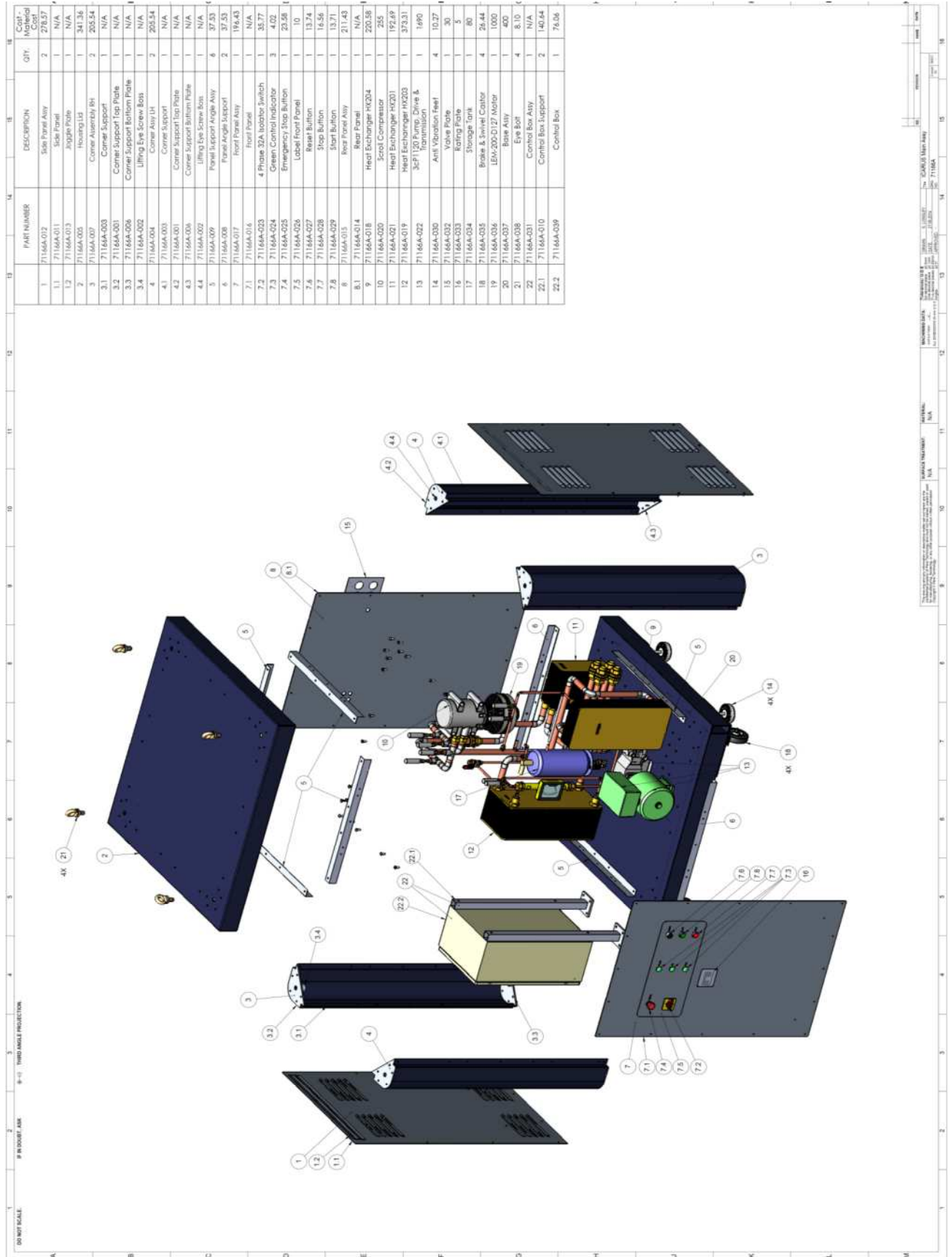


**Figure 9-2: Exploded view of the R1233zd(E) ORC prototype system.**

As shown in Table 9.2, the prototype has many components, more than the potential 5 kW and 20 kW systems. This is due to the fact that the 5 kW and 20 kW systems would be specified for mass manufacture and not all the components on the prototype are required for the mass manufacture version, as some components on the prototype were for testing and experimental purposes only. For example, it can be seen in Table 9.2 that not all the metal housing panels are applicable for the 5 kW and 20 kW systems. Therefore, the cost was revised so that the price of the 5 kW system was estimated as €640, while €896 was estimated for the 20 kW system. This is due to the housing on the prototype which are 'one-off' parts and cost a lot more than parts which are for mass manufacture. It is also assumed the metal work will be simpler and thinner which would also reduce labour and material costs.

From Table 9.2 it may also be seen that the estimated total cost for the 5 kW system is €6,33.84 while for the 20 kW system, it is €15,740.79. The 5 kW system has been estimated as cheaper than the prototype, the total cost of which is €10,679.60. However, the 20 kW system would be more expensive, as some components needed to be scaled up when compared to the prototype. These components are highlighted in yellow in Table 9.2. For instance, the 20 kW system's heat exchangers are required to be larger, due to the heat exchangers incorporated into the prototype being designed for a 5 kW system. Therefore, the heat exchangers for the 20 kW system are required to be four times the size. This subsequently contributes to the price increase. The components which need to be scaled up and which are therefore more expensive, are the pump, storage tank, pipes and valves and the amount of refrigerant gas. None of the 5 kW system components require scaling up, as all the components on the prototype system have been specified to produce 5 kW, apart from the cost of the extra 4 expanders, in order to produce 5 kW expander power output.

Table 9.3 presents the R1233zd(E) ORC system’s total and specific capital costs, where a 29% mark-up was added for each system’s cost upon assembly.

**Table 9.3: Specific cost of the R1233zd(E) ORC system.**

	Prototype [1 kW]	5 kW system	20 kW system
Cost [€]	10,350	6,633	15,740
Capital cost with 29% mark-up [€]	13,351	8,815	20,305
Specific capital cost [€]	13,351	1,763	1,015

Information on the ORC system installation costs was available from the development of the prototype system. Therefore, it was added as a one-off expense to the capital investment for the first year of each system’s lifetime. Table 9.4 shows the total, as well as a breakdown of the installation costs.

**Table 9.4: Installation costs for the R1233zd(E) ORC system.**

Civil works [€]	450
Permission/studies [€]	500
Transport [€]	500
Anchoring [€]	150
Connection to grid [€]	150
Supervision on site [€]	1000
Total [€]	2750

For a realistic approach, it was presumed that the expanders would need replacing every alternate year of the system’s lifetime, considering that the expanders utilised were modified automotive compressors and designed for the operation in automotive applications. Therefore, they might wear out before the end of their lifetime due to the heavy duty nature of the ORC system.

#### 9.4.2 Economic Analysis Results and Discussion

All amounts were converted to US dollars, using the current conversion rate, as shown in Table 9.5 for the economic feasibility model inputs for both systems.

**Table 9.5: R1233zd(E) ORC system’s economic model inputs.**

System capacity [kW]	5	20
Electrical conversion efficiency [%]	80	80
Power consumed by the R1233zd(E) pump [W]	189.7	758.8
Total capital cost [\$]	10,987.4	25,302.9
Specific capital cost [\$/kW]	2,197.47	1,265.14
Installation cost [\$]	3,427.71	3,427.71
System lifetime [years]	20	20
Price of electricity [\$/kW h]	0.144	0.144
System’s availability throughout the year	95	95
Electricity price escalation rate [%]	4.5	4.5
O&M costs [\$/kW h]	0.012	0.012
Consumer price index [%]	3	3
System’s annual depreciation rate [%]	8	8
Discount rate [%]	3.5	3.5

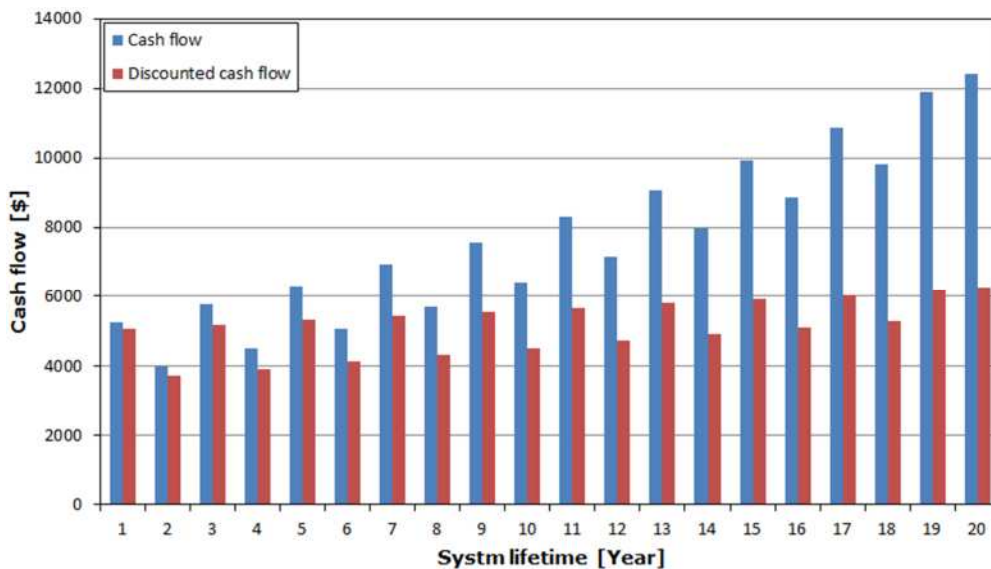
#### 9.4.2.1 The 5 kW R1233zd(E) ORC System

Table 9.6 presents the results of the economic model for the system’s lifetime and for the first 5 years of this lifetime. The results suggest that the investment in the 5 kW R1233zd(E) system is economically feasible and attractive, whereby the system can pay back the invested capital after 3.10 years and start generating profit. As shown, the NPV of the system after the end of the project would be \$887,711.83, which is very high. Besides this, the system would be able to withstand relatively high interest rates and remain a feasible investment of up to 37.1% with a very high magnitude of benefits in relation to expenses, as the ROI value indicates. Similarly, if the project’s lifetime is 5 years, one might be confident that the investment will be economically feasible, with an NPV of \$8,833.471 by the end of the fifth year and a maximum acceptable interest rate of 22.4%, which is also high and indicates a safe investment. However, the magnitude of benefits from the system would be 82.6% by the end of the fifth year, which is considerably attractive, even when the system has endured two replacements of expanders while recovering the capital investment. It is important to note that because of the relatively low cost of the system’s components, specifically the expanders, low pump power consumption, even at lower efficiencies, and the high magnitude of benefits, this economic model suggests the system remains feasible, even if the expanders were to be replaced on an annual basis throughout the system’s lifetime.

**Table 9.6: The 5 kW R1233zd(E) ORC system’s economic model results.**

	20 years	5 years
NPV [\$]	8,87711.83	8,833.471
Payback [years]	3.10	3.10
IRR [%]	37.1	22.4
ROI [%]	1198.8	82.6

Figure 9-3 shows the variation of cash flow and discounted cash flow over the lifetime of the system. Gradual, yet fluctuating increase in cash flow can be observed along this timeline. As shown, the reduction in cash flow every alternate year is due to the expanders replacements costs being added to the annual expenses. The increase in cash flow is mainly a result of the annual increase in electricity prices per unit. The R1233zd(E) pump does not consume high power input, even in its worst condition. Therefore, the increase in electricity prices will always come as a benefit of the system rather than as an expense for operating the pump. The effect of the discount rate on cash flow can also be seen in the Figure, where the cash flow varies from \$3,983.97 to \$12,428.12, while the discounted cash flow varies from \$3,719.08 to \$6,245.95.



**Figure 9-3: Cash flow variation for the 5 kW R1233zd(E) ORC system over 20 years.**

Figure 9-4 presents the cumulative discounted cash flow, where the invested capital is shown to be recovered at the beginning of the

fourth year. After breaking even, the system would start generating pure profit until the end of its lifetime.

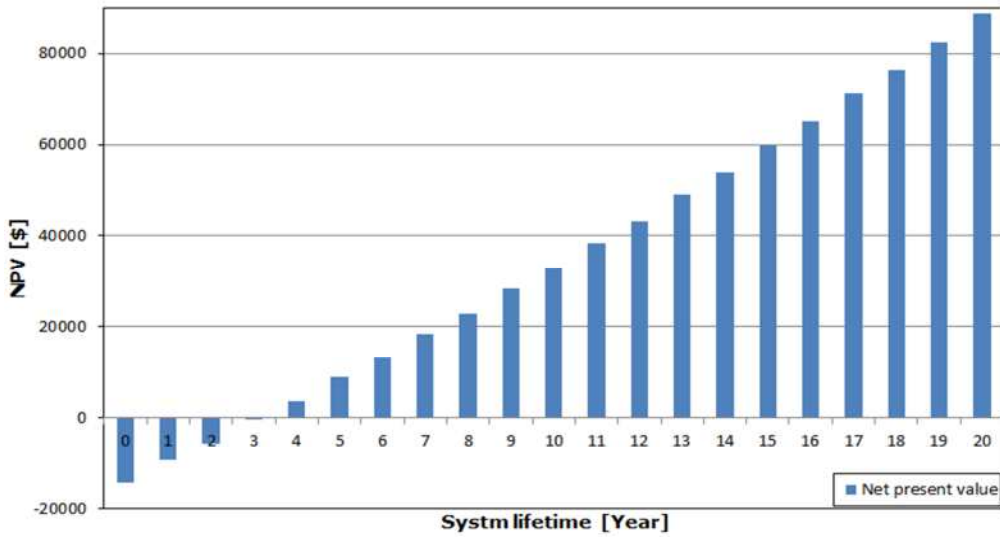


**Figure 9-4: Net present value of the 5 kW R1233zd(E) ORC system over 20 years.**

Figure 9-5 shows a zoomed-in view of the cumulative discounted cash flow for the first 5 years of the system's lifetime, where the invested capital is recovered. As shown, year zero shows the capital investment cost, installation and O&M costs, when the system is built and first commissioned, without generating any benefits. This negative value is reduced after operation and cash flow until the end of the third year, where the system would be just \$408.90 short of breaking even. In the fourth year, the invested amount would be recovered and an extra \$3,518.69 would be gained by the end of the fourth year.

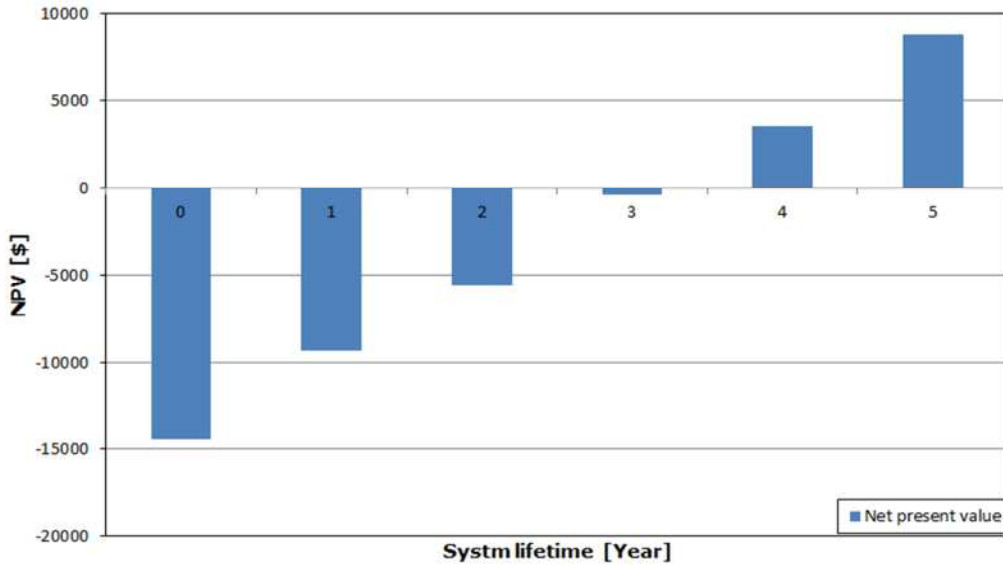
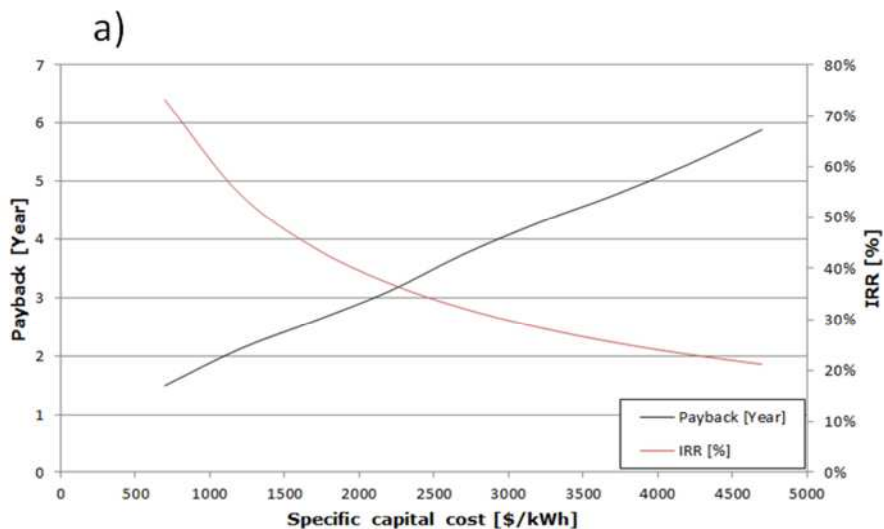


**Figure 9-5: Net present value of the 5 kW R1233zd(E) ORC system over 5 years.**

#### 9.4.2.1.1 Sensitivity Analysis

Once the economic model is established, it is important to analyse the effect of factors which have significant influence on the feasibility and profitability of the system. These factors are namely the specific capital cost of the system, which will have a direct influence on all evaluation indicators, and the electricity price which defines the benefits and major portion of the system costs represented by the pump power consumption.

##### 9.4.2.1.1.1 The Effect of the System's Specific Capital Cost



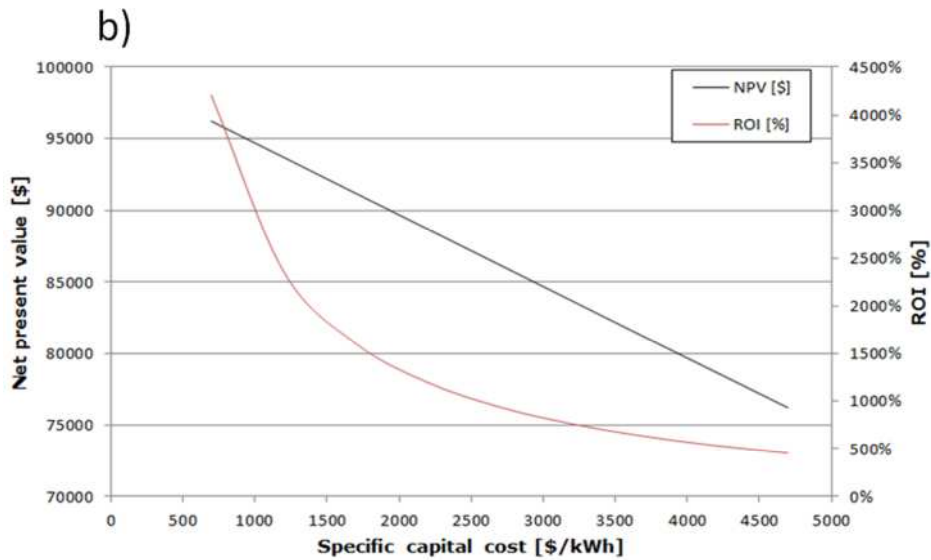


**Figure 9-6: The effect of specific capital cost on the 5 kW R1233zd(E) ORC system’s economic indicators.**

Figure 9-6 presents the effect of specific capital cost variation on the economic evaluation parameters. In Figure 9-6 (a), the payback period increases in a linear manner with the increase in specific capital cost. In the opposite direction, the IRR decreases gradually with the increase in specific capital cost. However, within the examined range of specific costs, one might be confident that the investment is feasible and able to withstand further higher specific costs per kW power. When the specific cost is at its minimum of \$697, the system will break even after just 1.49 years of operation and be able to withstand interest rates of up to 73% before the investment stops being feasible. At the maximum analysed specific capital cost of \$4,697.47, the system was found to break even and be capable of paying back the invested capital after 5.88 years, with the ability to withstand interest of up to 21.22%. Figure 9-6 (b) presents the effect of the capital’s specific cost variation on the NPV and ROI. It is clear that both parameters would reduce gradually as the specific capital costs increase, as is to be expected. The NPV would be \$96,211.83 by the end of the system’s lifetime when the specific capital cost is at its lowest value of \$697.47, with a superior ROI of 4,207.16%, showing that the magnitude of benefit from the system is superior to the expenses. At the maximum analysed specific capital cost of \$4,697.47, the NPV and

ROI would be \$76,211.83 and 454.37%, respectively, indicating a feasible and attractive investment. The very high ROI mainly relates to the cost of electricity per kWh and the power produced and consumed by the system. Since the power consumption is very low, expenses are also kept very low, compared to the benefit gained from the higher power output.

9.4.2.1.1.2 **The Effect of Electricity Costs**

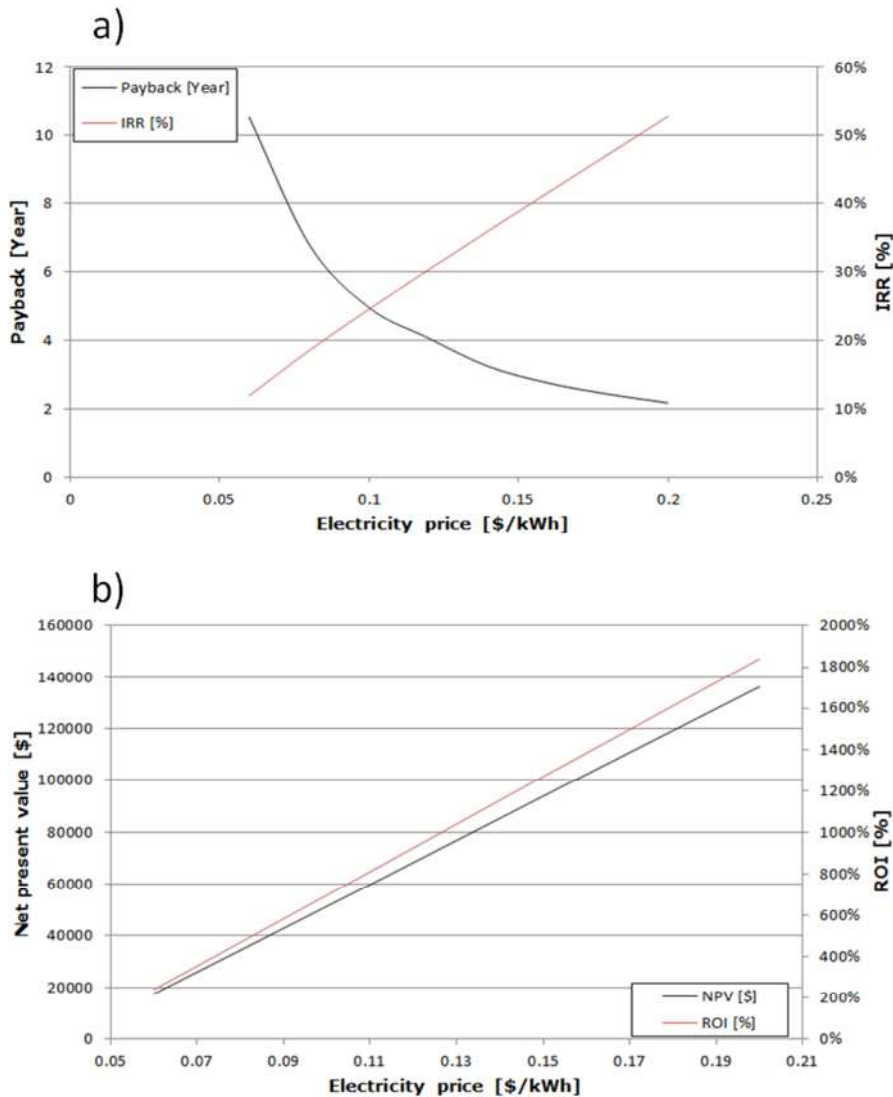


**Figure 9-7: The effect of electricity price on the 5 kW R1233zd(E) ORC system’s economic indicators.**

The effect of electricity cost per kWh was also investigated, as presented in Figure 9-7. The payback trend is presented in Figure 9-7 (a) and shows that the system’s payback period reduces gradually as the electricity price per kW increases, where the

system would generate 41,610 kW/year and consumes 1,578.68 kW/year to operate the pump. Therefore, the value of the power produced increases alongside the rise in electricity prices. Consequently, the cash flow and benefits from the system would increase and the system would break even sooner rather than later. On the other hand, the IRR increases in a linear way with the increase in electricity costs, indicating a safe investment and the high potential to survive, even with an interest rate of up to 52.83% when the maximum electricity price per kWh is \$0.2. The system would therefore be able to pay back after 2.17 years of its lifetime. When the price of electricity is at its lowest value of \$0.06, competition with the grid supply becomes harder, leading to a system payback period of 10.54 years. This could be considered feasible with up to 11.89% interest. However, the system remains positively feasible, aside from the fact that the price of grid power supply is not expected to drop as low as \$0.06 per kWh. Figure 9-7 (b) shows that both NPV and ROI increase in a linear manner with an increase in electricity price per kWh. Where the electricity price is \$0.06, the NPV is expected to be \$17,408.81 by the end of the system's lifetime, with an ROI of 238.71%. At the maximum analysed price of \$0.2/kWh, the NPV would increase to \$136,247.1, while the ROI rate would be 1,838.88%.

#### 9.4.2.2 The 20 kW R1233zd(E) ORC System

Similar to the 5 kW system, Table 9.7 presents the economic model's results for the 20 kW system over the system's lifetime and for the first 5 years, respectively. In general, the results indicate economically feasible and attractive investment, even superior to the 5 kW system, where the 20 kW system can pay back the invested capital very quickly after 1.6 years of operation. The NPV of the system after 20 years would be \$377,631.346 with an IRR of 69.5% and a high magnitude of benefit amounting to 2,194.3%. For a 5 year plan, the system would have an NPV of \$62,670.944 and an IRR of 62.4%, with an attractive ROI of 256%.

**Table 9.7: The 20 kW R1233zd(E) ORC system’s economic model results.**

	20 years	5 years
NPV [\$]	377,631.346	62,670.944
Payback [years]	1.6	1.6
IRR [%]	69.5	62.4
ROI [%]	2,194.3	256

The variation in cash flow and discounted cash flow over the system’s lifetime, shown in Figure 9-8, indicates similar behaviour to that observed for the 5 kW system, where an obvious reduction could be seen each alternate year, due to the need to replace the expanders. The cash flow would be at its minimum in the second year, with \$15,593 and at its maximum in the last year, with \$49,128.78. On the other hand, the discounted cash flow shows greatly reduced rates in relation to the cash flow, especially from the ninth year onward. However, the discounted cash flow would be at its minimum of \$14,556.24 by the second year and at its maximum of \$24,690.44 in the final year.

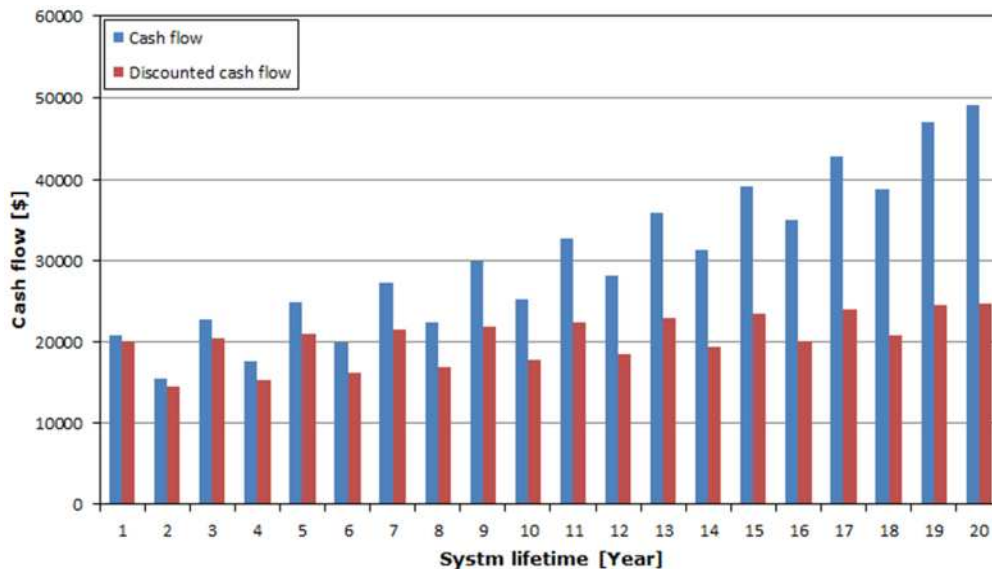


**Figure 9-8: Cash flow variation for the 20 kW R1233zd(E) ORC system over 20 years.**

The cumulative discounted cash flow presented in Figure 9-9 shows the payback point during the second year. After that, profit would be generated until the end of the system’s lifetime.

Chapter 9: Economic Feasibility Assessment of the R1233zd(E) ORC system and the CO<sub>2</sub> SRC Power Generation System

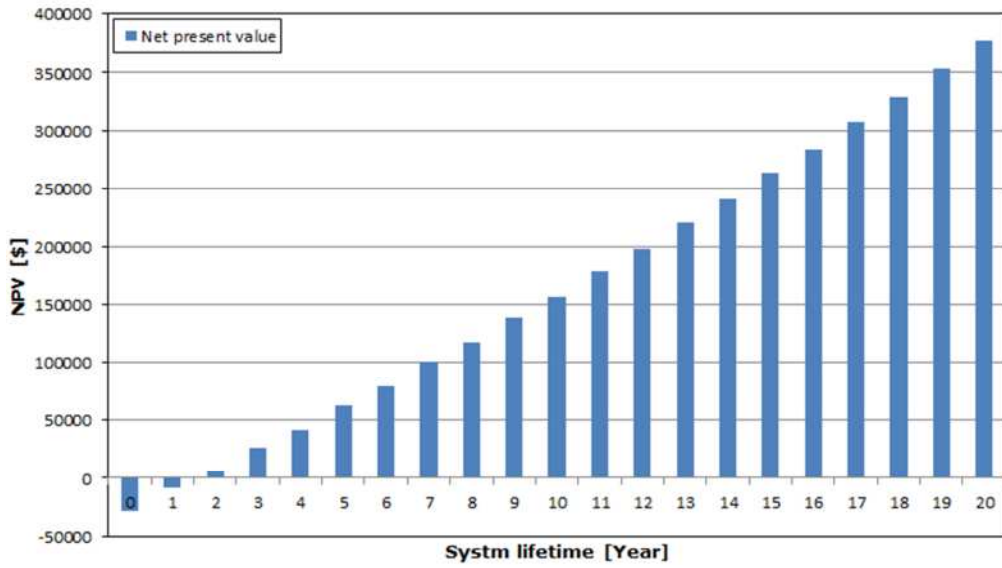


**Figure 9-9: Net present value of the 20 kW R1233zd(E) ORC system over 20 years.**

A zoomed-in view of the cumulative discounted cash flow in the first five years is provided in Figure 9-10, where most of the initial costs would be recovered within the first year before the year’s end, with \$8,703.5 short of breaking even. However, during the second year, the system would break even and start generating profit before the year’s end, with \$5,852.67 profit.

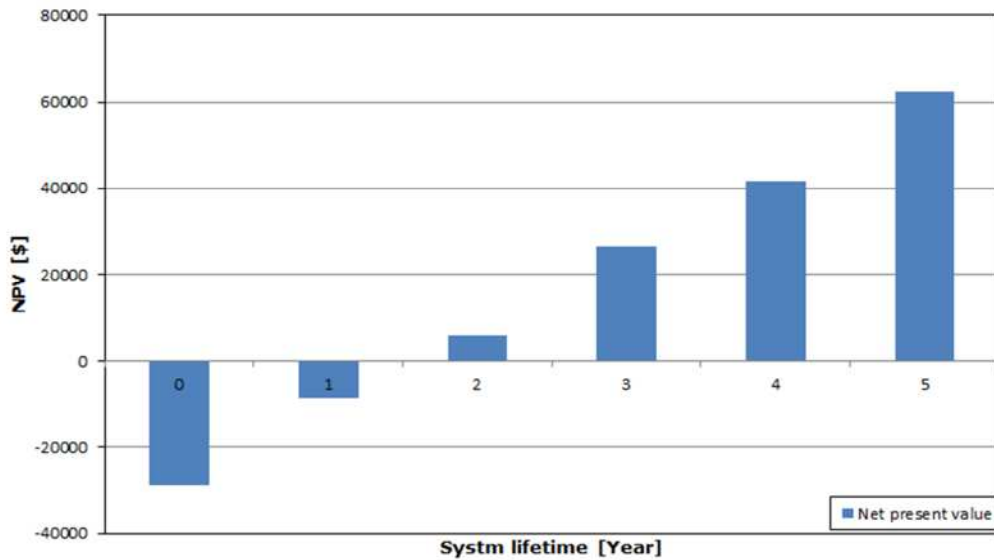


**Figure 9-10: Net present value of the 20 kW R1233zd(E) ORC system over 5 years.**

### 9.4.2.2.1 Sensitivity Analysis

#### 9.4.2.2.1.1 The Effect of the System's Specific Capital Costs

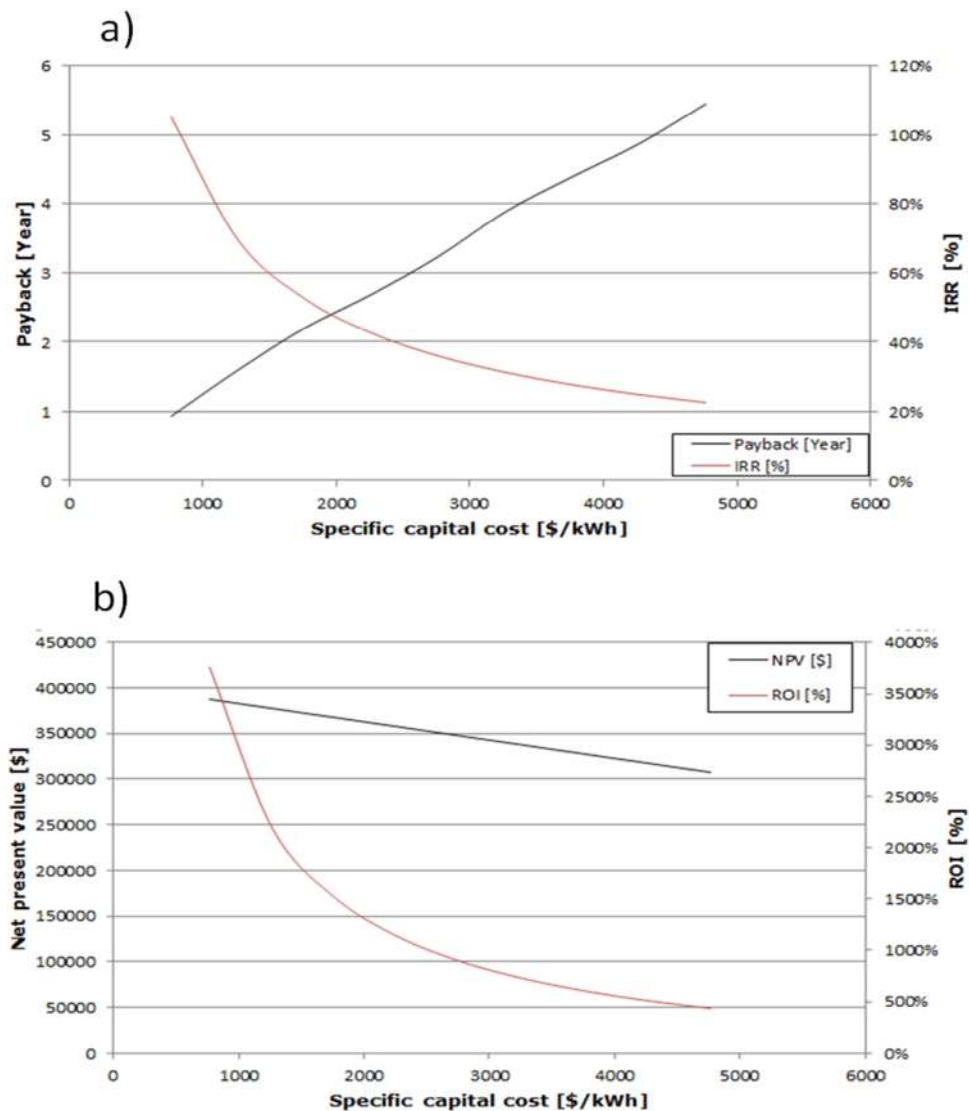


**Figure 9-11: The effect of specific capital cost on the 20 kW R1233zd(E) ORC system's economic indicators.**

Similar to the behaviour seen in the 5 kW sensitivity analysis, Figure 9-11 presents the effect of specific capital cost variation on the economic evaluation indicators and the system's feasibility. Figure 9-11(a) shows that the payback period increases with an increase in the specific capital cost per kW, while the IRR reduces gradually. In general, both the payback and IRR rate are shown to be within a similar range to what is observed in the 5 kW system, where the system would break even very quickly in the last month of the first year of operation, where the specific cost is at its

minimum of \$765 and the IRR is at 105%. At the maximum specific capital cost of \$4,765.14 analysed, the system would pay back after 5.45 years, with 22.6% IRR. Figure 9-11(b) shows that both the NPV and ROI decrease as the specific capital cost increases. Where the specific cost is \$765.14, the NPV would be \$38,7631.34 by the end of the system’s lifetime, while the ROI would be 105.1%. At the maximum specific capital cost, NPV would be \$307,631.34, while ROI would be 435.7%, which confirms the attractiveness of the investment.

9.4.2.2.1.2 **The Effect of Electricity Costs**

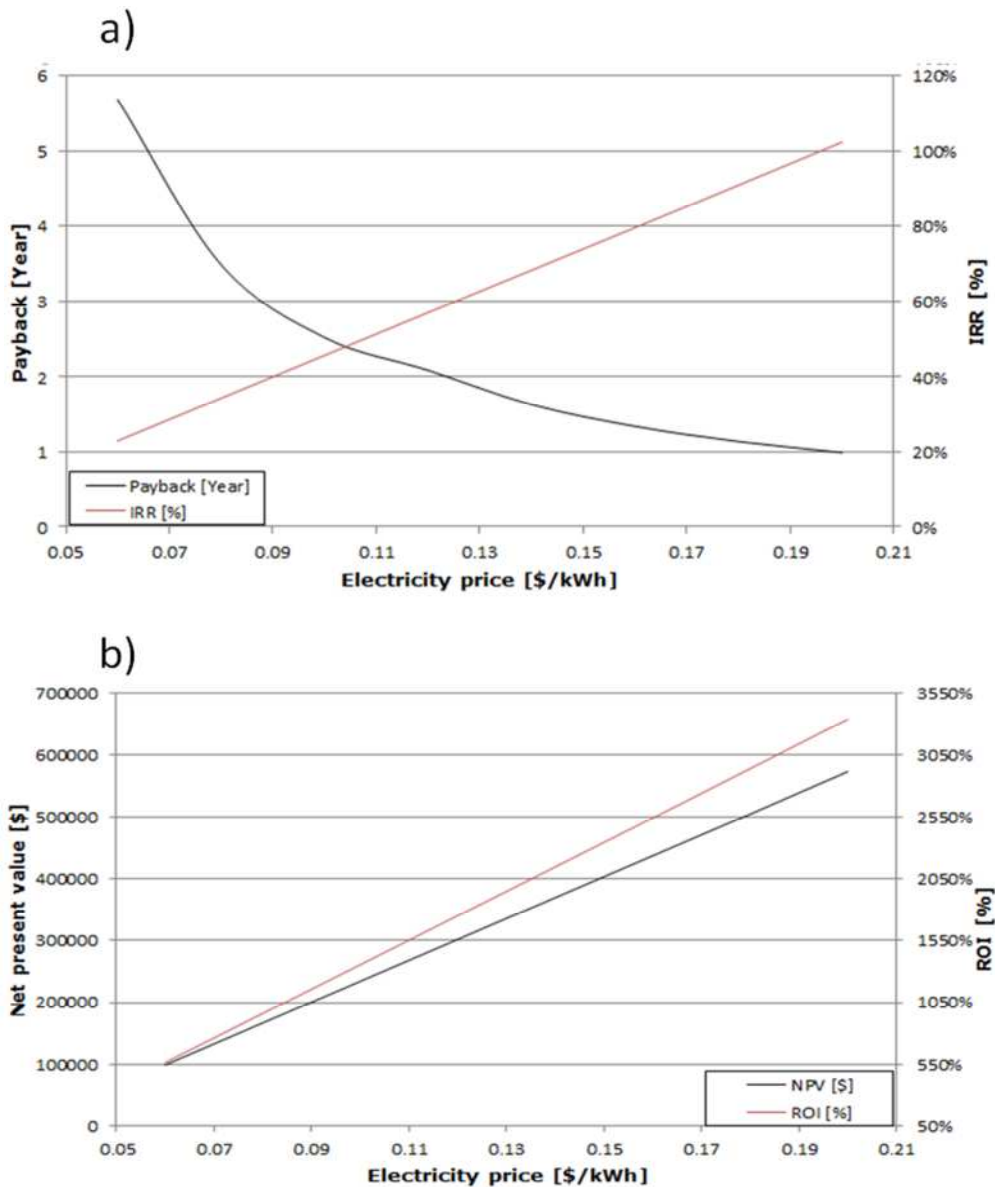


**Figure 9-12: The effect of electricity price per unit on the 20 kW R1233zd(E) ORC system’s economic indicators.**

Similar behaviour to what was observed for the 5 kW system may be seen in the 20 kW system. The payback period decreases while the IRR increases in line with electricity prices, as shown in Figure 9-12(a). At the minimum electricity price of \$0.06 kW/h the system indicates a maximum payback period of 5.69 years and the lowest IRR of 22.9%. When the maximum electricity price is 0.2 kW/h, the system's payback period would be 1 year, while IRR would 102.4%. In Figure 9-12(b), both the NPV and ROI increase in a linear manner and show \$98,565.12 and 562%, respectively at the minimum electricity price, and \$573,918.2 and 3,341.4%, at the maximum electricity price.

## **9.5 5 kW CO<sub>2</sub> SRC Power Generation System Economic Analysis**

### **9.5.1 System's Components Identification**

In order to construct a prototype of the 5 kW CO<sub>2</sub> SRC power generation system, the key components of the system should be identified. Nevertheless, the crucial requirement for the CO<sub>2</sub> system is to identify suitable equipment that can stand high operating pressure, which will consequently be at a higher cost in comparison to conventional equipment, and contribute significantly in the capital cost of the system. General auxiliary components which are not associated with high pressure are easily found commercially, such as thermocouples, electrical inverter drives, data loggers, etc. Therefore they will not be discussed in this section, although their cost values are added to the capital cost of the system.

#### **9.5.1.1 CO<sub>2</sub> Turbine**

According to the results of the theoretical analysis conducted in Chapter 6, the system's operating pressure and temperature range requires a turbine of special specifications to handle the operating conditions. The search carried out covers different types of expanders and turbines. However, most turbine manufacturers start

their product range at 20 kW, which is also the lowest limit for a so-called micro-turbine. However, the search scope was narrowed to consider turbines that are capable of producing 5 kW to 7 kW power output. The drawbacks encountered during the search were either the limitation of the operating pressure, or the very high cost of custom design. By the end of the search, two turbine manufacturers were identified: Infinity Turbines [338], who produce ITmini, with a rated output of 3 kW through compressed air and has a maximum operating pressure of 140 bar. IT10, by the same manufacturer has a rated output in the range of 5 kW to 10 kW and maximum operating pressure of 140 bar; however, IT10 has never been tested by the manufacturer. The initial price of the turbine is \$15K. Figure 9-13 shows the Infinity IT10 Turbine.

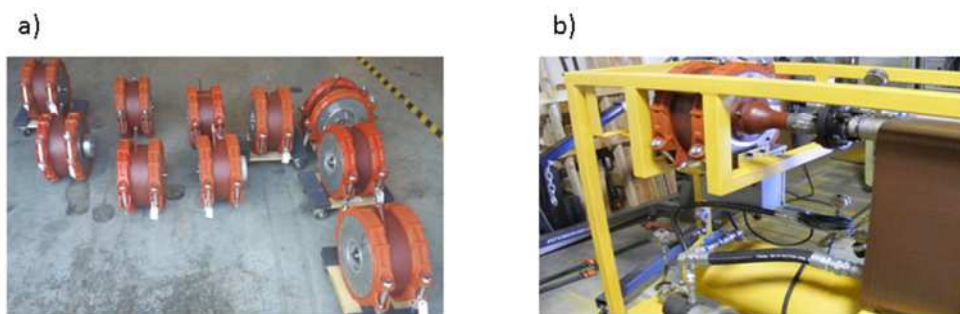


**Figure 9-13: Infinity IT10 turbine, a) IT10 turbine units and b) IT10 turbine in an ORC system. (Source: [338])**

The other turbine manufacturer is Enogia [339], which is known to design, assemble and sell thermodynamic cogeneration systems. The manufacturer mainly produces turbine systems for refrigerants, with a maximum pressure of 20 bar. However, they also manufacture custom turbines with specific given criteria within their engineering and manufacturing capabilities. A 6 kW electrical output turbine system would cost €13.5K, in addition to €11K for the turbine accessories, including a cooling circuit; dry cooler; oil circuit; separator, and an inverter for speed control. This adds more complexity to the system, where the turbine is actually a system in itself. However, including accessories, the total price of the system becomes €24.5K, which is very expensive. Unfortunately, the maximum system pressure is 80 bar and the maximum attainable

isentropic efficiency is 50%. Figure 9-14 (a) shows the Enogia 6 kW hermetic turbine, while Figure 9-14 (b) shows a metric view of the system.

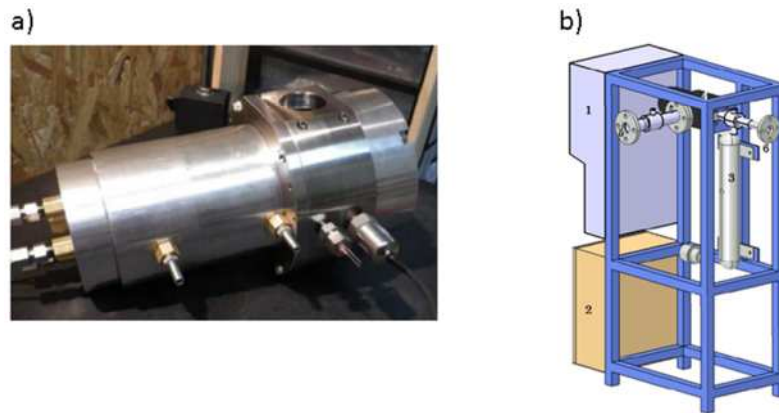


**Figure 9-14: Enogia CO<sub>2</sub> turbine, a) Enogia turbine unit and b) Enogia CO<sub>2</sub> system. (source: [340])**

The components shown in Figure 9-14 (b) are as follows:

1. Inverter
2. Electrical cabinet
3. Lubrication system
4. Turbine
5. Outlet flange
6. Inlet flange

#### 9.5.1.2 CO<sub>2</sub> pump

The dilemma over operating pressure was also found in the search for a suitable CO<sub>2</sub> compression device for the CO<sub>2</sub> power system. Few of the pumps identified could handle the high CO<sub>2</sub> pressure, but some were air-driven [341] and some were very expensive, which makes the system unfeasible [342, 343]. Other manufacturers [344] have pumps especially designed for CO<sub>2</sub> applications but which are not tested at the required operating conditions. The most suitable pump for the system proved to be a triple plunger pump, which is only suitable for pumping liquid CO<sub>2</sub> [345]. Figure 9-15 shows the Ninjang Yalong Technology CO<sub>2</sub> boosting pump.



**Figure 9-15: Ninjang Yalong Technology CO<sub>2</sub> boosting pump. (source: [345])**

**Table 9.8: The CO<sub>2</sub> pump's general specifications. (source: [346])**

Manufacturer	Ninjang Yalong Technology Co. Ltd.
Model	3ZRC75-5.22/10-1.5 boosting CO <sub>2</sub> injection pump
Type	Triple plunger pump
Unit cost [€]	13 K
Flow rate [L/min]	87
Inlet pressure [bar]	85
Discharge pressure [bar]	120
Inlet temperature [°C]	20 to 30
Power [kW]	2.7 to 4.4

### 9.5.1.3 Heat Exchangers

The heat exchangers identified for the system are counter-flow brazed plate heat exchangers manufactured by Kaori in Taiwan [288], the same manufacturer provided the R1233zd(E) ORC system's heat exchangers. However, the proposed heat exchangers for the CO<sub>2</sub> system are especially designed for CO<sub>2</sub> applications, and have high pressure ratings. Table 9.9 lists the heat exchangers in the CO<sub>2</sub> system, their cost, and general specifications.

**Table 9.9: CO<sub>2</sub> power system heat exchanger specifications. (source: [347])**

Heat exchanger	CO <sub>2</sub> heater	CO <sub>2</sub> cooler	Recuperator heat exchanger
Model	C097	C097	C202HP6
Unit cost [€]	376.47	424.33	1299.25
Pressure [bar]	140	140	140
Temperature [°C]	200	200	200
Number of plates	60	70	132
Heat transfer area [m <sup>2</sup> ]	2.755	3.230	34.02
Heat load [kW]	42.8	40.5	220

#### 9.5.1.4 Other System Components

Other identified system components that contribute significantly to the capital cost of the system are, e.g. piping, fittings and valves. Unlike ordinary thermal systems which use standard copper piping and fittings, the current system requires special piping and fittings to stand the operating pressure. The pipes identified for the system are stainless steel refrigeration pipes of various sizes that can stand very high pressure and a wide range of temperatures from -255C to 605 °C. It was estimated that 6 m of piping in total would be sufficient for the system. The average cost of the piping is £130 [348]. Similar to the required fittings, high pressure fittings were identified and the estimated total cost of the fittings amounted to £850 [349].

Due to the nature of the system’s operating conditions, solenoid valves are the best option for avoiding direct human contact with the system, for safety reasons. The solenoid valves identified are directly operated valves especially manufactured for CO2 applications. The valve can be mounted in any position and does not require minimum pressure for operation. Table 9.10 lists the solenoid valves specifications and cost.

**Table 9.10: General specifications for a CO2 solenoid valve. (source: [350])**

Manufacturer	Asco
Maximum pressure [bar]	70
Temperature range [°C]	-60 to 60
Maximum kinematic viscosity [Cst]	65
Response time [ms]	5 to 25
Unit cost [£]	165.06

#### 9.5.1.5 Measurement Devices

Similar to other components, the system requires measuring devices for high pressure; specifically, pressure transducers and CO2 flow sensors. The pressure transducers identified for the system are manufactured by Telemecanique, UK [351] and cost £78.60 per unit. The transducers are especially designed for

hydraulic and refrigeration applications and are capable of measuring pressure in the range of 0 to 100 bar, with an uncertainty of  $\pm 0.5\%$ . The flow sensor suitable for the system is an inline digital flow meter of turbine type. The flow sensor is G2H15I09LMA, manufactured by Bell Flow Systems, UK [352] and costs £1083. The flow sensor is capable of withstanding pressure of up to 207 bar, operating within a temperature range of -10 to 60 °C, and measures flow rates from 38 to 380 L/min, with an uncertainty of  $\pm 0.5\%$  of full scale. Figure 9-16 shows a general view of the high pressure flow sensor [352].



**Figure 9-16: General view of G2H15 high pressure flow sensor. (source: [352])**

After all the system components were identified, a bill of materials was generated as shown in Table 9.11 listing these components, alongside their quantities and cost in their original currencies. It was assumed that the capital cost of the system would be the sum of these costs, converted to US dollars. Furthermore, it was assumed that the equipment's installation costs were included in their original cost prices. The total capital cost was thus found to be \$40,811.

**Table 9.11: 5 kW CO<sub>2</sub> power system components and costs in original currencies.**

Component	Quantity	Component price in original currency	Remarks
Heat exchangers	3	€ 2100.05	
Expander	1	\$ 15000	
High pressure CO <sub>2</sub> liquid receiver	1	£ 300	Estimated
CO <sub>2</sub> liquid pump	1	\$ 13000	
CO <sub>2</sub> liquid pump inverter drive (Variable frequency drive)	1	£518	[353]
Cooling water circulation pump	1	£200	Estimated
Solenoid valves	4	£800	
Piping and fittings		£850	

Insulation for high temperature		£200	Based on existing material information
Pressure transduces	4	£ 314.4	
K- Type thermocouples	4	£164	[354]
CO <sub>2</sub> flow sensor	1	£1083	
CO <sub>2</sub>	1	£1500	Based on quotes for previous orders
System frame	1	£200	Based on the department technician and material costs.
Miscellaneous		£ 200	

#### 9.5.1.6 Components Identification Discussion

The research carried out identifies the suitable 5 kW CO<sub>2</sub> power system's components. However, the outcome of the research shows a lack of options in the selection of these components. The main limitation in these options is represented by the turbine and the pump. The CO<sub>2</sub> turbines found either have a complex configuration, lower operating pressure, or isentropic efficiency as in the Enogia CO<sub>2</sub> turbine, or good operating parameters, with unknown isentropic efficiency, as in the case of IT10 turbines by Infinity. The pump limitation is simply denoted as the ability of the pump to only pump liquid CO<sub>2</sub>. Therefore, and with reference to the simulated cases results for the CO<sub>2</sub> SRC power generation system in Table 6.10, Chapter 6, the first two cases are inapplicable in reality, due to the unsuitability of the identified pump to compress CO<sub>2</sub> in its gas state. The last two simulated cases are applicable when the system is fully operating above the critical region, specifically when the CO<sub>2</sub> on the low pressure side of the system is a fully developed CO<sub>2</sub> liquid, which allows proper operation of the CO<sub>2</sub> liquid pump. However, the relatively high power consumption of the CO<sub>2</sub> liquid pump indicated by the manufacturer and the low isentropic efficiency of the CO<sub>2</sub> turbine rationally suggests very poor system performance, if the third simulated case is applied in a real system. Moreover, an operational challenge might be experienced, where the CO<sub>2</sub> in the low pressure side of the system could be on the

edge of transformation from liquid to gas state, which would simply damage the CO<sub>2</sub> pump. Thus, the only case applicable would be the fourth simulated case, where the turbine inlet pressure is 100 bar. Nevertheless, a consideration of the 50% isentropic efficiency of the CO<sub>2</sub> turbine in the simulation of the fourth case will change the system characteristics. Table 9.12 lists the characteristics of the re-simulated optimum operating point, alongside the results of the formerly simulated optimum point.

**Table 9.12: CO<sub>2</sub> SRC power generation system's fourth case re-simulation results compared to the original results.**

Operation region	New simulation results	Old simulation results
Optimum CO <sub>2</sub> cooler pressure [bar]	85	82
CO <sub>2</sub> heater power [kW]	42.8	40.2
CO <sub>2</sub> cooler power [kW]	40.5	36.7
Recuperator exchanger power [kW]	220.5	93.7
Pump power [kW]	2.7	1.5
System thermal efficiency [%]	5.4	8.7
Net thermal power output [kW]	2.3	3.5
CO <sub>2</sub> mass flow rate [kg/s]	1.1	0.5

The comparison Table 9.12 shows that optimum CO<sub>2</sub> cooler pressure slightly increased when the turbine's isentropic efficiency dropped from 80% to 50%. Furthermore, a slight increase was observed in the CO<sub>2</sub> cooler and heater energy requirements. This is not the case for the recuperator heat exchanger, where the energy increased dramatically from 93.7 kW to 220.5 kW. The result also shows that the pump energy increased significantly. However, the pump energy requirements were found to be very close to what was suggested by the CO<sub>2</sub> liquid pump manufacturer. The system's overall thermal efficiency dropped markedly from 8.7% to 5.4%. Similar behaviour was seen for the net thermal power output, which decreased from 3.5 kW to 2.3 kW, while the mass flow rate of the refrigerant rose by 54%. In general, the results show acceptable characteristics, even though the operating pressure is considered very high. Furthermore, the operation is limited by the low

isentropic efficiency of the turbine and the ability of the CO2 pump to only pump liquid CO2.

### 9.5.2 Economic Analysis Results and Discussion

After all the analysis factors were established, they were listed in Table 9.13, and used as the economic feasibility model inputs.

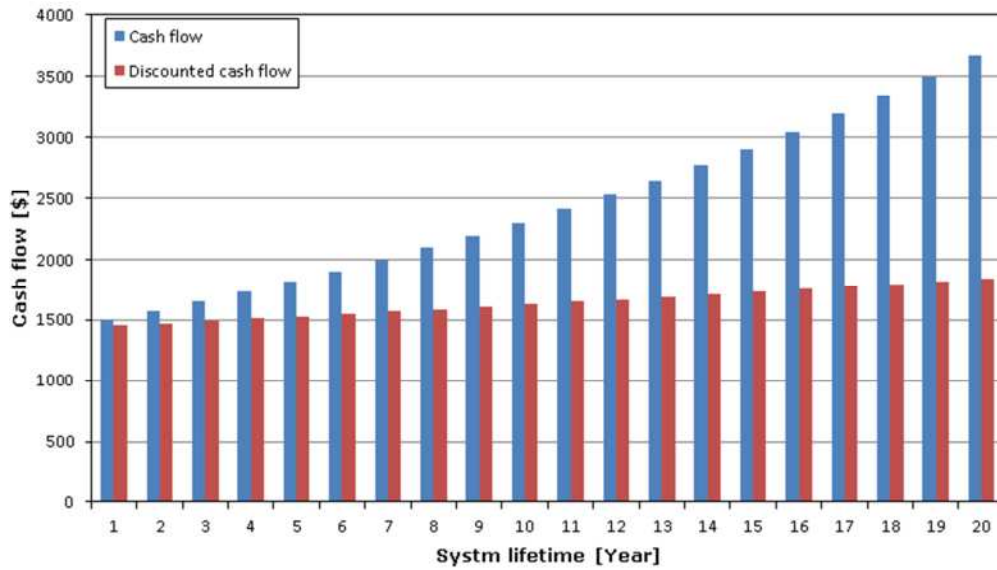
**Table 9.13: The 5 kW CO2 power system’s economic model inputs.**

System capacity [kW]	5
Electrical conversion efficiency [%]	80
Liquid CO2 Pump consumed power [kW]	2.7
Total capital cost [\$]	40811
Specific capital cost [\$/kW]	9602.59
System lifetime [years]	20
Electricity price [\$/kW h]	0.144
System availability throughout the year	95
Electricity price escalation rate [%]	4.5
O&M cost [\$/kW h]	0.012
Consumer price index [%]	3
System’s annual depreciation rate [%]	8
Discount rate [%]	3.5

Table 9.14 shows the results of the economic model. The results suggest that investment in the 5 kW CO2 SRC power generation system is not economically feasible. The NPV by the end of the project is negative and short by \$7953.97 to break even and recover the invested capital. In order to make a feasible investment, the system would require interest rates lower than 1.5%, which is impossible in reality. In addition, the magnitude of system costs is 80.5% higher than the rate of gains.

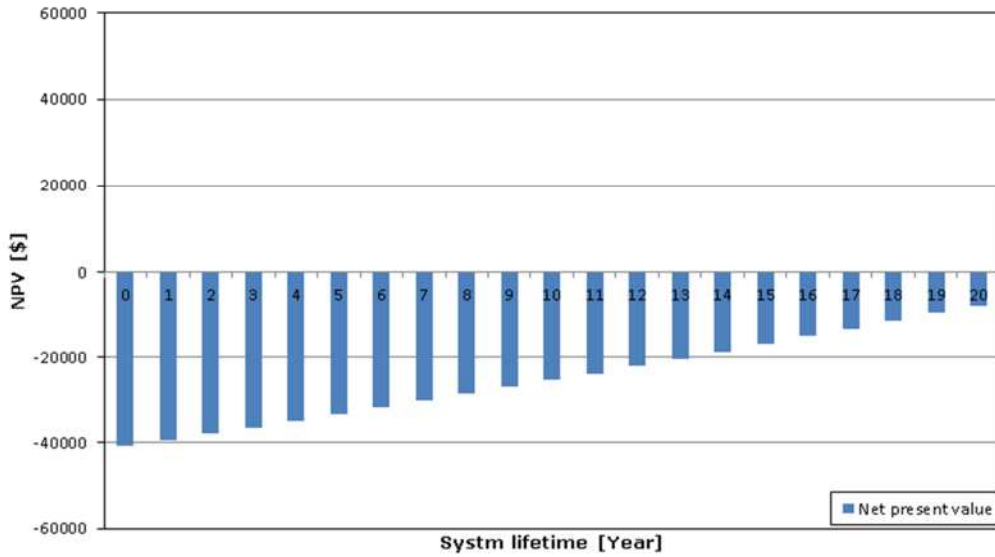
**Table 9.14: Results for the 5 kW CO2 power system economic model.**

NPV [\$]	-7953.97
Payback [Years]	N/A
IRR [%]	1.5
ROI [%]	-80.5



**Figure 9-17: Cash flow variation throughout the 5 kW CO<sub>2</sub> SRC power generation system lifetime.**

Figure 9-17 shows the variation of cash flow and discounted cash flow throughout the lifetime of the system. A gradual increase in cash flow can be observed along the timeline. This increase is a result of the annual increase in electricity prices and the fact that the power consumed by the CO<sub>2</sub> liquid pump is lower than the power produced by the system. On the other hand, the cost represented by the O&M annual increase rate is slightly lower than the electricity rate, which consequently increases the system's benefits. Despite the increase seen in the cash flow, the discount rate has a very significant effect on the cash flow, as shown. The discounted cash flow remains moderately within the range of \$1450 to \$1840 throughout the system's lifetime.

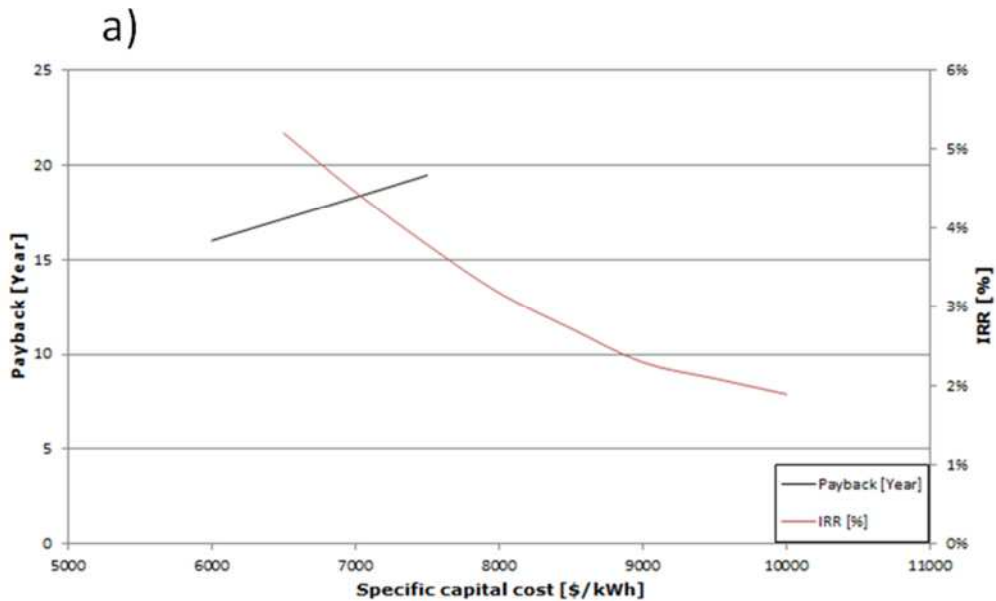


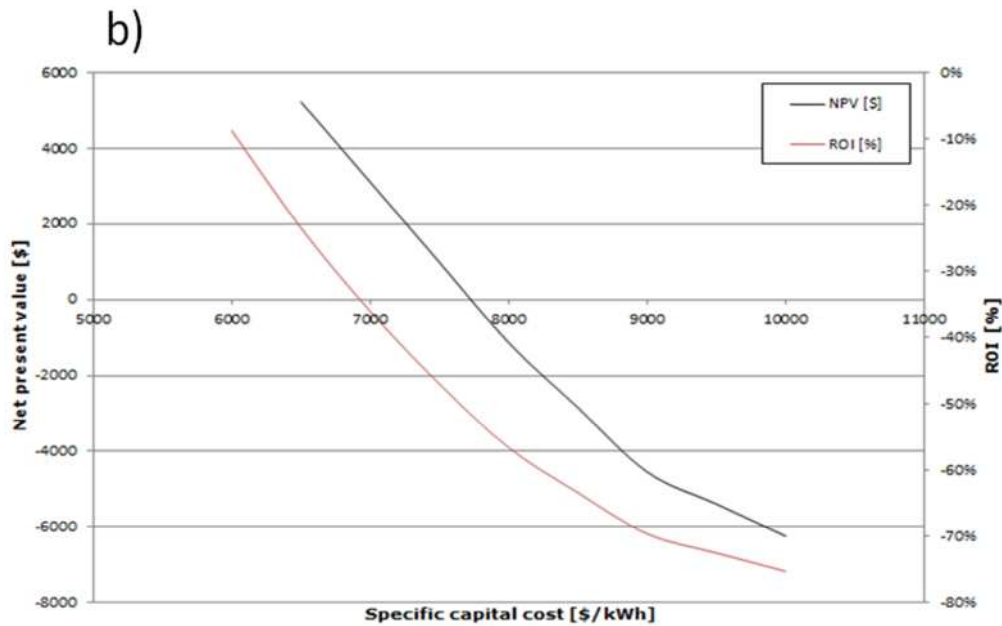
**Figure 9-18: Net present value of the 5 kW CO2 SRC power generation system.**

Figure 9-18 shows the cumulative discounted cash flow. The Figure suggests that the total capital cost of the system could not be recovered throughout the system’s lifetime. The NPV was determined as \$ -7953.97 by the end of the project’s lifetime, as shown by the end of year 20.

### 9.5.2.1 Sensitivity Analysis

#### 9.5.2.1.1 The Effect of the System’s Specific Capital Cost





**Figure 9-19: The effect of the specific capital cost of the 5 kW CO<sub>2</sub> SRC power generation system's economic indicators.**

Figure 9-19 (a) shows the effect of the system's specific capital cost on the payback period, where the capital invested is recovered, as well as the IRR rates. The results show that the IRR rates reduce as the specific cost of the system increases. This suggests low interest rates are required, in order for the system to be feasible. However, the system could be considered as a feasible investment at a maximum specific capital cost of \$7500/kW and IRR of 3.8%, where the supposedly invested capital cost of \$31500/kW could be recovered by 19.5 years of the system's lifetime. At specific capital costs lower than \$7500/kW, the system could also be considered feasible, as the payback period is reduced. However, this is not necessarily true since the cost of CO<sub>2</sub> equipment is almost impossible to be found at specific capital costs within these ranges, nowadays. Figure 9-19 (b) shows NPV and ROI at variable specific capital cost. As expected, the NPV of the specific cost of the system increases. Similar behaviour can be seen for ROI, where the rate tends to decrease in a negative direction as the specific cost increases, which indicates the system's infeasibility. Although, the NPV curve and the results from Figure 9-19 (a) suggest a feasible system at specific capital costs lower than \$7500/kW, the ROI suggests that the investment is still to be considered as unfeasible

and risky, where the magnitude of costs is higher than the magnitude of gains, represented by the negative results.

9.5.2.1.2 The Effect of Electricity Costs

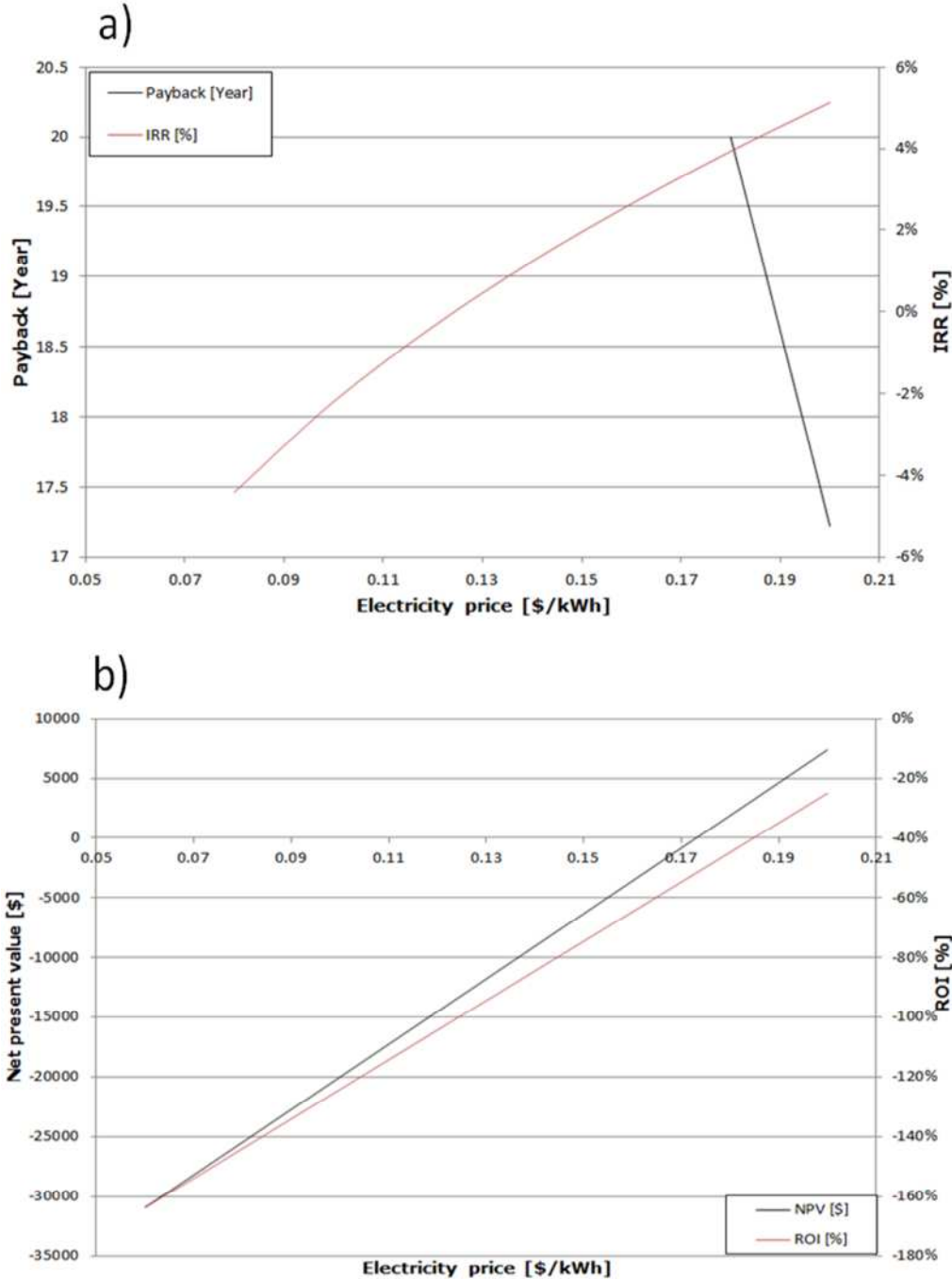


Figure 9-20: The effect of electricity price on the 5 kW CO2 SRC power generation system’s economic indicators.

Electricity prices have a very significant influence on evaluation indicators, as they can directly influence cash flow, as mentioned previously. Figure 9-20 (a) shows the effect of electricity price

variation on the payback period and IRR. The results suggest that the system is totally unfeasible as it cannot compete with the prices of electricity supplied by the grid. The only condition under which the system could break even and pay back its initial capital cost is when the kWh supplied by the grid is \$0.18/kWh or higher, which is not possible in reality. However, in that case, the system would pay back its capital cost by year 20, which is the maximum lifetime of the system. Figure 9-20 (b) shows the NVP and ROI results. The NPV results suggest that the system is feasible if the electricity prices are higher than \$0.17/kWh. The ROI shows that the cost magnitude is higher than the gains from the system, even when the NPV is positive at higher electricity prices.

## 9.6 Conclusion

This chapter analysed the economic feasibility and potential of two thermal power generation technologies, namely, the ORC system employing R1233zd(E), and the CO<sub>2</sub> SRC power generation system. For the conducted analysis, economic evaluation indicators were explained, and the economic parameters assumed for the analysis were taken from reported real life indicators. Furthermore, sensitivity analysis for all systems was carried out in order to investigate the effect directly of influential factors on the systems feasibility. These factors are namely, the specific capital cost of the system and electricity price per kWh.

For the R1233zd(E) ORC, and based on the optimum experimentally obtained performance results, the analysis included 5 kW and 20 kW R1233zd(E) ORC systems. A bill of materials was produced for the prototype system; this allowed the larger systems to be priced for mass manufacture. The predicted costs of the 5 kW and 20 kW systems allowed for economic evaluation. The analysis revealed that both systems have shown to be very attractive investments, with short payback periods of 3.10 and 1.6 years for the 5 kW and the 20 kW systems, respectively. Both systems showed very high NPV by the end of their lifetime, where the NPV would be

\$887,711.83 for the 5 kW system and \$377,631.346 for the 20 kW system. Similarly, both systems demonstrated high IRR, indicating a safe investment that could survive with high interest rates, with the IRR for the 5 kW system being 37.1% and for the 20 kW system, 69.5%. The magnitude of benefits from the systems was very high compared to the magnitude of expenses, where both systems showed outstanding ROI. Generally, the superior economic performance of both systems was in relation to the very low power consumed by the pump, compared to the power produced by the system. This consequently generates more benefits from the system, at escalated rates in relation to all expenses, including power consumption, O&M and expander replacements. However, even if the pump efficiency is taken to be very low, as seen in the experimental phase, the system remains economically feasible; attractive due to its relatively low power consumption.

For the CO<sub>2</sub> power generation system, the chapter presented the outcome of the extensive market research carried out to identify commercially available components suitable for the build and construction of a CO<sub>2</sub> SRC prototype system similar to that built for the R1233zd(E) ORC system. The research revealed very high costs and limited options for the main system's components, namely the CO<sub>2</sub> turbine which has low isentropic efficiency of 50%, and the CO<sub>2</sub> pump, which is only suitable for pumping liquid CO<sub>2</sub>. To incorporate these technical limitations into the 5 kW CO<sub>2</sub> SRC power system, the system was re-simulated, incorporating the low isentropic efficiency of the CO<sub>2</sub> turbine and the liquid phase in the pump inlet. It was found that the only technically feasible operating condition is when the turbine inlet pressure is 100 bar and the system operates completely above the CO<sub>2</sub> critical region, where the CO<sub>2</sub> on the lower pressure side is in its liquid phase. This constraint adds technical inflexibility to other disadvantages of the system, such as high operating pressure and high equipment costs.

However, similar to the R1233zd(E) ORC systems, the identified components were listed alongside their cost to produce the system's bill of materials. The analysis results showed that the system is economically unfeasible, as its NPV remains negative throughout the system's lifetime and the magnitude of the system's cost is higher than its gains, indicated by the ROI indicator. The sensitivity analysis has also revealed that the system remains unfeasible from an economic point of view. The system could be considered feasible if the specific capital cost of the system was lower than \$7500/kW, which would seem to be very far from achievable, at least in the near future. With regard to electricity prices, the system remains unfeasible until the kWh supplied by the grid cost \$0.18/ kWh, which is very expensive in comparison to the actual unit cost, especially at industrial rates with taxes included. The ROI indicator suggests that the magnitude of the costs and expenses throughout the lifetime of the system is always going to be higher than the benefits gained from it. This is mainly due to the relatively high cost of electricity consumed by the CO<sub>2</sub> liquid pump. Finally, although the 5 kW CO<sub>2</sub> power system proved its theoretical thermodynamic feasibility, the high cost, inflexibility of its component options and limitations in its operating conditions proved otherwise. This is emphasised by the economic model, which confirms the unfeasibility of the system in real life. The feasibility of the system is heavily dependent on the future evolution of CO<sub>2</sub> technology in general, which would add more options in terms of system's component flexibility and costs, consequently rendering the CO<sub>2</sub> SRC power generation system economically feasible.

## Chapter 10 : Conclusions and Further Work

---

### 10.1 Conclusions

This research was conducted with a step-by step investigative approach in order to fulfil its aims and objectives to develop and test a novel Rankine based, small-scale power generation prototype system for low-grade waste heat recovery. Four potential power generation systems employing environmentally friendly working fluids were proposed, namely, the CO<sub>2</sub>/lubricant absorption, the CO<sub>2</sub>/POE32 lubricant flood expansion, the CO<sub>2</sub> SRC and the ORC employing newly developed environmentally friendly HFOs and HCFO-R1233zd(E) refrigerants. The conclusions made from the current research can be summarised as follow:

- The computer based thermodynamic modelling and simulations revealed that the R1233zd(E) ORC system is the most suitable system for research purposes. The R1233zd(E) ORC system was shown to have a thermal efficiency of 14.34%, net thermal power output of 4.81 kW and pump power consumption of 0.189 when operating at evaporator pressure of 14 bar. In addition, the ORC system employing the new HFOs and HCFO-R1233zd(E) refrigerants has without doubt achieved the best performance overall, compared to other investigated systems. Furthermore, the new refrigerants demonstrated their ability to replace the conventional refrigerants in ORC and refrigeration applications where R1234yf, and R1234ze(E) showed a similar performance to R134a. R1234ze(Z) was shown to have a similar performance to R245fa, while R1233zd(E) showed a superior performance overall that is very similar to R123.
- The design and construction of the small-scale R1233zd(E) ORC prototype system was successfully carried out, which included the production of a scroll expander which was

converted from an air-conditioning scroll compressor. Furthermore, the R1233zd(E) heat exchangers' surface area sizing was successfully modelled for the first time by LMTD approach, and validated by the heat exchangers' sizes proposed by the manufacturer.

- The expander produced was successfully tested with an automotive alternator in an especially constructed test bench, using air as the working fluid. The maximum electric power produced was 416W, with an alternator efficiency of 22.39% when the expander produced a power output of 2 kW with an isentropic efficiency of 96.33%. The results show that the electric power generator has low efficiency which suggests either large power losses through the transmission mechanism, or a speed mismatch between the expander and the electric power generator.
- The small-scale R1233zd(E) ORC prototype system has successfully proved its technical feasibility by means of two sets of experiments. The best overall experimental performance was achieved in the second experiment where the system's thermal efficiency was 7.6%, the system's electrical efficiency was 1.46%, the expander power output was 1019.54W and electric power output was 250W. However, the best performance achieved was found to be lower than theoretically predicted, due to the sources of performance destruction identified. The primary source of performance limitation was identified as the steam humidifier's lower capability to reach the anticipated temperature of 120°C, besides supplying heat at a constant rate. In addition, the R1233zd(E) circulation pump was identified as a source of performance destruction where it showed low efficiencies. Nevertheless, the system performance could be significantly improved by resolving these issues, as the validation of the theoretical performance demonstrated indicated.

- The economic feasibility and potential of the 5 kW and 20 kW R1233zd(E) ORC systems revealed their attractiveness and superior economic performance where the payback periods were shown to be 3.10 and 1.6 years for the 5 kW and the 20 kW systems, respectively. Furthermore, both systems have very high gains magnitude and can survive with high interest rates.
- Although the CO<sub>2</sub> power system proved its theoretical thermodynamic feasibility, the high cost, inflexibility of its component options and limitations in its operating conditions proved otherwise. This is emphasised by the economic analysis, which confirms the infeasibility of the system in real life. The feasibility of the system is heavily dependent on the future evolution of CO<sub>2</sub> technology in general, which would add more options in terms of the system's component flexibility and costs, consequently rendering the CO<sub>2</sub> SRC power generation system economically feasible.

This thesis therefore concludes that the ORC remains the most efficient, flexible, technically and economically attractive Rankine based technology for low-grade waste heat recovery at the present time, compared to other technologies investigated. Also, the very attractive potentials R1233zd(E) has shown, promotes it to become the primary refrigerant in ORC applications to replace both R123 and R245fa. Although the experimental evaluation showed that the R1233zd(E) ORC system has a lower performance than that theoretically predicted, the technical feasibility of the system has been confidently confirmed with relatively higher thermal efficiencies compared to equivalent technologies that are close to 8%, even with the observed system's limitations.

## 10.2 Recommendations for Further Work

To resolve the R1233zd(E) ORC prototype system's limitations and achieve higher system performance, the following recommendations are made and justified for further work:

1. Expander power output is mainly related to temperature and pressure. However, although the expander power output showed a maximum of nearly 2 kW in the first experiment, it was not possible to achieve higher power output than this, mainly because of the limitations of the steam humidifier heat source. Therefore, it is recommended to replace the steam humidifier heat source with a boiler capable of supplying heat at a constant rate and higher temperatures than 100°C-104°C, in order to allow operation at higher temperatures, higher corresponding evaporation pressure and sufficient super-heating at the expander inlet. Therefore, enhanced expansion would take place, increasing the expander's isentropic efficiency and the expander's power output. Alternatively, if the current steam humidifier is to be used, heating clamps or jacket heating methods could be implemented on the expander pipe line, in order to raise the temperature to the required level up to 120°C.
2. The discussion and comparison analysis of performance showed that the automotive alternator utilised as an electric power generator has the ability to produce electric power output limited to less than 1 kW, even though the expander's power output is higher than this. This relates to the poor electric conversion efficiency of between 15% and 30% at most experimental points. Besides these points, two other points were observed to have efficiencies as high as nearly 70%. In general, the lower efficiency observed is related to major power loss through the transmission belt, or due to the speed mismatch between the expander and the electric power generator. On the other hand, the first experiment revealed that the automotive DC motor was unsuitable for

the system, since the rotational speed afforded was way lower than anticipated. Again, the rotational speed pertains to the expander's power output, which subsequently relates to the heat source input. However, to overcome the electric generator's drawbacks, it is suggested that expanders with internal electric generators are used, if available at the required size, or that a direct coupling power transmission method is applied in order to minimise power loss. Alternatively, it is recommended to replace the alternator utilised with an alternative that requires lower rotational speed to produce electric power output.

3. The R1233zd(E) circulation pump proved to be a major source of vibration and irreversibility in all experiments conducted and contributed heavily to the reduction in the thermal efficiency achieved, especially in the second experiment, where the pump power output was very high compared to the first experiment. Moreover, the pump's operation indicated some difficulty in pumping the refrigerant around at certain points during the experiment and the refrigerant may have flowed back into the pump. As the differential pressure across the expander is not very high and the mass flow rate employed is achievable with a wide range of other types of pumps, it is recommended that the pump be replaced by a smaller pump, to be placed at the lowest point of the system. The liquid line piping should also be replaced with piping of larger internal diameter size to ensure the free flow of the refrigerant stream and proper pumping operation.
4. During the experiments, there was difficulty in monitoring the refrigerant level in the liquid refrigerant receiver cylinder and around the system, since the prototype system was only equipped with one sight glass on the liquid line after the pump. Adding more sight glasses at the expander inlet and heat exchanger inlets and outlets is very important to enable visual observation of the refrigerant flow at different points,

as a means of ensuring a continuous flow and sufficient availability of refrigerant within the system.

5. After the above recommendations have been addressed, it is recommended that the performance of the scroll expander-electric generator arrangement utilised be compared with the performance of a hermetic type of scroll expander, where the electromechanical losses of the integrated electric power generator are expected to be very low and therefore higher power outputs, and isentropic efficiency are expected.

## Bibliography

1. U.S. Energy Information Administration, *International Energy Outlook 2013*. 2013.
2. Population Reference Bureau (PRB), *2013 World Population Data Sheet*. 2014, Population Reference Bureau.
3. International Energy, A., C.-o. Organisation for Economic, and Development, *World energy outlook, 2012*. 2012, Paris: OECD/IEA.
4. Tiwari, G.N., R.K. Mishra, and C. Royal Society of, *Advanced renewable energy sources*. 2012, Cambridge: RSC Publishing.
5. International Energy, A., *Key world energy statistics : from the IEA*. 2013, Paris: International Energy Agency.
6. Haldar, I., *Global warming : the causes and consequences*. 2011, New Delhi: Mind Melodies.
7. *NASA Finds 2011 Ninth-Warmest Year on Record*. 2012 [cited 2014 22/8/2014]; Available from: <http://www.nasa.gov/topics/earth/features/2011-temps.html>.
8. Ichikawa, A., *Global warming - the research challenges : a report of Japan's global warming initiative*. 2004, Dordrecht; [Great Britain]: Springer.
9. *Global Warming Impacts*. 2013; Available from: [http://www.ucsusa.org/global\\_warming/science\\_and\\_impacts/impacts/](http://www.ucsusa.org/global_warming/science_and_impacts/impacts/).
10. See, M., *Greenhouse gas emissions : global business aspects : with 26 tables*. 2001, Berlin [u.a.: Springer.
11. Hilgenkamp, K., *Environmental health : ecological perspectives*. 2005, Sudbury, Mass.: Jones and Bartlett Publishers.
12. Höhne, N., et al., *The Emissions Gap Report 2012-UNEP Synthesis Report*, in *United Nations Environment Programme*. 2012.
13. Adhya, T.K., et al., *The Emissions Gap Report 2013-UNEP Synthesis Report*, in *United Nations Environment Programme*. 2013.
14. Olivier, J.G.J., et al., *TRENDS IN GLOBAL CO2 EMISSIONS 2013 REPORT*. 2013, PBL Netherlands Environmental Assessment Agency; Institute for Environment and Sustainability (IES) of the; European Commission's Joint Research Centre (JRC): The Hague, Netherlands.
15. European Wind Energy, A. *Wind energy-- the facts a guide to the technology, economics and future of wind power*. 2009; Available from: <http://public.eblib.com/choice/publicfullrecord.aspx?p=476575>.
16. Faure, M. and M. Peeters, *Climate change liability*. 2011, Cheltenham, UK; Northampton, MA, USA: Edward Elgar.
17. *Draft decision -/CP.15: Copenhagen Accord*. 2009, United Nations: Copenhagen, 7-18 December.
18. *European Union climate and energy package*. [cited 2014 20/11/2014]; Available from: [http://en.wikipedia.org/wiki/European\\_Union\\_climate\\_and\\_energy\\_package#cite\\_note-5](http://en.wikipedia.org/wiki/European_Union_climate_and_energy_package#cite_note-5).
19. Marlier, E., *Europe 2020: towards a more social EU?* 2010, Bruxelles; Bern; Berlin; Frankfurt, M; New York, NY; Oxford; Wien: PIE Lang.
20. Intergovernmental panel on climate change (IPCC). *Emissions Scenarios-Halocarbons and Other Halogenated Compounds*. [cited 2014 20/11/2014]; Available from: <http://www.ipcc.ch/ipccreports/sres/emission/index.php?idp=123>.

21. Calm, J.M., *The next generation of refrigerants – Historical review, considerations, and outlook*. International Journal of Refrigeration, 2008. **31**(7): p. 1123-1133.
22. United, S. and A. Energy Information, *Emissions of greenhouse gases in the United States, 2000*. 2001, Washington, D.C.: Energy Information Administration.
23. POOL, R., *The Elusive Replacements for CFCs: As CFCs are phased out to protect the ozone layer, chemical companies scramble to find substitutes for these vital compounds and to develop economical ways to make them in large quantities*. Science, 1988. **242**(4879): p. 666-668.
24. Manzer, L.E., *The CFC-ozone issue: Progress on the development of alternatives to CFCs*. Science, 1990. **249**(4964): p. 31-35.
25. Oberthür, S., *Linkages between the Montreal and Kyoto Protocols – Enhancing Synergies between Protecting the Ozone Layer and the Global Climate*. International Environmental Agreements, 2001. **1**(3): p. 357-377.
26. Wikipedia. *Montreal Protocol*. [cited 2014 21/11/2014]; Available from: [http://en.wikipedia.org/wiki/Montreal\\_Protocol](http://en.wikipedia.org/wiki/Montreal_Protocol).
27. Pellegrino, J., et al., *Energy Use, Loss and Opportunities Analysis for U.S Manufacturing and Mining in ACEEE Summer Study on Energy Efficiency in Industry*. 2005.
28. Unit B2 Industrial Competitiveness Policy, E.a.I.D., *EU Manufacturing Industry: What are the Challenges and Opportunities for the Coming Years? First tentative findings of a sector-specific analysis carried out in DG Enterprise and Industry 2010* European commission: Brussels, Belgium.
29. Power, E., *ECOHEATCOOL- Work package1 - The European Heat Market*, E.I.E.E. Programme, Editor. 2005-2006, Ecoheatcool and Euroheat & Powe: Brussels, Belgium.
30. Rademaekers, K., S.S.Z. Asaad, and J. Berg, *Study on the Competitiveness of the European Companies and Resource Efficiency- Final report*. 2011, ECORYS: Rotterdam, Holland.
31. Market Observatory for Energy, *Europe's energy position-markets and supply*. 2009, Directorate general for energy- European commission.
32. Li, C.-Z., *Advances in the science of Victorian brown coal*. 2004, Amsterdam; London: Elsevier.
33. Kiameh, P., *Power generation handbook : selection, applications, operation, and maintenance*. McGraw-Hill handbooks. 2003, New York [u.a.]: McGraw-Hill.
34. Victor, R.A., J.-K. Kim, and R. Smith, *Composition optimisation of working fluids for Organic Rankine Cycles and Kalina cycles*. Energy, 2013. **55**(0): p. 114-126.
35. Henry A. Mlcak, P., *An Introduction to Kalina cycle*, in *Proceedings of the International Joint Power Generation Conference, Book No. H01077*, L. Kielasa and G.E. Weed, Editors. 1996: Huston, Texas.
36. Tchanche, B.F., et al., *Low-grade heat conversion into power using organic Rankine cycles – A review of various applications*. Renewable and Sustainable Energy Reviews, 2011. **15**(8): p. 3963-3979.
37. Bao, J. and L. Zhao, *A review of working fluid and expander selections for organic Rankine cycle*. Renewable and Sustainable Energy Reviews, 2013. **24**(0): p. 325-342.
38. Mathias, J.A., et al., *Experimental Testing of Gerotor and Scroll Expanders Used in, and Energetic and Exergetic Modeling of, an*

- Organic Rankine Cycle*. Journal of Energy Resources Technology, 2009. **131**(1): p. 012201-012201.
39. Pei, G., et al., *Construction and dynamic test of a small-scale organic rankine cycle*. Energy, 2011. **36**(5): p. 3215-3223.
  40. Larjola, J., *Electricity from industrial waste heat using high-speed organic Rankine cycle (ORC)*. International Journal of Production Economics, 1995. **41**(1-3): p. 227-235.
  41. Quoilin, S. and V. Iemort, *Technological and Economical Survey of Organic Rankine Cycle Systems in Fifth European conference economics and management of energy in industry*. 2009: Algrave, Portugal.
  42. Chen, H., D.Y. Goswami, and E.K. Stefanakos, *A review of thermodynamic cycles and working fluids for the conversion of low-grade heat*. Renewable and Sustainable Energy Reviews, 2010. **14**(9): p. 3059-3067.
  43. Vélez, F., et al., *A technical, economical and market review of organic Rankine cycles for the conversion of low-grade heat for power generation*. Renewable and Sustainable Energy Reviews, 2012. **16**(6): p. 4175-4189.
  44. Jung, H.C., S. Krumdieck, and T. Vranjes, *Feasibility assessment of refinery waste heat-to-power conversion using an organic Rankine cycle*. Energy Conversion and Management, 2014. **77**(0): p. 396-407.
  45. Shu, G., et al., *Parametric and working fluid analysis of a dual-loop organic Rankine cycle (DORC) used in engine waste heat recovery*. Applied Energy, 2014. **113**(0): p. 1188-1198.
  46. Li, M., et al., *Construction and preliminary test of a low-temperature regenerative Organic Rankine Cycle (ORC) using R123*. Renewable Energy, 2013. **57**(0): p. 216-222.
  47. Li, M., et al., *Experimental Evaluation of the Regenerative and Basic Organic Rankine Cycles for Low-Grade Heat Source Utilization*. Journal of Energy Engineering, 2013. **139**(3): p. 190-197.
  48. Wang, D., et al., *Efficiency and optimal performance evaluation of organic Rankine cycle for low grade waste heat power generation*. Energy, 2013. **50**(0): p. 343-352.
  49. Saleh, B., et al., *Working fluids for low-temperature organic Rankine cycles*. Energy, 2007. **32**(7): p. 1210-1221.
  50. Hung, T.-C., *Waste heat recovery of organic Rankine cycle using dry fluids*. Energy Conversion and Management, 2001. **42**(5): p. 539-553.
  51. Mago, P.J., et al., *An examination of regenerative organic Rankine cycles using dry fluids*. Applied Thermal Engineering, 2008. **28**(8-9): p. 998-1007.
  52. Intergovernmental panel on climate change (IPCC). *Net Global Radiative Forcing, Global Warming Potentials and Patterns of Forcing*. 2015 [cited 2015 20/4/2015]; Available from: [https://www.ipcc.ch/publications\\_and\\_data/ar4/wg1/en/tssts-2-5.html](https://www.ipcc.ch/publications_and_data/ar4/wg1/en/tssts-2-5.html).
  53. Defibaugh, D.R. and M.R. Moldover, *Compressed and Saturated Liquid Densities for 18 Halogenated Organic Compounds*. Journal of Chemical & Engineering Data, 1997. **42**(1): p. 160-168.
  54. Wikipedia. *List of refrigerants*. [cited 2015 21/04/2015]; Available from: [http://en.wikipedia.org/wiki/List\\_of\\_refrigerants](http://en.wikipedia.org/wiki/List_of_refrigerants).
  55. Bell, I., *CoolProp*. 2013. p. A cross-platform, open-source, alternative to NIST REFPROP. Based on reference-accuracy

equations of state and transport property correlations for many refrigerants

56. American Society of Heating, R., E. Air-Conditioning, and I. American National Standards, *Designation and safety classification of refrigerants (Forward)*. 2007, Atlanta, GA: American Society of Heating, Refrigerating and Air-Conditioning Engineers.
57. Brown, J.S., C. Zilio, and A. Cavallini, *The fluorinated olefin R-1234ze(Z) as a high-temperature heat pumping refrigerant*. International Journal of Refrigeration, 2009. **32**(6): p. 1412-1422.
58. Bigonha Tibiriçá, C., G. Ribatski, and J. Richard Thome, *Flow Boiling Characteristics for R1234ze(E) in 1.0 and 2.2 mm Circular Channels*. Journal of Heat Transfer, 2011. **134**(2): p. 020906-020906.
59. Beattie, R.J. and J.A. Karnaz, *Investigation Of Low GWP Refrigerant Interaction With Various Lubricant Candidates*, in *The International Refrigeration and Air Conditioning Conference*. 2012: Purdue University, West Lafayette, Indiana, USA.
60. Steven Brown, J., *HFOs: New low global warming potential refrigerants* ASHRAE journal, 2009.
61. Honeywell. *Honeywell Solstice® 1233zd(E) Technical Information*. [cited 2014 12 April 2014]; Technical Information]. Available from: <http://www.honeywell-blowingagents.com/?document=solstice-lba-technical-brochure&download=1>.
62. Honeywell. *Solstice Range of Refrigerants*. [Brochure] 2012 [cited 2014 15 April 2014]; Solstice Refrigerants Brochure]. Available from: <http://www.honeywell-refrigerants.com/europe/?document=the-future-begins-with-solstice&download=1>.
63. Hulse, R.J., et al., *Physical Properties of HCFO-1233zd(E)*. Journal of Chemical & Engineering Data, 2012. **57**(12): p. 3581-3586.
64. Walter, B., *Refrigerants: Now And In The Future (Presentation)*, in *Carrier's Sustainability Symposiums*. 2012: SYRACUSE, N.Y, USA.
65. Schmidt, T., et al., *Biotransformation of trans-1-chloro-3,3,3-trifluoropropene (trans-HCFO-1233zd)*. Toxicology and Applied Pharmacology, 2013. **268**(3): p. 343-351.
66. Bala Varma, D. and B. Joost. *Organic Rankine Cycle System Analysis for LowGWP Working Fluids*. in *The International Refrigeration and Air Conditioning Conference*. 2012. Purdue University, West Lafayette, Indiana, USA.
67. Liu, W., et al., *Investigation of hydrofluoroolefins as potential working fluids in organic Rankine cycle for geothermal power generation*. Energy, 2014. **67**(0): p. 106-116.
68. Yamada, N., M.N.A. Mohamad, and T.T. Kien, *Study on thermal efficiency of low- to medium-temperature organic Rankine cycles using HFO-1234yf*. Renewable Energy, 2012. **41**(0): p. 368-375.
69. Qiu, G., H. Liu, and S. Riffat, *Expanders for micro-CHP systems with organic Rankine cycle*. Applied Thermal Engineering, 2011. **31**(16): p. 3301-3307.
70. Wang, T., et al., *A review of researches on thermal exhaust heat recovery with Rankine cycle*. Renewable and Sustainable Energy Reviews, 2011. **15**(6): p. 2862-2871.
71. Quoilin, S., et al., *Techno-economic survey of Organic Rankine Cycle (ORC) systems*. Renewable and Sustainable Energy Reviews, 2013. **22**(0): p. 168-186.
72. Song, P., et al., *A review of scroll expanders for organic Rankine cycle systems*. Applied Thermal Engineering, (0).

73. Yamamoto, T., et al., *Design and testing of the Organic Rankine Cycle*. Energy, 2001. **26**(3): p. 239-251.
74. Smith, I.K., et al., *COST EFFECTIVE SMALL SCALE ORC SYSTEMS FOR POWER RECOVERY FROM LOW ENTHALPY GEOTHERMAL RESOURCES*. London, UK.
75. Mu, Y., et al., *Experimental Study of a Low-Temperature Power Generation System in an Organic Rankine Cycle*. Journal of Energy Engineering. **0**(0): p. 04014017.
76. Qiu, G., et al., *Experimental investigation of a biomass-fired ORC-based micro-CHP for domestic applications*. Fuel, 2012. **96**(0): p. 374-382.
77. Wang, X.D., et al., *Performance evaluation of a low-temperature solar Rankine cycle system utilizing R245fa*. Solar Energy, 2010. **84**(3): p. 353-364.
78. Kaltschmitt, M., W. Streicher, and A. Wiese. *Renewable energy technology, economics, and environment*. 2007; Available from: <http://dx.doi.org/10.1007/3-540-70949-5>.
79. Whitman, W.C., W.M. Johnson, and J. Tomczyk, *Refrigeration & air conditioning technology*. 2000, Albany, NY: Delmar Publishers.
80. Sugarman, S.C. *HVAC fundamentals*. 2004; Available from: <http://search.ebscohost.com/login.aspx?direct=true&scope=site&db=nlebk&db=nlabk&AN=127763>.
81. Jradi, M. and S. Riffat, *Experimental investigation of a biomass-fuelled micro-scale tri-generation system with an organic Rankine cycle and liquid desiccant cooling unit*. Energy, 2014. **71**(0): p. 80-93.
82. Jradi, M., et al., *Micro-scale ORC-based combined heat and power system using a novel scroll expander*. International Journal of Low-Carbon Technologies, 2014.
83. Tarique, M.A.U.o.O.I.o.T., *Experimental investigation of scroll based organic Rankine systems*. 2011, UOIT: Oshawa, Ont.
84. Ali Tarique, M., I. Dincer, and C. Zamfirescu, *Experimental investigation of a scroll expander for an organic Rankine cycle*. International Journal of Energy Research, 2014. **38**(14): p. 1825-1834.
85. Li, T., et al., *Experimental comparison of R245fa and R245fa/R601a for organic Rankine cycle using scroll expander*. International Journal of Energy Research, 2014: p. n/a-n/a.
86. Panesar, A.S., *A study of organic Rankine cycle systems with the expansion process performed by twin screw machines*. (Unpublished Doctoral thesis, ), in *Civil Engineering*. 2012, City University London: London, UK.
87. Schuster, A., et al., *Energetic and economic investigation of Organic Rankine Cycle applications*. Applied Thermal Engineering, 2009. **29**(8-9): p. 1809-1817.
88. Carcasci, C., R. Ferraro, and E. Miliotti, *Thermodynamic analysis of an organic Rankine cycle for waste heat recovery from gas turbines*. Energy, 2014. **65**(0): p. 91-100.
89. Manolakos, D., et al., *Experimental evaluation of an autonomous low-temperature solar Rankine cycle system for reverse osmosis desalination*. Desalination, 2007. **203**(1-3): p. 366-374.
90. Manolakos, D., et al., *Design of an autonomous low-temperature solar Rankine cycle system for reverse osmosis desalination*. Desalination, 2005. **183**(1-3): p. 73-80.
91. Guo, T., H. Wang, and S. Zhang, *Comparative analysis of natural and conventional working fluids for use in transcritical Rankine*

- cycle using low-temperature geothermal source*. International Journal of Energy Research, 2011. **35**(6): p. 530-544.
92. Chen, Y., et al., *A comparative study of the carbon dioxide transcritical power cycle compared with an organic rankine cycle with R123 as working fluid in waste heat recovery*. Applied Thermal Engineering, 2006. **26**(17-18): p. 2142-2147.
  93. Vélez, F., et al., *Low temperature heat source for power generation: Exhaustive analysis of a carbon dioxide transcritical power cycle*. Energy, 2011. **36**(9): p. 5497-5507.
  94. Li, X., H. Huang, and W. Zhao, *A supercritical or transcritical Rankine cycle with ejector using low-grade heat*. Energy Conversion and Management, 2014. **78**(0): p. 551-558.
  95. Chen, H., et al., *A supercritical Rankine cycle using zeotropic mixture working fluids for the conversion of low-grade heat into power*. Energy. **In Press, Corrected Proof**.
  96. Shengjun, Z., W. Huaixin, and G. Tao, *Performance comparison and parametric optimization of subcritical Organic Rankine Cycle (ORC) and transcritical power cycle system for low-temperature geothermal power generation*. Applied Energy, 2011. **88**(8): p. 2740-2754.
  97. Vidhi, R., et al., *Organic Fluids in a Supercritical Rankine Cycle for Low Temperature Power Generation*. Journal of Energy Resources Technology, 2013. **135**(4): p. 042002-042002.
  98. Cayer, E., N. Galanis, and H. Nesreddine, *Parametric study and optimization of a transcritical power cycle using a low temperature source*. Applied Energy, 2010. **87**(4): p. 1349-1357.
  99. Baik, Y.-J., et al., *Power-based performance comparison between carbon dioxide and R125 transcritical cycles for a low-grade heat source*. Applied Energy, 2011. **88**(3): p. 892-898.
  100. Vetter, C., H.-J. Wiemer, and D. Kuhn, *Comparison of sub- and supercritical Organic Rankine Cycles for power generation from low-temperature/low-enthalpy geothermal wells, considering specific net power output and efficiency*. Applied Thermal Engineering, 2013. **51**(1-2): p. 871-879.
  101. Zhang, X.R., H. Yamaguchi, and D. Uneno, *Thermodynamic analysis of the CO<sub>2</sub>-based Rankine cycle powered by solar energy*. International Journal of Energy Research, 2007. **31**(14): p. 1414-1424.
  102. Turchi, C.S., et al., *Thermodynamic Study of Advanced Supercritical Carbon Dioxide Power Cycles for Concentrating Solar Power Systems*. Journal of Solar Energy Engineering, 2013. **135**(4): p. 041007-041007.
  103. Besarati, S.M. and D. Yogi Goswami, *Analysis of Advanced Supercritical Carbon Dioxide Power Cycles With a Bottoming Cycle for Concentrating Solar Power Applications*. Journal of Solar Energy Engineering, 2013. **136**(1): p. 010904-010904.
  104. Kato, Y., T. Nitawaki, and Y. Muto, *Medium temperature carbon dioxide gas turbine reactor*. Nuclear Engineering and Design, 2004. **230**(1-3): p. 195-207.
  105. Riffat, S.B., et al., *Natural refrigerants for refrigeration and air-conditioning systems*. Applied Thermal Engineering, 1997. **17**(1): p. 33-42.
  106. Ananthanarayanan, P.N., *Basic refrigeration and air conditioning*. 2005, New Delhi: Tata McGraw-Hill.
  107. Cayer, E., et al., *Analysis of a carbon dioxide transcritical power cycle using a low temperature source*. Applied Energy, 2009. **86**(7-8): p. 1055-1063.

108. Guo, T., H. Wang, and S. Zhang, *Comparative analysis of CO<sub>2</sub>-based transcritical Rankine cycle and HFC245fa-based subcritical organic Rankine cycle using low-temperature geothermal source*. Science China Technological Sciences, 2010. **53**(6): p. 1638-1646.
109. Tuo, H., *Thermal-economic analysis of a transcritical Rankine power cycle with reheat enhancement for a low-grade heat source*. International Journal of Energy Research, 2013. **37**(8): p. 857-867.
110. Kim, Y.M., C.G. Kim, and D. Favrat, *Transcritical or supercritical CO<sub>2</sub> cycles using both low- and high-temperature heat sources*. Energy, 2012. **43**(1): p. 402-415.
111. Chen, Y., P. Lundqvist, and P. Platell, *Theoretical research of carbon dioxide power cycle application in automobile industry to reduce vehicle's fuel consumption*. Applied Thermal Engineering, 2005. **25**(14-15): p. 2041-2053.
112. Persichilli, M., et al., *Supercritical CO<sub>2</sub> Power Cycle Developments and Commercialization: Why sCO<sub>2</sub> can Displace Steam in Power-Gen India & Central Asia Conference 2012*, Echogen Power Systems LLC: Pragati Maidan, New Delhi, India.
113. Song, Y., et al., *Thermodynamic analysis of a transcritical CO<sub>2</sub> power cycle driven by solar energy with liquified natural gas as its heat sink*. Applied Energy, 2012. **92**(0): p. 194-203.
114. Zhang, X.R., et al., *Analysis of a novel solar energy-powered Rankine cycle for combined power and heat generation using supercritical carbon dioxide*. Renewable Energy, 2006. **31**(12): p. 1839-1854.
115. Zhang, X.-R., et al., *A Feasibility Study of CO<sub>2</sub>-Based Rankine Cycle Powered by Solar Energy*. JSME International Journal Series B Fluids and Thermal Engineering, 2005. **48**(3): p. 540-547.
116. Zhang, X.R., et al., *Theoretical analysis of a thermodynamic cycle for power and heat production using supercritical carbon dioxide*. Energy, 2007. **32**(4): p. 591-599.
117. Zhang, X.R., et al., *Experimental Performance Analysis of Supercritical CO<sub>2</sub> Thermodynamic Cycle Powered by Solar Energy*. AIP Conference Proceedings, 2006. **832**(1): p. 419-424.
118. Zhang, X.-R., H. Yamaguchi, and D. Uneno, *Experimental study on the performance of solar Rankine system using supercritical CO<sub>2</sub>*. Renewable Energy, 2007. **32**(15): p. 2617-2628.
119. Zhang, X.R., et al., *Study of solar energy powered transcritical cycle using supercritical carbon dioxide*. International Journal of Energy Research, 2006. **30**(14): p. 1117-1129.
120. Yamaguchi, H., et al., *Solar energy powered Rankine cycle using supercritical CO<sub>2</sub>*. Applied Thermal Engineering, 2006. **26**(17-18): p. 2345-2354.
121. IBRAHIM, O.M., *Evaluation and Design of Absorption Power Cycles*. 1991.
122. Ibrahim, O.M. and S.A. Klein, *Absorption power cycles*. Energy, 1996. **21**(1): p. 21-27.
123. Srihirin, P., S. Aphornratana, and S. Chungpaibulpatana, *A review of absorption refrigeration technologies*. Renewable and Sustainable Energy Reviews, 2001. **5**(4): p. 343-372.
124. Jawahar, C.P. and R. Saravanan, *Generator absorber heat exchange based absorption cycle--A review*. Renewable and Sustainable Energy Reviews, 2010. **14**(8): p. 2372-2382.
125. Zhang, N. and N. Lior, *Development of a Novel Combined Absorption Cycle for Power Generation and Refrigeration*. Journal of Energy Resources Technology, 2007. **129**(3): p. 254-265.

126. Martin, C. and D.Y. Goswami, *Effectiveness of cooling production with a combined power and cooling thermodynamic cycle*. Applied Thermal Engineering, 2006. **26**(5-6): p. 576-582.
127. Sarbu, I. and C. Sebarchievici, *Review of solar refrigeration and cooling systems*. Energy and Buildings, 2013. **67**(0): p. 286-297.
128. Maloney, J.D. and R.C. Robertson, *Thermodynamic study of ammonia-water heat power cycles*. 1953.
129. Kalina, A.I., *Combined-Cycle System With Novel Bottoming Cycle*. Journal of Engineering for Gas Turbines and Power, 1984. **106**(4): p. 737-742.
130. Jawahar, C.P., B. Raja, and R. Saravanan, *Thermodynamic studies on NH<sub>3</sub>-H<sub>2</sub>O absorption cooling system using pinch point approach*. International Journal of Refrigeration, 2010. **33**(7): p. 1377-1385.
131. Li, X., Q. Zhang, and X. Li, *A Kalina cycle with ejector*. Energy, 2013. **54**(0): p. 212-219.
132. Wang, J., Y. Dai, and L. Gao, *Parametric analysis and optimization for a combined power and refrigeration cycle*. Applied Energy, 2008. **85**(11): p. 1071-1085.
133. Xu, F., D. Yogi Goswami, and S. S. Bhagwat, *A combined power/cooling cycle*. Energy, 2000. **25**(3): p. 233-246.
134. Sadrameli, S.M. and D.Y. Goswami, *Optimum operating conditions for a combined power and cooling thermodynamic cycle*. Applied Energy, 2007. **84**(3): p. 254-265.
135. Vidal, A., et al., *Analysis of a combined power and refrigeration cycle by the exergy method*. Energy, 2006. **31**(15): p. 3401-3414.
136. Sun, L., et al., *A power and cooling cogeneration system using mid/low-temperature heat source*. Applied Energy, 2013. **112**(0): p. 886-897.
137. Mirolli, M.D. *The Kalina cycle for cement kiln waste heat recovery power plants*. in *Cement Industry Technical Conference, 2005. Conference Record*. 2005.
138. Zheng, D., et al., *Thermodynamic analysis of a novel absorption power/cooling combined-cycle*. Applied Energy, 2006. **83**(4): p. 311-323.
139. Zhang, N. and N. Lior, *Methodology for thermal design of novel combined refrigeration/power binary fluid systems*. International Journal of Refrigeration, 2007. **30**(6): p. 1072-1085.
140. Liu, M. and N. Zhang, *Proposal and analysis of a novel ammonia-water cycle for power and refrigeration cogeneration*. Energy, 2007. **32**(6): p. 961-970.
141. Wang, J., Y. Dai, and Z. Sun, *A theoretical study on a novel combined power and ejector refrigeration cycle*. International Journal of Refrigeration, 2009. **32**(6): p. 1186-1194.
142. Youbi-Idrissi, M., et al., *Impact of refrigerant-oil solubility on an evaporator performances working with R-407C*. International Journal of Refrigeration, 2003. **26**(3): p. 284-292.
143. Yun, R., Y. Hwang, and R. Radermacher, *Convective gas cooling heat transfer and pressure drop characteristics of supercritical CO<sub>2</sub>/oil mixture in a minichannel tube*. International Journal of Heat and Mass Transfer, 2007. **50**(23-24): p. 4796-4804.
144. Dang, C., et al., *Effect of lubricating oil on cooling heat transfer of supercritical carbon dioxide*. International Journal of Refrigeration, 2007. **30**(4): p. 724-731.
145. Marsh, K.N. and M.E. Kandil, *Review of thermodynamic properties of refrigerants + lubricant oils*. Fluid Phase Equilibria, 2002. **199**(1-2): p. 319-334.

146. Youbi-Idrissi, M., et al., *Oil presence in an evaporator: experimental validation of a refrigerant/oil mixture enthalpy calculation model*. International Journal of Refrigeration, 2004. **27**(3): p. 215-224.
147. Conde, M.R., *Estimation of thermophysical properties of lubricating oils and their solutions with refrigerants: An appraisal of existing methods*. Applied Thermal Engineering, 1996. **16**(1): p. 51-61.
148. García, J., et al., *Experimental and PC-SAFT volumetric and phase behavior of carbon dioxide+PAG or POE lubricant systems*. The Journal of Supercritical Fluids, 2008. **47**(1): p. 8-16.
149. Hodder, R.S.T.J.L., *Dictionary of materials and testing*. 2000, Warrendale, Pa: Society of Automotive Engineers.
150. Totten, G.E., *Fuels and lubricants handbook : technology, properties, performance, and testing*. 2003, West Conshohocken, Pa.: ASTM International.
151. Youbi-Idrissi, M., et al., *Solubility of CO<sub>2</sub> in a Synthetic Oil*, in *21st, International congress of refrigeration*. 2003, International Institute of Refrigeration (IIR): Washington, DC, USA.
152. Seeton, C. and P. Hrnjak, *MEASUREMENTS OF SOLUBILITY, LIQUID DENSITY, AND LIQUID VISCOSITY FOR CO<sub>2</sub>-LUBRICANT MIXTURES*, in *3rd International Institute of Refrigeration (IIR) Conference on Thermophysical Properties and Transfer Processes of Refrigerants*. 2009: Boulder, Colorado, USA.
153. Neto, M.A.M. and J.R. Barbosa, *Experimental and Theoretical Analysis of CO<sub>2</sub> Absorption in Polyolester Oil Using the PC-SAFT Equation of State to Account for Nonideal Effects*. Industrial & Engineering Chemistry Research, 2011. **51**(2): p. 1027-1035.
154. Pensado, A.S., et al., *Viscosity and density measurements for carbon dioxide + pentaerythritol ester lubricant mixtures at low lubricant concentration*. The Journal of Supercritical Fluids, 2008. **44**(2): p. 172-185.
155. Leung, M., et al., *Measurements of Absorption Rates of HFC Single and Blended Refrigerants in POE Oils*. HVAC&R Research, 1998. **4**(2): p. 141 - 151.
156. Dijk, M.A.v. and A. Wakker. *Concepts of polymer thermodynamics*. 1997; Available from: <http://search.ebscohost.com/login.aspx?direct=true&scope=site&db=nlebk&db=nlabk&AN=32581>.
157. Bobbo, S., L. Fedele, and R. Stryjek. *Oil Structure Influence on the Solubility of Carbon Dioxide in POE Lubricants*. in *The International Refrigeration and Air Conditioning Conference*. 2006. Purdue University, West Lafayette, Indiana, USA.
158. *2010 ASHRAE Handbook - Refrigeration (SI Edition)*. American Society of Heating, Refrigerating and Air-Conditioning Engineers, Inc.
159. Willing, A., *Oleochemical esters — environmentally compatible raw materials for oils and lubricants from renewable resources*. Lipid / Fett, 1999. **101**(6): p. 192-198.
160. Schnubel, M., *Automotive heating & air conditioning*. 2009, Clifton Park, N.Y.: Delmar.
161. Li, H., K.C. Lilje, and M.C. Watson, *Field And Laboratory Evaluations Of Lubricants For CO<sub>2</sub> Refrigeration*, in *The International Refrigeration and Air Conditioning Conference*. 2002: Purdue University, West Lafayette, Indiana, USA.
162. Booser, E.R., *CRC handbook of lubrication and tribology. Volume III, Volume III*. 1994, Boca Raton; Ann Arbor; London [etc.]: CRC press.

163. Dincer, I.K.M.W.I., *Refrigeration systems and applications*. 2010, Chichester, West Sussex, U.K.: Wiley.
164. Rudnick, L.R.S.R.L. *Synthetic lubricants and high-performance functional fluids*. 1999.
165. Bobbo, S., et al., *SOLUBILITY OF CARBON DIOXIDE IN SOME COMMERCIAL POE OILS*, in *7th IIR Gustav Lorentzen Conference on Natural Working Fluids*. . 2006, International Institute of Refrigeration (IIR): Trondheim, Norway.
166. American Society of Heating, R. and A.N.S.I. Air-Conditioning Engineers, *Refrigeration oil description (foreword)*. 2006, Atlanta, GA: American Society of Heating, Refrigerating and Air-Conditioning Engineers.
167. *2010 ASHRAE Handbook - Refrigeration (I-P Edition)*. American Society of Heating, Refrigerating and Air-Conditioning Engineers, Inc.
168. Majumdar, S.R., *Oil hydraulic systems : principles and maintenance*. 2001, New Delhi: Tata McGraw-Hill.
169. Denis, J.B.J.D.G.H.J.-C.I.F.d.P., *Lubricant properties analysis & testing*. 2000, Paris: Ed. Technip.
170. Zhao, X. and P. Bansal, *Critical review of flow boiling heat transfer of CO<sub>2</sub>-lubricant mixtures*. International Journal of Heat and Mass Transfer, 2009. **52**(3-4): p. 870-879.
171. Hauk, A. and E. Weidner, *Thermodynamic and Fluid-Dynamic Properties of Carbon Dioxide with Different Lubricants in Cooling Circuits for Automobile Application*. Industrial & Engineering Chemistry Research, 2000. **39**(12): p. 4646-4651.
172. Fandiño, O., et al., *Solubilities of Carbon Dioxide in a Dipentaerythritol Ester and in a Polyether†*. Journal of Chemical & Engineering Data, 2010. **55**(12): p. 5483-5488.
173. Randles, S.J., et al. *A critical assessment of synthetic lubricant technologies for alternative refrigerants*. in *Proceedings of X European Conference on Technological Innovations in Air Conditioning and Refrigeration Industry with Particular Reference to new Refrigerants, new European Regulation New Plants-The Cold Chain*. 2003. Milan.
174. Ikeda, H., J.I. Yagi, and Y. Kawaguchi, *The Development of PAG Refrigeration Lubricants for Hermetic Compressors With CO<sub>2</sub>*, in *The International Refrigeration and Air Conditioning Conference*. 2004: Purdue University, West Lafayette, Indiana, USA.
175. Kawaguchi, Y., et al., *Performance study of refrigerating oils with CO<sub>2</sub> in The SAE Automotive Alternate Refrigerants System Symposium*. 2000: Scottsdale, Arizona, USA.
176. Yokozeki, A., *Solubility correlation and phase behaviors of carbon dioxide and lubricant oil mixtures*. Applied Energy, 2007. **84**(2): p. 159-175.
177. Zhao, C.-R., P.-X. Jiang, and Y.-W. Zhang, *Flow and convection heat transfer characteristics of CO<sub>2</sub> mixed with lubricating oil at super-critical pressures in small tube during cooling*. International Journal of Refrigeration, 2011. **34**(1): p. 29-39.
178. Bobbo, S., et al., *Solubility of CO<sub>2</sub> in Commercial POE Oils with Different Standard Viscosity*, in *The International Refrigeration and Air Conditioning Conference*. . 2008: Purdue University, West Lafayette, Indiana, USA.
179. Kierzkowska-Pawlak, H. and A. Chacuk, *Carbon Dioxide Desorption from Saturated Organic Solvents*. Chemical Engineering & Technology, 2010. **33**(1): p. 74-81.

180. Mantor, P.D., et al., *Solubility of carbon dioxide in propylene carbonate at elevated pressures and higher than ambient temperatures*. Journal of Chemical & Engineering Data, 1982. **27**(3): p. 243-245.
181. Murrieta-Guevara, F., A. Romero-Martinez, and A. Trejo, *Solubilities of carbon dioxide and hydrogen sulfide in propylene carbonate, N-methylpyrrolidone and sulfolane*. Fluid Phase Equilibria, 1988. **44**(1): p. 105-115.
182. SIGMA-ALDRICH, *Propylene Carbonate Material Safety Data Sheet*. 31/3/2013.
183. Seeton, C. and P. Hrnjak, *Thermophysical Properties of CO<sub>2</sub>-Lubricant Mixtures and Their Affect on 2-Phase Flow in Small Channels (Less than 1mm)*, in *The International Refrigeration and Air Conditioning Conference*. 2006: Purdue University, West Lafayette, Indiana, USA.
184. Marcelino Neto, M.A. and J.R. Barbosa Jr, *Phase and volumetric behaviour of mixtures of carbon dioxide (R-744) and synthetic lubricant oils*. The Journal of Supercritical Fluids, 2009. **50**(1): p. 6-12.
185. Hauk, A., *Thermo- und Fluidodynamik von synthetischen Schmierstoffen mit Kohlendioxid als Kältemittel in PKW-Klimaanlagen [in German]*. 2001, Ruhr-Universitt Bochum.
186. BOC industrial gases. *Refrigerant Grade CO<sub>2</sub> (R744)*. [cited 2014 24/11/2014]; Available from: <http://www.boconline.co.uk/en/products-and-supply/refrigerant-gases/natural-refrigerants/co2-r744/co2-r744.html>.
187. Lubrizol. *Lubrizol Website*. [cited 2014 12/10/2014]; Available from: <https://www.lubrizol.com/>.
188. Bredin, A., A.V. Larcher, and B.J. Mullins, *Thermogravimetric analysis of carbon black and engine soot—Towards a more robust oil analysis method*. Tribology International, 2011. **44**(12): p. 1642-1650.
189. Stuart, B., *Polymer analysis*. 2002, Chichester: John Wiley & Sons.
190. Akhavan, J., *Chemistry of Explosives (3rd Edition)*. Royal Society of Chemistry.
191. Bredin, A., *The influence of contaminant particles and filtration regime on fibrous mist-filter performance, in Department of Mechanical Engineering*. 2012, Curtin University: Perth, Australia.
192. Licari, J.J. and L.A. Hughes, *Handbook of Polymer Coatings for Electronics - Chemistry, Technology and Applications (2nd Edition)*. William Andrew Publishing/Noyes.
193. TA, I. *TA Instruments, SDT Q600 brochure*. 2014 [cited 2014 23 March 2014]; TA Instruments, TGA, SDT Q600 brochure]. Available from: <http://www.tainstruments.com/pdf/brochure/sdt.pdf>.
194. Lewis, R.J., Sr., *Hawley's Condensed Chemical Dictionary (15th Edition)*. John Wiley & Sons.
195. Plechkova, N.V.S.K.R. *Ionic liquids unCOILed critical expert overviews*. 2013; Available from: <http://search.ebscohost.com/login.aspx?direct=true&scope=site&db=nlebk&db=nlabk&AN=497775>.
196. Isochema, H. *Dynamic Mixed Gas Sorption Analyzer IGA-003*. 2014 [cited 2014 03/04/2014]; Available from: [http://www.hidenisochema.com/our\\_products/instruments/?id=8&title=iga\\_003](http://www.hidenisochema.com/our_products/instruments/?id=8&title=iga_003).
197. Fluid-o-Tech. *TMFR series (Rotary vane pumps)*. [cited 2014 21/09/2014]; Available from: [http://www.fluidotech.it/Pages/en\\_fo\\_fa\\_30\\_200\\_literature.aspx](http://www.fluidotech.it/Pages/en_fo_fa_30_200_literature.aspx).

198. Fluid-o-Tech. *Fluid-o-Tech TMFR series rotary vane pumps (specification sheet)*. [cited 2014 22/09/2014]; Available from: [http://www.becktech.co.uk/pdf/fot\\_tmfr\\_rvp\\_data\\_sheet.pdf](http://www.becktech.co.uk/pdf/fot_tmfr_rvp_data_sheet.pdf).
199. RS components. *K-type thermocouple with welded tip*. 2014 [cited 2014 21/09/2014]; RS -75 → +250 °C 5 m Cable K Type Thermocouple, 150 mm Probe]. Available from: <http://docs-europe.electrocomponents.com/webdocs/10d2/0900766b810d2904.pdf>.
200. RS components. *IND series-Industrial Pressure Transducer - Ceramic*. 2014 [cited 2014 20/09/2014]; RS -1 to 24 bar absolute Pressure transducer specification ]. Available from: <http://docs-europe.electrocomponents.com/webdocs/12b5/0900766b812b5a01.pdf>.
201. Thermo Fisher Scientific Australia Pty Ltd. *Data taker DT80 Series 3 Data logger (Specification sheets)*. [cited 2014 21/09/2014]; Available from: <http://www.datataker.com/documents/specifications/TS-0059-F1%20-%20DT80.pdf>.
202. Thermo Fisher Scientific Australia Pty Ltd. *Datataker DT80 range user's manual*. [cited 2014 21/09/2014]; Available from: <http://www.datataker.com/documents/manuals/UM-0085-B7%20-%20DT8x%20Users%20Manual.pdf>.
203. Microsoft, *Microsoft Excel*. 2010: Redmond, Washington, USA.
204. Lemmon, E.W., M.L. Huber, and M.O. McLinden, *NIST Standard Reference Database 23: Reference Fluid Thermodynamic and Transport Properties-REFPROP*. 2013, National Institute of Standards and Technology: Gaithersburg. p. Standard Reference Data Program.
205. Corporation, V.K. *EMKARATE RL 32H Material Safety Data Sheet*. 2004 [cited 2011 03/10/2011]; Available from: <http://www.halltherm.com/uploads/library/RL32H.pdf>.
206. Powell, R., *Experimentally obtained POE32 physical properties*. 2011.
207. Neto, M.A.M. and J.R. Barbosa Jr, *General empirical equation to predict the bubble point pressure/solubility relationship in CO<sub>2</sub>/POE68 and CO<sub>2</sub>/AB32 mixtures*, S.B. Riffat and F. Albatati, Editors. 2013: Florianopolis , Brazil.
208. Yokozeki, A., *Theoretical performances of various refrigerant-absorbent pairs in a vapor-absorption refrigeration cycle by the use of equations of state*. *Applied Energy*, 2005. **80**(4): p. 383-399.
209. Youbi-Idrissi, M. and J. Bonjour, *The effect of oil in refrigeration: Current research issues and critical review of thermodynamic aspects*. *International Journal of Refrigeration*, 2008. **31**(2): p. 165-179.
210. Burton, C., A.M. Jacobi, and S.S. Mehendale, *Vapor-liquid equilibrium for R-32 and R-410A mixed with a polyol ester: non-ideality and local composition modeling*. *International Journal of Refrigeration*, 1999. **22**(6): p. 458-471.
211. Yokozeki, A., *Solubility of Refrigerants in Various Lubricants*. *International Journal of Thermophysics*, 2001. **22**(4): p. 1057-1071.
212. García, J., X. Paredes, and J. Fernández, *Phase and volumetric behavior of binary systems containing carbon dioxide and lubricants for transcritical refrigeration cycles*. *The Journal of Supercritical Fluids*, 2008. **45**(3): p. 261-271.
213. Fedele, L., et al., *Solubility Temperature Dependence and Data Correlation of Carbon Dioxide in Pentaerythritol Tetra-2-*

- methylbutyrate*. Journal of Chemical & Engineering Data, 2009. **54**(11): p. 3104-3107.
214. Medvedev, O.O., P.V. Zhelezny, and V.P. Zhelezny, *Prediction of phase equilibria and thermodynamic properties of refrigerant/oil solutions*. Fluid Phase Equilibria, 2004. **215**(1): p. 29-38.
  215. Thome, J.R., *Comprehensive Thermodynamic Approach to Modeling Refrigerant-Lubricating Oil Mixtures*. HVAC&R Research, 1995. **1**(2): p. 110-125.
  216. Grebner, J.J. and R.R. Crawford, *The Effects of Oil on the Thermodynamic Properties of Dichlorodifluoromethane (R-12) and Tetrafluoroethane (R-134a)*, in *Air Conditioning and Refrigeration Center TR-13*. 1992, University of Illinois at Urbana-Champaign.: Urbana-Champaign, Illinois, USA.
  217. *(Hearing at a meeting with Prof. S.B.Riffat) Confirmation that POE32 and POE68 used by Christopher J. Seeton and Predrag S. Hrnjak are ICI EMKARATE brand*, in Kenneth C. Lilje, PhD-Senior Advisor-CPI Engineering Services-kcl@cpieng.com. 2013.
  218. Cavestri, R.C., *MEASUREMENT OF VISCOSITY, DENSITY, AND GAS SOLUBILITY OF REFRIGERANT BLENDS IN SELECTED SYNTHETIC LUBRICANTS*. 1995, Imagination Resources, Inc.: Dublin, Ohio, USA.
  219. Rao, Y.V.C., *Chemical engineering thermodynamics*. 1997, Hyderabad, India: Universities Press (India).
  220. Reid, R.C., J.M. Prausnitz, and B.E. Poling, *The properties of gases and liquids*. 1987. Medium: X; Size: Pages: 741.
  221. Bobbo, S., et al., *Solubility measurements and correlation of carbon dioxide in pentaerythritol tetra-2-methylhexanoate. Comparison with other pentaerythritol esters*. Fluid Phase Equilibria, 2010. **290**(1-2): p. 115-120.
  222. Bobbo, S., et al., *Solubility of carbon dioxide in 2-methylbutyric, 2-methylvaleric and 2-methylhexanoic ester oils*. Fluid Phase Equilibria, 2007. **256**(1-2): p. 81-85.
  223. Bobbo, S., et al., *Solubility Measurements and Data Correlation of Carbon Dioxide in Pentaerythritol Tetrahexanoate (PEC6)*. Journal of Chemical & Engineering Data, 2008. **53**(11): p. 2581-2585.
  224. Fedele, L., et al., *Solubility of carbon dioxide in pentaerythritol tetraoctanoate*. Fluid Phase Equilibria, 2009. **277**(1): p. 55-60.
  225. Fedele, L., et al., *Solubility Measurements and Data Correlation of Carbon Dioxide in Pentaerythritol Tetra(2-ethylbutanoate) (PEBE6)*. Journal of Chemical & Engineering Data, 2010. **56**(1): p. 62-64.
  226. Pernechele, F., et al., *Solubility of Carbon Dioxide in Pentaerythritol Tetrabutyrate (PEC4) and Comparison with Other Linear Chained Pentaerythritol Tetraalkyl Esters*. International Journal of Thermophysics, 2009. **30**(4): p. 1144-1154.
  227. Stryjek, R., et al., *Gas Chromatographic Measurements of Activity Coefficients at Infinite Dilution for Refrigerants with a Polyol Ester Oil as a Stationary Phase*. Journal of Chemical & Engineering Data, 1999. **44**(3): p. 568-573.
  228. Musso, E., *ICI EMKARATE POE32 Molar Mass confirmation (Personal communication)*, R. Stryjek, et al., Editors. 1998, Ausimont S.P.A.
  229. Fandiño, O., et al., *Solubility of Carbon Dioxide in Two Pentaerythritol Ester Oils between (283 and 333) K*. Journal of Chemical & Engineering Data, 2008. **53**(8): p. 1854-1861.
  230. Fandiño, O., et al., *Solubility of carbon dioxide in pentaerythritol ester oils. New data and modeling using the PC-SAFT model*. The Journal of Supercritical Fluids, 2010. **55**(1): p. 62-70.

231. Fandiño, O., et al., *High pressure densities of carbon dioxide + dipentaerythritol hexaheptanoate: New experimental setup and volumetric behavior*. The Journal of Supercritical Fluids, 2011. **58**(2): p. 189-197.
232. Fandiño, O., et al., *PpT Measurements and Equation of State (EoS) Predictions of Ester Lubricants up to 45 MPa*. Industrial & Engineering Chemistry Research, 2006. **45**(3): p. 1172-1182.
233. Fandiño, O., et al., *Compressed Liquid Densities of Squalane and Pentaerythritol Tetra(2-ethylhexanoate)*. Journal of Chemical & Engineering Data, 2006. **51**(6): p. 2274-2274.
234. Fandino, O., et al., *Volumetric behaviour of the environmentally compatible lubricants pentaerythritol tetraheptanoate and pentaerythritol tetranonanoate at high pressures*. Green Chemistry, 2005. **7**(11): p. 775-783.
235. Razzouk, A., et al., *Vapor pressure measurements in the range 10–5 Pa to 1 Pa of four pentaerythritol esters Density and vapor-liquid equilibria modeling of ester lubricants*. Fluid Phase Equilibria, 2007. **260**(2): p. 248-261.
236. Teodorescu, M., L. Lugo, and J. Fernández, *Modeling of Gas Solubility Data for HFCs–Lubricant Oil Binary Systems by Means of the SRK Equation of State*. International Journal of Thermophysics, 2003. **24**(4): p. 1043-1060.
237. Lee, B.I. and M.G. Kesler, *A generalized thermodynamic correlation based on three-parameter corresponding states*. AIChE Journal, 1975. **21**(3): p. 510-527.
238. Isaacs, E.E., F.D. Otto, and A.E. Mather, *Solubility of H<sub>2</sub>S and CO<sub>2</sub> in propylene carbonate solvent*. The Canadian Journal of Chemical Engineering, 1977. **55**(6): p. 751-752.
239. MATLAB, 7.12.0 (R2011a). 2011, The MathWorks Inc.: Natick, Massachusetts, USA.
240. Soave, G., *Equilibrium constants from a modified Redlich-Kwong equation of state*. Chemical Engineering Science, 1972. **27**(6): p. 1197-1203.
241. Redlich, O. and J.N.S. Kwong, *On the Thermodynamics of Solutions. V. An Equation of State. Fugacities of Gaseous Solutions*. Chemical Reviews, 1949. **44**(1): p. 233-244.
242. Hall, K.R., G.A. Iglesias-Silva, and G.A. Mansoori, *Quadratic mixing rules for equations of state: Origins and relationships to the virial expansion*. Fluid Phase Equilibria, 1993. **91**(1): p. 67-76.
243. Marcelino Neto, M.A. and J.R. Barbosa Jr, *Solubility, density and viscosity of a mixture of R-600a and polyol ester oil*. International Journal of Refrigeration, 2008. **31**(1): p. 34-44.
244. Daintith, J. and E. Martin, *Dictionary of Science (6th Edition)*. Oxford University Press.
245. Technology, A., *A property Methods and Calculations (Appendix A)*, in *HYSYS 3.2 Simulation Basis (Software Manual) 2003*, Hyprotech-Aspen Technology: Cambridge, MA, USA.
246. Chemstations, *Chemcad (Software manual)*. 2012, Chemstations, Inc.: Houston, Texas, USA.
247. Williams, L.L., E.M. Mas, and J.B. Rubin, *Vapor–Liquid Equilibrium in the Carbon Dioxide–Propylene Carbonate System at High Pressures*. Journal of Chemical & Engineering Data, 2002. **47**(2): p. 282-285.
248. Aprhornratana, S. and I.W. Eames, *Thermodynamic analysis of absorption refrigeration cycles using the second law of thermodynamics method*. International Journal of Refrigeration, 1995. **18**(4): p. 244-252.

249. He, L.J., L.M. Tang, and G.M. Chen, *Performance prediction of refrigerant-DMF solutions in a single-stage solar-powered absorption refrigeration system at low generating temperatures*. Solar Energy, 2009. **83**(11): p. 2029-2038.
250. Kuppan, T. *Heat exchanger design handbook*. 2013; Available from: <http://www.crcnetbase.com/isbn/978-1-4398-4213-3>.
251. Sabir, H., *Heat and Mass Transfer Processes in Absorption Systems*. 1993: University of London.
252. Gyftopoulos, E.P. and G.P. Beretta, *Thermodynamics - Foundations and Applications*. Dover Publications.
253. Igobo, O.N. and P.A. Davies, *Review of low-temperature vapour power cycle engines with quasi-isothermal expansion*. Energy, 2014. **70**(0): p. 22-34.
254. Woodland, B.J., et al., *Performance Benefits for Organic Rankine Cycles with Flooded Expansion and Internal Regeneration*, in *The International Refrigeration and Air Conditioning Conference*. 2010: Purdue University, West Lafayette, Indiana, USA.
255. Woodland, B.J., et al., *Thermodynamic comparison of organic Rankine cycles employing liquid-flooded expansion or a solution circuit*. Applied Thermal Engineering, 2013. **61**(2): p. 859-865.
256. Bell, I.H., E.A. Groll, and J.E. Braun, *Performance of Vapor Compression Systems with Compressor Oil Flooding and Regeneration*. Publications of the Ray W. Herrick Laboratories. Purdue University, 2010. **Paper 4**.
257. Bell, I., et al., *Liquid flooded compression and expansion in scroll machines - Part II: Experimental testing and model validation*, in *The International Refrigeration and Air Conditioning Conference*. 2012: Purdue University, West Lafayette, Indiana, USA.
258. Hugenothe, J., et al., *Liquid-Flooded Ericsson Cycle Cooler: Part 1 – Thermodynamic Analysis*, in *The International Refrigeration and Air Conditioning Conference 2006*: Purdue University, West Lafayette, Indiana, USA.
259. Bell, I.H., et al., *Liquid-flooded compression and expansion in scroll machines – Part I: Model development*. International Journal of Refrigeration, 2012. **35**(7): p. 1878-1889.
260. Sanden International Inc. *Sanden TRSA09 scroll compressor Performance*. [cited 2014 20/10/2014]; Available from: [http://www.sanden.com/objects/TRSA09\\_Performance.pdf](http://www.sanden.com/objects/TRSA09_Performance.pdf).
261. Lemort, V., S. Declaye, and S. Quoilin, *Experimental characterization of a hermetic scroll expander for use in a micro-scale Rankine cycle*. Proceedings of the Institution of Mechanical Engineers, Part A: Journal of Power and Energy, 2011.
262. Bell, I.H., et al., *Impact of Oil Solubility and Refrigerant Flashing on the Performance of Transcritical CO<sub>2</sub> Vapor Compression Systems with Oil Flooding and Regeneration*, in *The International Refrigeration and Air Conditioning Conference*. 2010: Purdue University, West Lafayette, Indiana, USA.
263. Brasz, J.J., I.K. Smith, and N. Stosic, *Development of a Twin Screw Expander as a Throttle Valve Replacement for Water-Cooled Chillers*, in *The International Compressor Engineering Conference*. 2000: Purdue University, West Lafayette, Indiana, USA.
264. Stosic, N., I.K. Smith, and A. Kovacevic, *A Twin Screw Combined Compressor And Expander For CO<sub>2</sub> Refrigeration Systems*, in *The International Compressor Engineering Conference*. 2002: Purdue University, West Lafayette, Indiana, USA.
265. Smith, I.K., et al., *Steam as the working fluid for power recovery from exhaust gases by means of screw expanders*. Proceedings of

- the Institution of Mechanical Engineers, Part E: Journal of Process Mechanical Engineering, 2011. **225**(2): p. 117-125.
266. Stosic, N., I.K. Smith, and A. Kovacevic, *POWER RECOVERY FROM LOW COST TWO-PHASE EXPANDERS*, in *Centre for Positive Displacement Compressor Technology*. City University, London: London, UK.
  267. Chen, Y., *Thermodynamic Cycles using Carbon Dioxide as Working Fluid : CO2 transcritical power cycle study*, in *Applied Thermodynamics and Refrigeration*. 2011, KTH Royal Institute of Technology(KTH): Stockholm.
  268. Mexichem Fluor. 2014 [cited 2014 19/10/2014]; Available from: [www.mexichemfluor.com](http://www.mexichemfluor.com).
  269. CAREL. *HumiSteam: the next generation of electrode humidifiers (Data sheet)*. [cited 2014 28/10/2014]; Available from: <http://www.carelusa.com/lit/+302238348.pdf>.
  270. COREMA (UK). *Industrial chillers*. [cited 2014 30/10/2014]; Available from: <http://www.coremauk.co.uk/chillers.htm>.
  271. Quoilin, S., *Sustainable energy conversion through the use of Organic Rankine Cycles for waste heat recovery and solar applications*, in *Faculty of Applied Science*. 2011, University of Liège: Liège, Belgium. p. 183.
  272. Chen, Y., et al., *Mathematical modeling of scroll compressors—part I: compression process modeling*. *International Journal of Refrigeration*, 2002. **25**(6): p. 731-750.
  273. Sanden International Inc. *Sanden TRSA09 Scroll compressor*. 2014 [cited 2014 12/07/2014]; Available from: <http://www.sanden.com/scrollcompressors.html>.
  274. Automotive Electricity and Electronics (Website). *AC Generators*. [cited 2014 28/10/2014]; Available from: <http://autosystempro.com/ac-generators/>.
  275. Santini, A., *Automotive Electricity and Electronics (2nd Edition)*. Cengage Learning, Inc.
  276. Emadi, A., *Handbook of automotive power electronics and motor drives*. 2005, Boca Raton: Taylor & Francis.
  277. Whaley, D.M., W.L. Soong, and N. Ertugrul, *EXTRACTING MORE POWER FROM THE LUNDELL CAR ALTERNATOR*, in *Australasian Universities Power Engineering Conference (AUPEC 2004)*. 2004: Brisbane, Australia.
  278. Lynch Motor Company Ltd. *Motors LEM-200 (Data sheet)*. 2014 [cited 2014 28/10/2014]; Available from: [http://www.parvalux.co.za/sites/default/files/lem\\_datasheet\\_lem-200\\_v2.pdf](http://www.parvalux.co.za/sites/default/files/lem_datasheet_lem-200_v2.pdf).
  279. Cloud electric. *Motor LEM200-D127*. 2014 [cited 2014 28/10/2014]; Electrical products for vehicles]. Available from: <http://www.cloudelectric.com/product-p/mo-lem200-d127.htm>.
  280. Autoelectro. *AEC1761 alternator*. 2014 [cited 2014 29/10/2014]; Available from: <http://www.autoelectro.co.uk/aec1761>.
  281. Balmar DC charging systems. *6-Series Alternators (Data sheet)*. [cited 2014 29/10/2014]; Available from: <http://www.balmar.net/PDF/alternator%20info/6-series-sheet-web.pdf>.
  282. DELCO REMY. *22SI (150 Amps 12 V) performance curve* [cited 2014 29/10/2014]; Available from: <http://delcoremy.com/Images/PerformanceCurve-22SI-12v.aspx>.
  283. Cat pumps Ltd. 2014 [cited 2014 6/10/2014]; Available from: <http://www.catpumps.co.uk/>.

284. Cat pumps Ltd. *3CP Plunger Pump standard models data sheet*. 2014 [cited 2014 28/10/2014]; Available from: [http://www.catpumps.com/products/pdfs/3CP1120\\_G.pdf](http://www.catpumps.com/products/pdfs/3CP1120_G.pdf).
285. ALFA LAVAL, *Brazed plate heat exchangers- A product catalogue for refrigeration*. 2004.
286. Kaori. *How BPHEs Work*. [cited 2014 1/11/2014]; Available from: [http://www.kaori-bphe.com/en/products/page/How\\_BPHEs\\_Work](http://www.kaori-bphe.com/en/products/page/How_BPHEs_Work).
287. Wang, L.S.B.M.R.M., *Plate heat exchangers : design, applications and performance*. 2007, Southampton; Billerica, [Massachusetts]: WIT Press.
288. Kaori. *Kaori, Taiwan (heat exchangers)*. 2014 [cited 2014 6/10/2014]; Available from: <http://www.kaori-taiwan.com/index.html>.
289. Sugarman, S.C., *Testing and Balancing HVAC Air and Water Systems (4th Edition)*. Fairmont Press, Inc.
290. Madhawa Hettiarachchi, H.D., et al., *Optimum design criteria for an Organic Rankine cycle using low-temperature geothermal heat sources*. *Energy*, 2007. **32**(9): p. 1698-1706.
291. Quoilin, S., et al., *Thermo-economic optimization of waste heat recovery Organic Rankine Cycles*. *Applied Thermal Engineering*, 2011. **31**(14–15): p. 2885-2893.
292. Hesselgreaves, J.E., *Compact Heat Exchangers - Selection, Design, and Operation*. Elsevier.
293. Kaori heat treatment co Ltd. *Brazed Plate Heat Exchanger*. 2014 [cited 2014 10/11/2014]; BPHEs catalogue]. Available from: <http://www.kaori-bphe.com/uploads/editor/files/English.pdf>.
294. Han, D.-H., K.-J. Lee, and Y.-H. Kim, *The Characteristics of Condensation in Brazed Plate Heat Exchangers with Dierent Chevron Angles*. *Journal of the Korean Physical Society*, 2003. **43**(1): p. 66-73.
295. Gebrehiwot, T.H., *HEAT TRANSFER IN PLATE HEAT EXCHANGERS*, in *Chemical and Process Engineering*. 2009, LAPPEENRANTA UNIVERSITY OF TECHNOLOGY: Lappeenranta, Finland.
296. Claesson, J., *Thermal and hydraulic performance of compact brazed plate heat exchangers operating as evaporators in domestic heat pumps*, in *School of Industrial Engineering and Management (ITM), Energy Technology*. 2005, KTH: Stockholm.
297. Shah, R.K., et al., *Heat transfer equipment design*. 1988, New York: Hemisphere Pub. Corp.
298. Naik, V.R. and V.K. Matawala, *Experimental Investigation of single phase Chevron Type Gasket Plate Heat Exchanger*. *International Journal of Engineering and Advanced Technology (IJEAT)*, 2013. **2**(4): p. 362-369.
299. Longo, G.A., *Refrigerant R134a condensation heat transfer and pressure drop inside a small brazed plate heat exchanger*. *International Journal of Refrigeration*, 2008. **31**(5): p. 780-789.
300. Muley, A. and R.M. Manglik, *Experimental Study of Turbulent Flow Heat Transfer and Pressure Drop in a Plate Heat Exchanger With Chevron Plates*. *Journal of Heat Transfer*, 1999. **121**(1): p. 110-117.
301. Kuo, W.S., et al., *Condensation heat transfer and pressure drop of refrigerant R-410A flow in a vertical plate heat exchanger*. *International Journal of Heat and Mass Transfer*, 2005. **48**(25–26): p. 5205-5220.
302. Quoilin, S., V. Lemort, and J. Lebrun, *Experimental study and modeling of an Organic Rankine Cycle using scroll expander*. *Applied Energy*, 2010. **87**(4): p. 1260-1268.

303. Bogaert, R. and A. Böles, *GLOBAL PERFORMANCE OF A PROTOTYPE BRAZED PLATE HEAT EXCHANGER IN A LARGE REYNOLDS NUMBER RANGE*. *Experimental Heat Transfer*, 1995. **8**(4): p. 293-311.
304. Muley, A., *Heat transfer and pressure drop in plate heat exchanger*, in *Department of Mechanical, Industrial, and Nuclear Engineering 1997*, University of Cincinnati: Cincinnati, Ohio, USA.
305. Donowski, V.D. and S.G. Kandlikar, *CORRELATING EVAPORATION HEAT TRANSFER COEFFICIENT OF REFRIGERANT R-134a IN A PLATE HEAT EXCHANGER*, in *Engineering Foundation Conference on Pool and Flow Boiling*. 2000: Alaska, USA.
306. Kaori heat treatment co Ltd, *Quotation for R1233zd(E) ORC heat exchangers*, U.o. Nottingham, Editor. 2014: Chung-Li city, Taiwan.
307. Agilent Technologies Inc. *Agilent 34970A Data Acquisition/Switch Unit Family Product Overview 2012* [cited 2014 30/10/2014]; Available from: <http://cp.literature.agilent.com/litweb/pdf/5965-5290EN.pdf>.
308. RS components. *HPS-A Series 4-20mA Output Pressure Transmitter*. [cited 2014 1/11/2014]; Available from: <http://docs-europe.electrocomponents.com/webdocs/0c35/0900766b80c35d80.pdf>.
309. Parr, E.A., *Industrial control handbook*. 2000, New York: Industrial Press.
310. Roxspur Measurement & Control Ltd. *Platon flow meter (Specification)*. [cited 2014 30/10/2014]; Available from: <http://www.roxspur.com/Product/Platon-GMT-Screwed-Metal-Tube-VA-Flowmeter#productspec>.
311. Key instruments. *FR4500 Series: 0.5-5 GPM (Water)*. [cited 2014 30/10/2014]; Available from: [http://www.kidirect.com/FR4500-Series-05-5-GPM-Water\\_p\\_29.html](http://www.kidirect.com/FR4500-Series-05-5-GPM-Water_p_29.html).
312. Telonic instruments Ltd. *Multifunctional Electronic Load PLZ-4W Series (product overview)*. 2013 [cited 2014 31/10/2014]; Available from: [http://www.telonic.co.uk/products/pdfs/kikusui/PLZ-4W\\_1401\\_Telonic.pdf](http://www.telonic.co.uk/products/pdfs/kikusui/PLZ-4W_1401_Telonic.pdf).
313. Whitfield, J.F. and E. Institution of Electrical, *Electrical craft principles*. 1995, London, U.K.: Institution of Electrical Engineers.
314. Keljik, J., *Electricity 4 : AC/DC motors, controls, and maintenance*. 2013, Clifton Park, N.Y.: Delmar, Cengage Learning.
315. SMC. *SMC digital flow switches (Air flow sensor)*. 2014 [cited 2014 27/10/2014]; PF2A703H]. Available from: [http://content.smcetech.com/pdf/PF2A\\_EU.pdf](http://content.smcetech.com/pdf/PF2A_EU.pdf).
316. CAMOZZI. *Filter-regulators Series C*. Available from: <http://store.camozzi.co.uk/files/d11c9656-029a-45ff-a390-9d720100628f/Filter-regulators%20Series%20C.pdf>.
317. Zhou, N., et al., *Experimental study on Organic Rankine Cycle for waste heat recovery from low-temperature flue gas*. *Energy*, 2013. **55**(0): p. 216-225.
318. Twomey, B., *Experimental test results from QGECE laboratory small-scale organic Rankine cycle using a scroll expander*, in *Technical report no. 2012/03*. 2012, School of Mechanical Engineering-University of Queensland.
319. Basu, P. *Biomass gasification, pyrolysis and torrefaction practical design and theory*. 2013; Available from: <http://search.ebscohost.com/login.aspx?direct=true&scope=site&db=nlebk&db=nlabk&AN=486017>.
320. Megginson, W.L.S.S.B., *Introduction to corporate finance*. 2009, Mason, Ohio: South-Western Cengage Learning.

321. Röhrich, M., *Fundamentals of investment appraisal : an illustration based on a case study*. 2007, München [u.a.]: Oldenbourg.
322. Solution Matrix Limited. *Return on Investment ROI Explained Definition, Meaning, and Example Calculations*. [cited 2014 14/10/2014]; Available from: <https://www.business-case-analysis.com/return-on-investment.html>.
323. United, S., Congress, and A. Office of Technology, *Industrial and commercial cogeneration*. 2002, Miami: Books for Business.
324. Obernberger, I. and G. Thek. *The Pellet Handbook the Production and Thermal Utilization of Biomass Pellets*. 2010; Available from: <http://public.eblib.com/choice/publicfullrecord.aspx?p=605291>.
325. ASHRAE. *ASHRAE Equipment Life Expectancy chart*. [cited 2015 27/04/2015]; Available from: [http://www.f22designs.com/cullum/wp-content/uploads/2013/02/ASHRAE\\_Chart\\_HVAC\\_Life\\_Expectancy%201.pdf](http://www.f22designs.com/cullum/wp-content/uploads/2013/02/ASHRAE_Chart_HVAC_Life_Expectancy%201.pdf).
326. Rentizelas, A., et al., *Comparative techno-economic analysis of ORC and gasification for bioenergy applications*. *Energy Conversion and Management*, 2009. **50**(3): p. 674-681.
327. Kosmadakis, G., D. Manolakos, and G. Papadakis, *Simulation and economic analysis of a CPV/thermal system coupled with an organic Rankine cycle for increased power generation*. *Solar Energy*, 2011. **85**(2): p. 308-324.
328. Nafey, A.S., M.A. Sharaf, and L. García-Rodríguez, *Thermo-economic analysis of a combined solar organic Rankine cycle-reverse osmosis desalination process with different energy recovery configurations*. *Desalination*, 2010. **261**(1-2): p. 138-147.
329. David, G., F. Michel, and L. Sanchez, *Waste heat recovery projects using Organic Rankine Cycle technology – Examples of biogas engines and steel mills applications in World Engineers Convention*. 2011: Geneva, Switzerland.
330. Promo Bio. *Biomass-CHP-Plant based on ORC-cycle, Admont*. 2014 [cited 2014 12/10/2014]; Available from: [http://www.promobio.eu/tiedostot/tiedotteet/Fact%20sheet\\_admont\\_be2020\\_final1.pdf](http://www.promobio.eu/tiedostot/tiedotteet/Fact%20sheet_admont_be2020_final1.pdf).
331. U.S department of energy. *Office of energy efficiency and renewable energy (geothermal FAQ)*. [cited 2014 12/10/2014]; Available from: <http://energy.gov/eere/geothermal/geothermal-faqs>.
332. Nuclear Energy Institute (NEI). *Costs: Fuel, Operation, Waste Disposal & Life Cycle*. [cited 2014 13/10/2014]; Available from: <http://www.nei.org/Knowledge-Center/Nuclear-Statistics/Costs-Fuel,-Operation,-Waste-Disposal-Life-Cycle>.
333. HM Treasury, *THE GREEN BOOK: Appraisal and Evaluation in Central Government*, in *Long-term discount rates*. 2011: London, UK.
334. Office for national statistics, *Consumer Price Indices - CPI annual percentage change: 1989 to 2014*. 2014: UK.
335. Department of energy and climate change. [cited 2014 12/10/2014]; Available from: <https://www.gov.uk/government/organisations/department-of-energy-climate-change>.
336. Department of Energy & Climate Change, *Statistical data set: International industrial energy prices*. 2013: UK.
337. Department of Energy & Climate Change, *Statistical data set: International domestic energy prices*. 2013: UK.

338. Infinity Turbines. 2014 [cited 2014 6/10/2014]; Available from: [http://www.infinityturbine.com/ORC/ORC\\_Waste\\_Heat\\_Turbine.html](http://www.infinityturbine.com/ORC/ORC_Waste_Heat_Turbine.html).
339. Enogia. 2014 [cited 2014 6/10/2014]; Available from: <http://www.enogia.com/>.
340. Enogia, *6 kW CO2 turbine system (Technical proposal)*, University of Nottingham, Editor. 2013, Enogia: Marseille, France.
341. Haskel Milton Roy. 2014 [cited 2014 6/10/2014]; Available from: [http://www.haskel.co.uk/corp/details/0,10294,CLI1\\_DIV118\\_ETI10\\_044,00.html](http://www.haskel.co.uk/corp/details/0,10294,CLI1_DIV118_ETI10_044,00.html).
342. Michael Smith Engineers Limited. 2014 [cited 2014 6/10/2014]; Available from: wannerleads.com.
343. Speck Pumps. 2014 [cited 2014 6/10/2014]; Available from: <http://www.speck.co.uk/Pumps%20Index%20Page.htm>.
344. Beinlich Feedpumps 2014 [cited 2014 6/10/2014]; Available from: <http://www.beinlich-pumps.com/english/>.
345. Nanjing yalong technology CO ltd. 2014 [cited 2014 6/10/2014]; Available from: <http://en.jspump.cn/>.
346. NANJING YALONG TECHNOLOGY CO LTD, *CO2 plunger pump quotation.*, University of Nottingham, Editor. 2013: China.
347. Kaori heat treatment co Ltd, *Quotation for CO2 power system heat exchangers.*, University of Nottingham, Editor. 2013: Chung-Li city, Taiwan.
348. RS components. *Parker 2 m long stainless steel pipe.*, 2014 [cited 2014 6/10/2014]; Available from: <http://uk.rs-online.com/web/p/products/4324603/>.
349. Swagelok Manchester, *Tube fittings Quotation.* 2013: Warrington, Cheshire, UK.
350. ASCO. *SOLENOID VALVES direct operated for liquid CO2 applications 1/8 (data sheet).* 2014 [cited 2014 6/10/2014]; Available from: <http://docs-europe.electrocomponents.com/webdocs/0b2b/0900766b80b2b68b.pdf>.
351. Telemecanique. *Electronic pressure sensors OsiSense XM, type XML P for control circuits (datasheet).* 2014 [cited 2014 6/10/2014]; Available from: <http://docs-europe.electrocomponents.com/webdocs/0ff9/0900766b80ff9e01.pdf>.
352. Bell flow systems. *G2H15 flow meter (datasheet).* 2014 [cited 2014 6/10/2014]; Available from: <http://www.bellflowsystems.co.uk/files/PDF/G2H15I09LMA.pdf>.
353. RS components. *Inverter Drive, 0.1 → 600 Hz, 14 A, 460 V, IP20 For Use With 5.5 kW AC Motor.* 2014 [cited 2014 7/10/2014]; Available from: <http://docs-europe.electrocomponents.com/webdocs/1236/0900766b812364f6.pdf>.
354. RS components. *Jumo -200 to +800°C J Type Thermocouple, 1000mm Probe.* 2014 [cited 2014 8/10/2014]; Available from: <http://docs-europe.electrocomponents.com/webdocs/11cf/0900766b811cfc14.pdf>.

# Appendix A

---

## A.1 IGA Experimental Results

Table A.1:CO2/PC IGA absorption results.

	CO2 mass fraction [%]	Pressure [bar]
Min-1hr Max-2hr at -2°C	1.474179	3.996484
	2.454874	4.994352
	4.542872	6.992643
	10.70551	11.9883
	15.25506	14.98379
	16.96013	15.98166
	20.74463	17.98223
	23.97865	19.48852
	25.02351	19.93679
Min-12hr Max-18hr at -1.3°C	0.650154	0.769531
	0.939848	1.103813
	3.622594	4.011557
	4.736275	5.013596
	6.792212	7.011214
	13.06788	11.97808
	17.66123	14.96212
	19.34002	15.97843
	23.24401	18.0502
	26.59348	19.56092
	27.48043	19.96048

**Table A.2: CO<sub>2</sub>/POE5 IGA absorption results.**

	CO <sub>2</sub> mass fraction [%]	Pressure [bar]
Min-1hr Max-2hr at -2.4°C	0.485616	0.758796
	0.711707	1.097385
	2.760677	3.995304
	3.550446	4.994382
	5.208324	6.995365
	10.1612	11.99466
	13.9397	14.99418
	15.52792	15.98626
	18.79569	18.01726
	21.65834	19.51776
Min-12hr Max-18hr at 1.6°C	2.699535	3.985888
	8.106668	10.00996
	18.78133	18.90612

**Table A.3: CO<sub>2</sub>/POE32 IGA absorption results.**

	CO <sub>2</sub> mass fraction [%]	Pressure [bar]
Min-30min Max-1hr at -5.9°C	0.022572	0.103756
	0.061454	0.198362
	0.301411	0.758728
	0.352975	0.848489
	0.512561	1.097048
	0.938048	1.996406
	2.063171	3.995236
	3.058908	4.991892
	4.007277	5.993931
	4.949601	6.993682
	6.83545	8.993992
	9.061605	10.99565
	10.30909	11.9954
	12.62966	13.99706
	13.32623	15.00878
	16.18082	17.00546
	18.70389	18.4999
	19.62794	18.99877
	20.58813	19.50571
	21.26351	19.94833
Min-1hr Max-2hr at -1°C	0.331056	0.757061
	0.547007	1.098341
	2.168204	3.992357
	2.945084	4.992647
	4.410264	6.989458
	8.714841	12.00988
	11.83421	15.00267
	13.03339	15.99489
	15.60433	18.00704
	16.95368	19.49328
17.27029	19.94303	

**Table A.4: CO<sub>2</sub>/POE68 IGA absorption results.**

	CO <sub>2</sub> mass fraction [%]	Pressure [bar]
Min-1hr Max-2hr at 0°C	0.292269	0.760484
	0.48703	1.095843
	1.896118	3.996319
	2.652674	4.993244
	3.939564	6.989786
	7.786928	11.9845
	10.62928	14.99991
	11.89935	16.01554
	14.23429	18.02486
	16.17517	19.51877
Min-12hr Max-18hr at -1.1°C	0	2.75E-04
	2.265813	3.971961
	6.56329	10.01663
	12.06787	15.92564
	15.72569	18.98532

## **A.2 General Empirical Equation to Predict Bubble Point Pressure/Solubility**

Relationship in CO<sub>2</sub>/POE68 and CO<sub>2</sub>/AB32 mixtures:

$$P = \zeta_1 x_1 + \zeta_2 x_1 T + \zeta_3 x_1^2 + \zeta_4 x_1^2 T + \zeta_5 x_1^2 T^2$$

Where  $T$  is in kelvin and  $P$  is in MPa. The empirical coefficients ( $\zeta_i$ ) for the two systems are shown in Tables A.5 and Table A.6. The equations should not be used outside the data range. Figures 1 to 4 show comparisons between the empirical equations and the data.

**Table A.5: Coefficients for the CO<sub>2</sub>/POE 68 system.**

$\zeta_1$	$\zeta_2$	$\zeta_3$	$\zeta_4$	$\zeta_5$
-93,15	0,3863	-97,12	0,5151	-0,0008038

**Table A.6: Coefficients for the CO<sub>2</sub>/AB 32 system.**

$\zeta_1$	$\zeta_2$	$\zeta_3$	$\zeta_4$	$\zeta_5$
-105,8	0,4524	-96,2	0,3081	-0,0001254

## Appendix B

### B.1 Solubility, Density and Viscosity Correlation

#### Coefficients of CO<sub>2</sub>/Absorbents

Solubility correlation coefficients for CO <sub>2</sub> /absorbents				
Coefficient	CO <sub>2</sub> /POE32 solubility correlation (5.1) [183]	CO <sub>2</sub> /POE68 solubility correlation (5.6)	CO <sub>2</sub> /POE68 polynomial solubility correlation (5.8)	CO <sub>2</sub> /PC polynomial solubility correlation (5.10)
a1	6.59664	4.862	-3.363	-1.819
a2	-1.62E+03	-938.9	0.02215	0.01064
a3	7.01E+04	24.61	0.9401	0.195
a4	3.88634	0.05952	-2.64E-05	-1.605E-05
a5	-1.47E+03	-239	0.02036	-0.0009949
a6	1.19E+05	94.29	-11.37	-0.0001974
a7	3.41E-01	-2.675	-1.98E-05	1.356E-06
a8	-2.54E+02	204.8	-0.0003121	-7.166E-08
a9	2.11E+04	-114.1	8.954	1.693E-06
a10		-1.195		
a11		102.3		
a12		-140.2		
Suitability of fit				
SSE		0.00291	0.0009303	0.00742
$R^2$	0.99996	0.9989	0.9997	0.9814
RMSE		0.01019	0.005478	0.02066

Keys:

Summed square of residuals (SSE)

Coefficient of determination ( $R^2$ )

Root mean square error (RMSE)

CO <sub>2</sub> /absorbent density correlation			
Coefficient	CO <sub>2</sub> /POE32 density correlation (5.2) [183]	CO <sub>2</sub> /POE68 density correlation (5.7)	CO <sub>2</sub> /POE68 polynomial density correlation (5.9)
b1	1.33306	1.623	1.454
b2	-1.59E-03	-0.00205	-0.00095
b3	1.27E-06	1.93E-06	-4.792
b4	1.68E-02	-38.28	1.92E-07
b5	2.77E-04	0.2251	0.003391

b6	0	-0.00036	37.68
b7	8.58E-01	348	-3.60E-06
b8	-3.62E-03	-2.14	-0.06154
b9	0	0.003393	-74.73
b10		-697.8	7.78E-05
b11		4.352	0.0252
b12		-0.00691	59.11
Suitability of fit			
SSE		0.005678	0.000773
$R^2$	0.9977	0.9871	0.9982
RMSE		0.01239	0.004569

Keys:

Summed square of residuals (SSE)

Coefficient of determination ( $R^2$ )

Root mean square error (RMSE)

CO2/absorbent viscosity correlation		
Coefficient	CO2/POE32 viscosity correlation (5.3) [183]	CO2/POE68 viscosity correlation (5.3)
c1	3.16E+01	-46.99
c2	-7.08386	20.05
c3	3.14E-01	-2.022
c4	-3.40E+02	751.7
c5	1.29E+02	-254.9
c6	-1.22E+01	21.4
c7	1.30E+03	-1191
c8	-4.69E+02	399.4
c9	4.23E+01	-33.38
Suitability of fit		
SSE		0.07272
$R^2$	0.996	0.9977
RMSE		0.04625

Keys:

Summed square of residuals (SSE)

Coefficient of determination ( $R^2$ )

Root mean square error (RMSE)

## B.2 Ideal Heat Capacity of Pure POE Compounds

Polynomial correlation and coefficients for pure POE compounds [208]

$$C_p^0 = C_0 + C_1T + C_2T^2 + C_3T^3$$

(B.1)

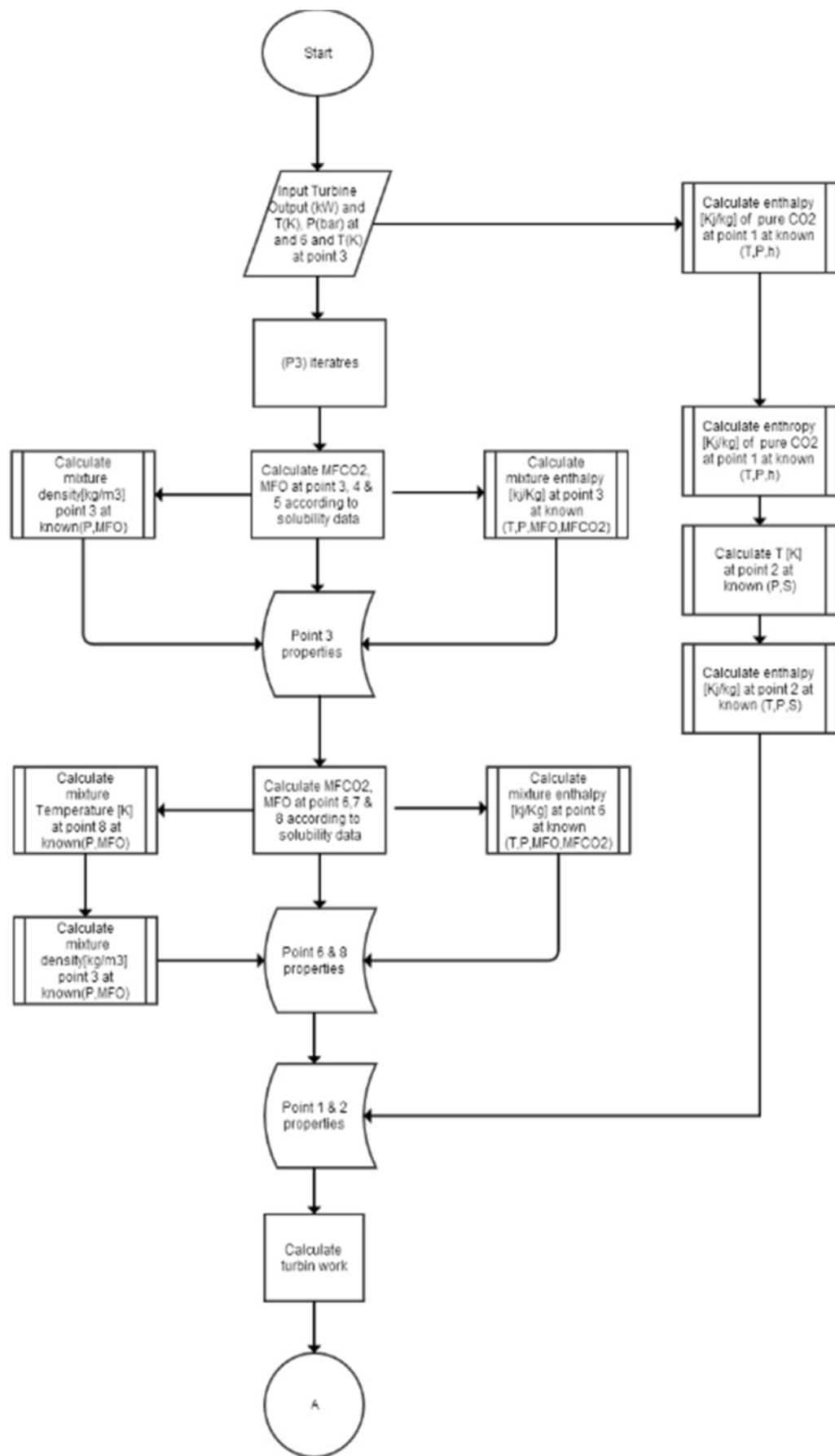
Ideal gas heat capacity coefficients for pure POE compounds [208]				
Compound	c0	c1	c2	c3

PEC5	57.97	2.1551	-1.01E-03	2.62E-07
PEC9	84.34	3.5852	-1.81E-03	4.36E-07
PEB6	2.594	2.728	-1.42E-03	5.43E-07
PEB8	15.8	3.443	-1.82E-03	6.30E-07

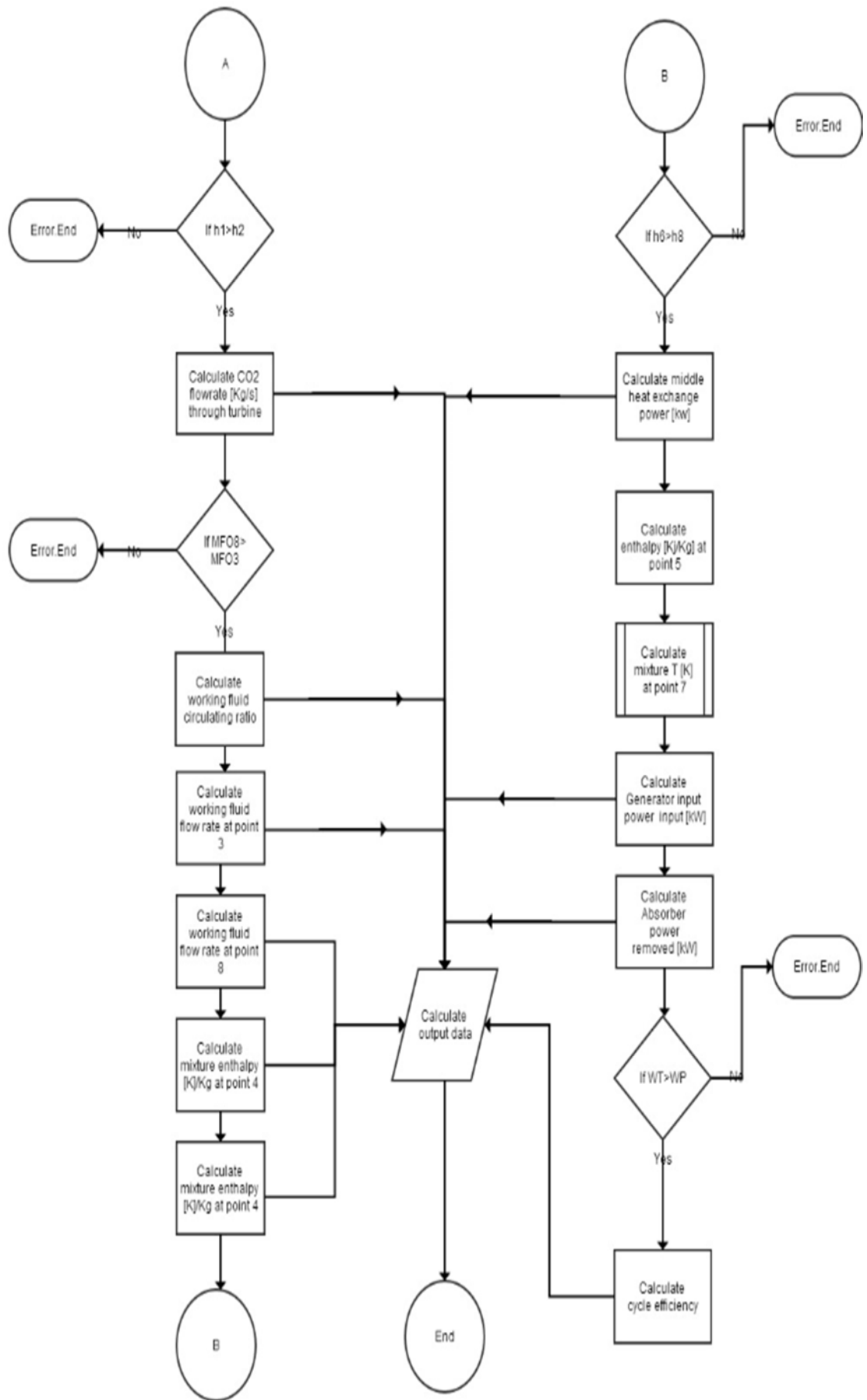
## Appendix C

---

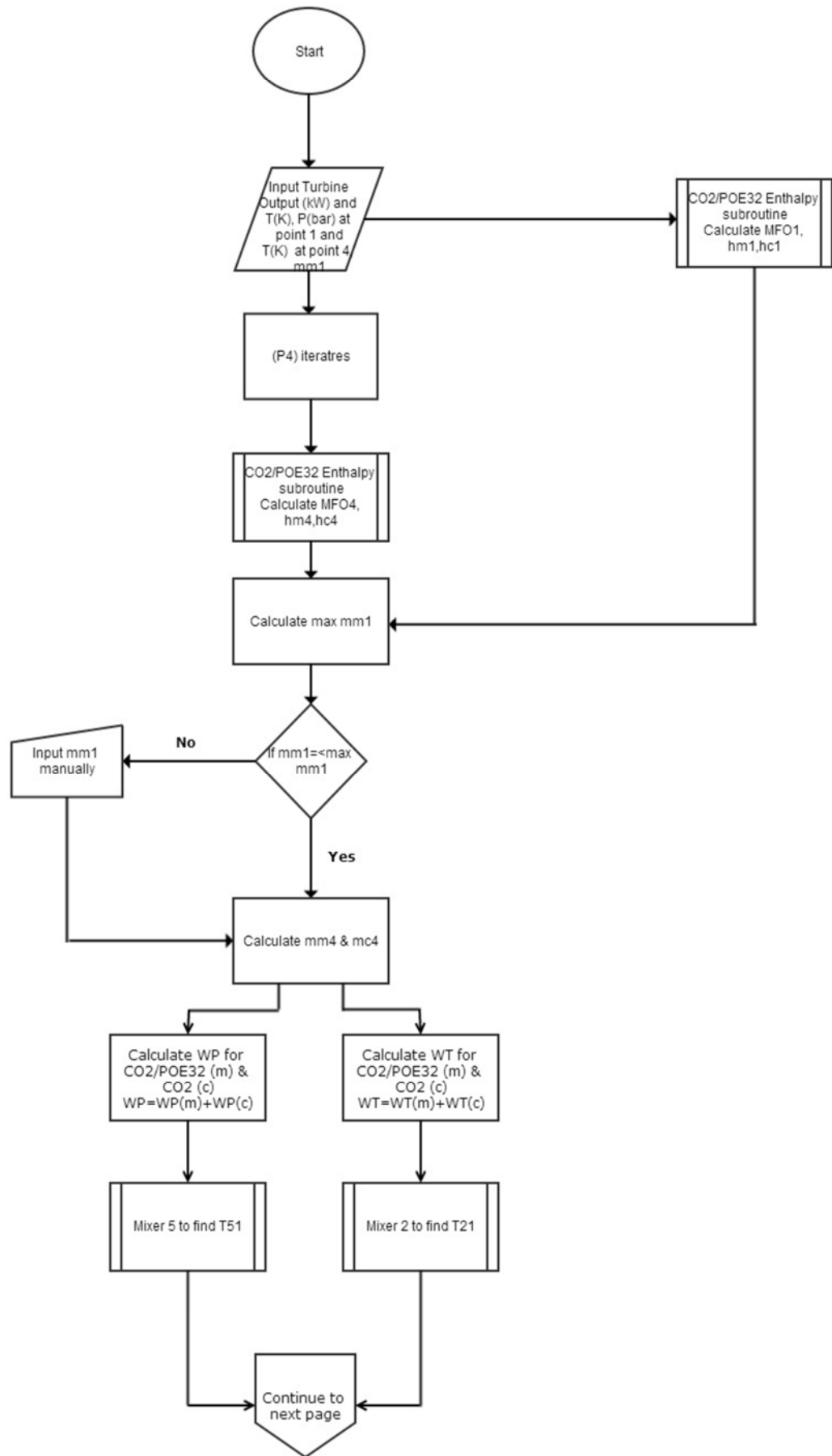
### **C.1 CO<sub>2</sub>/Lubricant Absorption Power Generation System Simulation Program Flow Chart**

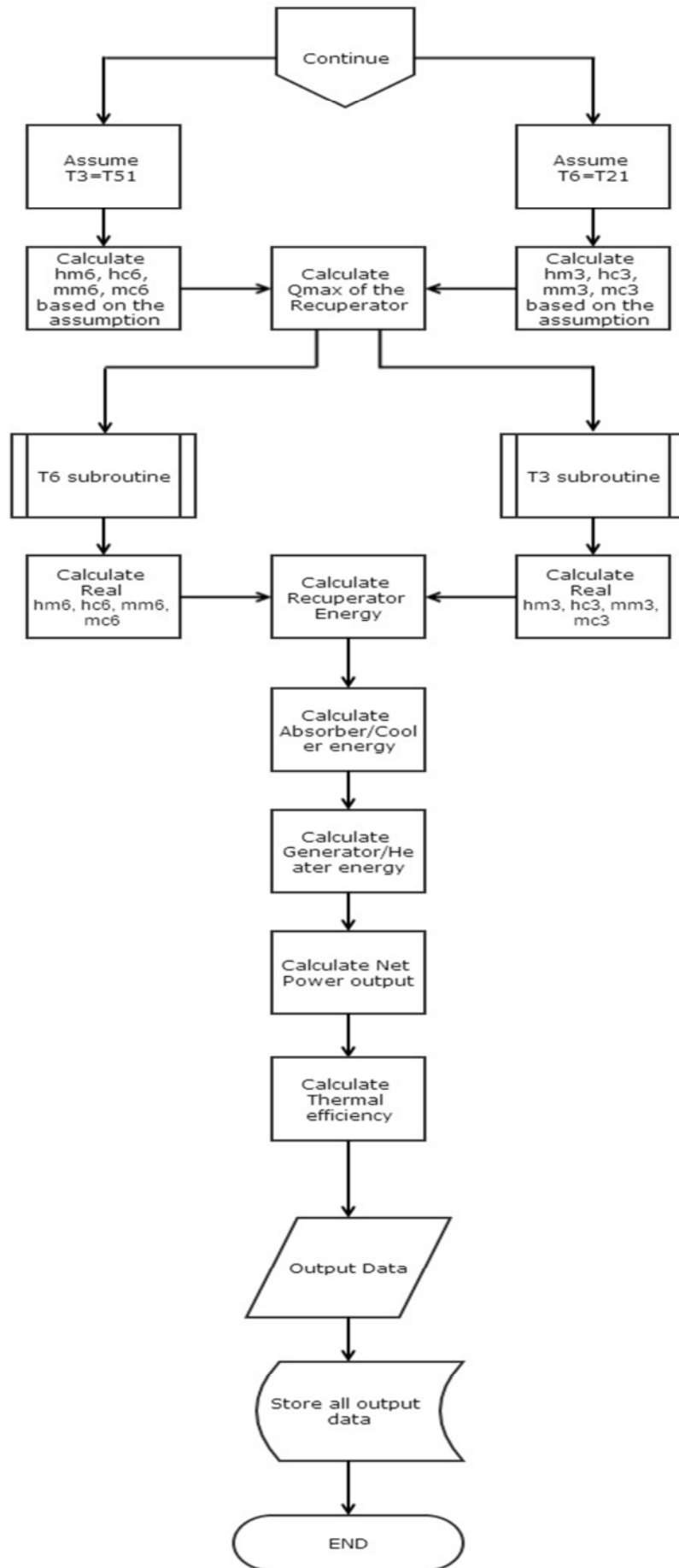


(continued)

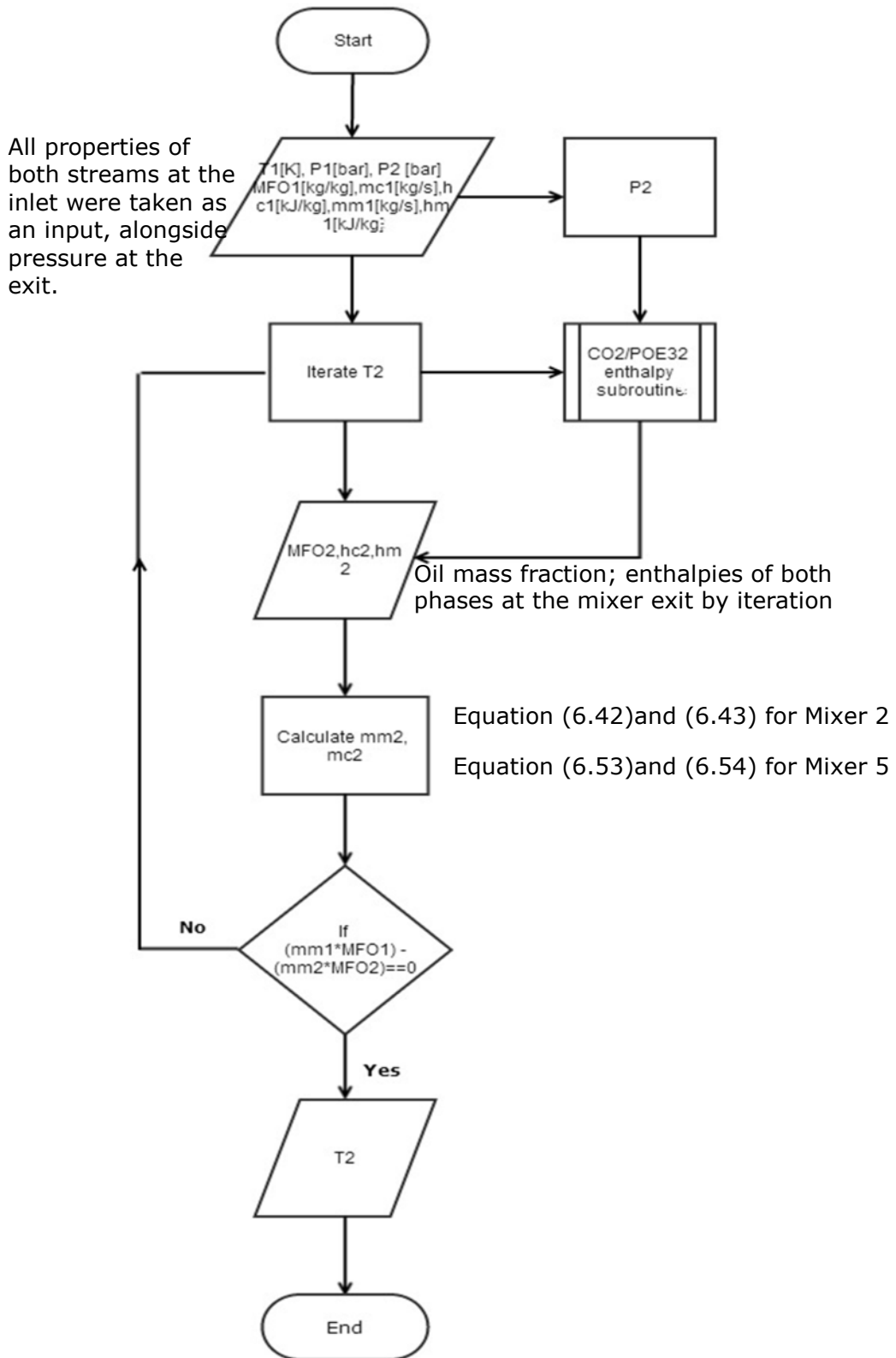


**C.2 CO2/POE32 Flood Expansion Power Generation  
System Simulation Programme Flow Chart**

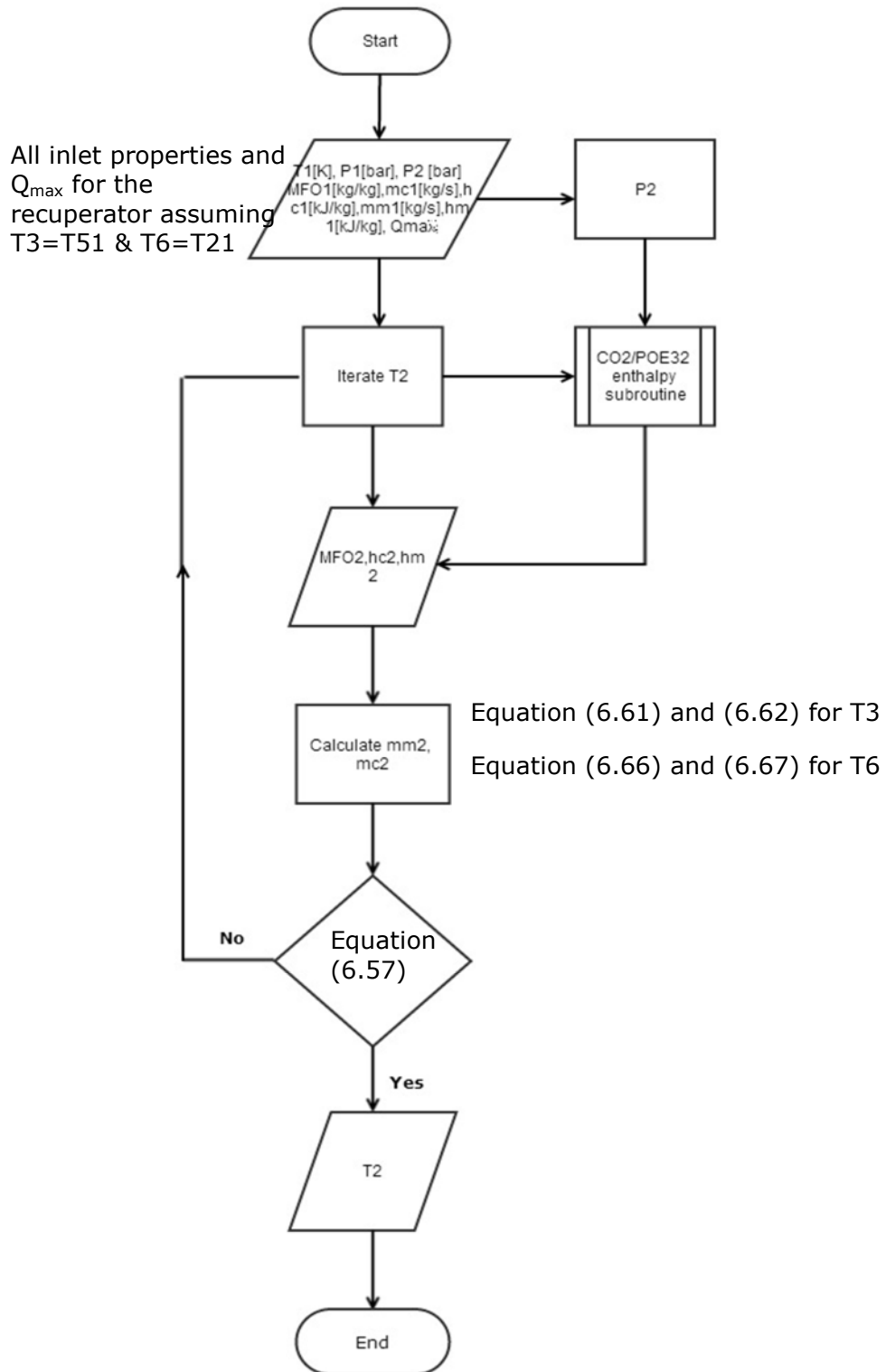




### C.3 Mixer Sub-routine Flow Chart



### C.4 T3 and T6 Recuperator Exit Temperature Sub-routine Flow Chart



## C.5 R1233zd(E) ORC System Thermodynamic Model

### Code

```
%  
%-----  
% Properties  
%Q Quality [-]  
%T Temperature [K]  
%P Pressure [bar]  
%D Density [kg./m3]  
%C Specific heat at constant pressure [kJ./kg]  
%H Enthalpy [kJ./kg]  
%S Entropy [kJ./kg./K]  
%V Dynamic viscosity [Pa-s]  
%L Thermal conductivity [kW./m./K]  
%  
%-----  
%Cycle State points  
%a Condensed saturation 100% liquid  
%sub sub cooled for pump (at pump inlet)  
%b2 Pump output conditions  
%c After addition of sensible heat in middle heat exchanger  
(HEX)  
%e After addition of latent heat - Evap saturation 100%  
vapour  
%es After addition of superheat - expander inlet condition  
%f2 Actual conditions at expander out after expander  
efficiency  
%g After removing superheat from exhaust (HEX outlet)  
%  
%-----  
%Turbine efficiency  
Teff=0.8;  
%pump efficiency  
WPeff=0.9;  
%Heat exchangers effectiveness  
effect=0.8; %  
%critical pressure  
Pcri=REFPROPm('R1233zd(E)', 'pcrit')./100;  
%  
%-----  
%required Turbine Power output  
WT=input ('kW');  
%condenser saturation temperature  
Ta=303.15+5%  
%Sub-cooling temperature  
Tsub=303.15;  
%Properties at Condenser saturation Temperature  
Pa=REFPROPm('P', 'T', Ta, 'Q', 0, 'R1233zd(E)')/100;  
%ha=REFPROPm('H', 'P', Pa*100, 'Q', 0, 'R1233zd(E)');  
ha=REFPROPm('H', 'P', Pa*100, 'Q', 0, 'R1233zd(E)');  
sa=REFPROPm('S', 'P', Pa*100, 'Q', 0, 'R1233zd(E)');  
%Properties at sub cooled Temperature  
if Tsub==Ta  
    hsub=ha;  
    ssub=sa;  
else  
hsub=REFPROPm('H', 'T', Tsub, 'P', Pa.*100, 'R1233zd(E)');  
ssub=REFPROPm('S', 'T', Tsub, 'P', Pa.*100, 'R1233zd(E)');
```

```

end
Tcin=Tsub-5;
Pf=Pa;
%Turbine inlet temperature
for i=[0:1:25];
Pe(i)=[4+i*0.5]
try
    Pb(i)=Pe(i);
if Pe(i)>=Pcri
    continue
end
if Pe(i)<=Pcri
%Properties at evaporator saturation pressure
he(i)=REFPROPm('H','P',Pe(i).*100,'Q',1,'R1233zd(E)');
Te(i)=REFPROPm('T','P',Pe(i).*100,'Q',1,'R1233zd(E)');
if Te(i)>393.15
    continue
end
%Properties at expander inlet (superheated)
Tes(i)=Te(i)+5;
if Tes(i)>393.15
    continue
end
hes(i)=REFPROPm('H','T',Tes(i),'P',Pe(i).*100,'R1233zd(E)');
ses(i)=REFPROPm('S','T',Tes(i),'P',Pe(i).*100,'R1233zd(E)');
else
    continue
end
%Turbine outlet enthalpy for ideal expansion
hf(i)=REFPROPm('H','P',Pf.*100,'S',ses(i),'R1233zd(E)');
Tf(i)=REFPROPm('T','P',Pf.*100,'H',hf(i),'R1233zd(E)');
%ideal turbine work
WTideal(i)=hes(i)-hf(i);
%Real turbine work
WTreal(i)=WTideal(i).*Teff;
%Real turbine outlet enthalpy
hf2(i)=hes(i)-WTreal(i);
%Properties at turbine outlet
Tf2(i)=REFPROPm('T','P',Pf.*100,'H',hf2(i),'R1233zd(E)');
%Mass flow rate through the turbine
mr(i)=WT./(hes(i)-hf2(i));
%Ideal pump exit enthalpy
hb(i)=(REFPROPm('H','P',Pb(i).*100,'S',ssub,'R1233zd(E)'));
%Ideal pump exit Temperature
Tb(i)=REFPROPm('T','P',Pb(i).*100,'H',hb(i),'R1233zd(E)');
%ideal Pump work
WPideal(i)=(hb(i)-hsub);
%Real pump work
WPwork(i)=WPideal(i)./WPeff;
%Pump Power
WP(i)=WPwork(i).*mr(i);
if WP(i)>WT
    continue
end
%Real Pump exit enthalpy and properties
hb2(i)=hsub+WPwork(i);
Tb2(i)=REFPROPm('T','P',Pb(i).*100,'H',hb2(i),'R1233zd(E)');
Pg=Pf;
Pc(i)=Pb(i);
%
% Recuperator calculation

```

```

%assume Tg=Tb2(i)
hgb(i)=REFPROPm('H','T',Tb2(i),'P',Pg.*100,'R1233zd(E)');
Qxmax1(i)=mr(i).*(hf2(i)-hgb(i));
%assume Tc=Tf2(i)
hcf(i)=REFPROPm('H','T',Tf2(i),'P',Pc(i).*100,'R1233zd(E)');
Qxmax2(i)=mr(i).*(hcf(i)-hb2(i));
%smallest Qmax value represent maximum he(i)at transfer.
if Qxmax1(i)<Qxmax2(i);
    Qxmax(i)=Qxmax1(i);
else
    Qxmax(i)=Qxmax2(i);
end
%Enthalpy and properties at Condenser inlet
hg(i)=hf2(i)-((Qxmax(i).*effect)./mr(i));
Tg(i)=REFPROPm('T','P',Pg.*100,'H',hg(i),'R1233zd(E)');
%Enthalpy and properties at Evaporator inlet
hc(i)=hb2(i)+((Qxmax(i).*effect)./mr(i));
Tc(i)=REFPROPm('T','P',Pc(i).*100,'H',hc(i),'R1233zd(E)');
%
if hes(i)>hc(i)
%Power input (Evaporation and super heating)
QG(i)=mr(i).*(hes(i)-hc(i))
else
    continue
end
%Evaporation power input
Qev(i)=mr(i).*(he(i)-hc(i));
%Super heating power input
Qsup(i)=mr(i).*(hes(i)-he(i));
if hg(i)>hsub
%Power output (Condensation and subcooling)
QA(i)=mr(i).*(hg(i)-hsub)
%Condensation power output
Qcond(i)=mr(i).*(hg(i)-ha)
%Sub-cooling power output
Qsub(i)=mr(i).*(ha-hsub)
else
    continue
end
if hf2(i)>hg(i)
%middle he(i)at exchanger power
Qx(i)=mr(i).*(hf2(i)-hg(i))
else
    continue
end
Qin(i)=QA(i)+WT
Qout(i)=WP(i)+QG(i)
if WT>WP(i)
% Cycle efficiency
Cycleeff(i)=((WT-WP(i))./QG(i)).*100
% Net thermal power output
Net(i)=WT-WP(i)
% Sub-routines for heat exchangers sizing by (LMTD)
[Atcond(i),Ucond(i),mrcool(i)] = condense(Tg, Pg, Tsub, Qcond,
Qsub, mr, effect)
[Atrec(i),Urec(i)] = recuperator(Qx, Tf2, Tg, Tb2, Tc, Pg, Pc,
mr)
[Atev(i),Uev(i),mrsteam(i)] = evaporator(Qev, Qsup, Tc, Te,
Tes, mr, Pc, effect)
%
catch err

```

```

end
%Results Matrix
X2=[Pe.' Cycleeff.' Net.' QG.' QA.' Qx.' mr.' Tb2.' Tc.'
Tf2.' Tg.']
X=X2(find(X2(:,2)>0),:);
end

```

## C.6 Thermal Efficiency Comparison of the ORC System and the CO2 SRC power generation system

The CO2 SRC power generation system was compared to both conventional and environmentally friendly ORC refrigerants under the same working conditions presented in Chapter 6, section 6.7.4.1. However, for the CO2 system, three CO2 cooler pressures of 74, 85 and 95 bar were kept constant in the simulation, while varying the CO2 heater pressure, in order to establish a comparison under similar conditions. The actual isentropic efficiency of the only suitable, commercially available CO2 turbine was 50%, and was used in the simulation. Figure C- and Figure C-show the simulation results for thermal efficiency at 100°C and 120°C, respectively.

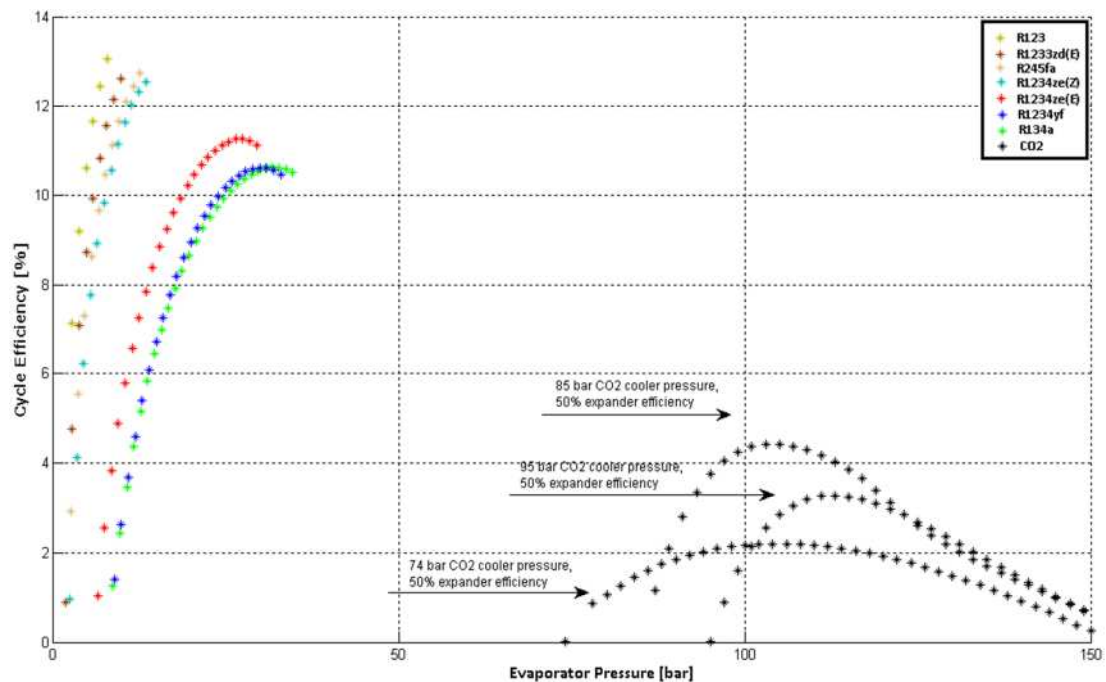


**Figure C-1: ORC working fluids efficiency comparison with the CO2 SRC power system at 100°C.**

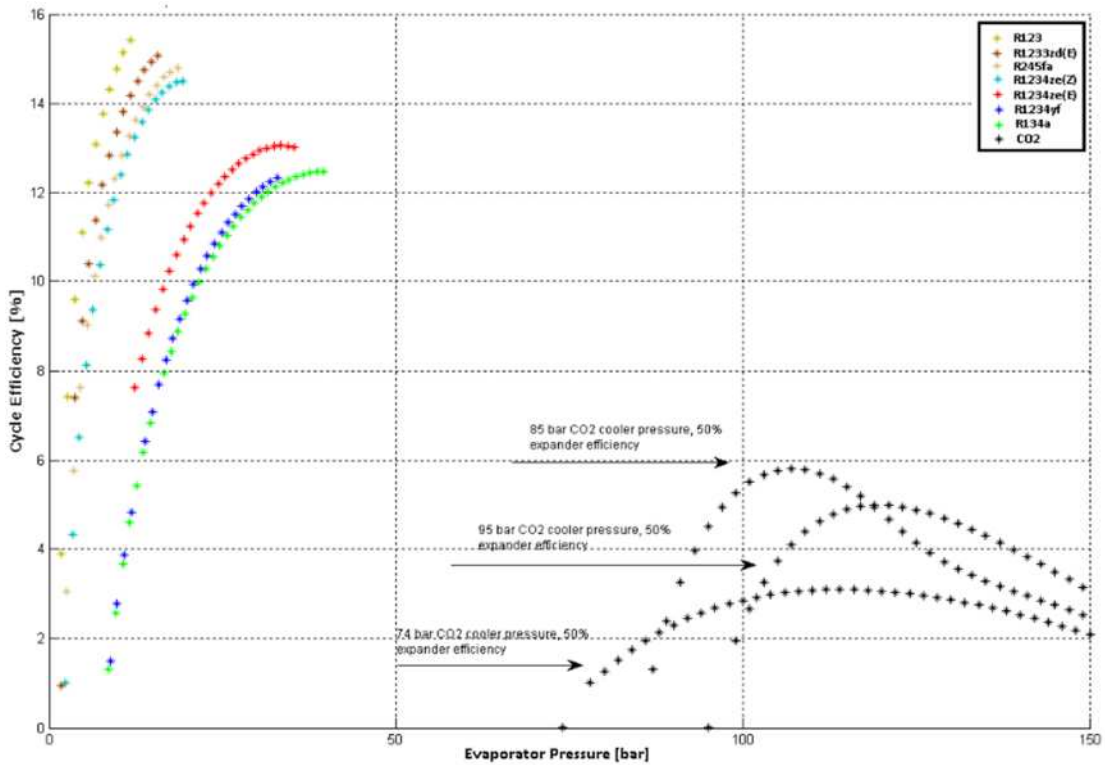


**Figure C-2: ORC working fluids efficiency comparison with the CO2 SRC power system at 120°C.**

As shown in both figures, the CO2 SRC power generation system generally showed very low thermal efficiency when compared to the ORC system, with the highest thermal efficiency achieved being with the 85 bar CO2 cooler pressure in both cases. Further increases in CO2 cooler pressure had a negative effect on thermal efficiency, where it was reduced when the CO2 cooler pressure was increased to 95 bar. In all three CO2 cooler pressure curves, the thermal efficiency increased gradually as the CO2 heater pressure rose, until maximum thermal efficiency was achieved. After that, a further increase in CO2 heater pressure tended to reduce the system's thermal efficiency.

# Appendix D

## D.1 R1233zd(E) Safety Data Sheet



### SAFETY DATA SHEET

#### 1. IDENTIFICATION OF THE SUBSTANCE / PREPARATION AND COMPANY / UNDERTAKING

<b>Product Name</b>	<b>HFCO 1233 zd-E</b>
<b>Manufacturer</b>	Mexichem UK Limited PO Box 13 The Heath Runcorn Cheshire WA7 4QX Tel: +44(0) 1928 511192 Fax: +44(0) 1928 517592 E-Mail: info@mexichem.com
<b>Emergency Phone No.</b>	IN AN EMERGENCY DIAL 999 (UK Only) For specialist advice in an emergency telephone +44(0) 1928 572000
<b>Use</b>	Subject to Member State regulations, applicable uses are: refrigerant

#### 2. HAZARDS IDENTIFICATION

This material is only for research and development purposes as a refrigerant.

Low acute toxicity. Very high atmospheric concentrations may cause an abnormal heart rhythm, anaesthetic effects and asphyxiation.  
Liquid splashes or spray may cause freeze burns to skin and eyes.

EC Classification Not classified as dangerous according to EC Directive 67/548/EEC.

#### 3. COMPOSITION / INFORMATION ON INGREDIENTS

Alternative names Hydrofluorochloro-olefin 1233 zd-E

##### HAZARDOUS INGREDIENT(S)

Hazardous ingredient(s)	%(w/w)	CAS No.	EC No.	EC Classification
trans-1-chloro-3,3,3-trifluoroprop-1-ene (HFCO 1233 zd-E)	99.5			

#### 4. FIRST AID MEASURES



The first aid advice given for skin contact, eye contact, and ingestion is applicable following exposures to the liquid or spray. See also section 11.

<b>Inhalation</b>	Remove patient from exposure, keep warm and at rest. Administer oxygen if necessary. Apply artificial respiration if breathing has ceased or shows signs of failing. In the event of cardiac arrest apply external cardiac massage. Obtain immediate medical attention.
<b>Skin Contact</b>	Thaw affected areas with water. Remove contaminated clothing. Caution: clothing may adhere to the skin in the case of freeze burns. After contact with skin, wash immediately with plenty of warm water. If irritation or blistering occur obtain medical attention.
<b>Eye Contact</b>	Immediately irrigate with eyewash solution or clean water, holding the eyelids apart, for at least 10 minutes. Obtain immediate medical attention.

## SAFETY DATA SHEET

Ingestion	Unlikely route of exposure. Do not induce vomiting. Provided the patient is conscious, wash out mouth with water and give 200-300 ml (half a pint) of water to drink. Obtain immediate medical attention.
Further Medical Treatment	Symptomatic treatment and supportive therapy as indicated. Adrenaline and similar sympathomimetic drugs should be avoided following exposure as cardiac arrhythmia may result with possible subsequent cardiac arrest.

### 5. FIRE-FIGHTING MEASURES

General	This refrigerant is not flammable in air under ambient conditions of temperature and pressure. Certain mixtures of this refrigerant and air when under pressure may be flammable. Mixtures of this refrigerant and air under pressure should be avoided. Certain mixtures of HFOs and chlorine may be flammable or reactive under certain conditions. Thermal decomposition will evolve very toxic and corrosive vapours. ( hydrogen fluoride ) Containers may burst if overheated.
Extinguishing Media	As appropriate for surrounding fire. Keep fire exposed containers cool by spraying with water.
Fire Fighting Protective Equipment	A self contained breathing apparatus and full protective clothing must be worn in fire conditions. See Also Section 8

### 6. ACCIDENTAL RELEASE MEASURES

Personal Protection	Ensure suitable personal protection (including respiratory protection) during removal of spillages. See Also Section 8
General	Provided it is safe to do so, isolate the source of the leak. Allow small spillages to evaporate provided there is adequate ventilation. Large spillages: Ventilate area. Contain spillages with sand, earth or any suitable adsorbent material. Prevent liquid from entering drains, sewers, basements and workpits since the vapour may create a suffocating atmosphere.

### 7. HANDLING AND STORAGE

Handling	Avoid inhalation of high concentrations of vapours. Atmospheric levels must be controlled in compliance with the occupational exposure limit. The vapour is heavier than air, high concentrations may be produced at low levels where general ventilation is poor, in such cases provide adequate ventilation or wear suitable respiratory protective equipment with positive air supply. Avoid contact with naked flames and hot surfaces as corrosive and very toxic decomposition products can be formed. Avoid contact between the liquid and skin and eyes.
Process Hazards	Liquid refrigerant transfers between refrigerant containers and to and from systems can result in static generation. Ensure adequate earthing. Certain mixtures of HFOs and chlorine may be flammable or reactive under certain conditions. Care must be taken to mitigate the risk of developing high pressures in systems caused by a temperature rise when liquid is trapped between closed valves or in cases where containers have been overfilled.
Storage	Keep in a well ventilated place away from fire risk and avoid sources of heat such as electric or steam radiators. Avoid storing near to the intake of air conditioning units, boiler units and open drains.
Specific use	Subject to Member State regulations, applicable uses are: refrigerant

SAFETY DATA SHEET

**8. EXPOSURE CONTROLS / PERSONAL PROTECTION**

**General** Wear suitable protective clothing, gloves and eyeface protection. Wear thermal insulating gloves when handling liquefied gases. In cases of insufficient ventilation, where exposure to high concentrations of vapour is possible, suitable respiratory protective equipment with positive air supply should be used.



Eye Protection



Gloves

**Occupational Exposure Limits**

Occupational Exposure Limits	CAS No.	LTEL (8 hr TWA ppm)	LTEL 8 hr TWA mg/m <sup>3</sup>	STEL (ppm)	STEL mg/m <sup>3</sup>	Note:
trans-1-chloro-3,3,3-trifluoroprop-1-ene (HFCO 1233 zd-E)		10				COM (provisional)

**9. PHYSICAL AND CHEMICAL PROPERTIES**

**Form** liquefied gas  
**Colour** colourless  
**Odour** slight ethereal  
**Solubility (Water)** insoluble  
**Solubility (Other)** Soluble in: alcohols , chlorinated solvents , esters  
**Boiling Point (° C)** 19

**10. STABILITY AND REACTIVITY**

**Hazardous Reactions** Certain mixtures of HFOs and chlorine may be flammable or reactive under certain conditions. Incompatible materials: finely divided metals , magnesium and alloys containing more than 2% magnesium . Can react violently if in contact with alkali metals and alkaline earth metals - sodium , potassium , barium

**Hazardous Decomposition Product(s)** hydrogen fluoride by thermal decomposition and hydrolysis.

**11. TOXICOLOGICAL INFORMATION**

This material is only for research and development purposes as a refrigerant.

**Inhalation** Low acute toxicity  
 Very high atmospheric concentrations may cause an abnormal heart rhythm, anaesthetic effects and asphyxiation.

**Skin Contact** Liquid splashes or spray may cause freeze burns. Unlikely to be hazardous by skin absorption.

**Eye Contact** Liquid splashes or spray may cause freeze burns.

**Ingestion** Highly unlikely - but should this occur freeze burns will result.

**Long Term Exposure** No information available.

## SAFETY DATA SHEET

### 12. ECOLOGICAL INFORMATION

Environmental Fate and Distribution	Vapour
Persistence and Degradation	Decomposed rapidly in the lower atmosphere (troposphere). May influence photochemical smog (i.e. may be a VOC under the terms of the UNECE agreement). Does not deplete ozone. Has a Global Warming Potential (GWP) of 20 (relative to a value of 1 for carbon dioxide at 100 years).
Effect on Effluent Treatment	Discharges of the product will enter the atmosphere and will not result in long term aqueous contamination.

### 13. DISPOSAL CONSIDERATIONS

Recommended:	Best to recover and recycle. If this is not possible, destruction is to be in an approved facility which is equipped to absorb and neutralise acid gases and other toxic processing products.
--------------	---

### 14. TRANSPORT INFORMATION

#### Hazard Label



Road/Rail UN No.	3163
ADR/RID Class	2.2
ADR/RID Proper Shipping Name	LIQUEFIED GAS, N.O.S. (trans-1-chloro-3,3,3-trifluoroprop-1-ene)
SEA IMDG Class	2.2
Marine Pollutant	Not classified as a Marine Pollutant
AIR ICAO/IATA	2.2

### 15. REGULATORY INFORMATION

#### European Regulations

EC Classification	Not classified as dangerous according to EC Directive 67/548/EEC.
-------------------	---

### 16. OTHER INFORMATION

This data sheet was prepared in accordance with Regulation (EC) No. 1907/2006.

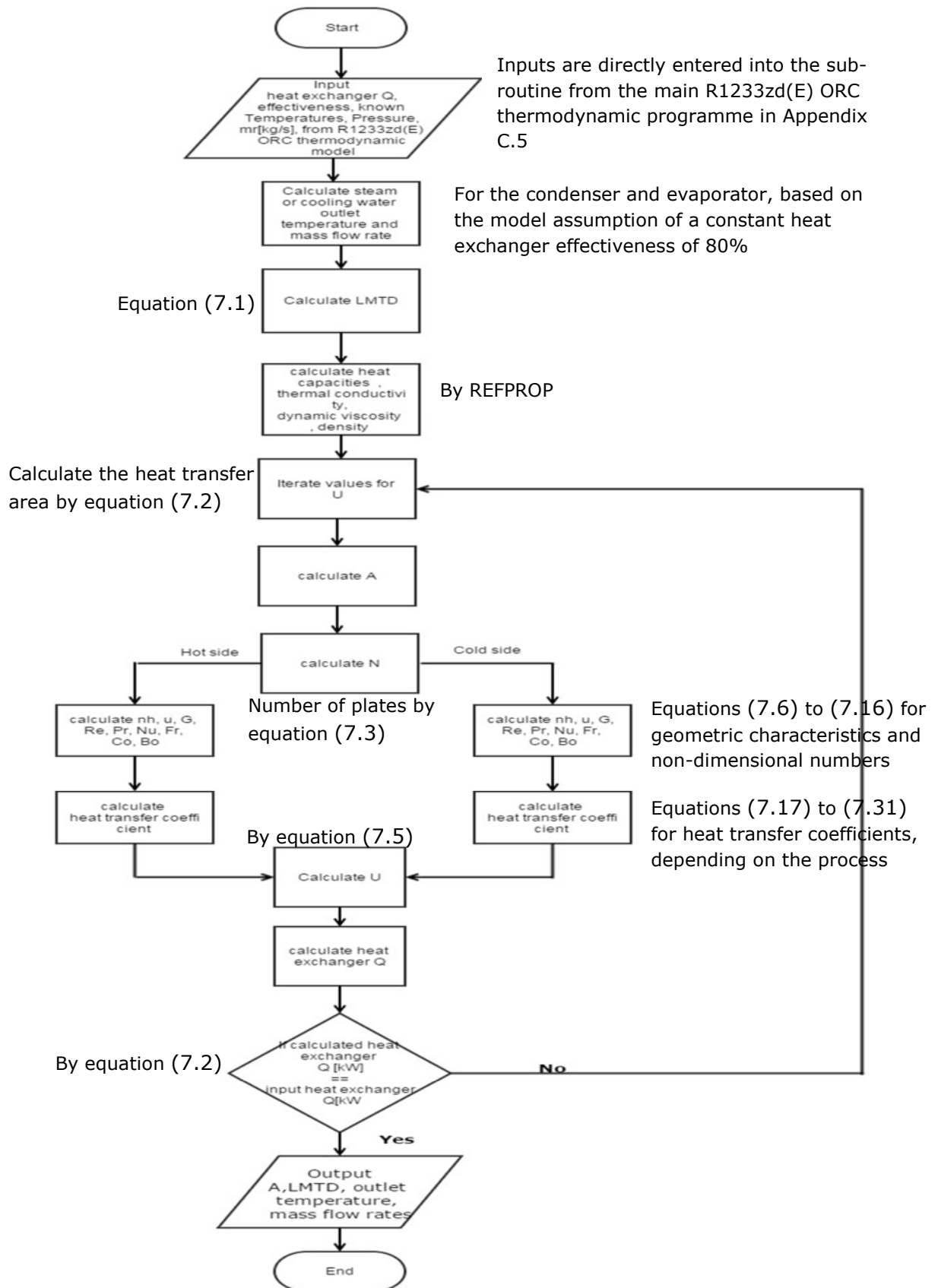
Information in this publication is believed to be accurate and is given in good faith, but it is for the User to satisfy itself of the suitability for its own particular purpose. Accordingly, Mexichem UK Limited gives no warranty as to the fitness of the Product for any particular purpose and any implied warranty or condition (statutory or otherwise) is excluded except to the extent that such exclusion is prevented by law. Freedom under Patent, Copyright and Designs cannot be assumed. Mexichem Fluor™ is a trademark, the property of Mexichem SAB de C.V. Mexichem UK Limited is Registered in England No 7088219. Registered Office The Heath Business & Technical Park, Runcom, Cheshire WA7 4QX. © Mexichem UK Limited 2010.

## SAFETY DATA SHEET

### Glossary

WEL: Workplace Exposure Limit (UK HSE EH40)  
COM: The company aims to control exposure in its workplace to this limit  
TLV: The company aims to control exposure in its workplace to the ACGIH limit  
TLV-C: The company aims to control exposure in its workplace to the ACGIH Ceiling limit  
MAK: The company aims to control exposure in its workplace to the German limit  
Sk: Can be absorbed through skin  
Sen: Capable of causing respiratory sensitisation  
Bmgv: Biological monitoring guidance value (UK HSE EH40)

## D.2 BPHE LMTD Sub-Routine Flow Chart



## Appendix E

---

### E.1 Compressed Air Open Loop Expander-Alternator

#### Experiment's Electrical Measurements

**Table E.7: Preliminary expander-electric power generator's electrical measurements.**

Load measurement			Battery measurement			Total current [I]	Electric power output [W]
Current [I]	Voltage [V]	Power [W]	Shunt voltage [mV]	Current [I]	Power [W]		
13.35	14.52	193.84	1.70	5.67	82.28	19.02	276.12
13.32	14.50	193.14	1.48	4.93	71.53	18.25	264.67
13.32	14.51	193.27	1.45	4.83	70.13	18.15	263.40
13.29	14.53	193.10	1.35	4.50	65.39	17.79	258.49
13.29	14.50	192.71	1.28	4.27	61.87	17.56	254.57
13.29	14.52	192.97	1.18	3.93	57.11	17.22	250.08
13.32	14.53	193.54	1.14	3.80	55.21	17.12	248.75
13.35	14.51	193.71	1.02	3.40	49.33	16.75	243.04
16.5	14.51	239.42	1.00	3.33	48.37	19.83	287.78
16.5	14.49	239.09	0.94	3.13	45.40	19.63	284.49
16.5	14.50	239.25	0.89	2.97	43.02	19.47	282.27
19.86	14.49	287.77	0.78	2.60	37.67	22.46	325.45
19.89	14.48	288.01	0.78	2.60	37.65	22.49	325.66
23.64	14.44	341.36	0.78	2.60	37.54	26.24	378.91
23.67	14.46	342.27	0.69	2.30	33.26	25.97	375.53
26.61	14.44	384.25	0.66	2.20	31.77	28.81	416.02
18.81	14.49	272.56	0.61	2.03	29.46	20.84	302.02
23.64	14.47	342.07	0.53	1.77	25.56	25.41	367.63

## **E.2 R1233zd(E) ORC Prototype's Experimental Results**

### **E.2.1 Experiment 1**

**Table E.8: ORC experiment 1, first run - measured quantities.**

Time [sec]	T Pump out [°C]	T evaporator in [°C]	T expander in [°C]	T expander Out [°C]	T condenser In [°C]	T condenser Out [°C]	T Chiller in [°C]	T Chiller out [°C]	P expander in [bar]	P expander out [bar]	P pump out [bar]	P condenser out [bar]	Expander pressure ratio [-]	R123zd(E) mass flow rate [kg/s]	Cooling water flow rate [l/m]	Boiler heat input [kW]
136	11.01	42.20	90.82	58.16	41.76	9.68	9.62	16.22	8.27	1.41	8.55	1.22	5.88	0.07	20	16.88
249	11.13	42.90	92.35	59.45	42.98	9.76	9.62	16.21	8.66	1.50	8.89	1.31	5.76	0.07	20	16.88
487	11.15	48.94	94.27	63.99	48.89	9.81	9.71	16.61	9.03	1.97	9.21	1.81	4.57	0.07	20	20.25
670	11.30	48.78	92.49	61.91	47.86	9.96	9.86	17.03	8.62	1.86	8.95	1.71	4.63	0.07	20	23.63
846	11.40	47.72	93.36	62.53	46.99	10.02	9.93	16.84	8.85	1.83	9.25	1.69	4.84	0.07	20	27
1400	11.47	41.68	94.01	60.03	40.78	10.34	10.30	18.01	9.10	1.41	9.28	1.17	6.46	0.09	20	30.38
1587	11.65	43.39	93.07	58.94	42.67	10.55	10.39	18.37	8.83	1.51	9.07	1.27	5.85	0.11	20	30.38
1704	11.76	42.99	94.11	59.97	42.62	10.58	10.47	18.05	9.06	1.54	9.23	1.25	5.88	0.11	20	33.75
1831	11.74	42.77	94.11	59.80	42.30	10.66	10.57	18.04	9.11	1.52	9.27	1.23	6	0.11	20	33.75
1939	11.88	41.83	92.51	57.61	40.58	10.77	10.67	18.45	8.82	1.37	8.99	1.09	6.42	0.11	20	33.75
2078	11.98	41.95	93.27	57.95	40.97	10.88	10.82	18.42	8.92	1.41	9.09	1.14	6.33	0.11	20	33.75
2178	12.05	42.06	93.45	57.78	41.27	10.85	10.73	18.35	8.91	1.41	9.15	1.12	6.31	0.11	20	33.75
2491	12.48	43.20	92.91	60.64	44.27	11.12	11.05	17.78	8.76	1.53	8.85	1.34	5.71	0.07	20	33.75
2782	12.53	44.68	93.11	61.16	44.32	11.16	11.11	18.99	8.82	1.50	9.11	1.33	5.89	0.08	20	33.75
3025	12.66	38.52	93.80	60.17	39.57	11.39	11.27	18.32	8.98	1.22	9.23	1.02	7.36	0.08	20	33.75
3138	12.75	40.58	93.62	59.79	41.90	11.39	11.34	18.46	8.98	1.37	9.30	1.16	6.54	0.08	20	33.75
3589	12.97	39.56	93.91	59.40	39.21	11.60	11.56	18.86	9.11	1.26	8.98	1.04	7.22	0.08	20	33.75
3712	13.01	38.71	92.62	57.25	37.60	11.67	11.58	19.26	8.79	1.17	8.73	0.93	7.49	0.08	20	33.75
3803	12.99	39.26	93.50	59.43	38.50	11.75	11.71	19.12	8.92	1.20	8.89	1	7.45	0.08	20	33.75
3913	13.11	39.30	93.80	58.85	38.77	11.79	11.74	19.02	8.98	1.24	9.25	0.96	7.24	0.08	20	33.75
4236	13.18	38.91	93.23	58.45	37.87	11.87	11.78	19.41	8.86	1.18	8.90	0.99	7.50	0.08	20	33.75

Table E.9: ORC experiment 1, results of first run.

Evaporator energy [kW]	Condenser			Recuperator		Recuperator HP energy [kW]		Expander		Net			Electric		System thermal efficiency
	energy [kW]	LP energy [kW]	HP energy [kW]	power output [W]	isentropic efficiency [%]	RPM	Pump power [W]	Pump efficiency [%]	power output [W]	Transmitted power	power output [W]	generator efficiency	System thermal efficiency		
15.43	16.25	0.99	2.80	1156.59	47.14	1198	137.76	29.52	1018.83	1040.93	107	10.28	6.60		
15.41	16.30	1	2.85	1139.44	47.05	1272	141.80	29.67	997.63	1025.49	107	10.43	6.47		
14.94	16.57	0.93	3.40	1005.38	47.66	1250	139.17	29.50	866.21	904.84	107	11.83	5.80		
14.88	16.50	0.87	3.37	1053.53	49.56	1220	138.68	28.97	914.85	948.17	107	11.28	6.15		
15.01	16.46	0.94	3.26	1036.99	47.43	1263	143.33	29.25	893.65	933.29	107	11.46	5.96		
18.67	19.38	1.37	3.25	1367.87	44.30	1205	147.39	36.66	1220.49	1231.08	107	8.69	6.54		
23.83	25.12	1.51	4.41	1854.56	49.02	1226	184	36.46	1670.56	1669.10	107	6.41	7.01		
23.95	25.12	1.61	4.34	1824.16	48.06	1243	195.16	35.16	1629	1641.75	107	6.52	6.80		
23.97	25.09	1.62	4.31	1823.14	47.57	1188	182.38	37.93	1640.76	1640.83	107	6.52	6.85		
23.98	24.94	1.57	4.16	1888.82	47.61	1048	185.12	36.69	1703.69	1699.93	117.60	6.92	7.10		
24.02	24.94	1.56	4.16	1927.09	48.84	1110	184.34	37.09	1742.75	1734.38	128	7.38	7.25		
24.02	24.97	1.52	4.16	1965.88	49.86	1000	199.09	34.69	1766.79	1769.29	140	7.91	7.35		
15.37	16.14	1.06	2.75	1091.62	45.35	1230	141.08	29.54	950.54	982.46	110	11.20	6.18		
16	16.95	1.14	3.02	1111.37	43.23	1220	149.56	30.33	961.81	1000.23	110	11	6.01		
17.40	17.47	1.44	2.54	1217.28	40.27	1300	148.44	33.76	1068.84	1095.55	110	10.04	6.14		
17.57	17.98	1.30	2.80	1280.42	44	1275	160.34	31.68	1120.09	1152.38	110	9.55	6.38		
17.27	17.50	1.32	2.61	1261.02	42.21	1260	156.66	30.91	1104.36	1134.92	110	9.69	6.39		
17.31	17.41	1.28	2.52	1345.28	44.23	1190	153.61	30.99	1191.66	1210.75	122	10.08	6.88		
17.30	17.44	1.37	2.58	1249	41.12	1225	143.75	33.49	1105.26	1124.10	122	10.85	6.39		
17.31	17.46	1.31	2.57	1310.16	43.73	1190	152.90	33.09	1157.26	1179.14	134	11.36	6.69		
17.32	17.39	1.34	2.53	1300.95	42.69	1172	150.77	32.03	1150.18	1170.85	134	11.44	6.64		

**Table E.10: ORC experiment 1, measured quantities and results of the second run.**

Time [sec]	T Pump out [°C]	T evaporator in [°C]	T expander in [°C]	T expander Out [°C]	T condenser In [°C]	T condenser Out [°C]	T Chiller in [°C]	T Chiller out [°C]	P expander in [bar]	P expander out [bar]	P pump out [bar]	P condenser out [bar]	Expander pressure ratio [-]	R1233zd(E) mass flow rate [kg/s]	Cooling water flow rate [l/m]	Boiler heat input [kW]
419	12.26	39.31	93.05	60.84	37.94	10.99	10.97	18.39	8.75	1.19	9.07	0.99	7.37	0.07	20	33.75
478	12.33	38.63	93.32	58.76	38.22	11.13	11.07	18.48	8.92	1.19	9.23	0.97	7.50	0.07	20	33.75
595	12.62	39	93.35	60.16	38.24	11.44	11.38	18.77	8.89	1.20	9.02	0.97	7.40	0.07	20	33.75
1256	13.56	39.91	93.63	60.58	39.26	12.20	12.12	19.54	8.93	1.24	8.78	0.98	7.20	0.07	20	33.75
1915	13.84	41.43	93.51	58.89	40.56	12.45	12.34	19.81	8.98	1.35	9.09	1.13	6.68	0.07	20	33.75
2085	13.78	39.87	93.41	58.58	38.51	12.48	12.33	19.89	8.96	1.22	9.07	0.96	7.32	0.07	20	33.75
2340	14.02	38.11	93.85	56.87	37.20	12.66	12.53	19.77	9.03	1.15	9.01	0.93	7.83	0.07	20	33.75
2451	13.99	36.98	93.65	54.69	35.55	12.61	12.51	19.83	9.01	1.01	9.01	0.84	8.91	0.07	20	33.75

Evaporator energy [kW]	Condenser energy [kW]	Recuperator LP energy [kW]	Recuperator HP energy [kW]	Expander power output [W]	Expander isentropic efficiency [%]	RPM	Pump power [W]	Pump efficiency [%]	Net power output [W]	Transmitted power [W]	Electric power output [W]	Electric generator efficiency	System thermal efficiency	System electrical efficiency	Energy in [kW]	Energy out [kW]
15.74	15.93	1.36	2.42	1043.14	37.88	1200	134.10	33.43	909.05	938.83	107	11.40	5.77	0.32	15.88	16.97
15.79	15.91	1.23	2.35	1164.41	42	1250	128.54	35.66	1035.87	1047.97	107	10.21	6.56	0.32	15.92	17.07
15.76	15.89	1.30	2.36	1085.54	39.41	1250	126.02	35.46	959.53	976.99	107	10.95	6.09	0.32	15.88	16.98
15.66	15.84	1.28	2.35	1077.49	39.69	1170	140.69	30.73	936.80	969.74	119	12.27	5.98	0.35	15.80	16.92
15.50	15.86	1.10	2.46	1179.02	45.21	1200	144.13	30.62	1034.89	1061.12	130	12.25	6.68	0.39	15.64	17.04
15.64	15.79	1.18	2.33	1177.12	43.10	1170	137.29	32.74	1039.83	1059.40	142	13.40	6.65	0.42	15.78	16.97
15.81	15.69	1.16	2.15	1292.75	45.80	1088	142.02	31.58	1150.72	1163.47	167	14.35	7.28	0.49	15.95	16.98
15.90	15.61	1.12	2.05	1394.83	46.61	920	143.86	31.50	1250.97	1255.34	180	14.34	7.87	0.53	16.05	17

## E.2.2 Experiment 2

**Table E.11: Experiment 2, measured quantities and results.**

Time [sec]	T Pump out [°C]	T evaporator in [°C]	T expander in [°C]	T expander out [°C]	T condenser in [°C]	T condenser out [°C]	T Chiller in [°C]	T Chiller out [°C]	P expander in [bar]	P expander out [bar]	P pump out [bar]	P condenser out [bar]	Expander pressure ratio [-]	R1233zd(E) mass flow rate [kg/s]	Cooling water flow rate [l/m]	Boiler heat input [kW]
52	15	36	91.51	58.02	32.49	19.78	11.58	11.87	7.36	0.82	7.62	0.82	8.99	0.09	3	20.25
83	44.84	55.73	97.66	58.72	53.62	39.67	12.84	53.74	9.38	2.15	11.02	2.15	4.37	0.05	4	16.88
191	29.17	53.46	97.29	63.03	38.80	28.89	13.12	38.09	9.29	1.15	10.82	1.15	8.04	0.05	4	16.88
222	30.15	55.52	97.46	64.80	38.99	29.20	13.35	38.54	9.31	1.17	9.49	1.17	7.93	0.05	4	16.88
407	19.18	50.86	95.54	65.90	33.31	25.74	14.70	32.06	8.83	0.84	7.71	0.84	10.50	0.08	4	16.88
551	33.19	56.53	96.73	67	41.37	31.86	15.50	41.15	9.25	1.36	9.95	1.36	6.81	0.07	4	20.25
920	31.34	53.77	95.92	66.53	40.95	32.01	17.74	40.36	9.23	1.34	8.74	1.34	6.90	0.09	4	20.25
1019	36.08	58.49	95.98	67.68	43.50	34.31	18.32	43.33	9.07	1.52	9.25	1.52	5.99	0.07	4	16.88
1172	35.69	49.92	95.48	52.79	46.04	35.89	19.16	45.14	8.98	1.56	8.01	1.56	5.76	0.06	4	16.88

Evaporator energy [kW]	Condenser energy [kW]	Recuperator LP energy [kW]	Recuperator HP energy [kW]	Expander power output [W]	Expander isentropic efficiency [%]	Pump power [W]	Pump efficiency [%]	Net power output [W]	Transmitted power [W]	Electric power output [W]	Electric generator efficiency	System thermal efficiency	System electrical efficiency	Energy in [kW]	Energy out [kW]
19.83	18.89	1.73	2.16	1580.05	41.42	383.56	11.78	1196.49	1422.04	211.32	14.86	6.03	1.04	20.21	20.47
9.44	9.14	0.16	0.62	1019.02	75.42	300.71	9.27	718.31	917.12	245.99	26.82	7.61	1.46	9.75	10.16
10.58	10.73	1.07	1.51	818.61	38.94	533.26	6.26	285.35	736.75	510.35	69.27	2.70	3.02	11.11	11.55
10.44	10.69	1.14	1.58	746.47	35.80	563.53	5.92	182.95	671.82	465	69.21	1.75	2.76	11	11.44
16.36	16.86	2.20	2.97	944.47	26.16	664.44	7.43	280.03	850.03	206.23	24.26	1.71	1.22	17.03	17.81
14.39	14.65	1.58	2.03	877.46	32.66	699.57	6.49	177.89	789.72	316.57	40.09	1.24	1.56	15.09	15.52
17.41	17.52	1.90	2.32	1010.03	31.35	692.49	7.82	317.54	909.03	199.51	21.95	1.82	0.99	18.10	18.53
13.43	13.71	1.41	1.86	783.96	32.99	642.84	6.44	141.12	705.56	212.10	30.06	1.05	1.26	14.07	14.50
11.31	11.04	0.25	0.93	1325.77	71.24	436.46	7.47	889.31	1193.19	265.42	22.24	7.86	1.57	11.75	12.37

**Table E.12: Experiment 2, electrical measurements.**

Load measurement			Battery measurement				
Current [I]	Voltage [V]	Power [W]	Shunt voltage [mV]	Current [I]	Power [W]	Total current [I]	Electric power output [W]
8.07	12.05	97.20	2.84	9.47	114.07	17.54	211.32
16.14	12.21	196.20	1.20	4.01	48.92	20.15	245.99
29.30	11.98	350.00	3.99	13.30	159.33	42.60	510.35
33.80	11.85	400.00	5.45	18.17	215.28	51.97	615.81
16.10	12.30	200.00	0.20	0.67	8.20	16.77	206.23
21.42	12.12	261.00	1.41	4.70	56.96	26.12	316.57
12.39	12.59	155.70	1.04	3.46	43.52	15.85	199.51
16.26	12.36	200.10	0.27	0.90	11.12	17.16	212.10
18.30	12.50	222.00	0.88	2.93	36.67	21.23	265.42

## E.3 R1233zd(E) ORC Prototype System Performance

### Improvement Simulated Cases State Points' Properties

**Table E.13: First simulated case state points' properties.**

State point	Temperature [°C]	Pressure [bar]	Enthalpy [kJ/kg]	Entropy [kJ/kg-°C]
Evaporation	95.553	9.3809	462.33	1.7569
2	97.663	9.381	464.62	1.7631
3	58.721	2.147	443.06	1.7845
5	53.623	2.147	438.6	1.771
Condensation	39.88	2.1518	245.5	1.1549
7	39.674	2.147	245.26	1.1541
8	40.12	9.3809	245.99	1.1546
9	55.733	9.381	264.83	1.2132

**Table E.14: Second simulated case state points' properties.**

State point	Temperature [°C]	Pressure [bar]	Enthalpy [kJ/kg]	Entropy [kJ/kg-°C]
Evaporation	95.553	9.3809	462.33	1.7569
2	100.5486	9.381	467.7077	1.7714
3	60.3966	2.147	444.535	1.7889
5	39.88	2.147	420.3287	1.7336
Condensation	39.88	2.147	245.5	1.1549
7	34.88	2.147	239.5937	1.1359
8	35.3128	9.3809	240.3234	1.1363
9	55.4917	9.3809	264.5297	1.2123

**Table E.15: Third case and initial thermodynamic model state points' properties.**

State point	Temperature [°C]	Pressure [bar]	Enthalpy [kJ/kg]	Entropy [kJ/kg-°C]
Evaporation	114.3775	14	472.19	1.7636
2	119.3775	14	478.18	1.779
3	61.5167	1.8351	446.15	1.8032
5	35	1.8351	416.58	1.7322
Condensation	35	1.8351	239.73	1.1364
7	30	1.8351	233.88	1.1173
8	30.7051	14	235.09	1.1181
9	55.519	14	264.66	1.2116